Monolithic metal oxide thin-film transistors (TFTs) via photonic processing of sol-gel precursors

MATTHEW GEORGE SPINK

A thesis submitted in partial fulfilment of the requirements of Nottingham Trent University for the degree of Doctor of Philosophy

This research programme was carried out in collaboration with King Abdullah University of Science and Technology, Saudi Arabia and University of Ioannina, Greece

School of Science and Technology

Nottingham Trent University

March 2025

Copyright Statement

Abstract

The intrinsic limitations of traditional vacuum-based techniques and silicon electronics enforce restrictions that prevent the realisation for new device paradigms such as the Internet of Things. Large-area electronics aims to circumvent these roadblocks, using processes and techniques amenable to scalable, high throughput manufacturing with materials with mature properties. Photonic processing such as laser annealing has recently shown some promise utilising the electrical stability and versatility of metal oxides in solution processed forms. However, using photonic processing for solution processed materials effectively means further understanding of the photochemical conversion process, light-matter interactions as well as how this translates to electrical device performance. This work developed vital electrical devices for modern electronics (i.e. thin-film transistors and Schottky diodes) while investigating light-matter interactions via coupled self-consistent opto-thermal simulations. For the first time, opto-thermal simulations are used to determine the temperature rise in metal oxide thin films and solution precursors due to pulsed laser annealing (LA), with these temperature rises also correlated to electrical device performance. These opto-thermal simulations gave way to experimental parameters for investigating the photochemical conversion of metal oxide sol-gel dielectrics to thin films which would act as the base for TFTs. For the first time, Infra-Red Spectroscopic Ellipsometry (IRSE) with metallic substrates was employed for high sensitivity detection of chemical groups in sol-gel LA dielectrics. Finally, the developed sol-gel dielectric and opto-thermal simulations were combined to demonstrate the first fully sol-gel LA TFTs. In addition, laser processing was used as a novel patterning technique for developing nano-Schottky diodes with GHz operation.

Acknowledgments

Firstly, I would like to thank Dr Nikolaos Kalfagiannis and Dr Demosthenes Koutsogeorgis who have both been Director of Studies during this PhD. The wealth of support, guidance and patience has contributed to my growth as a researcher and having the tools to eventually obtain the position or job I desire. Nikos had the fun of dealing with all the teething issues that many experience during the PhD, as well as imparting the specialist knowledge for ellipsometry and the simulations that make half of these results. Demos then had to deal with the thesis and several personal circumstances that made the last couple of years a further challenge than anticipated, guiding me through the tumultuous process. Their inputs are greatly appreciated.

Of course, I would also like to thank the many collaborators during this project: Professor Thomas Anthopoulos, Dr Hendrik Faber and their associates at KAUST, Saudi Arabia for allowing me to work on a small part of their extremely promising adhesion lithography work, as well as Thomas being the PI and funder for my project. To Associate Professor Elefterios Lidorikis and his team at the University of Ioannina, Greece - for providing, troubleshooting and commenting on the outputs of the opto-thermal simulation code. The simulations were an enjoyable part of this project that allowed me to properly revisit some fundamental physics and made the last year of experiments possible (or at least less time consuming!). More locally, I would like to thank Associate Professor Chris Mellor from the University of Nottingham for allowing use of the NIR-VIS-UV ellipsometer, the measurements from which provided vital measurements for every chapter of this work.

I would also like to express gratitude to some specific people in iSMART and MTIF of past, present and future in no particular order. Dr Josh Barkby, Dr Gary Mudd, Dr Magda Patel, Elene Aberywickrama, Jorge Sacristan, Luke Blythe, Russell Metcalfe, Alex Webster and Ethan Phillips for your supporting roles in the group that helped to make the atmosphere what it was. Dr James Hillier, who was a kindred spirit in winding people up, making pop culture references and generally being completely ridiculous. Dr Jodie West, for being a great friend, confidant and guide since my MSci and during the PhD. Thomas Howe, for his joining me in being completely ludicrous and masking it by occasionally doing physics well. Also, along with Jodie, you were the weird metal people in the corner with me! Parvin Ebrahimi for our cathartic coffee sessions and your entertaining sassiness. I wish you the best for the rest of your PhD. Dr Domonic Craske (Dr Dom), not only for your assistance with microscopy (with a hefty dose of verbal abuse) but for your goodwill and humour. Maybe we'll actually go for a pint when I'm in Beeston sometime. Finally, to Dr Christina Koutsiaki, who has not only been a fellow iSMART group member, but

someone who I worked alongside for some time during this PhD. Most of all, she's been my best friend and confidant even after she left NTU. Here's to many years more friendship!

I need to show my gratitude to all my family and their continued patience with my moaning, perpetual ghost-like behaviour and silence. I mean, even more than usual. To Mum, for our regular chats, your unconditional love and for providing the means at the end of the PhD for me to focus and finish this thesis. To Dad, for your general support and regular visits. I may finally come down to clear my stuff out your garage! To my brother and sister-in-law, Dan and Sarah, for always offering an ear or refuge for the many downs of the last few years. To Anthony, for your support and whose interest and knowledge for the general background of my PhD was very up-to-date, leading to some great conversations. Bill and Lisa – hopefully I will make it out to Florida in the near future. Thank you for your support and interest in what I do. To Victoria, for checking on my wellbeing despite her own health being in a poor state. Finally, thanks to the rest of my family – Grandad, Jean and the cousins – who I hope to see more of now this is over.

I would be remiss to not remember Uncle David, Nanna and Grandma who passed during the duration of this PhD. You are all missed, and I would hope finally finishing this would have made you proud as you have been before with me. Finally, to the furrier, stubborn members of family that were Moo and Freckles. Thank you both for your mix of sassiness, indifference to my existence and ability to tolerate my bothersome self. I miss you both.

Finally, to Hannah Southern. Hannah, the list of things you have done for me and the memories we've created since we've been together just before the PhD started require their own chapter. Thank you for your support, encouraging my idiocy and for being the best person I know that continues to make me better. I love you.

List of Publications

1. **M. G. Spink**, D. C. Koutsogeorgis, N. Kalfagiannis – Fabrication of sol-gel, laser annealed ZrO_x dielectrics for capacitors and TFTs with physicochemical analysis via IRSE – In preparation.

2. H. Faber, L. Panagiotidis, **M. G. Spink,** D. C. Koutsogeorgis, N. Kalfagiannis, T. D. Anthopoulos – journal article on radio frequency nanogap Schottky diodes enabled by laser patterning and adhesion lithography - In preparation.

List of Conference Presentations

1. **M. G. Spink**, E. Lidorikis, T. D. Anthopoulos, D. C. Koutsogeorgis, N. Kalfagiannis - "Large-Scale Electronics Manufactured with Light". **A poster presentation at the 15th International Summer School on Nanotechnologies (ISSON21), 3rd-10th July, - (Thessaloniki, Greece).**

2. **M. G. Spink,** D. C. Koutsogeorgis, N. Kalfagiannis - "Metal oxide thin-film transistors via photonic processing of sol-gel precursors". – **An oral presentation at School of Science and Technology 15th Annual Research (STAR) Conference, 15-16th June 2022 (Nottingham Trent University, Nottingham – UK)**

3. **M. G. Spink**, D. C. Koutsogeorgis, N. Kalfagiannis "Solution processed and laser annealed ZrO_2 and Al_2O_3-based capacitors for implementation into TFT devices". – **An oral presentation at the 19th International Conference on Nanosciences and Nanotechnologies (NN22), 5th-8th July 2022 – (Thessaloniki, Greece)**

4. **M. G. Spink**, C. Koutsiaki, D. C. Koutsogeorgis, N. Kalfagiannis – "Fully solution-processed metal oxide TFTs on Si via laser annealing". **An oral presentation at 8th International Symposium on Transparent Conductive Materials & 12th International Symposium on Transparent Oxide and Related Materials for Electronics and Optics (TCM-TOEO2022), 16th-21st October 2022 – (Crete, Greece)**

5. **M. G. Spink**, D. C. Koutsogeorgis, N. Kalfagiannis – "Laser annealing and Infra-Red Spectroscopic Ellipsometry: Promising Alternatives for manufacturing and quality control for LAE". **An oral presentation at the 10th Innovations in Large-Area Electronics Conference (innoLAE 2024), 20th-22nd February – (Cambridge, UK)**

Table of Contents

List of Symbols

λ	Wavelength	$I(\delta)$	Wave intensity after propagation
k	Critical dimension coefficient	I_0	Original wave intensity
Ga	Gallium	δ	Depth
Ge	Germanium	δ_p	Penetration depth
Si	Silicon	$\Xi(t)$	External electric field/electromagnetic plane wave
μ	Carrier mobility	m	Mass
eV	Electron volt	γ	Damping constant
MoS_2	Molybdenum sulphide	$r(t)$	Electron displacement
WS_2	Tungsten sulphide	e	Electron charge
$M-O$	Metal-oxide bond	m_e^*	Electron effective mass
ZrO_x	Zirconium oxide (non-stochiometric)	K	Spring constant
InO_x	Indium oxide (non-stoichiometric)	ω_0	Oscillator frequency
AlO_x	Aluminium oxide	χ_e	Electron susceptibility
$\mathbf{D}$	Electric displacement	N_L	Number of Lorentz oscillators per unit volume
$\mathbf{B}$	Magnetic induction	$P_b(\omega)$	Background electric displacement
$\boldsymbol{\Xi}$	Electric field	ε_∞	High frequency permittivity
$\mathbf{H}$	Magnetic field	A_L	Oscillator amplitude
q	Charge	SiO_2	Silicon dioxide
$\mathbf{j}$	Current density	d_{H_ik}	Thickness of oxide dielectric
$\mathbf{r}$	Spatial vector	k_{SiO_2}	Dielectric constant of silicon dioxide
t	Time	k_{H_ik}	Dielectric constant of oxide
ε_0	Permittivity of free space	E_G	Bandgap
$\mathbf{P}$	Electric polarisation	Ta_2O_5	Tantalum pentoxide
$\mathbf{M}$	Magnetisation	Y_2O_3	Yttrium oxide
μ_0	Permeability of free space	HfO_2	Hafnium oxide
$\mathbf{k}$	Wavevector	ZrO_2	Zirconium oxide (stoichiometric)
ω	Angular frequency	Al_2O_3	Aluminium oxide (stoichiometric)
ε_r/k	Relative permittivity/dielectric constant	MO_x	Metal oxide film (non-stoichiometric)
μ_r	Relative permeability	N	Carrier concentration
c	Speed of light	In_2O_3	Indium oxide (stoichiometric)
σ	Conductivity	ZnO	Zinc oxide
$\tilde{\varepsilon}(\omega)$	Complex permittivity	SnO_2	Tin oxide
$\varepsilon_1(\omega)$	Real permittivity	NiO	Nickel oxide
$\varepsilon_2(\omega)$	Imaginary permittivity	Cu_2O	Copper oxide
$\boldsymbol{\Xi}_o$	Electric field amplitude	$SrCu_2O_2$	Strontium copper oxide

$\mathbf{H}_o$	Magnetic field amplitude	$CuAlO_2$	Copper aluminium oxide
$\tilde{\mathbf{k}}$	Complex wavevector	n	Principal quantum number
$\underline{\hat{\mathbf{e}}}$	Real unit vector	E_F	Fermi level
$\tilde{n}(\omega)$	Complex refractive index	R	Alkyl group
$n(\omega)$	Refractive index	$M(NO_3)_x$	General nitrate formula
$\kappa(\omega)$	Extinction coefficient	$M(CH_3COO)_x$	General acetate formula
$v(\omega)$	Phase velocity	$M(ClO_y)_x$	General chlorate formula
$\alpha(\omega)$	Absorption coefficient	$In(NO_3)_3$	Indium nitrate
$M-O-M$	Metal-oxide-metal network	υ_d	Electron drift velocity
Φ_M	Work function of metal	μ_n	Carrier mobility in the channel
E_C	Energy to release metal from conduction band	$V(x)$	Channel voltage at distance x
E_0	Vacuum energy	$I_{DS,sat}$	Saturation current
Φ_S	Work function of semiconductor	μ_{lin}	Linear mobility
$E_{F,M}$	Fermi level of metal	μ_{sat}	Saturation mobility
χ_{ox}	Oxide electron affinity	$I_{On/Off}$	On-off current ratio
χ_S	Semiconductor electron affinity	SS	Subthreshold swing
$E_{F,S}$	Semiconductor Fermi level	V_{on}	On-voltage
E_I	Energy level of intrinsic semiconductor	Fe	Iron
E_V	Energy level of valence band	PbS	Lead sulphide
V_G	Gate voltage	Φ_B	Schottky barrier height
Q	Electron density in semiconductor	I_o	Reverse bias saturation current
n_e	Density of electrons	n	Diode ideality factor
k	Boltzmann constant	S	Diode area
φ_S	Semiconductor surface potential	A^*	Effective Richardson constant
$\Delta\varphi_{ox}$	Potential drop across oxide layer	R_S	Series resistance
$\xi(x)$	Electric field in depletion region	Φ_{B0}	Apparent barrier height
N_D	Concentration of semiconductor dopants	Φ_{BFB}	Flat-band barrier height
ϵ_S	Dielectric permittivity of semiconductor	N_C	Density of states in the conduction band
x_d	Depletion region length	V_{Bi}	Built-in voltage
$\varphi(x)$	Potential across semiconductor	$N_{A/D}$	Dopants of materials in accumulation region
ξ_{ox}	Electric field across oxide	N_{CB}	Effective density of states
t_{ox}	Thickness of oxide	h	Planck's Constant
ϵ_{ox}	Oxide dielectric constant	$I_F(V)$	Diode forward current
C_{ox}	Parallel plate capacitance per unit area of oxide layer	$I_R(V)$	Diode reverse current
V_{TO}	Threshold voltage	$f_{c,int}$	Intrinsic frequency
φ_{ms}	Metal-semiconductor correction	$f_{c,ext}$	Extrinsic frequency
V_{FB}	Flat-band voltage factor	R_b	Barrier resistance
Q_{SS}	Surface charge density of dielectric	C_j	Metal-semiconductor junction capacitance

Q_i	Surface charge density due to semiconductor implant dopants	X_C	Reactance associated with junction capacitance
V_{th}	(Corrected) threshold voltage	V_{in}	Input voltage
Q_{inv}	Inversion charge density	V_{Out}	Output voltage
V_{DS}	Source-drain voltage	h_f	Spin-coated film thickness
I_{DS}	Source-drain current	h	Thickness of solution layer
V_{SB}	Source-to-substrate bias	ρ	Density of solution
V_{GS}	Source-gate voltage	η	Viscosity of solution
L	Channel length	t	Rotating time
W	Channel width	h_0	Thickness of film at $t = 0$
q_{ch}	Total charge per channel area	E_{evap}	Solvent evaporation rate of solvent per unit area
τ_{DS}	Average time for carrier to accelerate from source to drain	C	Volume fraction of solute in film
C_0	Initial solution concentration	c_p^f	Latent heat of fusion
Au	Gold	T_m	Melting point
E_M	Monitor laser energy	$\Psi\,(E)$	Ellipsometry angle related to amplitude
J_L	Target laser fluence	$\Delta\,(E)$	Ellipsometry angle related to phase
E_L	Target laser energy	r_p	Fresnel reflection coefficient of p-polarised light
$E_{M,Desired}$	Desired monitor laser energy	r_s	Fresnel reflection coefficient of s-polarised light
$J_{L,Desired}$	Desired laser fluence	N	Modulated ellipsometry function
$E_{M,Actual}$	Actual monitor energy	C	Modulated ellipsometry function
$J_{L,Actual}$	Actual laser fluence	S	Modulated ellipsometry function
$Nd:YVO_4$	Vanadate	$< \tilde{\varepsilon}(E,\theta) >$	Pseudo-permittivity
M^2	Laser beam quality number	$\tilde{\varepsilon}_{Gaussian}(E)$	Complex permittivity of Gaussian oscillator
r	Reflected amplitude	A_n	Peak amplitude for oscillator
t	Transmitted amplitude	En	Peak central energy
$I_{\tilde{n}_{Sub}\tilde{n}_f}$	Interface matrix from film to substrate	Γ	Kramers-Kronig consistency term
$P_{\tilde{n}_f l_{tot}}$	Propagation matrix in the films	Br_n	Oscillator broadening at FWHM
$I_{\tilde{n}_f n_a}$	Interface matrix from air to film	σ_n	Gaussian oscillator function
M	Transfer matrix	m	Number of fitting parameters
n_a	Refractive index of air	SiC	Silicon carbide
$\tilde{n}_f$	Effective refractive index of film	θ	Measuring angle for ellipsometry
$\tilde{n}_{sub}$	Refractive index of the substrate	$T(E)$	Frequency-dependent transmittance
k_f	Wave vector in the film	$r_F(E)$	Fresnel reflection coefficient

d_{tot}	Total thickness	$t_F(E)$	Fresnel transmission coefficient
P_i	Propagation matrix	$\tilde{\varepsilon}_i(E)$	Complex permittivity of material before interface (incidence)
$I_{i,i+1}$	Interface matrix	$\tilde{\varepsilon}_t(E)$	Complex permittivity of material after interface (transmitted)
E_f	Electric field forward reflection	$k_i(E)$	Wavevector of incident wave
E_b	Electric field backward reflection	$k_t(E)$	Wavevector of transmitted wave
$F(x)$	Forward wave	θ_i	Angle of incidence
$B(x)$	Backward wave	θ_t	Angle of refraction
x_s	Distance from film-substrate interface	θ_r	Angle of reflection
k_s	Wave vector in the substrate	$R(E)$	Frequency dependent reflectance
S	Poynting vector	ξ_n^+	Electric vector of wave in the direction of incidence
$I(x)$	Electromagnetic flux	ξ_n^-	Electric vector of wave opposite to direction of incidence
Δx	Discrete increment of computational grids	$I_L(E)$	Spectral light intensity of the lamp
$A(x)$	Absorption per increment	$I_D(E)$	Dark intensity
c_p	Specific heat capacity	$I_s(E)$	Reflective light intensity of sample
ρ_m	Mass density	$R_{th}(E)$	Theoretical reflectivity of mirror
$T(x,t)$	Local temperature transient	R_a	Arithmetic roughness
k	Thermal conductivity	R_q	Root-mean-square roughness
$\dot{q}$	Time dependent thermal load due to light absorption	Z_{range}	Difference of maximum and minimum vertical AFM distances
a, b, c	Thermal property fitting parameters	C_i	Areal capacitance
		A	Surface area of electrodes
		d	Thickness

List of Abbreviations

2-ME	2-methoxyethanol	M1	Metal 1
AC	Alternating current	M2	Metal 2
AFM	Atomic force microscopy	MEA	Monoethanolamine
ALD	Atomic layer deposition	MO	Metal oxide
a-lith	Adhesion lithography	MOS	Metal oxide semiconductor
BGTC	Bottom gate top contact	MOS capacitor	Metal oxide semiconductor capacitor
CAD	Computer aided design	MOSFET	Metal oxide semiconductor field effect transistor
CB	Conduction band	MSE	Mean squared error
CBM	Conduction band minimum	NA	Numerical aperture
CCD	Charge-coupled device	NFC	Near field communication
CD	Critical dimension	NIR	Near infrared
CMOS	Complementary metal oxide semiconductor	NTU	Nottingham Trent University
C-V	Capacitance-voltage	ODPA	Octadecylphosphonic acid
CVD	Chemical vapour deposition	ORS	Optical reflectance spectroscopy
D	Drain	PECVD	Plasma enhanced chemical vapour deposition
DC	Direct current	PET	Polyethylene terephthalate
DI	Deionised (water)	PI	Polyimide
DPSS	Diode pumped solid state	PLD	Pulsed laser deposition
DUT	Device under test	PTFE	Polytetrafluroethylene
DUV	Deep ultraviolet	R2R	Roll-to-roll
EFM	Electrostatic force microscopy	RCE	Rotating compensator element
EMA	Effective medium approximation	ReLA	Reactive environment laser annealing
EOT	Equivalent oxide thickness	RF	Radio frequency
EUV	Extreme ultraviolet	RFID	Radio frequency identification tag
FET	Field effect transistor	RH	Relative humidity
FLA	Flash lamp annealing	RO	Research objective
FTIR	Fourier transform infrared	RPM	Revolutions per minute
FWHM	Full width half maximum	RTA	Reflection-transmission-absorption
G	Gate	S	Source
GSG	Ground-signal-ground	S2S	Sheet-to-sheet
IC	Integrated circuit	SAM	Self-assembled monolayer
IGZO	Indium gallium zinc oxide	SE	Spectroscopic ellipsometry

IIS	Ionised impurity scattering	SMU	Source measuring unit
IoT	Internet of Things	TA	Thermal annealing
IPA	Isopropanol	TE	Transverse electric
IRSE	Infrared spectroscopic ellipsometry	TFT	Thin-film transistor
IRT	Infrared transmission	TGBC	Top gate bottom contact
iSMART	Innovation in Surface Materials and Related Technologies	TM	Transverse magnetic
ITO	Indium tin oxide	UoI	University of Ioannina
I-V	Current-voltage	UV	Ultraviolet
IZO	Indium zinc oxide	VASE	Variable angle spectroscopic ellipsometry
KAUST	King Abdullah University of Science and Technology	VB	Valence band
KrF	Krypton Fluoride	VBM	Valence band minimum
LA	Laser annealing	VIS	Visible
LAE	Large area electronics	VNA	Vector network analyser
LEV	Local Exhaust Ventilation	XPS	X-ray photoelectron spectroscopy

1. Introduction and Motivation

The unprecedented development of technology critical to everyday modern life is running into roadblocks due to economic and technological constraints, threatening the further advancement of key electronics elements. Applications such as displays [1], memory devices [2], and sensors [3] are reliant on ubiquitous components in integrated circuits (ICs) including thin-film transistors (TFTs) [4], diodes [5] and photovoltaics [6], [7]. The current pathway aims to bring these applications together into a perpetually data communicating network as the Internet of Things (IoT) [8], which has spurred several new areas of interest to do so. For 60 years, silicon (Si) has been used as the active material. While some paradigms like extreme ultraviolet lithography (EUV) allow the performance demand to be met, the ever-decreasing node level is reaching its material limit at great economic cost. Alternative materials including metal oxides (MOs) are increasingly adopted instead of Si due to their optical transparency, electrical properties and processing versatility, including in completely diverging disruptive pathways such as large-area electronics (LAE) that utilise roll-to-roll (R2R) lines with flexible substrates to produce abovementioned technologies [9], [10], [11] at a fraction of the cost. Solution processing has gone hand-in-hand with this exhaustive material and methodologies research due to its potential for high throughput manufacturing at atmospheric conditions [12]. However, solution processed MOs typically require a high temperature, longer duration thermal annealing (TA) step to achieve their desirable properties. As well as being undesirable for manufacturing process flows, the implementation of flexible substrates with typically lower melting temperatures becomes near impossible. Laser annealing (LA) has been suggested as a superior alternative to TA. The absorption of photons with near-singular energies into MOs thin film precursors causes a localised high temperature rise in the targeted material, with a low thermal budget for the substrate that makes LA amenable to flexible substrates. This comes with the potential to achieve properties rivalling or exceeding their TA counterparts. However, the theoretical understanding for photochemical conversion is not well known yet, along with experimental parameters needing to be tuned for optimal results.

The research presented in this PhD thesis investigates the photochemical conversion mechanism of MO sol-gel thin films via LA, uses the knowledge to develop functional thin films for integration into TFTs and metal oxide capacitor devices and also links the LA-induced temperature rise to electrical characteristics with aid from a theoretical model in simulations. Additionally, laser processing is used as a material patterning methodology in tandem with sol-gel semiconductor layers to produce nano-Schottky diodes with radio frequency operation.

1.1 Motivation and Challenges

The semiconductor and microchip sectors have been in a dynamic and disruptive state in the last few years [13], with nations seeking to bolster their own strategic assets for semiconductor manufacturing for automotive industries, defence systems and data storage as well as a broad range of electronic applications. The tendency of industries both young and old building a reliance on semiconductors and chips became evident during the COVID pandemic and several accidents parallel to the pandemic timeline, leading to large-scale disorder. Factories were shuttered due to COVID induced lockdowns [14] while demand for work-from-home facilities (PCs, laptops) sharply rose [15], meaning demand for all industries could not be met. The inability to meet demand was severely hampered in 2021 by an earthquake and fire (separate occasions) in the Renesas Electronics factory in Japan [16], [17] specialising in automotive and microcontrollers, winter storms across Texas that hindered production by NXP [18], Samsung and Infineon [19] and extended lockdowns in Malaysia where chip assembly takes place [20]. TSMC – the global semiconductor leader responsible for an incredible proportion of the world's most advanced logic chips [21] – experienced Taiwan's worst draught in 50 years, halting production as the ultra-pure water used for manufacturing was unavailable [22]. The lithography scanner company ASML experienced a fire in their Berlin factory in 2022, preventing distribution of extreme ultraviolet (EUV) lithography machines used in all of the most advanced chips [23].

Social, geopolitical and economic elements further contributed toward the chip shortage. During the COVID pandemic, China and the US became entangled in a trade war revolving around restriction of each other's chip manufacturer's operating in each other's countries. US imposing the necessity of trade licenses for export of software and advanced chips to China [24] led to the vitriolic response of placing an embargo on Gallium and Germanium shipments [25], who's use in the semiconductor sector is prevalent. For perspective, in 2022 around 90 % of global supply for Ga and 60 % of Ge originated from China [26]. The Russia-Ukraine war and various allegiances with each side has heavily reduced distribution of key gases (particularly noble gases) [27] for wide use in the semiconductor industry including use in lasers that are commonplace for lithography, marking and processing. The cross-strait political tension between China and Taiwan [28] prospectively acts as a further issue, where war or political turmoil would globally disrupt chip supply chains. Several countries sit on fault lines where earthquakes and further natural disasters are commonplace. In essence, a domino effect from a myriad of sources disrupted the global supply chain to an extent could not be overlooked nor predicted. The advent of AI, particularly generative AI such as ChatGPT, is the most recent

technological progression that has pushed this demand over the edge and caused a power sway in the key players in the semiconductor industry.

In all chains of events in the above of past, present and future, critical issues are persistent: despite globalisation, there is reliance on a few certain companies that utilise only a few materials that are in shortage. This has led to unprecedented levels of funding via the Europeans Chips Act 2023 [29] and US CHIPS and Science Act 2022 [30] for $€43\ \text{billion}$ and $\$52.7\ \text{billion}$, respectively. Principally, the funding seeks to establish technological sovereignty in their respective unions to reduce dependency on select countries and firms for chips, via investment in next generation technologies, the companies (start-ups to large established companies) and their networks. The problem with this is the investment in foundries that utilise the traditional silicon electronics. Maintaining the current pathways and implementing new paradigms faces technological barriers and huge capital cost, all in the name of fulfilling the industry goalpost of Moore's Law [31] via miniaturisation of the integrated circuits (ICs) components of transistors, capacitors, resistors and diodes. In particular, thin-film transistors (TFTs) and metal oxide semiconductor field effect transistors (MOSFETs) devices used for electronic circuit switching and amplification, found in the backplanes of optical displays for example, radically transformed electronics after their discovery and are responsible for the investment and ambition to maximise their performance and advance the rest of modern technology manufacturing. As demonstrated by Dennard [32], the downscaling of MOSFETs for many years held very few to no compromises when it comes to performance but only to a certain extent. The new archetype, detailed by the roadmap from world-leading semiconductor research institute IMEC [33], seeks to establish sub $-1\ \text{nm}$ process nodes via novel Gate All Around nanosheets and Complementary FET transistors from 2030 onwards. These unfathomable extremes are only achieved via high numerical aperture (High-NA) EUV [34] which the company ASML has monopolised especially in the last few years. This orbits back to the original problem to the reliance on select few companies. Furthermore, photolithography has an intrinsic problem with producing perpetually shrinking feature sizes that is best illustrated by the Rayleigh criterion describing the resolution limit [35]:

$$\text{CD} = \frac{\text{k}\lambda}{\text{NA}} \tag{1.1}$$

where CD is the critical dimension (smallest possible feature size), k is a coefficient relating to several factors of the chip manufacturing process, λ is the wavelength of the light source and NA is the numerical aperture of the optics, a number that describes the ability for optics in a photolithography system to collect and focus light to print a pattern on a chip. Increasing

resolution (lower value of CD) relies on lowering λ or increasing NA. k has a physical limit of 0.25, which can be pushed via refinement of the lithography process and computational lithography [36]. λ has already seen its lowest values yet for chips in active production - Samsung in collaboration with TSMC adopted an extreme UV (EUV) photolithography system from ASML, using a $13.5\ \mathrm{nm}$ plasma source [37]. Achieving this was via the very unconventional route of using a laser on liquid Sn droplets to vaporise them and induce a plasma that emits EUV light [38]. However, all materials have strong absorption into the UV, thus additional coatings, photoresists and modifications to lithography equipment and optics are required. This leads to a vicious circle of higher cost, lower throughput and highly complex methodologies. These electronics can also only operate on a wafer scale, typically employing large $300\ \mathrm{mm}$ wafers. This may be sufficient for chips in mobile phones or small devices assembled elsewhere, but area-intensive applications such as solar cells, displays, and radio frequency applications suffer in throughput via these traditional methods. For some, the imminent end of Moore's Law has led to skyrocketing prices and alternative routes, with some leading companies already declaring Moore's Law dead [39].

The necessity to find diverging pathways from the current standard facilitating new, emerging or future technologies that become integrated into the growing Internet of Things (IoT) ecosystem has created a new industry pathway known as large-area electronics (LAE). Utilising high-throughput fabrication routes on roll to roll (R2R), sheet-to-sheet (S2S) with large-area flexible, lightweight substrates without the bottleneck of vacuum-based processing techniques and advantageous optoelectronic materials potentially relieves the demand of these conventional methods and meets the quantity demand of modern consumers. Furthermore, the inherent nature of flexible substrates results in the use of foils, plastics and papers that are recyclable [40]. Sustainability and green technologies have become a focal point to mitigate the effects of chip manufacturing on climate change [41], [42], reusing the substrates and extracting critical raw materials of the thin films to prevent wastage. LAE is far more inclined to this approach. However, the rollout of LAE faces technical challenges in several facets including the lab-to-fab scale-up of production, optimisation of materials (which is discussed further down) and the thermal budget. The component of thermal budget is particularly unique and critical to LAE, since plastic flexible substrates markedly degrade with temperature and compromise the electrical device. Certain thermoplastics such as polyimide counteracts this somewhat, but depending on the material far higher temperatures above its melting point are still readily researched and materials cannot be extracted and recycled to the same capability as other plastics [43]. This recycling issue scratches the surface of green technologies and making the IC and chip industry cleaner, whose output of $\mathrm{CO_2}$ exceeds $900\ \mathrm{Mt}$ [44].

Aside from the limitations currently faced by LAE overall, the dichotomy of material selection must be considered. Amorphous Si (a − Si) commonly used for low cost and scalable applications lacks the necessary performance (charge carrier mobility) to be viable for traditional or LAE methodologies and faces pushing past its critical dimensions to do so with huge economical drawbacks. Consequently, several alternative materials have exploded into prominence in recent years to meet the demands of the state-of-the-art. Table 1.1 gives examples of some of the more commonly appearing material classes, with comparisons of mobility and opto-electronic properties. Note these are overarching summaries of the material properties in the literature and that exceptions do occur. An example is graphene, where the hurdle of deposition has been overcome by the UK company Paragraf to produce wafer-scale graphene [45].

Table 1.1. Comparison of different opto-electronic material types and their typical enabling physical and electronic properties. The large variation in values for some properties is attributed to different deposition techniques.

Material	Deposition Techniques	Bandgap (eV)	μ (cm^2/Vs)	Spatial Uniformity	Electrical Stability	Ref
a-**Si**	PECVD	1.1	$0.1 - 1$	High	Low	[46]
nano-**Si**			10	Medium	Medium	
Poly-**Si**	High temp annealing.		100	Low	High	
Metal Oxides	Sputtering, PLD, thermal evaporation, spin-coating, printing.	$2.0 - 4.5$	$0.01 - 100$	High	High	[47]
Organics	Spin-coating, printing.	$1.5 - 4.0$	$10^{-4} - 10$	Low	Low	[48], [49]
Carbon nanotubes	CVD, spin-coating.	1.0	$0.1 - 10^4$	Low	Low	[50]
Graphene	Exfoliation, CVD, spin-coating, printing.	≈ 0	$0.1 - 10^4$	Low	Med	[51]
MoS_2/WS_2	Exfoliation, CVD, spin-coating, printing.	$1.3 - 1.8$	$1 - 100$	Low	High	[52]

Out of all the emerging materials, metal oxides (MOs) [53] have demonstrated they are amongst the most promising due to their combination of optical transparency, outstanding electrical performance (with mobilities rivalling poly-Si) and electrical stability. This is already evident via their integration into TFTs [54]. Their adaptability to a gamut of deposition and processing methodologies combined with their performance mean exploitation of semiconductors in shortage can potentially be reduced, with MO technologies being fabricated

at a fraction of the cost and complexity while exploring new possibilities [55]. This includes solution processing, which is lucrative due to assembly at atmospheric pressures, lower raw material costs, adaptable chemistry and formatting to printing for LAE. The sol-gel process is such an example of a solution process, dissolving solid precursor salts within a solvent to form a solution (sol) that is deposited onto the target substrate and dried to form the thin film (gel). Solution processed MOs within LAE theoretically alleviates the strain currently plaguing the semiconductor industry, but this revolutionary change is yet to surface since the electrical properties of as-deposited solution processed materials tend to be inferior for their desired application to those of their vacuum-processed counterparts, unless they are further processed with high temperature thermal annealing (TA) of $300℃$ or more at long dwell times ($> 1\ \mathrm{hr}$). The TA process densifies and condenses the film, altering the crystal structure, chemical homogeneity and stoichiometry to a required state. This contradiction of reliance on high temperature to the original purpose of implementing MOs in LAE (and in place of Si) restricts substrate materials due to the undesirable increase in thermal budget and increases process cost.

To circumvent this issue, interjections at each possible stage of the fabrication have been made including trialling a variety of precursors or chemical pathways in the sol-gel route (and other solution processes) [56] and post-deposition processing steps such as microwave annealing or plasma treatments [57], [58], [59]. Different families of precursor salts such as nitrates, acetylacetonates and perchlorates each have corresponding chemical pathways towards an $\mathrm{M-O}$ network for thin film formation, occurring at different temperatures and atmospheric conditions, thus alternative routes may yield lower temperature due to the decomposed products having increased volatility. Work has been conducted to clarify the chemical composition of MO thin films and understand how they evolve with temperature via the characterisation stalwarts of Fourier transform infrared spectrometry (FTIR) and X-ray photoelectron spectroscopy (XPS). Despite these endeavours and progress, solution processed MOs have fallen short of performance and stability requirements for functional applications. Analogous to vacuum-process techniques and the current conventional techniques, these instruments have provided invaluable input but are not compatible with LAE and the ultra-low scales of the future. On one hand, XPS operates with sufficient sensitivity albeit at ultra-high vacuum and is invasive to chemical species due to standard approaches of Argon etching. Thus, only a single product can be analysed as the sample is irreversibly modified. FTIR is non-invasive and covers the spectral range of organometallic building blocks for many MO precursors but lacks the sensitivity to analyse thin films of $10\ \mathrm{nm}$ such as those of semiconductors in TFTs. For a ubiquitous characterisation technique that detects chemical species from solution deposition

to thin film formation, on a lab scale or via in-line monitoring of a high throughput R2R production line [60], a non-invasive and highly sensitive technique operating at atmospheric conditions is essential.

From this overview of the semiconductor sector and possible routes of progression, there are three challenges identified that epitomise why sol-gel MO thin films are not massively prolific:

1) Lack of widespread alternative and fast post-deposition processing techniques that sufficiently elevate the temperature of the MO sol-gel precursor while leaving the substrate macroscopically cold.
2) Absence of knowledge on MO sol-gel precursor conversion mechanism including the use of a universal technique with sufficient sensitivity for low scale electronics and fitting to a LAE production line.
3) Patterning techniques that fit to high throughput manufacturing protocols, removing the necessity for masks and vacuum-based technologies.

For the processing route instead of TA, photonic processing has already demonstrated successful fabrication via deep ultra-violet (DUV) lamp irradiation, flash lamp annealing (FLA) and laser annealing (LA) [61]. The use of short, high intensity pulses that are absorbed into a thin film or precursor raises the temperature in the material nearly instantaneously, with the short irradiation time and thermal mismatch between thin film and substrate ensuring low thermal budget for the substrate. LA is accompanied by other benefits including highly specific area selectivity, the lack of necessity for a patterning mask and shorter exposure time compared to DUV and FLA. This selective energy delivery to the target material allows for controlled temperature elevation in the target material to a desired penetration depth to reduce substrate temperature load.

Recent work [61], [62], [63], [64] has begun to demonstrate the capabilities and novelty of LA for sol-gel MO thin films , but detailed understanding of how to precisely control the optical and electrical properties of the thin films, the physicochemical phenomena during precursor decomposition and thermally induced photochemical conversion mechanisms are elusive. Only by deconvoluting the MO sol-gel precursor conversion mechanism can these thin films begin to reach their vast expectations. This entails both theoretical and experimental routes. IRSE can act as a self-referencing technique with high sensitivity in the IR regions where chemical building blocks of organometallic precursors reside, giving way to detail about the optoelectronic properties, composition and structure of the sol-gel thin films. Concurrently, the temperature rises based on the precursor opto-thermal and electronic properties can be modelled and linked

to these changes during precursor decomposition. This step may establish IRSE as an in-line quality control tool for LAE production lines.

While the development of materials to substitute Si can be solved via sol-gel MO layers and LA, the quandary of ever diminishing feature sizes and reliance on photolithography to achieve these features reliably while patterning samples remains. While these techniques continue to prove their competence, their application can only take place on Si-based platforms and not LAE platforms. Thus, a different patterning or lithography technique must be employed. Due to the development of the adhesion lithography (a-lith) methodology [65], nanogap electrodes have exploded recently, demonstrating their abilities in several different electronic devices including transistors and diodes. In short, a-lith uses adaptability of surface chemistries of two different conductive materials (i.e. the electrodes) to selectively remove areas of the conductive materials leaving a nanogap between them, providing co-planar electrodes composed of two different materials. Subsequent materials are then deposited and photonically processed to complete the device in question (e.g. a sol-gel MO semiconductor directly on top to form a nano Schottky diode). Further detail is given in subsequent chapters on the a-lith methodology. However, the patterning of the first metal has still been reliant on standard photolithography, thus a maskless technique to pattern it with minimal distraction to the substrate is required. Patterning with a laser source offers a suitable alternative, as a monochromatic (uniform energy) source with highly flexible parameterisation and area selectivity can ablate the metal on the substate in any desired pattern while leaving the substrate surface without excessive roughness that inhibits the a-lith methodology. As with LA, realising this concept depends on the parameter optimisation and linking the effect on the ablation quality with the change in a laser parameter.

1.2 Novelty and Impact

The work presented in this thesis is novel on several fronts. Firstly, the use of nanosecond pulse duration LA for fabricating sol-gel MO thin films for TFTs and capacitors is a novel processing methodology amenable to scalable electronics. The use of LA to efficiently convert the sol-gel MO precursor to a thin film also lowers the substrate thermal budget, expanding the palette to flexible polymer substrates that are commonly used in LAE, thus constituting a methodology that uniquely increases the scalability and throughput. In this thesis, this is demonstrated on ZrO_x for the first time and with the fabrication of TFTs composed of sol-gel MO dielectrics and sol-gel InO_x semiconductor (also for the first time), building on previous demonstration of this technique [62], [63], [64].

Adding further to these exhibitions of the new materials and devices fabricated is the theoretical modelling of LA induced temperature rises through developing a universal modelling tool, contributing to the understanding of photochemical conversion. The combination of optical behaviour of the system coupled to the thermal properties of the system, while accounting for the pulsed laser spectral and temporal profiles, thermal non-linearities and phase changes of the material system with different thermodynamic boundaries is absent from the literature. This is advanced further when it is applied to sol-gel materials, whose temperature changes and volatility underline the chemical pathway and the thin films formed. Effective utilisation of the opto-thermal simulations when combined with experimental results will allow further optimisation of deposition and LA processing parameters for tuning the material properties and build new understanding of the effect of LA on precursor conversion to functional thin films. As part of the experimental work to reinforce this, InfraRed Spectroscopic Ellipsometry (IRSE) is used to investigate the chemical composition of thin films processed with LA at different fluences and reinforces its prospects as a highly sensitive, non-invasive characterisation technique to study the properties of sol-gel, MO thin films. The foundations of this were previously laid at NTU recently [66].

Finally, the adoption of laser patterning for the a-lith process is innovative and fixes a crucial missing piece in the puzzle. The a-lith methodology has already demonstrated rapid progression in its range of applications and competence within them on Si and flexible substrates, with laser processing replacing the role of photolithography. Additionally, laser patterning benefits from the removal of masks to pattern the sample, replacing it with ultra—fast processing capable of high throughput manufacturing. Overall, the implementation of the characterisation and processing methodologies can drive innovation of photonic processing-based electronics, further increase their adoption and bolster the understanding of MO, sol-gel fabrication.

1.3 Research aim and objectives

The overarching aim of this project was to generate new knowledge in light-matter interactions to efficiently convert and process MO precursors to sequentially stacked thin films for fabricating high performance, state-of-the-art TFTs on large-area flexible substrates. By combining extensive experimental techniques with a comprehensive theoretical modelling platform, electronic and photonic technologies are created. To work towards this aim, three distinctive research objectives (ROs) were decided.

- **RO1:** Develop LA processing protocols for growth and patterning of sol-gel MO precursors to produce conductors, semiconductors and dielectrics. This accesses vital

information on the applicability and limitations of LA for processing sol-gel MO precursors.

- **RO2:** Gain knowledge on the light-matter interactions which are critical for efficient photochemical conversion of precursor material to its targeted stoichiometric state. Linking their understanding to performance of material and devices and associated LA protocols will enable improved precursors and allow better conversion control.
- **RO3:** Utilise cultivated results on LA parameterisation for best performing material systems to develop and demonstrate prototype MO-based electronic devices. The development of fully sol-gel, LA TFTs using MOs demonstrates the utilisation of the cultivated knowledge of RO1 and RO2 for proof-of-concept, novel technologies.

1.4 Methodology Overview

In this work, solution processing via spin-coating and post-deposition processing via LA are primarily used as the experimental techniques for fabricating sol-gel MO thin films. A solution is prepared with a known concentration of solute (precursor salt) diluted appropriately in a solvent, with the concentration partially dictating the thickness of the resultant thin film. This solution is dispensed on a cleaned substrate surface (e.g. Si wafer) via spin-coating with a given spinning speed and time duration. The control over deposition variables makes spin-coating an ideal choice for lab-scale (research) fabrication. The MO sol-gel precursor spin-coating and solvent removal – during the spin-coating, evaporation and post-deposition thermal stabilisation – causes gel solidification that forms a uniform thin film.

As previously discussed, conventional TA processes at a minimum of $300℃$ are normally used for post-deposition processing of the MO precursors to promote higher electrical performance via conversion into MO thin films. Due to TA processing having long dwell times, high thermal budget and incompatibility with flexible substrates (thus low throughput), LA was implemented as the main processing technique (though TA samples were produced as a reference). The flexibility of LA parameterisation, combined with the localised heat transfer from photon transfer in a highly precise manner at ultra-short pulse durations, promotes the possibility of high-speed processing with no limitation on substrate. LA was performed in atmospheric conditions, with experimental parameters of fluence (energy per unit area) and number of pulses systematically varied to investigate and optimise the changes in sol-gel, MO precursor conversion.

To inform the parameters of the LA experiments, investigate temperature rises of the thin films during LA and address the thermal budget of the substrate during processing, a modelling and optimisation platform was developed and run in tandem. The model uses coupled,

self-consistent opto-thermal simulations that account for material optical and thermal properties (and their non-linearities), laser spatial and temporal profiles, phase changes and thermodynamic boundaries. Fresnel equations are solved using optical constants of the materials to determine reflection and transmission, followed by electromagnetic flux within a known discretisation of computational space within a grid to calculate absorption. Then, thermal property relationships are mapped onto the grid with the optical, to determine the temperature rise.

The advantages of laser processing were extended to other processes that have demonstrated potential for fabricating a range of technologically vital components. The methodology, known as adhesion lithography (a-lith) creates asymmetric laterally aligned contacts of two different metals with a nanogap that permits reduced parasitic capacitances, lower leakage currents and amenability to LAE. Laser processing was used to pattern a substrate by selectively ablating a thermally evaporated Al thin film (metal 1, M1) with a computer-aided design (CAD) design. Laser parameters such as repetition rate and hatch spacing were varied to achieve the smoothest substrate surface after M1 patterning. A self-assembling monolayer (SAM) with an alkyl tail is deposited, which modifies the adhesion properties of materials deposited hereafter. A uniform deposition over the full area with gold (Au) (metal 2, M2) via electron beam evaporation takes place. Then, a removal of Au and the SAM takes place via physical agitation in solvent or using adhesive tape. Due to Au having poor adhesion to M1 from the presence of the SAM, M2 detaches from the regions above M1 leaving M2 only in the areas where M1 is missing (ablated during laser patterning). The selective removal of M2, followed by a final removal of the leftover SAM, completes the a-lith process, with subsequent material depositions and architecture modifications dictating the device. In the case of this work, an MO sol-gel semiconductor is deposited and processed with flash lamp annealing to create a RF Schottky diode.

With the variety of thin films and devices in this work, characterisation covered a suite of optical, compositional, topographical and electronic techniques to determine the effect of post-deposition processing on the MO sol-gel thin film and device performance.

1.5 Structure of Thesis

The structure of this thesis is as follows:

- Chapter 1 introduces the research work, its motivation and novelty, research aims and objectives. A short methodology overview is also given.
- Chapter 2 explains the background information and fundamental science vital to completing and understanding this work. The optical properties of solids and opto-

electronic properties of metal oxides are presented, with some specific focus on certain MO dielectrics and semiconductors. The basics of sol-gel are subsequently provided, demonstrating the required knowledge for understanding the formation of the MO thin film and how LA comprises a vital and novel component to this work. Finally, the basics of optoelectronic device operation are explained.

- Chapter 3 explains the fabrication, post-deposition processing and characterisation techniques employed for the sample preparation and analysis in this thesis.
- Chapter 4 presents the results of self-consistent opto-thermal simulations of LA $In(NO_3)_3$ on different thicknesses of SiO_2 to create TFTs, using experimental results of previous studies at NTU as the platform. The theoretical results are compared to the experimental electrical characterisation to link temperature rise in the MO sol-gel precursor to TFT performance, as well as help to build understanding of MO precursor conversion. Commentary on the validity of the theoretical model is offered and rationalises its application throughout the rest of the thesis.
- Chapter 5 presents the development and electrical characterisation of fully sol-gel, LA TFTs and MOS capacitors, with a heavy focus on the development of MO, sol-gel dielectrics (ZrO_x and AlO_x). The effects of dielectric thickness and LA conditions on MOS capacitor performance for ZrO_x are reported, before using both aforementioned dielectrics in TFTs and discussing their performance. Opto-thermal simulations were also employed to discuss possible pathways to improving their performance.
- Chapter 6 reports the IRSE investigation of TA and LA MO dielectrics (ZrO_x and AlO_x), exploiting Al substrate for heightened sensitivity in the mid IR and far IR to determine their composition at different processing conditions and unravel the photochemical conversion process. Additionally, opto-thermal simulations were used to generate input LA parameters (i.e. fluence) relative to standard Si processing conditions.
- Chapter 7 demonstrates laser patterning as an alternative technique to lithography for fabricating RF Schottky diodes via the adhesion lithography process. The process of testing different laser sources, laser parameterisation and effect of laser parameters on surface character post-ablation is discussed, with its implications demonstrated via fabrication of the RF Schottky diodes.
- Chapter 8 summarises the conclusions of this work, along with briefly explaining several possible avenues for future work on sol-gel, LA MO devices and understanding their photochemical conversion.

2. Background and Literature Review

This chapter provides background information and fundamental science necessary for the cultivating and understanding of results in this thesis. The fundamentals of the optical properties of solids and TFT operation are explained. Furthermore, the key properties of MOs are displayed with a focus on dielectrics and semiconductors. An overview of sol-gel chemistry is also given.

2.1 Optical Properties of Solids

2.1.1 Electromagnetism

Due to the use of multiple optical characterisation techniques (e.g. spectroscopic ellipsometry) and a light-based processing technique, understanding the optical properties of solids and light-matter interactions is beyond vital. All descriptions of the optical properties of solids originate from describing the interactions between electromagnetic radiation (light) and matter via solving the Maxwell equations in differential form, which are written as [67], [68]:

$$\nabla \cdot \mathbf{D}\,(\mathbf{r},\mathrm{t}) = \mathrm{q}(\mathbf{r},\mathrm{t}) \tag{2.1}$$

$$\nabla \cdot \mathbf{B}(\mathbf{r},\mathrm{t}) = 0 \tag{2.2}$$

$$\nabla \times \Xi(\mathbf{r},\mathrm{t}) = \frac{\delta \mathbf{B}(\mathbf{r},\mathrm{t})}{\delta \mathrm{t}} \tag{2.3}$$

$$\nabla \times \mathbf{H}(\mathbf{r},\mathrm{t}) = \frac{\delta \mathbf{D}(\mathbf{r},\mathrm{t})}{\delta \mathrm{t}} + \mathbf{j}(\mathrm{r},\mathrm{t}) \tag{2.4}$$

where $\mathbf{D}$ is the electric displacement ($\mathrm{C/m^2}$), $\mathbf{B}$ is the magnetic induction (T), Ξ is the electric field ($\mathrm{V/m}$), $\mathbf{H}$ is the magnetic field ($\mathrm{A/m}$), q is the charge (C) and j is the current density ($\mathrm{A/m^2}$). $\mathbf{D}, \mathbf{B}, \Xi$ and $\mathbf{H}$ comprise functions of time t and spatial vector $\mathbf{r}$. $\mathbf{D}$ and $\mathbf{H}$ are also described by [69]:

$$\mathbf{D}(\mathbf{r},\mathrm{t}) = \varepsilon_0 \Xi(\mathbf{r},\mathrm{t}) + \mathbf{P}(\mathbf{r},\mathrm{t}) \tag{2.5}$$

$$\mathbf{H}(\mathbf{r},\mathrm{t}) = \frac{1}{\mu_0}\mathbf{B}(\mathbf{r},\mathrm{t}) - \mathbf{M}(\mathbf{r},\mathrm{t}) \tag{2.6}$$

where $\mathbf{P}(\mathbf{r},\mathrm{t})$ is the electric polarisation (average electric dipole moment per unit volume), $\mathbf{M}(\mathbf{r},\mathrm{t})$ is the magnetisation (average magnetic dipole per unit volume), ε_0 is the permittivity of free space ($\approx 8.854 \times 10^{-12}\ \mathrm{F/m}$), and μ_0 is the permeability of free space ($\approx 1.257 \times 10^{-6}\ \mathrm{H/m}$). To describe the response of matter to the aforementioned fields (in a linear and isotropic medium, without charges or currents), eqs. 2.1 - 2.4 are supplemented with the constitutive relations [67], [69]. Combining with eqs 2.3 - 2.4 - with the assumption of a time-harmonic field – gives:

$$\mathbf{D}(\mathbf{k},\omega) = \varepsilon_0\varepsilon_r(\mathbf{k},\omega)\boldsymbol{\Xi}(\mathbf{k},\omega) \quad 2.7$$

$$\mathbf{B}(\mathbf{k},\omega) = \mu_0\mu_r(\mathbf{k},\omega)\mathbf{H}(\mathbf{k},\omega) \quad 2.8$$

$$\mathbf{j}(\mathbf{k},\omega) = \sigma(\mathbf{k},\omega)\boldsymbol{\Xi}(\mathbf{k},\omega) \quad 2.9$$

where $\mathbf{k}$ is the wavevector and ω the angular frequency. $\varepsilon_r(\mathbf{k},\omega)$ and $\mu_r(\mathbf{k},\omega)$ are the dimensionless relative permittivity and permeability of a material, respectively. ε_r is commonly known as the dielectric constant of a material and is a value defining by how much the electric field strength is reduced in a material compared to vacuum. $\mathbf{j}(\mathbf{k},\omega)$ is the current density and $\sigma(\mathbf{k},\omega)$ the conductivity of a material. It is observed that eq. 2.9 is identical to Ohm's Law [69].

In eqs. 2.7 - 2.9, it is observed that a wavevector and angular frequency dependence of ε_r, μ_r and σ exists. For wavelengths ($\lambda = \frac{c}{\omega}$ where $c = 2.998 \times 10^8$ m/s) that are much smaller than the material dimensions, the wavevector dependence can be neglected. Regardless of material dimensions, the frequency dependence is essential to consider when discussing optical and opto-electronic phenomena. The frequency dependent optical response of a material is described by the dielectric function $\varepsilon(\omega)$ (permittivity) of a material. Assuming a uniform, isotropic and non-magnetic material (i.e. $\mu_r(\omega) = 0$ for all ω values), the Helmholtz equation can be derived [70]:

$$\nabla^2\boldsymbol{\Xi}_\omega(\mathbf{r}) + \frac{\omega^2}{c^2}\varepsilon(\omega)\boldsymbol{\Xi}_\omega(\mathbf{r}) = 0 \quad 2.10$$

If a current source is added to said material (i.e. $j(\omega) \neq 0$), the Helmholtz equation is modified to be:

$$\nabla^2\boldsymbol{\Xi}_\omega(r) + \frac{\omega^2}{c^2}\left(\varepsilon(\omega) + i\frac{\sigma(\omega)}{\omega\varepsilon_0}\right)\boldsymbol{\Xi}_\omega(\mathbf{r}) = 0 \quad 2.11$$

Comparing eqs. 2.10 - 2.11 reveals permittivity is a complex value in the presence of a current, such that $\varepsilon(\omega) \rightarrow \tilde{\varepsilon}(\omega) = (\varepsilon_1(\omega) + \frac{i\sigma(\omega)}{\omega\varepsilon_0})$. Thus, the frequency dependent properties of a material can be described by the complex permittivity:

$$\tilde{\varepsilon}(\omega) \rightarrow \varepsilon_1(\omega) + i\varepsilon_2(\omega) \quad 2.12$$

where $\varepsilon_1(\omega)$ and $\varepsilon_2(\omega)$ are the real and imaginary components of complex permittivity $\tilde{\varepsilon}(\omega)$. In general, the absolute permittivity that defines the electric polarizability of a material is related to the relative permittivity as $\varepsilon_r = \frac{\varepsilon}{\varepsilon_0}$.

2.1.2 Optics

Optics is the study of interaction (reflection, transmission and absorption) of electromagnetic waves with materials. The simplest form of electromagnetic waves are the plane waves [68]:

$$\boldsymbol{\Xi}(\mathbf{r},t) = \boldsymbol{\Xi}_o e^{i(\tilde{\mathbf{k}}\cdot\mathbf{r}-\omega t)} \quad 2.13$$

$$\mathbf{H}(\mathbf{r},t) = \mathbf{H}_o e^{i(\tilde{\mathbf{k}}\cdot\mathbf{r}-\omega t)} \quad 2.14$$

where $\boldsymbol{\Xi}_o$ and $\mathbf{H}_o$ represent the electric and magnetic field amplitudes, respectively, and are complex vectors. The wavevector is also complex such that $\tilde{\mathbf{k}} = \mathbf{k_1} + i\mathbf{k_2}$. If one assumes a homogeneous electromagnetic wave with $\tilde{\mathbf{k}} = (\mathbf{k_1} + i\mathbf{k_2})\hat{\mathbf{e}} = \tilde{k}\hat{\mathbf{e}}$ (where $\underline{\hat{\mathbf{e}}}$ is a real unit vector in the direction of propagation) and no charge or current density is present ($\mathbf{j} = 0$), it can be shown that:

$$\varepsilon(\omega)\mathbf{k}\cdot\boldsymbol{\Xi}_o = 0 \quad 2.15$$

$$\mathbf{k}\cdot\mathbf{H_o} = 0 \quad 2.16$$

$$\mathbf{k}\times\boldsymbol{\Xi}_o = \omega\mu_0\mathbf{H}_o \quad 2.17$$

$$\mathbf{k}\times\mathbf{H}_o = -\omega\varepsilon_0\tilde{\varepsilon}(\omega)\boldsymbol{\Xi}_o \quad 2.18$$

Via these assumptions, all properties of $\tilde{\varepsilon}(\omega)$ arise from the material properties. According to eq. 2.13 and eq. 2.14, $\mathbf{k}$ is perpendicular to $\boldsymbol{\Xi}_o$ and $\mathbf{H_o}$ meaning there is a transverse wave. Combining eqs. 2.15- 2.16 gives rise to the dispersion relation:

$$\tilde{k}(\omega) = \sqrt{\tilde{\varepsilon}(\omega)}\frac{\omega}{c} = \tilde{n}(\omega)\frac{\omega}{c} \quad 2.19$$

where $\tilde{n}(\omega)$ is the complex refractive index:

$$\tilde{n}(\omega) = \sqrt{\varepsilon(\omega)} = n(\omega) + i\kappa(\omega) \quad 2.20$$

where $n(\omega)$ is the normal refractive index that determines the phase velocity, $v(\omega)$, of a plane wave through the material, (i.e. $n(\omega) = \frac{c}{v(\omega)}$) and $\kappa(\omega)$ is the extinction coefficient that determines the absorption coefficient, $\alpha(\omega)$, via the following relationship:

$$\alpha(\omega) = 2\frac{\omega}{c}\kappa(\omega) = \frac{4\pi\kappa(\omega)}{\lambda} \quad 2.21$$

Furthermore, the description of electromagnetic wave intensity attenuation for a material with a known $\alpha(\omega)$ can be found according to Beer's Law [71]:

$$I(\delta) = I_0 e^{-\alpha(\omega)\delta} \quad 2.22$$

where $I(\delta)$ is the wave intensity after propagating along the z-direction through a material of depth δ and I_0 is the original intensity value. From Beer's Law, the penetration depth δ_p can be calculated at the point where $I(z) = \frac{I_0}{e}$ (33% of original value).

The now defined refractive index n and extinction coefficient κ can be used to calculate the real and imaginary parts of complex permittivity - $\varepsilon_1(\omega)$ and $\varepsilon_2(\omega)$, respectively:

$$\varepsilon_1(\omega) = n^2(\omega) - \kappa^2(\omega) \quad 2.23$$

$$\varepsilon_2(\omega) = 2n(\omega)\kappa(\omega) \quad 2.24$$

$$n^2(\omega) = \frac{1}{2}\sqrt{\varepsilon_1^2(\omega) + \varepsilon_2^2(\omega)} + \frac{\varepsilon_1(\omega)}{2} \quad 2.25$$

$$\kappa^2(\omega) = \frac{1}{2}\sqrt{\varepsilon_1^2(\omega) + \varepsilon_2^2(\omega)} - \frac{\varepsilon_1(\omega)}{2} \quad 2.26$$

Throughout this thesis, $\varepsilon_1(\omega)$ and $\varepsilon_2(\omega)$ were used to evaluate materials during use of optical characterisation techniques. $\varepsilon_2(\omega)$ is particularly inspected due to its indication of absorption, scaled by the real refractive index. n and κ are used for optical constants of materials during opto-thermal simulations (chapter 3, section 3.3).

2.1.3 Lorentz Oscillators

Each change in the complex permittivity of a material is influenced by optical absorptions at a specific frequency, arising from a physical mechanism related to the material properties. Each absorption can be modelled by an oscillator. The most used oscillator, known as the Lorentz oscillator, uses a model of a negatively charged electron bound to a positively charged ion due to its parallels to the classic damped oscillator with a restoring force (analogous to a mass on a spring) [68]. This oscillator model restoring force has a resonant frequency ω_0, as well as any bound dipoles. The equation of motion for electrons in response to an external electric field, $\Xi(t)$, derives from Newton's laws of motion and includes damping, driving and spring forces [68]:

$$F_{acceleration} = m\frac{d^2r}{dt^2} = F_{Driving} + F_{Damping} + F_{Spring} \quad 2.27$$

Using Hooke's Law for a harmonic oscillator to describe the spring force [72], Coulomb's law to describe $\Xi(t)$ driving force [73] and assuming damping is linearly proportional to mass velocity, it can be shown that:

$$\frac{d^2r(t)}{dt^2} + \gamma\frac{dr(t)}{dt} + \omega_0^2 r(t) = \frac{e}{m_e^*}\Xi(t) \qquad 2.28$$

where γ is the damping constant, $r(t)$ is the electron displacement, e is the electron charge and m_e^* is the electron effective mass. For the spring constant K associated with oscillator frequency ω_0, it can be found that $\omega_0 = \sqrt{\frac{K}{m_e^*}}$. Assuming the electric field is induced via an electromagnetic plane wave ($\Xi(t) = \Xi_0(\omega)e^{-i\omega t}$), eq. 2.28 can be solved for $r(t) = r_0(\omega)e^{-i\omega t}$ to give:

$$r_0(\omega) = \frac{e}{m(\omega_0^2 - \omega^2 - i\gamma\omega)}\Xi_0(\omega) \qquad 2.29$$

In eq. 2.29, an electric dipole moment $\mu_0(\omega)$ can be substituted by $er_0(\omega)$. Polarisation vectors can also be considered, since $P = N\mu_0(\omega) = Nqr_0(\omega)$. By also noting $P(\omega) = \varepsilon_0\chi_e(\omega)\Xi_0(\omega)$ [74] the complex permittivity can be derived as [75], [76]:

$$\tilde{\varepsilon}(\omega) = 1 + \frac{N_L e^2}{\varepsilon_0 m_e^*}\cdot\frac{1}{\omega_0^2 - \omega^2 - i\gamma\omega} \qquad 2.30$$

where N_L is the number of Lorentz oscillators per unit volume. For a real material, all transitions and real interactions must be considered along with the Lorentz oscillator similar to the consideration of dipoles and polarisation vectors previously. To do this, the electric displacement is separated into the resonant part, $P(\omega) = \varepsilon_0(\tilde{\varepsilon}(\omega) - 1)\Xi(\omega)$, and the background part $P_b(\omega) = \varepsilon_0(\varepsilon_\infty - 1)\Xi(\omega)$. The resonant part describes the Lorentz oscillator itself, while the background contributions are represented by a high frequency permittivity ε_∞. Therefore, the complex permittivity can be written as:

$$\tilde{\varepsilon}(\omega) = \varepsilon_\infty + \frac{f_L^2}{\omega_0^2 - \omega^2 - i\gamma.\,\omega} \qquad 2.31$$

where $f_L^2 = \frac{N_L e^2}{\varepsilon_0 m_e^*}$ gives the oscillator amplitude A_L. At the resonant condition (i.e. $\omega = \omega_0$):

$$\varepsilon_2(\omega = \omega_0) = A_L = \frac{f_L^2}{\gamma\omega_0} \qquad 2.32$$

$\tilde{\varepsilon}(\omega)$ can be then be written as:

$$\tilde{\varepsilon}(\omega) = \varepsilon_1(\omega) + i\varepsilon_2(\omega) = \varepsilon_\infty + \frac{A_L \gamma \omega_0}{\omega_0^2 - \omega^2 - i\gamma\omega} \quad 2.33$$

$\tilde{\varepsilon}(\omega)$ can be further separated into its constituent components:

$$\varepsilon_1(\omega) = \varepsilon_\infty + \frac{(A_L \gamma \omega_0)(\omega_0^2 - \omega^2)}{(\omega_0^2 - \omega^2)^2 + (\gamma\omega)^2} \quad 2.34$$

$$\varepsilon_2(\omega) = \frac{(A_L(\gamma^2 \omega_0 \omega)}{(\omega_0^2 - \omega^2)^2 + (\gamma\omega)^2} \quad 2.35$$

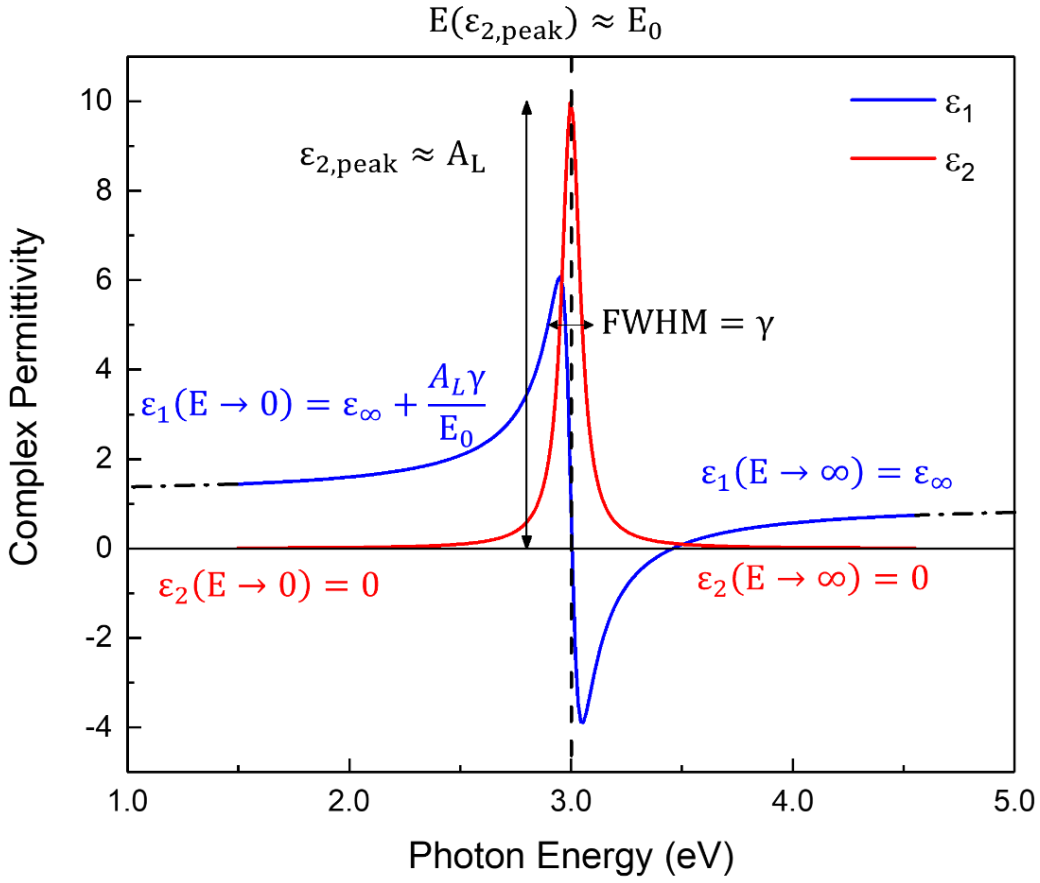

Figure 2.1. Example of the real (blue) and imaginary (red) permittivity of a Lorentz oscillator with $\varepsilon_\infty = 1$, $A_L = 10$, $\gamma = 0.1$ eV and $E_0 = 3$ eV. The origin of the shape of each curve is described by inset equations.

In the above equations, A_L equals $\varepsilon_2(\omega)$ at its peak value ($\omega = \omega_0$) if $\gamma \ll \omega_0$. Figure 2.1 shows an example of a Lorentz oscillator with $\varepsilon_\infty = 1, A = 10, \gamma = 0.1$ and $E_0 = \hbar\omega_0 = 3$ eV. Note that photon energy is often expressed in a variety of ways instead of ω (in s^{-1}) such as the wavenumber (cm^{-1}) or photon energy E (in eV). Figure 2.1 uses eV instead. While several other oscillators exist and differ in distinctive ways (e.g. Gaussian, Tauc-Lorentz), the principles here extend to these oscillators for extracting complex permittivity, particularly via IRSE data analysis in this work (extensively utilised in chapter 6). The imaginary permittivity (ε_2) follows a

simpler line shape of a bell curve, with associated amplitude A_L, broadening as a full width at half maximum (FWHM) (γ) and centre E_0 (indicated by the vertical black dashed line in Figure 2.1). As energy tends towards extreme values of either ∞ or 0 away from E_0, ε_2 also tends towards 0. Real permittivity has a more complex shape that is described here moving from left to right (low energy to high energy). Starting from a stable value of ε_1 dictated by $\varepsilon_\infty + \frac{A\gamma}{E_0}$ (black horizontal dotted line), as E_0 is approached ε_1 increases to a maximum of $E_0 - \gamma$. This is known as normal dispersion. When $E_0 - \gamma < E < E_0 + \gamma$, ε_1 then immediately undergoes rapid decrease to negative values, into the anomalous dispersion region. When $E > E_0 + \gamma$, normal dispersion is re-obtained so ε_1 becomes positive again, trending toward ε_∞.

2.2 Properties of metal oxides

The emergence of thin films in modern electronics for TFTs has led to a radical transformation in our daily quality of life while also paving the way to the revolutionary Internet of Things (IoT) [8], building an interconnected network of devices such as smart windows [77], [78], [79], optical displays [80], [81], [82], solar cells [83], [84] (sustainable energy in general [85]) and sensors [86], [87] – with high frequency radio frequency ID (RFID) tags and near-field communication (NFC) tags distinguishing between them [88]. Many of these devices in the modern age are based on thin films. This unprecedented expansion, not only ascertaining the importance of these devices but also dramatically increasing the number of devices, has led to new industry paths such as flexible electronics and large-area electronics that are necessarily attempting to meet this up-scaling. This has led to the fabrication of these devices on flexible components, such as flexible displays [4], [9], [89], TFTs [89], [90], [91] and solar cells [92], since flexible substrates are able to be printed on cm and m scale for higher throughputs.

However, this progression is at a crossroads. Thus far, thin film technologies utilised for the devices in the IoT infrastructure have been reliant on Si nanoelectronics that remain constrained by the technological and economic factors in vacuum-based fabrication techniques and photolithography [93], [94]. To meet performance increases and the increase of electronic components as described by Moore's Law [31] (which is used as a goal in industry), semiconductor device dimensions in TFTs and integrated circuits (ICs) are accelerating to as low as 2 nm process node in tandem with other innovations in technology [95], [96], aiming to meet transistor performance doubling every 18 months. Miniaturization has allowed the continued success of this paradigm for decades since it allows reduced power consumption for each chip [97], at the expense of the low charge carrier mobility for a − Si, incompatibility with LAE for higher performance polycrystalline Si (lower potential throughput) and high manufacturing cost

of most forms of Si [98], [99]. The incompatibility is further exaggerated by conventional photolithography – previously the most viable semiconductor patterning process [100] - not being compatible with flexible electronics. This means alternative materials and processes are required for flexible, large-area electronics. Metal oxides (MOs) initially emerged in the early 1960s, demonstrating their implementation in TFTs and surface coatings [101], [102]. However, significant attention and progress would only be initiated after noteworthy performance characteristics reported by Nomura *et al* for TFTs with both crystalline and amorphous MO semiconductors [54], [103]. Metal oxides have become a focal point of the alternative materials [104], [105], [106] and offer several advantages that tackle these challenges including outstanding electrical and optical properties (high mobility [107] and transparency), spatial uniformity and mechanical stability [108]. Their assembly into low-dimension (ultra-thin) heterostructures [6], [109] and nanosheets has been shown to result in charge carrier mobilities rivalling poly-Si [7], [110], [111], [112], [113] and unique fabrication possibilities to further enhance performance, such as quantised energy states for quantum effect devices [55]. Importantly, they offer unrivalled processing versatility with both physical and solution processing methodologies with adaptable chemistry in either case [114], [115].

Within electronics, three classes of materials exist that are differentiated by electrical conductivity and behaviour and MO materials can be categorised by: metals, dielectrics and semiconductors. While metals (or high carrier concentration MOs) have the necessary electrical conductivity to carry charge and activate the transistor, they lack the switching ability, transparency and adaptability sought for active layers in electrical devices. Thus, MO dielectrics and semiconductors are employed as charge storage and active layers respectively, while metal or MO electrodes are deposited within the structure (see chapter 2, section 2.4.2 for transistor behaviour). Dielectrics and semiconductor materials are both derived from ceramics. MO ceramics are chosen due to a wide bandgap ($E_G > 3$ eV, transparent in the visible range) with a wide range of carrier concentrations. Those with lower carrier concentrations (dielectrics) are employed as charge storage layers, while those of higher carrier concentration (semiconductors) as active layers for optoelectronics. As dielectrics and semiconductors are the materials of interest in this thesis, these are discussed further below.

2.2.1 Metal oxide dielectrics

A dielectric is an electrical insulator that is polarised in the presence of an electric field. Due to their lack of free carriers, localised charges are shifted from equilibrium and redistributed when under the influence of an electric field (i.e. applied bias) to counteract the electric field. This forms a net dipole moment describing a vector summation of each charge displacement product from the superposition principle (sometimes referred to as the transition dipole

moment) [116]. Within the context of TFTs, the dielectric underpins the operation of the device and for what application the TFT is incorporated into. When any voltage with a high frequency alternating current (AC) component is applied to the TFT, the dielectric charges opposing the field orientate and relax at rate determined by the frequency. A high-performance dielectric will successfully orientate at a variety of frequencies from kHz to several MHz ensuring opposition to the field and charging the device, while a poor dielectric will fail to the extent the TFT performance is completely impeded. In several TFT configurations (details in chapter 2, section 2.4.3), the dielectric is placed between a "gate" electrode (thus becomes the gate oxide). The electric field is applied by carrier transport through a bias supplied between the "source" and "drain" electrodes, whose magnitude is modulated by the "gate" electrode bias.

Certain requirements have been identified for a MO dielectric to be realistically considered in transistors [117]. A high dielectric constant, k, at a pragmatically low film thickness permits high charge storage with the reduced power consumption required for miniaturised electronics. MO dielectrics are often normalised for comparison to $\mathrm{SiO_2}$ (to confirm if the same capacitance per unit area is achieved) via a figure known as the equivalent oxide thickness (EOT), which is calculated as:

$$\mathrm{EOT} = \frac{\mathrm{d_{H_iK}} \cdot \mathrm{k_{SiO_2}}}{\mathrm{k_{H_iK}}} \qquad 2.36$$

where $\mathrm{d_{H_iK}}$ is the thickness of the oxide dielectric, $\mathrm{k_{SiO_2}}$ is the dielectric constant of $\mathrm{SiO_2}$ and $\mathrm{k_{H_iK}}$ is the dielectric constant of the oxide. A high bandgap is necessary to advance this low power consumption, as this hinders charge injection to the conductive electrodes due to lower parasitic electrical conduction [118]. The dielectric surface should be smooth for interface planarisation, as roughness or other topographical features cause electrostatic boundaries that impede carrier transport through the channel at the dielectric-semiconductor interface [119]. Dielectric-semiconductor planarisation has been shown to improve TFT carrier mobility [120]. Finally, structural defects (e.g. oxygen vacancies, pinholes [121]) in the dielectric layer should be minimised so the dielectric polarisation process is unaffected and charge scattering is minimised. Comparison to the industry standard unveils where these critical requirements are derived from. Due to its fabrication via thermal oxidation permitting a perfect interface with Si, $\mathrm{SiO_2}$ has been the dielectric of choice for decades. However, while it does have an extraordinary bandgap $\mathrm{E_G}$ of $8.9\ \mathrm{eV}$ [117], it fails to meet the desired high-k value, commonly only demonstrating a k of $3.8 - 4.2$. Furthermore, the $5\ \mathrm{nm}$ scales of electronics currently employed by leading technology companies such as Samsung and TSMC [37] have forced $\mathrm{SiO_2}$ to its intrinsic limit, leading to enormous gate leakages only emphasised by tunnelling mechanisms. The

technological cost for manufacturing at low nm scales combined with devices drawing excessive power drives economical cost up dramatically, making the current manufacturing route increasingly untenable. Thus, research into MO dielectrics meeting the aforementioned criteria becomes increasingly vital. MO dielectrics fabrication in amorphous phase is also facile and advantageous, preventing easy paths for leakage currents to the gate electrode [122].

The research into dielectrics has particularly accelerated in recent years. It's particularly pertinent as the ideal situation of high bandgap and high- k values so far has not been found, requiring innovation in new dielectric materials and device design. Figure 2.2 demonstrates this need for innovation via a plot of dielectric constant vs E_G for bulk and thin film forms for several candidate materials commonly appearing in the literature [117], [123], [124], [125], [126], [127], [128], [129], [130], [131], [132], [133], [134], [135], [136], [137], [138]. While there are several candidates, certain materials have been championed and promoted in the literature.

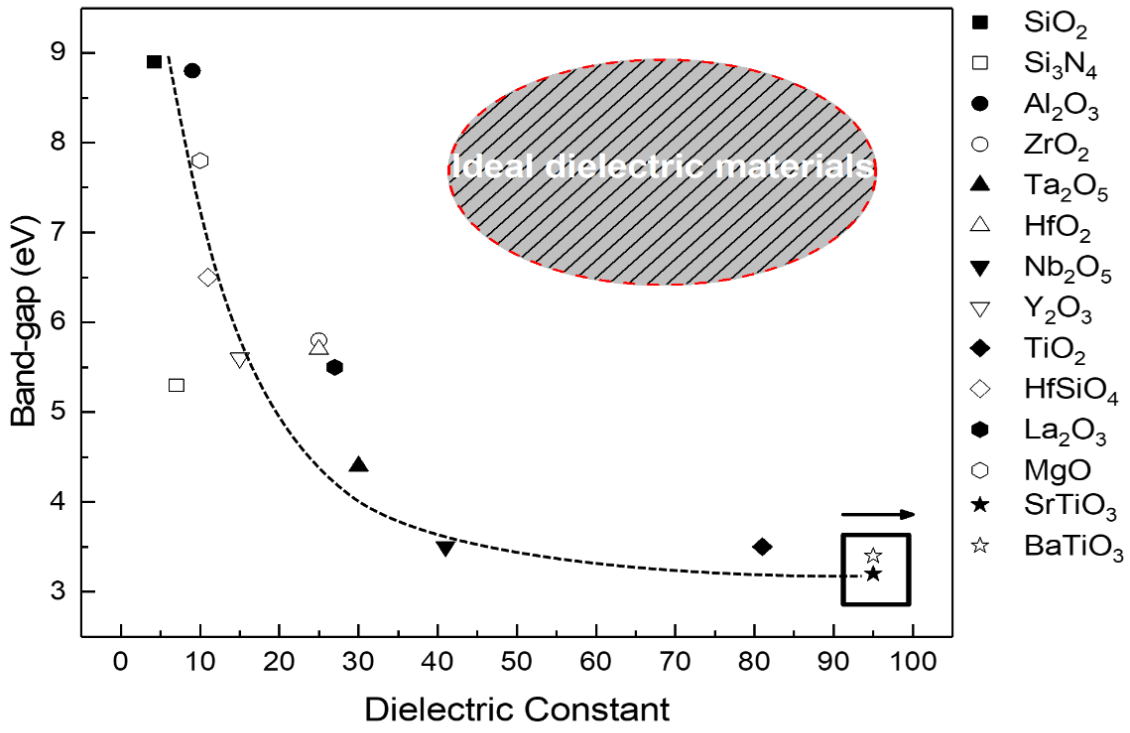

Figure 2.2. A plot of band-gap vs dielectric constant for several dielectric materials that are common in the literature for electronics and opto-electronics, including TFTs and diodes. Note that values here are representative and can vary greatly depending on a plethora of variables. The shaded rectangular area in the top right of the graph indicates how these (and hundreds of other materials) fail to meet the ideal criteria of high band gap and high dielectric constant, with band gap and dielectric constant commonly being inverse to each other (as indicated by the curved dashed line on the graph). The box around the points in the bottom right of the scatter graph are accompanied by an arrow, to indicate their dielectric constant values extend far beyond the limits of the axes here.

Tantalum pentoxide (Ta_2O_5) [139], [140] and yttrium oxide (Y_2O_3) [141], [142] have been utilised with different semiconductors in TFTs with promising performance characteristics. However, they are far less prevalent and utilised, since there is a compromise between bandgap and high dielectric constant. Hafnium oxide (HfO_2) [143], [144] has higher prevalence since there is less compromise between bandgap and dielectric constant, as well as previous computational calculations and experiments revealing its ability to be a stable, high performance gate dielectric [145]. For many of these materials, these experiments span vacuum and solution processed fabrication routes for more immediate and future integration to current and future industry manufacturing. Recent calculations and simulations have also investigated over 1800 materials in the Inorganic Crystal Structure Database to further identify new candidates [146].

Perhaps of equal occurrence to HfO_2 is its partner oxide zirconium oxide (ZrO_2). The bulk k of 25 is very high while maintaining a reasonable bandgap of 5.8 eV. It has demonstrated the ability of being fabricated as an amorphous sol-gel layer with high electrical performance, using different chemical precursors. Al_2O_3 has also been of utmost interest for reasons aside from meeting the aforementioned criteria. While its k value is far lower than its counterparts, Al_2O_3 boasts a unique advantage over other MO gate dielectrics. Since flexible substrates for LAE such as polyethylene (PET) and polyimide (PI) are themselves not conducting or semiconducting, Al metal is commonly deposited to act as the gate electrode. Thus, a situation analogous to the $Si-SiO_2$ interface occurs, where formation of a dielectric material with a highly favourable interface occurs with the substrate. Additionally, the higher dielectric constant of 9 and band-gap comparable to SiO_2 is appealing for increased charge accumulation without sacrificing electrical stability. Finally, its ability to be fabricated in amorphous thin film by solution processing routes for an array of different devices – as well as established fundamental understanding of different chemical pathways for various precursors – makes it highly advantageous. For these reasons, Al_2O_3 and ZrO_2 were selected as the dielectrics of choice for this work.

Finally, certain distinguishments should be made regarding the difference between solution processed dielectrics and their stoichiometric counterparts. Solution processed MO dielectric thin films typically have lower dielectric constants than stoichiometric films or bulk materials, due to organic residuals and their amorphous nature. Furthermore, the chemical pathways of each precursor (e.g. nitrate, acetate) form different by-products such as hydroxides that may render conversion incomplete, thus straying even further from stoichiometry. Thus, MO dielectric thin films throughout this film are more accurately referred to as MO_x, where M is the metal.

2.2.2 Metal oxide semiconductors

MO semiconductors have the beneficial high optical transparency ($E_G > 3$ eV leading to 80% or higher transparency in the visible range) [147] that reduces their parasitic leakage currents and capacitances in optoelectronics. The transparency of metal oxide semiconductors compared to other semiconductors is credited to the large electronegativity of oxygen and low energy of the valence band states [147], [148]. However, of the plethora of metal oxides, very few in their intrinsic form typically have the carrier concentration N (conductivity) necessary to compete with the industry standard Si or state-of-the-art methodologies since they remain in a ceramic form. Of this variety, indium oxide In_2O_3, zinc oxide ZnO and tin oxide SnO_2 are some of the most widely adopted. To meet the needs for conductivity for a given application, many metal oxides are further degenerately doped with extrinsic materials like metals to achieve a higher electrical conductivity and carrier concentration. Just a few examples of these materials include indium-gallium zinc oxide (IGZO) [143], [149], [150] , indium zinc oxide (IZO) [151], [152], aluminium zinc oxide (AZO) [153], zinc tin oxide (ZTO) [154] and ITO [155], [156]. Otherwise, conductivity can be boosted via intrinsic defects such as altering oxygen vacancies concentration [157]. Doping has also led to an increase in the number of p-type MOs.

Due to the materials and their doping selection, most MO semiconductors typically demonstrate n-type behaviour. However, the development of NiO [158], Cu_2O [159] and doped or alloyed derivatives such as $SrCu_2O_2$ [160] and $CuAlO_2$ [161] in the 1990s within electronics has led to an increasing prevalence and implementation of p-type candidates. The properties of all these semiconductors (p and n-type) varies wildly with deposition technique and conditions, as well as their doping versatility [53]. Large stoichiometry deviations and defects result in free carrier generation, depending on dopant's energy level with respect to E_G of the seed oxide. Bandgap, optical properties and electrical properties can drastically vary depending on deposition technique and conditions due to the stoichiometry and defects, as well as altered charge transport due to differences between crystalline, polycrystalline and amorphous samples [162]. Since MO semiconductors constitute the active layer for TFTs in this work (Chapters 4 and 5) and complete the fabrication of the Schottky diodes (chapter 7), fundamental understanding of the optical and electrical properties of key candidate materials is required to unravel the mechanism of LA on them and how these differences may influence the performance of vital electrical devices such as TFTs.

<u>Indium Oxide</u>

As indium oxide constitutes the main semiconductor used in this work (chapters 4 and 5), substantially more detail is given about it compared to other semiconductors. Indium oxide

is an n-type, direct band-gap semiconductor championed due to the optical transparency and highly tuneable conductivity due to vast differences between stoichiometric and thin film form [163]. Furthermore, the undoped In_2O_3 from solution processing and laser processing achieves surplus conductivity due to shallow oxygen vacancy defect states [157], leading to higher conductivity. Previous work at NTU has shown this conductivity can be tuned [63] for several deposition techniques for different applications. Due to these attractive properties, it has been trialled for several applications [164], [165], [166].

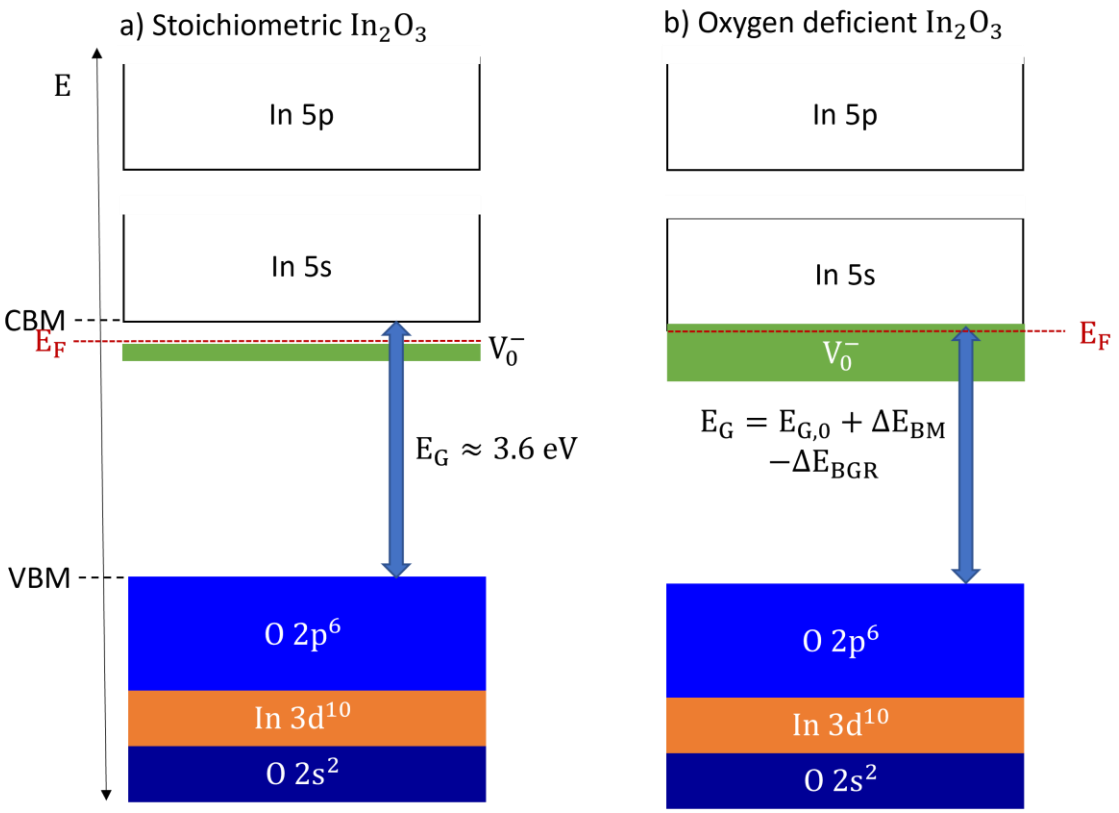

Figure 2.3. Energy band diagrams representing the simplified electronic band structure of a) stoichiometric In_2O_3 and b) oxygen deficient In_2O_3. The orbital state and occupation are labelled within the band, with CBM and VBM indicated on the energy (y) axis. The band gap is indicated by the blue arrow, while the Fermi level is indicated by the red dotted line. Note the shifted band gap in the oxygen deficient In_2O_3, highlighting the importance of defects within MO semiconductors.

For a semiconductor, an understanding of electrical behaviour can be found via the electronic band structure (valence band, VB, and conduction band, CB) and electron configurations in a simplified band structure diagram, representing only the direct band transitions. Figure 2.3 gives the band diagrams for stoichiometric and oxygen vacancy rich In_2O_3. Oxygen vacancies are used as an example of how defects affect the band structure, especially since they are one of the most prominent and important defects in In_2O_3. Due to a vested increase in indium oxide and its expansive range of carrier mobility, extremely detailed models and calculations of electronic configuration have been assembled for undoped and doped

forms[167], [168], [169], [170], [171]. In this case, isotropic parabolic conduction bands are sufficient to describe the relevant main properties for this work.

Indium oxide contains oxide anions with $2s^2\ 2p^6$ valence electron configurations, with the $2p$ orbital filled to form the valence band maximum (VBM). Metallic cations with ns^0 conduction band configuration are present (n dictating the principal quantum number of the orbital), with empty metallic s-orbitals forming the conduction band minimum (CBM). Between the $2s$ and $2p$ exists the filled $3d$ orbital, while above the $5s$ orbital exists the $5p$ orbital and together form the CBM with a single-free-electron-like behaviour. The Fermi level, E_F, in many stoichiometric oxides normally exists somewhere centrally between the VBM and CBM. The definition and position of E_F is fundamental to understanding the electrical properties of semiconductors. E_F does not necessarily refer to a physical energy level of an electron; instead, its position reflects the level at which the probability of finding an electron (cloud) is 50%. Depending on the dominance of carriers in the semiconductor – holes in p-type semiconductors and electrons in n-type semiconductors – E_F will shift closer to the VB or CB, respectively, to reflect the increased probability of finding holes or electrons. Certain materials including In_2O_3, when experiencing extremely high carrier concentration, cause a relative shift in E_F due to certain phenomena such as Burstein-Moss shift and a lower CBM due to the introduction of defects [172]. The aforementioned bandgap E_G is given as the difference between the VBM and CBM. The type of symmetry of the valence bands restricts promotion of charge carriers to the CB, forcing a minimum direct (and forbidden) band-gap of $2.9\ eV$ [173]. The first allowed transition occurs at $0.8\ eV$ below the VB, causing the $3.6\ eV$ direct bandgap [174]. The metal cations of lower ionisation energy in $5s$ and oxygen atoms with higher electron affinity in $2p$ undergo charge transfer, predominantly leading to ionic bonding. This ionic bonding is extremely noteworthy. As previously mentioned and elucidated by the band diagrams, crystal structure and defect variation plays a huge part in opto-electronic properties for In_2O_3.

Substantial efforts have been made to determine how this affects band structure and charge transport. Hosono *et al* [175] determined that since large and spherical ns orbitals (cation sources) overlap with the $2p$ orbitals more easily than other materials ($5s$ orbitals for indium oxide), conduction pathways and charge transfer is maintained to some degree regardless of crystal structure. This means amorphous, non-stoichiometric In_2O_3 can still exhibit high mobility [147]. This remains true as long as $n > 4$ to achieve sufficiently large orbitals that overlap their neighbours regardless of the amorphicity and establish an efficient conduction pathway [103], [176]. In essence, the nature of the ionic bonding maintains a higher degree of mobility compared to other material classes explored for modern electronics (e.g. organics, Si). Covalent bonded materials such as Si consist of highly sensitive directional and anisotropic sp^3

orbitals, hence changes in stoichiometry and crystallinity with large bond angle cause distortions that lead to highly localised traps below the CBM (in the band-gap). This impedes charge transport, since it is limited to hopping between trap states in the band gap [177], [178]. An illustration of the overlapping orbitals for metal oxides can be seen in Figure 2.4.

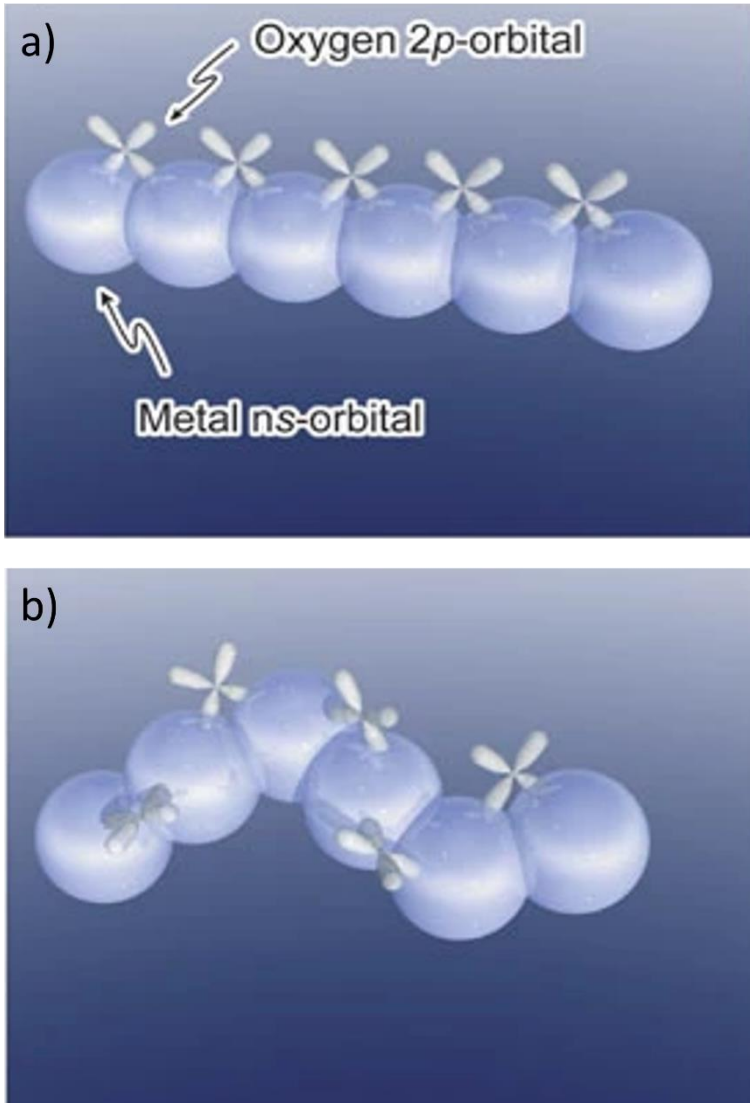

Figure 2.4. Schematics of orbitals of metal oxide semiconductors in a) crystalline and b) amorphous phase. The light blue and white spheres denote the metal ns-orbitals, while the white dumbbell-shaped orbitals are the oxygen 2p-orbitals. Note the large overlap of metal orbitals and the small overlap between 2p orbitals and metal orbitals in both crystalline and amorphous phases. Re-used with permission from [101].

However, the degree of mobility retained for amorphous metal oxides compared to a crystalline sample has been shown to be influenced both by the charge carrier transport and scattering mechanisms. These are not necessarily independent of each other. For example, grain boundaries themselves facilitate diffusion of ionised trap states, forming negatively charged boundaries that act as potential barriers that must be overcome to fill carrier depleted regions. These carrier depleted regions cause a large reduction in carrier mobility. Seto [179] and Baccarani [180] revealed in polycrystalline MO materials how overcoming this barrier is

dependent on several variables including the grain size, carrier concentration, trap state density and energy in the depletion zone. Thus, films that contain large grains and grain boundaries hinder performance in electronic devices and amorphous films are sought as a consequence of this.

In metal oxides including indium oxide, ionised impurity scattering (IIS) has previously been presented as a principal mechanism hindering carrier transport for higher carrier concentration materials [181]. Charge donors to the CB leave localised ionised impurities for charge preservation which carriers then scatter off during transport. While this can be dependent on a plethora of variables, at a uniform temperature IIS becomes limited to dependency on the charge and concentration of the ionised impurity. Greater charge - due to oxygen vacancies or highly charged interstitials – cause greater reductions in mobility.

In a fabrication context where lower temperatures are sought such as LAE using flexible substrates, amorphous films are sought to minimise mobility reduction due to some of these scattering mechanisms. In wider industry today, such an approach has been taken using $\mathrm{a-Si}$ in place of polycrystalline Si (to the detriment of performance). Oxides categorised as having post-transition cations with a $(\mathrm{n}-1)\,\mathrm{d}^{10}\,\mathrm{s}^{0}$ electronic configuration result in an amorphous configuration rivalling the polycrystalline films. However, some scattering will still occur due to lattice vibrations and polycrystalline films with many deposition techniques are common [182]. Since high temperatures are typically used to induce the desired semiconductor charge mobility and carrier concentration [183], an alternative is required to make MO semiconductors of any kind amenable to devices on flexible substrate.

2.3 Sol-gel Process

The fabrication of the advantageous metal oxides has evolved radically since the introduction and integration of thin films to vital technological components, including TFTs. While the metal oxides have appeared in various forms (bulk single crystals [53], nanoparticles [184], frameworks [185]), thin film fabrication is especially important to MOs as it acts as a scalable, lower economical cost method to implement thin films in modern technologies. Generally, these thin films follow two divergent groups of fabrication methods:

i) Physical “dry” processes centred around including sputtering, pulsed laser deposition (PLD) and evaporation processes. Here, a bulk source material is gradually eroded in some means (e.g. ion bombardment) with the removed material being deposited onto the sample.

ii) Chemical “wet” processes in controlled or ambient atmosphere including chemical vapour deposition (CVD), atomic layer deposition (ALD) and sol-gel processes. These

methods form the thin film by forming a network structure between atoms and molecules using chemical precursors.

The selection of thin film deposition methods depends on a plethora of factors. In the scope of this thesis, where context resides in the LAE paradigm with flexible substrates, a low temperature process without vacuum technologies was required. In the case of implementing metal oxides with scalable, disruptive methodologies such as LAE, physical processes or controlled atmosphere chemical processes (CVD, ALD) are processes that are constrained by the economical and technological necessities of vacuum chambers, providing discontinuities in the production line. Thus, solution processes based on sol-gel offer an attractive alternative. Since the inception of sol-gel for oxides in 1930 [186], the prevalence and sophistication of sol-gel has since grown dramatically, permitting extensive control over structure and composition for different applications at a range of temperatures. Sol-gel processes escape current technological boundaries as they can be conducted in ambient atmosphere with a variety of techniques adaptable to large flexible substrates including (but not limited to) ink-jet printing [187] and spray pyrolysis [188], [189]. Solution processes can then be further divided into i) liquid solution precursor compounds involving the mixture of a powder and solvent ("sol"), which is deposited and converted through a chemical reaction after energy is supplied to form a solid networked structure ("gel"). ii) Synthesisation of nanocrystals [190] that are dispersed in a solvent and subsequently deposited, before evaporation of the solvent to leave the nanocrystals behind. These solution processes can be further enhanced when combined with other methodologies, such as UV treatment [191], [192] or additives [193]. This section explores the fundamentals of sol-gel for MOs, as well as the current state of sol-gel for electronics.

2.3.1 Sol-gel Fundamentals

Sol-gel can be separated into three distinct stages. Steps 1 and 2 are associated with the mixing of precursor reagent with a solvent, while step 3 is associated with the subsequent deposition and drying of the sol-gel film. The net reaction is that of a series of hydrolysis, polymerisation and polycondensation processes to form a solid phase thin film material. A representation of this process can be seen in Figure 2.5.

1) Hydrolysis of the precursor reagent powder via dissolution in water (aqueous route) or alcohols (non-aqueous route), occurring during fabrication of the solution. The solvent provides oxygen, which is necessary for the conversion route. Additives can be used to aid in hydrolysis or the precursor and full dissolution of the precursor reagent in the solvent. Generically, hydrolysis is described as [184]:

$$M - OR + H_2O \rightarrow M - OH + ROH \quad (2.37)$$

where M is the metal and R is the alkyl group C_nH_{2n+1}. The quantity of water can be altered to change the gel formation. Increasing water content increases the ratio of bridging to nonbridging oxygens, producing a more polymerised and branched structure in the next steps [194].

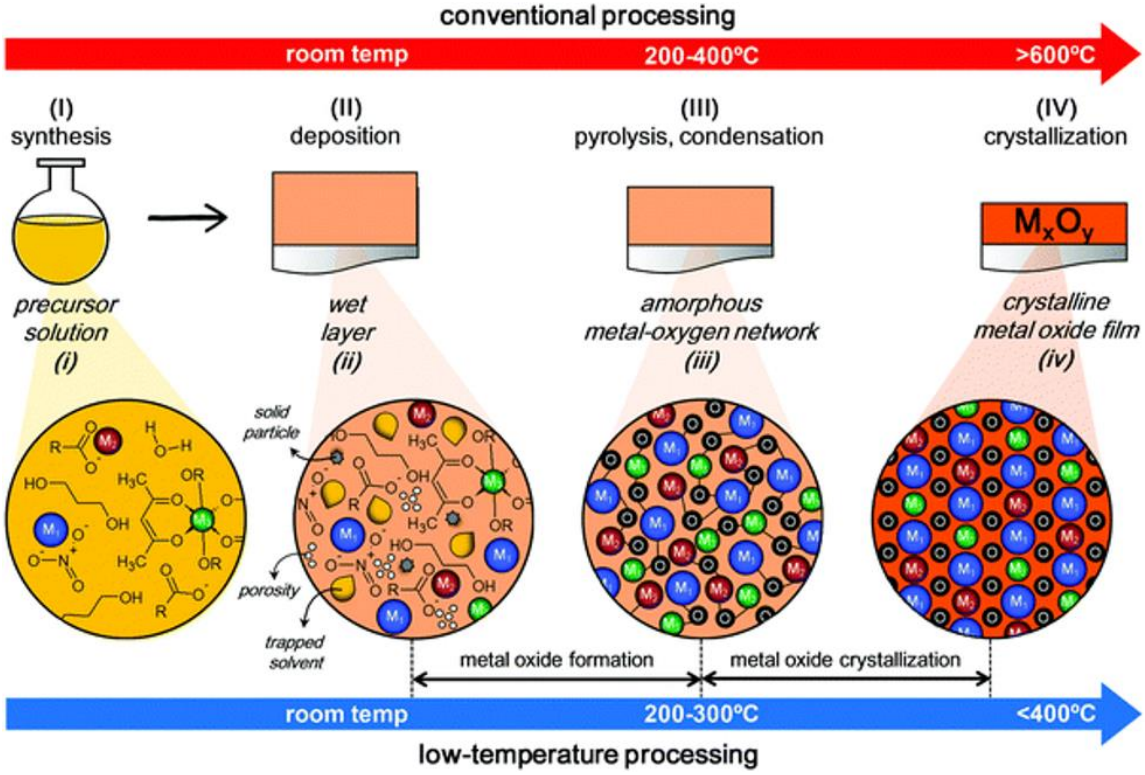

Figure 2.5. Schematic demonstrating the key steps of sol-gel fabrication and deposition, alongside the different evolution stages the material undergoes. Re-used with permission from [195].

2) Gel formation via polycondensation reactions to form metal-oxo-metal or metal-hydroxy-metal bonds. Excess water, alcohol and organic residues are removed while adjacent hydrated metal molecules condense to begin forming metal oxide bonds. Formation occurs either via i) olation, where a hydroxyl bridges between two metal centres ($M - OH - M$) or ii) oxolation, where an oxo bridge is formed between two metal centres ($M - O - M$) [184]. Several of these condensation reactions occur, with highly branched agglomerates forming in the 'sol' that eventually crosslink to form a porous structure (but still maintaining a liquid form) that constitute the 'gel' [196]. The formation of the gel via networking agglomerates is heavily dependent on the solution parameters, such as the type of precursor [197], solvent pH [198] or concentration [199]. The condensation process can be described as [184]:

$$\mathrm{M-OH+XO-M\ \rightarrow M-O-M+XOH} \qquad 2.38$$

where X is either a hydrogen (H) or an alkyl group. In this step of the synthesis, these condensation reactions are encouraged early on in pre-condensation reactions within the precursor solution, promoting atomic level mixing of multi-component systems [200]. Solution viscosity increases with further condensation reactions to form the gel.

3) Drying of the gel. The forming network adheres to the substrate and remaining solvent and organic residues evaporate. At this point, the gel (a dense xerogel) is also formed. The gel drying can be chemically complex, as removal of water and organic components disturbs the bonding to the metal atoms in different ways, leading to a variety of by-products depending on the precursor selected. Further drying at sufficiently elevated temperatures is subsequently employed to decompose those precursor by-products or intermediates, completely evaporate solvent and condense metal-hydroxides ($\mathrm{M-O-M}$) to form the metal-oxide molecular network. This additional temperature rise results in the organometallic conversion of the precursor into the desired thin film. Several variables including relative humidity (RH), atmosphere and temperature can vary the quality of the gel network and extent of drying [201]. The deposition technique used to deposit the solution can also initiate drying at differing rates. Spray coating aggressively induces drying upon contact with the substrate, since the substrate is heated to utilise the Leidenfrost effect [202], while the aggressive substrate rotation of spin-coating initiates the drying step during the deposition itself, before being further heated to densify the film and remove the remaining solvent.

The temperature threshold for complete drying and conversion of the organometallic precursor to a thin film is defined by the selection of MO precursor, with each providing a distinct chemical pathway of different by-products with varying volatilities, thus different temperatures for the drying stages. In all cases, higher levels of RH present during fabrication results in changes of chemistry due to additional water, which negatively affects the stability of the film [203]. Various salt precursors including nitrates ($\mathrm{M(NO_3)_x}$), acetates ($\mathrm{M(CH_3COO)_x}$) and chlorates $\mathrm{M(ClO_y)_x}$), have been chosen in the past [204], though only nitrates and acetates appear in this work. Nitrates offer several advantages – via more volatile by-products during precursor decomposition, the metal-oxide network and organometallic precursor conversion is achieved at lower temperatures [200], [205], [206]. This leads to nitrates being more amenable to implementation with large-scale plastic substrates in flexible electronics due to lower thermal budget. However, many nitrates (e.g. $\mathrm{In(NO_3)_3}$, $\mathrm{Al(NO_3)_3}$) are more susceptible to becoming too unstable due to water absorption in elevated RH. Acetates, while requiring a higher

conversion temperature (thus increased thermal budget) and being less naturally miscible in both aqueous and non-aqueous routes, do not absorb as readily in higher RH, prospectively leading to a more stable and consistent film. The use of additives such as monoethanolamine (MEA) can also aid in the miscibility in the solvent, circumventing one of their main issues [207]. Both nitrates and acetates have been shown to be successfully utilised for conductive [208], [209], [210] , semiconducting [206], [211] and dielectric [212], [213], [214] thin films.

2.3.2 Sol-gel thin films for LAE

As alluded to throughout this thesis, solution processed MOs boast several factors that make them promising for the next generation of electronics and amenable to LAE methodologies and R2R manufacturing, with these advantages demonstrated in TFTs containing sol-gel dielectrics and semiconductors. However, the input of energy for precursor conversion into a thin film still proposes a challenge to fully realising large-scale implementation of sol-gel, MO thin films. Mechanisms for organometallic precursors into functional thin films (with any precursor) typically occur above $250℃$, a temperature sufficiently high to damage several common (lower cost) flexible substrates such as PET [215]. In reality, precursors such as acetates can require up to $500℃$. Insufficient temperature rise of the precursor in semiconductors results in the presence of a variety of by-products that are dependent on chosen precursor, but commonly forming $\mathrm{M-OH}$ networks [216] - instead of $\mathrm{M-O-M}$ networks - that have been shown to disrupt device performance [217]. Thus, alternative processing methodologies for the end of the drying step – when densification and full conversion takes place - are required.

Consideration of optimising the hydrolysis and polycondensation stages via altering the solution chemistry has become evident as one of the first approaches. As previously mentioned, selection of the precursor is vital to this since certain precursors (e.g. nitrates) are removed of chemical impurities at lower temperatures. Further to this are additives mixed with the powder and solvent, which has previously been mentioned as an aid to improve solubility in some cases but can also be used as reaction catalysts to consume remaining hydroxide anions and encourage $\mathrm{M-O-M}$ bonding [218], [219]. Other additives, such as acetylacetone or urea [220], [221], [222], cause an endothermic redox reaction after a temperature threshold that causes an extreme temperature release into the solution, promoting precursor conversion at a lower temperature. This process, known as solution combustion synthesis, uses the additive as a fuel that is consumed after the temperature threshold, thus not altering the chemical pathway of the precursor. This has shown excellent and consistent results in the literature [223], [224], [225], [226] while using conventional drying methodologies such as thermal annealing on a hot plate.

The second change is new methodologies to the drying step itself. Instead of hot plates and ovens, light-based sources have become increasingly utilised in the form of microwaves [227], [228], flash lamps (for flash lamp annealing, FLA) [229], [230], UV lamps (DUV annealing) [231] and lasers (laser annealing, LA) [232], [233], [234] to produce high performance electrical materials. Apart from FLA sources that tend to be more broadband, UV irradiation is the focus of these photonic processes since MOs and their precursor solutions demonstrate higher absorption in the UV wavelength ranges due to their high bandgaps, advocating higher localised temperature rises that cause dissociation of the chemical impurities. The increased absorption subsequently leads to a lower penetration depth in the material, thus thermal budget to a flexible substrate is heavily reduced in comparison to other photonic sources or conventional methodologies. However, DUV lamps comprise a ratio of different UV wavelengths, exhibiting lower control over this process. Laser sources counteract this since they are monochromatic, thus the photothermal heating in the MO precursor is more precise and controllable. Despite these advantages, laser sources for LA remain far less explored than the DUV source.

UV radiation can affect the precursor or formed $\mathrm{M-O-M}$ network in different ways via electronic and thermal excitation phenomena. Initially, the bonds of the photosensitive compounds of the organometallic precursor are cleaved. Subsequently, the potential for electronic excitations of the organic and inorganic components increases. Oxidants such as ozone are produced, removing surface impurities and promoting bond dissociation of the organic components (-OR groups) via ozonolysis. However, certain reactive species such as $\mathrm{-OH}$ groups remain. The dissociation of these organic components encourages the condensation and densification process. The inorganic $\mathrm{M-O}$ bonds consequently form a $\mathrm{M-O-M}$ network that develops as the condensation and densification processes are completed. Atomic oxygen dissociated in the structure can also react with oxygen vacancies, changing the stoichiometry of certain MOs. Further thermal excitation - due to the increased energy provided by UV radiation or factors external to the UV radiation - leads to the complete densification and crystallisation of the precursor, leading to the formation of the thin film.

The combination of the sol-gel fundamentals and LA as an alternative processing methodology for photochemical conversion of the sol-gel MO is explored in chapter 3 (methodology), and chapters 5-6 (results chapters).

2.3.3 LA for sol-gel thin films

LA has seen well-established use of processing of MOs in the literature for novel methodologies and material processing with several justifiable reasons. Aside from the monochromatic nature providing a rapid and precise means of energy delivery, the nanosecond

pulse duration allows short exposure for a low thermal budget. These two factors are customised further via the myriad of LA parameters. The energy delivery can be changed with customisable spot sizes and geometries, as well as the energy itself, to control changes in areas of interest and avoid penetration into the substrate underneath (depending on opto-thermal properties). The high spatial resolution ($10\ \mu m$) and control over sample stage movement ($200\ ms^{-1}$ in 1D and accurate to $1\ \mu m$) allows precision in the chosen area for precursor conversion and patterning the film while still enabling high throughput. These factors lead to LA being amongst the most promising candidates for processing and patterning materials into commercial applications. This includes LAE, since decreased processing times, thermal budget and rapid scan speeds are compatible with R2R systems. In sol-gel materials, the use of UV wavelength LA using excimer lasers on the sol-gel materials with UV photosensitive compounds only bolsters this viewpoint.

LA has already evidenced potential for the fabrication of TFTs, LEDs and photosensors by fabricating well-know sol-gel conductors [235], [236], [237], semiconductors [238], [239], [240] and dielectrics [241] and processing vacuum-based materials for TFTs and diodes [242], [243], [244]. Work can still be done to expand the LA material library for electrical devices and expand into the combining of devices for full logic circuitry. However, there is especially one glaring omission centred on the understanding the underlying physiochemical phenomena in precursor conversion for achieving optimal electrical and optical characteristics. Many phenomena such as thermally induced chemical reactions, layer crystallisation, densification and growth due to photochemical conversion aren't fully understood due to their complex nature. Theoretical studies of LA on vacuum processed materials have been conducted, but don't capture the information necessary for sol-gel materials and material non-linearities [245], [246], [247]. The multiparametric nature of LA means 10 parameters must be optimised and thin film changes correlated to each change, the information for which must be discovered. For LA to be a standardised methodology for state-of-the-art, solution-processed flexible electronics and for the resultant realisation of high-throughput, high performance devices, new knowledge in light-matter interactions and the underlying mechanism for photochemical conversion is necessary.

2.4 Operation of fundamental electronics

For decades, transistors have been the fundamental building blocks in the electronics of the everyday. In layman's terms, transistors act as an electrical switch in a circuit. The backplanes of computers and phone displays are formed via the combination of many transistors with other devices (e.g. diodes) into integrated circuits on chips, amplifying signals, realising logic circuits or controlling pixel outputs in a display. The operation and different categories of transistors are

described below, alongside the capacitor structure that underpins the charge storage in a transistor. Additionally, the operation and origin of the Schottky diode, fundamental to radio frequency communication, is discussed.

2.4.1 Metal oxide-semiconductor capacitor (MOS capacitor)

As previously mentioned, the dielectric underpins the function of the TFT or MOS-field effect transistor. Thus, careful analysis of the dielectric in an isolated state separate from the semiconductor permits highly selective material and processing choices for the dielectric for optimal transistor performance, while understanding the fundamental electronic phenomena allows extraction of values necessary to define TFT performance. Figure 2.6 shows the energy band diagrams of the ideal MOS capacitor with an n-type semiconductor under different bias conditions. The MOS capacitor typically comprises a bulk substrate (also acting as the n-type semiconductor in this case), the oxide dielectric and a conductive gate electrode (typically a metal) combined into a simple stacked structure. Within the band diagram, important quantities are seen that need to be defined. Φ_M is the work function of the metal, representing the required energy to release an electron from the metal conduction band energy, E_C, to the vacuum energy, E_0. Similarly, Φ_S is the work function of the semiconductor. The metal has an associated Fermi level, $E_{F,M}$. The oxide electron affinity, χ_{ox}, signifies the energy difference between the conduction band of the oxide and the vacuum energy. Therefore, χ_S signifies the energy difference between the conduction band of the semiconductor and the vacuum energy. Since semiconductors are commonly subjected to doping, χ_S is of critical importance as its value is an intrinsic property of the material, thus doesn't depend on the shifting height of the semiconductor Fermi level, $E_{F,S}$ (or E_I for an intrinsic semiconductor). χ_S can also be related to work function via $\Phi_S = \chi_S + E_C - E_f$. As a result, it is more beneficial to refer to χ_S when describing the fluctuation in band diagrams in Figure 2.6. The semiconductor valence band level, E_V should also be noted.

In the absence of an applied voltage to the gate electrode (i.e. $V_G = 0$) of the device in Figure 2.6a, no electric charge accumulates at the oxide-semiconductor (O-S) interface, causing no alteration to the flat energy bands. This is referred to as the flat-band condition, which will act as a point of reference in certain explanations of the MOS capacitor fundamental operation. Once a non-zero gate voltage is applied (i.e. $V_G \neq 0$), the Fermi levels of the metal and semiconductor shift according to:

$$qV_G = E_{F,M} - E_{F,S} \qquad 2.39$$

where q is the elementary charge (1.6×10^{-19} C).

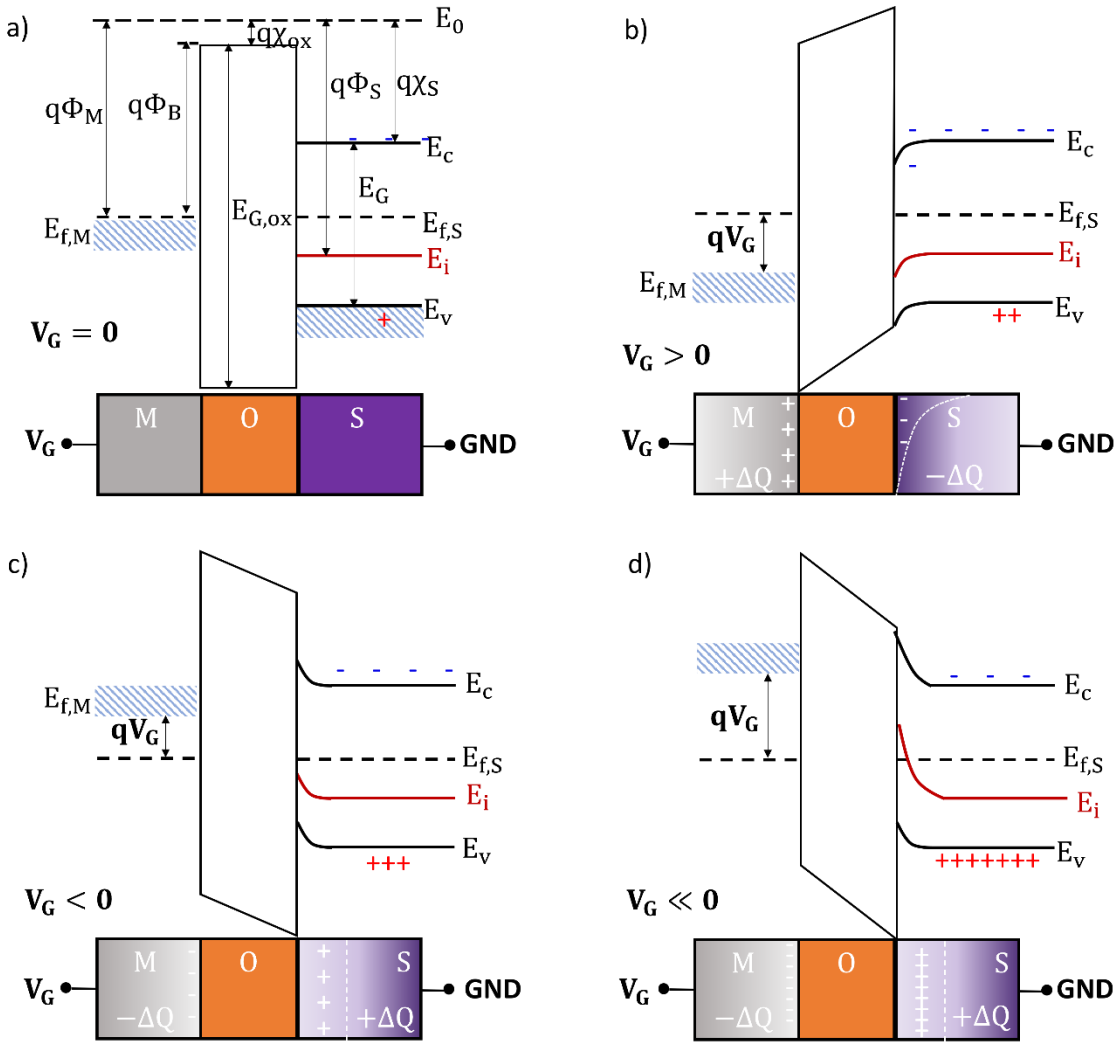

Figure 2.6. Schematic energy band diagrams for an ideal MOS capacitor device with an n-type semiconductor. a) Under zero bias, known as the flatband condition. b) Under positive gate bias, known as accumulation. c) Under negative bias, creating a depletion region. d) Under large negative gate bias, creating strong inversion. Red crosses throughout the figure indicate the presence of holes, while blue dashes indicate negative charges above the conduction band.

If $V_G > 0$, positive charges will accumulate to the metal-oxide (M-O) interface according to Gauss's Law [248] resulting in an increase of electron density in the semiconductor, $-\Delta Q$, and band bending of E_C, E_V and E_I of the semiconductor in proximity of the O-S interface. The band bending causes an apparent shift of E_C towards $E_{F,S}$ at the O-S interface. This band bending is visualised in Figure 2.6b, with its impact shown when reviewing its effect on the density of electrons, n_e, in the semiconductor:

$$n_e = n_i e^{\frac{E_{F,S} - E_i}{kT}} \qquad 2.40$$

where n_i is the intrinsic semiconductor electron density, k is the Boltzmann constant and T is the temperature. In the $V_G > 0$ case, $E_{F,S} - E_i$ increases at the O-S interface which increases n_e.

Due to the increased electron density, this regime is known as accumulation. In the opposing case of a negative voltage ($V_G < 0$ for small values, represented by Figure 2.6c), negative charges accumulate at the M-O interface. Consequently, a positive charge is formed at the O-S interface via repulsion of electrons inside the semiconductor and the O-S interface, forming a region depleted of electrons. This "depletion region" ensures charge neutrality in the layers. $E_{F,S}$ moves closer towards E_i via band bending, so semiconductor electron density reduces.

Where larger negative voltages are applied to the gate electrode ($V_G \ll 0$, represented by Figure 2.6d), $E_{F,S}$ moves even further towards and below E_i via band bending at the O-S interface, causing a greater concentration of holes than electrons at the O-S interface. This "inversion" condition occurs for small differences between $E_{F,S}$ and E_i, with larger differences due to larger negative voltages powering further increases in hole density at the O-S interface. At certain voltages, the Fermi levels either side of the O-S interface will align:

$$\left|E_{F,S} - E_i\right| = \left|E_i - E_{F,S}\right| \qquad 2.41$$

In the above equation, $\left|E_{F,S} - E_i\right|$ accounts for the O-S interface condition, while $\left|E_i - E_{F,S}\right|$ accounts for the bulk semiconductor, thus defining a condition where holes in the interface are equal to the electron density in the bulk semiconductor. This is known as "strong inversion." Eventually, increasingly negative V_G no longer fuels increased hole density as the depletion region reaches a threshold length. Thus, a strong inversion layer, consisting of a thin layer of holes close to the O-S interface, forms to contribute to the charge neutrality.

The origin of the hole layer without external charge contributions depends on thermal equilibrium phenomena, which inherently involve slow (low energy) constituents and processes. In this case, generation and recombination of electron-hole pairs in the bulk region takes place. To determine the effect of increasingly negative V_G on these processes, the relationship between V_G and the bulk semiconductor surface potential, φ_S, must be ascertained:

$$V_G = \varphi_s + \Delta\varphi_{ox} \qquad 2.42$$

where $\Delta\varphi_{ox}$ is the potential drop across the oxide layer. The electric field across the depletion region in the semiconductor, $\xi\,(x)$, is given by:

$$\xi\,(x) = \frac{qN_D}{\epsilon_s}(x - x_d) \qquad 2.43$$

where N_D is the concentration of semiconductor dopants, ϵ_s is the dielectric permittivity of the semiconductor, x is the distance from the O-S interface and x_d is the depletion region length. The potential across the area of the semiconductor, $\varphi(x)$, is given as:

$$\varphi(x) = -\int_{x_d}^{x} \xi(x) = -\frac{qN_D}{\epsilon_s}\int_{x_d}^{x}(x - x_d) = \frac{qN_D}{2\epsilon_s}(x - x_d)^2 \qquad 2.44$$

The potential at the O-S interface ($x = 0$) is:

$$\varphi_s = \frac{qN_D}{2\epsilon_s}x_d^2 \qquad 2.45$$

In inversion, the absence of a net charge causes a constant electric field ξ_{ox} across the oxide:

$$\xi_{ox} = \Delta\varphi_{ox}t_{ox} \rightarrow \Delta\varphi_{ox} = \frac{\xi_{ox}}{t_{ox}} \qquad 2.46$$

where t_{ox} is the thickness of the oxide layer. Due to boundary conditions across the interface, the electric displacement vector D should be continuous across the interface. Therefore:

$$D_{ox} = D_s \rightarrow \xi_{ox}\epsilon_{ox} = \xi_s\epsilon_s \qquad 2.47$$

Where ϵ_{ox} is the dielectric permittivity of the oxide and ξ_s is the electric field at the semiconductor side of the interface. Rearranging and substituting the equation for chemical potential gives:

$$\Delta\varphi_{ox} = \frac{\epsilon_s}{\epsilon_{ox}}\xi_s t_{ox} \qquad 2.48$$

The equation for V_G can then be expressed as:

$$V_G = \varphi_s + \frac{\epsilon_s}{\epsilon_{ox}}\xi_s t_{ox} \qquad 2.49$$

where the electric field at the interface ($x = 0$) following eq. 2.43 is:

$$\xi_s = \frac{qN_D}{\epsilon_s}x_d \qquad 2.50$$

And:

$$\varphi_s = \frac{qN_D}{2\epsilon_s} x_d^2 \rightarrow x_d = \sqrt{\frac{2\epsilon_s \varphi_s}{qN_D}} \quad 2.51$$

Combining the above equations for V_G, ϵ_s and φ_s leads to:

$$V_G = \varphi_s + \frac{\epsilon_s}{\epsilon_{ox}} t_{ox} \sqrt{\frac{2qN_D}{\epsilon_s}} \varphi_s = \varphi_s + \gamma\sqrt{\varphi_s} \quad 2.52$$

where $\gamma = \sqrt{2q\epsilon_s N_D}/C_{ox}$ and $C_{ox} = {}^{\epsilon_{ox}}/_{t_{ox}}$. This defines step 1 of increased V_G application. Step 2 aims to define the point of strong inversion by arbitrarily defining a relationship between φ_s and φ_f so $q \cdot \varphi_{f,s} = E_{f,s} - E_I$. This relationship describes the Fermi level energy difference at the point of strong inversion. Since $\varphi_f = ({}^{kT}/_{q}) \ln({}^{N_D}/_{n_i})$, φ_s can be defined as:

$$\varphi_s = 2\varphi_f = \frac{2kT}{q} \ln(\frac{N_D}{n_i}) \quad 2.53$$

The voltage initiating the strong inversion, known as the threshold voltage (V_{TO}), is subsequently:

$$V_{TO} = 2\varphi_f + \gamma\sqrt{2\varphi_f} \quad 2.54$$

While strong inversion has been somewhat defined, it has only done so under the flat-band condition. Thus, correction factors must be included to meet this condition (i.e. where the work functions of the metal and semiconductor are equal, at $V_G = 0$). The metal-semiconductor correction, φ_{ms}, is given as:

$$\varphi_{ms} = \frac{1}{q}(\Phi_M - \Phi_S) = \frac{1}{q}(\Phi_M - \chi_S - E_C + E_F) \quad 2.55$$

Another correction factor is the inhomogeneous charge density across the O-S interface due to impurities and charge traps in the dielectric, as well as semiconductor implant dopant influence. A flat-band voltage factor, V_{FB} ,is introduced that summates these in relation to the metal-semiconductor junction:

$$V_{FB} = \varphi_{ms} - \frac{Q_{SS}}{C_{ox}} - \frac{Q_i}{C_{ox}} \quad 2.56$$

where Q_{SS} represents the charge density of the dielectric and Q_i is the surface charge density due to semiconductor implant dopants. The corrected threshold voltage, V_{th}, can then be written as:

$$V_{th} = V_{FB} + 2\varphi_f + \gamma\sqrt{2\varphi_f} \quad 2.57$$

Any voltage above V_{th} linearly increases the inversion charge, Q_{inv}:

$$Q_{inv} = C_{ox}(V_G - V_{th}) \quad 2.58$$

The expression of V_{th} with the inclusion of V_{FB} reveals how the charge accumulated, as well as low-voltage operation, are influenced by the level of defects in the dielectric and semiconductor. Results of MOS capacitors using sol-gel, metal oxide dielectrics are discussed in chapter 5, section 5.1.

2.4.2 Metal-Oxide-Semiconductor Field Effect Transistors (MOSFETs)

The transformation from a MOS capacitor to a MOSFET device occurs via two highly doped semiconductor areas at the oxide-semiconductor interface to form source and drain electrodes, with the doped areas being opposed to the bulk semiconductor doping (e.g. bulk n-type semiconductor has p-doped source-drain and vice versa). The oxide electrically insulates the gate from the other elements of the MOSFET. Figure 2.7a shows a schematic of a MOSFET with a bulk p-type semiconductor and doped n-type source-drain regions under equilibrium ($V_{DS} = 0$), which will be referenced for explanation of MOSFET operation hereafter. Alongside the MOSFET schematics throughout this section is the measurement of current between source and drain electrodes, I_{DS}, due to an applied bias between the electrodes, V_{DS}. To maintain simplicity, the MOSFET is considered a 3-terminal device and ignores the "body effect" that considers a source-to-substrate (V_{SB}) bias that operates as a second bottom gate terminal. The additional bias causes a larger threshold voltage, thus a larger gate voltage is required to operate and populate the channel with carriers [248]. Understanding the operation of the MOSFET - and subsequently the TFT – allows derivation of the key performance metrics for the transistors in this work. Visually, it can be seen that the architectural differences between a MOS capacitor and MOSFET are very few. The key difference is the addition of the doped (n-type) regions that allows perpetual contribution to the generation of free carriers, including under the absence of a source-drain bias ($V_{DS} = 0$). Thus, free carrier generation is achieved far quicker than the MOS capacitor. With a non-zero V_{DS} and a sufficient modulating voltage applied at the gate (V_{GS}), the electron cloud formed at the oxide-semiconductor interface during an inversion process accelerates from source to drain via a channel, collecting current I_{DS} at the drain. The channel dimensions are defined by the length (L) and width (W) of the source-drain electrodes, and will later be displayed to be linked to the carrier mobility in the channel. Figures 2.7 b-d presents the MOSFET in the state where V_{DS} is non-zero. This current collection occurs in distinct operating regimes of inversion charge.

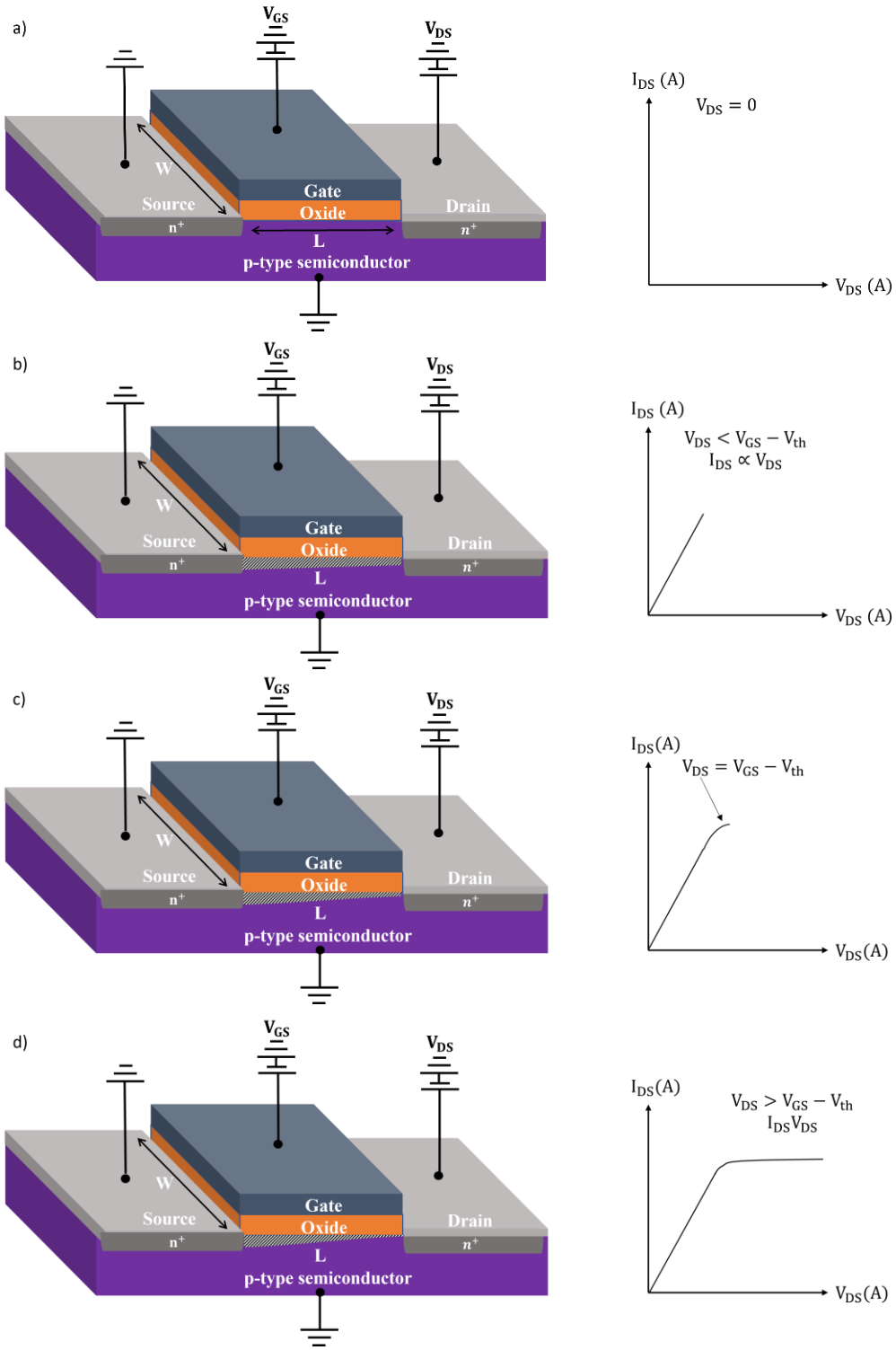

Figure 2.7. Schematic showing the architecture and key components of a MOSFET device, as well as the evolution of operating regimes with increasing V_{DS}. In each figure, p-doped Si semiconductor is shown in purple, the oxide/dielectric in orange, source-drain electrodes in light grey, n-doped regions of the Si in dark-grey and gate electrode in the blue grey. a) $V_{DS} = 0$, where no current is collected at the drain. In 2.7a, the channel length L and width W are also indicated. b) $V_{DS} < V_{GS} - V_{th}$, yielding the linear region of operation. In this and following figures, the formed channel and charge transport between source-drain is indicated by the black and white striped area between source and drain. c) $V_{DS} = V_{GS} - V_{th}$, where incremental increases in V_{DS} gradually narrow the channel at the drain end. This eventually leads to pinch-off. d) $V_{DS} > V_{GS} - V_{th}$, producing the saturation regime after pinch-off is reached.

i) In the linear regime, where small values (relative to the materials used) of V_{DS} are used ($V_{DS} < V_{GS} - V_{th}$ where V_{th} is the threshold voltage), the inversion charge has an even distribution throughout the MOSFET channel, described by:

$$q_{ch} = W \cdot L \cdot Q_{inv} = W \cdot L \cdot C_{ox}(V_{Gs} - V_{th}) \quad 2.59$$

where q_{ch} is the total charge per channel area, Q_{inv} the is inversion charge density and C_{ox} is the capacitance of the oxide layer. Furthermore, the average time for a carrier to accelerate from source to drain, τ_{DS}, is:

$$\tau_{DS} = \frac{L}{\upsilon_d} = \frac{L}{\mu_n E} = \frac{L}{\mu_n V_{DS} L^{-1}} = \frac{L^2}{\mu_n V_{DS}} \quad 2.60$$

where υ_d is the electron drift velocity, μ_n is the carrier mobility in the channel (in this case electrons) and E is the electric field. In one of its most trivial forms, $I = \frac{Q}{t}$, therefore:

$$I_{DS} = \frac{q_{ch}}{\tau_{DS}} = \frac{W \cdot L \cdot C_{ox}(V_{Gs} - V_T)}{\frac{L^2}{\mu_n V_{DS}}} \Rightarrow I_{DS} = \frac{W \cdot \mu_n \cdot C_{ox}}{L}(V_{Gs} - V_T) \cdot V_{DS} \quad 2.61$$

This current-voltage relationship that's linear in nature describes a resistor following Ohm's Law, thus deriving the MOSFET linear regime at low values of V_{DS} where $V_{DS} < V_{GS} - V_{th}$. This is schematically described in Figure 2.7b.

ii) If it is now assumed V_{DS} has continued to increase, according to equations 2.59—2.61 inversion charge density around the drain area will be altered (as V_{GS} and V_{DS} interfere). By further assuming the channel as a set of infinitesimal MOSFETS in series, V_{DS} can be expressed as the summation of infinitesimal voltage drops dV across an infinitesimal distance dx. One MOS transistor with a voltage drop dV across distance dx and an incremental inversion charge dq thus leads to:

$$dq = W \cdot C_{ox} \cdot dx \cdot [V_{GS} - V(x) - V_{th}] \quad 2.62$$

where $V(x)$ is the channel voltage at x. To maintain conservation of charge, I_{DS} in each of the MOS transistors across the channel should be identical to the current through the entire transistor:

$$I_D = \frac{dq}{d\tau} = W \cdot C_{ox} \cdot dx \cdot \frac{[V_{GS} - V(x) - V_{th}]}{(dx^2/\mu dV)} = \mu C_{ox} W[V_{GS} - V(x) - V_{th}]\frac{dV}{dx} \quad 2.63$$

Integrating across the channel to solve the differential gives:

$$I_D = \int_0^{V_{DS}} dx = \mu C_{ox} W \int_0^{V_{DS}} [V_{GS} - V(x) - V_{th}] dV \qquad 2.64$$

Substituting for equivalent terms and completing the integration gives:

$$I_D = \frac{\mu C_{ox} W}{L} \left[(V_{GS} - V_{th}) V_{DS} - \frac{V_{DS}^2}{2} \right] \qquad 2.65$$

Eq. 2.65 only holds when the channel extends across the entire source-drain area, where $V_{DS} < V_{GS} - V_{th}$. Once $V_{DS} = V_{GS} - V_{th}$, inversion charge dq across the drain $(V(x) = V_{DS})$ will become 0.

This leads to a narrowing of the channel, as depicted by Figure 2.7c, which is known as pinch-off. The current at $V_{DS} = V_{GS} - V_{th}$ that initiates pinch-off is known as the saturation current, $I_{DS,sat}$, and is extracted from eq. 2.66:

$$I_{DS,sat} = \frac{\mu C_{ox} W}{2L} (V_{GS} - V_{th})^2 \qquad 2.66$$

The voltage at one end of the channel remains defined and stable according to $V_{GS} - V_{th}$, since this initiates the strong inversion that forms the channel. Once $V_{DS} \geq V_{GS} - V_{th}$, pinch-off begins to move to the left and the channel begins to shorten. When an increasing V_{DS} is applied to the shorter channel, I_{DS} does not increase with it. Instead, electrons are brought into-pinch-off via drift and collected in the drain by the electric field. The voltage drop across the shortened channel is $V_{GS} - V_T$, which is not dependent on V_{DS}, so I_{DS} remains constant. This is demonstrated in Figure 2.7d.

Eq. 2.66 (saturation regime) is valid at the onset of $V_{DS} \geq V_{GS} - V_{th}$ using a channel length L that is assumed to be constant. This analytical approach is known as the "gradual channel approximation." However, it is clear the effective channel length in post-pinch-off is smaller than L which was not a parameter included in the model. The measurement of I_{DS} vs V_{DS} with gradually increasing V_{GS} modulating the magnitude of I_{DS} is known as the output curve, and is typically conducted first to determine the TFT is switching and is accumulating charge as desired. An example of an output measurement is given in Figure 2.8a.

The extracted performance metrics of MOSFETS rely on the definitions for onset of the linear and saturation regimes according to changes in I_{DS} modulated by V_{DS} and V_{GS}. For carrier mobility μ, different mobilities are attributed to each regime. For the linear regime, eq. 2.65 is rearranged to determine μ_{lin}:

$$I_{DS} = \frac{W \cdot \mu_{lin} \cdot C_{ox}}{L}(V_{Gs} - V_{th}) \cdot V_{DS}$$

$$\Rightarrow \quad \frac{\partial I_{DS}}{\partial V_G} = \frac{W \cdot \mu_{lin} \cdot C_{ox}}{L}\frac{\partial (V_{GS} - V_{th})}{\partial V_G} V_{DS}$$

$$\Rightarrow \quad \mu_{lin} = \frac{L}{W \cdot C_{ox} V_{DS}}\frac{\partial I_{DS}}{\partial V_G} \qquad 2.67$$

In the saturation regime, saturation mobility μ_{sat} is obtained by rearranging eq. 2.66:

$$I_{DS,sat} = \frac{\mu_{sat} \cdot C_{ox} \cdot W}{2L}(V_{GS} - V_{th})^2$$

$$\Rightarrow \quad \frac{\partial^2 I_{DS,sat}}{\partial V_G^2} = \frac{\mu_{sat} \cdot C_{ox} \cdot W}{2L}\frac{\partial^2 [(V_{Gs} - V_{th})^2]}{\partial V_G^2}$$

$$\Rightarrow \quad \mu_{sat} = \frac{L}{C_{ox} W}\frac{\partial^2 I_{DS,sat}}{\partial V_G^2} \qquad 2.68$$

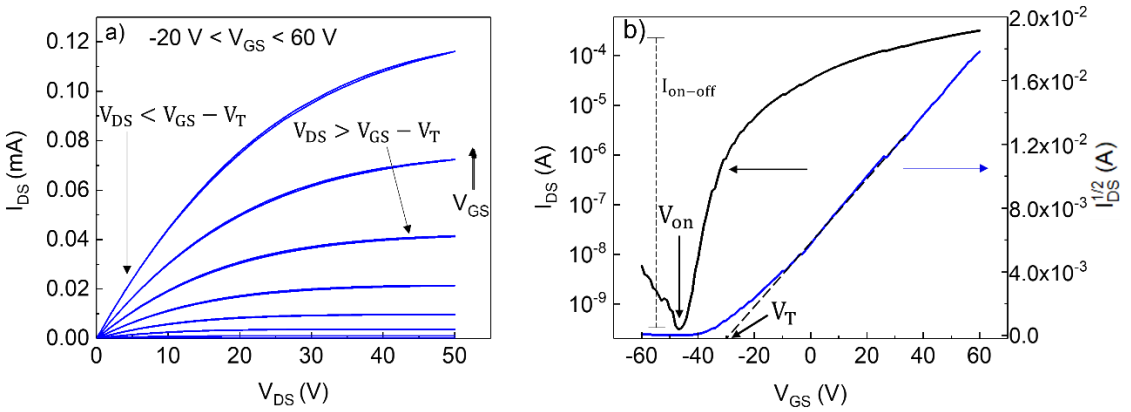

Figure 2.8. a) Example of the measurement of a family of output curves for an n-channel TFT. The linear region and saturation regions, as well as the V_{GS} values swept, are indicated. b) Example of a transfer curve for an n-channel TFT with $I_{DS}^{1/2}$ plotted on the second y-axis, used to extract μ, $I_{On/Off}$, V_{on} and S.

Higher values of mobility are sought as they represent maximum output performance via I_{DS} and the ability to operate TFTs at higher frequencies. Aside from μ, there is also the on-off current ratio ($I_{On/Off}$), threshold voltage (V_{th}) and subthreshold swing (SS). $I_{On/Off}$ is the ratio between maximum I_{DS} in the on state (i.e. when $V_{GS} > V_{th}$) and minimum I_{DS} in the off state (i.e. when $V_{GS} < V_{th}$). A higher ratio is demonstrative of better switching capability and lower power consumption (in some cases). The value of the ratio is inherently limited by the lower value of I_{DS}, since leakage current paths in the dielectric will prevent this from being exceedingly low. Also important is V_{th}, the gate voltage required to form the TFT channel in the oxide-semiconductor interface, with this initiating the linear regime. It is typically extracted via

extrapolation of the $\sqrt{I_{DS}}$ vs V_{GS} linear plot, with the x-intercept of the plot representing V_{th}. A near—zero V_{th} is desired to permit low-voltage operation for lower power consumption. In some cases, the onset voltage, V_{on}, is expressed instead, where I_{DS} is minimised before a substantial increase. Differences between V_{th} and V_{on} can be minimal to substantial depending on the accuracy of the extrapolation used to extract V_{th}. Throughout the results of this report, V_{on} is used far more frequently for that reason. The maximisation of $I_{On/Off}$ and minimisation of V_{on} to 0 is required for a TFT with reduced power consumption.

Subthreshold swing SS is a parameter used to describe the transition between the off state and maximum I_{DS}, which is characterised by the amount of V_{GS} required to increase I_{DS} over one decade:

$$SS = \frac{\ln(10)nkT}{q} \tag{2.70}$$

where n is an ideality factor accounting for non-ideal MOSFET behaviour. SS is extracted via the inverse slope of I_{DS} vs V_{GS} below the value of V_{th}. Small values of SS indicate a steep transition to the maximum I_{DS}, thus smaller values are more desirable. From eq. 2.70, it can be observed that SS becomes theoretically limited with electrical measurements at room temperature due to the thermal energy of the electrons, sometimes referred to as the Boltzmann limit. Reducing to low temperatures (< 50 K) produces lower values and a step-like switching behaviour. By applying $T = 300K, n = 1$ (i.e. ideal MOSFET behaviour) and the values of the physical constants, the value corresponding to a room temperature theoretical limit is obtained:

$$S = \ln(10)\frac{300(1.38 \times 10^{-23})}{1.6 \times 10^{-19}} = 59.6\ \text{mV/decade} \tag{2.71}$$

Extracting μ, $I_{On/Off}$, V_{on} and S for a TFT is conducted via an electrical measurement known as the transfer curve, with an annotated version of a typical measurement displayed in Figure 2.8b. Certain values are not alluded to in these metrics, but are noteworthy for reviewing transistor performance and imparting useful information about the film properties. Tracking of the increasing current through the gate, I_{GS}, denotes unwanted current pathways from the gate through the insulating dielectric. Hysteresis is also monitored, as the directionality and magnitude of a hysteresis can be linked to defects in the TFT layers, among other important features. It is desirable for hysteresis and I_{GS} to be minimised as much as possible.

2.4.3 Thin-Film Transistors (TFTs)

The core differences in MOSFETS and TFTs lies in their operating modes and architecture. MOSFETs employ inversion mode between the source-bulk semiconductor drain area for channel formation, attracting charge carriers that are opposing charge to the bulk at an interface and forming an inversion layer. TFTs rely on a metal-semiconductor-metal structure that enforces the accumulation mode, attracting the same charge carrier type that is dominant in the semiconductor to an interface.

The difference in operation mode is derived from the difference in architectures and difference in properties of the materials involved. TFTs use deposited layers of semiconductor in proximity to the oxide, as well as conductive (metallic) electrodes - to form the channel instead of highly doped semiconductor areas on crystalline bulk Si. Aside from different operating modes, the use of deposited layers leads to freedom of different device architectures such as those in Figure 2.9 that are adopted for different reasons. For example, a bottom gate, top contact (BGTC) sandwich structure in Figure 2.9a is very simple to fabricate while co-planar electrodes can be staggered electrodes so parasitic capacitances can be reduced [249]. This less rigid approach to transistor fabrication constitutes the main benefit, since a plethora of material classes fabricated, processed and implemented in different ways paves the way to potentially improved performance.

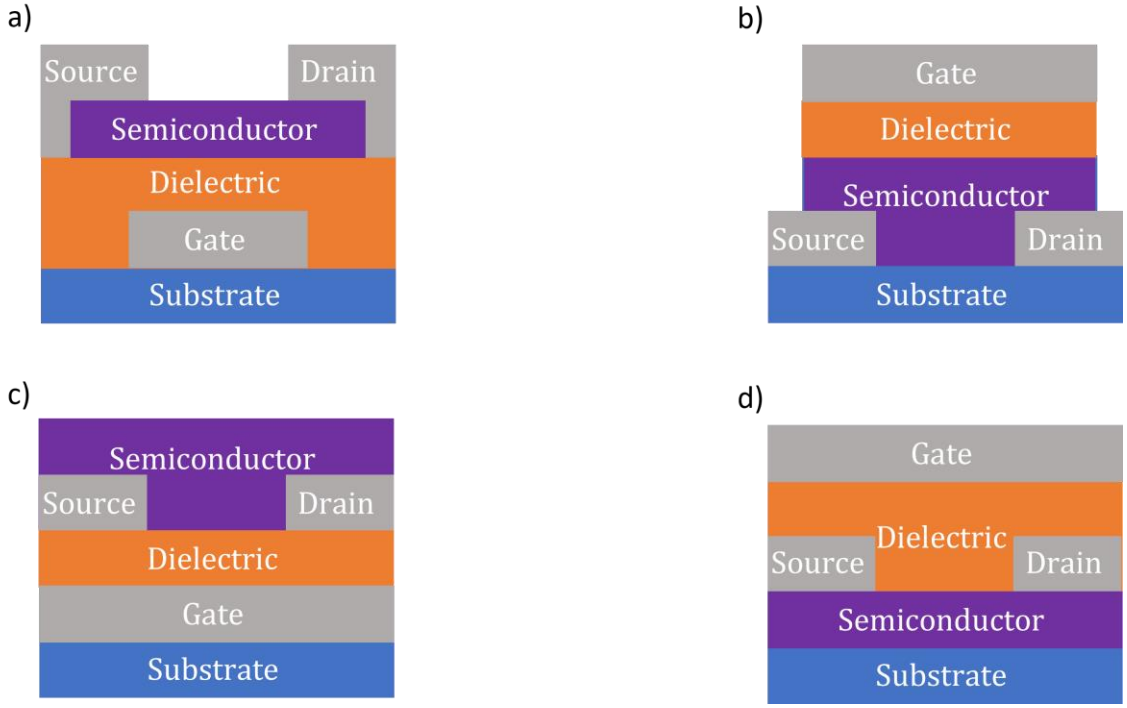

Figure 2.9 Example of different TFT architectures. a) Bottom-gate, top contact. b) Top-gate, bottom contact. c) Bottom gate, bottom contact. d) Top contact, top gate.

2.4.4. Schottky Diodes

Diodes of various types were the first semiconductor electronic devices, taking form in 1874 (far before transistors around 1947 [250]) when Ferdinand Braun[251] tested interaction of metal contacts with Cu, Fe and PbS crystals. The most basic definition of a diode is a device permitting a one-way flow of electrical current. Like transistors, diodes are fundamental to modern electronics since they have been integrated into various displays, logic circuits and radiation detectors among other applications. Particularly of interest in the modern age and development of the IoT are radio frequency (RF) diodes which are key to realising the IoT network via fast, seamless device intercommunication. Within any device compatible to the IoT exists a RF identification tag (RFID), that characterise the object and allows carriage of information to each device. RFIDs are comprised of an antenna, rectifier (including the RF diode) and logic circuitry. The antenna receives the AC signal from another IoT device, which is then rectified to a DC signal as a power supply for the logic circuit to operate the modulating transistor between an on or off state [252]. RFID tags can be powered by the RF wave being received (passive) or powered by a separate battery (active). Since each device within the IoT requires RFID tags, LAE using flexible substrates presents an attractive solution to meeting device volume demands, since the Si-based electronics lack the mechanical flexibility to do so. This drive to realise large-scale RFIDs in RF electronics is driving technological development in 5G/6G communication and wireless energy harvesting. By the inherently cheaper nature of passive tags (since a battery doesn't have to be manufactured and integrated), passive tags dominate the market and are more viable for the LAE approach.

In this thesis, a chapter of results is dedicated to fabrication of RF diodes via photonic processing and methodologies amenable to LAE. Therefore, it is necessary to delve into the fundamental understanding of the physics of the diode to interpret the results. In particular, Schottky diodes (and the metal-semiconductor-metal junction) are a focal point for RF diodes due to their demonstrated low turn-on voltage, high switching speed and low junction capacitance which lends them to fast, high frequency operation [253]. Thus, they have been implemented with a wide variety of material classes including metal oxides.

The theory for modern rectifying diodes was established by Mott [254] and Schottky [255] in the 1930s, investigating the interaction and formation of potential barriers between metal-semiconductor interfaces (contacts). The investigations by Mott led to establishing Ohmic contacts, while Schottky's investigations led to Schottky contacts. Ohmic contacts are formed when the work function Φ_{M} of the metal is aligned with the work function of the semiconductor Φ_{SC}. The equal work functions cause no barrier to charge carrier injection thus $\mathrm{I}-\mathrm{V}$ characteristics follow Ohm's Law. With Schottky contacts, the work function of the metal and

semiconductor are misaligned, causing a barrier that limits charge carrier injection. Figure 2.10 shows the band structures of a Schottky junction before contact (Figure 2.10a) and after contact (Figure 2.10b), assuming an n-type semiconductor like that of the metal oxide semiconductors in this work.

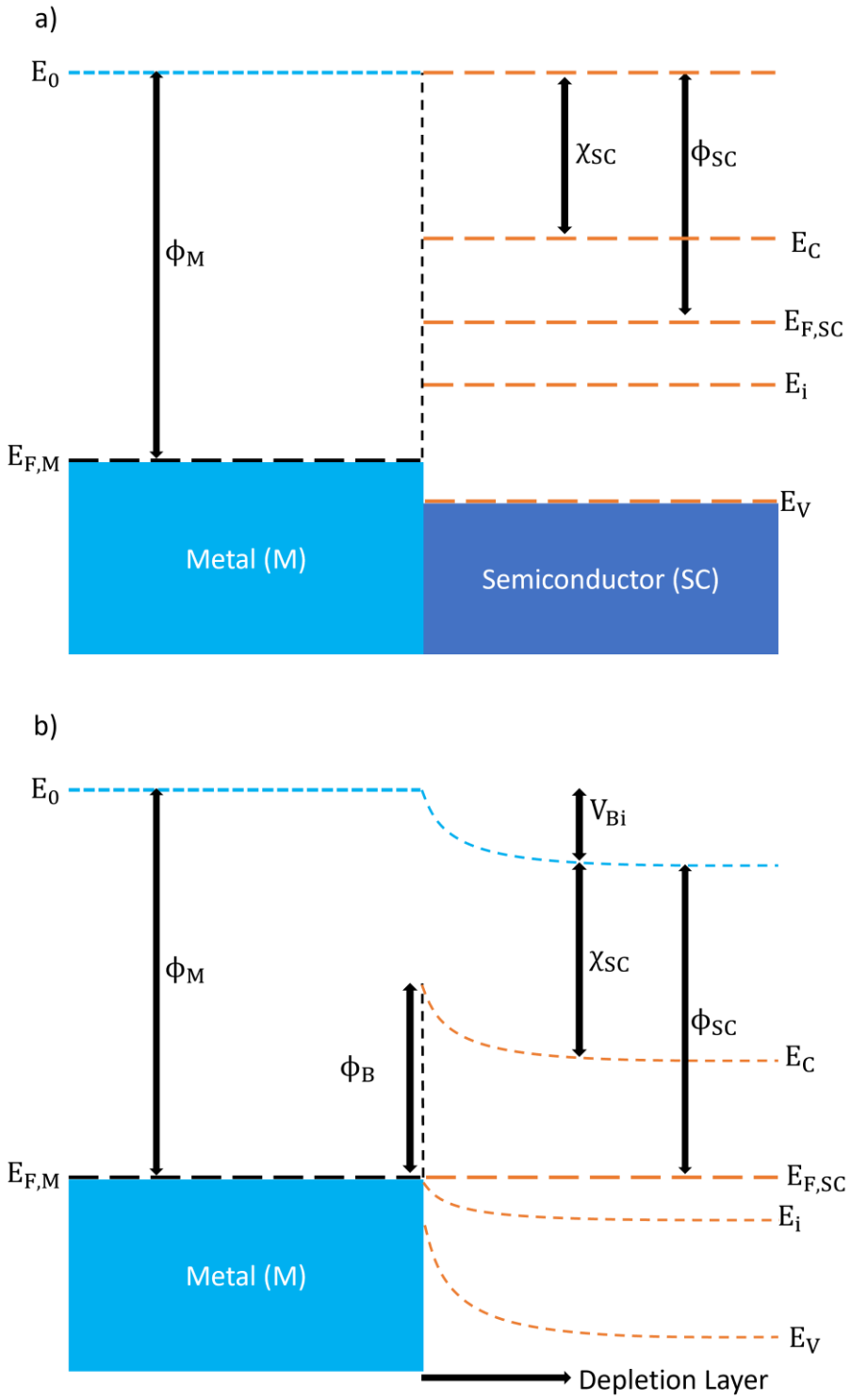

Figure 2.10 Energy band diagram for a Schottky junction between a metal and an n-type semiconductor a) before contact; b) after contact. Before contact, the Fermi levels of metal and semiconductor are misaligned and the bands straight. After contact, electrons flow from semiconductor to metal until Fermi levels align, causing semiconductor band bending.

With a metal-semiconductor junction with mis-aligned work functions under thermal equilibrium, electrons flow from semiconductor to the metal until the Fermi levels are aligned. This leads to band bending in the semiconductor with the formation of an energy barrier and a depletion region at the junction. The extent of band bending defines the barrier height that charge carriers have to overcome at the metal-semiconductor junction [256]. The barrier for electrons is known as the Schottky barrier with height Φ_B, and is given as:

$$\Phi_B = \Phi_M - \chi_{SC} \qquad 2.72$$

where χ_{SC} is the electron affinity of the semiconductor. Eq. 2.72 gives the barrier purely in terms of electron affinity, but several practical cases will also have to account for other effects such as interfacial states/defects, tunnelling-induced dipoles and surface states to accurately represent barrier formation and charge carrier transport in semiconductors [256]. Charge (electron) transport across the Schottky barrier can occur via several mechanisms. In a lightly doped semiconductor where charge carrier density is relatively low, a thermionic emission model can be followed such that only electrons with sufficiently high thermal energy can overcome the energy barrier (i.e. $\Phi_B \gg kT$) [257]. With a moderately doped semiconductor, a narrow barrier width permits tunnelling of the charge carriers as well as thermionic emission. Heavily doped semiconductors favour tunnelling as the dominant mechanism. Schematics of the various mechanisms are shown in Figure 2.11. Ultimately, the barrier height and semiconductor doping defining the charge transport, thus the diode behaviour. Hence determining the barrier height is of importance.

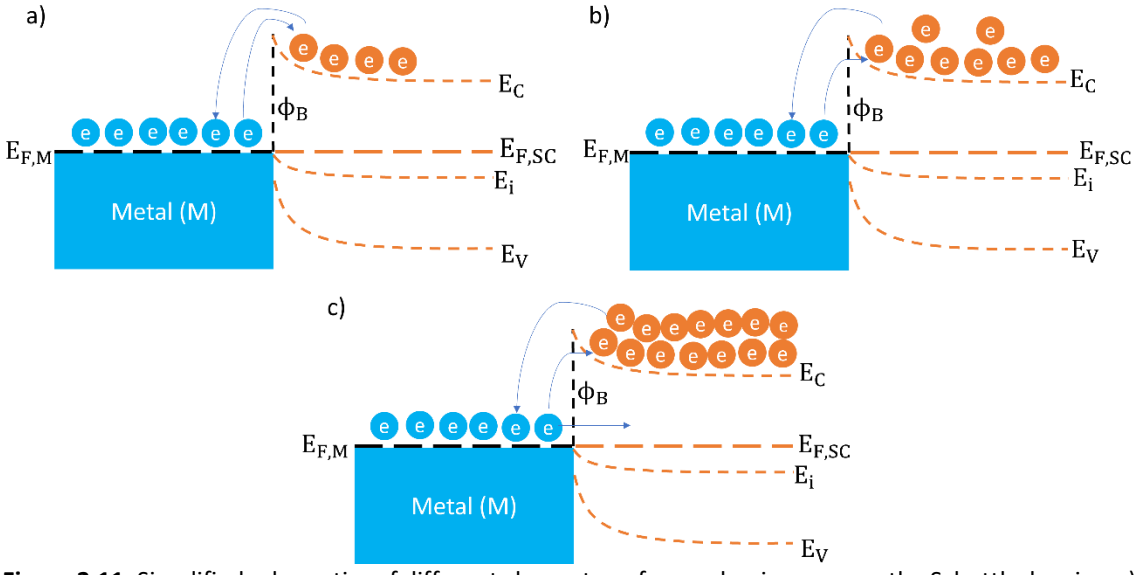

Figure 2.11. Simplified schematics of different charge transfer mechanisms across the Schottky barrier. a) Thermionic emission. b) A combination of thermionic emission (over the barrier) and barrier tunnelling (through the barrier). c) Emission entirely via tunnelling.

If one side of a metal-semiconductor contact forms an Ohmic contact while the other metal semiconductor junction forms a Schottky (rectifying) contact, a Schottky diode is formed. A Schottky diode will conduct electricity in forward bias and not reverse bias. The forward bias is predominantly due to thermionic emission, but tunnelling mechanisms can contribute along with carrier recombination in the depletion region and the semiconductor. The current transport due to dominant thermionic emission is given by:

$$\mathrm{I} = \mathrm{I_o} e^{\frac{\mathrm{qV}}{\mathrm{nkT}}} \tag{2.73}$$

and $\mathrm{I_o}$ is the reverse bias saturation current given as:

$$\mathrm{I_o} = \mathrm{SA^* T^2} e^{\frac{\mathrm{q}\Phi_\mathrm{B}}{\mathrm{kT}}} \tag{2.74}$$

In the above equations, q is electron charge (Coulombs), V is the voltage, n is the diode ideality factor, k is Boltzmann's constant (1.381×10^{-23} J/K), T is the temperature in K, S is the diode area in cm^2, A^* is the effective Richardson constant and Φ_B is the Schottky barrier height. Rearranging eq. 2.74 into a linear form unveils that the plot of $\ln \frac{\mathrm{I_o}}{\mathrm{ST^2}}$ vs $\frac{1}{\mathrm{kT}}$ can extract Φ_B and A^*, which is known as a Richardson plot. Aforementioned deviations from ideal behaviour can be due to a series resistance, $\mathrm{R_S}$, which is the combination of semiconductor sheet resistance, Ohmic contact resistance and Schottky contact resistance. This can be modelled as [258]:

$$\frac{\mathrm{dV}}{\mathrm{d(\ln I)}} = \mathrm{RI} + \frac{\mathrm{n}}{\beta} \tag{2.75}$$

where $\beta = \frac{\mathrm{q}}{\mathrm{kT}}$. Plotting $\frac{\mathrm{dV}}{\mathrm{d(\ln I)}}$ vs I and fitting the linear region outputs a value of $\mathrm{R_S}$ from the slope, while n is the intersect. To determine the barrier height, an additional function is used:

$$\mathrm{H(I)} \equiv \mathrm{V} - \frac{\mathrm{n}}{\beta} \ln\left(\frac{\mathrm{I}}{\mathrm{A_{eff} A^* T^2}}\right) \tag{2.76}$$

Plotting $\mathrm{H(I)}$ against I and fitting the linear region gives a second different approximation of $\mathrm{R_S}$ and Φ_B as the slope and intersect, respectively:

$$\mathrm{H(I)} = \mathrm{RI} + \mathrm{n}\Phi_\mathrm{B} \tag{2.77}$$

Thus, $\mathrm{I-V}$ characteristics can be used to estimate Φ_B and A^*. As there is a temperature dependency (eq. 2.76), the $\mathrm{I-V}$ characteristics must be temperature dependent ($\mathrm{I-V-T}$)

characteristics). Further modifications to the Richardson plot to extract Φ_B and A^* more accurately include the temperature dependence, using a temperature dependent function for the ideality factor and barrier height [259]:

$$n(T) = a + \frac{b}{T} \tag{2.78}$$

$$\Phi_B(T) = \Phi_{B0} - \alpha T \tag{2.79}$$

where Φ_{B0} is the apparent barrier height at T=0, T is temperature and a, b and alpha are constants. The true flat band barrier height, Φ_{BFB}, is obtained by:

$$\Phi_{BFB} = n\Phi_B - (n-1)\frac{kT}{q}\ln(\frac{N_C}{N_D}) \tag{2.80}$$

where N_C is the density of states in the conduction band and N_D is the doping concentration. Incorporating these temperature dependencies to the rearrangement of eq. 2.74 derives a modified saturation current:

$$n(T)\ln\left(\frac{I_0}{ST^2}\right) = -\frac{1}{kT}(\Phi_B - kb\ln(A)) + a\ln(A) + \frac{\alpha}{k} \tag{2.81}$$

By plotting $n(T)\ln\left(\frac{I_0}{ST^2}\right)$ against $\frac{1}{kT}$ and obtaining a line of best fit, Φ_B and A^* can be more precisely extracted.

The above completes the demonstration of extracting these values via $I-V$ and $I-V-T$ characteristics. However, $C-V$ characteristics can also act as an alternative to precisely determine Φ_B. Specifically, the Mott-Schottky plot, $f(V) = \frac{1}{C^2}$, can calculate the voltage at which there is no band bending, known as the built-in voltage (V_{Bi}). At V_{Bi}, there is also no charge depletion that causes separation between the depletion region, the accumulation region and any doped regions of concentration $N_{A/D}$. In full, the Mott-Schottky plot is:

$$\frac{1}{C^2} = \frac{2(V_{Bi} - V - \frac{kT}{q})}{A^2 q\varepsilon\varepsilon_0 N_{A/D}} \tag{2.82}$$

where ε is the semiconductor dielectric constant. Φ_B can then be calculated from the extracted values of V_{Bi} and $N_{A/D}$:

$$\Phi_B = V_{Bi} + \frac{kT}{q}(\ln\frac{N_{CB}}{N_{A/D}} + 1) \tag{2.83}$$

where N_{CB} is the effective density of states in the conduction band:

$$N_{CB} = 2\left(\frac{2\pi m^* kT}{h^2}\right)^{3/2} \quad 2.84$$

where m^* is the effective mass of electrons in the semiconductor. For the capacitance values, a device with no semiconductor present can measured to determine the capacitance contribution from the complete device [260].

Similar to transistors, there are key performance metrics that define the quality of the Schottky diode. Principally, there is the rectification ratio that is expressed as the ratio of the forward current to the reverse current with the same absolute value of voltage:

$$\text{Rectification ratio} = \left|\frac{I_F(V)}{I_R(V)}\right| \quad 2.85$$

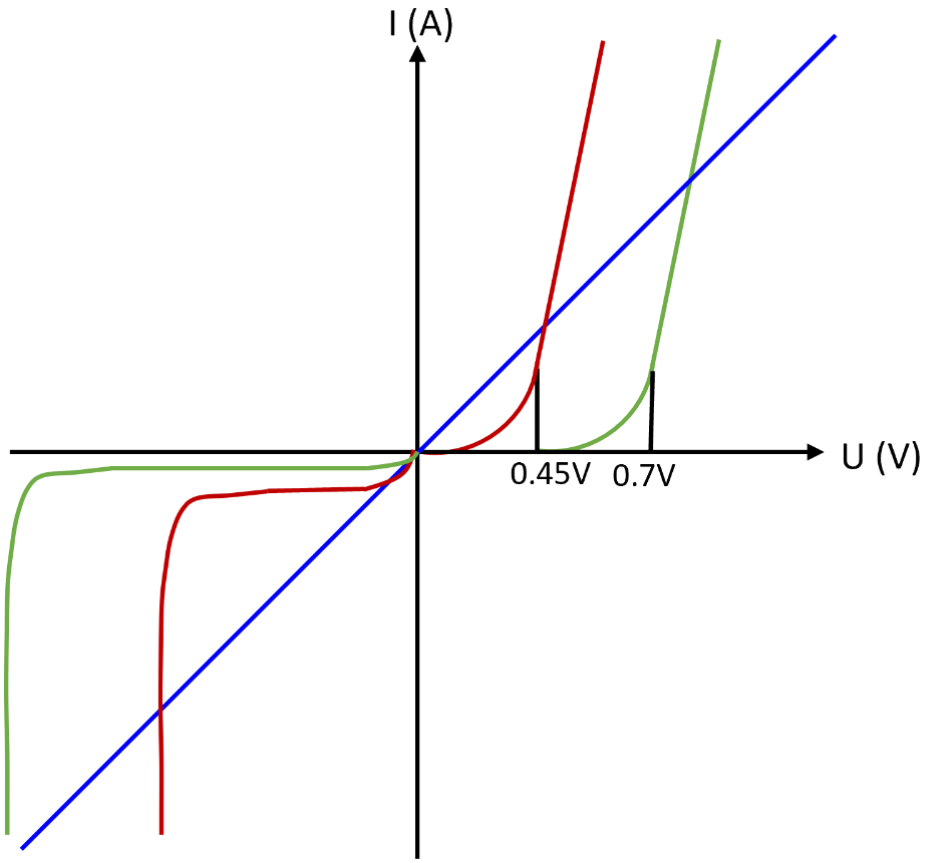

Figure 2.12. The differing current-voltage (I-V) characteristics of metal-semiconductor contacts for a n-type semiconductor. The linear blue line is that of an Ohmic contact, the curved steep red line a rectifying Schottky diode and the curved shallower green line describes a pn junction diode. The differences in turn-on voltage between Schottky and pn junction diodes are indicated.

Also relevant is the turn-on voltage, which for Schottky diodes is expected to be lower than typical Si pn junctions due to the formation of a low depletion region at one side of the metal-semiconductor junction, with coincides with a lower barrier height that requires a lower

potential to overcome [256]. Turn-on voltage is extracted from fitting 2 linear lines to different regions of the $\mathrm{I}-\mathrm{V}$ curve, then extracting the point at which they intersect. Figure 2.12 shows examples of an Ohmic, Schottky and pn junction behaviour. The blue line shows the Ohmic contact, the curved steep red line is the Schottky diode and curved, shallower green line a pn junction diode.

Non-linearity values of a diode may also be extracted. This value measures the deviation of the Schottky diode from Ohmic behaviour via the ratio of differential conductance ($\frac{\mathrm{dI}}{\mathrm{dV}}$) to the conductance ($\frac{\mathrm{I}}{\mathrm{V}}$):

$$\mathrm{Non-linearity\ (V)} = \frac{\frac{\mathrm{dI}}{\mathrm{dV}}(\mathrm{V})}{\frac{\mathrm{I\ (V)}}{\mathrm{V}}} \qquad 2.86$$

Ideally, a non-linearity of 3 or greater is obtained [261].

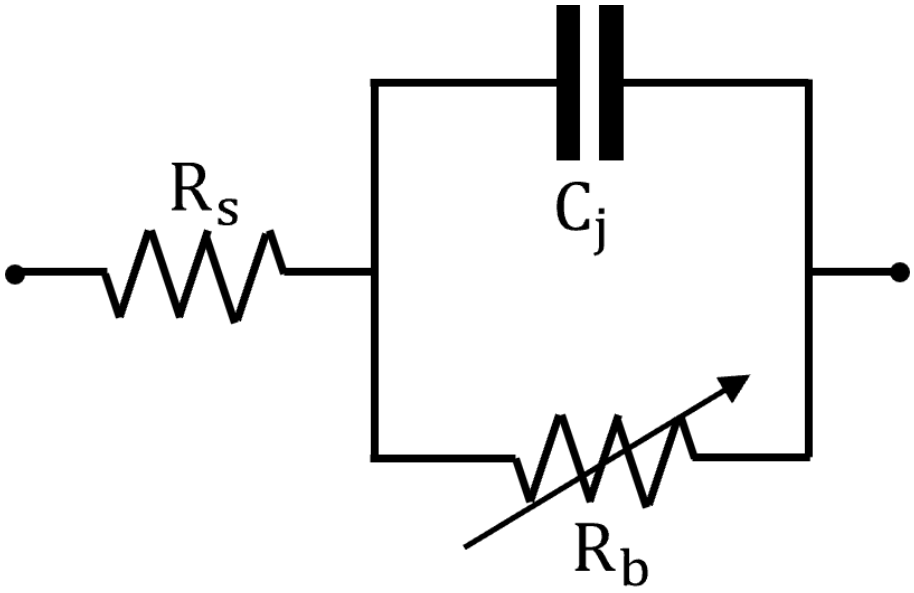

Figure 2.13. Equivalent circuit model of a Schottky diode. The model comprises a series resistance $\mathrm{R_S}$ due to intrinsic semiconductor resistance and contact resistance, barrier resistance $\mathrm{R_b}$ due to resistance of emission past the Schottky barrier and junction capacitance $\mathrm{C_j}$ between the metal and semiconductor.

The cut-off frequency value dictates the high frequency operation range of the diode. It is important to distinguish that two types of cut-off frequency exist and are reported in the results of this work for the diode's efficacy in RF electronics [252]. Intrinsic frequency ($\mathrm{f_{c,int}}$) is measured by one-port $\mathrm{S_{11}}$ dynamic reflection measurements that allows losses from reflection, impedance mismatching and dielectric losses [261] to be neglected when evaluating voltage progression with frequency, thus demonstrating a theoretical limit of the DUT. On the other hand, extrinsic frequency ($\mathrm{f_{c,ext}}$) measures this voltage progression when in a rectifier circuit,

thus losses are incorporated and a more practical value for real systems. By definition, $f_{c,int}$ is always higher than $f_{c,ext}$. $f_{c,int}$ is extracted via an equivalent circuit model of the device as in Figure 2.13, with a device resistance R_S in parallel with a non-linear barrier resistance R_b and metal-semiconductor junction capacitance C_j.

The source of R_S arises from inherent semiconductor sheet resistance and metal-semiconductor contact resistance:

$$V_{Out} = V_{in} \frac{X_c}{\sqrt{R_s^2 + X_c^2}} \qquad 2.87$$

where X_C is the reactance associated with C_j, and is given as:

$$X_C = \frac{1}{\omega C_j} = \frac{1}{2\pi f C_j} \qquad 2.88$$

where f is the frequency. Two cases occur in eq. 2.87: in lower frequencies, when $X_C \gg R_S$, the series resistance domination allows rectification to occur. At higher frequencies, when $X_C \ll R_S$, current flow shorts through the capacitor and prevents further rectification. $f_{c,int}$ is defined as the threshold between these two behaviours at reasonably high frequencies (i.e. $X_C = R_S$) [252]. From knowing $f_{c,int}$, the RC constant can be calculated:

$$f_c = \frac{1}{2\pi R_s C_j} \qquad 2.89$$

Eq. 2.89 shows that minimisation of R_S and C_j maximises the frequency and increases the chance of the diode being applicable to RF electronics.

While one port S_{11} dynamic reflection measurements are effective at extracting the series resistance, frequency dependent series resistance and junction capacitance values are more reliable for extracting the impedance of the diode and predicting the intrinsic frequency [262], [263]. Once obtained, the impedance of the Schottky diodes is plotted against frequency, with the intersection between real and imaginary components of impedance marking the value for $f_{c,int}$. An example of this is shown in Figure 2.14a [264]. The device impedance is then matched with input RF signal to observe the proportion of input signal allowed. $f_{c,ext}$ is extracted via implementation of the diode to a rectifier circuit such as that in Figure 2.14b. Voltage across the load resistor is measured at incrementing frequency to extract the -3 dB point, which is defined as the frequency where the output voltage, V_{out}, reaches $\frac{1}{\sqrt{2}}$ of the peak value. Figure 2.14c shows an example of an $f_{c,ext}$ measurement [265]. Finally, consideration of the reverse current may be pertinent. The current level in the reverse bias condition, aside from being vital to establish the rectification ratio, contributes to losses in the diode. It is also known that this

current is highly temperature sensitive in Schottky diodes, thus $I-V-T$ characteristics can become necessary.

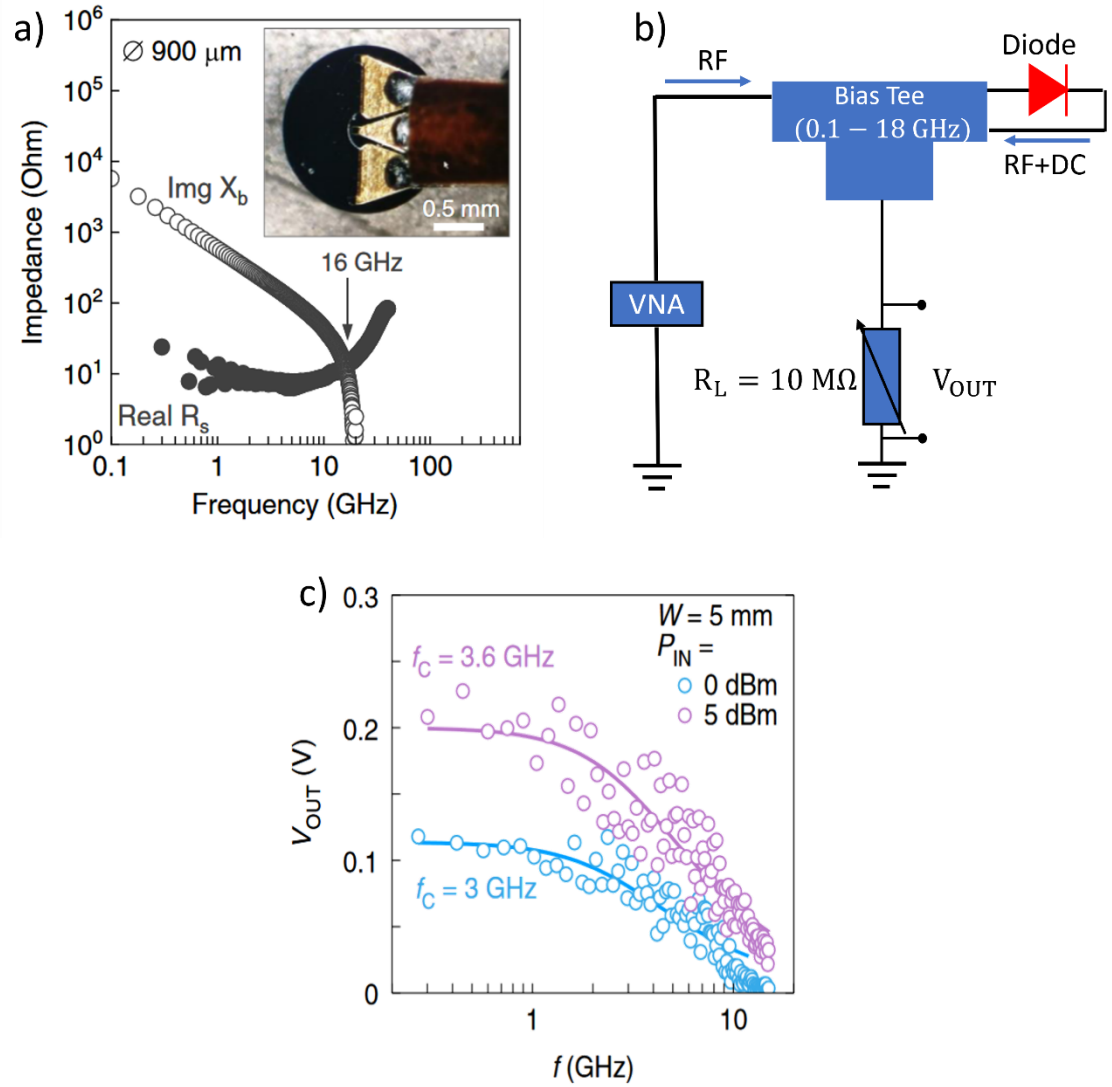

Figure 2.14. a) An example from Loganathan *et al* [264] of an intrinsic cut-off frequency measurement via S_{11} scattering parameter measurement, using a vector network analyser (VNA) and ground-signal ground (GSG) probes in contact with a co-planar diode to measure frequency dependent impedance. The crossover between R_S and X_b outputs the value for $f_{c,int}$. b) The rectifier circuit employed for extrinsic cut-off frequency measurements. The set-up comprises a VNA, a bias tee with suitably high frequency capabilities, a diode and a resistor. The output the rectified RF signal is measured across the load resistor. c) An example from [265] of an extrinsic frequency measurement on a diode using the a-lith methodology and ZnO.

2.4.5 Roadblocks in RF applications

While RFIDs have clearly demonstrated importance and LAE is conceptually a promising manufacturing pathway, several issues must continue to be progressed. The read distance has been continually developed as larger read distances allow communication and scanning in a

wider range of applications. Originally, high frequency tags at $13.56\ \mathrm{MHz}$ were used with a limited read distance of $5-10\ \mathrm{cm}$. Near-field communication (NFC) tags and protocols continue to use this frequency band for purposes such as contactless card and mobile payments at close range, as well as download of digital content at close range. Other ultra-high frequency tags have increased the read distance dramatically to $10-100\ \mathrm{m}$ at frequencies of $2.4\ \mathrm{GHz}$ or higher, allowing bidirectional information transmission - *via* wireless communication and Bluetooth - for wearable health and exercise devices, sensors or headphones, among a litany of other devices [266] [267], [268].

The development of high frequency operation also led to the miniaturisation of tags. Aside from smaller tags being more easily implemented into other applications, this also drove the necessity of more efficient, fast rectifying circuits with low power consumption. Miniaturisation size of the full RFID itself is currently hindered by the size of the antenna, which can potentially be bypassed with novel design [269]. In essence, the epicentre to overcoming several roadblocks of state-of-the-art RFIDs is the operating frequency. By increasing the operating frequency, higher read distances are achieved while lowering power consumption and increasing the range for novel applications and faster electronics in the IoT.

However, the developments of the above were conducted via exploitation of the conventional materials and processes that are increasingly restrictive, namely Si-based CMOS technologies and EUV lithography for metallic electrodes and semiconductors. As these technologies become increasingly restrictive, their cost of manufacturing and complexity increases. Additionally, these materials and processes aren't amenable to LAE which has led to the scrutinization of other patterning methods for metallic electrodes. Soft lithography methods such as scanning probe lithography [270] and moulding [271] have been studied. However, in the last decade the performance exhibited by diodes with metallic electrodes separated by nanogaps are immutable. While nanogaps have been fabricated via mechanical break junctions [272], [273], [274], electrochemical deposition [275], [276], e-beam lithography [277], [278] and nanostructure templating [279], adhesion lithography has proven its capability of producing devices with feature sizes and nanogaps as low as $10\ \mathrm{nm}$ with high yield and admirable performance of $100\ \mathrm{GHz}$ [265]. A-lith uniquely allows the fabrication of asymmetric electrodes with potential of excluding vacuum processes or masks, using two different metals. In short, the process uses a self-assembled monolayer (SAM) to modify the adhesion properties of the first deposited metal (M1) before depositing and selectively removing the second metal (M2) from the SAM/M1 areas that M2 overlaps with. This forms the nanogap as the interface between M1 and M2. The initial a-lith method in 2014[280] utilised photolithography for M1 patterning, thermal evaporation for M1 and first contact glue with electrical tape by the user to manually

remove M2, but astonishing progression in the methodology has since been made on material deposition parameters, chemistry optimisation, sample architecture, electrode shape and the peel-off technique to remove the human element and improve nanogap uniformity and device yield. A recent example is the use of inherent material stresses between an intelligently chosen M1 and M2 causing peel-off [264]. Importantly, the use of sol-gel semiconductors processed with photonic processing (FLA in many recent cases) means the entire process can be macroscopically cold. The automation of the peel-off step and low substrate thermal budget makes a-lith viable with LAE and flexible substrates, with previous a-lith methodologies already being carried out on flexible substrates [10], [281], [282]. It's application also extends beyond ultra-high frequency diodes, having been demonstrated in self-aligned gate TFTs [283], memory devices [284], photodetectors [285] and LEDs [283]. Despite this progress, the patterning of M1 is still largely reliant on photolithography. The results of chapter 7 of this thesis addresses this discrepancy in the methodology using a laser ablation process to pattern M1, followed by application of the a-lith process to fabricate RF diodes.

3. Experimental Methodology

This chapter explains the fundamentals of the thin film fabrication, post-deposition processing and characterisation techniques used in this work to consult the current challenges facing the overarching semiconductor industry and the adoption of MO sol-gel thin films in LAE, via the consultation of the research objectives of this project. The thin film deposition techniques of spin-coating (for MO sol-gel precursors) and thermal evaporation (for metallic thin films and contacts) are explained, along with the post-deposition processing technique of laser annealing that is used in place of TA to convert the MO precursor. The modelling platform used to simulate temperature rises of thin films and explain the LA mechanism is also explained in detail. The adhesion lithography process is explained and how laser patterning can replace lithography within it to move to a maskless, vacuum free process. Finally, a description of various advanced characterisation techniques is given that were used to determine thin film or precursor composition, optical properties, electrical properties and surface topographies.

3.1 Thin Film Fabrication

3.1.1 Spin-coating

Sol-gel synthesis requires the dissolution of a compound (e.g. powder or salt) in a solvent to create a precursor solution, which proceeds to the desirable material after processing. One of the most common methods to distribute a solution across a substrate (wafer size or smaller) is spin-coating, especially for polymer films or photoresist in photolithography in the wider semiconductor industry. During spin-coating, a thin film of solution is deposited evenly across a planar substrate before (or simultaneously) rotating at a constant angular velocity, with the rotation contributing a centrifugal force that spreads the solution across the substrate. Combined with the adaptability of the solution chemistry, multi-stage recipes allow for customisable manufacturing of different architectures via variations in rotating speed, rate of acceleration, spin duration, solution concentration and solvent boiling point. The subsequent critical drying process via exposure to heat and radial solvent evaporation further modifies the properties of the resultant thin film [286].

In this work, rotation speed, solution concentration and spin-coating duration are the primary variables altered for spin-coating, although solvent boiling point and solution concentration (viscosity) also influence the spin-coating. Choice of rotation speed is based on substrate size and geometry, precursor solution viscosity and thus solution concentration. For smaller substrate sizes, non-circular geometries and low rotation speeds ($< 1000\ \mathrm{RPM}$) are avoided as this leads to inadequate flow across the substrate and large edge effects (poor uniformity). Figure 3.1 shows the progression of the thin film during spin-coating.

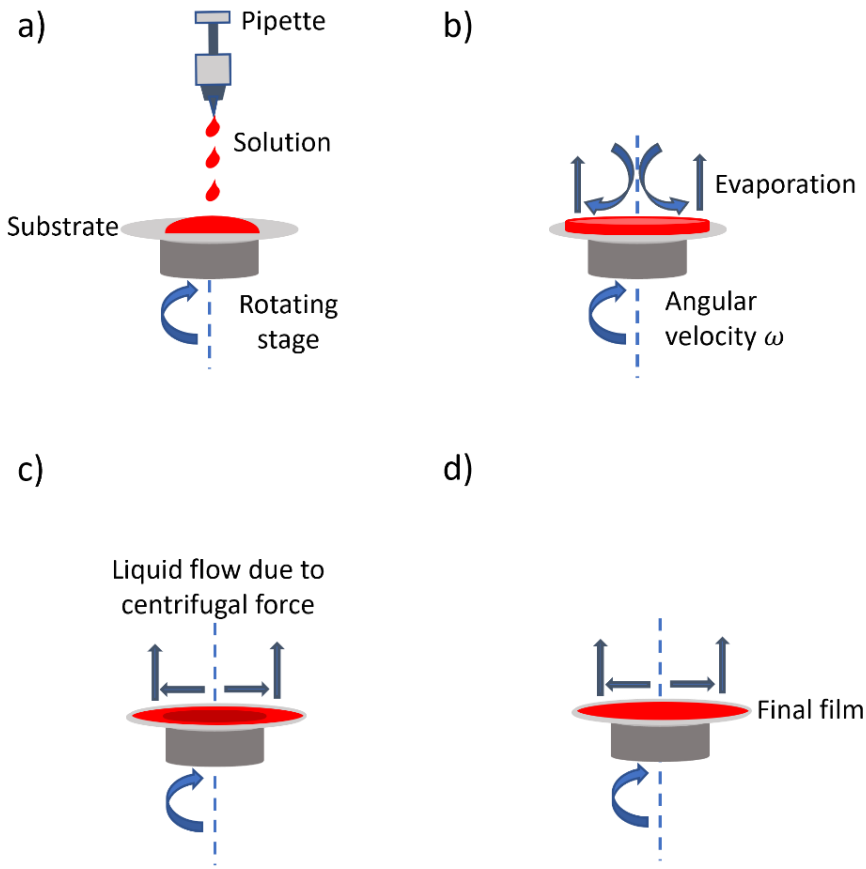

Figure 3.1 Mechanistic steps of the spin-coating process. a) Solution is dispensed onto the substrate surface via a micropipette, which slowly spreads. Substrate rotation is then initiated as soon as possible. b) Immediately after rotation starts, the solution spreads across the substrate due to centrifugal force. c) The solution film thickness continues to decrease with time as rotation continues, with solvent evaporation concurrently reducing thickness further. Evaporation is exaggerated at the edges, where the film is thinner. d) Once rotation is completed, evaporation occurs across the solution thin film that leads to solid thin film formation.

As the film thickness in electronics manufacturing and our opto-thermal simulations plays a crucial role, it is imperative to understand precisely how spin-coating parameters including rotation speed alter thickness. Broadly, spin-coating film thickness is described by:

$$h_f \propto \omega^{-1/2} \qquad 3.1$$

where h_f is the obtained film thickness (as opposed to a nominal thickness) and ω is the substrate angular velocity. While this possibly describes the film thickness due to substrate rotation speed, it omits the influence of several other important parameters previously mentioned (e.g. solution concentration). Several attempts have been made in the literature to obtain precise relations including these parameters. Emslie, Bonner and Peck[287] expanded into the complexity of adding non-Newtonian fluids with associated properties and how these relate to spin-coating parameters, as seen in the below equation:

$$\frac{\partial h}{\partial t} + \frac{\rho\omega^2 r}{\eta} h^2 \frac{\partial h}{\partial r} = -\frac{2\rho\omega^2 h^3}{3\eta} \quad 3.2$$

where h is the thickness of the solution layer, t is the rotating time, ρ is the density of the solution, r the distance to the rotating centre and η is the viscosity of the solution. The time differential $\frac{\partial h}{\partial t}$ represents the dynamic thickness change while radial change $\frac{\partial h}{\partial r}$ is the spreading rate. If the initial film deposition is uniform, the fluid thickness can be described as:

$$h = \frac{h_0}{\left(1 + \frac{4\rho\omega^2}{3\eta} h_0^2 t\right)^{1/2}} \quad 3.3$$

where h_0 represents the uniform film thickness at $t = 0$. However, it omits anything associated with solvent evaporation parameters (radial or temperature-related) thus is incomplete.

Meyerhofer Model

The Meyerhofer model in 1978 [288] attempts to amend this by incorporating a physical constant relating to any evaporation of solvent. They reported the following equation:

$$\frac{\partial h}{\partial t} = \frac{\rho\omega^2 h^3}{3\eta} - E_{evap} \quad 3.4$$

where E_{evap} is the solvent evaporation rate of solvent per unit area, per unit time. The model describes solution thinning to be dominated by different processes at different times. In the early stages of spin-coating, flow (i.e. fluid viscosity) initially dominates the film thinning process where solution spins off due to the high angular velocity. Further thickness reduction after this arises from evaporation phenomena. If the transition is rapid to instantaneous (thus there are well-defined stages of film thinning), the critical point where spin off transitions to thinning by solvent evaporation can be described analytically as:

$$E = \frac{(1 - C)2\omega^2\rho h_0^3}{3\eta} \quad 3.5$$

where h_o is the film thickness at the transition point and C the volume fraction of solute in the film. From rearranging eq. 3.5 and assuming the film thickness of the dried film can be extracted:

$$h_f = \left(\frac{3\eta_0 E}{2(1 - C_0\rho\omega^2}\right)^{1/3} \quad 3.6$$

where C_0 is the initial solution concentration and $n_0 = n(C_0)$. Eq. 3.6 holds as long as C_0 is constant until the critical point. Further calculations excluded the evaporation parameter via an assumption there is constant laminar flow during spin-coating:

$$h_f = \left(\frac{3}{2}\right)^{\frac{1}{3}} k^{\frac{1}{3}} C_0 (1 - C_0)^{-\frac{1}{3}} \rho^{-\frac{1}{3}} \eta_0^{\frac{1}{3}} \omega^{-\frac{1}{2}} \qquad 3.7$$

where k is a solvent dependent constant. Comparing eq. 3.1 to eq. 3.7 reveals an alignment since eq. 3.7 also shows $h_f \propto \omega^{-1/2}$. Thus, the proportionality constant of $\left(\frac{3}{2}\right)^{\frac{1}{3}} k^{\frac{1}{3}} C_0 (1 - C_0)^{-\frac{1}{3}} \rho^{-\frac{1}{3}} \eta_0^{\frac{1}{3}}$ is dependent on the plethora of other factors influencing spin-coating. Despite this myriad of factors, spin-coating rotation speed remains the primary factor for final thin film thickness and quality.

Solution Preparation

The deposition parameters for each solution, as well as the resulting dried product and its significance in this work, are displayed in Table 3.1. The process flow for fabricating sol-gel, MO thin films – including solution preparation, substrate preparation, spin-coating and post-deposition processing – is shown in Figure 3.2. This process flow applies for a single layer, with the large arrow beneath indicating the initiation of the process again for following layers (e.g. for a semiconductor on top of a dielectric to form a BGTC TFT).

In several cases, 2-methoxyethanol ($2-\mathrm{ME}$, $99\ \%$ anhydrous, Fisher Scientific) was chosen as the solvent in which the precursor powders were dissolved in to perform the sol-gel method. For ultra-thin semiconductor layers of InO_x in TFTs, a $30\ \mathrm{mg/ml}\ (0.1\mathrm{M})$ solution of indium (III) nitrate hydrate $In(NO_3)_3 \cdot xH_2O$ ($99.99\ \%$ trace metal basis, Alfa Aesar) was dissolved in $2-\mathrm{ME}$. For dielectrics, AlO_x and ZrO_x were both pursued for application in MOS capacitors and TFTs. Aluminium (III) nitrate nonahydrate $Al(NO_3)_3 \cdot 9H_2O$ (99.997% trace metal basis, Sigma Aldrich) was dissolved in $2-\mathrm{ME}$ at concentrations of $37.5\ \mathrm{mg/ml}\ (0.1\ \mathrm{M})$ or $100\ \mathrm{mg/ml}\ (0.266\ \mathrm{M})$. The use of different concentrations in this work is clearly differentiated when necessary. In both concentrations, urea CH_4N_2O ($\geq 98\ \%$, Sigma Aldrich) as part of the solution combustion synthesis process is added after $1\ \mathrm{hr}$ of mixing in a ratio of $2.5{:}\ 1\ Al^{3+}{:}\ \mathrm{urea}$ to maintain the redox chemistry. Zirconium (IV) acetylacetonate, $Zr(C_5H_7O_2)_4$, hereafter $Zr(AcAc)_4$ ($\geq 98\ \%$, Sigma Aldrich) was dissolved at $72\mathrm{mg/ml}\ (0.15\ \mathrm{M})$ in $2-\mathrm{ME}$. Ethanolamine (MEA, $\geq 99\ \%$, Sigma Aldrich) was added in a $1{:}\ 1$ molar ratio to aid the dissolution of the powder in $2-\mathrm{ME}$ and act as a crosslinker to protect against humidity exposure in ambient environment. For the Schottky diodes, undoped ZnO was used as the semiconductor atop the coplanar electrodes. Zinc oxide powder ($99.99\ \%$ trace metal basis,

Sigma Aldrich) was dissolved in ammonium hydroxide solvent (50 % v/v aqueous, Alfa Aesar) to a concentration of 10 mg/ml. For all samples, the solutions were stirred overnight (minimum of 12 hrs) on a hotplate (Cole-Parmer Stuart UC152D) with a magnetic stirrer at a temperature of 50℃ at 600 RPM until clear and homogenous. Finally, solutions are passed through a 0.2 μm PTFE syringe filter to remove any particulates and undissolved material. For the ZnO deposition details after this, further details can be found in chapter 3, section 3.1.3 due to its drastically different circumstances in use (substrate and a-lith). All solution preparation and deposition took place in room temperature, ambient conditions.

After solution preparation, substrates are cleaned and prepared for spin-coating. Si wafer die cut from 4" wafers (MI-NET) – either coated in $100\mathrm{nm}$ Al or with the $2\mathrm{nm}$ $\mathrm{SiO_2}$ native oxide – underwent sequential cleaning steps of 10 mins ultrasonication in DI water, acetone and IPA with high $\mathrm{N_2}$ flow between each wash. The substrates were then exposed to a UV-ozone treatment for 90 mins at room temperature to increase the wettability of the substrate surface. After this, spin-coating of the sol-gel dielectrics took place. Cleaned and UV treated Si wafer die were placed in the spin—coater (Laurell WS650) and secured using the vacuum chuck, using a $50-200$ μL adjustable micropipette to evenly deposit precursor solution across the substrate. Precursors were then spin-coated using the conditions in Table 3.1, followed immediately by a thermal stabilisation treatment on a hot plate at 150℃ for 15 mins to remove remaining solvent and organic residues while initiating the precursor decomposition process. If several layers of the precursor are to be deposited to achieve an increased nominal thickness, the spin-coated layer is instead treated at 150℃ for 1 min and the sample left to briefly cool before subsequent further depositions of the same precursor solution. Where thermally treatments were performed to induce the chemical conversion to the MO thin film, the samples were further annealed at 300℃ for 1 hr or 450℃ for 1 hr, depending on the precursor that was used.

As explained in chapter 2, section 2.3.1, temperature and humidity (atmospheric conditions) can have a drastic influence on the sol-gel quality. As the sol-gel deposition and processing took place entirely outside of a glovebox or dry environment, it was vital to consider these atmospheric conditions before each deposition. Two environments were used to fabricate the samples. A standard lab was used for mixing of precursor powders and solvents, as well as substrate cleaning, UV lamp treatment and post-deposition processing *via* LA or TA. In this environment, temperature typically remained at 21 ± 1 ℃, while humidity fluctuated in a large range of $30-80\%$. All steps of sol-gel fabrication and processing in this lab environment took place below 60%. Attempts at samples fabricated or processed above 60% showed visible defects in thin films, poorer $\mathrm{I-V}$ characteristics and decreased reproducibility. Thus, with a

certain lack of control over humidity in this environment, sample preparation and fabrication was limited to times when humidity was below this threshold.

Humidity in the standard lab environment was monitored in the fumehood, the ambient lab and the desiccator in which the metalorganic powders resided. The desiccator storage container was filled with $1\ \mathrm{kg}$ silica beads that were regularly changed and restored to maintain drier conditions. Powders during storage were not exposed to above 15% until they were removed for use, including the use of decant vials to protect the rest of the unused product. A second environment - a cleanroom - was used for spin-coating and hot plate stabilisation, maintaining humidity from $45-55\%$ and temperature at $22\pm1\ ^{\circ}\mathrm{C}$. Due to the more controlled environment of this lab, no impact of atmospheric conditions was traced to fabrication or processing steps in this environment. All steps could not take place in the cleanroom due to certain restrictions (e.g. particle count limit prevents weighing and using precursor powders).

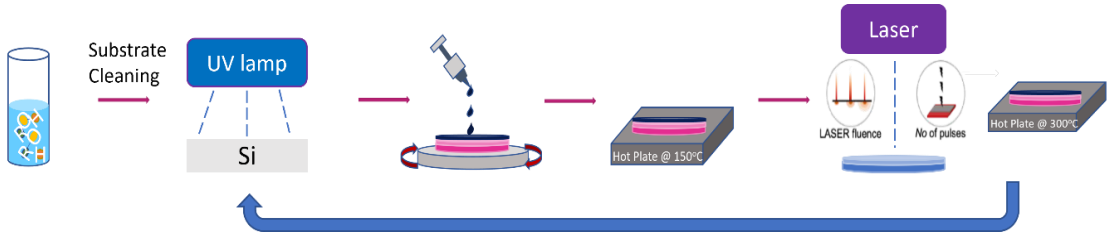

Figure 3.2 The process flow for fabricating MO, sol-gel thin films and the post-deposition processing. The large blue arrow indicates the restarting of the process to deposit further layers.

Table 3.1 Summary of the MO sol-gel thin film fabrication details.

Material	Precursor	Solvent	Concentration $(\mathrm{mg/ml})$	Additive	Spin-coat
$\mathbf{InO_x}$	$\mathrm{In(NO_3)_3 \cdot xH_2O}$	$2-\mathrm{ME}$	30	None	4000 RPM, 30s
ZnO	ZnO powder	$\mathrm{NH_4OH}$	10	None	3000 RPM, 30s
$\mathbf{AlO_x}$	$\mathrm{Al(NO_3)_3 \cdot 9H_2O}$	$2-\mathrm{ME}$	37.5	Urea, $2.5{:}1\ \mathrm{Al^{3+}}$: urea	2000 RPM, 35s
$\mathbf{AlO_x}$	$\mathrm{Al(NO_3)_3 \cdot 9H_2O}$	$2-\mathrm{ME}$	100	Urea, $2.5{:}1\ \mathrm{Al^{3+}}$: urea	4000 RPM, 30s
$\mathbf{ZrO_x}$	$\mathrm{Zr(AcAc)_4}$	$2-\mathrm{ME}$	72	MEA, 1:1 molar ratio	2000 RPM, 35s

3.1.2 Thermal Evaporation of Metals

Thermal evaporation is a commonly used physical vapour deposition technique for the formation of thin film materials. In short, a material is placed in a basket (or crucible) in a vacuum

chamber and the basket supplied with a high voltage to induce a high temperature via Joule heating that eventually vaporises the chosen thin film material source and forming a thin film on the substrate. Current in the basket is measured as a relation to the temperature, with any fluctuations describing the status of the deposition in the absence of a viewing window. Temperatures typically reach thousands of degrees, with the exact rise dependent on the material of the basket. Figure 3.3 shows an illustration of how the thermal evaporation process occurs.

In this project, thermal evaporation of Al took place to fabricate Al electrodes for capacitors, TFTs and Schottky diodes, as well as Al thin films of $100\ \mathrm{nm}$ thickness. A tungsten basket (Kurt J. Lesker) was affixed to the high voltage (AC) source. The Al deposition source was Al wire, removed of its $\mathrm{Al_2O_3}$ native oxide layer via acetone cleaning and placed into the centre of the tungsten basket. The length of wire was determined by the desired nominal thickness. The custom-built vacuum chamber was placed under high vacuum to allow clean distribution of Al vapour onto the substrate, held at the top of the vacuum chamber in the substrate cradle.

The high vacuum also prevents oxidation of the basket and undesired reactions between the basket and deposition material that reduce the lifetime of the basket [289]. For the capacitor and TFT front electrodes, deposition took place at $10\ \mathrm{Å/s}$ for a nominal thickness of $200\ \mathrm{nm}$ to pattern the substrate via a shadow mask. Back contacts were also fabricated for the same devices via a blanket deposition across the back of the substrate. For the Schottky diodes fabricated via a-lith, a blanket deposition of $100\ \mathrm{nm}$ thin film took place on borosilicate glass substrates at a deposition rate of $3\ \mathrm{Å/s}$. After conducting the necessary steps of the a-lith methodology (including laser patterning – see chapter 7), blanket deposition of Au through a shadow mask also took place. Before Au deposition, a $5\ \mathrm{nm}$ underlayer is deposited with the same deposition parameters as M1 to promote adhesion of the Au layer. Then, a $95\ \mathrm{nm}$ Au layer from gold pellets (Kurt J. Lesker) is deposited at a rate of $1\ \mathrm{Å/s}$ using an alumina crucible (Kurt J. Lesker).

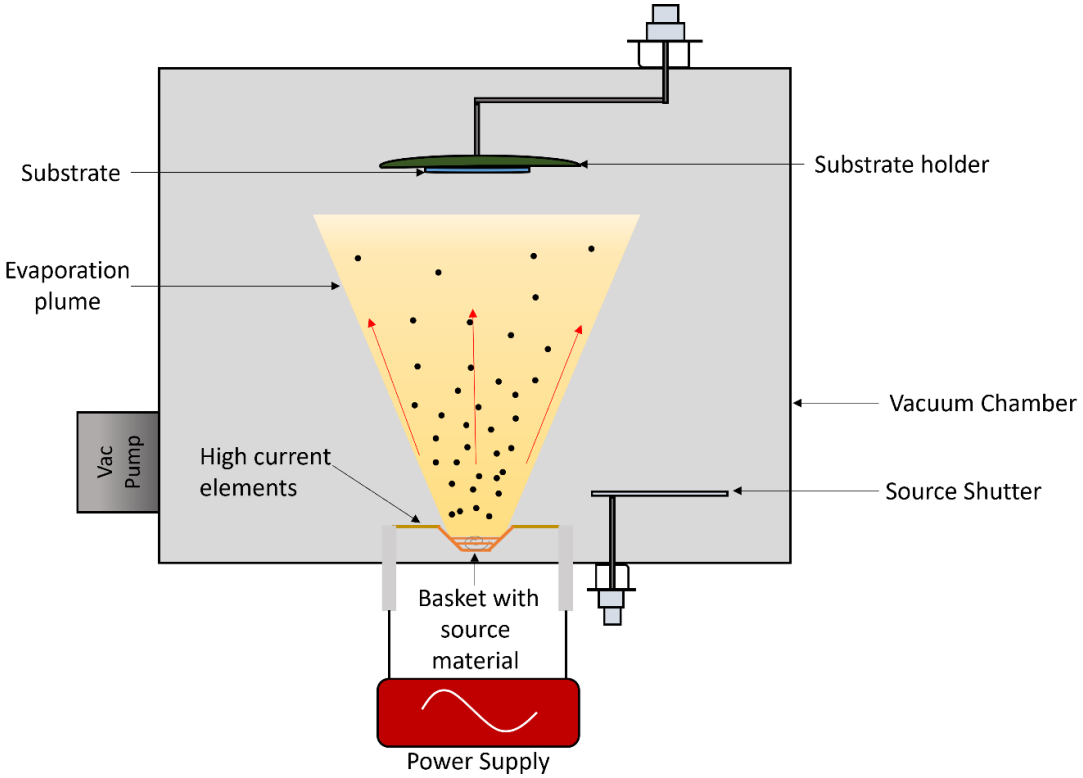

Figure 3.3. Schematic of the thermal evaporation chamber and process. The vacuum chamber houses conductive elements connected to a basket, with the elements transporting a high voltage (and current) from a power supply to the basket. A source material such as Al wire is placed inside the basket, which is vaporised by the temperature rise and drifts onto the substrate that is held above the tungsten basket at the top of the vacuum chamber.

Table 3.2 Summary of thermal evaporation deposition details. Different thicknesses and evaporation rates were necessary depending on the type of device or end purpose for the deposited metal.

Material	Thickness (nm)	Deposition Rate (Å/s)	Reason
Al	100	2.0	A-lith M1 deposition; 100 nm film for IRSE
Al	200	10.0	MOS capacitor /TFT electrodes
Au	95	1.0	A-lith M2 deposition

3.1.3 Adhesion Lithography

Patterning of materials for opto-electronic devices typically uses vacuum-based methods such as e-beam lithography or photolithography for the smallest features (5 – 100 nm), which limits the mass manufacturing of electronics with inexpensive substrates and strangles throughput. Full details of this can be found in chapter 2, section 2.4.5. As an

alternative patterning and fabrication route, adhesion lithography (a-lith) has excelled due to its ability to fabricate high performance diodes with asymmetric electrodes on large-scale substrates. The schematic in Figure 3.4 shows the individual steps.

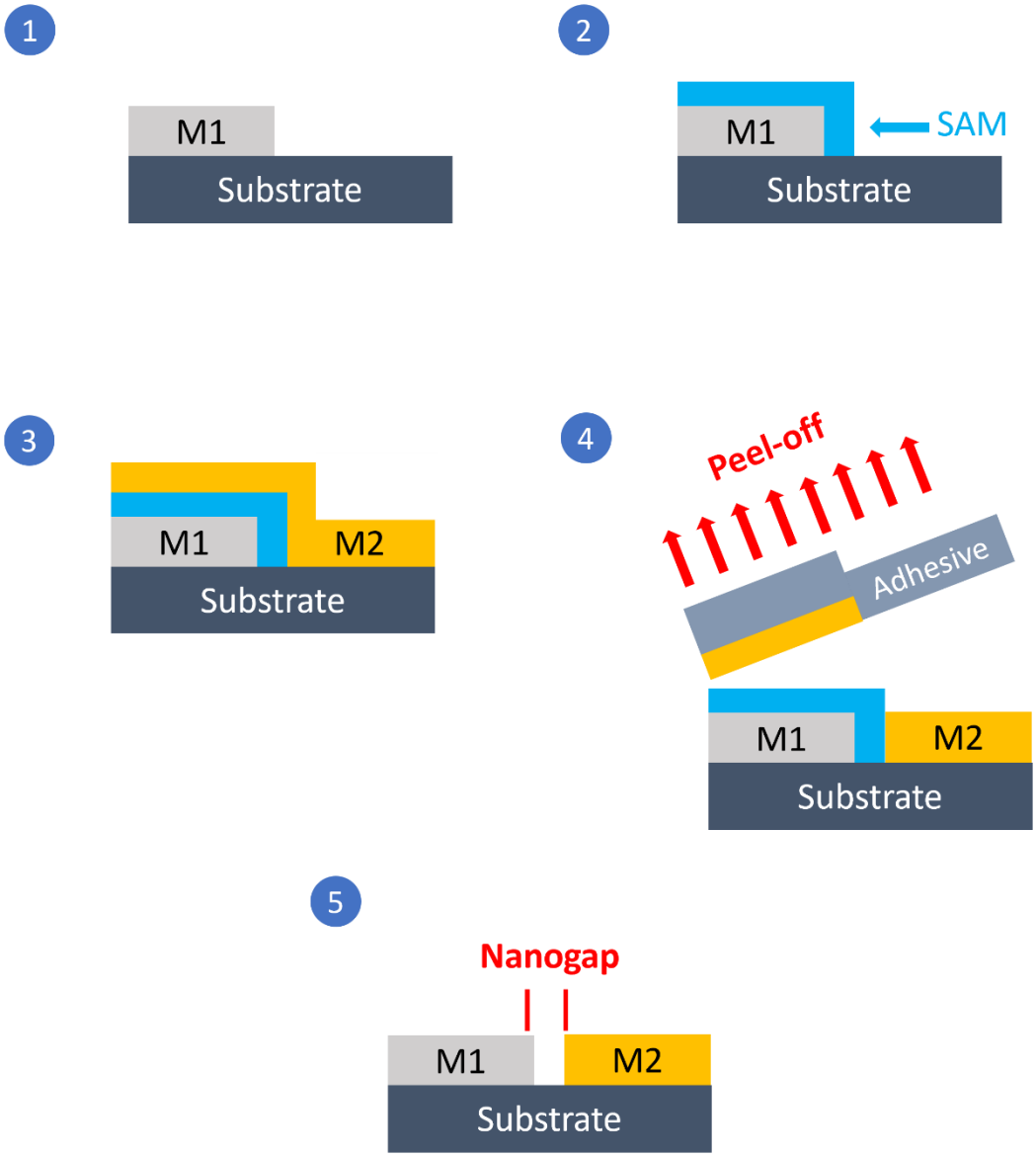

Figure 3.4 Steps of the adhesion lithography process. 1) Deposition and patterning of M1 on the substrate; 2) deposition of the SAM, functionalising M1. 3) Deposition of M2 onto the SAM-functionalised M1. 4) Application of the peel-off process, selectively removing M2 from atop the SAM-functionalised M1. In this diagram, the peel-off variation using adhesive and tape is shown but other methods have been utilised for peel-off. 5) Nanogap is formed after UV treatment of the surface to remove the remaining SAM.

While a-lith has been thoroughly investigated for a range of devices, certain roadblocks have prevented rollout to LAE beyond the lab. Firstly, the manual peel-off step had remained. The use of a manual peel-off with a human operator has variation from person to person which affects the range of size of the nanogap, uniformity, and capability to be established as a

patterning methodology in a LAE automated manufacturing line. Second is the use of photolithography and wet etching to pattern M1, after its blanket deposition on the substrate and prior to the other a-lith steps. Photolithography using any deep UV wavelengths (e.g. below the $\mathrm{ArF}\ 198\ \mathrm{nm}$ excimer laser wavelength) requires vacuum systems, enclosed beams and purge lines which is incompatible with high throughput LAE production lines. While the peel-off step has been addressed with bimetal combinations for M2 that selectively peel as well as chemical removal of the SAM and M2, progress in patterning of M1 has remained sedentary.

The critical step that makes a-lith effective since its conception is the deposition and formation of the self-assembled monolayer as per part two of Figure 3.4. The selection of the SAM is dependent on the chemical affinity between the SAM and the M1 surface. For Al, a commonly employed material for M1, the phosphonic ($-\mathrm{POOH}$) group attaches to the $\mathrm{AlO_x}$ native oxide on the Al, while the methyl ($-\mathrm{CH_3}$) tail groups point outwards and organise over time. Since the alkyl chain and methyl tail are chemically non-reactive, the M1/SAM surface becomes hydrophobic and adhesion with any further deposited layers becomes further reduced. Thus, the M2 layer forming the other electrode can be selectively removed due to this low adhesion.

In this work, Al and Au were used as the metals for M1 and M2 for the coplanar, nanogap separated, asymmetric electrodes. Borofloat borosilicate glass slides of $1.1\ \mathrm{mm}$ thickness (Instrument Glasses Ltd) underwent sequential cleaning steps of $10\ \mathrm{min}$ ultrasonication each with DI water, acetone and IPA. The blanket deposition of Al on borosilicate glass follows the details described at the end of chapter 3, section 3.1.2. After this deposition, the $100\ \mathrm{nm}\ \mathrm{Al}$ was laser patterned, testing with a variety of laser sources to obtain optimised Al ablation with minimised disruption to the glass surface. Full details of this optimisation process and the laser parameters are discussed in chapter 7, sections 7.1 and 7.2 of this thesis. Afterwards, the SAM deposition took place to functionalise the surface of M1. For the SAM solution, $0.26\ \mathrm{mg/ml}$ of octadecylphosphonic acid (ODPA, Sigma Aldrich) is mixed in IPA and stirred for several hours until everything is fully dissolved. The samples were placed inside a petri dish, the ODPA solution poured over them so they are fully submersed in the liquid and were rested in the liquid for $20\ \mathrm{hrs}$, so a SAM film is formed on the surface of M1 (the Al native oxide) and the glass without a SAM layer. Afterwards, the samples were removed and rinsed thoroughly with IPA, dried in an $\mathrm{N_2}$ stream and placed on a hotplate at $80^{\circ}\mathrm{C}$ for $10\ \mathrm{min}$ to remove physically adsorbed ODPA molecules. UV/ozone treatment before deposition of the solution-based SAM is avoided to prevent activation of the glass substrate and reduce the chances of the SAM attaching to the substrate surface. Finally, SAM deposition is followed by blanket deposition of the Au via thermal evaporation with a $5\mathrm{nm}\ \mathrm{Al}$ underlayer, as described in

chapter 3, section 3.1.2. The Al underlayer promotes adhesion of the metal to the glass substrate.

The removal of M2 in this work was tested via both lift-off with tape and a chemical agitation method. First contact adhesive was applied uniformly with a brush or spray-coated to the $\mathrm{Al-SAM-Au}$ structure and left to dry for $20\ \mathrm{mins}$. The adhesive and Au on top of the SAM-functionalized Al were then peeled off using electrical tape. For chemical agitation, the samples after Au blanket deposition were submerged in acetone and ultrasonicated, followed by further ultra sonication for $1\ \mathrm{min}$ in IPA. This step finalizes the fabrication of the electrodes via a-lith. In this thesis, the electrodes for the subsequent diodes were not isolated. To remove the SAM from M1 after the peel-off step, UV-ozone treatment was carried out for $15\ \mathrm{mins}$. To fabricate the Schottky diodes, a sol-gel, ZnO semiconductor was spin-coated on top following the spin-coating recipe in chapter 3, section 3.1.1. In the case of ZnO, the precursor was processed via FLA using a Novacentrix Pulse Forge 1300 by collaborators at KAUST.

3.2 Thin Film Processing

3.2.1 Excimer Laser Annealing

As discussed in previous chapters, many thin film materials in a plethora of wet or dry deposition techniques do not immediately exhibit the desired properties for implementation in functional devices. Sol-gel MOs are no exception. For sol-gel thin film MOs to be viable, post-deposition processing via some form of annealing takes place. Typically, this requires some form of external thermal energy (e.g. hot plate, furnace annealing, rapid thermal annealing) applied to the substrate backside for a specific amount of time, transmitting the heat to the thin film before allowing to cool. Because TA at the necessary high temperatures limits substrate choice for LAE, photonic processing has been pitched as an alternative.

In this work, excimer laser annealing (ELA, commonly in this thesis as LA) is used. In LA, high energy UV photons greater than several of the MO material bandgaps are used to deliver a near instantaneous high temperature rise by strong light absorption into the materials, as well as contributions via reflection. The light absorption leads to excited electrons that trigger a multi-phonon cascade emission as they de-excite. The emitted phonons carry the heat (energy rise) throughout the material via diffusion. Additionally, materials below the thin film at the top of the material stack will be heated. The LA mechanism, including its modelling for the purpose of simulations predicting temperature rises, is discussed in more detail later in chapter 3, section 3.3.

Experimental Details

Figure 3.5a demonstrates the schematic of the LA system used for this research. The LA system itself is complex to ensure control over all the laser parameters and obtain a reliable recipe for obtaining specific material properties while retaining a certain degree of freedom. In the context of LAE, this recipe can then be applied uniformly to a lower cost R2R mass production line using a LA system appropriate for the requirements of the production line [61]. A conceptual example is shown in Figure 3.5c, while an illustrative synopsis of the LA parameters is given in Figure 3.5b.

a)

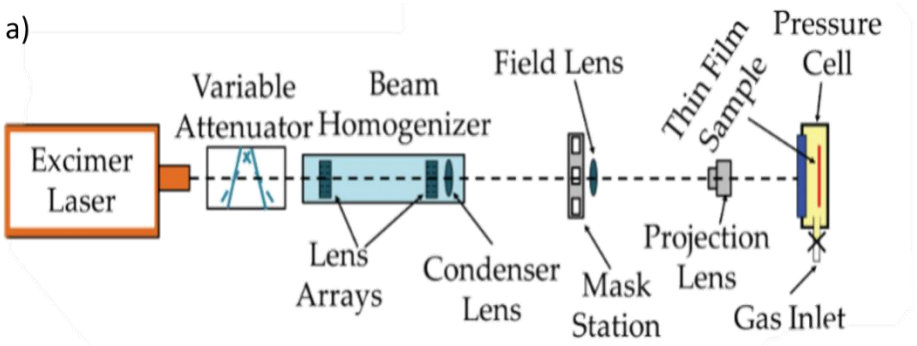

b)

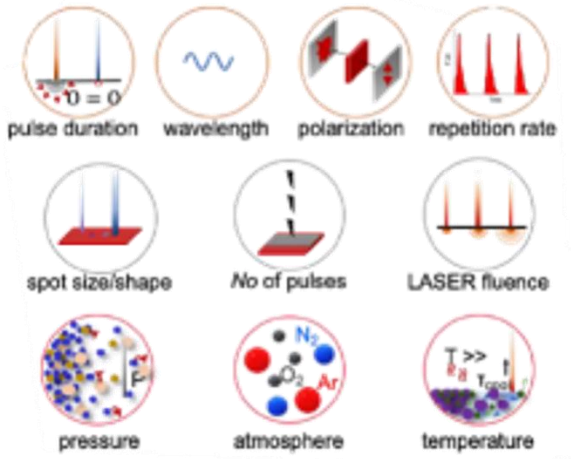

c)

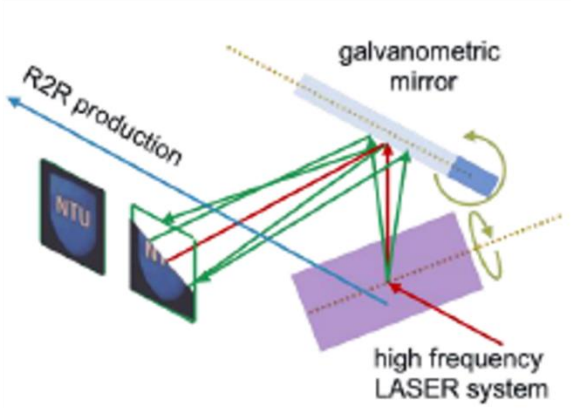

Figure 3.5 a) Schematic of the typical excimer LA system, including the one used in this work. b) The various LA parameters with the pulsed excimer laser. c) Conceptual example of the implementation of LA to a LAE (R2R) production line, using galvanometric components to orientate the laser path to the desired location.

LA systems including this one can be split into three key components [290]:

i) the laser source, providing the high energy photons for processing. The LA system uses a Krypton Fluoride (KrF) excimer laser (Lambda Physik LPX 305i) that emits unpolarised light with a wavelength of $\approx 248\ \mathrm{nm}\ (5\ \mathrm{eV})$, a pulse with FWHM of $\sim 25\ \mathrm{ns}$ and energy per pulse up to $1500\ \mathrm{mJ/cm^2}$. The raw beam is a Gaussian profile on the long axis with a $30\ \mathrm{mm} \times 15\ \mathrm{mm^2}$ are. Via a control panel, the laser can fire with different repetition rates and pulse intensities. For the purposes of processing sol-gel materials, the ns pulse duration is preferable since photon absorption is via lattice vibration to induce heat transfer through the material.

ii) the beam delivery system, transforming and directing the light to the sample position. Light is transported through an iris and a variable attenuator to adjust the energy of each pulse. The variable attenuator uses a partially reflective plate at variable angles to reflect the laser beam, followed by a second plate that compensates for the parallel displacement of the beam caused by the first plate. Depending on the angle of the first plate, anywhere from 10% to 90% of the beam is transmitted through before reaching the beam homogeniser. The beam homogeniser (Exitech Ltd, type EX-HS-700D) is comprised of two lens arrays and a condenser lens. The condenser lens provides a pre-determined laser spot size of $13\ \mathrm{mm} \times 13\ \mathrm{mm^2}$ at a correct position, as well as providing a top-hat profile on both axes with a uniformity better than $\pm\ 2\%$ across the irradiated area. This homogenised beam is incident on a mask contained in a carousel, allowing easy cycling between masks, whose image is projected onto the sample with a combination of a field lens and projection lenses. The projection lenses can be swapped and put into positions to achieve $\times 1$,$\times 1.8$ or $\times 5$ magnification depending on setup. Various mirrors are also positioned to guide the beam through each component and towards the sample position. In this work, a $\times 5$ magnification of the $13\ \mathrm{mm} \times 13\ \mathrm{mm^2}$ spot was used to achieve processed areas of sol-gel MO dielectric or semiconductor of area $2.5\ \mathrm{mm} \times 2.5\ \mathrm{mm^2}$.

iii) sample stage. The cell itself contains the sample, while the cell is transported around on a computer-controlled x-y-z translation stage with precision to $1\ \mu\mathrm{m}$. Specialised software can also externally trigger the laser. In some cases, a pressure cell with a UV transparent window may be fixed to the sample stage for processing in highly pressurised, non-ambient environments (e.g. $\mathrm{O_2}, \mathrm{Ar}, \mathrm{N_2}$) during Reactive Environment Laser Annealing (ReLA) [291]. However, this was not utilised for any experiments in this work.

Adjacent to the beam delivery and sample stage component is the energy monitoring system to ensure precise energies were delivered for the desired fluence. Energy monitoring was performed both in-line and at the sample position where the laser energy is targeted; in-

line utilises a beam splitter between the field lens and projection lens towards an energy monitor (Gentec ED200) composed of a CCD array, while the sample position is a one-time measurement taken with a different energy monitor (Gentec QE50) below the stage, thus below the point of focus to fill the CCD array for a more reliable reading. From this, a ratio between the two can be determined so laser energies can be continually monitored via the in-line monitor ($\mathrm{E_M}$ with fluence $\mathrm{J_L} = \frac{\mathrm{E_M}}{\mathrm{A}}$) in comparison to the target laser energy $\mathrm{E_L}$ with associated fluence $\mathrm{J_L} = \frac{\mathrm{E_L}}{\mathrm{A}}$ on a spot with irradiated area A.

The precise measurement of the target laser energy is of utmost importance for accurate and reproducible LA experiments. Because the exact value of $\mathrm{E_L}$ may not be attainable due to natural fluctuations in laser energy, the target laser energy fluence and monitored energy are distinguished from each other, documented, and an error range for the energy derived from the standard deviation of several pulses. To compensate for this during LA experiments, the "desired" monitor energy $\mathrm{E_{M,Desired}}$ compares to the desired fluence $\mathrm{J_{L,Desired}}$ (eq. 3.8) and how the actual monitor energy $\mathrm{E_{M,Actual}}$ measured before LA compared to $\mathrm{E_{M,Desired}}$ (eq. 3.9):

$$\mathrm{E_{M,Desired}} = \mathrm{A} \cdot \mathrm{J_{L,Desired}} \tag{3.8}$$

$$\mathrm{J_{L,Actual}} = \mathrm{J_{L,Desired}} \cdot \frac{\mathrm{E_{M,Actual}}}{\mathrm{E_{M,Desired}}} \tag{3.9}$$

Since fluence is also dependent on the spot sizes, precise measurements of the spot size were also made. For this work, a microscope with a webcam was used to determine the dimensions. A photograph of a known scale (e.g. callipers) was sued to determine a calibration for $\mathrm{pixels/mm}$. A photo of the spot at the same magnification was taken and the length and width measured using this calibration and the area subsequently calculated.

This versatile setup allows the tuning of nine different laser annealing parameters:

1) Wavelength (nm): for LA, wavelengths reside in the UV region as most materials experience higher absorption and smaller penetration depths in the UV wavelengths, allowing increased temperature rise of the targe material and not the underlying materials. Venturing into even deeper wavelengths than the KrF excimer (e.g. ArF excimer lasers) brings unique issues, as $\mathrm{O_2}$ molecules have high UV absorption which leads to toxic ozone production. Thus, deep UV wavelength lasers should ideally have their beam delivery system enclosed in sealed tubes, allowing simultaneous $\mathrm{N_2}$ flow during the process.
2) Pulse duration (ns): the time duration of a single laser pulse. Systems used for annealing purposes typically have short pulses of ns duration.

3) Polarisation: light produced from most excimer lasers is randomly polarised, but can be orientated using optical filters (polarisers) to block waves of other polarisations out to convert it to a wave with a well-defined polarisation state.
4) Fluence ($\mathrm{mJ/cm^2}$): the energy density per unit area delivered to the sample in the sample position, typically adjusted through the laser energy via the variable attenuator. The fluence can also be vary due to the size of the mask and the objective lens used to project the laser spot onto the sample's surface, since these influence the irradiated area. The laser spot size is determined by a combination off field and projection lenses along with the mask selected.
5) Number of pulses: the number of pulses at the desired fluence applied to the sample. Combined with fluence, this controls the temperature rise in the target materials and the photochemical conversion in sol-gel MO precursors.
6) Repetition rate (Hz): number of pulses per second. This is externally controlled and can vary from $1\ \mathrm{Hz}$ to $50\ \mathrm{Hz}$.
7) Environment temperature (℃): ambient temperature in which the sample is processed in, which will affect the cooling rate of the sample after laser irradiation and the properties of the materials. The custom-built LA system can be held at an elevated temperature, room temperature or cooled via liquid nitrogen to -196℃.
8) Environment composition: the pressure cell that the sample sits in can be supplied with several different gases including $\mathrm{Ar}, \mathrm{N_2}, \mathrm{O_2}$ and $5\%\ \mathrm{H_2}$ in Ar. Selection of gas composition depends on the targeted properties (e.g. conductivity, interstitial vacancies) of the material, possible doping purposes (e.g. $\mathrm{N_2}$ hyperdoping) or the desire for an inert or reactive environment
9) Pressure (psi): low vacuum or high pressure of the chosen gaseous composition during LA is often used to attenuate the detrimental effects of ablation.

3.2.2 Laser Metal Ablation (Marking Lasers)

The LA system in chapter 3, section 3.2.1 proposes a highly flexible route to low thermal budget MOs for LAE and can conceptually be used for highly area selective patterning, making it a ubiquitous tool for the next generation. However, excimer lasers are inherently limited to deep UV wavelengths. For the a-lith process, where both minimal surface roughness to the substrate and thin films and sharp, defined edges where the nanogap is formed, limiting to the UV wavelengths may be counterproductive. For the exploration of patterning, marking lasers of $532\ \mathrm{nm}$ (Trumpf Trumark 3230 OEM) and $1064\ \mathrm{nm}$ (Trumpf Trumark 3330 OEM) were used. The $355\ \mathrm{nm}$ (Trumpf Trumark 3130 OEM) was also available but was not explored in this work. Instead of high energy pulses and low repetition rates with reliance on the deep UV absorption

of the target materials, low energy and high frequency laser pulses are scanned across a CAD design made by the user to mark the sample. The CAD design is marked via a hatch of vertical and horizontal lines that overlap the spots in to smooth these differences in temperature rise and ensure complete coverage of the selected area. Like the excimer, the diode pumped solid state (DPSS) lasers - built with industry suitability in mind - can be split down into key functions:

i) The laser device: each laser uses an active medium of $\mathrm{Nd{:}\,YVO_4}$ (Vanadate), which has a typical laser emission wavelength of $1064\ \mathrm{nm}$. The lower wavelengths of $532\ \mathrm{nm}$ and $355\ \mathrm{nm}$ are achieved by frequency doubling and tripling the output of the laser, respectively [292]. Pulse duration and maximum energy output varies depending on the repetition rate during processing but can be anywhere from $8-20\ \mathrm{ns}$ and up to $40\ \mathrm{kW}$ per pulse. The beam profile follows a Gaussian profile on each axis, with a beam quality number ($\mathrm{M^2}$) typically around 1.2. Note that a figure of 1 for the $\mathrm{M^2}$ number indicates a perfect Gaussian. Table 3.3 offers more information on the laser device parameters for each laser source.

ii) Optics: Focus of the laser is achieved with manual manipulation of the stage and with an internal focal position adjustment unit, using a variable beam expander and defocusing unit. There is a high precision beam deflection system, using galvanometer mirrors to guide from laser source and through the lens towards the sample. All 3 lasers have a F-Theta focusing lens with focal length $\mathrm{f} = 160\ \mathrm{mm}$ and a marking field size of $110\ \mathrm{mm} \times 110\ \mathrm{mm}$ when in focus. The use of the F-Theta lens reduces the need for electronic correction and keeps the focus consistent across the marking field when scanning.[293] The marking of a design onto the sample can be simulated with an integrated pilot laser diode (Trumark Series 3000) to improve positioning of the sample prior to processing.

iii) Operation and programming: the laser is operated via a modular supply unit and control computer, containing various software provided by Trumpf. The proprietary TruTops Mark software is used to monitor the laser status, control laser parameters and offer overall structured management to the laser. A CAD design software is supplemental to this, allowing extremely customisable design that can be marked or processed onto a sample. Part of this software is a Navigator Grid, which is a software-based wizard to output a range of suitable parameters depending on the desired application. Use of the navigator allows rapid determination of suitable laser parameters for optimisation or immediate transfer to a new sample. There is an internal power measurement to evaluate the exact laser power.

Table 3.3 Comparison of specifications for each wavelength of the Trumpf DPSS marking lasers.

Wavelength (nm)	Peak pulse power (kW)	Pulse Duration (ns)	Spot Size (μm)	Focal Length (mm)	Beam Quality M^2
355	15	< 20	25	160	1.2
532	> 14	< 20	25	160	< 1.2
1064	> 40	15	45	160	< 1.5

Due to their large differences to the excimer lasers, the Trumpf marking lasers have several laser parameters that are different to the excimer laser:

1) Scan speed ($\mathrm{mm/s}$): how quickly the laser scans across the sample. A slower scan speed results in a longer dwell time for the laser on a certain area, thus increasing the temperature rise. The software is precise up to 0.001 mm (1 μm).
2) Repetition rate (kHz): number of laser pulses per second, at the prescribed conditions. The full consequence in relation to power and effect on the sample is discussed later.
3) Hatch spacing (mm): the spacing between laser spots. Processing the area occurs via horizontally scanning the laser across the area with the preset laser parameter scan speed and repetition rate, before tracing the outline of the shape around the ablated area.
4) De-focus (mm): the Trumpf lasers have a built-in feature to change the focus from the current position by ± 8 mm. Doing so can bring the current position into (or out of focus), drastically altering the fluence and depth of the hatch during the laser scan.
5) Power ($\%$): how much of the laser power is used for each pulse. The details of how this relates to frequency below.
6) Number of passes: the number of times the chosen conditions are used to process an input CAD pattern.

A further consideration with the marking lasers in this work is that the power expressed by the laser varies with frequency. Figure 3.6 shows how the power varies for the three different wavelengths of Trumpf lasers, determined via measurements internal to NTU. Generally, peak power is achieved with 20 kHz. For applications such as wafer dicing, where hundreds of passes of the same pattern are required, this is vital information for timely processing and the die edges to be clean.

For the fabrication of RF Schottky diodes with nanogap electrodes using the a-lith methodology, the patterning of M1 must take place. These types of lasers have been utilised for annealing in the past [294], but not during this work. Multiple laser sources were tested, including the 532 nm (Trumpf Trumark 3230 OEM) and 1064 nm (Trumpf Trumark 3330 OEM).

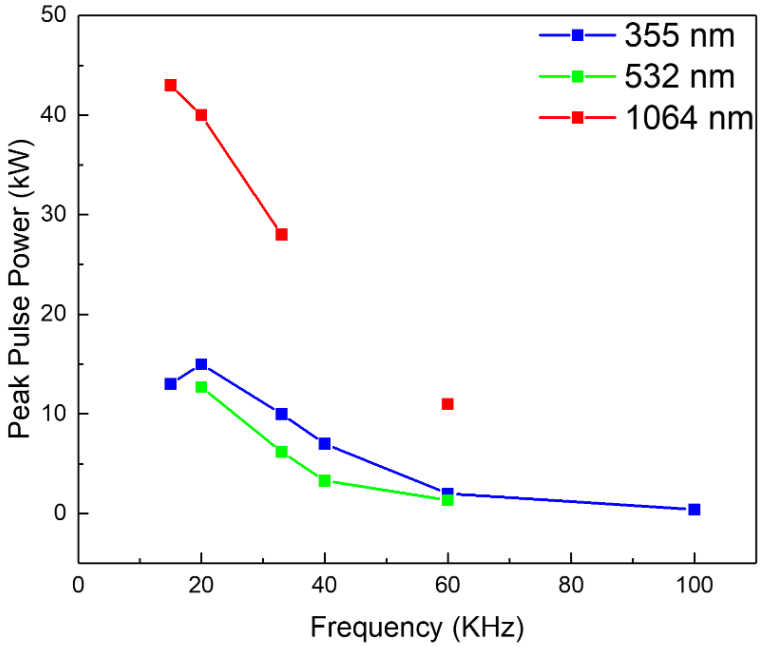

Figure 3.6. Demonstration of how the Trumpf laser power across the three sources (355 nm, 532 nm and 1064 nm) vary their output power with frequency. Power per pulse is generally maximised around 20 kHz, then reduces at lower or higher frequencies.

Figure 3.7a shows the experimental schematic for laser ablation with the use of the Trumpf lasers. Samples are placed on a Newport 9204-M Variable Height Platform (with a resolution of 0.05 mm). As the high frequency, low scan speeds are extremely powerful with any wavelength of these lasers, the sample was placed upside down and processed through the backside in some tests to add a defocus via the change in refractive index between air and glass. Other tests placed the sample with the film side facing towards the laser. When the processing through the backside occurred, the sample was elevated with spacers of 5 mm thickness to prevent the high temperature fusion of Al nanoparticles and debris to the frontside of the glass. The laser processing chamber was also ventilated with a Local Exhaust Ventilation (LEV) to remove Al nanoparticles. First, the sample position height was varied to determine focus. Figure 3.7b shows an example focus test. A dummy sample of the same thickness and materials in an identical processing configuration was utilised to mark three thin lines with line distance spacing between of 0.3 mm and group distance of 1.5 mm. Each group represented a different level of z-heights (defocus), initially across a z-distance of ± 8 mm. The best focus (thinner, darker lines) was selected. A further focus test was conducted with a limited range of z-heights of ± 1 mm to achieve sub-mm focus at the film. The sub-mm focus test was inspected with a Lumenera Infinity2 zoom camera.

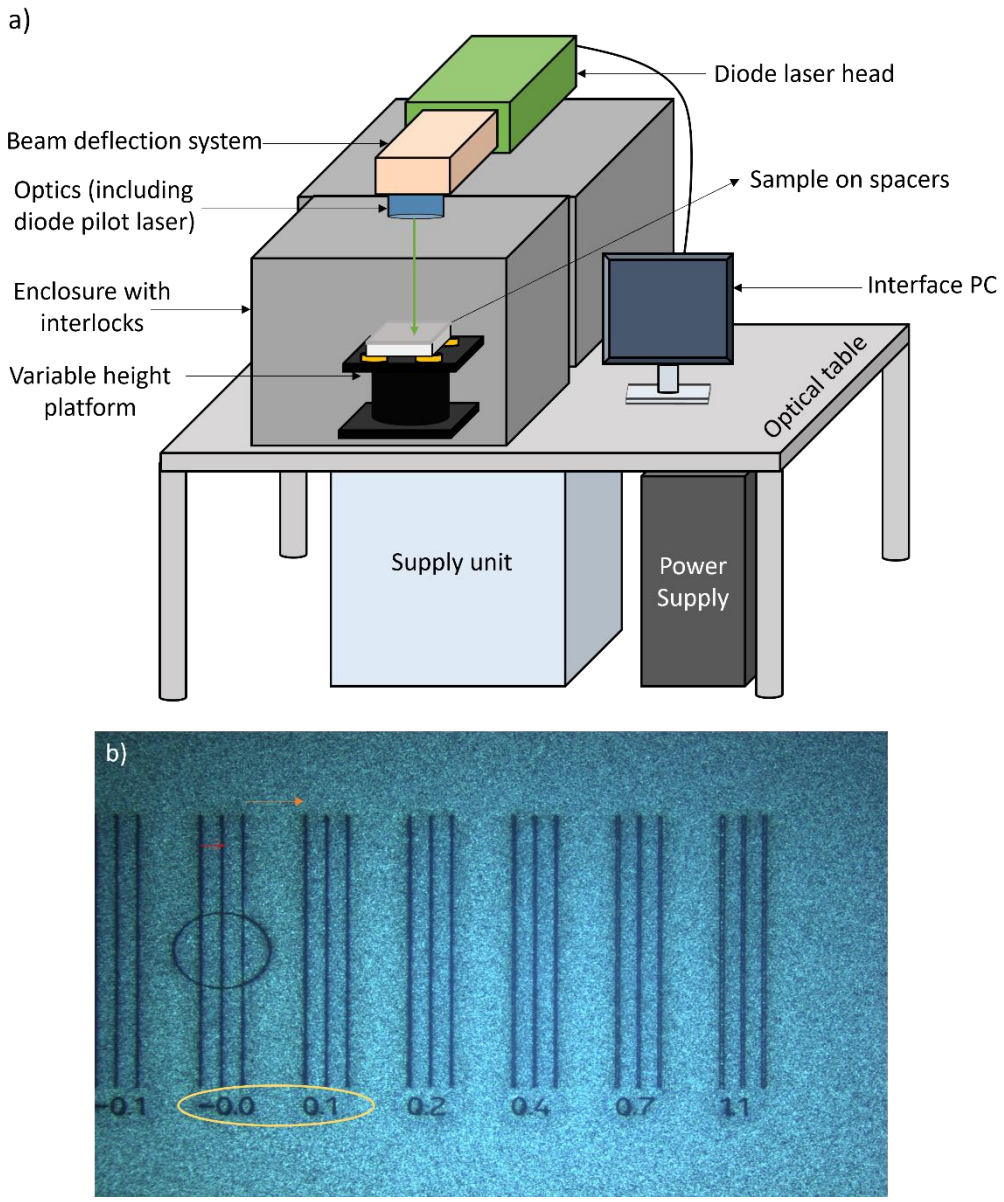

Figure 3.7 a) Schematic of the Trumpf marking laser. Samples are placed on a stage vertically positioned so the side being processed is in focus. The sample is then aligned using the pilot laser and processed with a CAD design. All actions take place via the interface PC. b) An example of a focus test using groups of lines at various levels of defocus. The line distance spacing (red arrow) in this test is $0.3\ \mathrm{mm}$, the group distance (orange arrow) $1.5\ \mathrm{mm}$ and a z-distance (gold circle) variation of $\pm\ 1.1\ \mathrm{mm}$.

Samples were mounted securely via tape or other means onto the surface atop the stage. The CAD design was then highlighted and outer dimensions traced with a red pilot laser to align the sample. For the samples that would become the base of the Schottky diodes via a-lith, the $20\ \mathrm{mm} \times 20\ \mathrm{mm} \times 1.1\ \mathrm{mm}$ glass slide (Borofloat Glass, Instrument Glasses) with a $100\ \mathrm{nm}$ Al thin film was placed film side down on the $5\ \mathrm{mm}$ spacers. The CAD design that may be comprised of several geometries and feature sizes was then marked, using a webcam mounted to the ceiling of the laser enclosure to monitor the process. The patterned samples were then subjected to the rest of their methodologies, such as the a-lith methodology for the patterned

glass substrates. Further details of the laser parameters used are given in results chapters. Additionally, the $532\,\mathrm{nm}$ Trumpf was used for wafer dicing of 4" Si wafers down to $25\,\mathrm{mm} \times 15\,\mathrm{mm}$ wafer die for spin-coating. Si wafers were placed faced down and the laser focused on the backside using the same procedure as described above. The Si wafers were mounted on dicing tape to protect the polished frontside surface. Laser parameters were set as 300 passes at a power of $100\,\%$, scan speed of $100\,\mathrm{mm/s}$, pulse frequency of $20\,\mathrm{kHz}$ and hatch spacing of $0.01\,\mathrm{mm}$. Any additional uses of the marking lasers are mentioned in subsequent chapters.

3.3 Modelling the Laser Annealing Mechanism

While LA is potentially extremely advantageous for LAE production lines when compared to its conventional TA counterparts, the use of an optical process to induce a thermal effect introduces additional complexity via coupled processes between additional variables. Understanding these processes will elucidate the photochemical pathway from sol-gel precursor to a functional MO thin film. Optically, the absorption of photons into the material being defined by the imaginary permittivity (thus absorption) leads to different energy (heat) transfer phenomena depending on the bandgap of the material [295], [296].

In the case where bandgap is lower than the photon energy, strong interband and intraband excitations occur that lead to phonon energy transfer (lattice vibrations) and an increased number of free carriers in some materials. The extent of these is further dependent on the temperature rise due to photon absorption [296]. Bandgaps higher than the photon energy lead to weak interband electronic excitations, unless the material permits a mechanism for multiphoton absorption [297].

Aside from optical phenomena in the material, interference phenomena from reflections of other materials also take place. The aforementioned temperature rise and heat transfer throughout the system after absorption of photons is also dependent on the thermal properties of the materials in the system, such as heat capacity, thermal conductivity and (for sol-gel precursors) melting temperatures. Since increased absorption of photons leads to a temperature rise in the material, these optical and thermal (opto-thermal) properties and phenomena naturally become coupled. For sol-gel materials, whose evolution from precursor to thin film follows distinct steps in a chemical pathway marked by temperature, consideration of how to understand and manipulate the temperature rise is vital. UV photons are perhaps one of the more extreme examples that show these differences in behaviour in MOs. Due to the high bandgaps of MOs, UV photons are necessary in many cases to achieve the prerequisites of

photochemical conversion to a functional thin film with shallow penetration depth to preserve substrate integrity [298], [299].

The light-matter (photon-electron) and phonon transport interactions responsible for heating becomes increasingly complex when the laser properties are further integrated for consideration of temperature rise and heat transfer. The laser spatial and temporal profiles, combined with the opto-thermal properties of the materials, restrict the time scale of temperature rise via the laser pulse duration. The time for the different mechanisms of heat transfer (electron excitation or phonon transfer) also occur on different time scales (fs compared to ms), thus the heat transfer between each laser pulse is governed by bandgap and laser pulse duration also. Beginning to understand the interplay of these processes and how they contribute to a photothermally induced chemical reaction to fabricate a thin film is critical and would be a beyond extensive (and non-pragmatic) experimental undertaking.

To overcome this, a specialised simulation tool on opto-thermal modelling is employed to gain insight into the laser annealing of a material system with known optical and thermal properties. Strongly coupled and thermal simulations are used that account for the optical properties (n, κ), thermal properties (heat capacity, thermal conductivity including temperature dependent non-linearities), density, phase changes (melting temperature and latent heat of fusion) and laser profiles (temporal and spatial profiles).

3.3.1 Optical Simulation

First, the optical constants of the materials in the laser wavelength ranges of interest are considered in combination with the geometry of the multi-layer structure. The complex refractive index:

$$\tilde{\mathrm{n}}_{\mathrm{i}} = \sqrt{\tilde{\varepsilon}_{\mathrm{i}}} = \mathrm{n}_{\mathrm{i}} + \mathrm{i}\kappa_{\mathrm{i}} \qquad 3.10$$

where the i subscript refers to the number material in the system, $\tilde{\mathrm{n}}$ is the complex refractive index, $\tilde{\varepsilon}_{\mathrm{i}}$ is the complex dielectric function and n_{i} and κ_{i} is the real and imaginary components of the material complex refractive index, respectively.

The optical component of laser annealing is solved in 1D under normal incidence within the Fresnel equations using the transfer matrix method [300], [301]. “Propagation” and “interface” matrices (P_{i} and $\mathrm{I}_{\mathrm{i,i+1}}$) are formulated based on the propagation properties and boundary conditions of the electromagnetic fields of the two counter propagating waves within the structure, at the material’s bulk and interfaces, respectively. Then the total optical problem at a specific time instance is solved by multiplying the respective transfer matrices, starting from

the incident side (unitary incidence and reflected amplitude r) all the way to the back side of the device (transmitted amplitude t):

$$\begin{pmatrix} \mathrm{t} \\ 0 \end{pmatrix} = \mathrm{I}_{\tilde{\mathrm{n}}_{\mathrm{Sub}}\tilde{\mathrm{n}}_{\mathrm{f}}} \mathrm{P}_{\tilde{\mathrm{n}}_{\mathrm{f}}\mathrm{l}_{\mathrm{tot}}} \mathrm{I}_{\tilde{\mathrm{n}}_{\mathrm{f}}\mathrm{n}_{\mathrm{a}}} \begin{pmatrix} 1 \\ \mathrm{r} \end{pmatrix} = \begin{pmatrix} \mathrm{M}_{11} & \mathrm{M}_{12} \\ \mathrm{M}_{21} & \mathrm{M}_{22} \end{pmatrix} \begin{pmatrix} 1 \\ \mathrm{r} \end{pmatrix} = \mathrm{M} \begin{pmatrix} 1 \\ \mathrm{r} \end{pmatrix} \quad 3.11$$

where $\mathrm{I}_{\tilde{\mathrm{n}}_{\mathrm{Sub}}\tilde{\mathrm{n}}_{\mathrm{f}}}$ is the interface matrix from film to substrate, $\mathrm{P}_{\tilde{\mathrm{n}}_{\mathrm{f}}\mathrm{l}_{\mathrm{tot}}}$is the propagation matrix in the films, $\mathrm{I}_{\tilde{\mathrm{n}}_{\mathrm{f}}\mathrm{n}_{\mathrm{a}}}$ is the interface matrix from air to film and M is the transfer matrix. From the above, M is more generally is a product of P_{i} and $\mathrm{I}_{\mathrm{i,i+1}}$:

$$\mathrm{M} = \mathrm{I}_{\mathrm{n-1,n}} \mathrm{P}_{\mathrm{n-1}} \dots \mathrm{I}_{2,3} \mathrm{P}_{2} \mathrm{I}_{1,2} \quad 3.12$$

with the index running over all layers in the multilayer structure. The individual matrices are:

$$\mathrm{I}_{\tilde{\mathrm{n}}_{\mathrm{f}}\mathrm{n}_{\mathrm{a}}} = \frac{1}{2\tilde{\mathrm{n}}_{\mathrm{f}}} \begin{pmatrix} \tilde{\mathrm{n}}_{\mathrm{f}} + \mathrm{n}_{\mathrm{a}} & \tilde{\mathrm{n}}_{\mathrm{f}} - \mathrm{n}_{\mathrm{a}} \\ \tilde{\mathrm{n}}_{\mathrm{f}} - \mathrm{n}_{\mathrm{a}} & \tilde{\mathrm{n}}_{\mathrm{f}} + \mathrm{n}_{\mathrm{a}} \end{pmatrix} \quad 0.13$$

$$\mathrm{P}_{\tilde{\mathrm{n}}_{\mathrm{f}}\mathrm{l}_{\mathrm{tot}}} = \begin{pmatrix} \mathrm{e}^{\mathrm{i}\mathrm{k}_{\mathrm{f}} d_{\mathrm{tot}}} & 0 \\ 0 & \mathrm{e}^{-\mathrm{i}\mathrm{k}_{\mathrm{f}} d_{\mathrm{tot}}} \end{pmatrix} \quad 0.14$$

$$\mathrm{I}_{\tilde{\mathrm{n}}_{\mathrm{Sub}}\tilde{\mathrm{n}}_{\mathrm{f}}} = \frac{1}{2\tilde{\mathrm{n}}_{\mathrm{Sub}}} \begin{pmatrix} \tilde{\mathrm{n}}_{\mathrm{Sub}} + \tilde{\mathrm{n}}_{\mathrm{f}} & \tilde{\mathrm{n}}_{\mathrm{Sub}} - \tilde{\mathrm{n}}_{\mathrm{f}} \\ \tilde{\mathrm{n}}_{\mathrm{Sub}} - \tilde{\mathrm{n}}_{\mathrm{f}} & \tilde{\mathrm{n}}_{\mathrm{Sub}} + \tilde{\mathrm{n}}_{\mathrm{f}} \end{pmatrix} \quad 0.15$$

where n_{a} is the refractive index of the air, $\tilde{\mathrm{n}}_{\mathrm{f}}$ is the effective refractive index of the film, $\tilde{\mathrm{n}}_{\mathrm{sub}}$ the refractive index of the substrate, k_{f} the wave vector inside the film and $\mathrm{d}_{\mathrm{tot}}$ the total thickness. Since $\mathrm{n}_{\mathrm{a}} = 1$, $\tilde{\mathrm{n}}_{\mathrm{f}} \equiv \tilde{\mathrm{n}}_{\mathrm{i}}$ and $\mathrm{k}_{\mathrm{f}} = \frac{2\pi\tilde{\mathrm{n}}_{\mathrm{f}}}{\lambda}$, eqs. 3.13-3.15 can be turned into the general form below:

$$\mathrm{I}_{\mathrm{i,i+1}} = \frac{1}{2} \begin{pmatrix} 1 + \mathrm{n}_{\mathrm{i}}/\mathrm{n}_{\mathrm{i+1}} & 1 - \mathrm{n}_{\mathrm{i}}/\mathrm{n}_{\mathrm{i+1}} \\ 1 - \mathrm{n}_{\mathrm{i}}/\mathrm{n}_{\mathrm{i+1}} & 1 + \mathrm{n}_{\mathrm{i}}/\mathrm{n}_{\mathrm{i+1}} \end{pmatrix} \quad 3.16$$

$$\mathrm{P}_{\mathrm{i}} = \begin{pmatrix} \mathrm{e}^{\mathrm{i}2\pi\mathrm{n}_{\mathrm{i}}\mathrm{d}_{\mathrm{i}}/\lambda} & 0 \\ 0 & \mathrm{e}^{-\mathrm{i}2\pi\mathrm{n}_{\mathrm{i}}\mathrm{d}_{\mathrm{i}}/\lambda} \end{pmatrix} \quad 3.17$$

From eq. 3.11 and eq. 3.16, the complex components of the transfer matrix, M, can be derived:

$$\mathrm{M}_{11} = \frac{1}{2}\left(1 + \frac{\mathrm{n}_{\mathrm{a}}}{\tilde{\mathrm{n}}_{\mathrm{Sub}}}\right) \cos\left(\frac{2\pi\tilde{\mathrm{n}}_{\mathrm{f}}\mathrm{d}}{\lambda}\right) + \frac{\mathrm{i}}{2}\left(\frac{\mathrm{n}_{\mathrm{a}}}{\tilde{\mathrm{n}}_{\mathrm{f}}} + \frac{\tilde{\mathrm{n}}_{\mathrm{f}}}{\tilde{\mathrm{n}}_{\mathrm{Sub}}}\right) \sin\left(\frac{2\pi\tilde{\mathrm{n}}_{\mathrm{f}}\mathrm{d}}{\lambda}\right) \quad 3.18$$

$$\mathrm{M}_{21} = \frac{1}{2}\left(1 - \frac{\mathrm{n}_{\mathrm{a}}}{\tilde{\mathrm{n}}_{\mathrm{Sub}}}\right) \cos\left(\frac{2\pi\tilde{\mathrm{n}}_{\mathrm{f}}\mathrm{d}}{\lambda}\right) + \frac{\mathrm{i}}{2}\left(\frac{\mathrm{n}_{\mathrm{a}}}{\tilde{\mathrm{n}}_{\mathrm{f}}} - \frac{\tilde{\mathrm{n}}_{\mathrm{f}}}{\tilde{\mathrm{n}}_{\mathrm{Sub}}}\right) \sin\left(\frac{2\pi\tilde{\mathrm{n}}_{\mathrm{f}}\mathrm{d}}{\lambda}\right) \quad 3.19$$

The other matrix element of M can be realised as the complex conjugates of eq. 3.18 and eq. 3.19 i.e. $\mathrm{M}_{22} = \mathrm{M}_{11}^{*}$and $\mathrm{M}_{12} = \mathrm{M}_{21}^{*}$. By combining eq. 3.11 with eqs. 3.16-3.19, the

reflection amplitude via $r = \frac{-M_{21}}{M_{22}}$ and transmission amplitude $t = \frac{|M|}{M_{22}}$ are obtained. Solving throughout the structure reveals the total response for r and t.

After light is reflected or transmitted, there are subsequent coherent electromagnetic waves in forwards (E_f) or backwards (E_b) directions. Associating the waves from before the air-film interface with those after the air-film interface obtains the electromagnetic fields after:

$$\begin{pmatrix} E_{f0} \\ E_{b0} \end{pmatrix} = I_{\tilde{n}_f n_a} \begin{pmatrix} 1 \\ r \end{pmatrix} = \begin{pmatrix} N_{11} & N_{12} \\ N_{21} & N_{22} \end{pmatrix} \begin{pmatrix} 1 \\ r \end{pmatrix} \quad 3.20$$

The fields after the air-film interface are thus:

$$E_{f0} = \frac{N_{11}M_{22} - N_{12}M_{21}}{M_{22}} \quad 3.21$$

$$E_{b0} = \frac{N_{21}M_{22} - N_{22}M_{21}}{M_{22}} \quad 3.22$$

These waves are counter propagating in the film and at a distance x from the interface they are described by the wave equations $F(x) = F_0 e^{ik_f x}$ and $B(x) = B_0 e^{-ik_f x}$, both waves decreasing exponentially with distance along the propagation direction ($+x$ for the forward wave, $-x$ for the backward wave) according to Beer's Law. Also, the wave propagating in the semi-infinite substrate is described as:

$$t(x_s) = t_0 e^{ik_s x_s} \quad 3.24$$

where x_s is the distance from the film-substrate interface and $k_s = \frac{2\pi\tilde{n}_s}{\lambda}$ is the wave vector in the substrate. By calculating the Poynting vector, S, at each point in the film and in the substrate, we obtain the net electromagnetic flux $I(x)$ in the structure:

$$S = I(x) = Re\{\tilde{n}_f\}(|E_f(x)|^2 - |E_b(x)|^2) - 2Im\{\tilde{n}_f\}Im\{E_f(x)E_b^*(x)\} \quad 3.25$$

$$S(x_s) = Re\{\tilde{n}_f\}(|t(x_s)|^2) \quad 3.26$$

The first term in eq. 3.25 is associated with the forward $F(x)$ and backward $B(x)$ waves, as if each of them was propagating independent of each other. The second term, which is absent in the case of non-absorbing media, appears here because of the interference between the counter-propagating waves in the absorbing film. The absorption within a Δx element is then calculated as:

$$A(x) = (\partial I(x)/\partial x)\Delta x \quad 3.27$$

This absorption calculation is done at every point in the device based on the discretization Δx we have assumed. This obtains a full optical response – known as the RTA response hereafter – upon which the heat transport simulation is performed. By implementing this optical model in a computational space with discrete intervals defined by the user, we obtain a grid that allows simulations via a semi-analytical model. By coupling with the laser spectral profile, a spectral absorption profile is obtained. Integrating over all wavelengths yields the total absorption distribution of the whole structure for unit power incidence. Finally, this spectral absorption profile is coupled with the laser temporal profile to obtain the distributed time-dependent heating source used in the heat diffusion simulations. Throughout these simulations, temperature independent refractive index is assumed for all materials. It is also assumed that thermal properties are homogenous throughout the thickness of the film. Other cases involving stratification in layers or matrices, while useful and have been reported, is not described explicitly in this model.

3.3.2 Thermal Simulation

The heat diffusion equation in 1D is solved on the above-mentioned grid. The obtained absorption distribution $A(x)$ combined with the experimental laser pulse profile $\phi(t)$ are used as the laser induced heating source:

$$\dot{q}(x,t) = A(x)\phi(t) \tag{3.28}$$

and solved numerically in the 1D heat diffusion equation:

$$(c_p\rho_m)(x)\frac{\partial T(x,t)}{\partial t} = \frac{\partial}{\partial t}\left(\kappa\frac{\partial}{\partial x}\right) + \dot{q}(x,t) \tag{3.29}$$

where c_p is the specific heat capacity (in $J/kg\cdot K$), ρ_m is the mass density (in kg/m^3), $T(x,t)$ is the local temperature transient, κ is the thermal conductivity (in $W/m\cdot K$), and $\dot{q}$ is the time-dependent thermal load coming from light absorption, as explained in the optical section, above. All above quantities are a function of space (different materials) and temperature (nonlinear response). Eq. 3.29 is solved using the 4^{th}-order Runge-Kutta integration scheme [302] (integrating over time), outputting the transient temperature at each discrete point in the multilayer. Boundary conditions are implemented on both sides including thermal insulation, fixed temperature, natural or forced convection, and thermal radiation.

Material thermal non-linearities are included via a three-parameter model. For c_p, temperature dependence follows the relationship:

$$c_p(T) = a + b\frac{\left(\frac{T}{300}\right)^c - 1}{\left(\frac{T}{300}\right)^c + b/a} \quad 3.30$$

where a, b and c the adjustable parameters fitted to heat capacity experimental data from the literature. In this three-parameter model, a represents the room temperature ($298\ K$) value, b signifies the linear regime and c represents the high temperature limit. The temperature dependence for k follows the relation:

$$\kappa(T) = a\left(\frac{T}{300}\right)^b + c \quad 3.31$$

where a, b and c the adjustable parameters fitted to thermal conductivity experimental data from the literature. In many cases, the model does not hold for low temperature cases ($< 200\ K$), where phonons are frozen out, but is valid for cases at room temperature or above. For the case of simulating LA-induced temperature rises where all interest is above room temperature, this is deemed a satisfactory approach.

Phase changes are also accommodated for. Sol-gel nitrate and acetate salts and gels are volatile [200], with salt melting (or decomposition) temperatures well within reach of LA at remarkably low fluence. Certain metals commonly used in electronics (e.g. Au, Al) have thermal properties and melting temperatures only slightly above the temperatures required for metal-oxygen-metal bond formation [196], [200], [303], [304], [305]. Thus, phase change models are necessary. The latent heat of fusion can be modelled as:

$$c_p^f(T) = \frac{a}{b\sqrt{\pi}} e^{-\frac{(T-T_m)^2}{b^2}} \quad 3.32$$

where c_p^f is the latent heat of fusion, T_m is the melting point and b is a non-zero bandwidth (typically around $10\ K$) to allow smooth evaluation of temperature derivatives.

3.3.3 Opto-thermal Simulation Parameters and Material Database

For the opto-thermal simulations to output accurate results for the basis of experiments and modelling the photochemical phenomena for MO sol-gel conversion, accurate input parameters and simulation variables must be used. Aside from the material properties contained within the material files, several other variables must be set for the simulations to correctly predict temperature rises:

1) Material thickness (nm): each layer must be named and have a defined thickness (including air). A thickness of 0 is used to define a semi-infinite layer thickness for a bulk material such as a substrate. Due to the infinite nature of the material, temperature rise cannot be simulated in a material with $0\ nm$ thickness.

2) Spare layer: a simulated very high thickness layer of several thousand nm of substrate material, measuring the temperature change and heat dispersion at the top of the bulk material. This was used for all simulations in this work, simulating the top $10000\ \mathrm{nm}$ of Si wafer. This is necessary since heat transfer cannot be calculated in a semi-infinite layer thickness used for bulk materials, as the computational grid is not imposed on semi-infinite layers. Heat transfer in this "spare layer" was tested with increasing thickness until convergence of the temperature rise and thermal properties was achieved as well as observation of the heat decay. This required a minimum of $7\ \mu\mathrm{m}$.
3) Ambient initial temperature (K): the temperature of the materials and environment before a laser pulse is applied. For all simulations, $300\ \mathrm{K}$ was set as the starting temperature.
4) Non-linearity selection: opto-thermal simulations can preset to be linear (i.e. ignore a, b and c from equations) or include non-linearities. In this work, all opto-thermal simulations included non-linearities.
5) Boundary conditions: a range of boundary conditions exist. For each simulation, the boundary conditions at the top and bottom of the structure must be defined. The three conditions are i) Isolation, where there is no heat exchange with the environment and thus flux at the point of boundary condition should be 0; ii) Fixed T, where a temperature is set based on the processing conditions the sample would be in (e.g. ambient, cooling device); iii) Convection, where a heat transfer coefficient from environment to sample or from top layer to bottom layer is inputted. This heat transfer coefficient in $\mathrm{W/m^2K}$ will depend on what kind of surface the sample is being placed on. In this work, as all simulations took place in ambient atmosphere, the top boundary was set to a fixed temperature of $300\ \mathrm{K}$. The bottom boundary condition was set to isolation.
6) Laser fluence: a non-normalised fluence that is applied, without an input area. The input fluence is changed before each simulation.
7) Grid spacing: the discrete step taken on the computational grid where the calculations of the optical model and coupling to the thermal simulations are performed. Increased grid spacing comes at the expense of far longer time for the code to complete the simulation, while extremely low grid spacing insufficiently captures temperature rise throughout each layer. Thus, optimised grid spacing creates the shortest simulation possible while capturing key aspects about the temperature rise. For this work, $5\mathrm{nm/grid}$ was a universal starting point.
8) Duration: length of time the simulation is run for. While the pulse duration of the KrF excimer is only $25\ \mathrm{ns}$, temperature rise will disperse over the course of hundreds to thousands of ns depending on the thin film materials and thicknesses involved. Opto-thermal simulation time should be set to capture the peak temperature rise as well as a large

portion of the structure's return to thermal equilibrium. In the case of nearly all material systems in this work, $500\ \mathrm{ns}$ was satisfactory.

9) Time step: how often the opto-thermal model is applied to a discrete point, until the time duration is met. Increased resolution results in longer simulations but with better measurement of the temperature rise. To capture phase changes of the materials accurately, a time step of $0.1\ \mathrm{ns}$ was used for all simulations.

A material database was created accumulating the NIR-VIS-UV optical constants from optical characterisation at NTU and various databases, and thermal properties from the literature. This was for bulk materials and thin films depending on a plethora of factors including modelling assumptions, material thicknesses and further relevant information extracted from the literature. This was for materials both used and not used in this study, as part of the overarching aim of the project was for establishing a ubiquitous coding and simulation platform for photonic processing. Table 3.4 contains some of this database, comprising materials used throughout this work as well as other materials mentioned that are of potential interest.

Along with the collation of thermal non-linearities and physical properties, adjustments were made to more accurately model thin films in some cases. In particular, sol-gel materials do not commonly report c_p many of the necessary values or non-linearities. Where thin film data for values of are unavailable (e.g. for InO_x or $In(NO_3)_3$), other properties that are available are used to derive c_p. For example, if κ is known (since it is more widely reported in the literature), the kinetic theory-based thermal conductivity in non-metals can be described as [306]:

$$\kappa = \frac{C_p \cdot L \cdot v}{3} \qquad 3.33$$

where κ is thermal conductivity, C_p is the heat capacity, L is the mean free path and v is the phonon velocity). In this equation, $\kappa \propto C_p$. Although the phonon velocity and mean free path aren't known, a first approximation can be taken to scale down the bulk values of In_2O_3 C_p based on thin film κ values in the literature. This approach was taken for InO_x, ZrO_x and AlO_x thin films and their precursors, whose properties were scarce.

This approach was also taken for latent heat of fusion, as some precursors used did not have reported values in the literature. Using known parameters about the fabrication for each solution, the latent heat for the organometallic precursors was derived from [307]:

$$\mathrm{Ln}\ x_2 = \frac{-\Delta^{\circ}_{fus}}{R}\left(\frac{1}{T} - \frac{1}{T_{fus}}\right) \qquad 3.34$$

Where x_2 is the mole fraction, $-\Delta^{\circ}_{fus}$ is the heat of fusion (a.k.a latent heat), R is the molar gas constant ($8.314\ J/mol \cdot K$), T is the absolute temperature and T_{fus} is the melting temperature. While the value is very low, comparison to other latent heat values of MO precursors and salts that do exist in the literature demonstrate these low values may be reasonable [308], [309].

Table 3.4. Summary of opto-thermal properties of a wide range of metals, semiconductors, dielectrics and organometallic precursors for use in opto-thermal simulations.

Material	$n-K$	$c_p\ (J/kg \cdot K)$	$\kappa\ (W/m \cdot K)$	$\rho\ (kg/m^3)$	$c_p^f\ (J/kg)$	$t_m\ (K)$
Si	VIS-UV SE measurements of bulk	[310] Nanowires	[311] Bulk	[303]	[303]	[303]
SiO_2	VIS-UV SE measurements of thin films	[312]Bulk	[312]Bulk	[303]	[303]	[303]
Al	VIS-UV SE measurement	[303], [313]Bulk	[303]	[303]	[303]	[303]
Au	VIS-UV SE measurements of thin films	[314], [315]	[303]Bulk	[303]	[316]	[316]
$Al(NO_3)_3$ /AlO_x	VIS-UV SE measurements of thin films	[317]Bulk	[318], [319]Amorphous thin film	[62] Sol-gel stab, TA and LA [320]Thin film, ALD [321]Bulk	-	[230], [304]
$Zr(AcAc)_4$ ZrO ,	VIS-UV SE measurements of thin films	[321]Bulk [322]Thin film	[323]Polycrystalline [324]Thin film [325]Bulk [326]Sintered nanoparticles	[317]Bulk [327], [328]	-	[230]
HfO_2	VIS-UV SE measurements of thin films	[329], [330]Bulk	[331]Amorphous thin films [332]Ultra-thin films	[303]Bulk [332]Ultra-thin film	-	
$In(NO_3)_3$ /InO_x	VIS-UV SE measurements of thin films	[333], [334], [335]Bulk	[336], [337], [338]Thin film	[339], [340]	-	[230]

3.4 Thin Film and Device Characterisation

3.4.1 Electrical Characterisation

As this work revolves around the performance of electrical devices such as TFTs and MOS capacitors, the accurate measurement of capacitance-voltage $(C-V)$ and current-voltage $(I-V)$ characteristics is fundamental. Figure 3.8 shows a labelled picture of the electrical characterisation setup used for the devices in this work.

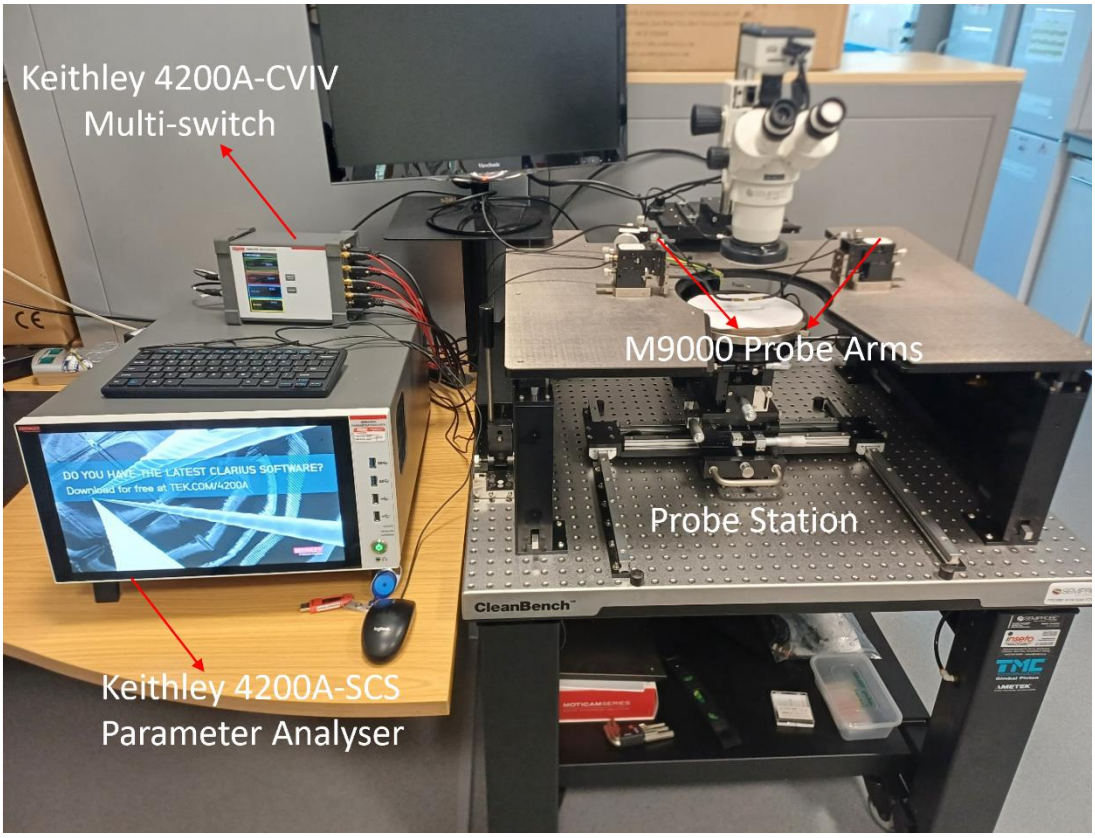

Figure 3.8 Labelled picture for the probe station used for electrical characterisation in this work. The setup involved the probe station and associated probe arms connected to the Keithley 4200A-SCS Parameter Analyser via the Keithley 4200A-SCS multi-switch. The probe station comes with equipment to view the x-y adjustable stage.

- Keithley 4200A-SCS Parameter Analyser: the primary tool for designing and performing C-V or I-V measurements. This acts as the interface between the sample, probe station and the operator.
- Keithley 4200A-CVIV Multi-switch: the four channels of the multi-switch are connected to the Keithley 4200A-SCS. Via operation of the 4200A-SCS, channels can be automatically configured between any desired state without removing the coaxial cables. For TFTs, this is extremely beneficial as contact can be maintained when switching from $I-V$ to $C-V$ characterisation.

- SemiProbe PS4L SMU Probe Station: where the sample is placed prior to measurement. The sample stage is initially covered to protect it from dust and detritus. After the cover removal, the sample is placed is placed on the table atop the vacuum chuck to ensure good contact (as the table also acts as an SMU) and stop excessive movement of the sample during probing. The probe station is accompanied by a microscope with webcam viewing through the microscope and connected to a screen, allowing precise probing of a device without excessively lowering the tungsten probe. Lowering the probe too harshly will pierce the electrode and cause mechanical strain to the thin films underneath, potentially altering the CVIV results. The sample stage also stands on an air table, elevated with compressed air to isolate the system from vibrations that can affect probing (thus the $\mathrm{CV}-\mathrm{IV}$ measurements).
- SemiProbe M9000 Probing arms: the arms are magnetically mounted above the table to prevent movement, with coaxial cables leading out the back to the SMUs of the multi-switch. Tungsten probing tips are pinned on the probing arm's edge.

In short, the probe station and M9000 probe arms make contact with the device under test (DUT) and acts as an interface with the other hardware and instrumentation. The subsequent $\mathrm{C}-\mathrm{V}$ and $\mathrm{I}-\mathrm{V}$ characteristics of a DUT are sensed by the source-measuring units (SMUs) of the multi-switch, which sends the data to the parameter analyser.

Experimental Details

For the characterisation of MOS capacitors that were atop a $\mathrm{p}^{+}-\mathrm{Si}\ (1-2\ \Omega\cdot\mathrm{cm})$ substrate, three measurement types were utilised. Capacitance-voltage $(\mathrm{C}-\mathrm{V})$ measurements were operated from $1\ \mathrm{V}$ to $-3\ \mathrm{V}$ in steps of $0.1\ \mathrm{V}$ on a dual sweep to observe the hysteresis in the reverse sweep. Capacitance-frequency $(\mathrm{C}-\mathrm{f})$ measurements were subsequently used to test the dielectric's ability to perform at a wide frequency range, in addition to investigating dispersion within the dielectric and what physical significance this holds. $\mathrm{C}-\mathrm{f}$ measurements from $1\ \mathrm{kHz}-1\ \mathrm{MHz}$ in logarithmic steps were made in the saturation regime of the $\mathrm{C}-\mathrm{V}$ curve at $-3\ \mathrm{V}$ constant bias. Breakdown field, $\mathrm{E_{br}}$, $\mathrm{I}-\mathrm{V}$ measurements operated under the JEDEC 35 standard procedure for wafer level testing of thin dielectrics [341], [342], using voltage steps scaled to the dielectric thickness (extracted from ORS or VIS-UV-SE) at a fixed step time. A voltage sweep delay of $83\ \mathrm{ms}$ with a hold time of $16.6\ \mathrm{ms}$ for a $100\ \mathrm{ms}$ step time with a correctly determined linear voltage for the film thickness allows an increase of $0.1\ \mathrm{MV/cm}$ per step. An addition $0.2\ \mathrm{s}$ hold time on the first voltage step is used to allow displacement current to settle before voltage sweeps. The value for the breakdown filed is defined as by a sudden

increase in current exceeding either ten times the expected value or a specified current compliance.

For TFTs fabricated on test grade Si $(1 - 20\ \Omega \cdot \mathrm{cm})$, $\mathrm{I} - \mathrm{V}$ characteristics via the output ($\mathrm{I_{DS}}$ vs $\mathrm{V_{DS}}$ at incrementing $\mathrm{V_{GS}}$) and transfer ($\mathrm{I_{DS}}$ vs $\mathrm{V_{GS}}$ with incrementing $\mathrm{V_{DS}}$) curves previously described in chapter 2, section 2.3 are used to discern sample information and obtain critical values for extracting μ_{FE}, $\mathrm{I_{On/Off}}$ and $\mathrm{V_{th}}$. For TFTs, $\mathrm{C} - \mathrm{V}$ measurements were also operated since areal capacitance is necessary for the calculation of mobility, as well as imparting other useful information about the sample. $\mathrm{C} - \mathrm{V}$ measurements were operated from $1\ \mathrm{V}$ to $-3\ \mathrm{V}$ in steps of $0.1\ \mathrm{V}$ unless information extracted from the $\mathrm{I} - \mathrm{V}$ measurements suggested an alternative range was necessary.

In the case of the Schottky diodes via the a-lith process, collaborators at KAUST carried out the electrical characterisation with their equipment. The Schottky diode $\mathrm{I} - \mathrm{V}$ characterisations were carried out with a Keysight B2912A precision SMU. High-frequency scattering parameter ($\mathrm{S_{11}}$) measurements were carried out in air using an Agilent PNA N5225A operating from $10\ \mathrm{MHz} - 50\ \mathrm{GHz}$. Rectifier circuit measurements were conducted in ambient atmosphere with a bias Tee ($10\ \mathrm{MHz} - 18\ \mathrm{GHz}$) through GSG Picoprobes. The output voltage was measured across a load resistor of $10\ \mathrm{M\Omega}$ connected to a Keysight 34465A Digital Multi Meter.

3.4.2 Infra-red Spectroscopic Ellipsometry (IRSE)

Spectroscopic Ellipsometry (SE) is a highly sensitive, reference-free and non-destructive optical characterisation capable of extracting optical properties, film thicknesses, compositional information, defect states and a plethora of other points of interest. It measures the change in polarisation after reflection from (or transmission through) a sample surface. This is specifically via measurement of ellipsometry angles $\Psi\ (\mathrm{E})$ and $\Delta\ (\mathrm{E})$ which are related to ratio of reflection of the p-polarised (parallel light) and s-polarisation (perpendicular light) states from the sample by [343]:

$$\rho(\mathrm{E}) = \frac{\mathrm{r_p}(\mathrm{E})}{\mathrm{r_s}(\mathrm{E})} = \tan\big(\Psi(\mathrm{E})\big)\mathrm{e}^{\mathrm{i}\Delta(\mathrm{E})} \qquad 3.35$$

where $\mathrm{r_p}$ and $\mathrm{r_s}$ are the Fresnel reflection coefficients of the p-polarised and s-polarised light respectively. After reflection, the ratio between $\mathrm{r_p}$ and $\mathrm{r_s}$ changes in amplitude and phase. $\Psi\ (\mathrm{E})$ relates to the ratio of reflected amplitude of light compared to the amplitude of incident light. Due to reflection from the sample, outgoing light amplitude in both p-polarised and s-polarised states is expected to be less. $\Delta(\mathrm{E})$ describes the phase difference between p-polarised

and s-polarised after reflection from the sample. The real numbers of $\Psi\,(\mathrm{E})$ and $\Delta\,(\mathrm{E})$ constitute the raw measurement data, but are not measured directly themselves. Instead, they are directly related to modulated intensities (i.e. always between -1 and 1) that are trigonometric functions of $\Delta\,(\mathrm{E})$. These quantities – N, C and S - are expressed as:

$$\mathrm{N} = \cos(2\Psi) \tag{3.36}$$

$$\mathrm{C} = \sin(2\Psi)\cos(\Delta) \tag{3.37}$$

$$\mathrm{S} = \sin(2\Psi)\sin(\Delta) \tag{3.38}$$

$\Psi\,(\mathrm{E})$ and $\Delta\,(\mathrm{E})$ are fitted with a suitable model to extract the dielectric function via the "pseudo-permittivity" $<\tilde{\varepsilon}(\mathrm{E},\theta)>$, calculating the measured value of $\rho(\mathrm{E})$ at each measurement angle θ [343]:

$$\begin{aligned} <\tilde{\varepsilon}(\mathrm{E},\theta)> &= <\varepsilon_1(\mathrm{E},\theta)> \; + \mathrm{i} <\varepsilon_2(\mathrm{E},\theta)> \\ &= \sin^2(\theta)\left(1 + \tan^2(\theta)\left[\frac{1-\rho(\mathrm{E})}{1+\rho(\mathrm{E})}\right]^2\right) \end{aligned} \tag{3.39}$$

However, $<\tilde{\varepsilon}(\mathrm{E},\theta)>$ is an extrinsic property of the sample that depends on both complex permittivity and geometry of each layer. Thus, a model comprised of a geometric part - accounting for the layer stack - and optical component for layer permittivity and thickness is necessary.

In spectroscopic ellipsometry, reliable fittings are only possible when more fitting variables are known than unknown. Assisting in all fittings in this thesis is that the optical constants of the Si wafer and its $\mathrm{SiO_2}$ native oxide are well known [344], thus only the fitting of the permittivity and thickness of the unknown thin film layer are required. Where multiple thin films are involved, the optical constants and thicknesses of the underlying layers are first derived to reduce the number of unknown variables and fit parameters, simplifying the model.

<u>B-Spline Model</u>

The B-Spline is an interpolation function that fits the shape of the optical constants ε_1 and ε_2 with a smooth and continuous curve consisting of multiple connected polynomial segments:

$$\mathrm{p_m}(\mathrm{x}) = \mathrm{a_m x^m} + \mathrm{a_{m-1} x^{m-1}} + \cdots + \mathrm{a_1 x} + \mathrm{a_0} \tag{3.40}$$

where $\mathrm{p_m}$ is $\mathrm{m^{th}}$ degree polynomial of the B-Spline, x is the location of knots on the x-axis for energy or wavelength (in eV) and a the control points. Johs [345] previously demonstrated the ability for B-Splines to accurately represent the dielectric function of a thin film, including complex structure in the absorption (ε_2) spectra. B-Splines can have several advantages, such as each polynomial only influencing the local shape of a curve and that the summed function can't

exceed the highest or lowest node amplitudes. B-Splines can act as a more straightforward method to obtain the dielectric function compared to the required accuracy of the oscillator model (see below), provided the correct resolution (number of knots) is used.

Oscillator Models

The optical model used to extract the permittivity of an unknown layer and represent the physical phenomena taking place in the material typically comprises a summation of individual oscillators representing contributions due to interband, intraband and optical phonon absorptions [68], [346]. The permittivity via this oscillator model is a summation of the high-frequency permittivity and the individual oscillators [333]:

$$\tilde{\varepsilon}(\mathrm{E}) = \varepsilon_{\infty} + \sum_{\mathrm{n}=1}^{\mathrm{m}} \tilde{\varepsilon}_{\mathrm{n}}(\mathrm{E}) \tag{3.41}$$

The most common oscillator used throughout SE fittings in this work is the Gaussian oscillator. The majority of features in the SE spectra are due to optical phonon absorptions, which Gaussians can accurately fit at the IR absorption centre:

$$\tilde{\varepsilon}_{\mathrm{Gaussian}}(\mathrm{E}) = \mathrm{A_n}\left\{\left[\Gamma\left(\frac{\mathrm{E}-\mathrm{En}}{\sigma_{\mathrm{n}}}\right) + \Gamma\left(\frac{\mathrm{E}+\mathrm{En}}{\sigma_{\mathrm{n}}}\right)\right] + \mathrm{i}\left(\exp\left[-\left(\frac{\mathrm{E}-\mathrm{En}}{\sigma_{\mathrm{n}}}\right)^2\right] - \exp\left[-\left(\frac{\mathrm{E}+\mathrm{En}}{\sigma_{\mathrm{n}}}\right)^2\right]\right)\right\} \tag{3.42}$$

$$\sigma_{\mathrm{n}} = \frac{\mathrm{Br_n}}{2\sqrt{\ln(2)}} \tag{3.43}$$

where E is the photon energy and $\mathrm{A_n}$ is the peak amplitude for ε_2 at peak central energy En. Γ is a convergence series term to ensure Kramers-Kronig consistency ε_1 and σ_{n} is a value defined to allow $\mathrm{Br_n}$ to approximate to the FWHM, whose calculation in seen in eq. 3.43. The parameters are fit using the Levenberg-Marquardt method in a nonlinear regression algorithm [347]. The errors are derived from the 90% confidence intervals of the algorithm and the quality of fit can be assessed via the root mean squared error (MSE) of the fit (see eq. 3.44). The MSE is best described as a summation of the difference between the measured data and the generated oscillator model:

$$\mathrm{MSE} = \sqrt{\frac{10^6}{3\mathrm{n}-\mathrm{m}}\sum_{\mathrm{i}=1}^{\mathrm{n}}\left[\left(\mathrm{N_{mes_i}} - \mathrm{N_{fit_i}}\right)^2 + \left(\mathrm{C_{mes_i}} - \mathrm{C_{fit_i}}\right)^2 + \left(\mathrm{S_{mes_i}} - \mathrm{S_{fit_i}}\right)^2\right]} \tag{3.44}$$

where n is the number of data points defined by each individual energy/frequency measured, m is the number of fitting parameters and N, C and S are the previously defined modulated intensities. The use of N, C and S is beneficial since they are bound between -1 and 1 which fits to the MSE definition, while maintaining precision and accuracy in these values for this rotating compensator ellipsometer configuration [348].

Experimental Details

IRSE measurements were performed with a J. A. Woollam Mark II IR Variable Angle Spectroscopic Ellipsometer (VASE) ($1.6-40\mu m; 250-8000\ cm^{-1}; 0.03-0.992\ eV$) and, in cases where optical constants in the NIR-VIS-UV were necessary, a J. A. Woollam Focused M2000-DI VASE ($0.193-1.69\ \mu m;\ 0.734-6.424\ eV$). In many cases, to remove instrumental noise that affect fittings, measurement spectra were restricted to produce models. The use of the IR-VASE is more prevalent in this work, hence a large portion of the focus shall be on this. A schematic of the IR-VASE can be found in Figure 3.9 [64].

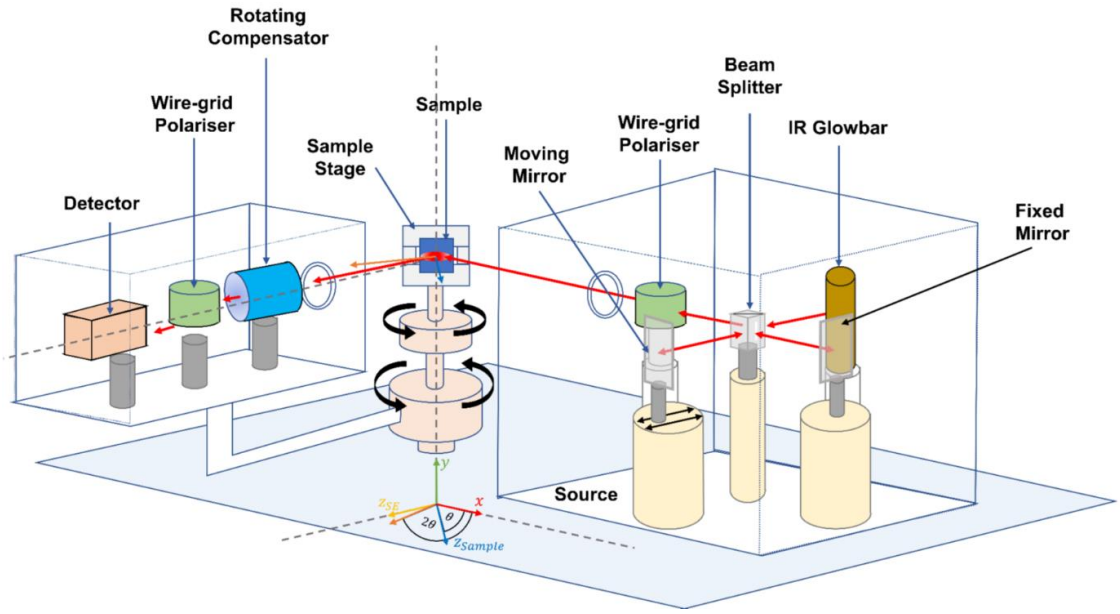

Figure 3.9 Schematic of the J. A. Woollam IR-VASE Mark II. The source in the right-hand side cube is comprised of a SiC glow bar, beam splitter, fixed mirror, moving mirror, wire-grid polariser and an iris. This delivers linearly polarised light to the sample surface. The sample surface is manipulated by a rotating sample stage to ensure light is incident at angle θ to the sample surface with the sample mounted on a semi-hollow stage with a vacuum chuck. The detector unit containing a wire-grid polariser, rotating compensator and a detector is held at angle 2θ. The rotating compensator allows the simultaneous measurements of $\Psi\ (E)$ and $\Delta\ (E)$. Borrowed with permission from [64].

The schematic shows the IR-VASE can be split into the IR source, the sample manipulator and the detector. The source is comprised of a SiC IR glowbar source, with a beam splitter diverting the IR radiation to a fixed mirror, moving mirror and wide band wire-grid polarisers.

This delivers linearly polarised light to the sample surface away from the source via an iris. The sample vertically mounted on the sample stage (affixed by a vacuum chuck) is rotated with the sample stage as required to meet the desired incident angle θ. One of the stages used is semi-hollow, to permit IR radiation to pass through for IRT measurements (see chapter 3, section 3.4.3 for information on IRT measurements). The detector unit is rotated in accordance with the sample stage and source unit so that a $\theta - 2\theta$ consistency between source and detector is maintained. The detector unit contains a rotating compensator, wire-grid polariser and detector. The use of an RCE in this setup allows for simultaneous measurements of $\Psi\,(\mathrm{E})$ and $\Delta\,(\mathrm{E})$ for multiple angles at a wide spectral range.

The ellipsometry parameters $\Psi\,(\mathrm{E})$ and $\Delta\,(\mathrm{E})$ were obtained using the acquisition parameters seen in Table 3.4. Measurements were taken at several angles of incidence, typically $55° - 75°$ by $10°$. There are several measurement parameters with different significances:

- Resolution (cm^{-1}): spectral measurement resolution. A higher resolution entails a lengthier measurement, but increases the number of measurement nodes so the shape of the line spectra can be more accurately captured. The best resolution is a compromise between accurately capturing the shape of the spectra in the minimal time while considering the purpose of the analysis and information gathered. For example, fitting mainly for the thickness of a metallic thin film will require far fewer data points and time than determining the composition of a sol-gel thin film.
- Spectra/revolution: number of measurement position per revolution of the rotating compensator.
- Scans/Spectrum: number of FTIR spectrometer mirror scans performed at each measurement position during a revolution.
- Cycles/angle: number of times one angle experiences a full complete measurement (i.e. all scans performed). The cycles are then averaged.

Table 3.4 IRSE parameters used for measuring various samples with IRSE and IRT in this work.

Measurement	Resolution (cm^{-1})	Spectra/Rev	Scans/Spectrum	Cycles/Angle	No. Angles
Short	16	15	1	1	1
Standard	8	15	10	2	3
Long	4	15	20	3	3

3.4.3 Infra-red transmission (IRT)

The J. A. Woollam Mark II IR-VASE can also perform IR transmission (IRT) measurements of the spectral transmission from $250 - 8000\ \mathrm{cm}^{-1}$ at normal incidence, which have their own merits or can be used for improving the confidence of experiments. For example, the typical finish on the backside of substrates leads to reflections from the back surface that are incoherent with the measured reflection from the surface. To avoid additional complexity in the model by accounting for these reflections, suppression via roughening the back surface [349] or index matching the backside with semi-solid materials (e.g. adhesive tape, paint) [350] can be employed. For this work, roughening was used exclusively instead of index matching, employing IRT measurements to confirm reduction or elimination of transmission across the majority of the IRSE spectral range. Specifically, the transmission was determined to be a maximum of 5% before proceeding to SE measurements.

For all samples in this work, the substrate backside (Si, Glass) was deliberately roughened before measurement. Roughening was conducted in two different methods. With small samples, samples were placed face-down on dicing tape to secure them before roughening using a Dremel tool with a diamond head, operating at $5000\ \mathrm{RPM}$. With larger samples or "seed" materials, samples were roughened using the Trumpf 3230 OEM $532\ \mathrm{nm}$ laser. The laser was brought into sub-mm focus, and a De Moire grid was laser marked into the substrate backside, with 10 passes of the pattern completed in sub-mm focus with $1000\ \mathrm{mm/s}$, $10\ \mathrm{kHz}, 100\%$ power and $0.1\ \mathrm{mm}$ hatch spacing. The sample was cleaned with ultrasonication in DI water and IPA for $10\ \mathrm{mins}$ each and dried with an N_2 stream. IRT measurements were performed immediately prior to measurement:

$$\mathrm{T(E)} = \frac{\mathrm{n_0(E)}\cos^2(\theta_{\mathrm{N+1}})|\xi_0^+|^2}{\mathrm{n_{N+1}(E)}\cos^2(\theta_0)\left|\xi_{\mathrm{N+1}}^+\right|^2} \tag{3.45}$$

where N is the total number of layers ($\mathrm{N} = 0$ is the layer of the incident light). ξ_0^+ and $\xi_{\mathrm{N+1}}^+$ can be extracted from the Fresnel coefficients from ORS as in eqs. 3.50-3.53, following the matrix method that is described. The acquisition parameters for IRT were the same as their subsequent IRSE measurements.

3.4.4 Optical Reflectance Spectroscopy (ORS)

Optical reflectance at normal incidences to the sample in the UV-VIS spectral range is known as ORS. Intensities from a sample are compared to the lamp intensity measured and known reference mirror ($\mathrm{Al}, \mathrm{Ag}, \mathrm{Au}$ and Si are commonly used) with subtraction of the background instrumental noise (known as the dark measurement).

If boundary conditions are established for plane waves at a plane interface between two materials of complex dielectric function $\tilde{\varepsilon}_i(E)$ and $\tilde{\varepsilon}_t(E)$ [351], Fresnel reflection and transmission coefficients ($r_F(E)$ and $t_F(E)$, respectively) at photon energy E can be derived. Figure 3.10 shows the interaction of light at the plane interface.

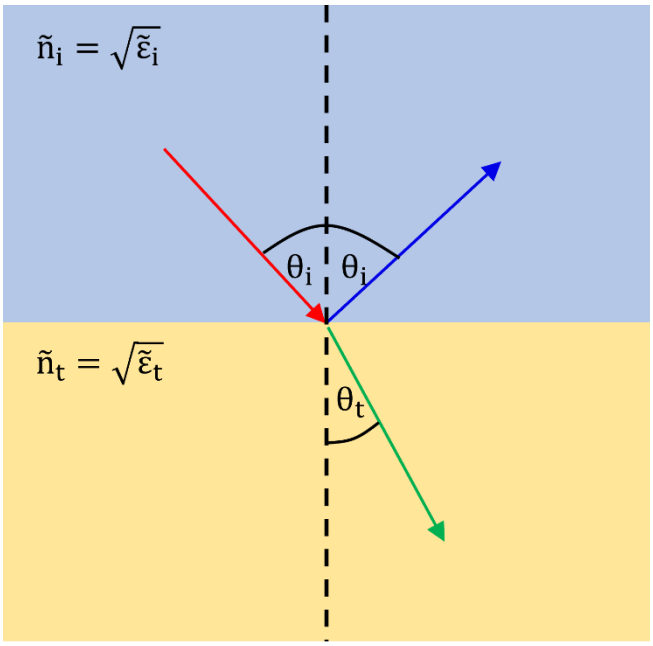

Figure 3.10 Schematic of light refraction and reflection at a boundary between two regions with different refractive indices, $\tilde{n}_i$ and $\tilde{n}_t$. The incoming light (red arrow) at angle of incidence θ_i normal to the interface is either transmitted (green arrow) at refracted angle θ_t or reflected at angle $\theta_r = \theta_i$.

The Fresnel coefficients are defined separately for cases of transverse electric (TE) and transverse magnetic (TM) modes. Thus, we describe two cases of a linearly polarised wave perpendicular to plane of incidence (TE, denoted as s-polarised) or parallel to plane of incidence (TM, denoted as p-polarised). The state of polarisation is indicated within the superscript of the forthcoming equations.

$$r_F^p(E) = \frac{\tilde{\varepsilon}_t(E)k_i(E) - \tilde{\varepsilon}_i(E)k_t(E)}{\tilde{\varepsilon}_t(E)k_i(E) + \tilde{\varepsilon}_i(E)k_t(E)} \quad 3.46$$

$$r_F^s(E) = \frac{k_i(E) - k_t(E)}{k_i(E) + k_t(E)} \quad 3.47$$

$$t_F^p(E) = \frac{2k_i(E)}{\tilde{\varepsilon}_t(E)k_i(E) + \tilde{\varepsilon}_i(E)k_t(E)} \quad 3.48$$

$$t_F^s(E) = \frac{2\tilde{\varepsilon}_t(E)k_i(E)}{k_i(E) + k_t(E)} \quad 3.49$$

where $k_i(E)$ and $k_t(E)$ are the wavevectors of the incident and transmitted wave perpendicular to the interface. The polarisation dependence of the Fresnel coefficients is fundamental for ellipsometry measurements [348].

In a non-absorbing incident medium (i.e. ε_i is real and positive), the Fresnel coefficients can be used to determine the frequency dependent reflectance and transmittance (($R(E)$ and $T(E)$) for p-polarised and s-polarised electromagnetic waves:

$$R^P(E) = \frac{|\xi_r(E)|}{|\xi_i(E)|} = \left|r_F^p(E)\right|^2 = \left|\frac{1 - \frac{\varepsilon_i(E)k_t(E)}{\tilde{\varepsilon}_t(E)k_i(E)}}{1 + \frac{\varepsilon_i(E)k_t(E)}{\tilde{\varepsilon}_t k_i}}\right| \quad 3.50$$

$$R^S(E) = \frac{|\xi_r(E)|}{|\xi_i(E)|} = \left|r_F^p(E)\right|^2 = \left|\frac{1 - \frac{k_t(E)}{k_i(E)}}{1 + \frac{k_t(E)}{k_i(E)}}\right| \quad 3.51$$

$$T^P(E) = \frac{|\xi_t(E)|}{|\xi_i(E)|} = 1 - R^P(E) = \frac{4\left(\frac{\varepsilon_i(E)k_t(E)}{\tilde{\varepsilon}_t(E)k_i(E)}\right)}{\left|1 + \frac{\varepsilon_i(E)k_t(E)}{\tilde{\varepsilon}_t(E)k_i(E)}\right|} \quad 3.52$$

$$T^S(E) = \frac{|\xi_t(E)|}{|\xi_i(E)|} = 1 - R^S(E) = \frac{4\frac{k_t(E)}{k_i(E)}}{\left|1 + \frac{k_t(E)}{k_i(E)}\right|} \quad 3.53$$

At normal incidence ($\theta_i = 0$), $R(E)$ is identical for p-polarised and s-polarised light:

$$R(E) = \left|\frac{n_i - \tilde{n}_t(E)}{n_i + \tilde{n}_t(E)}\right| \quad 3.54$$

where n_i is the refractive index of the non-absorbing incident medium (Air) and $\tilde{n}_t = \sqrt{\tilde{\varepsilon}_t} = n_i + i\kappa_i$ is the complex refractive index of the potentially absorbing material with real refractive index, n_t, and extinction coefficient, κ_t. For multi-layer structures (common in this work), back-reflections at material interfaces must be accounted for as they cause interference effects in the collected light. Determination of $R(E)$ and $T(E)$ for such multilayer structures requires the Matrix Method [352] utilising either 2×2 or 4×4 matrices for both reflection and transmission Fresnel coefficients for each layer. The overall optical response is then determined from the multiplication of the individual matrices. Heavens [353] provides a short description of the method by examining the electric vector ξ_n^+ of a wave travelling in the direction of incidence and in the opposite direction ξ_n^- within the nth layer. These waves are described by:

$$\xi_n^+ = \frac{1}{t_n}(\xi_{n-1}^+ \exp(i\theta_{n-1}) + r_n(\xi_{n-1}^- \exp(-i\theta_{n-1})) \quad 3.55$$

$$\xi_n^- = \frac{1}{t_n}(r_n\xi_{n-1}^+ \exp(i\theta_{n-1} -) + (\xi_{n-1}^- \exp(-i\theta_{n-1})) \quad 3.56$$

where t_n and r_n are the transmission and reflection Fresnel coefficients, respectively. The above equations can then be re-written into matrix form:

$$\begin{pmatrix}\xi_n^+\\ \xi_n^-\end{pmatrix}=\frac{1}{t_n}\begin{pmatrix}\exp(i\theta_{n-1}) & r_n\exp(-i\theta_{n-1})\\ r_n\exp(i\theta_{n-1}) & \exp(-i\theta_{n-1})\end{pmatrix}\begin{pmatrix}\xi_{n-1}^+\\ \xi_{n-1}^-\end{pmatrix}=\frac{1}{t_n}M_{n-1}\begin{pmatrix}\xi_{n-1}^+\\ \xi_{n-1}^-\end{pmatrix} \quad 3.57$$

For a stack of N layers, it can be derived that:

$$\begin{pmatrix}\xi_{N+1}^+\\ \xi_{N+1}^-\end{pmatrix}=\frac{M_N M_{N-1}\cdots M_2 M_1}{t_N t_{N-1}\cdots t_2 t_1}\begin{pmatrix}\xi_0^+\\ \xi_0^-\end{pmatrix} \quad 3.58$$

Finally, the reflectance can be calculated from:

$$R(E)=\frac{|\xi_{N+1}^-|^2}{|\xi_{N+1}^+|^2} \quad 3.59$$

Experimental Details

Where VIS-UV SE was unavailable and sample size was limited, ORS at normal incidence was used to determine both VIS-UV optical properties and film thickness, with the VIS-UV optical properties measured from $225-870\ \text{nm}$ $(1.425-5.510\ \text{eV})$. The ORS system comprises a balanced deuterium-halogen light source (Ocean Optics DH2000BAL), transparent co-axial fibre optics cables (Avantes Reflection Probe), a CCD detector as a tabletop spectrometer (Ocean Optics USB4000) and a high-line density grating in combination with the Ocean Optics Spectrasuite Software for acquisition. The experimental setup is shown in Figure 3.11a.

The spectral light intensity of the lamp $I_L(E)$ was recorded using several reference mirrors – $250\ \text{nm}$ Al thermally evaporated thin film deposited on Si, a $n-\text{Si}\ (1-20\ \Omega\cdot\text{cm})$ reference wafer, $100\ \text{nm}$ sputtered Au thin film on Si and a $100\ \text{nm}$ sputtered Ag thin film on Si. The inherent problem of a reference sample is changes in sample condition affect mirror quality, increasing the possibility of erroneous analysis (e.g. $R(E)>1$). The spacing between the transparent optical fibre and sample surface was adjusted to maximise reflection intensity. The number of counts was subsequently adjusted below its saturation point via reduction of integration time. The light source was then blocked to record the intrinsic noise of the spectrometer $I_D(E)$. The reflective light intensity of the samples ($I_S(E)$) was then measured.

$R(E)$ was calculated using the equation:

$$R(E)=\frac{I_S(E)-I_D(E)}{\left(I_L(E)-I_D(E)\right)}R_{th}(E) \quad 3.60$$

where $R_{th}(E)$ represents the theoretical reflectivity of the chosen mirror, which is determined via ellipsometry [354].

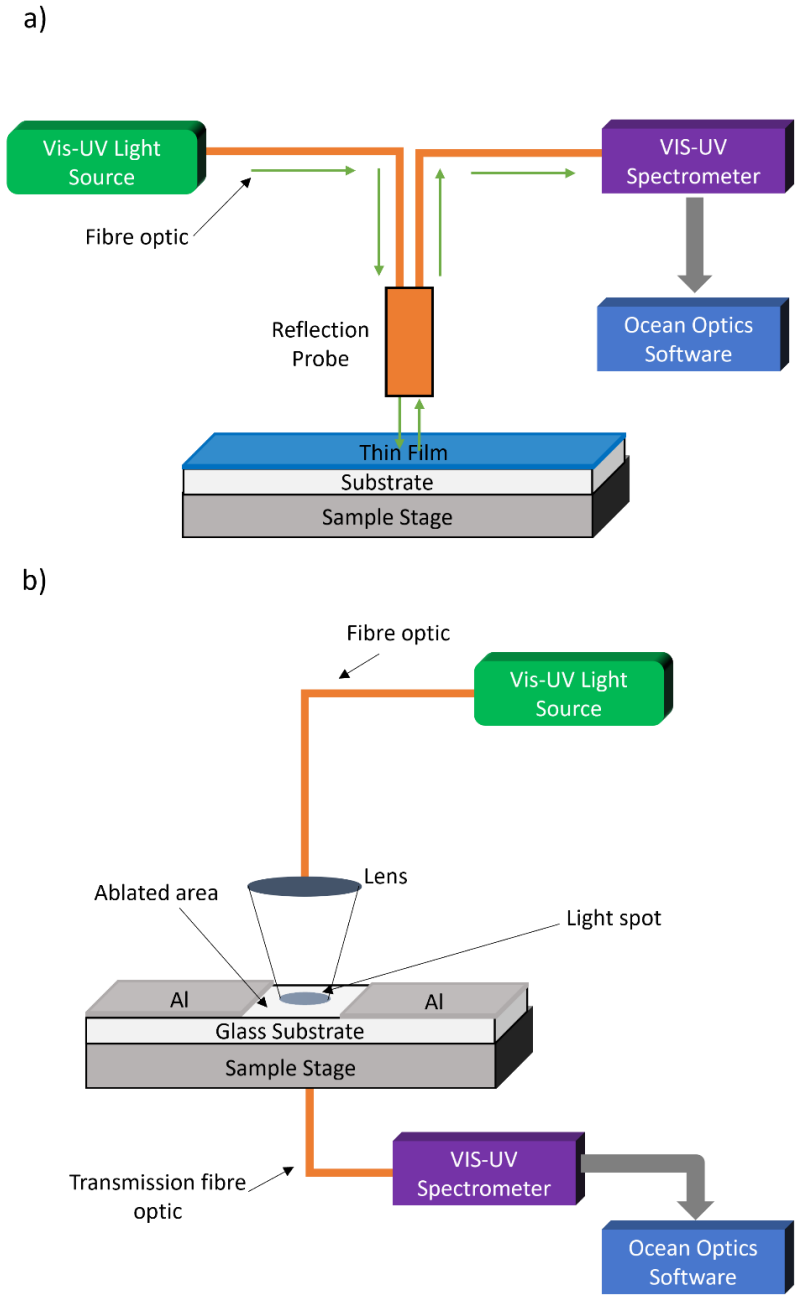

Figure 3.11 a) Illustration of experimental setup for ORS measurements. Light (green arrows) is directed via fibre optic cables towards a thin film sample on a reflective substrate through a probe hovering a short distance above the sample. Light reflects from the surface of the thin film, the interfaces between other layers or back-reflected from the surface and interface into the reflection probe and collected by a spectrometer so $R(E)$ can be determined. This method also works for determining thin film thickness as long as one or more back-reflections occurs, so interference fringes can be used to calculate the thickness. b) Schematic of the transmission spectroscopy measurements used on borosilicate glass substrates. The same light source as ORS is used to direct light via fibre optics cables and a fibre optic lens to create a light microspot smaller than the dimensions of the ablated area. A coaxial fibre optic sends light intensity to the spectrometer, which is used to determine $T(E)$.

The J. A. Woollam proprietary software was used to solve the matrix method for a combination of transparent and potentially semi-absorbing layers with a general incident angle. A geometric model is built layer by layer with $\tilde{n}$ or $\tilde{\varepsilon}$ for each layer. The region below the band-gap for the material is used to fit a constant n and d to the data with a Levenberg-Marquardt nonlinear regression algorithm [347].

3.4.5 Transmission Spectroscopy

As $T(E)$ can also be determined for a multilayer structure via the method described above in chapter 3, section 3.4.4, it follows that $T(E)$ can be measured with an adaptation of the ORS experimental setup. Taking eq. 3.52 and eq. 3.53 at normal incidence, where p-polarised and s-polarised waves return identical results reveals:

$$T(E) = \frac{|\xi_t(E)|}{|\xi_i(E)|} = 1 - R(E) = 1 - \frac{I_S(E) - I_D(E)}{\left(I_L(E) - I_D(E)\right)} R_{th}(E) \qquad 3.61$$

For the borosilicate glass, light will transmit but roughness will cause scattering, causing a change in transmission relative to the glass substrate. For the a-lith process, minimal damage and minimal change to transmission is desired. Thus, transmission spectroscopy can be used as a rapid method of quality control for determining the glass substrate quality.

Figure 3.11b shows the setup for transmission spectroscopy. The deuterium-halogen light source (Ocean Optics DH2000BAL) is projected towards the ablated area of the borosilicate glass substrate through a fibre optic lens, which produces a micro spot smaller than the ablated area width (or diameter) that avoids unwanted additional light collection from reflections off the adjacent Al. The sample sits atop a Filmetrics SS-3 sample stage, which comes with a transparent panel and coaxial fibre optic fitting directly beneath the sample position. The light projects through the glass and into a coaxial fibre optic cable, whose raw intensity is collected and processed in the OceanOptics Spectrasuite software to produce transmission values. For this processing, air with $T(E) = 1$ is used as the baseline, meaning the light source incident on any surface should experience a decrease in transmission. Measurement of the unprocessed glass acted as a further reference.

3.4.6 Atomic Force Microscopy (AFM)

Atomic Force Microscopy is a common form of scanning probe microscopy used to characterise the topography of a material surface. A surface is scanned with a sharp tip attached to a reflective cantilever, the total assembly of which is the probe. A laser is directed at the reflective cantilever and reflected to a photodetector. The detector is position sensitive, allowing tracking of vertical and lateral deflection and the creation of a 3D-high resolution height

map to pm level. AFM is extremely adaptable, with the use of different tips and environments (e.g N_2) to obtain properties such as surface roughness, work function, crystal topographies, particle size and true topographical measurements. Figure 3.12 gives a schematic of the fundamentals for an AFM setup.

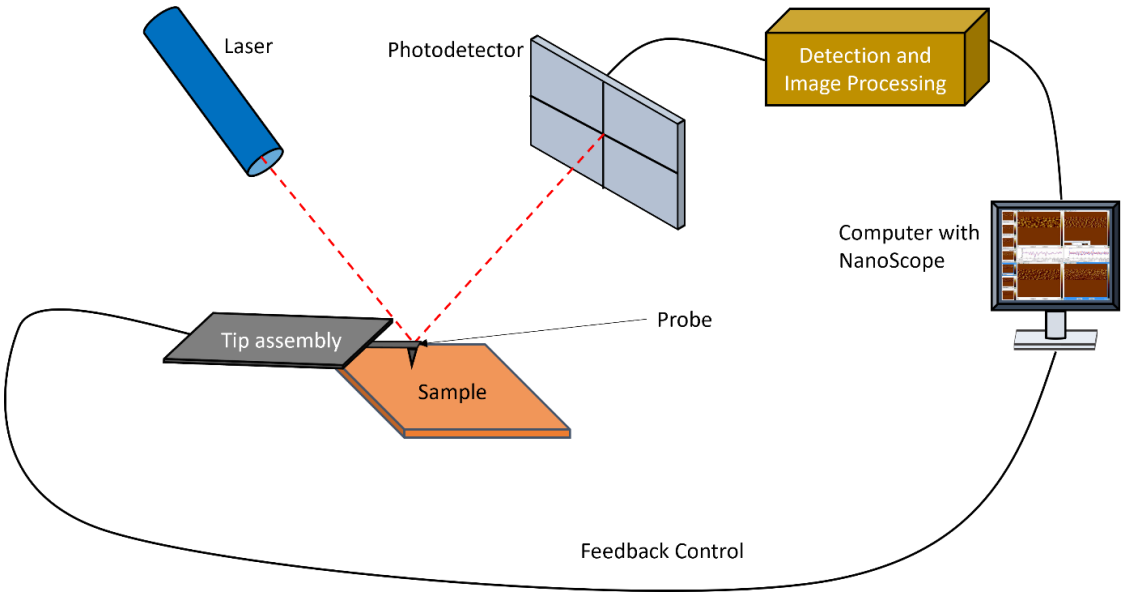

Figure 3.12 Basic principles and elements of an AFM setup.

AFM measurements in all modes rely on feedback loops based on changes of a parameter in relation to a "set point" which is then adjusted by an operator. The definition of set point depends on the type of AFM mode used. There are three common types of AFM modes: contact mode, tapping mode and force spectroscopy. Force spectroscopy is not discussed here. Contact mode maintains constant contact between the probe tip and the sample surface. Set point relates to how hard a probe presses into the samples surface via the changes in deflection of the cantilever. As the probe scans, the AFM will move the probe vertically to compensate for changes in deflection, with the changes in z-direction producing an image [355]. Contact mode has far fewer variables, thus a lower entry point that allows images to easily be taken. However, probes wear far quicker in contact mode than other modes which can lead to image artifacts and higher cost via throughput of tips [356]. Samples can also be damaged due to the constant probe interaction. Tapping mode undulates the cantilever in the z-direction while scanning along the sample surface so only intermittent contact with the surface is made, with the frequency of z-direction change governed by the resonant frequency of the cantilever. The amplitude of the vertical oscillation acts as the set point and is affected when the probe contacts the sample surface. The changes in z-direction are compensated for by returning the probe to the set point using a piezo actuator and the change in z-direction amplitude measured to produce a height map [357]. Tapping mode has far more parameters to adjust to obtain a high-quality image, but probe lifetime is increased, image resolution increased and potential damage to a sample

surface is reduced [358]. Furthermore, the increased parametrisation and wider material variety that can be imaged also means tapping mode acts as the basis for further advanced modes such as Electric Force Microscopy (EFM).

Several statistics can be extracted from the height maps [356]. In all aspects of this work, minimising roughness was of paramount importance for the dielectric-semiconductor interface in TFTs or for seamless a-lith methodology. From AFM measurements, roughness can be accounted for in a few different ways:

1) The arithmetic roughness, R_a, as the mean value of the surface height deviations, Z_i, from the arithmetic mean surface height, $\bar{Z}$, for the data points of the scanned area of number n:

$$R_a = \frac{1}{n}\sum_{i=1}^{n}(|Z_i - \bar{Z}|) \qquad 3.62$$

2) Root-mean-square roughness, R_{RMS} or R_q, as the standard deviation of the surface height values from the arithmetic mean height for the data points of the scanned area:

$$R_q = \left[\frac{1}{n}\sum_{i=1}^{n}(|Z_i - \bar{Z}|)^2\right]^{1/2} \qquad 3.63$$

3) Z_{range}, as the difference between maximum, Z_{max}, and minimum, Z_{min}, vertical distances in the scanned area:

$$Z_{range} = Z_{max} - Z_{min} \qquad 3.64$$

In this work, AFM was carried out in tapping mode using a Brucker Dimension Icon Scanning Probe Microscope - with NanoScope software - at ambient conditions to determine the surface roughness and character of ZrO_x and AlO_x dielectrics for TFT applications and of borosilicate glass substrate surfaces after ablation of a thin metal film. For the dielectrics, multiple sites across a laser spot were inspected to obtain images $2\ \mu m \times 2\ \mu m$ in size. For the glass substrates, far larger images of $50\ \mu m \times 50\ \mu m$ were taken to capture the full breadth of the Trumpf laser spot size.

3.4.7 Optical Profilometry

An optical profilometer acts a non-contact method to investigate the surface profile of a sample, using interferometry for a 3D reconstruction of a material surface. It's basic operating principle can be seen in Figure 3.13.

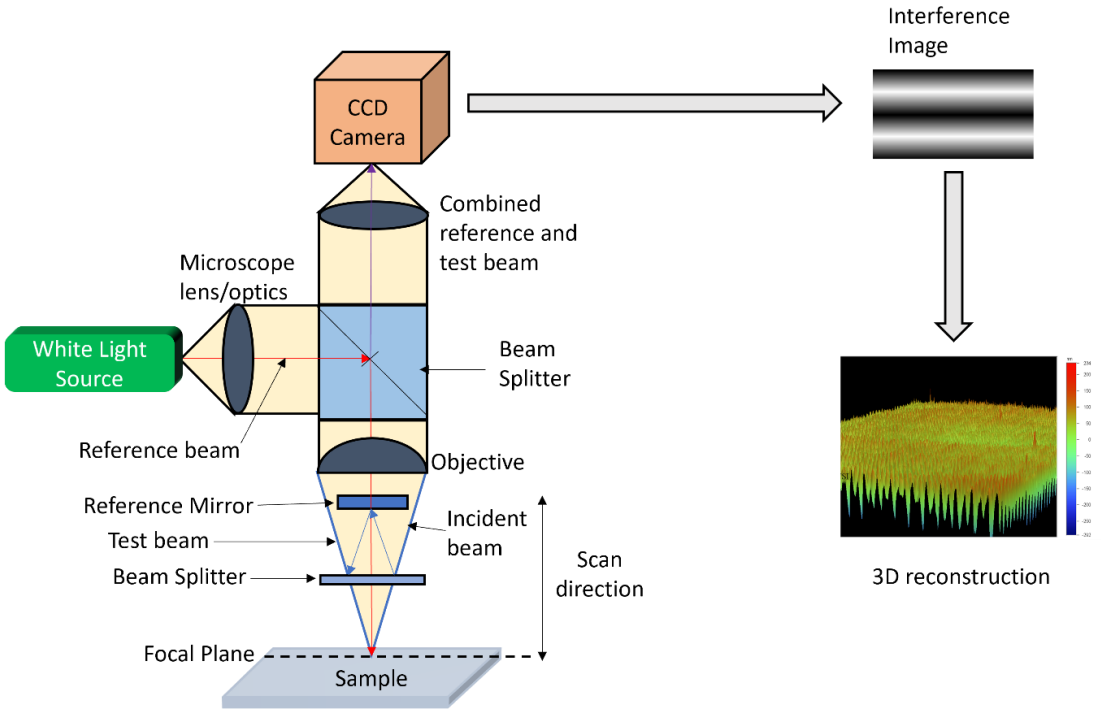

Figure 3.13 Simplified schematic of the operation of an optical profilometer. A white light source is sent to a beam splitter, creating a reference beam and test beam. The test beam is subjected to further optics and reflection from the sample at the focal plane, which recombines and interferes with the reference beam. The interference information is translated to an interference image, which is converted to a 3D reconstruction of the sample surface.

A white light source is projected onto a sample through a microscope lens before encountering a beam splitter, producing a reference beam and test beam. The reference beam reflection occurs at the mirror at the objective, while the test beam reflection occurs at the sample surface. These reflections recombine and interfere in transit back to the microscope lens and towards a CCD camera. The beam intensity is highest when the optical path of the test beam equals that of the reference beam. By scanning the objective vertically relative to the sample and documenting each vertical position where maximum beam intensity is achieved along with differences between projected and reflected light, calculations can be performed to produce a 3D reconstruction of the sample surface via an interference image [359].

Due to the inherent nature of the laser, samples ablated with the Trumpf DPSS lasers produce repetitive patterns of the hatch. Though AFM can confidently determine the topography and roughness of a surface, cross-verification of these results with an alternative non-contact method improves the confidence of these results by ruling out the possibility of artifacts. Thus, in this work, an optical profilometer (WYKO NT1100) was used for both verification of AFM results and for topography analysis across larger surface sizes than the maximum dimensions of AFM images, specifically regarding the state of the borosilicate glass

substrates after Al ablation. $1.2\ \mathrm{mm} \times 0.9\ \mathrm{mm}$ 3D images were produced upon investigating select laser processing conditions, with a maximum vertical resolution of $1\ \text{Å}$. A tungsten-halogen white light source was irradiated through a $\times 20$ objective lens and field of view lens, scanning vertically to find the focus at the glass surface.

4. Opto-thermal Simulations of sol-gel, LA InO_x TFTs

The work in this chapter was completed in collaboration with the University of Ioannina (UoI), Greece. The Computational Materials Science Laboratory team at UoI developed an initial version of the opto-thermal coding platform. NTU (Matthew Spink and Dr Nikolaos Kalfagiannis) conducted testing and troubleshooting of the code to aid UoI in producing more accurate iterations of code. Matthew Spink then solely conceived the idea for the work in this chapter and performed the opto-thermal simulations independently.

In order to achieve optimal electrical and optical characteristics in metal oxides (MOs) used for devices, it is crucial to attain a detailed understanding of the physicochemical phenomena and light-matter interactions that occur during precursor decomposition and subsequent growth. Although recent studies have explored the conversion process in certain materials, these investigations have largely been limited to thermal annealing (TA) procedures. The photochemical conversion process achieved via laser annealing (LA) remains largely unexplored. The nature of laser annealing necessitates a comprehensive process revolving around optical, thermal, and electronic regimes tailored to specific materials. The complexity and coupling of these regimes demand a comprehensive modelling strategy that encompasses optical and thermal non-linearities, material phase transitions, and LA process parameters.

This chapter introduces a methodological approach involving coupled self-consistent opto-thermal simulations. These simulations serve to predict temperature rise during single pulse laser annealing of indium nitrate $\mathrm{In(NO_3)_3}$ films of varying thicknesses applied to $\mathrm{SiO_2}$, supported on a silicon substrate. The study aims to correlate the predicted temperature rises with the electrical characteristics of previously fabricated devices of these architectures at NTU and the precursor conversion into a thin film of indium oxide ($\mathrm{InO_x}$).

The simulations targeted on single pulse, multi-fluence investigations, focusing on a $10\ \mathrm{nm}$ layer of $\mathrm{In(NO_3)_3}$ on $\mathrm{SiO_2}$ layers of $100\ \mathrm{nm}$, $200\ \mathrm{nm}$, and $400\ \mathrm{nm}$ thickness. This setup was processed with an excimer laser at a wavelength of $248\ \mathrm{nm}$. Error calculations due to thermal property variations and systematically propagated errors within optical constants were conducted throughout the modelling process. The resulting temperature rises were aligned with observed output and transfer curves alongside performance metrics of thin-film transistors (TFTs) previously developed at NTU. The comprehensive nature of these opto-thermal simulations, particularly the predictive modelling of temperature rises in thin films derived from sol-gel processes, is groundbreaking. It paves the way for the development of a universal tool for opto-thermal simulations, critically exploring the strengths and limitations of the current modelling framework using materials with well-characterized opto-thermal properties.

4.1 Simulation Set-up

NTU has previously conducted studies on fabricating TFTs using LA to induce conversion in organometallic precursors to fabricate sol-gel InO_x thin films on SiO_2, with a motivation of providing alternative processing paradigms for large-area electronics. NTU initially used $400\ nm\ SiO_2$ with a range of fluences and number of pulses, ultimately demonstrating optimised TFTs that had mobility μ_{FE} up to $13\ cm^2/Vs$, switching ratios $I_{On/Off} \approx 10^5$ and a threshold voltage (V_{th}) tuneable by a low temperature annealing [63]. Further work at NTU by Koutsiaki [64] using InO_x progressed this by further investigating the role of the gate dielectric thickness during LA of the organometallic precursor, investigating through the scope of device performance. Results showed LA had an extreme capability to tailor the conductivity of InO_x and induce conversion of the organometallic gel phase, culminating in TFTs with even higher carrier mobility than previously ($\mu_{FE} = 18\ cm^2V^{-1}s^{-1}$), high $I_{On/Off} \approx 10^5$ and V_{th} closer to $0\ V$ without additional processing steps.

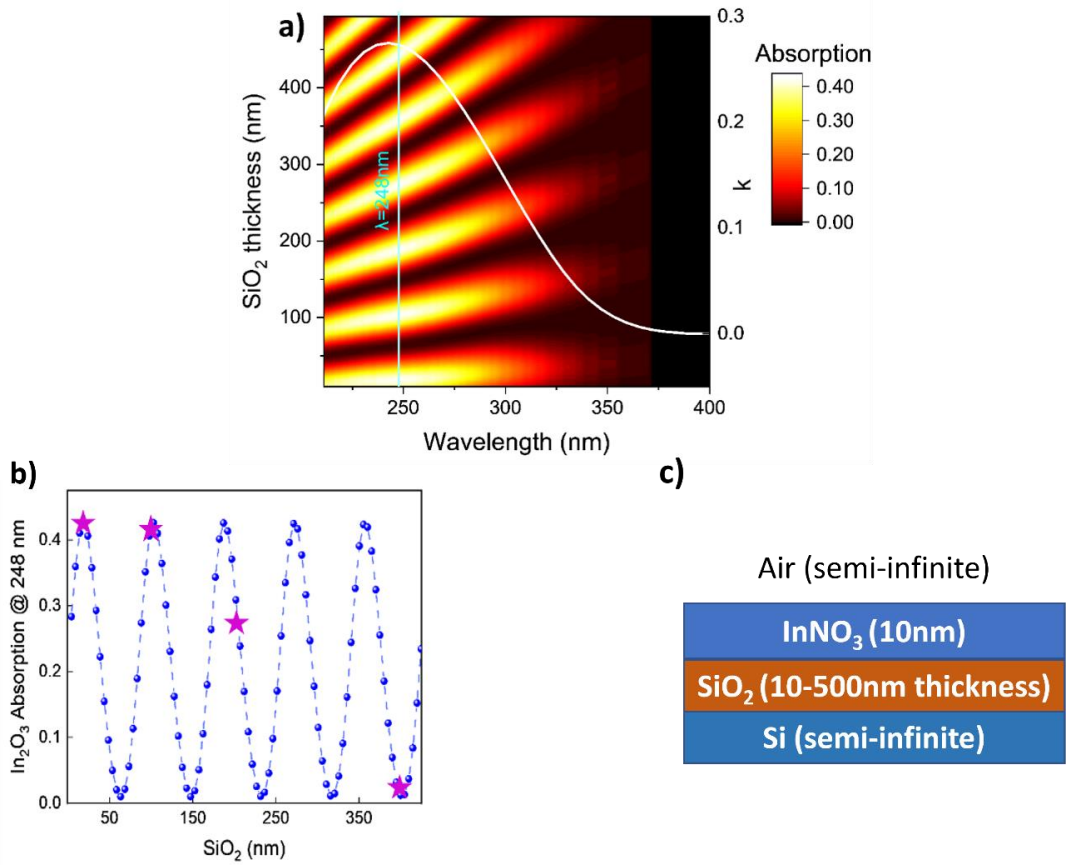

Figure 4.1. a) Numerical simulation of $InNO_3$ absorption coefficient in various SiO_2 thicknesses and irradiation wavelengths. White line shows the extinction coefficient of $In(NO_3)_3$. b) Absorption of $In(NO_3)_3$ at irradiation wavelength of $248\ nm$, for various SiO_2 thicknesses. Magenta stars denote the absorption for $20\ nm$, $100\ nm$, $200\ nm$ and $400\ nm$ SiO_2. c) Schematic illustration of the structure used during the numerical modelling.

The origin of these changes is attributed to the change in absorption in $In(NO_3)_3$ stemming from the interference effects that depend on the SiO_2 thickness. This relationship is elucidated through a numerical simulation of SiO_2 thickness ($10 - 500$ nm) vs laser irradiation wavelength that is represented in Figure 4.1a. The exact absorption at 248 nm (the excimer laser wavelength used for the fabrication of the devices) is shown in Figure 4.1b while Figure 4.1c shows the input architecture used to generate this multi-layer absorption calculation.

Although it is evident that high-performance TFTs can be fabricated using these materials through laser annealing, and conversion is achieved to a degree that facilitates device functionality, the connection between the temperature rise of thin films, the conversion mechanism from organometallic precursor to thin film and overall device performance remains inadequately understood. To address this, opto-thermal simulations with specific parameters were designed to determine the temperature rise and provide insights into this relationship, using the information in Figure 4.1 as a foundation.

The input file architecture can be seen in Figure 4.2a. The materials have thicknesses that were determined during the aforementioned experiments e.g. $In(NO_3)_3$ thickness determined by spectroscopic ellipsometry (SE), SiO_2 *via* optical reflectance spectroscopy (ORS) or a pre-determined thickness from a manufactured wafer. The purpose for using a thick layer of Si on top of semi-infinite Si was established in chapter 3, section 3.3.3. The 100 nm Si in the input file is determined by the absorption distribution, which shows the absorption moves to 0 after 100 nm. Figures 4.2b and 4.2c show the absorption distributions for $InNO_3$ on 100 nm SiO_2 and 200 nm SiO_2 at 1nm/grid. The optical constants used for all simulations are shown in Figures 4.2d-4.2f, which were extracted from NTU measurements or an ellipsometry database [360].

Figures 4.3a-4.3c demonstrate the heat capacities (C_p) of the materials and Figures 4.3d-4.3f the thermal conductivity (κ) used for the material properties in this simulation. The thermal properties of heat capacity and thermal conductivity are represented by a 3-parameter model (described in chapter 3, section 3.2 of this work), depicted by a red line, while the resultant constants a, b and c of the model are shown in the inset. The experimental data (shown as blue squares) were extracted from the literature [303], [310], [311], [312], [321], [334], [337]. O

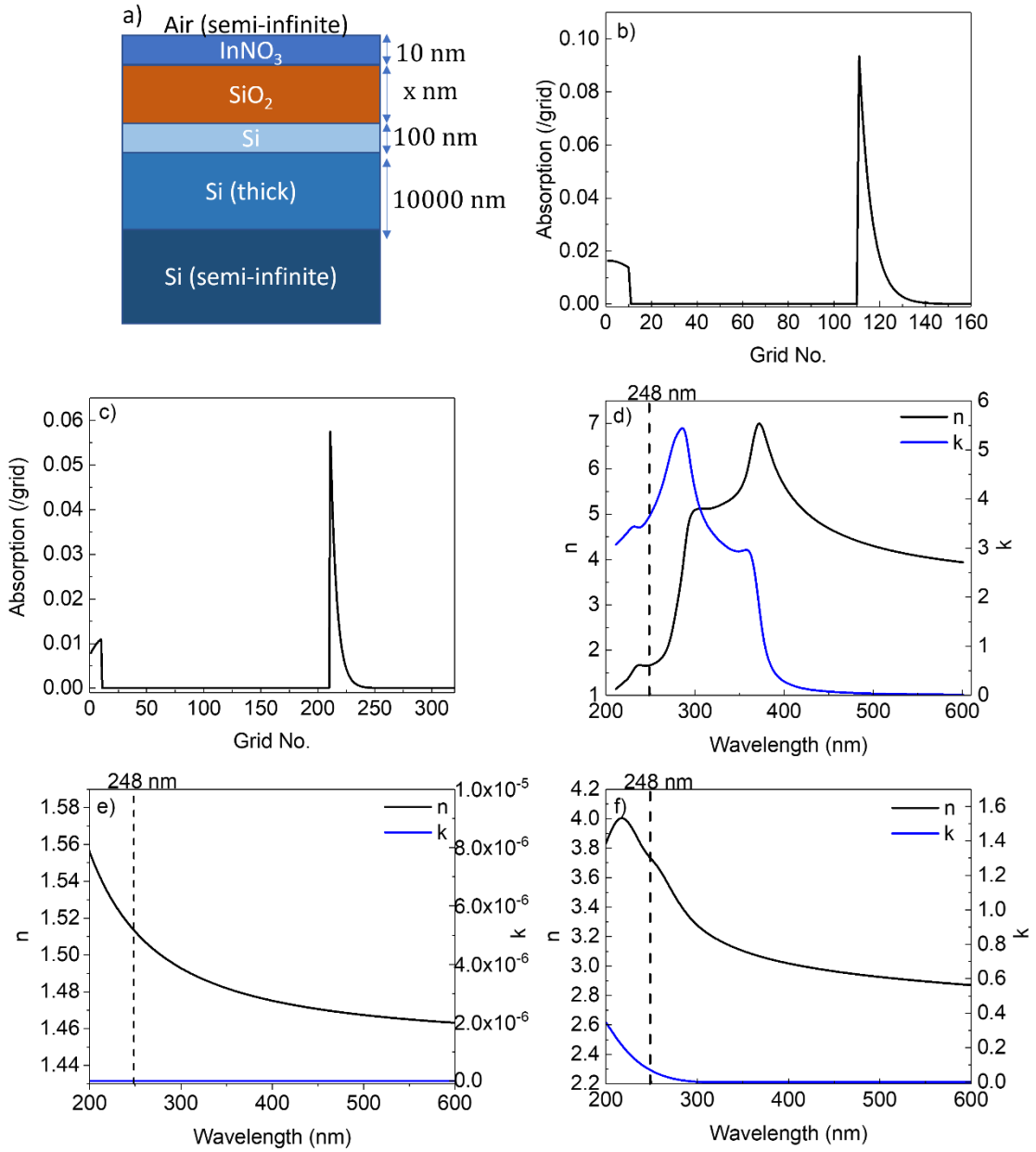

Figure 4.2 a) Material architecture used in the input file for the opto-thermal simulations. In this case, the SiO_2 thickness of x nm would change when necessary. b) Absorption distributions at $1nm/grid$ for $100\ nm$ SiO_2 c) Absorption distributions at $1nm/grid$ $200\ nm$ SiO_2. Both thicknesses show how absorption changes occur through the architecture. The small absorption from grids 0-10 are $In(NO_3)_3$, the flat region to transparent SiO_2 and highly absorbing region as Si. Note the different levels of absorption in $In(NO_3)_3$ because of the SiO_2 thickness. Optical constants representing the Si, SiO_2 and $In(NO_3)_3$ in the opto-thermal simulations are shown in d), e), and f) respectively. The dashed vertical line indicates the $248\ nm$ wavelength used in the simulations.

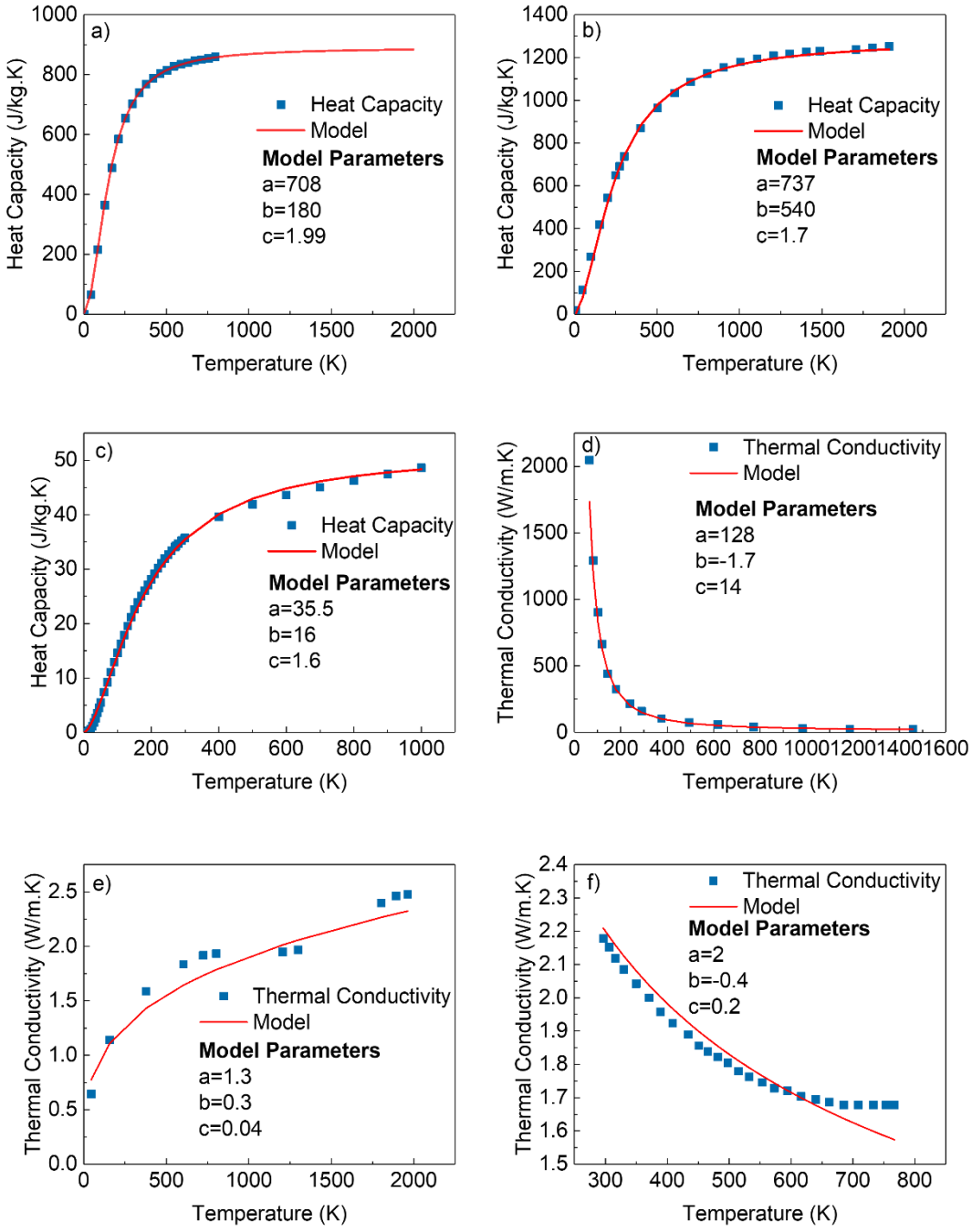

Figure 4.3. The heat capacity and thermal conductivity of the materials involved in this work, which were extracted from the literature. In all figures, the constants used for the 3-parameter model are inset. The data extracted from literature (blue squares) is compared to the 3-parameter model (red line). a)-c) are the heat capacities of Si, $\mathrm{SiO_2}$ and $\mathrm{In(NO_3)_3}$ respectively. Note in $\mathrm{In(NO_3)_3}$ the low heat capacity calculated due to its thin film nature. d-f) The thermal conductivities of Si, $\mathrm{SiO_2}$ and $\mathrm{In(NO_3)_3}$ respectively, with the model parameters inset. The thermal conductivity of $\mathrm{In(NO_3)_3}$ could not be fitted at temperatures $> 700\ \mathrm{K}$, suggesting an alternative model may be necessary here for very high temperatures and fluences.

Table 4.1 lists additional necessary values such as density ρ, melting point t_m and latent heat L_m of the materials, which were also extracted from the literature. Both Si and SiO_2 – due to their prevalence in the semiconductor industry – have well-known temperature dependent optical and thermal properties both in bulk and thin film form. As Si serves as a bulk substrate and the values for thicker SiO_2 layers converge with those of the bulk material, utilising bulk values for thermal properties and optical constants obtained via spectroscopic ellipsometry (SE) ensures an accurate approximation for these materials. The model for bulk materials can be considered established after recent published work utilised this model [361].

For $In(NO_3)_3$ (Figures 4.3c and 4.3f), adjustments were made to the bulk properties of $In(NO_3)_3$ and InO_x to better represent their thermal properties in thin film form. C_p of thin films are less prevalent in the literature, especially those of sol-gel materials since the precursor materials are volatile [200] and experience many phase changes which makes them unsuitable for applications where thermal stability is required. The process of the adjustment made in C_p values is explained in chapter 3, section 3.3.3. Note that at temperatures > 700 K $(426°C)$, the model for $In(NO_3)_3$ κ values don't fit well to the data despite different attempts at changing the model parameters. This may suggest an alternative model is necessary to represent this plateau at high temperatures, especially if it is present in other materials. The latent heat fusion followed a similar logic, using known parameters of the solution fabrication to derive a value. The process is also described in chapter 3, section 3.3.3. While the value is very low, comparison to other latent heat values of metal oxide precursors and salts (including nitrates) that do exist in the literature demonstrate these low values may be reasonable [308], [309].

Table 4.1. List of physical properties – aside from C_p and κ - used for the material files during the opto-thermal simulations of $InNO_3$ on SiO_2 gate dielectric.

Material	Density (kg/m^3)	Melting Point (K)	Latent Heat $(\frac{J}{kg})$
$InNO_3$	1020	373.0	94332.3
SiO_2	2650	1986.0	159800.0
Si	2330	1683.0	1409980.24

For the simulation input, the top boundary condition was set to be in isolation (no heat exchange is assumed with the environment). A fixed bottom boundary condition with $(300K)$ was used. Preliminary results showed indicated that the temperature response of $In(NO_3)_3$ is uniform, allowing for a lower resolution (greater grid spacing) to efficiently monitor temperature changes and quickly generate results from opto-thermal simulations. This approach maintains the same temperature rise accuracy as high resolution, ensuring no loss of precision. Consequently, a grid spacing of 5 nm was used. To accurately capture the change in

temperature rise due to latent heat after the melting point of $\mathrm{In(NO_3)_3}$ $(373\mathrm{K})$, a time step of 0.1 ns was utilised, applicable to all opto-thermal simulations. Finally, the laser temporal and spectral profiles are displayed in Figures 4.4a and 4.4b, respectively. Despite the temporal profile lasting only 110 ns, each simulation is run for 500 ns to adequately capture the materials' cooling phase. The spectral profile employs a Gaussian profile with a maximum at 248 nm.

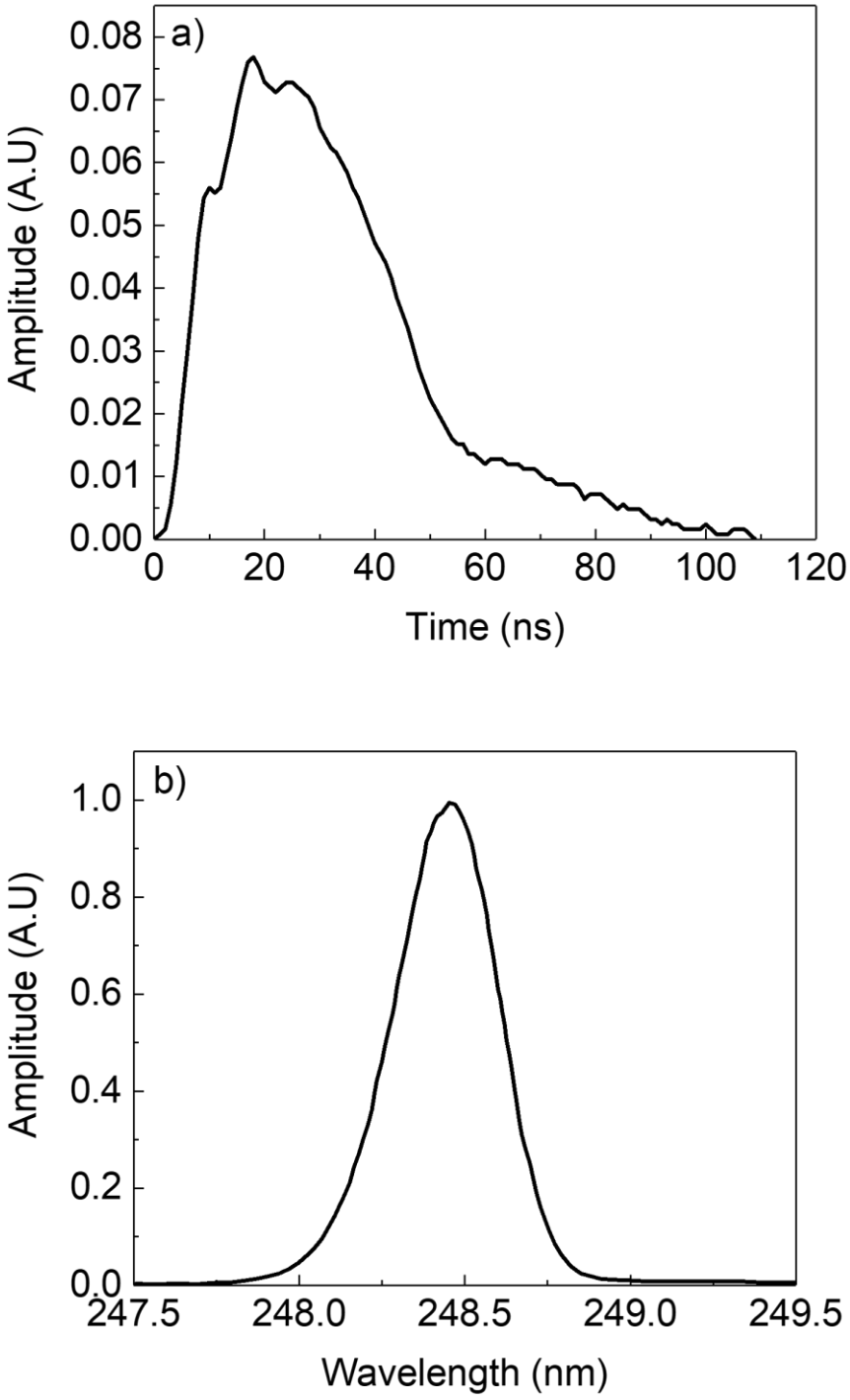

Figure 4.4. a) Laser temporal profile of the 248 nm KrF excimer laser used for the simulations and the experiments conducted at NTU. b) Laser spectral profile of the 248 nm KrF excimer laser.

4.2 Results and Analysis

Figure 4.5a displays the peak absolute temperature of the $In(NO_3)_3$ precursor on the various SiO_2 thicknesses. The temperatures on display are at the $InNO_3$- SiO_2 interface, as this is where the TFT channel formation occurs. As this is where charge carriers move, full conversion (sufficient temperature rise) is necessary to avoid charge carriers being impeded from organic ions and water that act as charge traps. Thus, a fully converted and tuned semiconductor should achieve higher performance metrics (e.g. μ_{FE}). The pink dashed line at $573\ K$ represents the minimum temperature required for the chemical conversion of $In(NO_3)_3$ to InO_x. Although no TFTs were tested using $50\ mJ\ cm^{-2}$, an opto-thermal simulation was performed at this fluence for $100\ nm\ SiO_2$ to obtain theoretical data below the conversion temperature of $In(NO_3)_3$. For the $100\ nm\ SiO_2$, even low fluences ($\geq\ 100\ mJ\ cm^{-2}$) result in a sufficiently high temperature to convert the $In(NO_3)_3$ precursor. For $200\ nm\ SiO_2$, fluences of $\geq 150\ mJ\ cm^{-2}$ can cause conversion of $In(NO_3)_3$to InO_x. For $400\ nm\ SiO_2$, only a fluence of $450\ mJ\ cm^{-2}$ predicts the achievement of a sufficient temperature for conversion.

These temperature rises were compared to electrical characteristics (output and transfer curves) and the linchpin metrics of $I_{On/Off}$, μ_{FE} and V_{th} to determine the significance of these temperature rises relative to device performance. Figure 4.5b, 4.5c and 4.5d respectively show $I_{On/Off}$, μ_{FE} and V_{th}. Note in some graphs a lack of coverage of some data - V_{th} for $100\ mJ\ cm^{-2}$ was not obtained as many devices were not swept through a sufficient gate-source voltage (V_{GS}) to prevent breakdown of the devices. The temperature rises associated with $100\ nm\ SiO_2$ and $200\ nm\ SiO_2$ have broad agreement with the electrical characteristics. Lower fluences that cause a sufficient (not excessive) temperature rise induces good performance – for example, $100\ mJ\ cm^{-2}$ on $100\ nm\ SiO_2$ produces devices with $I_{On/Off}$ approaching 10^5 while μ_{FE} reaches $8.28 \pm 1.42\ cm^2/Vs$. This balance of high performance and switching ability may be indicative of conversion expected at this temperature. However, the error bars for temperature rise indicate conversion is possibly not reached in a couple of cases across all SiO_2 thicknesses. These cases are discussed later with further information from the $I-V$ characteristics. In the cases of even higher temperature rises ($\geq 723\ K$) with $150\ mJ\ cm^{-2}$ and $200\ mJ\ cm^{-2}$ on $100\ nm\ SiO_2$ or $200\ nm\ SiO_2$, several similarities arise. Even with the consideration of error bars, the temperature rise exceeds $723\ K$ meaning full conversion would be reached. The excessive temperature rise leads to poor switching behaviour in the TFTs, drastically reducing $I_{On/Off}$ to below 10, but nearly doubling μ_{FE}. This drastic temperature rise would result in highly conductive InO_x, leading to the observed performance. This temperature rise has also been shown to leave nothing other than $In-O$ related products after processing [66]. The case of $400\ nm\ SiO_2$ presents far different temperature rises and a

bigger spread of electrical characteristics that don't fully agree with the opto-thermal simulations. Temperatures as low as $349 \pm 6\,\mathrm{K}$ are seen, which lead to poor device performances as expected. Where poor μ_{FE} and high $I_{On/Off}$ are present, so is an InO_x thin film that likely has lower carrier concentration (N_E) and a high density of carrier traps. However, fluences above $200\,\mathrm{mJ\,cm^{-2}}$ with temperature rises of $> 400\,\mathrm{K}$ display reasonable device characteristics (e.g. μ_{FE} up to $13\,\mathrm{cm^2/Vs}$, switching ratios $I_{On/Off} > 10^5$) despite being often being far from the conversion temperature. This contradicts many experimental observations so far, as the conversion of the organometallic precursor is critical to removing carrier traps and tuning N_E to a suitable value. Possible mechanisms for this are explored when the devices on $400\,\mathrm{nm}$ SiO_2 are discussed on a case-by-case basis.

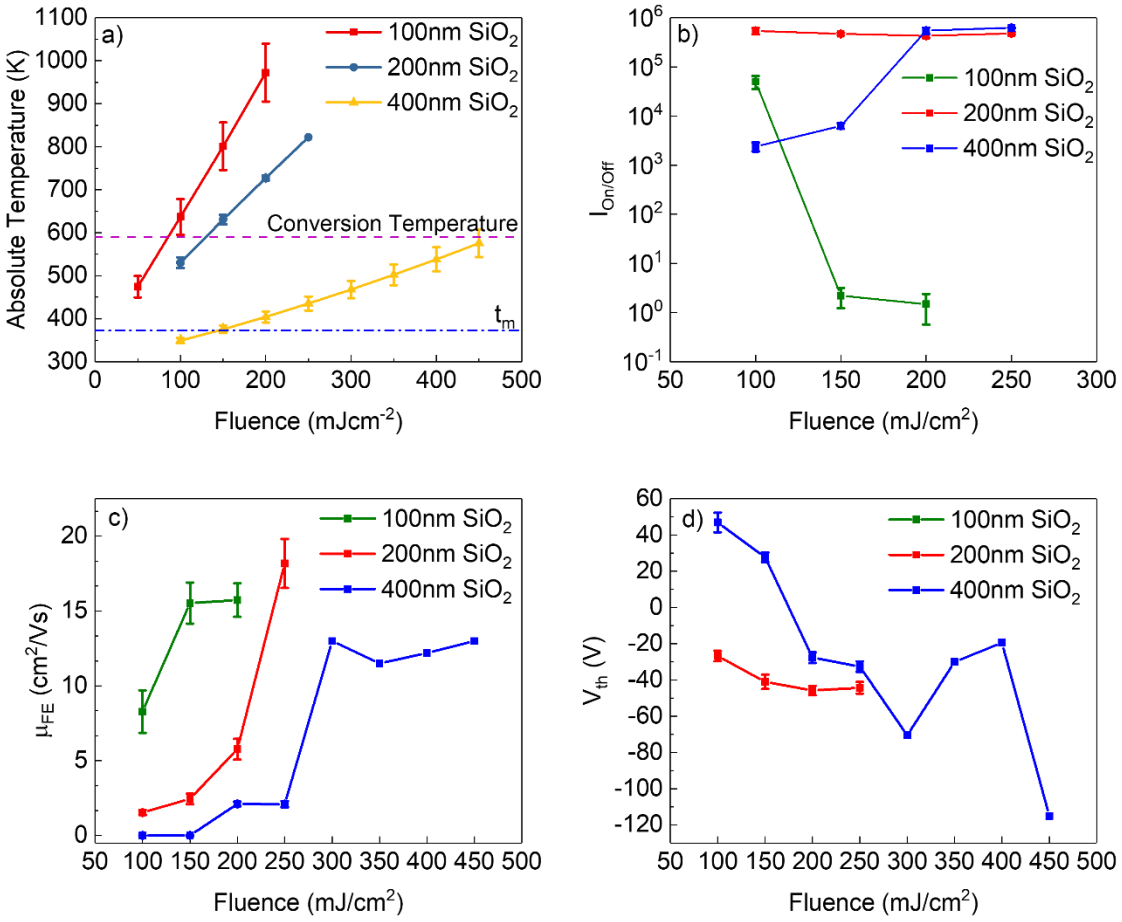

Figure 4.5. Peak absolute temperatures for the $InNO_3 - SiO_2$ boundary compared to key electrical characteristics of devices composed of $In(NO_3)_3$ on several SiO_2 thicknesses. a) Peak absolute temperatures at the $InNO_3 - SiO_2$ boundary for different fluences on various SiO_2 thicknesses. The magenta dashed line indicates the minimum temperature expected to convert the organometallic precursor to a thin film, while the blue dashed line indicates the melting temperature of $In(NO_3)_3$. b) $I_{On/Off}$ values of the $InNO_3$/ SiO_2/Si TFTs at different fluences Lower values typically correspond to semiconducting InO_x, while higher values are linked to extremely conductive InO_x. c) μ_{FE} values of the $InNO_3$/ SiO_2/Si TFTs at different fluences. d) V_{th} values of the $InNO_3$/ SiO_2/Si TFTs at different fluences.

4.2.1 100 nm SiO_2

Observation of the temperature evolution through the depth of the structure over time *via* contour plots, along with the output and transfer curves, reveals further information. Figure 4.6a-i show the contour plots (temperature vs time, colour scale indicating temperature) and $\mathrm{I-V}$ characteristics of $\mathrm{In(NO_3)_3}$ on $100\ \mathrm{nm}\ \mathrm{SiO_2}$ processed with $100\ \mathrm{mJ\ cm^{-2}}$ (Fig. 4.6 a-c), $150\ \mathrm{mJ\ cm^{-2}}$ (Fig. 4.6d-f) and $200\ \mathrm{mJ\ cm^{-2}}$ (Fig. 4.6g-i) respectively. The bold white lines of the contour plots are isolines indicating the exceeding - then falling - below the melting temperature of $\mathrm{In(NO_3)_3}$, while the green line indicates where the system exceeds the conversion temperature. Absence of the green isoline means this conversion temperature of $573\ \mathrm{K}$ was not reached. Note these contour plots do not account for any of the error bars seen in Fig. 4.5a. As previously mentioned, ambiguity arose concerning conversion of $\mathrm{In(NO_3)_3}$ into $\mathrm{InO_x}$ using $100\ \mathrm{mJ\ cm^{-2}}$ due to error bars dipping below the temperature rise whilst having good device performance. Clockwise hysteresis in the output (Fig. 4.5b) and transfer (Fig. 4.5c) supports being on this threshold, as organic ions ($\mathrm{NO_2}, -\mathrm{OH}$) act as charge traps after incomplete processing. Assuming the description above is correct, the application of a bias to this material in a device configuration promotes trap filling by the first voltage-induced charges. Unfilled traps also correspond to lower carrier concentration, explaining why μ_{FE} is lower than other conditions and does allow switching behaviour (where other conditions with this $\mathrm{SiO_2}$ thickness don't). The high $\mathrm{I_{DS}}$ in Figure 4.6b of $1\ \mathrm{mA}$ during saturation with high $\mathrm{V_{DS}}$ and lack of switching behaviour in the measured $\mathrm{V_{GS}}$ range demonstrates this excessive conductivity for TFT applications. Thus, experimental and theoretical data largely agree - the temperature rise induced (resulting in $637\ \pm 41\ \mathrm{K}$ absolute temperature) may be in a state where dissociation of nitrate ions has occurred, but water ions and by-products still exist. This agrees with a study performed at NTU, using Infra-Red Spectroscopic Ellipsometry (IRSE) to study the conversion of $\mathrm{In(NO_3)_3}$ at different processing stages [66]. Low leakage currents ($\mathrm{I_{GS}}$) in Figure 4.6c also indicate the fluence and temperature rise aren't so harsh that crystallinity or oxygen vacancies of $\mathrm{In(NO_3)_3}$ increases or that the dielectric is compromised. Note the hysteresis is clockwise – different directionalities of hysteresis can indicate different mechanisms. For example, an anticlockwise hysteresis can indicate ionic drift due to hole injection instead of charge traps [362].

For $150\ \mathrm{mJ\ cm^{-2}}$ and $200\ \mathrm{mJ\ cm^{-2}}$, the temperature rises of $801\ \pm 55\ \mathrm{K}$ and $972\ \pm 67\ \mathrm{K}$ in Figure 4.5a infers complete removal of by-products, nitrate ions and water for full chemical conversion into $\mathrm{InO_x}$. The contour plot (Figure 4.6d) shows this temperature is easily reached, with the green isoline for conversion temperature extending into the Si bulk. This leaves little to no charge traps, which is supported by a lack of hysteresis in the outputs of Figure

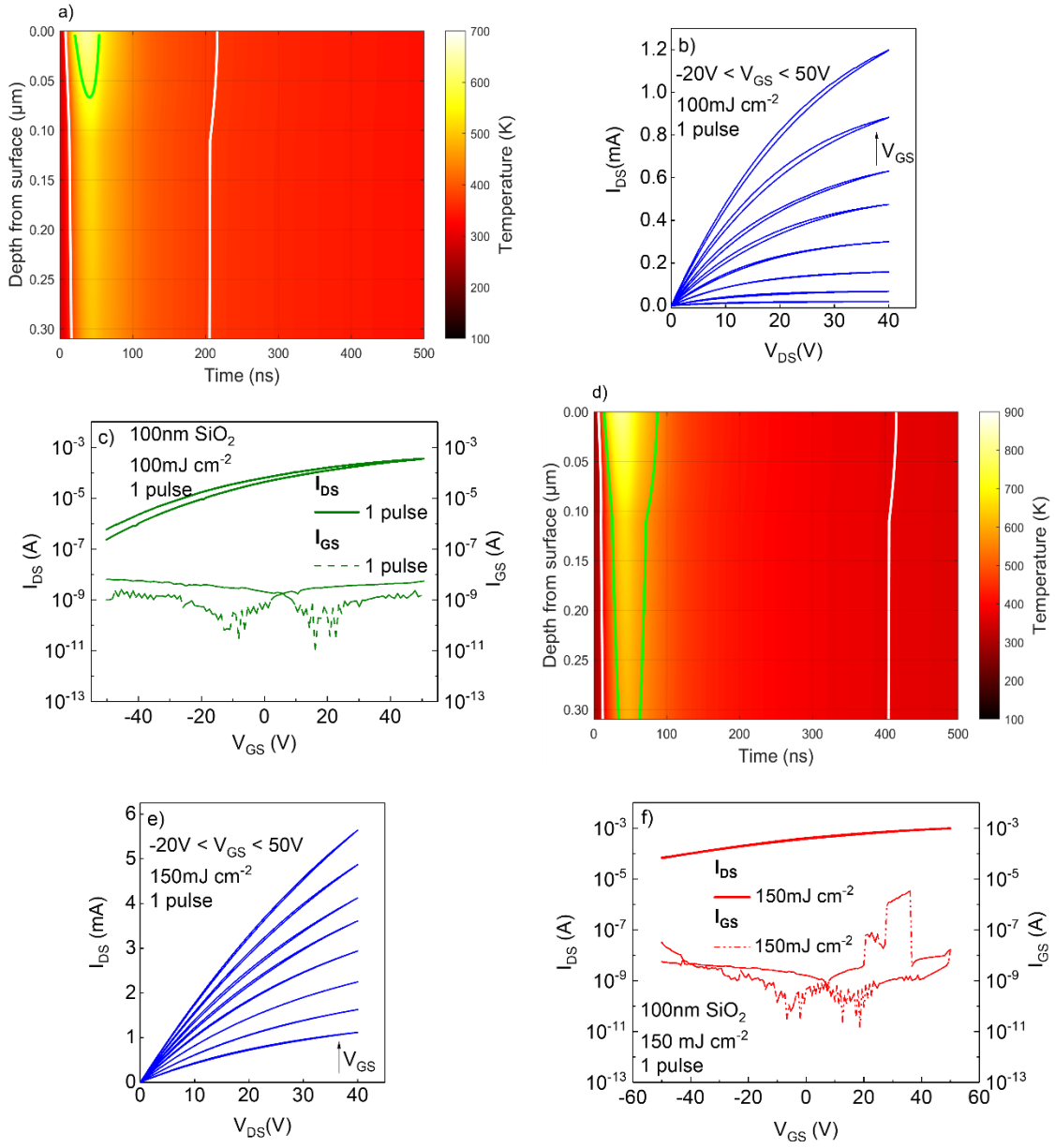

Figure 4.6. The opto-thermal simulation temperature rises for $10\ \mathrm{nm}\ \mathrm{In(NO_3)_3}$ on $100\ \mathrm{nm}\ \mathrm{SiO_2}$ compared to $\mathrm{I-V}$ characteristics for devices with each LA condition. In each contour plot, the colour scale indicates temperature through the depth of the structure against time, with white isolines indicating the melting temperature and green isolines when the conversion temperature is reached. a) Contour plot for $100\ \mathrm{mJ\ cm^{-2}}$. b) Output characteristics for $100\ \mathrm{mJ\ cm^{-2}}$. c) The transfer characteristics for $100\ \mathrm{mJ\ cm^{-2}}$. The analysis of the device characteristics matched with observations of the opto-thermal simulations for this fluence. d) Contour plot for $150\ \mathrm{mJ\ cm^{-2}}$. e) Output characteristics for $150\ \mathrm{mJ\ cm^{-2}}$. f) The transfer characteristics for $150\ \mathrm{mJ\ cm^{-2}}$. The analysis of the device characteristics showed good agreement with observations of the opto-thermal simulations for this fluence.

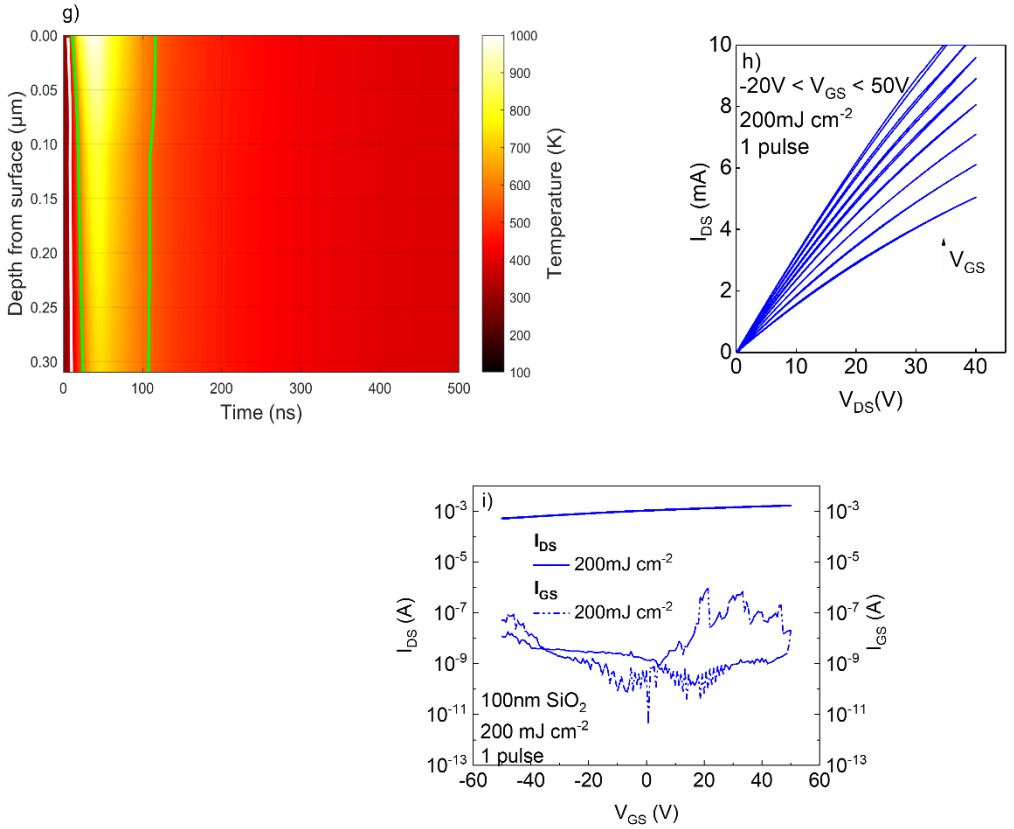

Figure 4.6 continued. g) Contour plot for $200\ \mathrm{mJ\ cm^{-2}}$. h) Output characteristics for $200\ \mathrm{mJ\ cm^{-2}}$. i) The transfer characteristics for $200\ \mathrm{mJ\ cm^{-2}}$. The analysis of the device characteristics showed strong agreement with observations of the opto-thermal simulations for this fluence.

4.6e and 4.6h, high values of $\mathrm{I_{DS}}$ even at low values of $\mathrm{V_{DS}}$, and no saturation behaviour suggesting the $\mathrm{InO_x}$ formed is more conductive than desired. The highly conductive layer leads to high μ_{FE} of above $15\ \mathrm{cm^2V^{-1}s^{-1}}$ with both these fluences, likely due to high $\mathrm{N_E}$. These values of $\mathrm{I_{DS}}$ in the outputs progress with fluence. Such a high $\mathrm{N_E}$ value would shift the Fermi level $\mathrm{E_F}$ close to the conduction band minimum (CBM) making it difficult to deplete the semiconductor with the range of $\mathrm{V_{GS}}$ values used here. The transfer curves seen for these conditions in Figure 4.6f and 4.6i supports these observations, with no hysteresis present and the material unable to switch off in the voltages tested. Figure 4.6f also shows $\mathrm{I_{GS}}$ increasing above 10^{-8} in the saturation regime of the device, suggesting the increased temperature rise has begun to compromise the dielectric or crystallised the semiconductor (either would permit paths for leakage current to propagate along). These effects are the same in $200\ \mathrm{mJ\ cm^{-2}}$, though more exaggerated with a larger hysteresis in $\mathrm{I_{GS}}$. Overall, there is a strong agreement between the experimental data and opto-thermal simulations for $10\ \mathrm{nm}\ \mathrm{In(NO_3)_3}$ on $100\ \mathrm{nm}\ \mathrm{SiO_2}$. The highly absorbing nature of the $\mathrm{In(NO_3)_3}$ at this $\mathrm{SiO_2}$ thickness was suggested to impede tailoring of the $\mathrm{InO_x}$ characteristics in the original work, which these large temperature rises at relatively low fluences also agrees with. The origin of this high $\mathrm{N_E}$ during

LA has been attributed in the past to the promotion of oxygen vacancies in InO_x, as well as other amorphous semiconductors [363].

Also of note for the contour plots are the temperature transients and how they will differ with the SiO_2 thicknesses. For the case of $100\ nm\ SiO_2$ at lower fluences used, a maximum temperature is reached very quickly after $40\ ns - 70\ ns$ and cool to the extent the materials can be considered to be fully cooled before subsequent pulses interact (assuming a $1\ Hz$ repetition rate is used). This means temperature transients contribute very little to the heating and chemical conversion for the $In(NO_3)_3$. The peak of this temperature rise in Figures 4.6a, 4.6d and 4.6g occurs at the top of the $In(NO_3)_3$ layer. For higher fluences and high temperature rises, due to the lack of modulation and low melting and decomposition temperatures of $In(NO_3)_3$, the melting temperature is exceeded easily and remains above this throughout the majority of the $500\ ns$ simulated time duration. In the case of $200\ mJ\ cm^{-2}$, the temperature never drops to below this melting temperature. It is unknown how the exposure of hundreds of ns durations of low heating to the material compare to the shorter duration, high temperature rises. The kink that occurs in the isolines for some of the contour plots systematically occurs at $0.11\ \mu m$, corresponding to the $SiO_2 - Si$ interface where there is a drastic change in opto-thermal properties. For the green conversion temperature isoline, a cone shape at the $40\ ns - 70\ ns$ is formed, with the narrower part at the deepest parts of the structure due to the aforementioned changes in opto-thermal properties. For cases where the conversion temperature is limited to above the Si bulk, a more normal cone shape is formed.

4.2.2 200 nm SiO_2

On $200\ nm\ SiO_2$, the $In(NO_3)_3$ layer exhibited a more tunable temperature rise, resulting in more distinctive outcomes for each fluence. These results frequently showed agreement between experimental data and opto-thermal simulations. Figures 4.7 a-l show the contour plots (temperature vs time, colour scale indicating temperature) and $I-V$ characteristics of $In(NO_3)_3$ on $200\ nm\ SiO_2$ processed with $100\ mJ\ cm^{-2}$ (Figures 4.7a-c), $150\ mJ\ cm^{-2}$ (Figures 4.7d-f), $200\ mJ\ cm^{-2}$ (Figures 4.7g-i) and $250\ mJ\ cm^{-2}$ (Figures 4.7j-l). For $100\ mJ\ cm^{-2}$ in Figures 4.5a and 4.7a, a maximum of $530 \pm 12\ K$ is reached which is not sufficient for organometallic conversion. Additionally, temperature drops extremely quickly below the melting point after $100\ ns$, meaning continued heating is minimal and removal of unwanted organic ions and water is minimal. The $I-V$ characterisation in Figures 4.7b and 4.7c supports this, as a large hysteresis up to $10\ V$ is present in the transfer (Figure 4.7c) due to organic ions. The output in Figure 4.7b also displays some of this hysteresis, especially in larger values of V_{GS}. In the highest values of V_{GS} at high V_{DS}, some noise is present which is attributed to either the presence of traps or series resistance between the Al contact and the InO_x layer.

In Figures 4.7b and 4.7c, mA values of $\mathrm{I_{DS}}$ are barely reached from a lower temperature rise that insufficiently processed the $\mathrm{In(NO_3)_3}$. Interestingly, Figure 4.7b shows a difficulty to reach saturation at most values of $\mathrm{V_{GS}}$ used for the measurements. $\mathrm{V_{th}}$ is far higher (less negative) than other conditions at $27\ \mathrm{V}$ and the value of $1.54\ \pm 0.16\ \mathrm{cm^2/Vs}$ for μ_{FE} is at the low end of any values recorded in these experimental results with any thicknesses of $\mathrm{SiO_2}$. The ability for this device to fully switch and have a high $\mathrm{I_{On/Off}}$ of nearly 10^6 can be attributed to the resulting $\mathrm{InO_x}$ film being semiconducting due to this low temperature rise. Something not considered thus far is that less dense films from lower temperature rises can be prone to more defects within the thin film in addition to the organic ion charge traps. This leads to amplification of previously discussed phenomena, such as the effects of unfilled traps. Regarding electronic structure, this low $\mathrm{N_E}$ has an $\mathrm{E_F}$ located further from the CBM within the bandgap. Thus, a large volume of traps must be filled before $\mathrm{E_F}$ reaches tail and extended states where induced carriers can be free to increase $\mathrm{I_{DS}}$. Overall, this condition mostly has agreement with experimental and opto-thermal simulation data.

For $150\ \mathrm{mJ\ cm^{-2}}$,$630\ \pm 11\ \mathrm{K}$ is reached which is in the region of removal of nitrate ions for conversion as shown in Figures 4.5a and 4.7d. The $\mathrm{I-V}$ characterisation in Figures 4.7e and 4.7f agrees with this as the hysteresis (Figure 4.7f) noticeably reduces, with the leftover hysteresis possibly due to structural water and by-products that are remaining. This higher temperature rise also gives a slight jump in μ_{FE}, more negative $\mathrm{V_{th}}$ of $-41\ \mathrm{V}$ and the same order of magnitude of $\mathrm{I_{On/Off}}$ in comparison to $100\ \mathrm{mJ\ cm^{-2}}$, though it can be argued μ_{FE} should have increased further. The output (Figure 4.7e) shows an increase in $\mathrm{I_{DS}}$ and, in contrast to the previous fluence, is able to saturate at most values of $\mathrm{V_{GS}}$. The origin of these changes can be heavily attributed to a minor increase in $\mathrm{N_E}$ of $\mathrm{InO_x}$ as it progresses towards a more stochiometric state. A small increase in $\mathrm{N_E}$ and a slightly denser resulting film would cause these changes in performance, but still leave the material in a state where the phenomena discussed for $100\ \mathrm{mJ\ cm^{-2}}$ are still dominant enough to hinder device performance. The remaining existence of $-\mathrm{OH}$ bonds to In at these predicted temperatures is experimentally validated [66] and would stop a major shift in device performance. An interesting comparison to make is between $\mathrm{In(NO_3)_3}$ on $200\ \mathrm{nm\ SiO_2}$ ($150\ \mathrm{mJ\ cm^{-2}}$) and $100\ \mathrm{nm\ SiO_2}$ ($100\ \mathrm{mJ\ cm^{-2}}$). Despite showing similar temperature rises, some device behaviours are notably different – the $200\ \mathrm{nm\ SiO_2}$ condition exhibits a far lower μ_{FE} of $2.45\ \pm 0.35\ \mathrm{cm^2/Vs}$ compared to $8.28\ \pm 1.42\ \mathrm{cm^2/Vs}$, with the lower μ_{FE} linked to lower values of $\mathrm{I_{DS}}$. $\mathrm{I_{On/Off}}$ shows an order of magnitude difference. The output of the $100\ \mathrm{mJ\ cm^{-2}}$ on $100\ \mathrm{nm\ SiO_2}$ (Figure 4.6b) shows hysteresis while the transfer (Figure 4.6c) struggles to show switching behaviour. Meanwhile, the $150\ \mathrm{mJ\ cm^{-2}}$ on $200\ \mathrm{nm\ SiO_2}$ shows no hysteresis in the output (Figure 4.7e) and switching

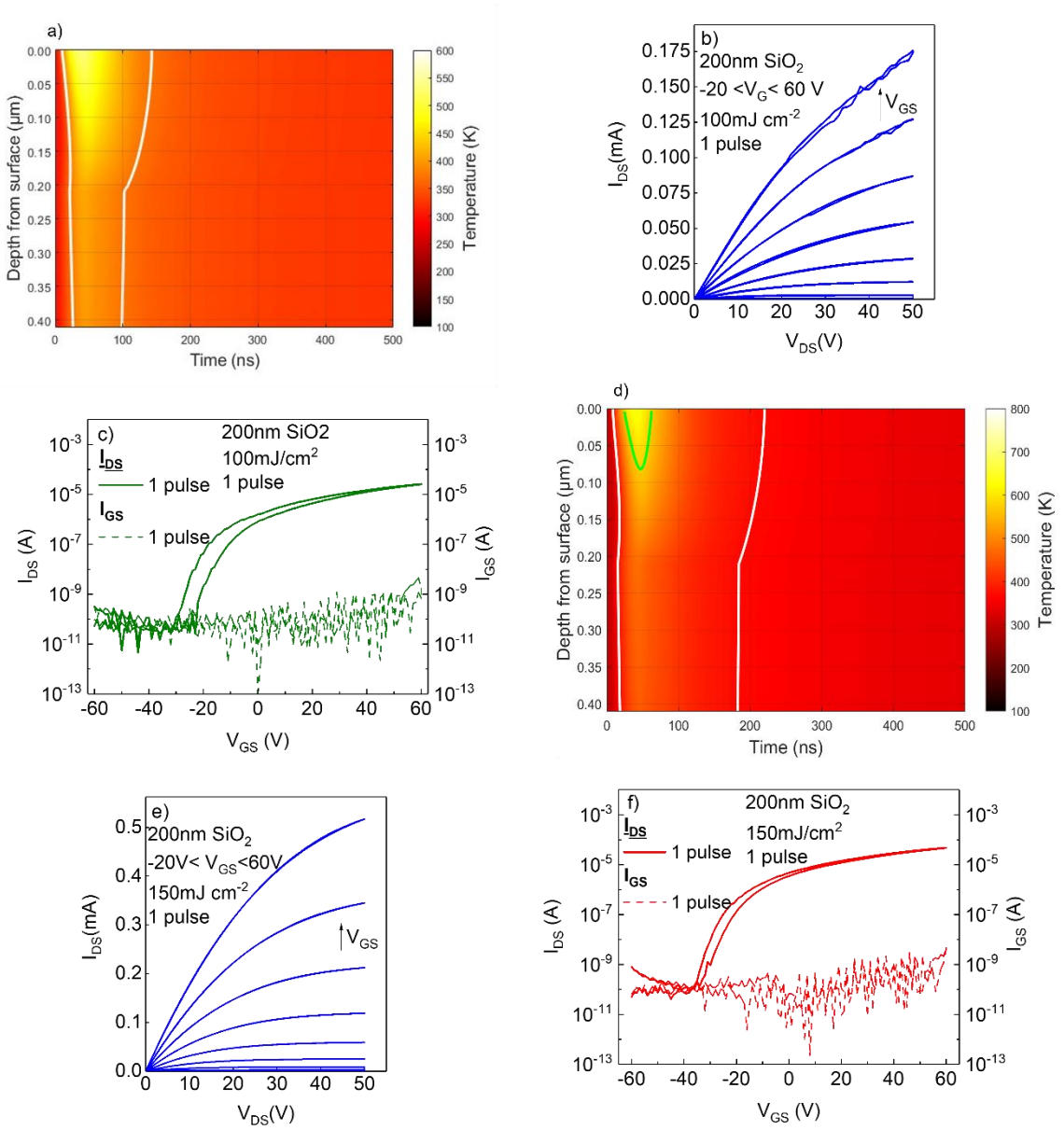

Figure 4.7. The opto-thermal simulation temperature rises for $10\ \mathrm{nm}\ \mathrm{In(NO_3)_3}$ on $200\ \mathrm{nm}\ \mathrm{SiO_2}$ compared to device $\mathrm{I-V}$ characteristics with each fluence. In each contour plot, the colour scale indicates temperature through the depth of the structure against time, with white isolines indicating the melting temperature and green isolines when the conversion temperature is reached. a) Contour plot for $100\ \mathrm{mJ\ cm^{-2}}$. b) Output characteristics for $100\ \mathrm{mJ\ cm^{-2}}$. c) The transfer characteristics for $100\ \mathrm{mJ\ cm^{-2}}$. The analysis of the device characteristics matched with observations of the opto-thermal simulations for this fluence. d) Contour plot for $150\ \mathrm{mJ\ cm^{-2}}$. e) Output characteristics for $150\ \mathrm{mJ\ cm^{-2}}$. f) The transfer characteristics for $150\ \mathrm{mJ\ cm^{-2}}$.The analysis of the device characteristics showed good agreement with observations of the opto-thermal simulations.

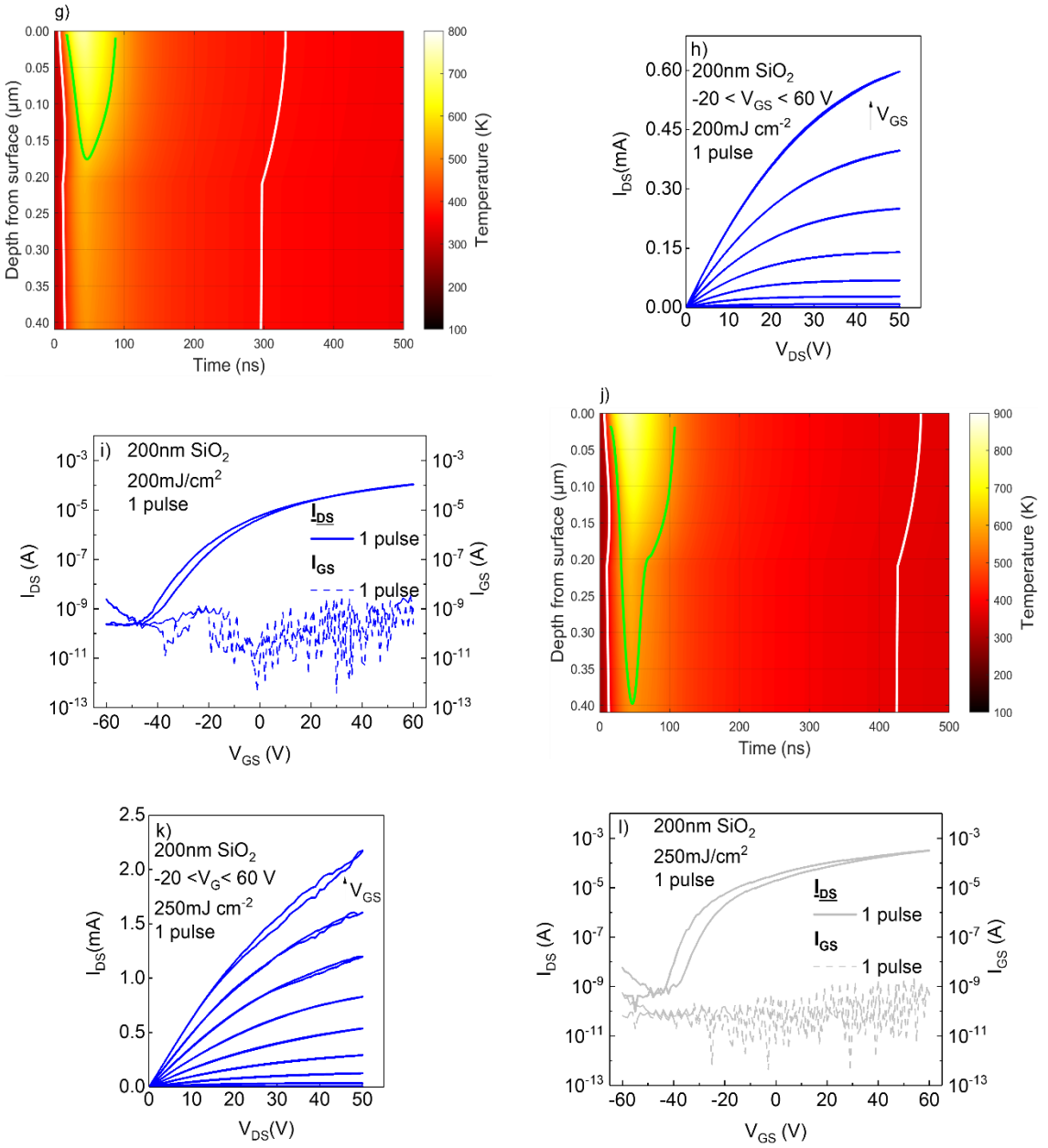

Figure 4.7 continued. g) Contour plot for $200\ \mathrm{mJ\ cm^{-2}}$. h) Output characteristics for $200\ \mathrm{mJ\ cm^{-2}}$. i) The transfer characteristics for $200\ \mathrm{mJ\ cm^{-2}}$. The analysis of the device characteristics showed strong agreement with observations of the opto-thermal simulations. j) Contour plot for $250\ \mathrm{mJ\ cm^{-2}}$. k) Output characteristics for $250\ \mathrm{mJ\ cm^{-2}}$. l) The transfer characteristics for $250\ \mathrm{mJ\ cm^{-2}}$. The analysis of the device characteristics showed some disparity compared to opto-thermal simulations, suggesting more insight into the effect of this temperature and the change in $\mathrm{InO_x}$ is needed.

behaviour in the transfer. At the time of writing, the cause of these differences is still being discussed and may require further experiments to confirm the composition of the $\mathrm{In(NO_3)_3}$. As an independent case, experimental data for $150\ \mathrm{mJ\ cm^{-2}}$ on $200\ \mathrm{nm\ SiO_2}$ agrees with opto-thermal simulations. However, this agreement is compromised when cross-referencing this I-V characterisation with others that experienced similar temperature rises.

For $200\ \mathrm{mJ\ cm^{-2}}$, there is far lower ambiguity. The temperature rises of $727\ \pm 6\ \mathrm{K}$ seen in Figure 4.5a and 4.7g imply an $\mathrm{InO_x}$ thin film that has fully removed nitrates, water and the $\mathrm{In-OH}$ bonds resulting in an amorphous and fully converted $\mathrm{InO_x}$ thin film. A smaller hysteresis in Figure 4.7i, doubling of μ_{FE} from $2.45\ \pm 0.35\ \mathrm{cm^2/Vs}$ to $5.77\ \pm 0.69\ \mathrm{cm^2/Vs}$ and retaining a very high $\mathrm{I_{On/Off}}$ of over 10^5 is indicative of this shift in composition. The complete conversion and increased fluence would lead to far fewer carrier traps and increase of $\mathrm{N_E}$. The increase in conductivity leads to the more negative $\mathrm{V_{th}}$ of $-45.8\ \mathrm{V}$. while the shift in μ_{FE} is linked to the decrease in carrier traps. The increase in conductivity can also be linked to the changes in $\mathrm{I-V}$ characteristics in Figures 4.7h and 4.7i. Figure 4.7h and 4.7i shows a small increase in $\mathrm{I_{DS}}$ with no change in the saturation behaviour (hence why carrier traps are linked to the doubling of μ_{FE}). Note in Figure 4.7i that $\mathrm{I_{DS}}$ is increasing towards $10^{-8}\mathrm{A}$ in its off state. Figure 4.7g shows the high temperature rise extending throughout most of the $200\ \mathrm{nm\ SiO_2}$, which could lead to thermal and mechanical stresses. As the $\mathrm{In(NO_3)_3}$ film is $10\ \mathrm{nm}$ and the absorption is small, the temperature profile is nearly flat and uninterrupted as it goes into the transparent $\mathrm{SiO_2}$, meaning the dielectric is fully exposed. Overall, the experimental data for this sample agrees with the opto-thermal simulation temperature rise.

The observations for $250\ \mathrm{mJ\ cm^{-2}}$ clash with everything previously discussed. An extremely high temperature ($822\ \pm 4\ \mathrm{K}$) is seen in Figures 4.5a and 4.7j, with the peak temperatures now extending throughout all of the $\mathrm{SiO_2}$. With this, we would expect to see a massive increase in μ_{FE}, more negative $\mathrm{V_{th}}$ and a lower $\mathrm{I_{On/Off}}$. μ_{FE} jumps from $5.77\ \mathrm{cm^2/Vs}$ to $18.18\ \pm 1.64\ \mathrm{cm^2/Vs}$, which is supportive of this fully converted material and temperature rise. This is likely due to increased oxygen vacancies and increased $\mathrm{N_E}$. However, $\mathrm{V_{th}}$ and $\mathrm{I_{On/Off}}$ remain the same, if not slightly increasing, which is contradictory to a TFT with a very conductive film expected from this temperature rise. The comparison of the temperature rise to $\mathrm{I-V}$ characterisation further opposes typical behaviour. The output (Figure 4.7k) shows the tripling of $\mathrm{I_{DS}}$ compared to the previous fluence which can be linked to the μ_{FE} tripling. However, unprecedented hysteresis and noise at high values of $\mathrm{V_{GS}}$ appears in this output, which at this temperature rise cannot be linked to remaining unconverted precursor. The two possibilities are that the temperature rises of these higher fluence are erroneous, or that another mechanism is responsible for these features. Similar confusion arises in the transfer in Figure 4.7l where larger hysteresis than the previous fluences is observed, despite $\mathrm{I_{DS}}$ values of $10^{-8}\mathrm{A}$ indicating the increased temperature incident on the dielectric. Such contradictory observations make it difficult to conclude on the agreement between experimental data and opto-thermal. Comparison to a sample with a similar temperature rise continues to add to this; the $100\ \mathrm{nm\ SiO_2}$ with $150\ \mathrm{mJ\ cm^{-2}}$ and $200\ \mathrm{nm\ SiO_2}$ with $250\ \mathrm{mJ\ cm^{-2}}$ have similar

temperature rises but exhibit different behaviours in electrical characterisation. Values for μ_{FE} are arguably within the same range of each other which is encouraging, but $I_{On/Off}$ are 5 orders of magnitude apart. V_{th} for $100\ nm\ SiO_2$ devices were either immeasurable due to device breakdown or extremely negative, while this case presents a value within the measurement range. Additionally, comparison between the $100\ nm\ SiO_2$ output and transfer (Figures 4.6e and 4.6f) and $200\ nm\ SiO_2$ output and transfer (Figures 4.7k and 4.7l) reveal completely different behaviours. Overall, there's some good agreement with opto-thermal and experimental data for $200\ nm\ SiO_2$ samples, but further consideration may be necessary due to certain observations in the transfer curves and comparison to other conditions.

In the contour plots, $100\ nm$ and $200\ nm\ SiO_2$ display similar behaviours – they reach a maximum temperature very quickly after $40\ ns - 70\ ns$ and heat dissipates quickly thereafter. $200\ nm\ SiO_2$ could be argued to have a slightly wider length of time for heating, due to the additional SiO_2 thickness acting as a thermal barrier. The kink in the white isolines occurs consistently at $0.21\ \mu m$, corresponding to the depth where the $SiO_2 - Si$ interface occurs. Where the green isolines permeate throughout most of the depth of the structure, a kink also occurs but in different places. In Figure 4.7g, an extremely small feature occurs at $0.15\ \mu m$ $(60\ ns - 70\ ns)$ that makes the cone shape irregular. As there is no interface or change in properties here, this is attributed to the change in intensity of the temporal profile of the laser. In Figure 4.7j, the kink occurs around $0.19\ \mu m$, close to the $SiO_2 - Si$ interface.

4.2.3 400 nm SiO_2

For the results of $400\ nm\ SiO_2$, results and figures are split in this discussion according to the two studies the experimental results originate from – either the lower fluence investigation by Koutsiaki [64] or the higher fluence study by Dellis *et al* [63], whose combined results provide large coverage of a range of experimental parameters. The two sets of data are then reviewed alongside each other at critical points to investigate the differences between the two studies. Figures 4.8 a-l show the contour plots (temperature vs time, colour scale indicating temperature) and $I - V$ characteristics of $In(NO_3)_3$ on $400\ nm\ SiO_2$ processed with $100\ mJ\ cm^{-2}$ (Figures 4.8a-b), $150\ mJ\ cm^{-2}$ (Figures 4.8c-e), $200\ mJ\ cm^{-2}$ (Figures 4.8f-h) and $250\ mJ\ cm^{-2}$ (Figures 4.8i-k). The data for the output curve for $100\ mJ\ cm^{-2}$ is currently unavailable.

For $100\ mJ\ cm^{-2}$, a maximum temperature of $349\ \pm 6\ K$ (Figure 4.5a) is reached which is insufficient to even melt or decompose the $In(NO_3)_3$ precursor. This is reflected in the poor device performance and $I - V$ characteristics different to any seen so far – a poor μ_{FE} of $0.0038\ \pm 0.005\ cm^2/Vs$, $I_{On/Off}$ of 2×10^3 and V_{th} of $46.96\ V$ are reached. Figure 4.8b

shows the low I_{DS} values, clockwise hysteresis that dominates throughout and lack of saturation in the measurement range. $150\ \mathrm{mJ\ cm^{-2}}$ shows similar behaviour to this also. The temperature rise of $375\ \mathrm{K}$ is given in Figures 4.5a and 4.8c. A low μ_{FE} of $0.0058\ \pm 0.05\ \mathrm{cm^2/Vs}$ is obtained, with a positive V_{th} of 27.7 V and $I_{On/Off}$ of the same order of magnitude as before. At these lower fluences, this can be explained by an exaggeration of phenomena related to carrier traps and low N_E materials as before. Such a low temperature rise means the precursor itself remains the same as originally fabricated, with no removal of organic bonds or structural water. The insufficient conversion from these low temperature rises can explain both these cases. With this comes fewer oxygen vacancies and defects within the InO_x, reducing N_E. These observations can be seen in the output and transfer in Figure 4.8d and 4.8e. I_{DS} is extremely low, with large clockwise hysteresis of many of the V_{GS} used. The bottom left of this output also displays abnormal current collection (highlighted by the red rectangle) during the return sweep. When V_{DS} changes sign and begins the return sweep, carriers cross the channel with hinderance from carrier traps and remain in position. The collection of these carriers occurs at an electrode and present as negative current. Ultimately, the origin of this is carrier traps from organic ions and water due to incomplete conversion which is supported by the low temperature rise. Overall, the experimental and opto-thermal simulation data agree for these fluences. Since the temperature rise is higher than previously, the transfer in Figure 4.8f shows a shift towards $0\ \mathrm{V}$, a smaller hysteresis and higher values for I_{GS}. Because the temperature rise maximises within the SiO_2, this may contribute to this.

$200\ \mathrm{mJ\ cm^{-2}}$ shows a notable difference in performance characteristics. There is a many-fold increase of μ_{FE} to $2.11\ \pm 0.14\ \mathrm{cm^2/Vs}$, V_{th} becomes negative at $-27.63\ \mathrm{V}$ and $I_{On/Off}$ increases by 2 orders of magnitude to $5.5\ \times\ 10^5$. However, this is in complete disparity to the temperature rises since only $404\ \pm 13\ \mathrm{K}$ is observed here in Figures 4.5a and 4.8f. Such a low temperature rise, while still decomposing the precursor, wouldn't have this large impact on device performance. The output in Figure 4.8g agrees with this observation since very little hysteresis and a mA level I_{DS} are present, despite a low temperature rise. Comparison to $\mathrm{I-V}$ characteristics on other SiO_2 thicknesses shows this output is similar to those of a higher temperature rise, further elucidating this discrepancy. The transfer in Figure 4.8h shows the massively increased I_{DS}, as well as a reduced hysteresis. An example to explain this disparity between experimental and opto-thermal data is that of $200\ \mathrm{nm}\ SiO_2$ with $100\ \mathrm{mJ\ cm^{-2}}$; this had a higher temperature rise of $530\ \pm 12\ \mathrm{K}$, but remained below the conversion temperature. Despite an even lower temperature rise in relation to this, the $200\ \mathrm{mJ\ cm^{-2}}$ here resulted in a better performing device, contradicting the observations and mechanisms responsible for device performance so far. The change in performance characteristics is expected, as the output

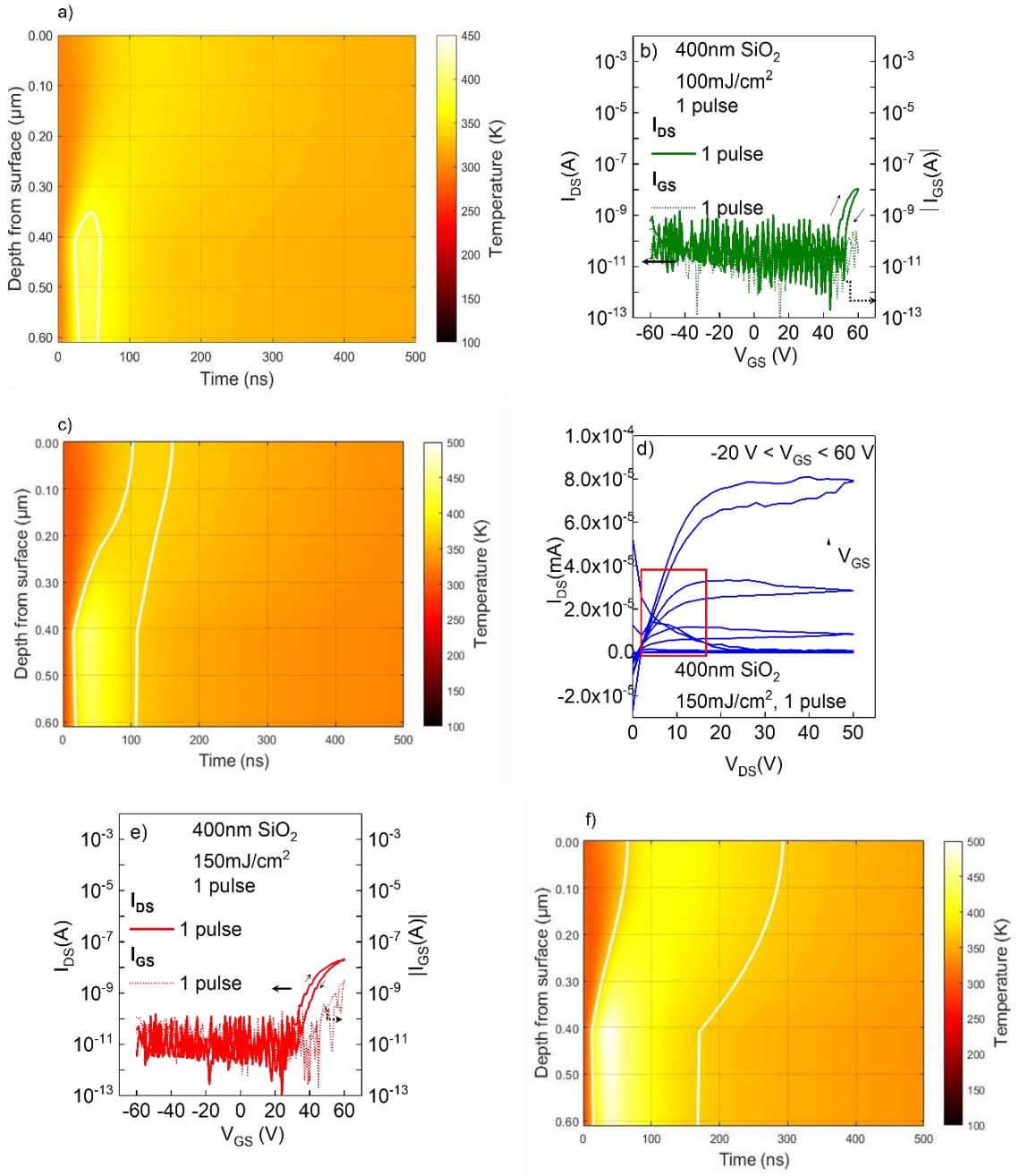

Figure 4.8. The opto-thermal simulation temperature rises of lower fluences for $10\ \mathrm{nm}\ \mathrm{In(NO_3)_3}$ on $400\ \mathrm{nm}\ \mathrm{SiO_2}$ compared to $\mathrm{I-V}$ characteristics for devices with each LA condition. In each contour plot, the colour scale indicates temperature through the depth of the structure against time, with white isolines indicating the melting temperature and green isolines when the conversion temperature is reached. a) Contour plot for $100\ \mathrm{mJ\ cm^{-2}}$. b) Output characteristics for $100\ \mathrm{mJ\ cm^{-2}}$. c) The transfer characteristics for $100\ \mathrm{mJ\ cm^{-2}}$. Comparison with the device characteristics supported observations of the opto-thermal simulations. d) Contour plot for $150\ \mathrm{mJ\ cm^{-2}}$. e) Output characteristics for $150\ \mathrm{mJ\ cm^{-2}}$. f) The transfer characteristics for $150\ \mathrm{mJ\ cm^{-2}}$. The analysis of the device characteristics showed good agreement with observations of the opto-thermal simulations.

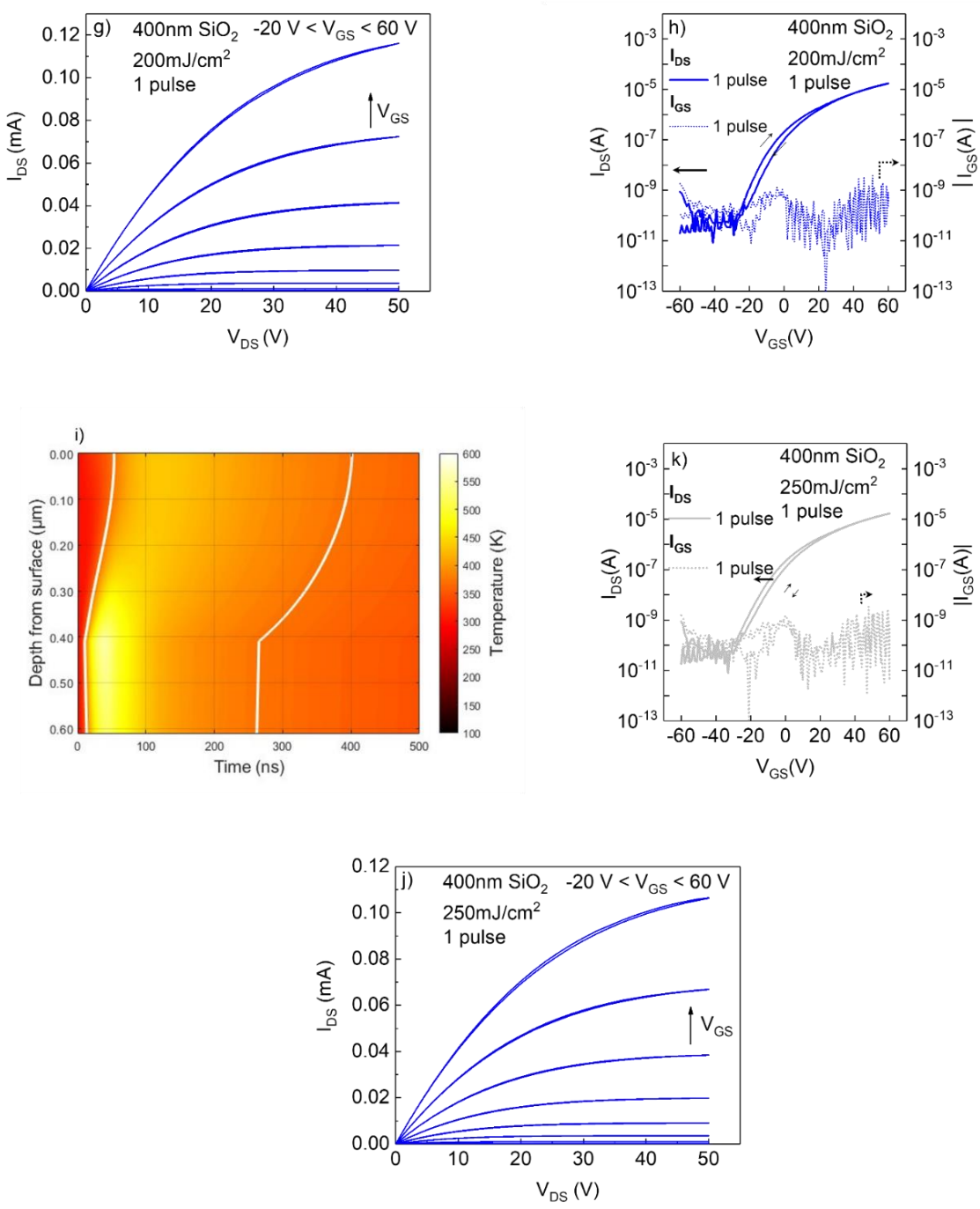

Figure 4.8 continued. g) Contour plot for 200 mJ cm^{-2}. h) Output characteristics for 200 mJ cm^{-2}. i) The transfer characteristics for 200 mJ cm^{-2}. The analysis of the device characteristics showed poor agreement with observations of the opto-thermal simulations. j) Contour plot for 250 mJ cm^{-2}. k) Output characteristics for 250 mJ cm^{-2}. l) The transfer characteristics for 250 mJ cm^{-2}. The analysis of the device characteristics showed large disparity compared to opto-thermal simulations.

in Fig. 4.8g shows a notable difference in I_{DS} to previous fluences. There is currently no suggestion for why these notable changes occur with such a low temperature rise. The absence

of explanation here suggests some alterations to the heating model are necessary with these low fluences so theoretical and experimental data corroborate each other.

The application of $250\ \mathrm{mJ\ cm^{-2}}$ to this same architecture gives similar device performance, with a μ_{FE} of $2.09\ \pm 0.2\ \mathrm{cm^2/Vs}$, $I_{On/Off}$ of $6\ \times\ 10^5$ and V_{th} of $-32.65\ \mathrm{V}$. This is despite a temperature rise of only $435\ \pm 16\ \mathrm{K}$. In the fabrication methodology of both NTU studies, this temperature is around the stabilisation temperature. A hotplate treatment of $150℃\ (423\ \mathrm{K})$ is used immediately after spin-coating the precursor onto the SiO_2/Si substrate to remove excess solvent and organic residues, as well as beginning the process of decomposing the $In(NO_3)_3$ precursor. The output characteristics in Figure 4.8j show I_{DS} values similar to those in Figure 4.8g. Since μ_{FE} values are also similar and I_{DS} values are relatively low, this explains both the low mobility and similar performance despite the fluence increase. However, a working device such as this wouldn't necessarily be expected at this insufficient temperature rise. At this stage of comparing the experimental and opto-thermal data, it isn't completely clear on the extent to which the opto-thermal simulations agree with the experimental data, hence why the additional data points at higher fluences become valuable for this SiO_2 thickness.

Figures 4.9a-l show the contour plots (temperature vs time, colour scale indicating temperature) and $I-V$ characteristics of $In(NO_3)_3$ on $400\ \mathrm{nm}\ SiO_2$ processed with $300\ \mathrm{mJ\ cm^{-2}}$ (Figures 4.9a-c), $350\ \mathrm{mJ\ cm^{-2}}$ (Figures 4.9d-f), $400\ \mathrm{mJ\ cm^{-2}}$ (Figures 4.9g-i) and $450\ \mathrm{mJ\ cm^{-2}}$ (Figures 4.9j-l). Note there are no outputs characteristics, as they were not preserved after the study was completed. For $I-V$ characteristics, V_{th} was obtained and reported within the article. However, transfer characteristics seen in Fig. 4.9 don't show distinctive switching behaviour in the measurement ranges (no clear regions where device is on and off). Thus, extracting $I_{On/Off}$ precisely is extremely difficult and an estimate is reported here, with no exact values reported in Fig. 4.5b.

The next fluence of $300\ \mathrm{mJ\ cm^{-2}}$ causes a sharp change in device characteristics, with an increase of μ_{FE} to $13.0\ \pm 0.2\ \mathrm{cm^2/Vs}$ and V_{th} becomes increasingly negative at $-70.5\ \mathrm{V}$. From the transfer characteristics seen in Fig. 4.9b, $I_{On/Off}$ can be estimated to have dropped to 10^2 – a decrease by 3 orders of magnitude. This is despite a minor temperature increase to $467\ \mathrm{K}$ in the semiconductor. It is worth mentioning that the device characteristics here are possible outliers. While the lines in Fig. 4.5b, 4.5c and 4.5d should mainly act as a guide to the eye, there is a clear trend that the data for $300\ \mathrm{mJ\ cm^{-2}}$ falls away from the data points around it. This is most notable in V_{th} (Fig. 4.5d), where a clear dip is seen at this data point when the pattern is clearly that of a plateau in V_{th}. If we choose to believe this data point is not erroneous with respect to the rest of the data, the sudden change in device characteristics with this

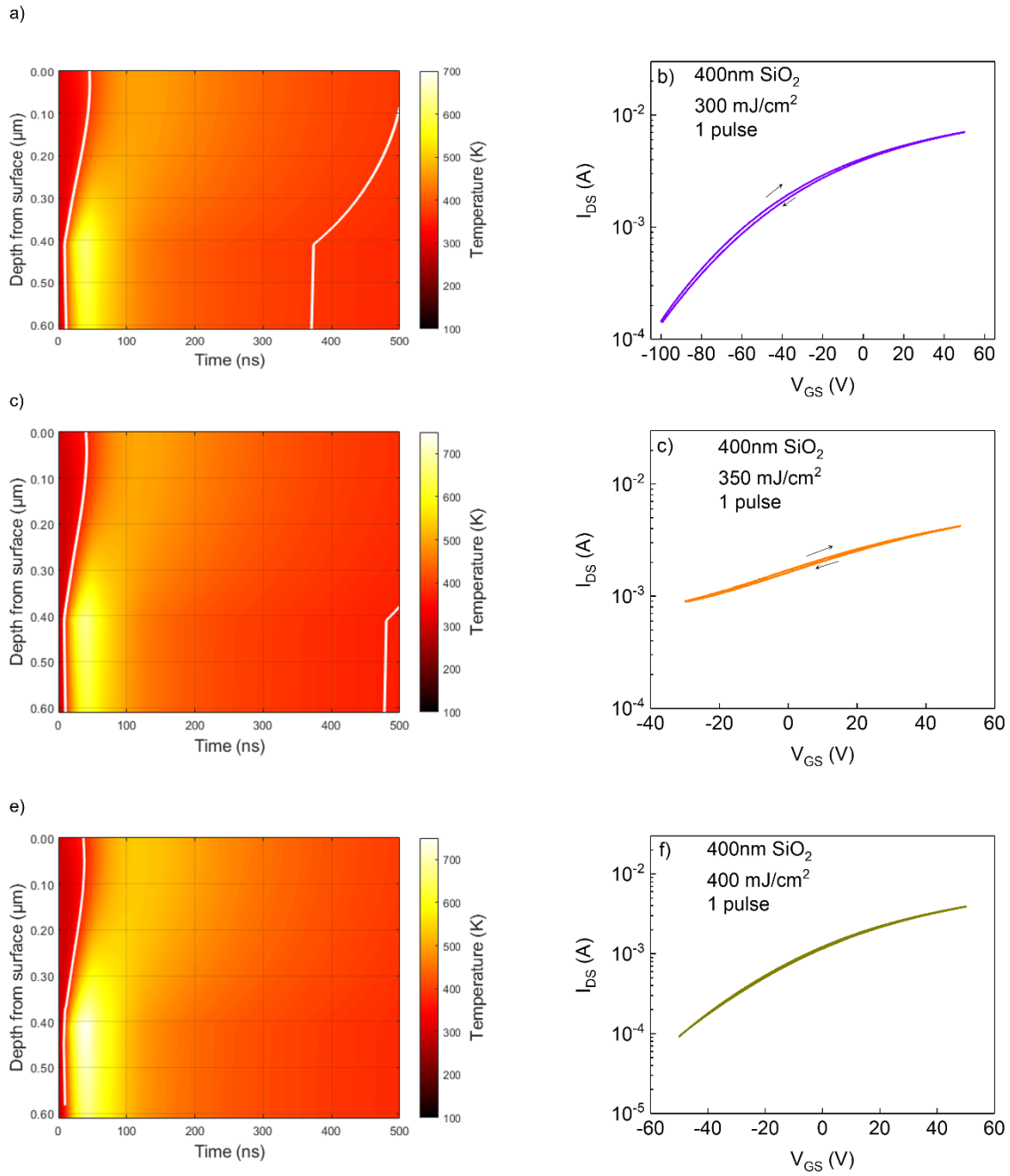

Figure 4.9. The opto-thermal simulation temperature rises of for $10\ \mathrm{nm}\ \mathrm{In(NO_3)_3}$ on $400\ \mathrm{nm}\ \mathrm{SiO_2}$ compared to device $\mathrm{I-V}$ characteristics for each fluence. a) Contour plot for $300\ \mathrm{mJ\ cm^{-2}}$. b) The transfer characteristics for $300\ \mathrm{mJ\ cm^{-2}}$. The analysis of the device characteristics does not match with observations of the opto-thermal simulations. c) Contour plot for $350\ \mathrm{mJ\ cm^{-2}}$. d) The transfer characteristics for $350\ \mathrm{mJ\ cm^{-2}}$. The analysis of the device characteristics showed slightly better agreement with observations of the opto-thermal simulations. e) Contour plot for $400\ \mathrm{mJ\ cm^{-2}}$. f) The transfer characteristics for $400\ \mathrm{mJ\ cm^{-2}}$. The analysis of the device characteristics showed strong agreement with observations of the opto-thermal simulations.

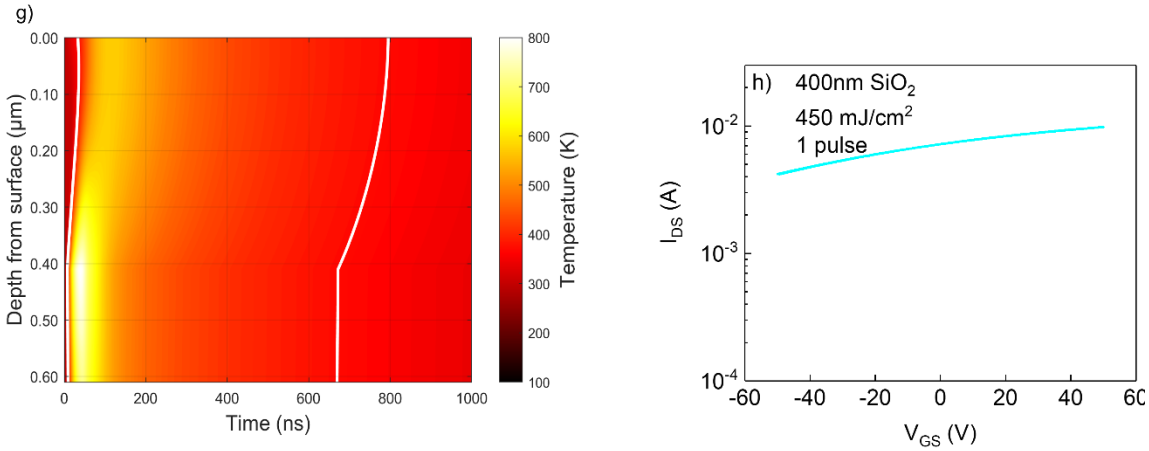

Figure 4.9 continued. g) Contour plot for $450\ \mathrm{mJ\ cm^{-2}}$. h) The transfer characteristics for $450\ \mathrm{mJ\ cm^{-2}}$.The analysis of the device characteristics showed some disparity compared to opto-thermal simulations.

temperature rise is difficult to explain. The agreement between experimental and opto-thermal simulation data doesn't improve with $350\ \mathrm{mJ\ cm^{-2}}$ and a temperature rise of $502\ \pm 24\ \mathrm{K}$ in the channel as seen in Figure 4.5a and 4.9a. Device characteristics are slightly less erroneous than the previous fluence, reporting μ_{FE} of $11.5\ \pm 0.2\ \mathrm{cm^2/Vs}$, V_{th} of $-30\ \mathrm{V}$ and $I_{\mathrm{On/Off}}$ less than 10. Note that V_{GS} is only swept from $-30\ \mathrm{V}$ to $50\ \mathrm{V}$. An increase in temperature, combined with peak temperature occurring towards the $\mathrm{SiO_2-Si}$ interface - leads to devices where sweeping at larger voltages leads to device breakdown. This is expected at far higher temperature rises than the $650\ \mathrm{K}$ observed in the dielectric. Furthermore, the lack of hysteresis in the transfer of Figure 4.9d suggests the precursor has been fully converted (including the removal of $\mathrm{In-OH}$), which is expected towards $823\ \mathrm{K}$. This is contradictory to the temperature rise observed here, thus experimental and opto-thermal results continue their trend of disagreement at this $\mathrm{SiO_2}$ thickness.

$400\ \mathrm{mJ\ cm^{-2}}$ shows some interesting variations in characteristics that can be explained in part by the increasing temperature rise. According to Figures 4.5a and 4.9e, a temperature rise of $538\ \pm 28\ \mathrm{K}$ occurs in the semiconductor leading to a device with μ_{FE} of $12.2\ \pm 0.2\ \mathrm{cm^2/Vs}$, $I_{\mathrm{On/Off}}$ of 10^2 and V_{th} of $-19.5\ \mathrm{V}$. Despite the increase in fluence and temperature rise, the device in Figure 4.9f achieves some switching behaviour and achieves higher voltages without device breakdown. The values of I_{DS} in the transfer curve are slightly elevated compared to previously, hence the increased μ_{FE} which can be linked to increasing conductivity. However, the problem of these characteristics manifesting at such a low temperature rise still persists.

$450\ \mathrm{mJ\ cm^{-2}}$ becomes a unique case for $400\ \mathrm{nm\ SiO_2}$ due to the massive change in V_{th}. According to Figures 4.5a and 4.9g, a temperature rise of $575\ \pm 32\ \mathrm{K}$ is observed at the

$InNO_3 - SiO_2$ interface. While μ_{FE} of $13.0 \pm 0.2\ cm^2/Vs$ continues the trend of slightly increasing μ_{FE}, V_{th} drops immensely to $-115.1\ V$ and $I_{On/Off}$ remains below 10. These changes are commensurate with increased conductivity and removal of water and nitrates, which is expected since the temperature is near the required temperature for conversion ($573\ K$). However, features of the transfer curve in Figure 4.9h disagree with this. At this temperature rise, some hysteresis and more semiconducting behaviour (instead of the very conductive behaviour) would be expected based on the $I - V$ characteristics of similar temperature rises in prior sections of this report. While the error bars indicate it is entirely possible to be as high as $610\ K$, this doesn't explain this disagreement between experimental and opto-thermal data.

One possible explanation of this disparity is that N_E being tuned sufficiently high via LA via a combination of mechanisms compensates for the high carrier trap density. From the perspective of temperature rise causing changes in material properties, $400\ nm\ SiO_2$ offers the greatest range of properties that result in a concurrent range of device characteristics. Since $400\ nm\ SiO_2$ causes poor absorption into the $In(NO_3)_3$ precursor, equivalent jumps in fluence on lower SiO_2 thicknesses cause lower temperature rises. Higher temperature rises into the structure below could cause dielectric damage, but smaller jumps in temperature rise into the $In(NO_3)_3$ precursor permit more accurate control over N_E which allows increased modulation of device performance. Such changes of N_E overcome excessive carrier traps and allow E_F to reach tail and extended states, thus a high performing semiconducting layer for TFTs is fabricated. In the higher fluences, this would then lead to overcompensation and a thin film semiconductor that didn't permit switching behaviour in a TFT.

In the case of $400\ nm\ SiO_2$, the maximum temperature in the $In(NO_3)_3$ in the contour plots occurs later than lower SiO_2 thicknesses at $120\ ns$ and retains this heat longer than lower thicknesses to the extent the sample remains above the melting point of $In(NO_3)_3$, despite lower temperature rises. An example of this in seen in Figure 4.9g, where the simulation is performed for $1000\ ns$ to demonstrate the full range of temperature transients, and when the temperature drops below the melting temperature. While this additional heating does occur, the temperature and the short length of exposure likely isn't long enough to induce any significant changes to the chemical conversion of the precursor. The highest temperature rise is seen in the $SiO_2 - Si$ interface and the top $100\ nm\ Si$. As many of the conditions do not meet the minimum temperature for conversion, green isolines were omitted from these contour plots. With all information considered (lower and higher fluences), the opto-thermal simulations temperature rises for $400\ nm\ SiO_2$ do not agree with the experimental data from $I - V$ characterisation.

4.3 Conclusions and Future Work

This chapter presents a methodological approach for predicting temperature profiles during laser annealing (LA) of indium oxide thin films derived from sol-gel processes. Coupled self-consistent opto-thermal simulations were used to model the temperature rise in $10\ \mathrm{nm}$ $\mathrm{In(NO_3)_3}$ films on $\mathrm{SiO_2}$ layers of varying thicknesses ($100\ \mathrm{nm}$, $200\ \mathrm{nm}$, and $400\ \mathrm{nm}$) during excimer laser annealing ($248\ \mathrm{nm}$ wavelength). The simulations accounted for thermal property variations and systematically propagated errors in optical constants. Thermal properties and non-linearities were extracted from the literature, with heat capacity and thermal conductivity in some cases adjusted to more closely resemble those of a thin film. Simulated temperature rises were generally consistent with experimentally observed output and transfer curves of thin-film transistors (TFTs) fabricated at NTU, especially for thinner $\mathrm{SiO_2}$ layers ($100\ \mathrm{nm}$ and $200\ \mathrm{nm}$). This correlation was particularly strong for fluences resulting in sufficient temperatures for complete conversion of $\mathrm{In(NO_3)_3}$ to $\mathrm{InO_x}$, also showcased by the TFT performance. However, significant discrepancies were observed for thicker $\mathrm{SiO_2}$ layers ($400\ \mathrm{nm}$) and at higher fluences, leading to more unpredictable results and less agreement between simulated and experimental data. The source of this discrepancy raises further questions about the $\mathrm{In(NO_3)_3}$ composition in each instance where this equivalence exists and the effect of the oxide dielectric thickness on the semiconductor conversion process. At higher temperatures ($>700\mathrm{K}$), limitations were revealed in the accuracy of the models used for $\mathrm{In(NO_3)_3}$ thermal properties, particularly thermal conductivity (κ). This suggests a need for refinement and alternative models. Discrepancies also existed between experimental and simulated results regarding certain fluences in the $400\ \mathrm{nm}\ \mathrm{SiO_2}$ cases. However, the comprehensive nature of the opto-thermal simulations, particularly the predictive modelling of temperature rises in thin films derived from sol-gel processes, is a significant advancement. The study highlights the need for further investigation to refine the opto-thermal models to account for the thickness-dependent effects observed, and specifically to improve the modelling of thermal properties of $\mathrm{In(NO_3)_3}$ at high temperatures. Additional research should focus on exploring the link between the precise conversion mechanism and thin film properties, which remains unclear in certain instances.

5. Fully sol-gel, laser annealed MOS capacitors and TFTs

This chapter explains the fabrication and characterisation of capacitors and TFTs fabricated entirely with sol-gel, LA MOs. For the first time, ZrO_x – selected due to its higher k (25) - is fabricated via sol-gel process and LA. The correlation between dielectric thickness, electrical performance *via* $C-V$, $C-f$ and E_{br} measurements, and LA parameters (fluence and number of pulses) was established to optimise thin film deposition, film thickness and LA processing parameters for high performance capacitors and their implementation into TFTs. Thin film thickness was investigated *via* ORS and VIS-UV SE, also allowing extraction of the bandgap for the ZrO_x thin film. AFM measurements of several LA conditions were conducted to determine the surface roughness and morphology, since smooth dielectric surfaces allow for easier charge transport when in TFTs. Afterwards, deposition of the electrodes - Al dots via thermal evaporation through a shadow mask - took place to complete fabrication of the capacitors. TA samples were made as references to the conventional methodology, undergoing the same characterisation as the LA films.

Afterwards, BGTC TFTS were fabricated by combining the optimised sol-gel, LA ZrO_x thin film with an InO_x semiconducting thin film, performing sequential deposition and processing steps for each film to produce the TFTs. Additionally, sol-gel, LA AlO_x thin films were integrated in with InO_x thin film based on a previous study at NTU, performing a comparative study using a dielectric with a lower k (9) but a higher bandgap 8.9 eV. The sol-gel, LA TFTs were compared to ALD AlO_x/InO_x TFTs and sol-gel, TA references of the same materials and structure. Devices with switching behaviour were demonstrated, demonstrating the first reported attempt of TFTs fabricated entirely from sol-gel MOs via LA with both dielectrics. Finally, opto-thermal simulations for both the dielectric thin films, AlO_x/InO_x and ZrO_x/InO_x structures are used to elucidate other LA conditions to improve sol-gel, LA TFT performance further.

5.1 Optimisation of ZrO_x MOS capacitors

For a sol-gel dielectric thin film, the functionality within a MOS capacitor or TFT depends heavily on the thickness and change in composition from precursor to thin film via chemical transformations. The effect of TA and LA processes on ZrO_x composition are explained fully in chapter 6 of this work, but a brief description is necessary to understand the requirements for realising novel sol-gel, LA ZrO_x thin films. It is well-regarded that chemical conversion of acetylacetonates to MO thin films, via removal of acetate complexes resultant from decomposition, requires higher temperatures than the more favoured nitrate precursors. Thus, a higher temperature via increased laser fluence is expected to achieve the desired performance in a MOS capacitor. With applied energy of any kind to a spin-coated precursor comes a

commensurate decrease in thickness that must be observed and controlled to not decrease excessive, potentially allowing increased leakage currents.

For ZrO_x, there are additional considerations. First, it is important to observe that areal capacitance C_i is related to electrode area A, film thickness d and dielectric constant k:

$$C_i = \frac{\varepsilon_0 kA}{d} \qquad 5.1$$

While the ZrO_x literature values for k (25) are high and lends itself to high areal capacitance in capacitors and TFTs as shown in eq. 5.1, the lower bandgap with lower thicknesses could lead to parasitic capacitances and high dispersion that work in opposition to this. Frequency-dependent dispersion can arise from this via a range of mechanisms such as tunnelling or Schottky emission [364] limiting the functionality of the eventual opto-electronic device. Additionally, the acetylacetonate precursor used ($Zr(AcAc)_4$) does not have the same high solubility as the nitrate precursors which would affect the number of spin-coated layers required since concentration is intrinsically limited. Thus, the numeric relationship between concentration, spin-coat number and thickness needed to be established first.

Initially, a concentration of $0.1\ M$ $(72.15\ mg/ml)$ of $Zr(AcAc)_4$ precursor in $2-ME$ was tested with spin-coating on heavily doped $p-Si$ ($1-2\ \Omega\cdot cm$) substrates, using $2000\ RPM$ for $35\ s$. Since acetylacetonate's chemical pathway to the MO thin film requires a higher temperature, a higher fluence window from $200-275\ mJ/cm^2$ was employed with 1, 2 and 3 pulses. TA films were fabricated using the same temperature in both cases, using $300℃$ hotplate for $1\ hr$. Thickness and bandgap measurements of the stabilised, LA and TA samples were obtained using ORS and NIR-VIS-UV SE. Thermal evaporation through a shadow mask consisting of $1\ mm$ diameter circles ($A = 0.785\ mm^2$) took place thereafter to finish the MOS capacitor fabrication.

Figure 5.1 displays the thicknesses of the ZrO_x films using $0.1\ M$ concentration at 1, 2 and 3 spin-coated layers, with the TA samples thicknesses shown with the stars. Thicknesses were determined via NIR-Vis-UV SE. As explained in chapter 3, section 3.4.2, the errors in thickness are extracted from CompleteEASE from the 90% confidence intervals of the regression algorithm used for analysis. In this case, a good fit with low MSE was obtained leading to extremely small (but present) errors in thickness.

In any high energy processing of a sol-gel precursor, extreme levels of film densification would be expected hence the low thicknesses observed, despite additional layer depositions. In 1-layer samples, LA causes a reduction thickness down to as low as $2\ nm$ at which point the role

of the dielectric would be questionable. Even with lower fluences of $200\ \mathrm{mJ/cm^2}$, thicknesses do not exceed $7.5\ \mathrm{nm}$. At these low thicknesses, particularly with the ZrO_x bandgap (whose thin film values are discussed later) tunnelling effects and extremely high leakage currents are commonly present. The 2-layer and 3-layer samples show a tendency to not densify as dramatically across most of the LA conditions, as thickness does not decrease to the extent of the 1-layer samples. The exception to this is with the 2-layer samples, where $275\ \mathrm{mJ/cm^2}$ does produce a large thickness decrease below $10\ \mathrm{nm}$. This threshold from higher temperature rise due to increased fluence can be implied to be a few things e.g. increased densification of a film when past the conversion temperature, removal of sol-gel by-products from conversion temperature being reached. This threshold in the 3-layer sample is far lower, seeing a decrease after $200\ \mathrm{mJ/cm^2}$. A change in thickness also represents a change in absorption into the sol-gel precursor, thus a lower fluence could permit the same temperature rise as that of a lower thickness with higher fluence. Since densification and by-products are removed, thickness then varies around a fixed range of $15 - 19\ \mathrm{nm}$.

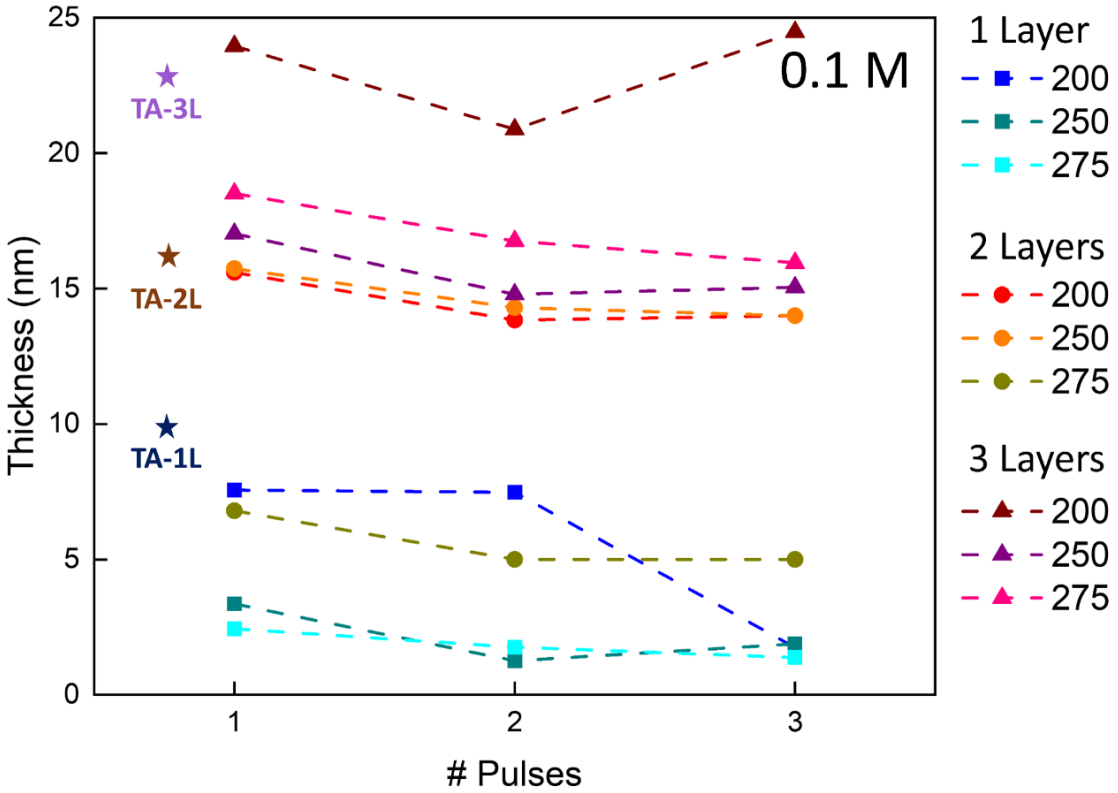

Figure 5.1 Comparison of thickness values of $1, 2$ and 3 layered thin films of ZrO_x using $0.1\ \mathrm{M}$ concentration of $Zr(AcAc)_4$ precursor spin-coated at $2000\ \mathrm{RPM}$ for $35\ \mathrm{s}$. Fluences of $200 - 275\ \mathrm{mJ/cm^2}$ were employed with $1, 2$ and 3 pulses for LA (squares, circles, triangles), while TA (stars) used hot plate annealing at $300°\mathrm{C}$ for $1\ \mathrm{hr}$.

While thickness trends might indicate certain outcomes based on known mechanisms, this is only speculative without electrical characterisation. Thus, $C - V$ and $C - f$

characterisation was carried out on the 0.1 M concentration thin films. Figure 5.2 a-c shows the $C-V$ curves and Figure 5.2 d-f the $C-f$ curves for the ZrO_x films of 0.1 M concentration at 1, 2 and 3 spin-coated layers. The $C-V$ curves use a dual sweep to observe any hysteresis in a reverse sweep. For the 1-layer samples (Figure. 5.2 a), the highest capacitance values are reached, with a maximum of $0.95\ \mu F/cm^2$ at $250\ mJ/cm^2$ for 2 pulses. Most of the LA conditions yield capacitance values of $0.6-0.8\ \mu F/cm^2$, with capacitance increasing with fluence or laser irradiation overall. At $250\ mJ/cm^2$ and above, near ideal behaviour is observed and there is a lack of (or very little) hysteresis. The absence of hysteresis is a positive indication that little or no charge traps exist at the metal-dielectric interface or within the dielectric film due to incomplete conversion (leading to organic byproducts). As the negative bias is applied to the electrode, a clearly defined accumulation region appears due to charge accumulation at the ZrO_x-Si (dielectric-substrate) interface, increasing capacitance values. Reversing the voltage sweep induces a depletion region and capacitance decreases as a result [365].

Similar observations are made for the 2-layer samples (Figure. 5.2b) with a similar spread between maximum and minimum capacitance values, though with a decreased maximum value of capacitance. This is attributed to the increased thickness, as Eq. 5.1 describes this inverse relationship (assuming the processing conditions give a similar dielectric constant). However, 3-layer samples (Figure. 5.2 c) shows far higher values of hysteresis and accumulation regions that are more difficult to define for multiple LA conditions. The increased hysteresis is likely due to the interfaces from multiple layers, as well as the shallow penetration depth of the 248 nm excimer laser into the $Zr(AcAc)_4$ precursor that means the entire depth of the laser may not be processed sufficiently at a particular fluence. Only the highest fluences with multiple pulses resolves this to bring the $C-V$ measurements closer to typical behaviour. Capacitance values are also further decreased. Across Figures 5.2 a-c, the TA sample shows non ideal behaviour in multiple ways, with accumulation regions not as well defined and hysteresis in all cases.

The $C-f$ measurements were utilised to help explain the observations in the $C-V$ measurements. In all cases (Figures 5.2 d-f), dispersion is witnessed in the higher frequency regimes for some or all laser conditions. In the 1-layer samples, a harsh drop occurs after 100 kHz regardless of processing condition. This is credited as a thickness related phenomenon, as below certain thickness thresholds charge is capable of conducting through the material via various tunnelling mechanisms and Schottky emission, for example. The $C-f$ measurements for 2-layer samples further confirm this, as the TA and select lower fluence LA samples demonstrate little to dispersion (increasing toward 1 MHz). However, dispersion occurs again

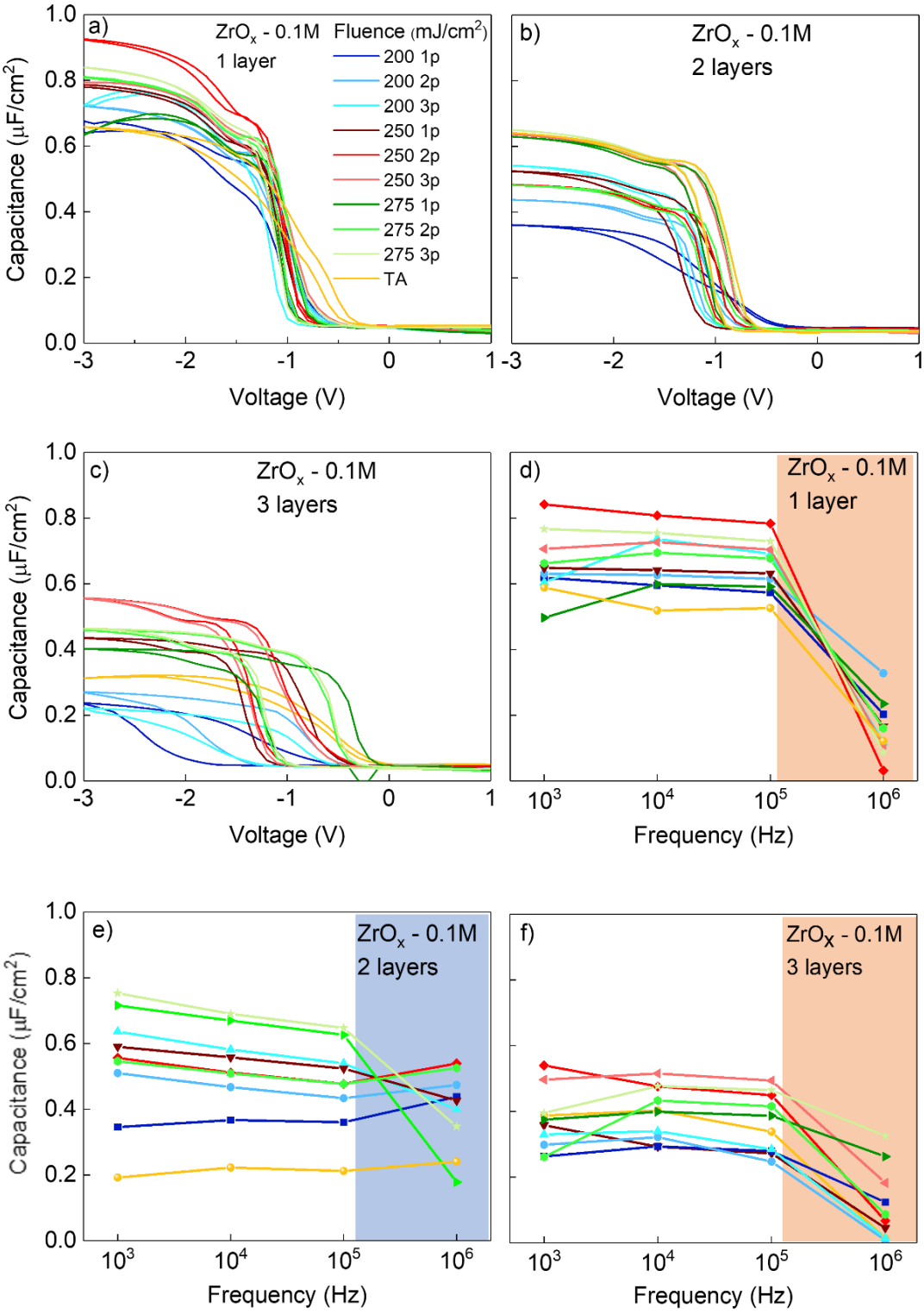

Figure 5.2. Capacitance-voltage $(C-V)$ and capacitance-frequency $(C-f)$ measurements of MOS capacitors utilising sol-gel, LA ZrO_x as a dielectric, using 0.1 M concentration and up to 3 spin-coatings of $Zr(AcAc)_4$ precursor on $p-Si$ substrates. For all different number of layers, $200\ mJ/cm^2$(blue lines), $250\ mJ/cm^2$ (red lines) and $275\ mJ/cm^2$ (green lines) for $1, 2$ and 3 pulses were used. A TA reference sample (gold line) was fabricated at $300°C$ for 1 hr. $C-V$ measurements were made from 1 V to -3 V in steps of 0.1 V. C-f measurements were made in logarithmic steps at a constant bias of -3 V. The graphs are split as: a) $C-V$ of 1-layer ZrO_x; b) $C-V$ of 2-layer ZrO_x. c) $C-V$ of 3-layer ZrO_x; d) $C-f$ of 1-layer ZrO_x; e) $C-f$ of 2-layer ZrO_x; f) $C-f$ of 3-layer ZrO_x.

after $250\ \mathrm{mJ/cm^2}$ for 3 pulses. Further thickness reductions and inducing charge traps and defects can both be linked in this case. Strangely, 3-layer samples contradict both of the above, as all conditions show dispersion at higher frequencies despite the increased thickness. Here, it is thought charge traps prevail entirely over this dispersion. The processes involved with charge trapping and escape when a bias is applied are far slower than those of other processes in the dielectric, thus the film cannot respond sufficiently quickly to the electric field.

Based on the above observations, 2-layer samples exhibit the better performance due to an optimised balance between capacitance values and frequency dispersion compared to 1-layer and 3-layer samples. Within the LA conditions of the 2-layer (optimised thickness) sample, it is necessary to find a condition that maximises capacitance and minimises frequency dispersion with the highest dielectric constant, k. The values of these devices have yet to be inspected. Thus, Figure 5.3 is used to compare k against frequency, taking the peak capacitance values at $-3\ \mathrm{V}$ in the accumulation region, to visually determine these conditions. Across all regions, k is low compared to the bulk value of 25. In nearly all cases, the highest values of k is obtained at low frequencies of $1\ \mathrm{kHz}$. At low frequencies, the AC signal modulates charge states at the interface that have a frequency-dependent capacitance. At higher frequencies, the states cannot follow the change in field of the AC signal and cannot contribute to the total measured capacitance [366]. Thus, values at $1\ \mathrm{kHz}$ will typically be higher than those of $1\ \mathrm{MHz}$ or $100\ \mathrm{kHz}$.

From Figure 5.3, three distinct regions can be identified. In region 1 (top, green), the highest k is achieved at the expense of the highest dispersion. Very few conditions achieve this, with only $250\ \mathrm{mJ/cm^2}$ (2 and 3 pulses) presenting the highest observed k of ≈ 12. This significantly drops between $100\ \mathrm{kHz}$ and $1\ \mathrm{MHz}$. No major change in thickness occurs, suggesting thin film structural modifications that cause pathways for leakage currents. Due to the low hysteresis from the $\mathrm{C-V}$ measurements, it is less likely that charge traps from remaining organic by-products are responsible for this. In region 2 (middle, blue), the frequency dispersion is minimised with moderate k. All conditions within this region (aside from the TA sample) are of low fluence or overall laser irradiation. The TA sample and single pulse LA samples ($200\ \mathrm{mJ/cm^2}$ and $250\ \mathrm{mJ/cm^2}$) are able to maintain k at $1\ \mathrm{MHz}$, contrary to all other LA conditions. Increase in the number of pulses leads to increased dispersion at $1\ \mathrm{MHz}$ with higher k at frequencies below $1\ \mathrm{MHz}$. Negligible thickness change in Figure 5.1 is observed, suggesting the additional pulses modify the structure of the thin film, such as crystallisation that induces grain boundaries as convenient paths for current leakage through the gate [367]. In region 3 (bottom, purple), there are the lowest k values of ≤ 4 with a small level of dispersion. This region contains only the highest fluence samples of $275\ \mathrm{mJ/cm^2}$ at $1, 2$ and 3 pulses. Single pulse shows no dependence on frequency, while 2 and 3 pulses show dispersion at $1\ \mathrm{MHz}$. This

is attributed to the slight decrease in thickness previously depicted in Figure 5.1, which may breach a threshold to where dispersion phenomena overwhelm at higher frequencies. From the observations of region 3, it could be concluded that LA with higher fluences, even at single pulses, may be unsuitable for ZrO_x for the purposes of MOS capacitors and TFTs and should be restricted to $250\ mJ/cm^2$.

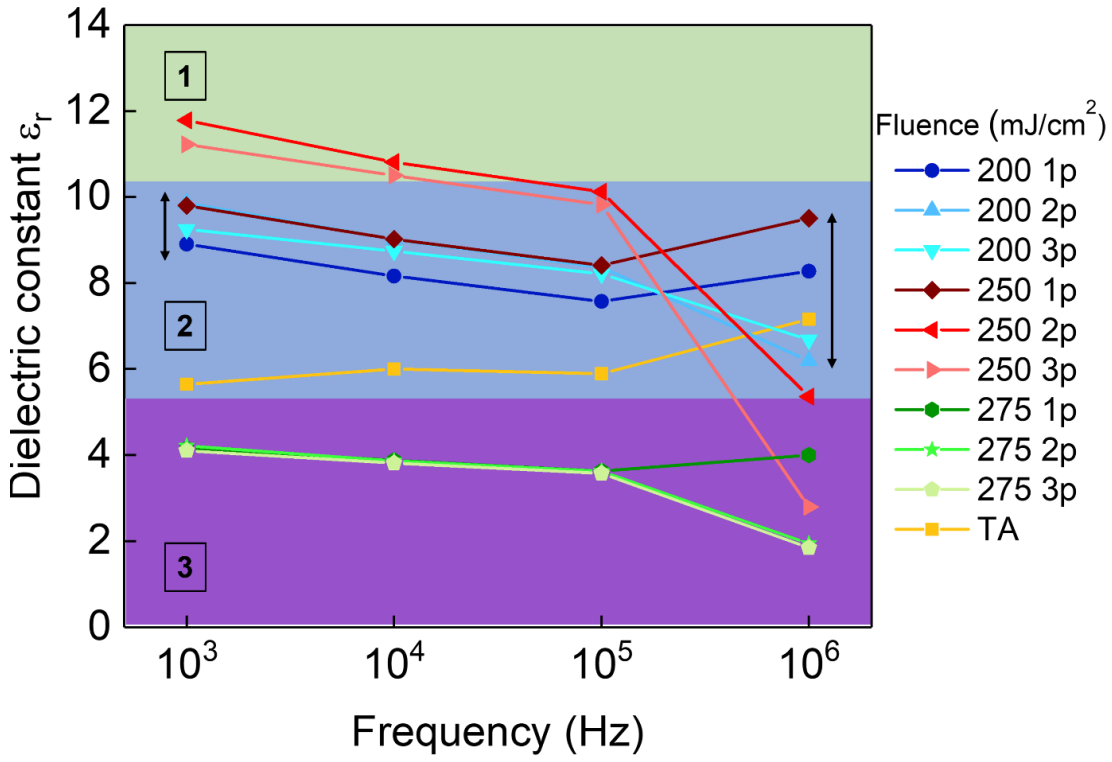

Figure 5.3. A plot of dielectric constant (k) against frequency for sol-gel, LA ZrO_x thin film dielectrics made of 2 spin-coated layers using $0.1\ M$ concentration of $Zr(AcAc)_4$ precursor. Dielectric constants were extracted using the maximum capacitance at the constant bias of $-3\ V$ from $C-f$ measurements (Figure 5.2), area of the circular Al electrodes of $1\ mm$ diameter and the thickness extracted via ORS and SE (Figure 5.1). Colour coded regions indicate distinct behaviours depending on LA condition - region 1 (green) indicates a high dielectric constant, high frequency dependent dispersion; region 2 (blue) a more moderate dielectric constant and low dispersion; and region 3 (purple) a low dielectric constant, low dispersion region.

In short, the observations of Figure 5.3 show the sensitivity of ZrO_x thin films to LA conditions and that acute care must be taken to reach an optimised condition. Even small steps of $25\ mJ/cm^2$ to $275\ mJ/cm^2$ can lead to drastic decrease in k with frequency dispersion due to tunnelling mechanisms (from decreased thickness) and thin film crystallisation. Due to the necessity for increased thickness and an adjustment of laser fluence, higher concentrations were trialled, while the lower concentration of $0.1\ M$ was set aside. New samples using $0.15\ M$ and $0.2\ M$ of $Zr(AcAc)_4$ in $2-ME$ were fabricated, with multiple layer samples and thickness

confirmation via SE and ORS utilised as previously to investigate higher thicknesses. Fluences were adjusted to $200 - 250\ \mathrm{mJ/cm^2}$ in steps of $25\ \mathrm{mJ/cm^2}$.

Figure 5.4 shows the $0.15\ \mathrm{M}$ film thickness for ZrO_x thin films at $1, 2$ and 3 layers, measured via ORS. In this case, after fitting both the transparent and semi-absorbing regions of the ZrO_x for $\tilde{n}$ and d in CompleteEASE, errors are outputted from the 90% confidence intervals of the region fitted below the bandgap.

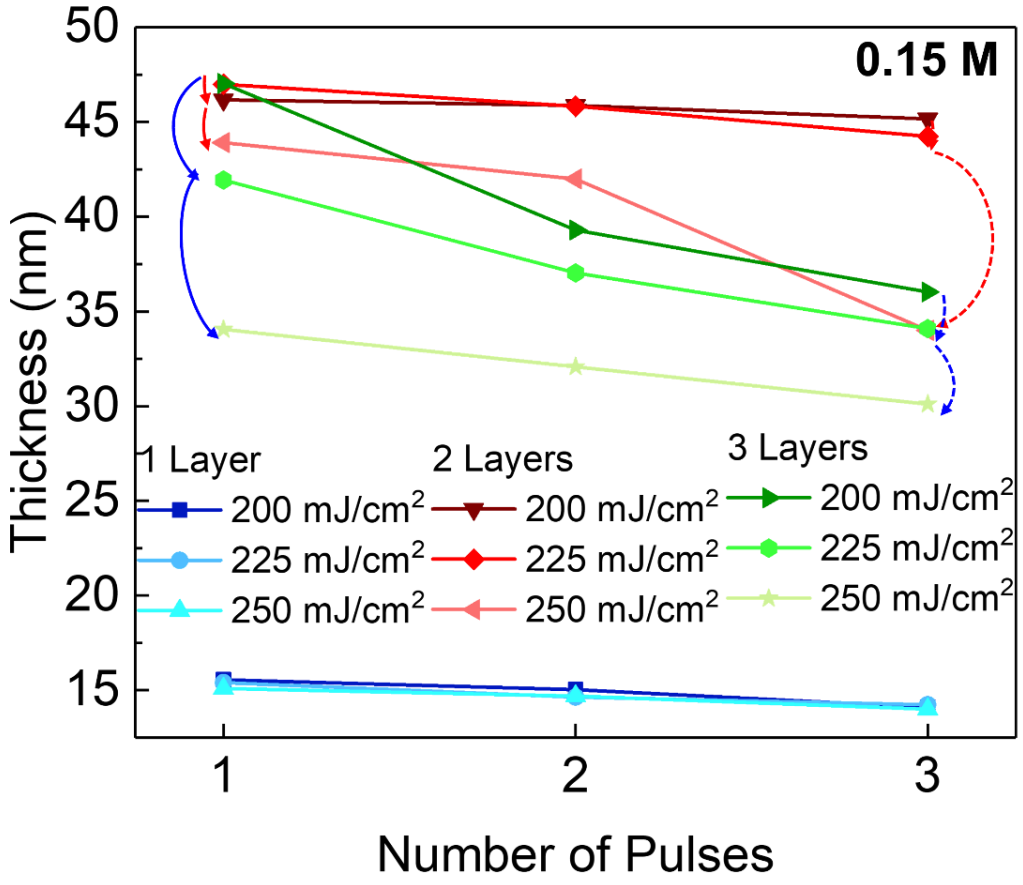

Figure 5.4. Comparison of thickness values of 1, 2 and 3 spin-coated layers for ZrO_x thin films using $0.15\ \mathrm{M}$ concentration of $Zr(AcAc)_4$ precursor. Fluences of $200\mathrm{mJ/cm^2}$, $225\ \mathrm{mJ/cm^2}$ and $250\ \mathrm{mJ/cm^2}$ were employed with 1, 2 and 3 pulses for LA (squares, circles, triangles), while TA (stars) used hot plate annealing at $300°C$ for $1\ \mathrm{hr}$.

The $0.15\ \mathrm{M}$ 1-layer sample demonstrates a stabilised thickness around $23\ \mathrm{nm}$, which can be corroborated with Figure 5.1 (from the $0.1\ \mathrm{M}$ samples) to be potentially thin enough for high dispersion after undergoing post-deposition processing, especially considering the densification of the film expected after LA. Subsequently, thicknesses after LA sit in a small range of $14 - 16\ \mathrm{nm}$, similar to those of Figure 5.1 of similar starting thickness. However, the use of a single layer to achieve this thickness may allow the MOS capacitor to benefit from a lack of interfaces from multiple layers, with fewer steps in the methodology for errors to contribute to thin film defects and device failure. For the $0.15\ \mathrm{M}$ 2-layer sample, a stabilised thickness of

around $47\ \mathrm{nm}$ is obtained, with LA parameters reducing this to a minimum of $\approx 33\ \mathrm{nm}$. The 2-layer samples show a resistance to thickness reduction, since the stabilised thickness and many of the LA thicknesses remain in proximity to each other. Surprisingly, $200\ \mathrm{mJ/cm^2}$ and $225\ \mathrm{mJ/cm^2}$ retain similar thickness values which could imply a fluence for a sufficient temperature rise that must be exceeded for sufficient energy to be imparted for photochemical conversion. This case of similar thickness values could be entirely duplicitous, as it could be linked to a thickness that results in low absorption that risks lack of densification and removal of organic groups (thus large volumes of charge traps exist) while being an adequate thickness to avoid dispersion in a wide frequency range. Thus, it's possible that the samples for $200\ \mathrm{mJ/cm^2}$ and $225\ \mathrm{mJ/cm^2}$ have a litany of faults preventing their functional use in devices. A sudden decrease in thickness with a single pulse of $250\ \mathrm{mJ/cm^2}$ and subsequent further pulses causes the eventual decrease in thickness to $\approx 33\ \mathrm{nm}$.

In contrast to the 2-layer samples, the 3-layer sample show large thickness reduction even at lower fluences. For example, a stabilised thickness of $\approx 70\ \mathrm{nm}$ quickly reduces to $47\ \mathrm{nm}$ after a single pulse at $200\ \mathrm{mJ/cm^2}$, which is a similar thickness to the 2-layer sample after processing with the same fluence. Subsequent further pulses with $200\ \mathrm{mJ/cm^2}$ reduce this even more heavily to $35.7\ \mathrm{nm}$. Higher fluences lead to even lower thicknesses than the 2-layer samples, despite the far higher starting thickness. There are a few potential causes could be speculated here. At the stabilised thickness of $\approx 70\ \mathrm{nm}$, the thin film may have increased absorption that leads to a dramatically high temperature rise with the same fluence. This could not be confirmed at the time these devices had been fabricated, as the opto-thermal simulation code had not been developed. The role of the interfaces with multi-layer spin-coating deposition could also contribute. Interaction of LA with interface defects from discontinuities between deposited layers, $-\mathrm{OH}$ radicals and $\mathrm{H_2O}$ from preparation in ambient conditions may cause their removal along with organic (carbon-related) by-products, leading to a heightened level of film densification.

For the $0.2\ \mathrm{M}$ thin films, while some stabilised and TA films were fabricated, issues arose during sample fabrication. $\mathrm{Zr(AcAc)_4}$ in this concentration within $2-\mathrm{ME}$ resulted in complete saturation, thus even heated at $50℃$ stirring at $1000\ \mathrm{RPM}$ (instead of $600\ \mathrm{RPM}$) with a magnetic stirrer until spin-coating took place resulted in large aggregates and particulates in the thin film precursor. These non-uniformities and inhomogeneities act as bulk material in the film, undergoing completely different chemical processes to the rest of the film during LA and would also act as charge traps in any resultant thin film. Thus, they were abandoned and not further characterised.

5. Fully sol-gel, laser annealed MOS capacitors and TFTs

As previously, to confirm the effects of thickness of device performance, $\mathrm{C}-\mathrm{V}$ and $\mathrm{C}-\mathrm{f}$ measurements were made after thermal evaporation of Al onto the processed thin films. Figure 5.5 shows the $\mathrm{C}-\mathrm{V}$ and $\mathrm{C}-\mathrm{f}$ characteristics of the $\mathrm{ZrO_x}$ MOS capacitors using a $0.15\ \mathrm{M}$ concentration. Similar to the $0.1\ \mathrm{M}$ 1-layer sample, the $0.15\ \mathrm{M}$ 1-layer sample (Figure 5.5 a) shows an extremely high capacitance of $1.0\ \mu\mathrm{F/cm^2}$ with very low hysteresis, likely due to the low film thickness that drives this value upwards along with the LA pulse penetrating throughout the depth of the precursor. Compared to the lower concentration, there is a slightly larger spread of capacitance values. A shoulder in many of the $\mathrm{C}-\mathrm{V}$ curves appears at $-1.8\ \mathrm{V}$, which disappears with 2-layer and 3-layer samples. The curves in some cases do not reach saturation in the accumulation region at the maximum of bias of $-3\ \mathrm{V}$. This is potentially detrimental to electrical stability – higher voltages for low thickness dielectrics that are inherently less stable than others could lead to premature dielectric breakdown before fully charging the device.

Akin to the $0.1\ \mathrm{M}$ samples is that the 2-layer sample for $0.15\ \mathrm{M}$ (Figure 5.5 b) drastically decreases in capacitance relative to the 1-layer, producing capacitance values of $0.33-0.44\ \mu\mathrm{F/cm^2}$. The 3-layer samples (Figure 5.5c) demonstrate a far broader range of capacitance values. This indicates a far larger dependency on fluence for the 3-layer samples to achieve desired dielectric properties. In both, the 2-layer and 3-layer samples, $250\ \mathrm{mJ/cm^2}$ for 3 pulses is clearly defined as the condition with the highest capacitance, at the expense of a larger hysteresis being produced compared to other LA conditions. The hysteresis with this LA condition was not thought to be due to lack of removal of organic groups during conversion due to the higher fluence and number of pulses, inducing a higher temperature rise than other conditions. The TA sample shows large anticlockwise hysteresis, which can be attributed to the presence of organic by-products since the $300^{\circ}\mathrm{C}$ treatment is not sufficiently high for full conversion via acetate dissolution. The accumulation region is not as well defined in the TA sample and lower fluence LA samples, which has been reported to arise from charge trapping sites in the dielectric-Si interface [368]. Aside from these conditions, the 2-layer and 3-layer sample LA conditions show extremely well-defined accumulation regions due to fast accumulation of charge carriers at the at the $\mathrm{ZrO_x}-\mathrm{Si}$ interface.

For the $\mathrm{C}-\mathrm{f}$ characteristics, the initial hypothesis of the 1-layer $0.15\ \mathrm{M}$ sample (Figure 5.5d) being too thin ($<20\ \mathrm{nm}$) is confirmed by every LA condition tested showing dispersion in frequencies above $100\ \mathrm{kHz}$. In contrast, the TA sample exhibits only mild dispersion, so capacitance remains nearly independent of frequency. Excessive densification and low thickness could both be correlated to this. The 2-layer $0.15\ \mathrm{M}$ sample (Figure 5.5e) shows little to no dispersion across the entire measured frequency range, with values dropping from $0.44-0.52\ \mu\mathrm{F/cm^2}$ to $0.38-0.42\ \mu\mathrm{F/cm^2}$. Values across the frequency range for LA samples are

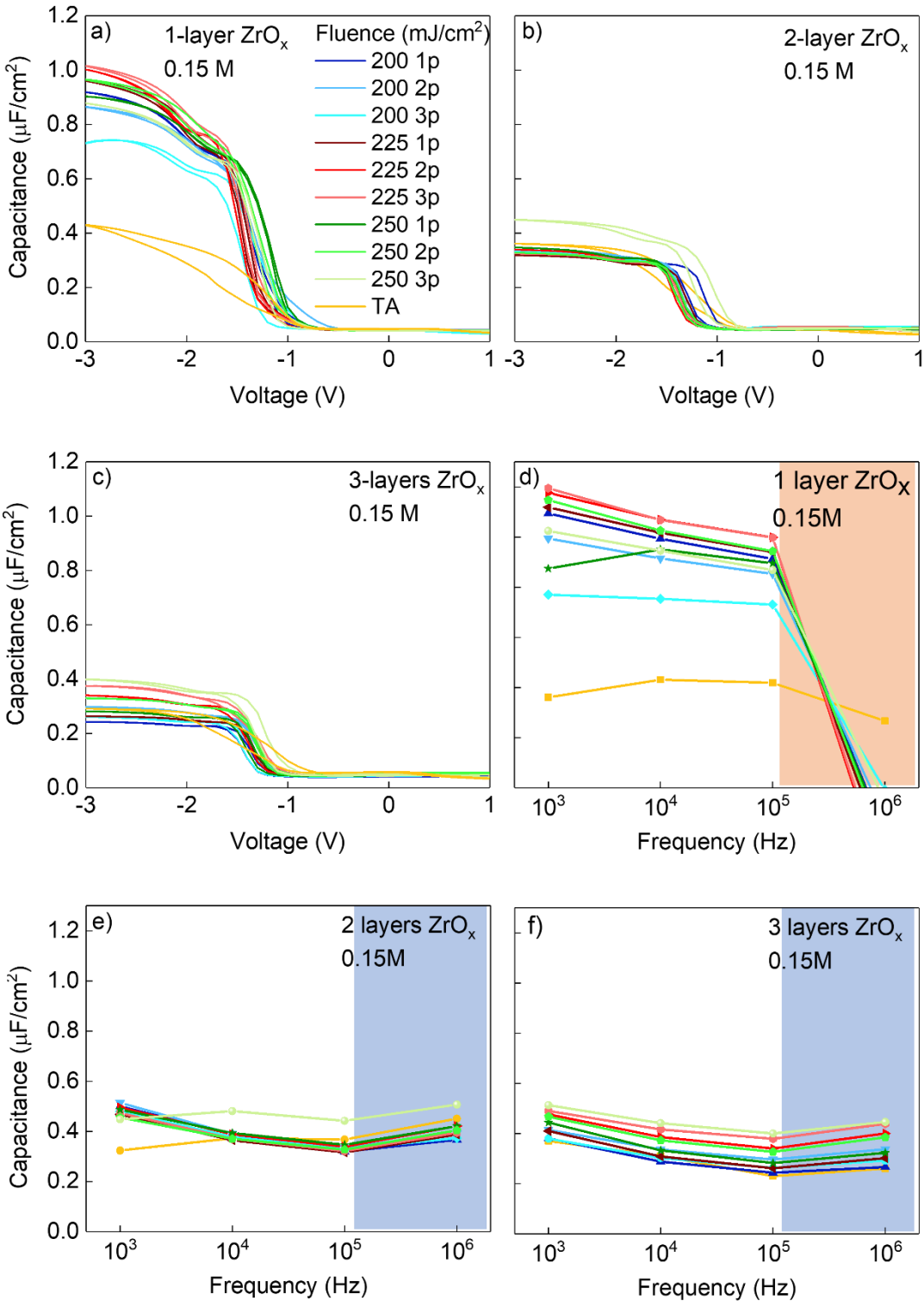

Figure 5.5. Capacitance-voltage $(C-V)$ and capacitance-frequency $(C-f)$ measurements of MOS capacitors utilising sol-gel, LA ZrO_x as a dielectric, using 0.15 M concentration and up to 3 spin-coatings of $Zr(AcAc)_4$ precursor on $p-Si$ substrates. For all different number of layers, 200 mJ/cm^2(blue lines), 225 mJ/cm^2 (red lines) and 250 mJ/cm^2 (green lines) for 1, 2 and 3 pulses were used. A TA reference sample (gold line) was fabricated at 300°C for 1 hr. $C-V$ measurements were made from 1 V to -3 V in steps of 0.1 V. C-f measurements were made in logarithmic steps at a constant bias of -3 V. The graphs are split as: a) $C-V$ of 1-layer ZrO_x; b) $C-V$ of 2-layer ZrO_x. c) $C-V$ of 3-layer ZrO_x; d) $C-f$ of 1-layer ZrO_x; e) $C-f$ of 2-layer ZrO_x; f) $C-f$ of 3-layer ZrO_x.

comparable or better than the TA sample. For the LA samples, $225\ \mathrm{mJ/cm^2}$ and $250\ \mathrm{mJ/cm^2}$ for any pulse number across most of the frequency range show higher capacitance values, meaning the fluence threshold previously demonstrated for the thickness can also be correlated to improved device performance. The 3-layer samples (Figure 5.5f) also show far lower dispersion across the frequency range than 1-layer samples. However, as discussed previously, 3-layer samples show the lowest capacitance values.

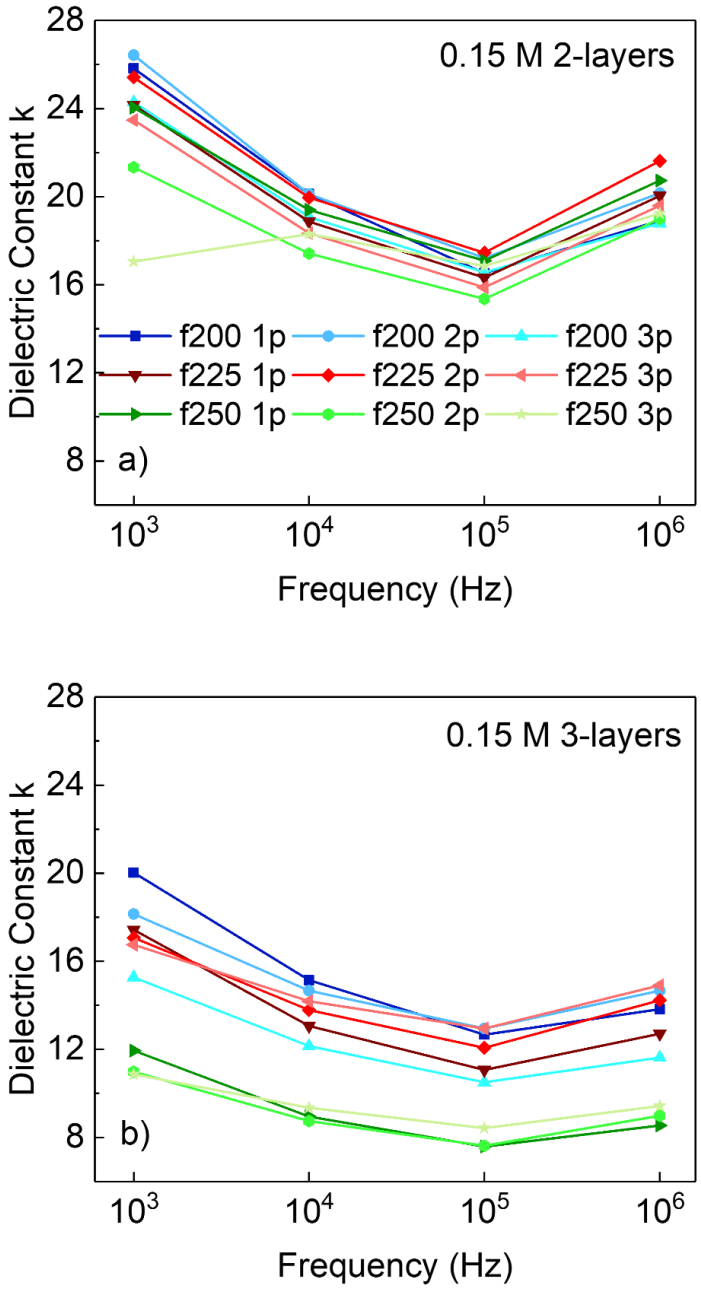

Figure 5.6. A plot of dielectric constant k against frequency for sol-gel, LA $\mathrm{ZrO_x}$ thin film dielectrics made of a) 2 and b) 3 spin-coated layers using $0.15\ \mathrm{M}$ concentration of $\mathrm{Zr(AcAc)_4}$ precursor. Dielectric constants were extracted using the maximum capacitance at the constant bias of $-3\ \mathrm{V}$ from $\mathrm{C-f}$ measurements (Figure 5.5), area of the circular Al electrodes of $1\ \mathrm{mm}$ diameter and the thickness extracted via ORS and SE (Figure 5.4).

The thickness, $C-V$ and $C-f$ data were combined to calculate and display dielectric constant values for LA samples in Figure 5.6. Since 1-layer samples showed overall undesirable performance, they were omitted from further study, leaving only 2-layer and 3-layer samples. The 2-layer $0.15\ M$ sample (Figure 5.6a) shows notably improved k across the measured frequency range compared to $0.1\ M$, reaching as high as 27 at $1\ kHz$ but ranging down to 17 at $100\ kHz$. The lowest values occur at higher frequency operation (arguably more relevance to modern device operation), returning values of $15-17$ with $250\ mJ/cm^2$ with 2 pulses producing the lowest value. There is seemingly an optimised region around $225\ mJ/cm^2$ for 2 pulses to $250\ mJ/cm^2$ with 1 pulse, maximising dielectric constant alongside minimal dispersion. That being said, at most frequencies, the deviation in value for k is very small. This is contrast to 3-layer samples (Figure 5.6b), where there is a far heavier dependency on LA parameterisation at all frequencies to improve dielectric constant. In 3-layer samples, there are lower dielectric constants compared to the 2-layer samples. As expected, values are maximised at $1\ kHz$ and range from $11.5-20$. Lowest values drop as low as 8 at $100\ kHz$. In particular, $250\ mJ/cm^2$ at any number of pulses shows a clear degradation in capacitive performance.

At this stage, there are clear identified trends between LA parameterisation, thin film thickness and several aspects of device performance that have led to a few candidate materials. The final device performance aspect to be inspected is electrical stability via measurement of the dielectric breakdown field, E_{br}. The process for conducting a breakdown field measurement is described in chapter 3, section 3.4.1, including the defined standard used. Figure 5.7 shows the breakdown field measurements for the 2-layer and 3-layer samples at $200\ mJ/cm^2$, $225\ mJ/cm^2$ and $250\ mJ/cm^2$ for $1, 2$ and 3 pulses. Dashed lines towards the x-axis are used to extrapolate and show the values for E_{br}. Across all samples of any type, current density prior to breakdown remains at a level of just above 10^{-5}. After breakdown, current density flatlines as it meets the maximum compliance of the Keithley SMU as opposed to a material-related phenomena. $200\ mJ/cm^2$ for 2 or 3 pulses (Figure 5.7a) produces higher breakdown fields than the TA reference at $1.7\ MV/cm$ and $1.9\ MV/cm$, respectively. $225\ mJ/cm^2$ for 1 pulse for the 2-layer samples (Figure 5.7b) produces values of $2.0\ MV/cm$ while 2 pulses permits $1.7\ MV/cm$, exceeding the reference. However, $250\ mJ/cm^2$ (Figure 5.7c) produces no samples with superior E_{br} to the reference. Across all LA parameters with 2-layer samples, increasing the pulse number from 2 to 3 results in a decrease in E_{br}.

Overall, the E_{br} measurements continue to support previous observations while showing sol-gel, LA ZrO_x can be suitable for electrical devices. $225\ mJ/cm^2$ for 1 pulse and 2 pulses were also identified as strong candidates in other electrical measurements, showing the highest dielectric constant with low dispersion. This gives them great potential for integration

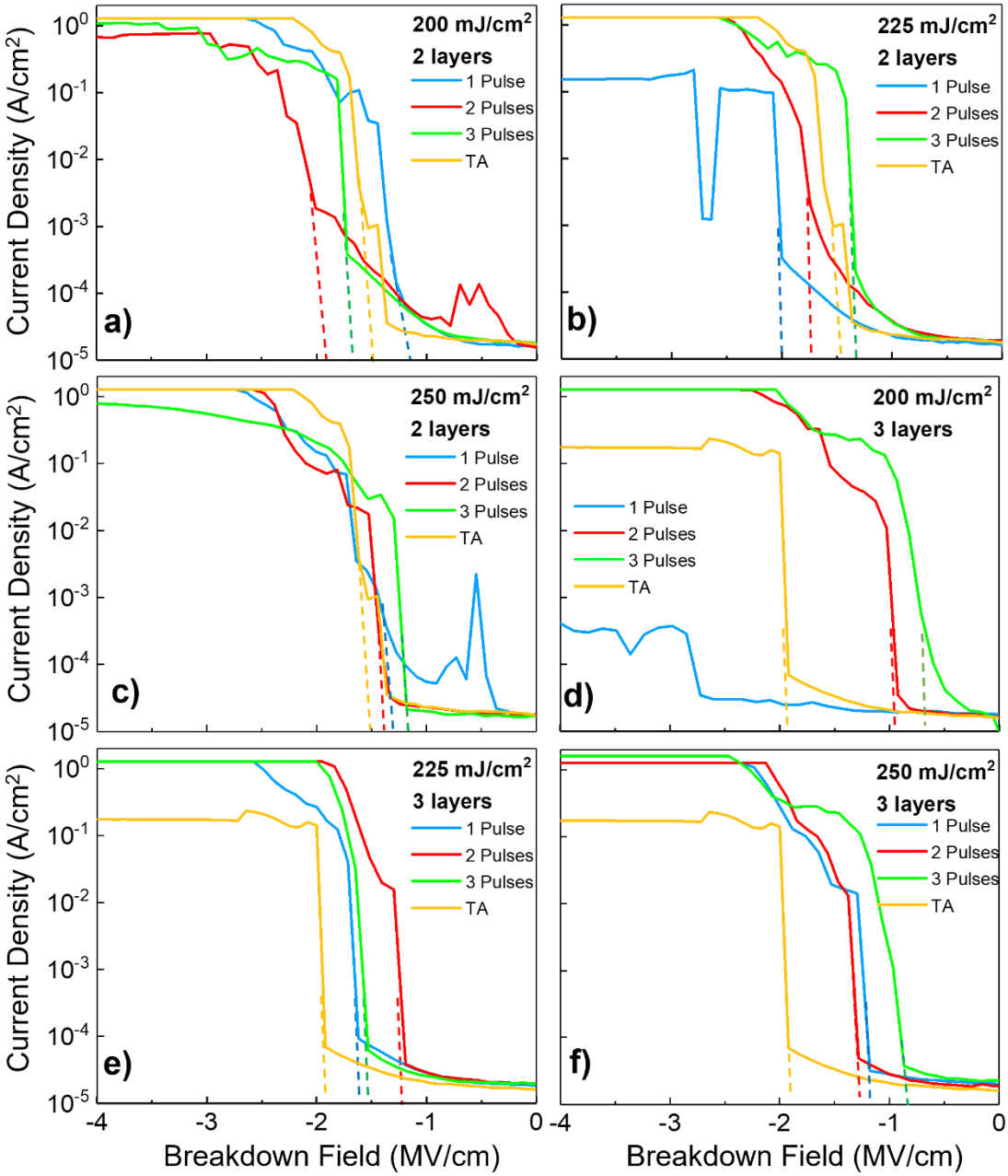

Figure 5.7. Breakdown field (in $\mathrm{MV/cm}$) of the $\mathrm{ZrO_x}$ dielectric thin films fabricated with 2 or 3 spin-coated layers of 0.15 M concentration $\mathrm{Zr(AcAc)_4}$, processed with LA at 200 $\mathrm{mJ/cm^2}$, 225 $\mathrm{mJ/cm^2}$ and 250 $\mathrm{mJ/cm^2}$ for 1, 2 and 3 pulses or TA at 300°C for 1 hr. Dotted lines with corresponding colour are used to extrapolate and indicate the approximate values of $\mathrm{E_{br}}$ on the x-axis.

into another device such as TFTs. The negative effect of moving from 2 to 3 pulses can be linked to the previously discussed change in structure with 2-layer samples at 0.15 M; as mentioned, thickness with LA didn't change until 250 $\mathrm{mJ/cm^2}$, thus the mechanism for changes in electrical performance must be inherent to film structure. Single pulses may not sufficiently raise the temperature of the precursor throughout the depth of the film, leading to incomplete conversion.

For 3-layer samples, far lower breakdown fields are experienced compared to the 2-layer samples. While the $200\ \mathrm{mJ/cm^2}$ single pulse does have a higher $\mathrm{E_{br}}$ than the TA sample, the other LA fluences show $\mathrm{E_{br}}$ below the TA reference. For $200\ \mathrm{mJ/cm^2}$ (Figure 5.7d), 2 and 3 pulses show $\mathrm{E_{br}}$ below $1\ \mathrm{MV/cm}$ (below the conventional $\mathrm{SiO_2}$ it is competing against) that the $\mathrm{ZrO_x}$ is aiming to improve upon. The lower fluence on an elevated thickness suggests incomplete conversion that allows formation of leakage pathways. $225\ \mathrm{mJ/cm^2}$ (Figure 5.7e) shows a continual decrease in $\mathrm{E_{br}}$ with pulse number, remaining lower than the TA reference but successfully increasing over $200\ \mathrm{mJ/cm^2}$. The decrease in capacitive performance at $250\ \mathrm{mJ/cm^2}$ seen in Figure 5.6b is seen in Figure 5.7f, where a decrease in $\mathrm{E_{br}}$ is seen compared to Figure 7.7e.

While there are clear advantages in using the 2-layer $0.15\ \mathrm{M}$ concentration samples compared to the 3-layer that have already been discussed, they both exhibit clear trends in relation to LA parameterisation. Overcoming certain fluence thresholds results in clear increases in key metrics for dielectric layers such as dielectric constant and reduction in frequency-dependent dispersion, with an accompanying decrease in thickness with removal of organic by-products and film densification. Of the tested LA parameters, $225\ \mathrm{mJ/cm^2}$ for both 2-layer and 3-layer samples exhibited the best of these, thus was isolated for further investigations into the thin film at both thicknesses.

Before integration into TFTs, the topography of the $\mathrm{ZrO_x}$ processed with $225\ \mathrm{mJ/cm^2}$ was determined via AFM. In a BGTC TFT such as those featured later in this chapter, the channel is established at the dielectric-semiconductor interface with the semiconductor on top. Aside from the dielectric's performance, a low surface roughness and uniform topography are desired. High surface roughness results in electrostatic boundaries that impedes charge carrier mobility [119] while surface non-uniformities can alter charge carrier paths through the channel by acting as charge traps.

Figure 5.8 shows $2 \times 2\ \mu\mathrm{m}$ AFM images of the $\mathrm{ZrO_x}$ thin films processed with LA at $225\ \mathrm{mJ/cm^2}$ for $1, 2$ and 3 pulses for 2-layer (Figure 5.8 a-d) and 3-layer samples (Figure 5.8 e-h). Table 5.1 gives the statistics of each AFM image to show $\mathrm{R_q}$, $\mathrm{R_a}$ and $\mathrm{Z_{range}}$. AFM roughness statistics were extracted before stretching the colour range of the images in the AFM software Gwyddion to elucidate the topography of the samples. For the 2-layer samples, $\mathrm{R_q}$ and $\mathrm{R_a}$ remain below $1\ \mathrm{nm}$ while $\mathrm{Z_{range}}$ does not stray above $2.351\ \mathrm{nm}$, showing a low surface roughness regardless of the number of pulses. There is also a visual consistency to the images and continuity within them, with each showing no indication of crystallisation or grains. The TA samples show increased surface roughness compared to the LA samples via a jump in $\mathrm{Z_{range}}$ to $6.018\ \mathrm{nm}$,

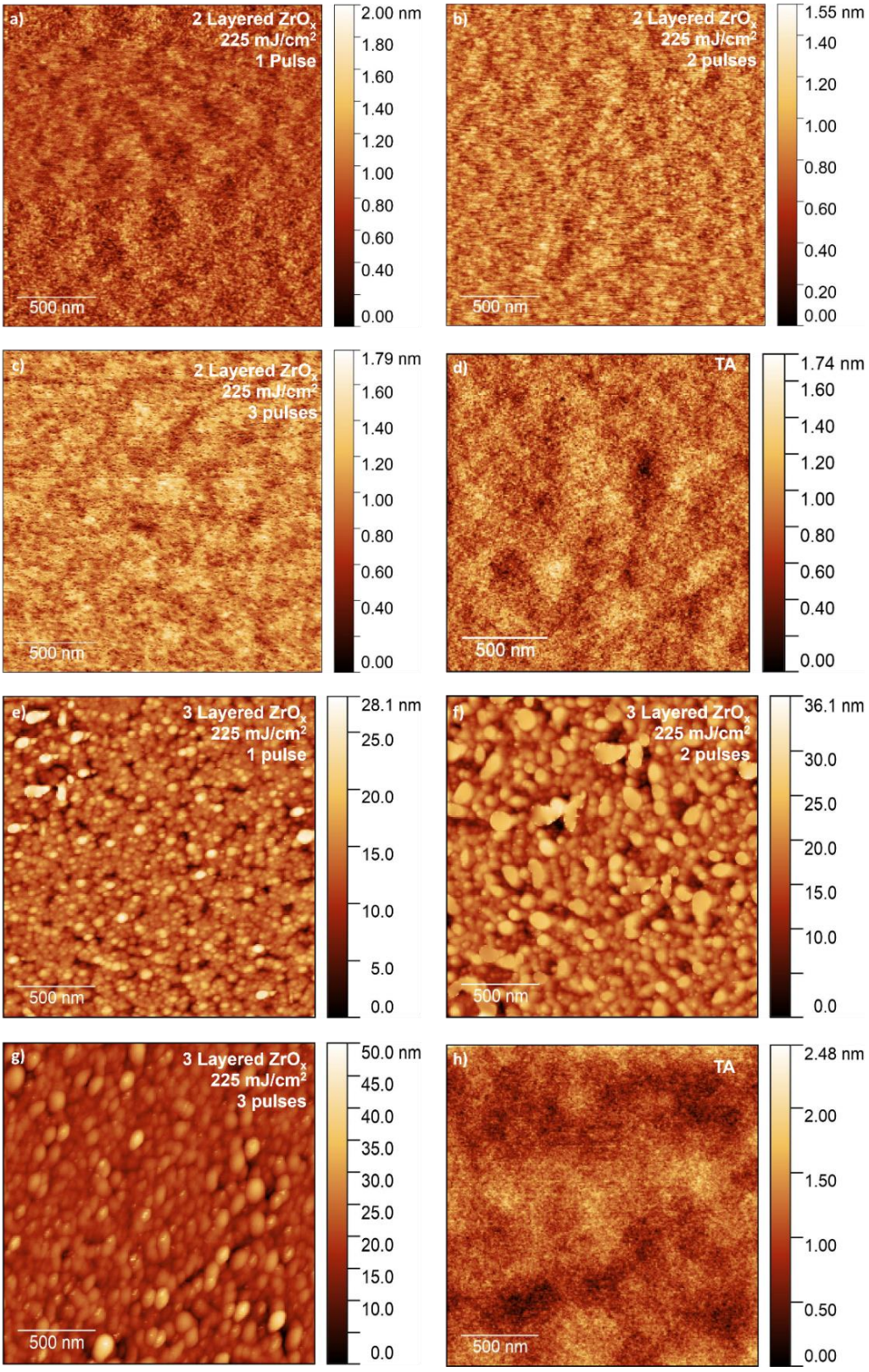

Figure 5.8. $2 \times 2\ \mu m$ AFM images of the ZrO_x thin films processed with LA at $225\ mJ/cm^2$, with TA samples also presented for reference. 2-layer samples at 0.15M concentration are presented in a)-d) as follows: a) $225\ mJ/cm^2$, 1 pulse; b) $225\ mJ/cm^2$, 2 pulses; c) $225\ mJ/cm^2$, 3 pulses; d) 2-layer TA. 3-layer samples are presented in e)-h) as: e) $225\ mJ/cm^2$, 1 pulse; f) $225\ mJ/cm^2$, 2 pulses; g) $225\ mJ/cm^2$, 3 pulses; h) 3-layer TA.

though R_q and R_a increases are minor. 3-layer samples show drastic differences in behaviour compared to the 2-layer samples. Even after a single pulse, R_q increases to $3.783\ \mathrm{nm}$ and Z_{range} to $50.74\ \mathrm{nm}$ with spherulite-shaped and ellipsoidal crystals. Additional pulses lead to the increase of size (width) of the crystals, and the density of the crystals increases. The sudden increase in Z_{range} to $112.3\ \mathrm{nm}$ for 2 pulses of $225\ \mathrm{mJ/cm^2}$ (Figure 5.8f) is attributed to one particular feature of the film in the bottom left of the AFM image, but is demonstration that such features can appear with the 3-layer samples. From 2 pulses to 3 pulses (Figure 5.8g), nanocrystals seemingly merge. The TA sample remains at low surface roughness without significant topographical structures.

Table 5.1. Statistics for roughness (R_q, R_a, Z_{range}) of the AFM images of Figure 5.8.

Number of Layers	Fluence ($\mathrm{mJ/cm^2}$)	Number of Pulses	R_q (nm)	R_a (nm)	Z_{range} (nm)
2	225	1	0.2080	0.1646	2.351
2	225	2	0.1941	0.1535	1.759
2	225	3	0.2244	0.1789	1.974
2	TA	N/A	0.3688	0.2444	6.018
3	225	1	3.783	2.531	50.74
3	225	2	8.901	5.735	112.3
3	225	3	4.773	3.498	48.98
3	TA	N/A	0.2732	0.2186	2.481

While there are drastic differences, they are not unexpected. Previous work has been done linking changes in ZrO_x film thickness to crystallisation and the nucleation barrier that must be surpassed to induce phase changes [369]. The increase or decrease of the nucleation barrier with ZrO_x thin films turning from amorphous to having crystallinity is defined by processes sensitive to thin film thickness. The nucleation barrier can only be exceeded above a certain temperature and critical thickness, after which the formation of nuclei and crystal growth can occur. [370] Formation of crystalline nuclei of a minimum size must occur, so they do not increase surface area and become unstable. After this, crystal growth occurs via mediation of atom diffusion to the crystal nuclei. The crystallisation temperature occurs when the both the energy required to overcome the nucleation barrier and the activation energy of the atom diffusion process are reached, allowing both steps to occur and overcome the energy barrier from an amorphous to crystalline state. For thin films of the nm scale, nuclei become constrained to 2D and the energy barrier for crystallisation is further reduced. This restriction that prevents the minimum nuclei size to be reached increases crystallisation temperature. Thus, an increase in thickness from 2-layer ZrO_x to 3-layer ZrO_x leads to a lower barrier for crystallisation and leads to the AFM images of Figure 5.8. Though not a sol-gel sample, this has also been seen in a study on vacuum-deposited molybdenum oxide [371] in which different

thicknesses were thermally annealed for a short time and assessed for growth of crystalline phases. Thinner films required longer annealing times to initiate the crystalline phase, which our observations corroborate with.

5.2 Fully sol-gel, LA TFTs

A key milestone of this project was the demonstration of TFT devices entirely based on sol-gel, LA MOs, as this has not been reported in the literature. This type of device also evidences the development of TFT devices using both the sol-gel dielectric and semiconductor layer fabricated at NTU. The constituent components of sol-gel dielectric and semiconductor have been partially have been laid out in previous NTU studies, as well as the work in this chapter for ZrO_x . Dellis *et al* [63] and Koutsiaki *et al* [64] have reported high performance InO_x semiconductor on conventional SiO_2 dielectric fabricated via thermal oxidation, while E. Carlos *et al* [62] fabricated sol-gel, LA AlO_x dielectric on Si via UV assisted solution combustion synthesis. It should be noted that Koutsiaki and Carlos used the same research facilities and equipment as this thesis. However, the work of Carlos used sputtered $IGZO$ films on sol-gel LA AlO_x films as a quick pathway to show efficacy of the AlO_x dielectric. This section of the thesis reports combining the previous and current sol-gel dielectrics and semiconductor research to reach the key milestone of a fully sol-gel, LA TFT. AlO_x dielectric was deployed as an additional dielectric for sol-gel, LA TFTs for its own merits, the previous cultivated knowledge and for comparison to ZrO_x since their dielectric properties are notably different from each other. Furthermore, a vacuum deposited (atomic layer deposition, ALD) Al_2O_3 can be fabricated as an additional reference of a high performance, smooth dielectric that removes the uncertainty of matching multiple sol-gel thin films.

Beforehand, some of the VIS-UV SE data for determining thickness was reevaluated to determine the material's bandgap, E_g. Photonic processing of the semiconductor on top of the dielectric to form the TFT ideally uses a material with E_g greater than the processing wavelength, reducing the impact of LA onto the dielectric to retain its previously measured properties and rendering it an optical spacer, whose thickness becomes an additional parameter to optimise absorption into the semiconductor (see chapter 4 for an example involving SiO_2 and InO_x). With

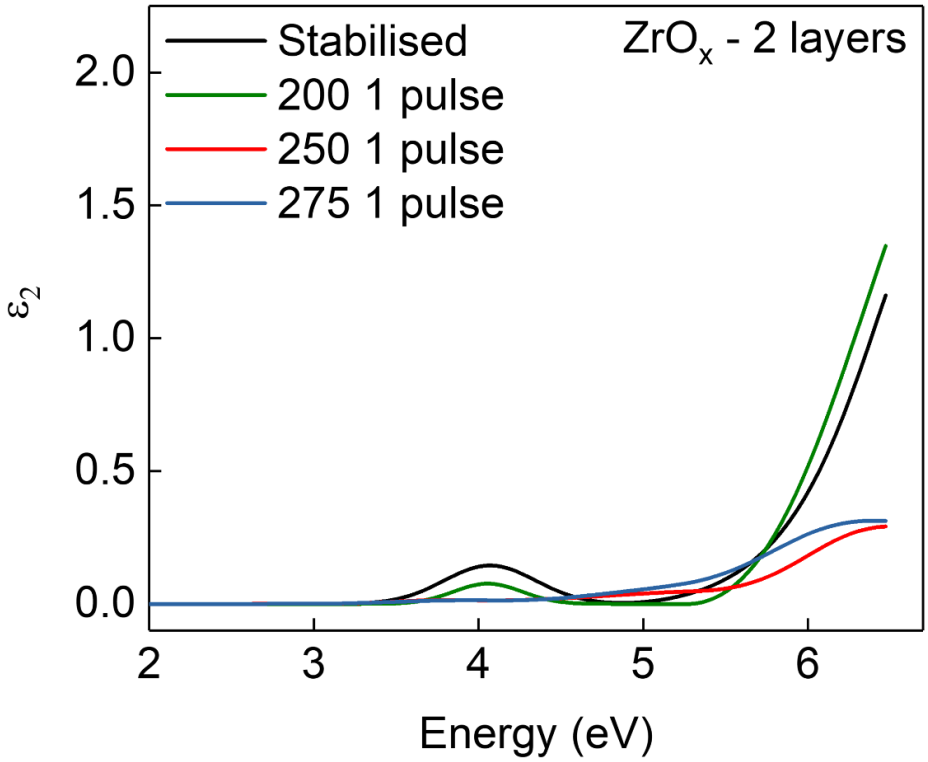

Figure 5.9. Absorption (ε_2) of the spin-coated 2-layer ZrO_x thin film at 0.1 M concentration in the NIR-VIS-UV wavelengths. Sufficiently processed LA films show absorption below 5 eV.

the E_g bulk value of 5.4 eV for ZrO_2 being in close proximity to the excimer laser wavelength, it is entirely possible the amorphous thin film falls under this value and will absorb radiation from the semiconductor processing. Figure 5.9 shows the absorption of the thin films via ε_2 of the 2-layer 0.1 M films. For the stabilised and low fluence conditions where the precursor has not been fully converted, absorption is demonstrated from $3.4 - 4.7$ eV so is only semi-transparent in nature. This confirmation affirms why the lower fluence window used may be appropriate for this material, since the precursor will absorb more than other MO dielectrics such as AlO_x or SiO_2. Further strong absorptions for these conditions occur above 5 eV, which LA at 248 nm does not affect. Higher fluences (thus lower thicknesses) where conversion is far more likely sees the removal of this absorption window from $3.4 - 4.7$ eV, but a more broadband absorption is seen via a continual increase in ε_2 at 4.26 eV onwards. The severity of this increase is fluence-dependent, with higher fluences causing higher absorptions.

Initially, the preference for LA condition for the dielectric needed to be decided. Multiple dielectric conditions combined with LA conditions for the semiconductor leads to a barely surmountable devices to be characterised, thus LA conditions for each material needed to be limited for pragmatic purposes. Aside from the electrical characteristics, surface roughness is also of importance.

For the ZrO_x, $225\ mJ/cm^2$ with 1 pulse was chosen due to its balance of dielectric constant, breakdown field, low dispersion across a wide frequency range and low surface roughness, using 2-layers for all reasons explained earlier in this chapter. Other conditions, while boasting a higher dielectric constant, could not be endorsed due to their lack of electrical stability. For the AlO_x, $175\ mJ/cm^2$ with 1 pulse was chosen. NTU's previous study using AlO_x and IGZO used $175\ mJ/cm^2$ with 2 pulses, producing good quality TFTs. While sol-gel AlO_x has a bandgap above $5\ eV$ so will not directly absorb the laser radiation, reflection from other layers and the Si substrate will cause further processing of the AlO_x layer that could push the layer past the desired level of processing. Aiming for slightly under the desired level in anticipation of this should match the different thin film LA processing conditions to each other. All fabrication, methodological details and characterisation for TFTs are featured in chapter 3. The TFTs were this time fabricated on heavily doped $(0.1 - 1.0\ \Omega/cm)$ n-type Si wafers. For both AlO_x and ZrO_x, a standard TA reference dielectric was fabricated, using hot plate annealing at $300℃$ for $1\ hr$ on both the dielectric and semiconductor in sequential steps. Further to these samples, a one-step process was also trialled. In this, the dielectric is first spin-coated and stabilised on the hot-plate as usual, but not further processed. Instead, the InO_x semiconductor is spin-coated on top of the stabilised dielectric and the entire bilayer processed via LA. All samples were electrically characterised via output and transfer curves, gate leakage measurements and $C-V$ measurements. Table 5.2 gives a summary of all the TFTs fabricated.

Table 5.2. Summary of all TFT samples fabricated using various combination of the sol-gel, LA ZrO_x (from this work), AlO_x from Carlos *et al* and ALD Al_2O_3.

Sample No.	Dielectric	Semiconductor
1	$AlO_x - 175\ mJ/cm^2$, 1 pulse	$InO_x - 150 - 250\ mJ/cm^2, 1 - 3$ pulses
2	$AlO_x - 300℃, 60\ min$	$InO_x - 300℃, 60\ min$
3	ALD $Al_2O_3 - 20\ nm$	$InO_x - 150 - 250\ mJ/cm^2, 1 - 3$ pulses
4	$ZrO_x - 225\ mJ/cm^2$, 1 pulse	$InO_x - 150 - 250\ mJ/cm^2, 1 - 3$ pulses
5	$AlO_x - 300℃, 60\ min$	$InO_x - 300℃, 60\ min$
6	One-step AlO_x/InO_x bilayer - $150 - 250\ mJ/cm^2, 1 - 3$ pulses	
7	One-step ZrO_x/ InO_x bilayer – $150 - 250\ mJ/cm^2$, $1 - 3$ pulses	

5.2.1 AlO_x-based TFTs

Figure 5.10 shows the $I-V$ characteristics of the LA (Figures 5.10a and 5.10 c) and TA (Figures 5.10b and 5.10d) AlO_x -based TFTs (Sample No. 1 and 2 in this work). Figure 5.10a shows the output of a InO_x TFT processed with one pulse of $150\ mJ/cm^2$. The TFT demonstrates no saturation regime with a continual linear increase in I_{DS} with V_{DS}, inferring the semiconductor

is more conductive than desired for a TFT. I_{DS} values due to this conductivity are high, being around the order of 10^{-4} A. There is a lack of hysteresis that combined with the other observations of this output suggest overprocessing of the semiconductor precursor. There is also an abnormal behaviour at $V_{DS} \leq 0$ V, where I_{DS} inflects upwards instead of saturating or remaining linear. The significance of this is discussed later.

The transfer curve for the LA device (Figure 5.10c) shows a small amount of switching behaviour since there is an increase in I_{DS} from 0 V to 2 V, with I_{DS} being around the order of 5×10^{-5} A. This increase becomes more apparent with higher V_{DS}. The values of V_{DS} swept are very low, as testing above this on similar devices caused dielectric breakdown, compromising the device. The TFT show similar I_{DS} values in on and off states that is possibly linked to the conductivity shown in the output curves, hence $I_{On/Off}$ is very poor when any accurately extracted V_{on} is taken. Above 2.5 V, I_{DS} starts to decrease again. Comparing the output and transfer curves to the

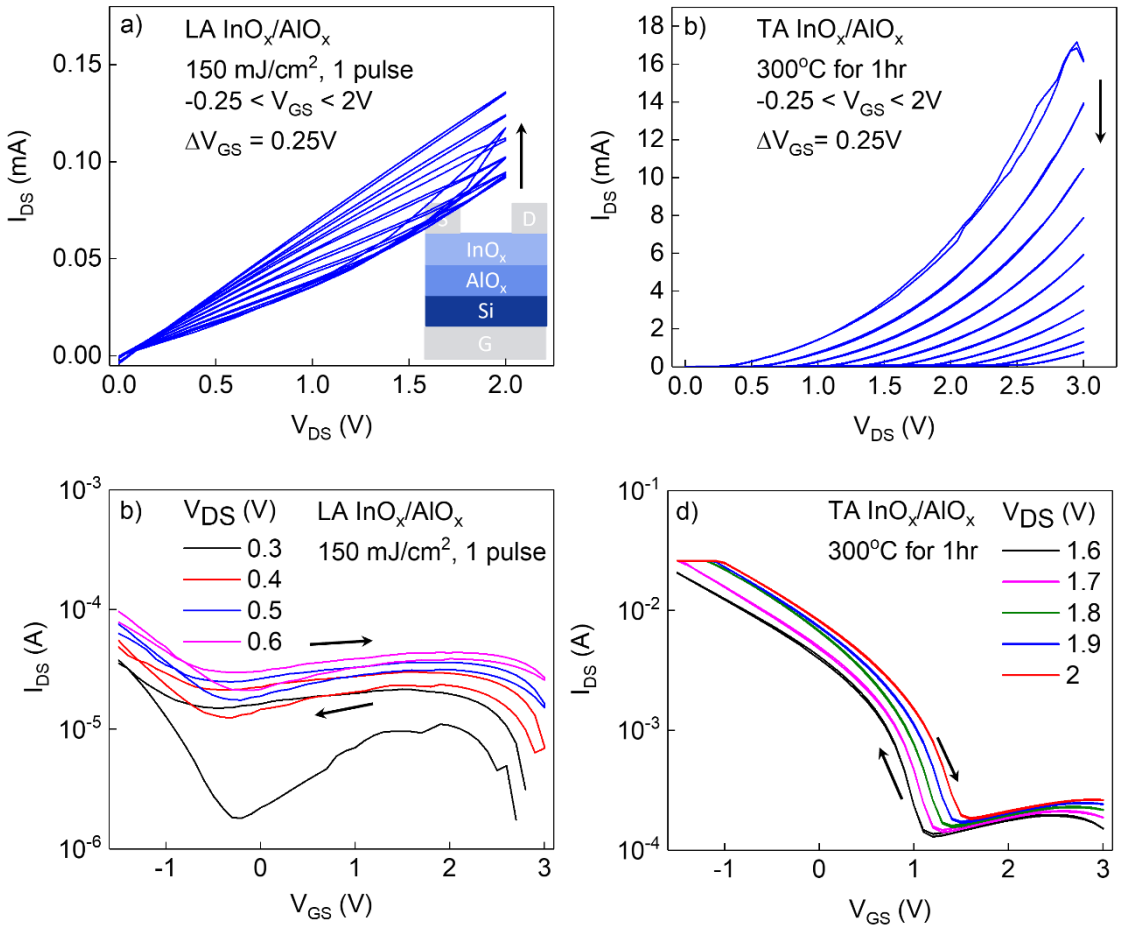

Figure 5.10. Electrical characteristics for sol-gel, LA TFTs using AlO_x and InO_x. The schematic for the measured device is inset. a) An example of an output for a sol-gel, LA TFT with the AlO_x processed with one pulse of 175 mJ/cm^2 and the InO_x processed with one pulse of 150 mJ/cm^2. b) Output curve for a typical TA device, where both layers are treated with 300°C for 1 hr. The output behaviour is extremely atypical. c) The transfer curve for the LA device. A small switching behaviour is visible. d) Typical transfer curve for the TA device. There is no switching behaviour observed, supported by the lack of saturation in the output curves.

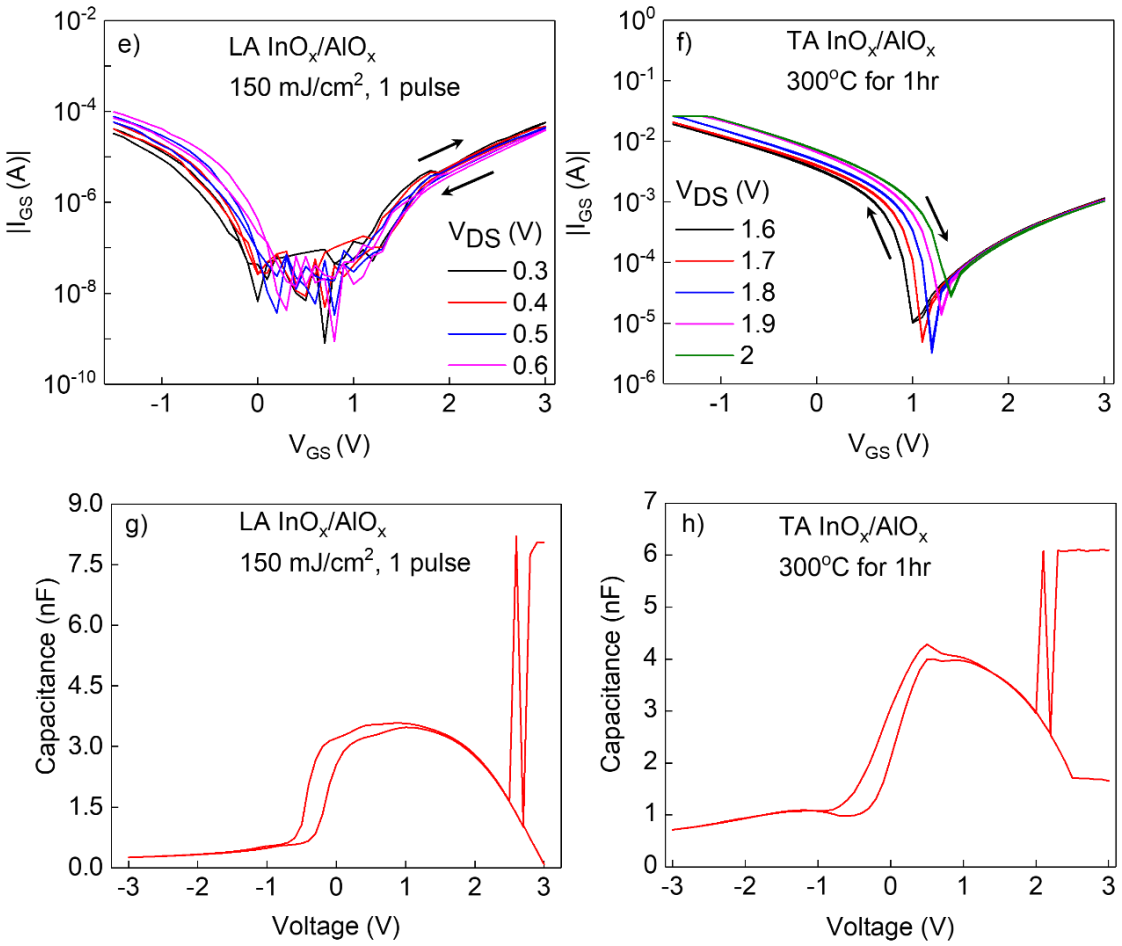

Figure 5.10 continued. e) Leakage currents for the LA device. There are increases when any bias is applied. f) Leakage currents for the TA device. The magnitude and shape match closely to the transfer, confirming the dominance of leakage currents. g) $C-V$ curve for the LA device. Decrease in accumulation and carrier overflow confirming operation during breakdown. h) $C-V$ curve for the TA device. Similar to the LA device, decrease during accumulation and carrier overflow occur.

leakage currents and C-V curves for the LA device in Figure 5.10e and Figure 5.10g reveals the origin of the many faults in this device. The magnitude of I_{GS} in the off-state below $0\ V$ reaches $10^{-4}\ A$, roughly the value of the abnormal inflected curves in the output curves and the off-state of the transfer curve. The instability between $0\ V$ and $1\ V$ suggests electrical instability. The C-V curve in Figure 5.10g shows decrease in capacitance after $1\ V$ (during accumulation) and carrier overflow at $2.5\ V$ during the forward and reverse sweep, both behaviours that occur during the progression to dielectric breakdown. The carrier overflow is linked to the decrease in I_{DS} that can be seen in the previously discussed transfer curve in Figure 5.10c. This dielectric breakdown is likely the onset of the other faults of the device. Cracks and large defects in the device occur due to breakdown, allowing current injection through the gate electrode via travelling through this crack (as well as gate carrier tunnelling). This charge is then collected at the drain electrode. The formation of a semiconductor channel in spite of this dielectric breakdown is contradictory, but could be linked to a continual degradation of the dielectric in

further measurements due to the dielectric sensitivity to high voltages. This cause of this sensitivity is contradictory to the literature and reproduced AlO_x, since both cases produced highly stable AlO_x with high breakdown fields.

The TA output in Figure 5.10b shows erroneous behaviour where the family of curves increase exponentially, with increasing V_{GS} decreasing I_{DS}. I_{DS} values reach $10^{-2} - 10^{-3}$ A, which are extremely high. No hysteresis is observed. The behaviour suggests no channel is formed for carrier transport, or that leakage currents dominate to the extent that their magnitude dwarfs I_{DS} through the channel. Either situation resolves the TFT as failing to perform. The transfer curve in Figure 5.10d shows large leakage currents of over 10^{-2} A in negative voltages are present and are two orders of magnitude larger than when the device is on. As per the output, no hysteresis is observed. Comparing to the leakage currents in Figure 5.10f reveals the origin of all behaviour is from the leakage currents, with increasing V_{DS} or V_{GS} reducing Ids (similar to the output) and the leakage currents replicating the transfer curve from -3 V to 1 V. The C-V curve further elucidates the origin of the poor performance of this TFT. There is a decrease in capacitance after 1 V (during accumulation) and carrier overflow at 2 V during the forward and reverse sweep, thus the device operates under breakdown and permits the same accumulation of current at the gat electrode as in the LA TFTs, only to a greater extent. One additional possibility applying to both LA and TA TFTs discussed so far is the very thin AlO_x (≈ 10 nm) may allow gate tunnelling current, thus a possible route to improving the device is to re-evaluate the thickness and architecture of the thin film stack. The depletion region width could also be as wide as the dielectric since the semiconductor and dielectric are similar thicknesses (semiconductor thicker than dielectric in some cases). Furthermore, hysteresis from $C - V$ curves indicate large numbers of defects within the dielectric layer; thus, a large hysteresis should be present in many of these curves.

As the potential of dielectric failure for the sol-gel AlO_x samples was high, the ALD Al_2O_3 became of increased importance to determine if the sol-gel transformation to a thin film was problematic or the interface with the InO_x was compromised. The proven robustness of a vacuum-deposited sample removes many of these variables. Figure 5.11 shows the electrical characteristics of the TFTs fabricated with 20 nm ALD Al_2O_3 and spin-coated InO_x processed (Sample 3 in Table 5.2) with either a single pulse of 150mJ.cm2 (Figure 5.11 a, c, e, g) or TA for 1 hr at 300℃ (Figure 5.11 b, d, f, h). 20 nm dielectric thickness was chosen to emulate the low thicknesses expected from the spin-coating recipe. The spin-coating conditions of InO_x were retained for these samples.

The LA TFT output (Figure 5.11a) shows a device with a highly conductive layer, with no saturation or pinch-off reached. There is no dependence of I_{DS} on V_{GS}, which is linked to this conductivity. The LA TFT transfer (Figure 5.11c) shows the device remains in the on-state due to the highly conductive InO_x thin film, with I_{DS} values in the low 10^{-4}. The lack of switching means $I_{on/off}$ value is poor. There is also substantial noise in both the forward and reverse sweep (with noise in the output curves also), possibly indicating instability when forming the channel. The leakage current (Figure 5.11e) increases to a minimum of 10^{-5} in both biases, meaning the devices are inefficient in any state. The $C-V$ curve (Figure 5.11g) shows clear depletion and accumulation regimes with a small amount of hysteresis, which may be linked to the noise observed in the transfer characteristics. The TA TFT output (Figure 5.11b) also resembles that of an overly conductive InO_x thin film due to lack of switching, saturation (and pinch-off) not being reached and the high I_{DS} values of 10^{-4}.

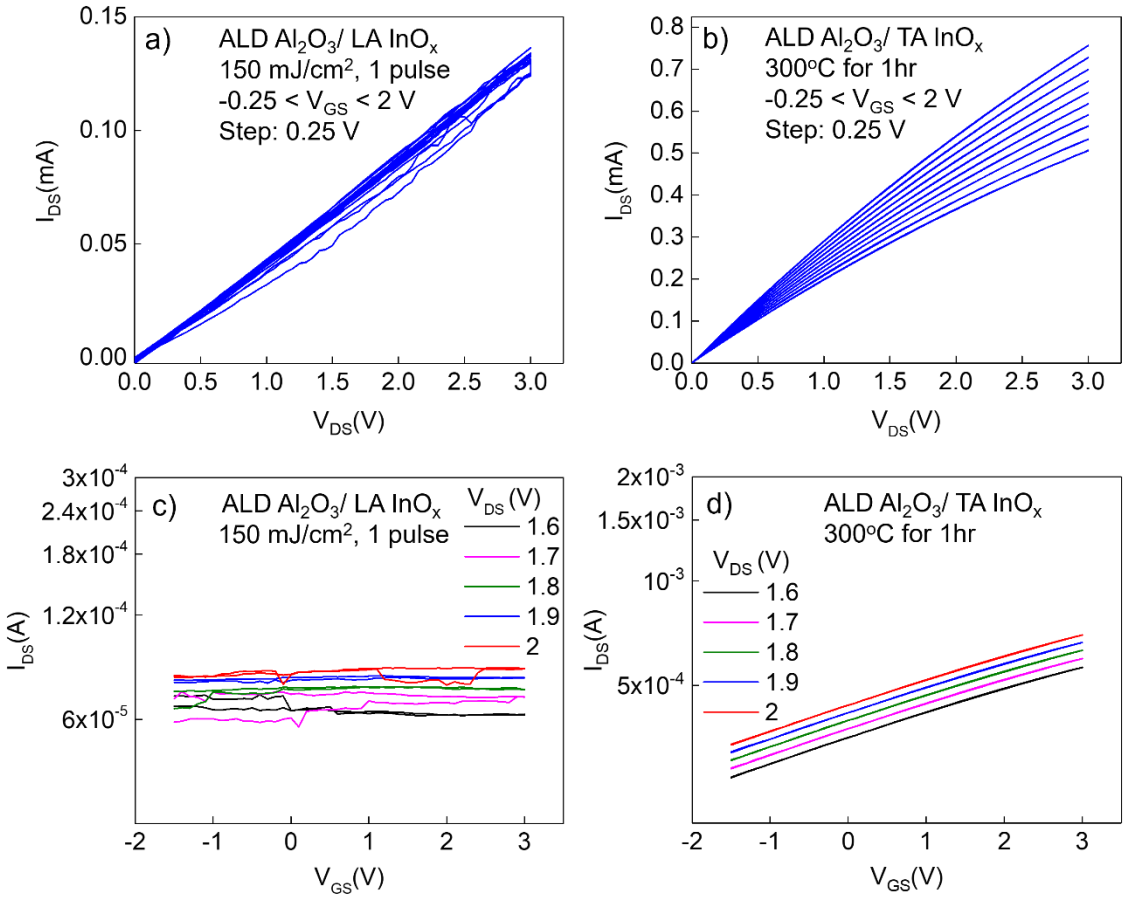

Figure 5.11. Electrical characteristics for sol-gel LA TFTs using $20\ nm$ ALD Al_2O_3 and sol-gel spin-coated InO_x. a) An example of an output for the Al_2O_3/InO_xTFT with the InO_x LA with one pulse of $150\ mJ/cm^2$. b) Output curve for a typical TA device, where the InO_x is treated with $300°C$ for $1\ hr$. c) The transfer curve for the LA device. d) Typical transfer curve for the TA device.

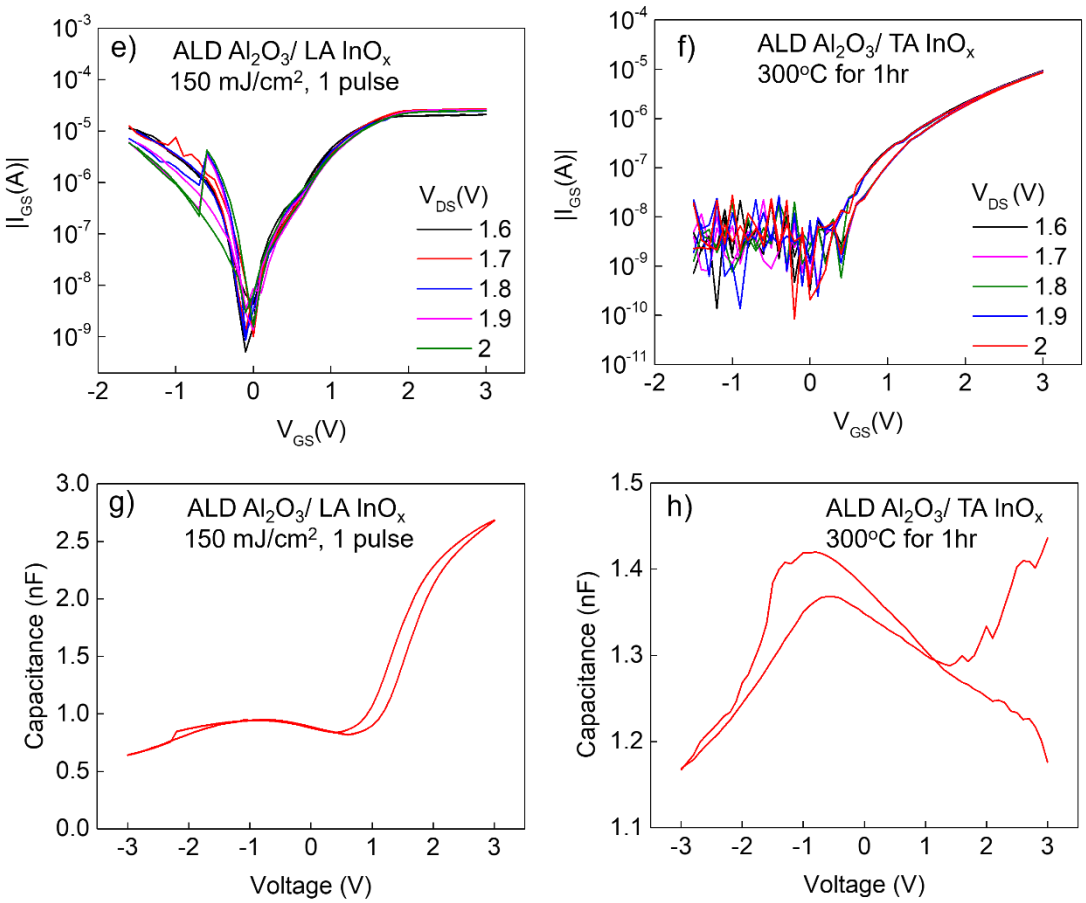

Figure 5.11 continued. e) Leakage currents for the LA device. f) Leakage currents for the TA device. g) $C-V$ curve for the LA device. h) $C-V$ curve for the TA device.

There is only a small dependence of I_{DS} on V_{GS}.There is also no hysteresis in the output and transfer (Figure 5.11d), opposite to the other thin films in this work. The I_{DS} values and lack of switching in the transfer are in accordance with the output, which means $I_{on/off}$ remains very low. However, there is far reduced noise compared to the LA sample, which combined with the hysteresis links to a lack of charge traps in the interface where the channel is. It is expected that the Al_2O_3 thin film has a very low surface roughness, contributing to these high I_{DS} values. Leakage currents (Figure 5.11f) are notably reasonably low, remaining below 10^{-8} before increasing to 10^{-5} under positive bias. These characteristics are overall superior to that of the LA device, since the device is both more stable and efficient. The $C-V$ curve (Figure 5.11h) shows a rapid increase in capacitance below 0 V before decreasing again where there should be an accumulation region, which may be linked to the conductivity of the InO_x preventing the anticipated storage of charge (as the $C-V$ curve will measure the capacitance of the entire structure).

5.2.2 ZrO_x-based TFTs

Figure 5.12 shows the $I-V$ characteristics of the LA (Figures 5.12a, c, e, g) and TA (Figures 5.12 b, d, f, h) of ZrO_x-based TFTs, which is Sample 4 and 5 in Table 5.2. Figure 5.12a

for the LA device shows an indicative output with relatively low I_{DS} of 10^{-6} and large hysteresis during the reverse section of the dual sweep. This can be attributed to carrier traps in the channel (dielectric-semiconductor interface), which has been seen in the literature for these materials. AFM shows ZrO_x does not present significant roughness after LA, so this can be excluded as a possible explanation. Values of $V_{GS} > 1\ V$ show no saturation. Lower values of V_{GS} produce irregular behaviour where inflection of the curve is mirrored to be opposite of typical output curves when V_{DS} reaches values typical for saturation. The effect of charge traps can be seen in the transfer also (Figure 5.12c), where reverse sweeps experience a large hysteresis. In the transfer around $0\ V$ (when devices are in the off-state), the curves have sawtooth waveform shape showing their instability. Due to low I_{DS} and these charge traps, μ_{FE} is calculated to be a very low $0.2\ cm^2/V^1s^1$ and $I_{On/Off} \approx 10^2$. Nevertheless, the results demonstrate proof-of-concept of sol-gel, LA TFTs. The source of charge traps attributed to many of these observations can originate from the incomplete photochemical conversion in either the

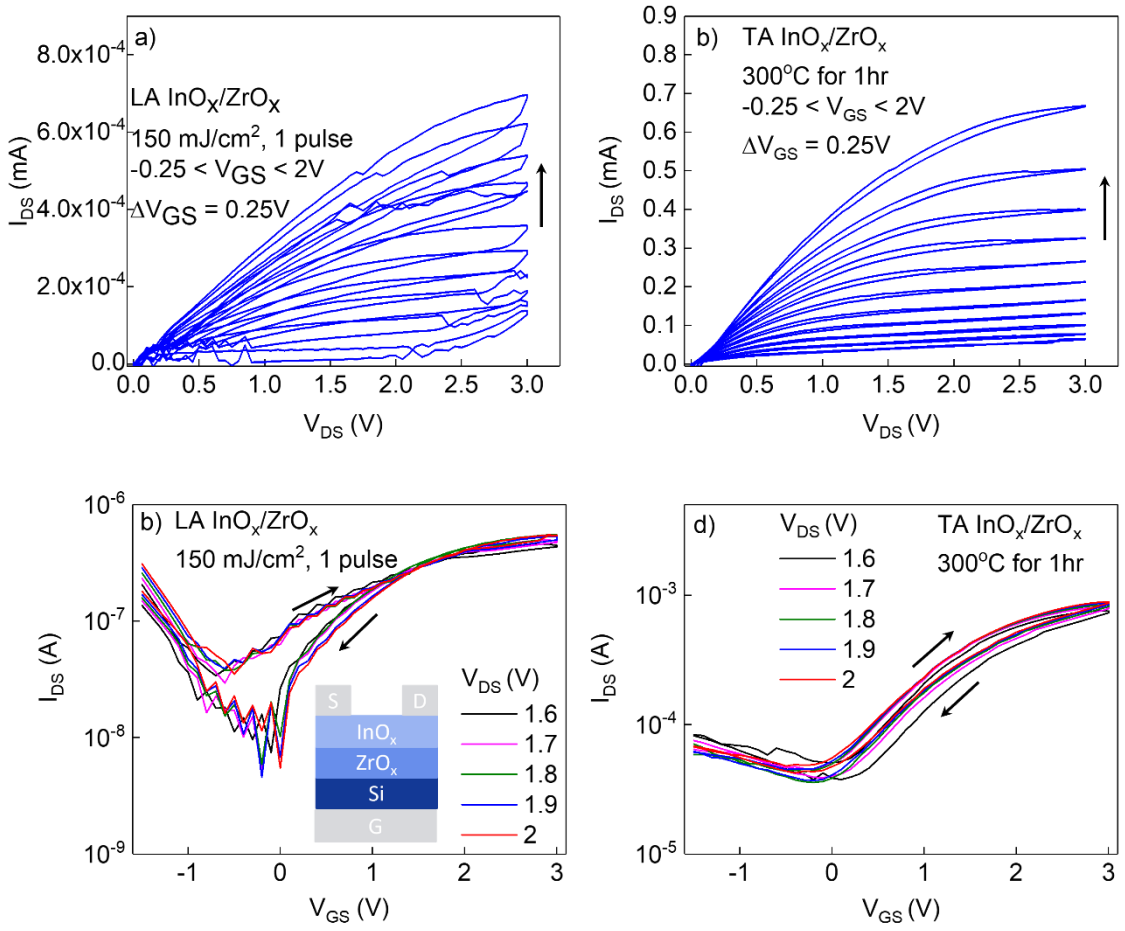

Figure 5.12. Electrical characteristics for sol-gel, LA TFTs using ZrO_x and InO_x. A schematic for the measured device is inset in the figure. a) An example of an output for a sol-gel, LA TFT with the ZrO_x processed with one pulse of $225\ mJ/cm^2$ and the InO_x processed with one pulse of $150\ mJ/cm^2$. b) Output curve for a typical TA device, where both layers are treated with $300°C$ for $1\ hr$. c) The transfer curve for the LA device, showing V_{DS} values during measurement displayed being in the saturation regime. d) Typical transfer curve for the TA device.

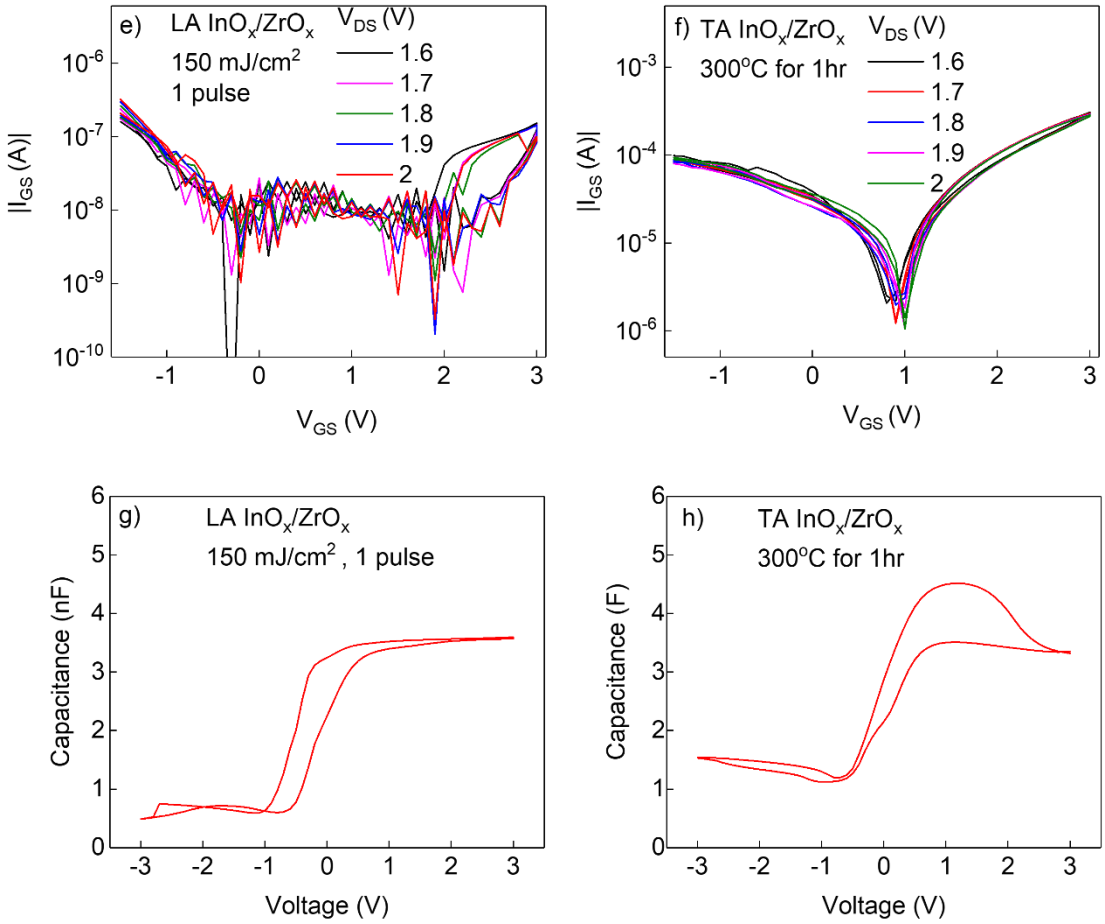

Figure 5.12 continued. e) The leakage current of the LA TFT. The leakage currents increase with V_{GS} in the saturation regime and with negative voltage during depletion, indicating possible increases in leakage currents due to the dielectric. f) The leakage current vs gate voltage curve of the TA TFT. Very high currents and very little hysteresis are demonstrated. g) The $C-V$ curve for the LA TFT. h) The $C-V$ curve for the TA TFT.

$(InNO_3)_3$ or the ZrO_x, with either promoting discontinuities and traps in the dielectric-semiconductor interface due to organic by-products.

Figure 5.12e shows the leakage currents of the LA TFT device. Magnitude of the leakages are approximately 10^{-7} A, which match those of the output and transfer curves. In this LA device, the steep rise to the maximum leakage currents occurs around V_{DS} values 2 V, which is also the V_{DS} value when the strange inflection occurs in the output curve in Figure 5.12a. Thus, the I_{DS} values in the output curve at $V_{GS} \leq 0.25$ V do not operate with I_{DS} greater than the leakage currents and we instead see the leakage currents in that section of the output. The C-V curve in Figure 5.12g shows a hysteresis that was not present in the C-V curves of the MOS capacitor devices, further fuelling the theory of charge traps in the dielectric-semiconductor interface or a lack of conversion in the $(InNO_3)_3$. There is possibly an incomplete semiconductor conversion and (at least more) complete dielectric precursor conversion. Despite this poor

semiconductor quality at the lower end of the LA fluence window tested, channel formation and switching behaviour took place demonstrating proof of concept for a sol-gel, LA TFT.

The TA TFT output in Figure 5.12b demonstrates far lower magnitude clockwise hysteresis and higher I_{DS} of 10^{-3} A than the LA device output, which is also reflected in the TA TFT transfer curve (Figure 5.12d). In the transfer curve, currents in the off-state, when the device is depleted, remain high at 10^{-3} A so $I_{On/Off}$ is negatively impacted. Despite the improvement in I_{DS} over the LA film, the mobility remains low at $0.4\ cm^2/V^1s^1$ while $I_{On/Off}$ remains the same. Leakage currents in Figure 5.12f are of the order of 10^{-4} A, which are high both absolutely and relative to the LA TFT leakages. This magnitude is very similar to the I_{DS} values seen in the transfer curve in Figure 5.12d, a comparison that could also be made to the LA device. Thus, it is also likely here that leakage currents contribute in some way to the transfer characteristics. For the TA sample, the loss of performance may be due to lack of conversion in the ZrO_x, since acetylacetonate precursors typically require > 300°C to achieve full conversion. This is in contrast to $(InNO_3)_3$, where previous work in the literature shows conversion would be achieved with this temperature during TA. Thus, an inverse case arises to the LA sample where high I_{DS} is achieved due to complete semiconductor precursor conversion and incomplete dielectric precursor conversion. The semiconductor precursor conversion is likely responsible for the high I_{DS} values and incomplete dielectric conversion responsible for high leakage currents. Furthermore, remaining $(ZrAcAc)_4$ by-products would result in organic residuals that contribute unwanted additional charges [372].

In both LA and TA samples, the necessity and confirmation of fully converted precursors becomes evident. The effect of both LA and TA on chemical conversion of $(ZrAcAc)_4$ to ZrO_x is fully explored via IRSE in chapter 6 of this thesis.

5.2.3 One-step LA TFTs

Figure 5.13 shows the electrical characteristics of the one-step LA process TFTs, comparing ZrO_x/InO_x TFTs (Figure 5.13a, c, e, g) to AlO_x/InO_x TFTs which are Sample 6 and 7 in Table 5.2. For the ZrO_x output (Figure 5.13a), I_{DS} is independent of V_{GS} and insufficient I_{DS} values of 10^{-9} are reached. Saturation is seemingly reached, though the point of saturation is not related to I_{DS} or V_{GS}. The ZrO_x transfer (Figure 5.13c) agrees with this, since sweeping V_{GS} or increasing V_{DS} does not increase I_{DS}. Furthermore, the leakage currents (Figure 5.13e) replicate most of those features but increases in I_{DS} above V_{GS} values of 2 V. This, along with the $C-V$ curve (Figure 5.13g) that shows clear depletion and accumulation regions, shows a ZrO_x film has been formed to some extent. Overall, the ZrO_x/InO_x with the one-step process failed to make a

functioning TFT with a well-defined channel and sharp interfaces. This is not unexpected; stabilisation for the ZrO_x and InO_x occur at $150℃$, which begins decomposition and removes the $2-ME$ solvent but does not initiate the conversion process. Thus, applying an LA pulse to the precursors with different conversion temperatures produces differing extents of photochemical conversion. Moreover, the sol-gel state of both layers with application of energy to cause a heat gradient could cause a ZrO_x- InO_x intermediate layer or blend that heavily reduces the possibility of a well-defined interface.

The AlO_x/InO_x demonstrate noticeably different behaviour. The output (Figure 5.13b) shows extremely high I_{DS}, with the value decreasing with increasing V_{GS}. This suggests an avalanche effect due to a gate to source junction. The transfer (Figure 5.13d) and leakage currents (Figure 5.13f) are nearly identical, which along with the output characteristics suggests a dielectric that has been damaged in some capacity so stores charge improperly and allows large conduction paths from the metallic electrodes. Finally, the C-V curve (Figure 5.13h) shows large hysteresis and an overflow above $2\,V$, indicating dielectric breakdown has been experienced.

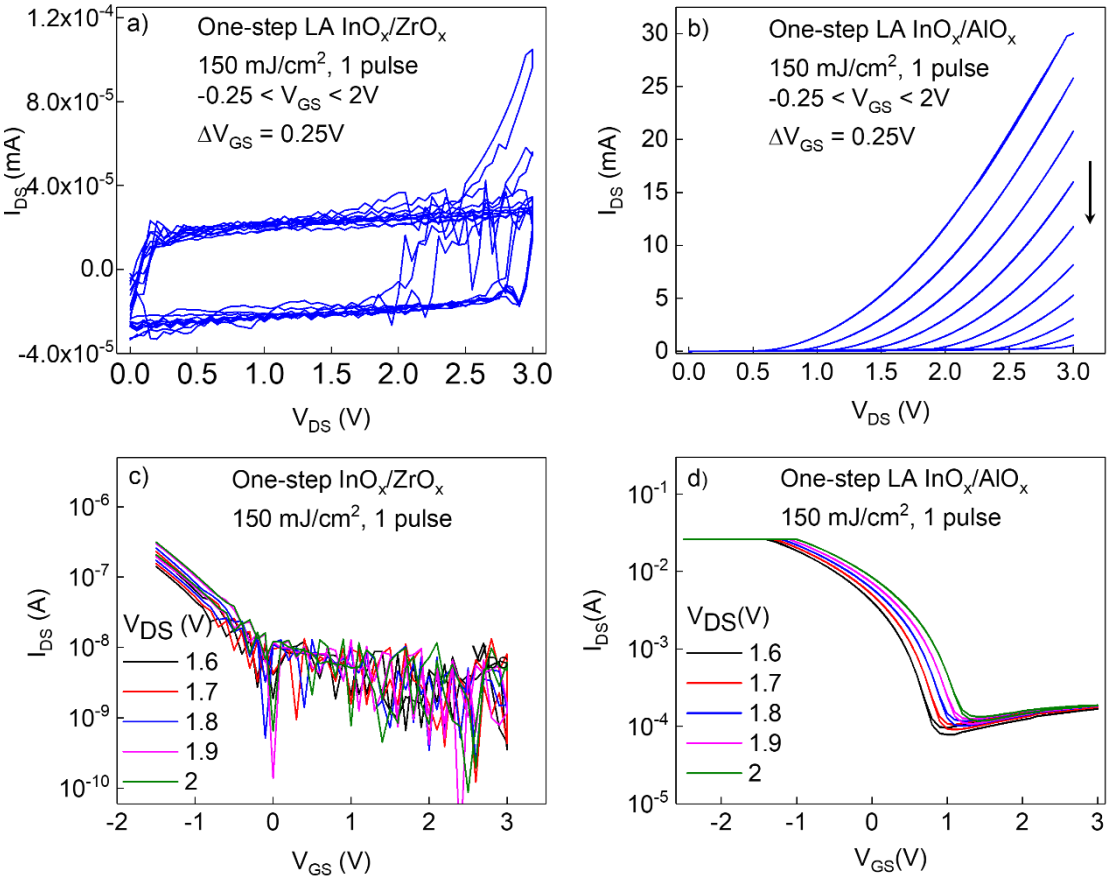

Figure 5.13. Electrical characteristics of the one-step process sol-gel, LA TFT using AlO_x and ZrO_x dielectrics with an InO_x semiconductor. Dielectric precursors were spin-coated and stabilised, immediately followed by InO_x spin-coating and single-pulse LA processing. a) ZrO_x/InO_x output curves. b) AlO_x/InO_x output curves. c) ZrO_x/InO_x transfer curve. d) AlO_x/InO_x output curves.

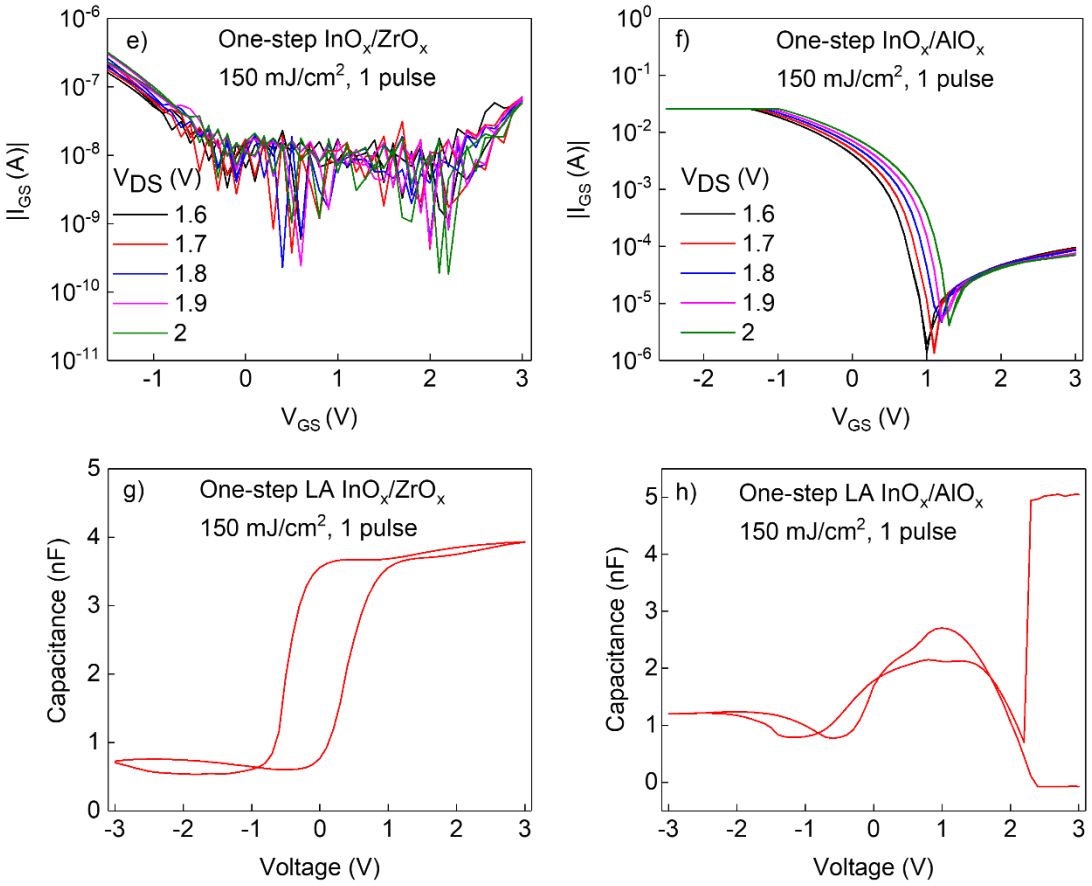

Figure 5.13 continued. e) ZrO_x/InO_x leakage currents. f) AlO_x/InO_x leakage currents. g) ZrO_x/InO_x $C-V$ curve. h) AlO_x/InO_x $C-V$ curve.

With these AlO_x/InO_x one-step devices, it is thus difficult to determine precisely the exact efficacy of the one-step process for AlO_x/InO_x since breakdown can occur in several different ways. It would be expected that, since both layers are nitrates following similar chemical pathways at similar temperatures, that the effect on each layer after LA is similar and the chances of detrimental intermediate layers is reduced.

5.3 Opto-thermal Simulations

Chapter 5.1 and 5.2 were completed without the availability of the opto-thermal simulations to determine the fluence window for the processing of ZrO_x, as well as InO_x, on either of the dielectrics. Testing the LA of structures with AlO_x, ZrO_x and InO_x, with their opto-thermal properties can aid in identifying the fluence window for MOS capacitors and TFTs to improve the devices in chapter 5, sections 5.1 and 5.2.

Figure 5.14a shows the simulated temperature rise for different thicknesses of $(ZrAcAc)_4$ and $(AlNO_3)_3$ precursors on Si with single pulse LA. The red dashed line indicates the expected minimum temperature rise $(300℃)$ of a nitrate precursor for complete

conversion, while the green dashed line specifies the higher temperature required for the conversion of an acetate $(450℃)$. In the case of both materials, the temperature profile is uniform (i.e. the temperature rise seen at the top and bottom of the layer is the same or extremely similar), thus only the top of the films is shown. Additionally, the top of the dielectric is where the carrier channel forms (at the semiconductor-dielectric interface) and is a vital region to control. Neither dielectric reaches its temperature for conversion with the previous LA conditions and fabrication methodologies. $44\ \mathrm{nm}\ (\mathrm{ZrAcAc})_4$, even at the high end of the fluence window at $250\ \mathrm{mJ/cm^2}$, remains around $60\ \mathrm{K}$ below the conversion temperature. At this thickness, destructive interference is prevalent so higher fluences are required for a desired temperature rise. In the context of TFTs such as those in this chapter, the lack of conversion causes charge carrier traps that impede performance. For $10\ \mathrm{nm}\ (\mathrm{AlNO_3})_3$, only fluences of $> 200\ \mathrm{mJ/cm^2}$ are sufficient for conversion (removal of nitrate groups). This means the dielectric used in these TFTs is potentially not converted, adding carrier traps that reduce mobility. This is in addition to the other possible drawbacks of using an ultra-thin dielectric, such as enhanced gate leakages. The thicknesses of these precursors have been confirmed via IRSE, so only minor deviations in thickness may be expected such as film thinning at the edge of the sample. In the case of any minor deviation, it could be argued that $(\mathrm{AlNO_3})_3$ achieves conversion, while $(\mathrm{ZrAcAc})_4$ could move toward this if a lower thickness was accidentally achieved. However, it is unclear if experimental work supports any of these observations and samples did show consistent thickness and behaviour. For example, a converted $(\mathrm{AlNO_3})_3$ ($> 175\ \mathrm{mJ/cm^2}$, 1 pulse) should see little hysteresis in the $\mathrm{C-V}$ curves in Figure 5.10, but does encounter this in many laser processing conditions.

The same methodology was then applied to the TFTs. The optical constants of the processed $\mathrm{AlO_x}$ and $\mathrm{ZrO_x}$ films were implemented with the $(\mathrm{InNO_3})_3$ precursor to investigate the $\mathrm{InO_x}$ conversion for TFT fabrication. Figure 5.14b shows the $10\ \mathrm{nm}\ (\mathrm{InNO_3})_3$ temperature rise with varying fluences on different thicknesses of $\mathrm{AlO_x}$ and $\mathrm{ZrO_x}$ thin films. The fluences shown here reflect previous fluences tested for fabrication of TFTs. The $10\ \mathrm{nm}\ \mathrm{AlO_x}$ and $44\ \mathrm{nm}\ \mathrm{ZrO_x}$ previously used demonstrate several LA conditions utilised for past $\mathrm{InO_x}$ TFTs would result in lack of conversion for the $(\mathrm{InNO_3})_3$, making it difficult to have a defined TFT channel formation. The issues of an only semi-converted semiconductor are compounded further with the non-converted dielectric. This can be linked to the non-satisfactory performance observed in NTU's sol-gel, LA TFTs in earlier in this chapter. However, with the knowledge that the dielectric could also not be converted, it is difficult to specifically attribute the TFT performance to a specific cause. Two things are clear from Figure 5.14: i) that minor deviations in dielectric thickness at certain points cause huge changes in temperature rise in the semiconductor, emphasising the

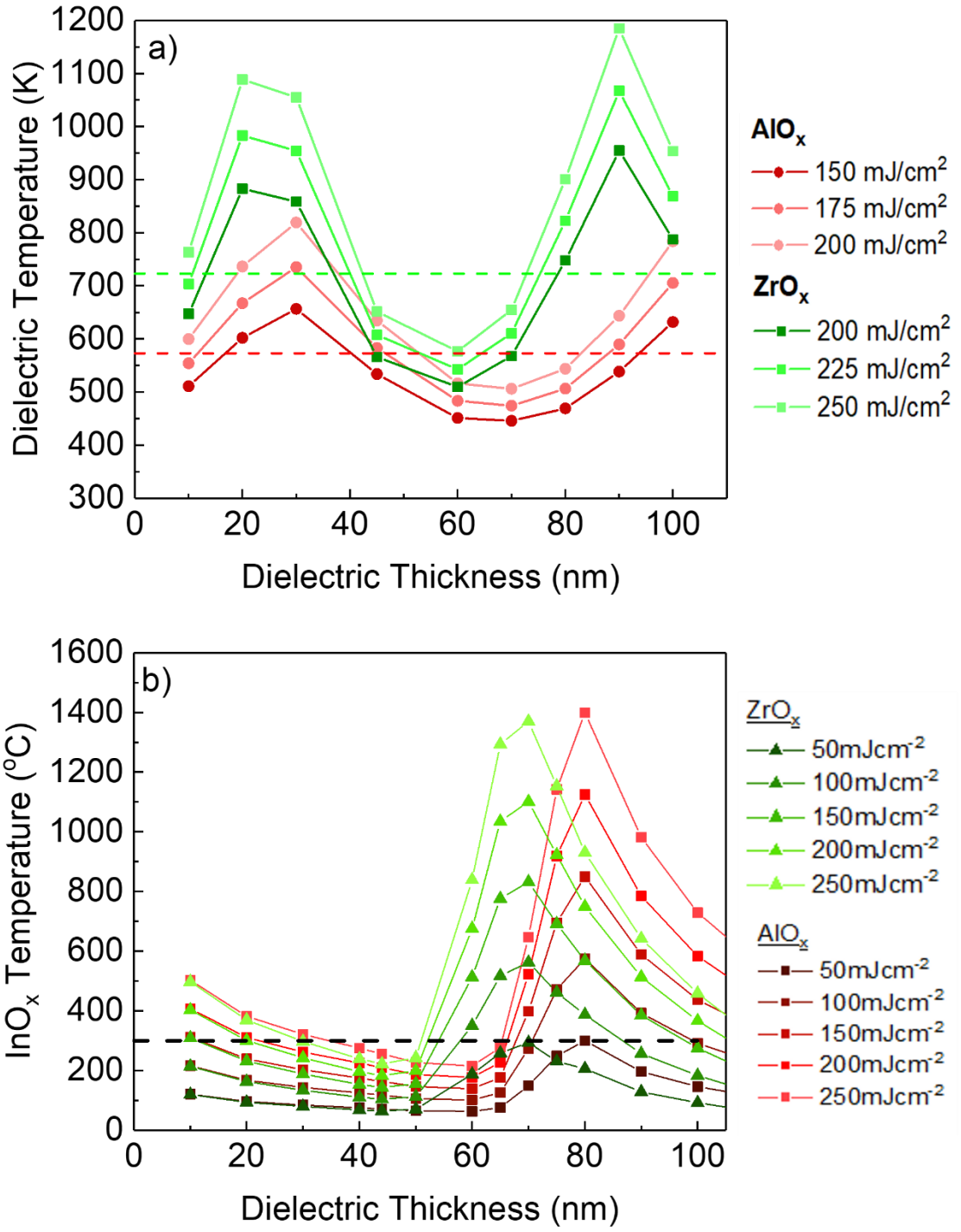

Figure 5.14: a) The opto-thermal simulation of the $AlNO_3$ (red lines with circles) and ZrAcAc (green lines with squares) stabilised precursors on Si. The dashed red line indicates the minimum temperature rise required for the nitrate conversion, while the green dashed line shows the minimum temperature rise required for the acetate to convert. Neither precursor has reached their minimum temperatures at previous thicknesses used in devices, suggesting the precursors might have not fully converted. b) The simulated temperature rise of $InNO_3$ precursor on AlO_x and ZrO_x precursors, with the black dotted line indicating the temperature required to convert $InNO_3$. 10 nm AlO_x permits conversion of the $InNO_3$ at previous fluences, while 44 nm ZrO_x does not allow conversion for $InNO_3$ with previous fluences.

requirement for precise measuring of sol-gel reagents during fabrication; ii) it is possible to target certain thicknesses for fabrication that will maximise the chance for $InNO_3$ conversion while tuning the TFT characteristics. For example, ZrO_x at $60\ nm$ or AlO_x at $25\ nm$ – the recipes for which exist already – can be used to achieve several fluences with multi-pulse opportunities.

Based on the result and conclusions of the experimental and theoretical work of this chapter, it was decided an experimental work package was necessary to corroborate the results of the simulation and precisely determine at what LA conditions the dielectric precursors are converted.

5.4 Concluding Remarks

This chapter investigated the LA parameterisation for sol-gel ZrO_x and its use as a dielectric in TFTs via implementation in MOS capacitor devices and TFTs. The relationship between LA fluence, number of pulses and thin film thickness was first established to target a sufficient thickness to avoid dispersion and tunnelling currents. Thickness was varied by solution concentration and number of spin-coat layers, then measured with ORS and ellipsometry. The different thicknesses were implemented in MOS capacitor devices and $C-V$ and $C-f$ measurements taken. The optimised concentration of $0.15\ M$ was tested rigorously with further optical, electrical and surface topography properties via electric field breakdown and AFM measurements. In all different permutations of ZrO_x films tested, fluence was the dominant parameter that influenced dielectric performance, with number of pulses having an additional smaller effect. In several cases for both dielectrics, LA samples exceeded the performance of the TA sample in one or more aspects, demonstrating high dielectric constant, high breakdown field and low dispersion. The MOS capacitors are the first demonstration of a sol-gel, LA ZrO_x thin film for electronics. An optimised ZrO_x thin film and LA condition of 2 layers of $0.15\ M$ concentration, processed with 1 pulse of $225\ mJ/cm^2$, was determined for further implementation to fully sol-gel, LA TFT devices with InO_x as the semiconductor. AlO_x was also introduced as a comparative dielectric, using a recipe in the literature (that was previously developed at NTU). While working TFTs were fabricated – demonstrating the first fully sol-gel, LA TFTs – several device defects were present that decreased the demonstrated performance including leakage currents dominating the output and transfer curves for the TFTs for both dielectrics and, in the case of AlO_x $C-V$ curves a decrease in capacitance before the full accumulation of electrons was completed. This was shortly followed by a carrier overflow and breakdown of the devices. These negative effects in the TFTs have been attributed to failure of fully controlling the temperature rise of both the dielectric and semiconductor during LA. Opto-thermal simulations of the dielectrics on an Si substrate and InO_x on the two different

dielectrics increases confidence of this hypothesis, demonstrating another effective use of the opto-thermal simulations.

Overall, both the theoretical opto-thermal simulation data and MOS capacitor/TFT experimental data underlines that compositional information and attention to the architecture of the TFT is critical to fully realising the potential of the sol-gel, LA paradigm.

6. Compositional analysis of sol-gel, LA MOs via IRSE

Chapter 5 established the feasibility of the fabrication of sol-gel-derived metal oxide (MO) dielectrics via laser annealing (LA) for capacitors and thin-film transistors (TFTs). It also highlighted several defects and areas for improvement in the electrical characteristics of the resulting devices. Addressing these challenges begins with a thorough understanding of the LA-induced precursor conversion mechanism into functional thin films, thereby enhancing control over the process and optimizing performance. This chapter employs Infra-Red Spectroscopic Ellipsometry (IRSE) to explore the physicochemical phenomena underlying the conversion of precursor materials into thin films of zirconium oxide (ZrO_x) and aluminum oxide (AlO_x). Conductive substrates (in this case Al) are utilized to heighten the sensitivity of IRSE in detecting organic and metal-oxygen peaks in both stabilised and thermally annealed (TA) sol-gel thin films of ZrO_x and AlO_x. Complementary opto-thermal simulations provide insights into temperature dynamics, guiding the experimental parameters for LA processing. Utilising the mid-to-far infrared spectral range and the non-destructive nature of IRSE, this study investigates bond absorptions in stabilized, single-pulse LA, and TA samples of ZrO_x and AlO_x. The aim is to elucidate the effects of LA on precursor conversion, compare it to conventional TA, and identify the fluence threshold where precursor conversion occurs. This research presents a pioneering exploration into the photochemical conversion processes enabled by LA, with a particular focus on the influence of fluence on organometallic precursors through IRSE. By leveraging these techniques, which are well-suited to laser-assisted fabrication, this work contributes critical insights into optimising LA processes for enhanced dielectric film performance in electronic applications.

6.1 Determining experimental parameters

Chapter 5 showed that while sol-gel, LA TFTS fabricated - with AlO_x and ZrO_x as dielectrics and InO_x as a semiconductor - demonstrated switching behaviour, their performance including μ_{FE} and $I_{on/off}$ was not satisfactory. Previous work indicated potential compromises in the dielectric integrity of AlO_x, contributing to dielectric breakdown and subsequent TFT channel formation issues. Additionally, opto-thermal simulations suggested that the previously used LA fluences ($150 - 200\ mJ/cm^2$ for $Al(NO_3)_3$, $200 - 250\ mJ/cm^2$ for $Zr(AcAc)_4$) might not suffice for effective conversion to the desired thin film composition. Therefore, compositional analysis became essential to explore these findings further.

Previous work by Koutsiaki *et al* [66] demonstrated the use of IRSE for compositional analysis on stabilised and TA sol-gel thin films, while presenting advantages over traditional X-

ray Photoelectron Spectroscopy (XPS) or Fourier Transform Infrared Spectroscopy (FTIR). The mid-IR region is particularly crucial due to the absorption wavelengths of organic groups (nitrates, acetates, acetylacetonates), metal-oxygen bonds, and structural water. The use of highly infrared reflective conductive substrates, specifically aluminum (Al) and gold (Au), enhances detection sensitivity and resolves challenges associated with ultra-thin films commonly used in modern electronics. Thus, highly IR reflective conductive substrates (Al, Au) are employed based on the findings of Koutsiaki *et al* [66] and Tompkins *et al* [76] to increase the sensitivity and detect these groups. An additional benefit is presented using Al, since its high carrier concentration makes it of common use in flexible electronics as the gate material (instead of the non-conductive/low carrier concentration substrate). Additionally, for any work where acetate or acetylacetonate precursors are used, Au becomes obsolete since its lower heat capacity allows its melting point to be reached extremely quickly during LA and melt, changing the properties of the metallic thin film considerably. Thus, Al was used exclusively as the conductive substrate for this IRSE work.

While the investigation of composition for stabilised and TA samples has been demonstrated, LA samples have not been investigated yet. The use of LA adds complexity, as the use of Al compared to Si (on which all samples so far have been based) heavily alters the optical and thermal properties of the system, hence the temperature rise of the sol-gel stabilised films is altered. Establishing a methodology for aligning experimental parameters between Si and Al-based systems is crucial to ensure consistent temperature behaviours and effective translation to large-scale device fabrication. Opto-thermal simulations have been instrumental in previous chapters, linking well-defined thin-film properties to empirical results. These simulations facilitate approximating new fluences on Al compared to Si by evaluating temperature elevations at various fluences, thereby negating the need for extensive preliminary experiments across a wide fluence range. In this case, Si (or any typical substrate in LAE) and have well known opto-thermal properties, minimising errors to the input material parameters of the dielectric thin film or precursor. Consequently, the most uncertainty arises from any differences between the literature thermal properties and those of our film.

For $\mathrm{AlO_x}$, further considerations of sample preparation were made in retrospect of the results of chapter 5, whose key relation to this chapter were previously explained. While the photochemical conversion of the aluminum nitrate precursor is a critical factor, the previously employed $10\ \mathrm{nm}$ thickness was inadequate to curb gate leakage currents via tunnelling, adversely affecting MOS capacitor and TFT yield. Thus, this chapter capitalizes on IRSE experiments to probe the conversion process of thicker $\mathrm{Al(NO_3)_3}$ films, targeting a thickness of

$45\ \mathrm{nm}$ using a $0.266\ \mathrm{M}$ solution concentration (nitrate precursors having excellent solubility in water and organic polar solvents [200] (i.e. $2-\mathrm{ME}$)) at $2000\ \mathrm{RPM}$ for $35\ \mathrm{s}$, with $\mathrm{Al}^{3+}\mathrm{:urea}$ maintained at a $2.5\mathrm{:}\ 1$ ratio. The $\mathrm{Zr(AcAc)_4}$ film recipe remained unchanged, since there was evidence of a TFT being manifested in the $\mathrm{I-V}$ characteristics. For the opto-thermal simulations, a duration of $500\ \mathrm{ns}$ was utilised to see the cooling effects after the temperature rise. The laser temporal and spatial profiles were identical to those in chapter 4, section 4.1. The optical properties involved used optical constants measured directly via SE for both bulk and thin film materials. For the thermal properties, bulk properties for Si and Al were used. For the precursors and dielectric thin films we used scaled thermal properties as described in chapter 3, section 3.3.3.

Figure 6.1a shows the simulated temperature rises of the $45\ \mathrm{nm}\ \mathrm{Al(NO_3)_3}$ spin-coated films atop both Al (red lines) and Si (blue lines) substrates. Since removal of the $\mathrm{NO_3^-}$ groups can occur at the temperature range between $250-300$℃ and by-products bonded with hydroxyl groups further refined at 400℃ and above, a fairly large range of temperatures were scanned. Shoulders in the curves at $20\ \mathrm{ns}$ and $85\ \mathrm{ns}$ in both graphs are tied to the exceeding and declination below the latent heat of fusion temperature, when the $\mathrm{Al(NO_3)_3\cdot 9H_2O}$ precursor crystal melts and decomposes. With fluences as low as $150\ \mathrm{mJ/cm^2}$ on Si ($700\ \mathrm{mJ/cm^2}$ on Al) and $200\ \mathrm{mJ/cm^2}$ on Si ($950\ \mathrm{mJ/cm^2}$ on Al), temperatures of 235℃ and 335℃ are obtained. Using the lowest fluence of $700\ \mathrm{mJ/cm^2}$ marks a baseline for which no progression of the conversion chemical pathway is achieved, followed by removal of the $\mathrm{NO_3^-}$ ions at high fluences (temperatures) that indicates partial conversion. Additionally, it has been found that dehydroxylation, which is part of the onset of the conversion for $\mathrm{Al(NO_3)_3\cdot 9H_2O}$, occurs at 220℃ and above which is only slightly exceeded and thus the LA conditions explore the full range of photochemical transformations [304]. The highest fluence of $250\ \mathrm{mJ/cm^2}$ on Si ($1200\ \mathrm{mJ/cm^2}$ on Al) ascends to 435℃, at which point it would be highly likely full chemical conversion is achieved [304].

Figure 6.1b shows the simulated temperature rises of the $45\ \mathrm{nm}\ \mathrm{Zr(AcAc)_4}$ on both Al (red lines) and Si (blue lines) substrates. Due to the higher temperature for conversion to a thin film, up to 500℃ temperature rises were investigated. In both thicknesses, the kink in the curve during the temperature rise at $16-17\ \mathrm{ns}$ is due to latent heat during decomposition of the precursor. This is accompanied by a commensurate sudden decrease in temperature at $106\ \mathrm{ns}$, when the temperature decreases below the melting/decomposition temperature. As alluded to in chapter 5 (sections 5.2 and 5.3), the fluence range identified for the films in the $45\ \mathrm{nm}\ \mathrm{Zr(AcAc)_4}$ MOS capacitors and TFTs was potentially too low, despite achieving satisfactory $\mathrm{C-V}$ characteristics. Thus, there is only some crossover in previous LA parameters.

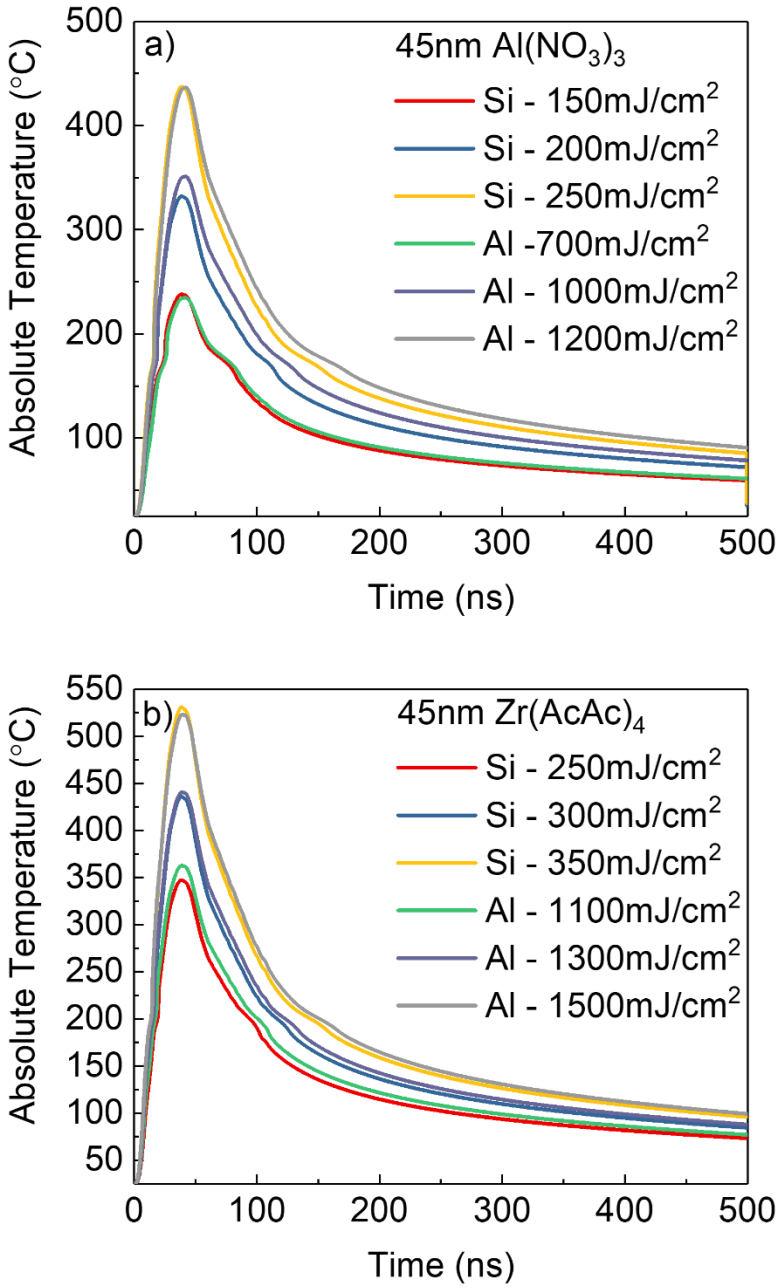

Figure 6.1. Absolute temperatures of the a) $Al(NO_3)_3$ and b) $Zr(AcAc)_4$ sol-gel precursors on $100\ nm$ Al and test-grade Si $(1-20\ \Omega \cdot cm)$ substrates, with both precursors at a nominal thickness of $45\ nm$. Near-identical temperature rises of the precursors on the different substrates were sought to replicate previous LA parameters from device fabrication.

This is apparent in Figure 6.1b, where the $250\ mJ/cm^2$ absolute temperature is $345℃$. For an acetylacetonate precursor with acetate products throughout the chemical pathway, this may be insufficient. A fluence of around $1100\ mJ/cm^2$ on Al replicates this temperature rise and can be used to test this hypothesis. For higher temperature rises to cause conversion, $300\ mJ/cm^2$ on Si (or $1300\ mJ/cm^2$ on Al) results in a temperature of $435℃$. A further increase to $350\ mJ/cm^2$ on Si ($1500\ mJ/cm^2$ on Al) reaches above $500℃$, a temperature that literature data dictates an almost certain conversion of the precursor.

Table 6.1. Experimental parameters for the fabrication and LA processing of $Al(NO_3)_3$ and $Zr(AcAc)_4$ precursor films.

Precursor	Concentration (M)	Additive	Nominal Thicknes (nm)	Spin-coating conditions	Si fluence (mJ/cm^2)	Al fluence (mJ/cm^2)
$Al(NO_3)_3$	0.26	Al^{3+}: urea at 2.5: 1	45	2000 RPM, 35 s, 2 layers	150	700
					175	825
					200	950
					225	1075
					250	1200
$Zr(AcAc)_4$	0.15	Zr^{4+}: MEA at 1: 1	45	2000 RPM, 35 s, 2 layers	250	1100
					275	1200
					300	1300
					325	1400
					350	1500

From these opto-thermal simulations, the LA parameters in Table 6.1 were derived. The five different fluences, as well as the different annealing steps (explained later), aims to unveil the effect of LA parameterisation on sol-gel precursor conversion and reveal the state of conversion of the dielectric thin films at different temperatures via IRSE, which is thus far unexplored in the literature. Conventional annealing treatments were also used following sequential steps: step 1 is a stabilisation step of $150°C$ for 15 mins for the final spin-coat layer. Step 2 is a TA treatment at $300°C$ for 1 hr to the films to promote precursor conversion or the LA processing. In some cases, a third TA step was added to the second TA step at $450°C$ for 1 hr.

6.2 Determining the Approach of IRSE Analysis

Several different types of models are used to eventually end up with the Oscillator models previously described in chapter 3, section 3.4.2 of this work. To obtain a baseline for thickness and material refractive index, a Cauchy model for a material with normal dispersion may be applied to a spectral region where the material is transparent [68]:

$$n(\lambda) = A + \frac{B}{\lambda^2} + \frac{C}{\lambda^4} + \cdots \qquad 6.1$$

In the case of the organometallic precursors, this can be more safely applied to a limited spectral range of $5000 - 6500\ cm^{-1}$ to an area free of absorption. After the Cauchy model finds these baselines, the Cauchy material is then applied to a B-Spline to fit $\Psi(E)$ and $\Delta(E)$, gradually adding more nodes as the algorithm is applied further to the mid-IR and far-IR wavelengths. The B-Spline fitting can be regulated by several means to ensure as physically real optical constants are extracted from the $\Psi(E) - \Delta(E)$ fitting as possible, including the tuning

of the resolution (i.e. number of nodes used for certain sections of the spectra), and ensuring Kramers-Kronig consistencies [373], [374] and that ε_2 remains positive while ε_1 follows logical corresponding changes with ε_2. Assuming a line shape representing physical optical constants are achieved, the B-Spline can then be parameterised, fitting the line shape of ε_2 with an oscillator model. While oscillator models can provide invaluable information, for the purposes of determining the extent of photochemical conversion of an organometallic precursor to a thin film a high-quality B-Spline may be sufficient.

To ascertain the validity of this hypothesis, B-Splines and oscillator models were compared for some of the $\mathrm{Al(NO_3)_3}$ samples. Figure 6.2 shows the fittings of $\Psi(\mathrm{E}) - \Delta(\mathrm{E})$ from CompleteEASE for the stabilised sample, both TA samples and an LA sample processed with 1 pulse of $700\ \mathrm{mJ/cm^2}$. These are presented alongside the optical constants (ε_1 and ε_2) of the B-Spline and oscillator model extracted from the fittings. In the $\Psi(\mathrm{E}) - \Delta(\mathrm{E})$ data, the red lines depict $\Psi(\mathrm{E})$, the green lines $\Delta(\mathrm{E})$ and the black dashed lines the B-Spline model applied to the data. In the graphs of optical constants, darker lines indicate the ε_1 and ε_2 values extracted from the B-Spline while lighter lines are those extracted from the oscillator model. These samples span a wide range of temperature rises, theoretically testing both fitting approaches for a range of compositions and line shapes. Alongside these graphs, Table 6.2 lists the location of each peak and their interpretation.

6.2.1 Stabilised Sample

The different optical phonon modes of metal-oxygen, nitrate groups and water (structural and surface adsorption) can all be identified within the stabilised sample in Figure 6.2 a-b. The $3209\ \mathrm{cm^{-1}}$ and $3474\ \mathrm{cm^{-1}}$ double peak result from $-\mathrm{OH}$ bonds of adsorbed water [375], [376], with the $1612\ \mathrm{cm^{-1}}$ and $1634\ \mathrm{cm^{-1}}$ peak appearing due to $\mathrm{H-O-H}$ bond bending from water structurally within the partially decomposed precursor [377]. The double peak between $1300 - 1400\ \mathrm{cm^{-1}}$ is related to $\mathrm{NO_2^-}$ ions from the precursor salt. Within hydrous nitrates, the origin of the double peak formation can be both free $\mathrm{NO_2^-}$ ions and bound $\mathrm{NO_2^- - H_2O}$ complexes [200], [378]. At the stabilisation step with $150℃$ hotplate treatment in atmospheric conditions, this level of water prevalence and $\mathrm{NO_2^-}$ ion presence is expected. Furthermore, their intensities relative to each other are similar to those in literature [304]. Peaks around $1049\ \mathrm{cm^{-1}}$ and $960\ \mathrm{cm^{-1}}$ are related to the deformation mode of an $\mathrm{Al-OH}$ bond [377], [379]. The detection and fittings of these peaks, based on the overlap between the B-Spline and oscillator model, can be conducted with either model with minor differences in the intensity of ε_2.

The major difference in B-Spline and oscillator models is first seen below $600\ \mathrm{cm}^{-1}$. For the B-Spline, a single peak at $520\ \mathrm{cm}^{-1}$ emerges, with unreasonably high ε_2 values and a corresponding large negative in ε_1. For many materials, this is typically a plasmonic or phononic behaviour associated with conductive (or phonon polariton) behaviour. As the literature has detailed previously, no phonon resonance modes for $\mathrm{Al_2O_3}$ lie anywhere near $400\ \mathrm{cm}^{-1}$ [380]. As for free carriers, $\mathrm{Al_2O_3}$ can demonstrate free carrier behaviour and transport but only in the case of extreme conditions such as near zero temperatures or highly granular films [381]. For the oscillator model, peaks centred at $696\ \mathrm{cm}^{-1}$ and $287\ \mathrm{cm}^{-1}$ are manifested instead. The $287\ \mathrm{cm}^{-1}$ peak is typically seen in aluminium oxide hydroxide ($\mathrm{Al-O-OH}$) compounds [382]. $696\ \mathrm{cm}^{-1}$ is attributed to the deformation mode of an $\mathrm{Al-O}$ bond, which considering the process temperature is due to the same oxide hydroxide compounds.

No peaks related to the $2-\mathrm{ME}$ solvent (e.g. $\mathrm{C-H}, \mathrm{C=O}$) are present, which is expected since the $150℃$ stabilisation temperature exceeds the $124℃$ boiling point of $2-\mathrm{ME}$. One query is the absence of peaks relating to urea. Some peaks for urea may not be decoupled from the precursor, since the absorption relating to $\mathrm{NH_2}$ bond stretching from $3210-3439\ \mathrm{cm}^{-1}$ [383] and bending vibrations from $1625-1680\ \mathrm{cm}^{-1}$ [384] coincide with the broadband $-\mathrm{OH}$ and $\mathrm{H-O-H}$ bonds of the $\mathrm{Al(NO_3)_3}$ precursor. The peaks relating to the $\mathrm{C-N}$ stretching vibration at $\approx 1460\ \mathrm{cm}^{-1}$, $\mathrm{NH_2}$ rocking vibration at $\approx 1160\ \mathrm{cm}^{-1}$, and $\mathrm{C=O}$ at $1596\ \mathrm{cm}^{-1}$ [383], [384] are absent. Decomposition of urea can occur from $150℃$ [385] while the solution combustion synthesis process occurs at $180℃$ [226] so stabilising at this temperature may lead to reactions and products that overlap with the broadband peaks. Alternatively, IRSE is not sensitive to the urea at this concentration or volume and avoids detection. For the stabilised sample at $150℃$, the chemical steps are well outlined and can be briefly outlined [304]. Below $170℃$, only hydrolysis and dehydration have occurred in a thermochemical process, leaving a mixture of crystalline and amorphous products. Hydrous nitrates cannot give anhydrous salts through decomposition alone, thus other processes must occur to remove the water. The products may consist of a mixture of the $\mathrm{Al(NO_3)_3}$ precursor itself, a decomposed by-product of $\mathrm{Al(OH)(NO)_3 \cdot 2H_2O}$ and various oxides and hydroxides, The combination of products here matches to the variety of peaks described above, verifying the composition of the $\mathrm{Al(NO_3)_3}$ stabilised film can be accurately determined by IRSE.

With regards to fitting of the IRSE data, there are many factors that lead to inconsistencies with the model and the data in the far-IR wavelengths such as those in Figure 6.2a, regardless of the use of the B-Spline or oscillator model. At $55°$ and $65°$, the model does not fit as well to the $2000-3500\ \mathrm{cm}^{-1}$ broad range related a peak relating to the $\mathrm{O-H}$ bonds, while $75°$ does not fit as well in the far-IR region describing the $\mathrm{Al-O}$ and $\mathrm{Al-OH}$ bonding. A

review of the data confirms a higher than desired level of depolarisation occurred especially for $75°$, which despite being accounted for in the model skews the fitting. The physical origin of this can be measurement related where the ellipsometer is misaligned from the $\theta - 2\theta$ geometry used for measurement or a sample related phenomena such as grading in the thin film or a layer with different refractive indices. Both cases were tested when this arose with another sample from the $Al(NO_3)_3$ sample set. EMA approximating 50% of a layer with a lower refractive index combined with 50% of a layer with a higher refractive index was tested, but provided no reduction of the MSE or improved fitting where the raw data and model become decoupled. Angle offsets where measurements are misaligned seemingly provide no benefit to the model at $55°$ and $65°$, but work in several cases for $75°$. However, this still leaves the model and data decoupled for this stabilised sample. Based on previous AlO_x fabrication, it is not expected roughness contributes to the depolarisation in these samples in the stabilised sample, though should always be trialled for an LA sample. Visual inspection of the sample shows no change in the surface due to light scattering. Since the majority of the samples do not experience this depolarisation at all or to a lesser extent, it is expected that the level of depolarisation affecting the fittings to this extent is a sample related phenomenon rather than a systematic measurement error. Since it affects both the B-Spline and oscillator model, the models remain valid in their description of the sample composition relative to each other. Additionally, for the stabilised sample spectra (and many spectra for samples in this work), precision of determining the $M - O$ bonds is affected by instrumental noise that sometimes extends as far as $500\ cm^{-1}$. Certain approaches can be taken to reduce this noise, such as very long (3 day) measurements to boost the signal-to-noise ratio. Before the measurements were undertaken, a new SiC glowbar was fitted to ensure the signal was increased. Further work investigating SE as a compositional characterisation technique may utilise Terahertz SE [386] to more clearly display the nature of the $M - O$ bonding in a variety of organometallic precursors. For the case of determining the removal of organic residues from the sol-gel to fabricate a functional thin film and the possible strength of the $M - O$ bonding, IRSE is seemingly capable of doing so.

6.2.2 LA Sample

For the LA sample using $700\ mJ/cm^2$ in Figure 6.2c-d ($235℃$ thin film temperature), depolarisation is not experienced, and a good fitting is achieved with both B-Spline and the oscillator model across most of the spectra to observe 8 peaks, reduced from the stabilised sample. The B-Spline and oscillator model both identify peaks at $3468\ cm^{-1}$, $3169\ cm^{-1}$ and $2020\ cm^{-1}$ relating to $-OH$ bonding and the $1630\ cm^{-1}$ relating to $H - O - H$ bending from the water bound to the precursor powder. The nitrate double peak at $1330\ cm^{-1}$ and $1394\ cm^{-1}$ remains. $Al - O$ bonding occurs at $567\ cm^{-1}$ in both models due to $Al - O$. This

has been linked to $\mathrm{Al-O}$ bond stretching in microcrystalline molecules with $\mathrm{Al-O_6}$ within an otherwise amorphous film [387].

Yet again, where the B-Spline and oscillator model differ is their interpretation of the peaks in the deepest wavelengths. For the B-Spline, a peak occurs around $440\ \mathrm{cm^{-1}}$, close to the origin of a peak related to the $\mathrm{Al-O-OH}$ of diaspore. For the oscillator model, a large sharp peak at $287\ \mathrm{cm^{-1}}$ occurs, whose origin was previously discussed as $\mathrm{Al-O-OH}$ related and is retained from the stabilised film. Furthermore, the increase is such that a dramatic negative ε_1 is presented, which (as discussed) is not expected in this sample. Hence, in this case, B-Spline results in the more reliable fit. However, both models identify a peak related to the same kind of aluminium oxide product, though both suffer in the far—IR as before due to the instrumental noise. Thus, peaks can't be identified and doubt is casted over the precision of the models in the region below $500\ \mathrm{cm^{-1}}$. Regardless, the reduction of ε_2 for organic peaks due to increased temperature and mass removal without full conversion is expected at this temperature and consistent in relation to the stabilised sample, showing the first signs that the photochemical conversion process via LA can be tracked and understood using IRSE. The decrease here is expected, as the dehydroxylation of the $\mathrm{Al(NO_3)_3}$ precursor can only occur above $220℃$. At this temperature, urea would have been fully removed via full decomposition or combustion so would not be related to any peaks in these spectra (or any $\mathrm{Al(NO_3)_3}$ spectra hereafter).

6.2.3 TA Samples

For the TA sample at $300℃$ (Figure 6.2e-f) that is used throughout the literature as a reference for the conventional sol-gel methodology, additional peaks emerge so 10 peaks are present. This is true for the B-Spline or oscillator model, which yet again closely match. As with previous samples, adsorbed water and $\mathrm{H-O-H}$ bending are present leading to peaks at $3500\ \mathrm{cm^{-1}}$, $3234\ \mathrm{cm^{-1}}$, $2100\ \mathrm{cm^{-1}}$ and $1620\ \mathrm{cm^{-1}}$, as is the nitrate double peak at $1346\ \mathrm{cm^{-1}}$ and $1412\ \mathrm{cm^{-1}}$. Arguably, the $1412\ \mathrm{cm^{-1}}$ peak is at too high a wavenumber due to the SE fitting process, but no other likely candidates were found. The change in line shape for $\Psi(\mathrm{E})$ in Figure 6.2e is the result of the growth of phases of $\mathrm{Al-O-OH}$, leading to peaks at $862\ \mathrm{cm^{-1}}$, $1072\ \mathrm{cm^{-1}}$ and $1186\ \mathrm{cm^{-1}}$[388]. Finally, a peak is presented at either $473\ \mathrm{cm^{-1}}$ ($\mathrm{Al-O}$) for the oscillator model or $526\ \mathrm{cm^{-1}}$ for the B-Spline. Due to the instrumental noise, the sudden increase in ε_2 from the B-Spline is not believed and the effect on the model is visible in Figure 6.2e, where unnecessary jumps are made to fit the line shape. Due to the shape of the peaks and amplitude of ε_2 in relation to other processing conditions, there is a high chance that some growth and prioritisation of $\mathrm{Al-O}$ and $\mathrm{Al-OH}$ bonds has occurred which is expected.

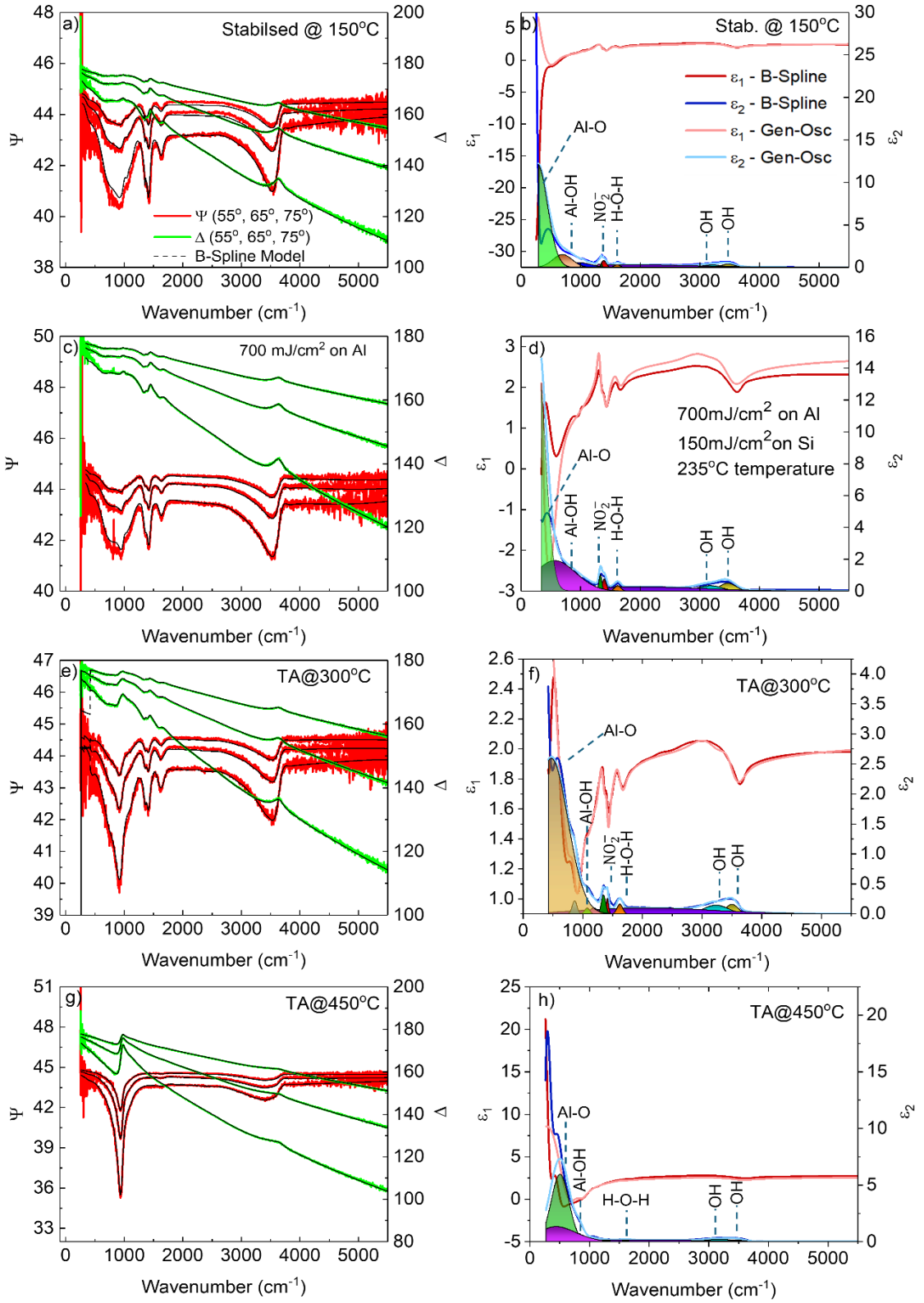

Figure 6.2. Measured $\Psi(E)$ (red lines) and $\Delta(E)$ (green lines), B-Spline models (blacked dashed line) and the optical constants with two different models (B-Spline in darker colours, oscillator model in lighter colours) for various $Al(NO_3)_3$ samples on Al substrate. a) $\Psi(E)$ and $\Delta(E)$ for the $Al(NO_3)_3$ sample stabilised at $150°C$, with the extracted ε_1 and ε_2 in b). c) $\Psi(E)$ and $\Delta(E)$ for the $Al(NO_3)_3$ sample LA with one pulse at $700\ mJ/cm^2$, with the extracted optical constants in d). e) $\Psi(E)$ and $\Delta(E)$ for the $Al(NO_3)_3$ sample TA at $300°C$, with the ε_1 and ε_2 in f). g) $\Psi(E)$ and $\Delta(E)$ for the $Al(NO_3)_3$ sample TA at $450°C$, with the extracted ε_1 and ε_2 in h).

Also, the amplitudes of the nitrate and water ions are lower than those of the sample processed with $700\ \mathrm{mJ/cm^2}$, demonstrating a reduction of the presence of the organic residues.

The lack of removal of the nitrate ions is possibly in contradiction to the work by Koutsiaki *et al* [66] that preceded this chapter and the wider literature that dictates $300°\mathrm{C}$ would be sufficient to do so for nitrates. Several similarities are shared between the $\mathrm{In(NO_3)_3}$ and $\mathrm{Al(NO_3)_3}$ precursors, including the large presence of bonded water, volatility of the nitrate precursors and low decomposition temperatures. One difference between them is the film thickness. The $\mathrm{In(NO_3)_3}$ investigated a film that was $12\ \mathrm{nm}$ thickness (at $30\ \mathrm{mg/ml}$ concentration) when stabilised compared to the highly elevated thickness arising from a $100\ \mathrm{mg/ml}$, 2-layer sample. Via IRSE, this confirms the standard TA temperature and dwell time has potential to be inadequate for possibly several dielectrics that have need of additional thickness above ultra-thin ($> 10\ \mathrm{nm}$) to promote low dispersion and electrical stability. The other possible factor is the complexity of the chemical pathways for $\mathrm{Al(NO_3)_3}$ and that the literature shows the removal of $-\mathrm{OH}$ bonds to a pure $\mathrm{AlO_x}$ can only occur at temperatures far beyond those used here [389].

The TA sample at $450°\mathrm{C}$ (Figure 6.2g-h) thus holds increased weight, as it progresses the precursor towards a high chance of conversion to a thin film. Here, a change in the $\Psi(\mathrm{E}) - \Delta(\mathrm{E})$ line shapes are seen and several of the peaks disappear. Initial observation already shows prioritisation of peaks between $500 - 1000\ \mathrm{cm^{-1}}$. Peaks due to $-\mathrm{OH}$ remain at $3468\ \mathrm{cm^{-1}}$ and $3177\ \mathrm{cm^{-1}}$, but the origin of these are now called into question since fully formed $\mathrm{Al-O-OH}$ compounds will also contribute to this instead of adsorbed water [390]. The $\mathrm{H-O-H}$ bending at $1605\ \mathrm{cm^{-1}}$ remains and follows. The nitrate double peak has been removed, demonstrating progression towards full conversion and supporting that $-\mathrm{OH}$ bonds relate to a more defined formation of $\mathrm{Al-O-OH}$ compounds. For $\mathrm{Al-OH}$ and $\mathrm{Al-O}$, peaks appear around $440\ \mathrm{cm^{-1}}$, $531\ \mathrm{cm^{-1}}$ and $831\ \mathrm{cm^{-1}}$. The temperature combined with the above observations indicates the conversion from the nitrate precursor to an aluminium oxide hydroxide as per the literature at this temperature. These peak locations are extremely similar regardless of the model used. Across these samples, certain trends emerge. In essence, for identifying the organic residues that are (or aren't) remaining in the sample after any post-deposition processing, either a B-Spline fitting or an oscillator model with IRSE will work to identify organic and organometallic peaks and find the amplitude of ε_2 relative to other samples up to $600\ \mathrm{cm^{-1}}$. However, instrumental noise can be a barrier to fully understanding the nature of $\mathrm{M-O}$ bonds within the materials, particularly for samples that have not been fully converted.

Table 6.2. ε_2 peaks for $Al(NO_3)_3$ samples on Al substrate, with the $Al(NO_3)_3$ precursor that is either stabilised, processed on a hot plate at 300°C or 450°C or LA with 1 pulse at $700\ mJ/cm^2$. Their corresponding physical interpretations are also given.

No of peak	Stab. $Al(NO_3)_3$	$Al(NO_3)_3$ – $700\ mJ/cm^2$	$Al(NO_3)_3$ – TA @ 300°C	$Al(NO_3)_3$ – TA @ 450°C	Interpretation
1	287	287	473	440	$Al-O-OH$
2	696	567	862	531	$Al-O-OH$
3	960	-	1072	831	$Al-O-OH$
4	1049	-	1186	-	$Al-O-OH$
5	1306	-	-	-	$\nu(NO_3^-)$
6	1346	1330	1346	-	Free NO_3^-
7	1386	1394	1412	-	Free NO_3^-
8	1612	1620	1620	1605	$H-O-H$
9	1900	2020	2100	2038	$H-O-H$
10	3209	3169	3234	3177	$\nu(O-H)$
11	3474	3468	3500	3468	$\nu(O-H)$

6.3 Ellipsometry Analysis of LA $AlNO_3$

Further to the $700\ mJ/cm^2$ sample and with the fitting strategy investigated, the rest of the LA samples can now be investigated to determine their composition. Figure 6.3 shows the fittings of $\Psi(E)-\Delta(E)$ from CompleteEASE for the LA samples processed with 1 pulse of different fluences. These are presented alongside the optical constants (ε_1 and ε_2) of the B-Spline and oscillator model extracted from the fittings. In the $\Psi(E)-\Delta(E)$ data, the red lines depict $\Psi(E)$, the green lines $\Delta(E)$ and the black dashed lines the B-Spline model applied to the data. Angle size increases from top to bottom of the graphs. In the graphs of optical constants, darker lines indicate the ε_1 and ε_2 values extracted from the B-Spline while lighter lines are those extracted from the oscillator model.

Throughout all of the spectra in Figure 6.3, peaks associated with $\mathrm{H-O-H}$ bending of structural water, $-\mathrm{OH}$ bonds from adsorbed water are present from $1620\ \mathrm{cm^{-1}}$, $\approx 3100\ \mathrm{cm^{-1}}$ and $\approx 3470\ \mathrm{cm^{-1}}$ with exact wavenumbers for peak amplitudes found in Table 6.3. Due to their commonality, there is little emphasis on the discussion of these peaks throughout chapter 6.3. For the $950\ \mathrm{mJ/cm^2}$ sample, these deviate slightly for reasons that will be explained in more detail later.

For now, $825\ \mathrm{mJ/cm^2}$ (Figure 6.3 a-b) is explained in more detail. With a temperature rise expected somewhere around $275℃$, some initiation of precursor conversion to a thin film might be expected but not to a high extent. Indeed, the nitrate double peak from $1300-1400\ \mathrm{cm^{-1}}$ remains indicating photochemical conversion was not achieved. As stated previously, this is not unexpected. Peaks thereafter at $420\ \mathrm{cm^{-1}}$, $920\ \mathrm{cm^{-1}}$ and $1088\ \mathrm{cm^{-1}}$ correspond to the $\mathrm{Al-O}$ and $\mathrm{Al-OH}$ bonds [388].

For the $950\ \mathrm{mJ/cm^2}$ (Figure 6.3 c-d), the B-Spline cannot be fitted at any thickness or with any parameters that result in a good fit for all angles across all wavelengths that all samples so far have returned. Attempting the same with a oscillator model returned the same difficulties, as well as $\Psi(\mathrm{E})$ only fitting well when $\Delta(\mathrm{E})$ fits poorly and vice versa, since the oscillator model stems from parameterising the B-Spline itself. Further advanced models involving a gradient in the film do not provide better fits with physical results. Thus, identification of the peaks may be treated with some scepticism due to these difficulties. A choice is also made that, if necessary, a poor fit in the wavelengths above $4500\ \mathrm{cm^{-1}}$ is taken to ensure a more cohesive fit from $400-4000\ \mathrm{cm^{-1}}$ where the $\mathrm{M-O}$, $\mathrm{M-OH}$ and organic bonds reside. This leads to more accurate ε_2 values that reveals the composition of the sample. The increased processing temperature of $335℃$ combined with the increased complexity of fitting means any model results in 11 identifiable peaks. The double peak of the nitrate ion has now merged into a single peak at $1379\ \mathrm{cm^{-1}}$. Since $\mathrm{H-O-H}$ bending and water complexes remains, this suggests a reduction of the $\mathrm{NO_2^-}$ free ions to the extent that they are eliminated. Instead of a single peak around $1088\ \mathrm{cm^{-1}}$, two separate peaks of $1128\ \mathrm{cm^{-1}}$ and $1048\ \mathrm{cm^{-1}}$ are present. Finally, peaks at $410\ \mathrm{cm^{-1}}$, $606\ \mathrm{cm^{-1}}$ are presented due to $\mathrm{Al-O}$ $(\mathrm{Al-O_2})$ transverse optical mode bond bending [387]. $806\ \mathrm{cm^{-1}}$ and $928\ \mathrm{cm^{-1}}$ are present due to $\mathrm{Al-O}$ bonds and $\mathrm{Al-OH}$ deformations.

For $1075\ \mathrm{mJ/cm^2}$ (Figure 6.3e-f), with a thin film temperature peak around $385℃$, some continuation of the observations of the $950\ \mathrm{mJ/cm^2}$ are seen here. The nitrate peak remains as a single peak at $1387\ \mathrm{cm^{-1}}$ and ε_2 is further diminished, suggesting removal of some of the $\mathrm{NO_2^- - H_2O}$ complexes. As mentioned, the $-\mathrm{OH}$ and $\mathrm{H-O-H}$ remains consistent.

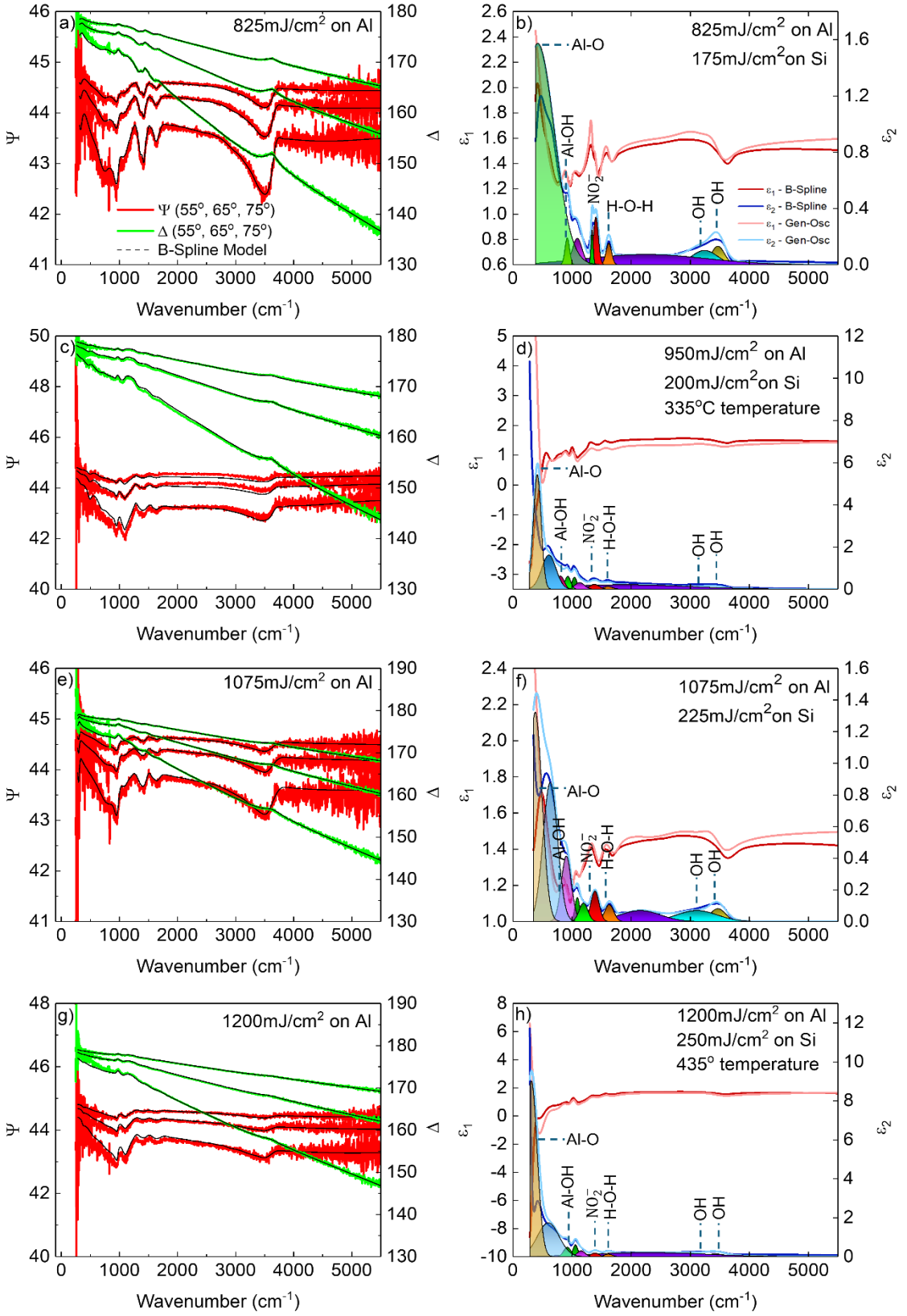

Figure 6.3. Raw data, B-Spline models and the optical constants for LA $Al(NO_3)_3$ samples. a) $\Psi(E)$ and $\Delta(E)$ for the $Al(NO_3)_3$ sample LA with one pulse at $825\ mJ/cm^2$, with the extracted ε_1 and ε_2 in b). c) $\Psi(E)$ and $\Delta(E)$ for the $Al(NO_3)_3$ sample LA with one pulse at $950\ mJ/cm^2$, with the extracted ε_1 and ε_2 in d). e) $\Psi(E)$ and $\Delta(E)$ for the $Al(NO_3)_3$ sample LA with one pulse at $1075\ mJ/cm^2$, with the ε_1 and ε_2 in f). g) $\Psi(E)$ and $\Delta(E)$ for the $Al(NO_3)_3$ sample LA with one pulse at $1200\ mJ/cm^2$, with the extracted ε_1 and ε_2 in h).

Table 6.3. ε_2 peaks for $Al(NO_3)_3$ samples on Al substrate, with the $Al(NO_3)_3$ precursor that is processed via LA with several different fluences. Their corresponding physical interpretations are also given.

No of peak	$Al(NO_3)_3$ – 825 mJ/cm^2	$Al(NO_3)_3$ – 950 mJ/cm^2	$Al(NO_3)_3$ – 1075 mJ/ cm^2	$Al(NO_3)_3$ – 1200 mJ/ cm^2	Interpretation
1	420	410	378	378	$Al-O-OH$
2	-	606	631	631	$Al-O-OH$
3	-	806	-	-	$Al-O-OH$
4	920	928	903	903	$Al-O-OH$
5	1088	1042	1088	1088	$Al-O-OH$
6	-	1128	1194	1194	$Al-O-OH$
7	1334	-	-	-	Free NO_3^-
8	1404	1379	1387	1389	Free NO_3^-
9	1620	1605	1630	1630	$H-O-H$
10	2250	2100	2154	2152	$H-O-H$
11	3240	3306	3113	3110	$\nu(O-H)$
12	3468	3501	3468	3475	$\nu(O-H)$

The peak deepest in the IR shifts down towards $370\ cm^{-1}$ and becomes sharper, which is characteristic of a peak in the $Al-O-OH$ compound boehmite that may occur at sufficiently high temperatures. This is further confirmed by the peak at $620-630\ cm^{-1}$, which originates from the $Al-O$ bonds from $Al-O-OH$. The similarities of the $1200\ mJ/cm^2$ sample (Figure 6.3g-h) ,with a $435°C$ thin film temperature peak, to the $1075\ mJ/cm^2$ sample suggest a stalling of the change of phases and precursor conversion to a thin film. The wavenumbers for each of the 10 peaks for the samples remain nearly identical, as can be seen in Table 6.3, with any shifts too minuscule to be outside of the bands of the previously identified peaks. This is agreeable, since conversion to aluminium oxide via the $Al(NO_3)$ precursor has been shown to remain in

stasis from $400-550$℃, leading to $\mathrm{Al-O}$ and $\mathrm{Al-O-OH}$ bonds spanning a wide spectral range [304], [389], [391]. Despite the peak temperature for the $1200\ \mathrm{mJ/cm^2}$ sample being close to the 450℃ TA sample, the $\Psi(\mathrm{E})-\Delta(\mathrm{E})$ and $\varepsilon_1-\varepsilon_2$ values and models are drastically different from each other.

While not being ideal for the fabrication of an $\mathrm{AlO_x}$ dielectric for opto-electronic devices as full photochemical conversion to a thin film was not achieved, these high fluence samples show the drastic differences between the TA and LA conversion process and the first sign that simply increasing fluence to induce the temperature rise required doesn't necessarily lead to photochemical conversion. It also demonstrates that IRSE can begin to unravel the photochemical conversion process v*ia* LA. Therefore, a multi-pulse approach should be investigated.

6.4 Ellipsometry Analysis of $Zr(AcAc)_4$ Samples

Since analysis of the $\mathrm{Al(NO_3)_3}$ samples revealed a B-Spline model is satisfactory for detecting chemical peaks and determining their origin, B-Spline models were used exclusively for analysis and modelling of the $\mathrm{Zr(AcAc)_4}$ spectra. Figure 6.4 shows the $\Psi(\mathrm{E})-\Delta(\mathrm{E})$ data and fittings of stabilised, TA and an LA sample. These are presented alongside the optical constants (ε_1 and ε_2) of the B-Spline. In the $\Psi(\mathrm{E})-\Delta(\mathrm{E})$ data, the red lines depict $\Psi(\mathrm{E})$, the green lines $\Delta(\mathrm{E})$ and the black dashed lines the B-Spline model applied to the data. In the graphs of optical constants, the highlighted areas below ε_2 are used to demonstrate the likely energy positions of each peak.

For the stabilised film (Figure 6.4a-b), multiple peaks are identified from $3000-3500\ \mathrm{cm^{-1}}$ from the phonon modes of $-\mathrm{OH}$ molecules in the zirconium acetate-acetoacetonate complex and adsorbed water. A broad peak with origin $\approx 2000\ \mathrm{cm^{-1}}$ cannot be directly attributed to a peak, but other spectroscopy techniques show absorbance (or decrease in transmittance) across this region previously [392]. Absorption peaks from $1000-1600\ \mathrm{cm^{-1}}$ indicate the presence of the acetate group, $(\mathrm{CH_3COO})_2$ [393]. Specifically, $1064\ \mathrm{cm^{-1}}$ is linked to $\rho\mathrm{CH_3}$, $1234\ \mathrm{cm^{-1}}$ to $\nu_{\mathrm{C-C}}$, $1428\ \mathrm{cm^{-1}}$ to $\delta_s\mathrm{CH_3}$ and $1556\ \mathrm{cm^{-1}}$ to $\nu_{\mathrm{C-O}}+\nu_{\mathrm{C-C}}$ phonon modes (where ρ is rocking mode, δ_s is plane bending, ν is bond stretching and the s subscript is the degenerate symmetric mode). The presence of the acetate group combined with peak at $590\ \mathrm{cm^{-1}}$ for propyne ($\mathrm{CH_3-C=CH}$) is indicative of partial decomposition process at 150℃ when a zirconium acetate-acetoacetonate complex is formed [393]:

$$\mathrm{Zr(C_5H_7O_2)_4} \underset{\mathrm{I}}{\rightarrow} \mathrm{Zr(C_5H_7O_2)_2\ (CH_3COO)_2} + 2\mathrm{C_3H_4} \qquad 6.2$$

The discovery of this process after stabilisation is beneficial for the conversion process. The acetate complex and the presence of the $\nu_{c-o} + \nu_{c-c}$ phonon mode causes a strain on one of the acetonates, making the complex and multi-stage decomposition process require lower energy. Thus, the acetylacetonate precursor is potentially advantageous over the standard acetate precursor for LA, since lower fluences for complete photochemical conversion - and even further reduced thermal budget to a substrate - become a consequence. Finally, a peak at $\approx 370\ \mathrm{cm}^{-1}$ is attributed to the $\mathrm{Zr-O}$ phonon mode [394].

Aside from the decomposition products, there is an additional peak at $1673\ \mathrm{cm}^{-1}$ that could result from the $\mathrm{N-H}$ vibration of the MEA stabilising agent [395], the ν_{c-o} of the AcAc group which remains in the acetate-acetoacetonate complex or the absorption band due to $\mathrm{C_3H_4}$ (though this is unlikely since it is gaseous). The boiling temperature of MEA is $170℃$ which may mean small amounts remain after stabilisation at $150℃$. The MEA solvent, while being potentially beneficial, adds the difficulty of multiple peaks coinciding with those of the initial decomposition process. For example, ν_{C-O} of the MEA may occur at $1074\ \mathrm{cm}^{-1}$ and ν_{C-N} at $1028\ \mathrm{cm}^{-1}$, which may redshift or blueshift depending on coordination or interaction with atoms in the surroundings [395]. In either case, the removal of these peaks is desirable and should occur at temperatures of $250℃$ or above.

For the $\mathrm{Zr(AcAc)_4}$ sample TA at $300℃$ (Figure 6.4c-d), elevated peaks around $3400\ \mathrm{cm}^{-1}$, $3081\ \mathrm{cm}^{-1}$ and $2100\ \mathrm{cm}^{-1}$ are linked to hydroxyl groups from large water adsorption into the film and in the sample itself. The single broad oscillator from $2000-3000\ \mathrm{cm}^{-1}$ can also have a contribution via stretching modes of the methyl group in the acetate ligand [396]. The increase in the size of the peak with respect to the stabilised film is linked to the zirconium acetate product being hydrophilic and water soluble [396]. This thin film also contains the acetate ion, as indicated by the peaks at $1044\ \mathrm{cm}^{-1}$, $1354\ \mathrm{cm}^{-1}$, $1513\ \mathrm{cm}^{-1}$ and $1584\ \mathrm{cm}^{-1}$ for the $\rho\mathrm{CH_3}$ mode, ν_{c-o} symmetric mode and ν_{c-o} antisymmetric mode, [397] respectively. The antisymmetric mode that is typically at $1556\ \mathrm{cm}^{-1}$ (such as in the stabilised sample) can split at low concentrations of acetate within a complex, resulting in the two peaks at $1513\ \mathrm{cm}^{-1}$ and $1584\ \mathrm{cm}^{-1}$. Note the shift of wavelengths for the bonds that are identified in both the stabilised and TA samples. The shifting of wavelengths and splitting of peaks for metal acetates has been shown to depend on the ratio between the two, thus the peaks for the acetate ion may shift with temperature as sample is advanced further along the chemical pathway. The acetate is expected at this stage in the form of $\mathrm{ZrO(CH_3COO)_2}$ (further supported by its related peak at $1170\ \mathrm{cm}^{-1}$) since increased temperature causes the decomposition of the acetate-acetoacetonate complex [393]:

$$\mathrm{Zr(C_5H_7O_2)_4\ (CH_3COO)_2} \underset{\mathrm{II}}{\rightarrow} \mathrm{Zr(OH)(CH_3COO)_3} \underset{\mathrm{III}}{\rightarrow} \mathrm{ZrO(CH_3COO)_2} \qquad 6.3$$

The peaks at this stage of decomposition and conversion manifest from the conversion being in stasis at the $250-350$℃ temperature range, which has been reported previously for $\mathrm{Zr(AcAc)_4}$ and acetates in general. Due to noise in the measurement in the far-IR, erroneous values for ε_2 are produced so the exact peak energies for ε_2 cannot be described. The value outputted is $545\ \mathrm{cm^{-1}}$, which resides close to the $\mathrm{Zr-OC}$ vibration band. However, this cannot be achieved during TA at 300℃. There is confirmation of $\mathrm{Zr-O}$ within this film due to a peak at $890\ \mathrm{cm^{-1}}$ [398].

The TA sample at 450℃ (Figure 6.4e-f) represents an interesting prospect for compositional characterisation. Specific IR spectra at this temperature exist, but not under sol-gel or atmospheric conditions, thus it is unclear if the evidenced formation of the carbonate and acetone will occur at this exact temperature *via* [393]:

$$\mathrm{ZrO(CH_3COO)_2} \underset{\mathrm{IV}}{\rightarrow} \mathrm{ZrOCO_3 + CH_3COCH_3} \qquad 6.4$$

The B-Spline fitting reveals peaks from $3000-3500\ \mathrm{cm^{-1}}$ from the phonon modes of $\mathrm{-OH}$ molecules remain. As with the sample TA at 300℃, all peaks from in the mid-IR region are due to $\mathrm{ZrO(CH_3COO)_2}$ with all the peaks blue-shifting to $1065\ \mathrm{cm^{-1}}$, $1387\ \mathrm{cm^{-1}}$, $1547\ \mathrm{cm^{-1}}$ and $1590\ \mathrm{cm^{-1}}$ for the $\rho\mathrm{CH_3}$ mode, $\nu_{\mathrm{c-o}}$ symmetric mode and $\nu_{\mathrm{c-o}}$ antisymmetric mode, respectively. The peak at $1161\ \mathrm{cm^{-1}}$ due to $\mathrm{ZrO(CH_3COO)_2}$ is the exception, which slightly redshifts. While a peak at $929\ \mathrm{cm^{-1}}$ can result from the presence of acetone ,$\mathrm{CH_3COCH_3}$, the lack of presence of other (more dominant) peaks suggests this is not the cause. Thus, the peak at $929\ \mathrm{cm^{-1}}$ is more likely to be $\mathrm{Zr-O}$ bond vibrations influenced by $\mathrm{-OH}$ groups shifting it to higher wavenumbers. The peak at $409\ \mathrm{cm^{-1}}$ results from $\mathrm{Zr-O}$ bond vibrations. Based on the described peaks, there is an absence of carbonate products described in eq. 6.4. This is connected to the increased levels of water in the thin film in comparison to the sample used in eq. 6.4 due to preparation in atmospheric conditions.

For the $\mathrm{Zr(AcAc)_4}$ sample processed with 1 pulse of $1100\ \mathrm{mJ/cm^2}$ (Figure 6.4g-h), where a peak thin film temperature of 345℃ is achieved, peaks from $3000-3500\ \mathrm{cm^{-1}}$ from the phonon modes of $\mathrm{-OH}$ molecules remain. In fact, in nearly all the $\mathrm{Zr(AcAc)_4}$ films of this chapter, water remains despite the use of MEA to reduce this. If a sample has been left in ambient environment after processing (i.e. MEA has been removed), this may result in adsorbed water being present in each thin film. The exceptions to this are other LA samples, the analysis for which will be discussed later. Peaks at $1065\ \mathrm{cm^{-1}}$, $1387\ \mathrm{cm^{-1}}$ and $1590\ \mathrm{cm^{-1}}$ represent the $\rho\mathrm{CH_3}$ mode, $\nu_{\mathrm{c-o}}$ symmetric mode and $\nu_{\mathrm{c-o}}$ antisymmetric mode, respectively. No peak splitting suggests the ratio of $\mathrm{CH_3COO}$ to $\mathrm{Zr^{4+}}$ is higher than in the TA samples previously.

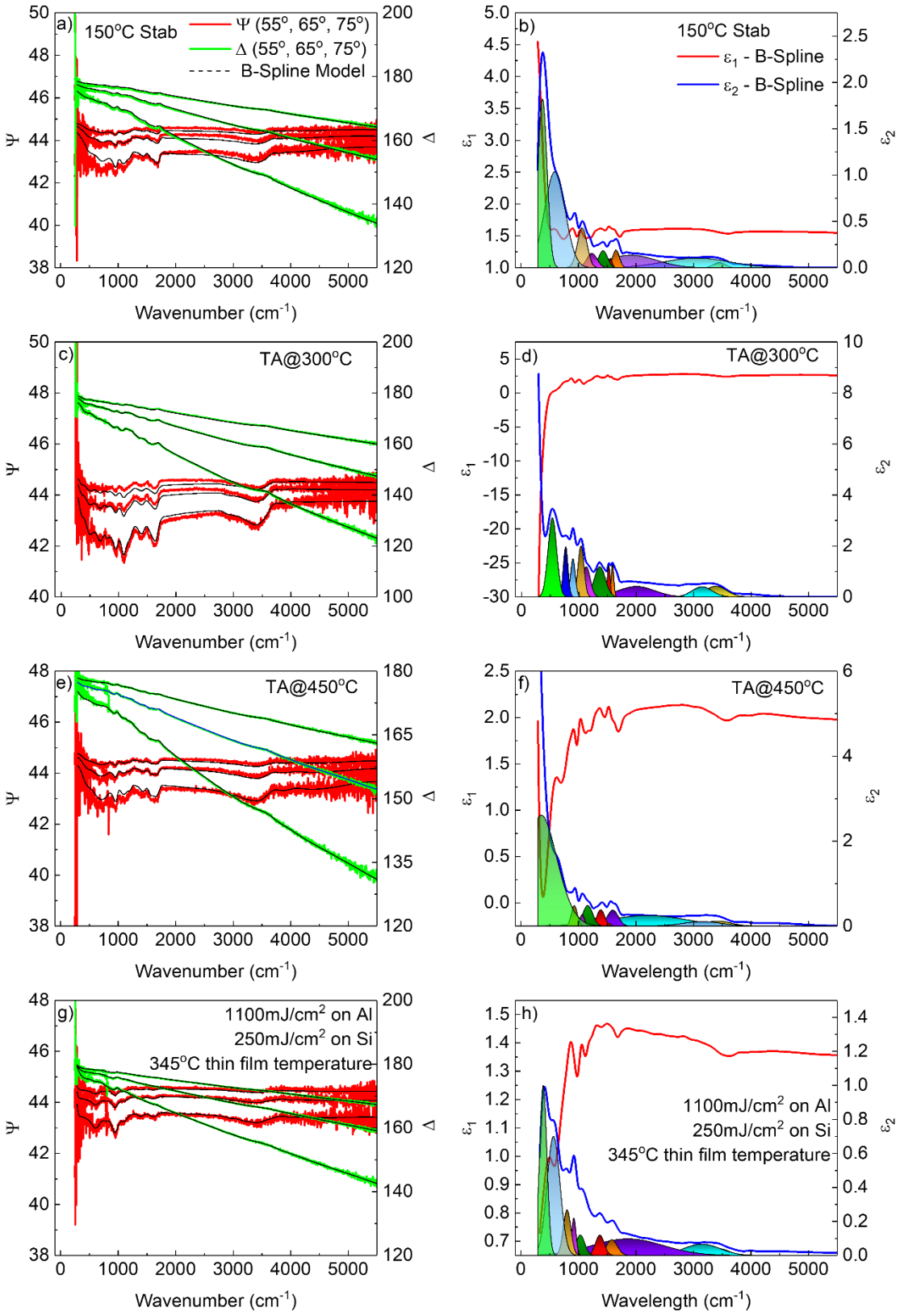

Figure 6.4. Measured $\Psi(E)$ (red lines) and $\Delta(E)$ (green lines) with the B-Spline models (blacked dashed line), and the optical constants extracted from the B-Spline, for various $Zr(AcAc)_4$ samples on Al substrate. a) $\Psi(E)$ and $\Delta(E)$ for the $Zr(AcAc)_4$ sample stabilised at $150°C$, with the extracted ε_1 and ε_2 in b). c) $\Psi(E)$ and $\Delta(E)$ for the $Zr(AcAc)_4$ sample TA at $300°C$, with the ε_1 and ε_2 in d). e) $\Psi(E)$ and $\Delta(E)$ for the $Zr(AcAc)_4$ sample TA at $450°C$, with the extracted ε_1 and ε_2 in f). g) $\Psi(E)$ and $\Delta(E)$ for the $Zr(AcAc)_4$ sample LA with one pulse at $1100\ mJ/cm^2$, with the extracted optical constants in h).

Table 6.4. ε_2 peaks for $Zr(AcAc)_4$ samples on Al substrate, with the $Zr(AcAc)_4$ precursor that is either stabilised, TA or LA with $1100\ mJ/cm^2$. Their corresponding physical interpretations are also given.

No of peak	Stab. $Zr(AcAc)_4$	$Zr(AcAc)_4$ – TA @ 300℃	$Zr(AcAc)_4$ – TA @ 450℃	$Zr(AcAc)_4$ – 1100 mJ/ cm^2	Interpretation
1	374	-	409	387	$Zr-O$
2	590	-	-	-	$CH_3-C=CH$
3	-	545	-	565	$Zr-O$
4	-	-	-	802	$Zr-O$
5	-	890	928	920	$Zr-O$
6	1064	1044	1065	1032	ρCH_3
7	-	1170	1161	-	$ZrO(CH_3COO)_2$
8	1234	-	-	-	$\nu(C-C)$
9	-	1354	1387	1371	ν_{c-o}
10	1428	-	-	-	$\delta_s CH_3$
11	1556	1513	1547	-	$\nu_{C-O}+\nu_{C-C}$
12	-	1584	1590	1580	$\nu(C-O)$ (acetate)
13	1673	-	-	-	$\nu(C-O)$ (AcAc)
14	1911	2100	2201	1900	$H-O-H$
15	3056	3081	3153	3179	$\nu(O-H)$
16	3450	3400	3420	3444	$\nu(O-H)$

A peak at $802\ \mathrm{cm^{-1}}$ is typically attributed to ν_{Zr-O} and sits within a broadband response linked to $\delta\ (Zr-O-H)$ vibrations from $770-820\ \mathrm{cm^{-1}}$. These are accompanied by the $Zr-O$ vibrations at $920\ \mathrm{cm^{-1}}$ and $387\ \mathrm{cm^{-1}}$. Aside from the adsorbed water, the sample could be stuck in an intermediate between reactions II and III of eq. 6.3 based on the presence of the peaks at $770-920\ \mathrm{cm^{-1}}$. This is further verified by the lack of splitting of the ν_{c-o} antisymmetric mode, since $CH_3COO:\ Zr^{4+}$ is $3:1$ in $Zr(OH)(CH_3COO)_3$ instead of the $2:1$ ratio of the fully decomposed acetate-acetoacetonate complex.

From the samples evaluated so far, the composition of the TA samples and $1100\ \mathrm{mJ/cm^2}$ sample for $Zr(AcAc)_4$ can be linked to the device performance from chapter 5, section 5.3.2. For these InO_x/ZrO_x TFTs, μ_{FE} was double in the TA InO_x/ZrO_x sample compared to the LA sample that used $225\ \mathrm{mJ/cm^2}$ for 1 pulse on the ZrO_x, which is lower than the equivalent fluence on Al (thus a lower temperature rise). Since the sample TA at $300°C$ converts the precursor to a higher extent than the LA sample, fewer organic ligands are present in the dielectric thin film so fewer charge traps exist and mobility is increased. However, in both cases, increased surface and thin film water adsorption due to the $ZrO(CH_3COO)_2$ being hydrophilic means $-OH$ groups form at the dielectric-semiconductor interface where channel formation occurs. This decreases the potential μ_{FE} for both LA and TA samples. Thus, IRSE compositional characterisation can be linked to device performance and unravel the conversion of the metal acetylacetonate precursor to a thin film. The summary of the peaks for ε_2 extracted from the fittings for the stabilised, TA samples and the sample LA with a fluence of $1100\ \mathrm{mJ/cm^2}$can be found in Table 6.4.

Figure 6.5 shows the $\Psi(E)-\Delta(E)$ data and fittings of the other LA $Zr(AcAc)_4$ samples. These are presented alongside the optical constants (ε_1 and ε_2) of the B-Spline. In the $\Psi(E)-\Delta(E)$ data, the red lines depict $\Psi(E)$, the green lines $\Delta(E)$ and the black dashed lines the B-Spline model applied to the data. In the graphs of optical constants, the highlighted areas below ε_2 are used to demonstrate the energy positions of each peak. Table 6.5 summarises the location of each peak from Figure 6.5 and their physical interpretation. The $1200\ \mathrm{mJ/cm^2}$ sample (Figure 6.5a-b) and $1300\ \mathrm{mJ/cm^2}$ sample (Figure 6.5 c-d) share several similarities in the peaks presented, showing lower or comparable amplitudes for ε_2 in the $1300\ \mathrm{mJ/cm^2}$. For the latter, a temperature rise of $435°C$ was achieved in the opto-thermal simulations. Peaks from $3000-3500\ \mathrm{cm^{-1}}$ from the phonon modes of $-OH$ molecules are present, though with lower amplitude than previously.

The peaks of the $1200\ \mathrm{mJ/cm^2}$ and $1300\ \mathrm{mJ/cm^2}$ samples are those that have already been presented in TA samples in Figure 6.4 c-f that demonstrate the presence of $ZrO(CH_3COO)_2$.

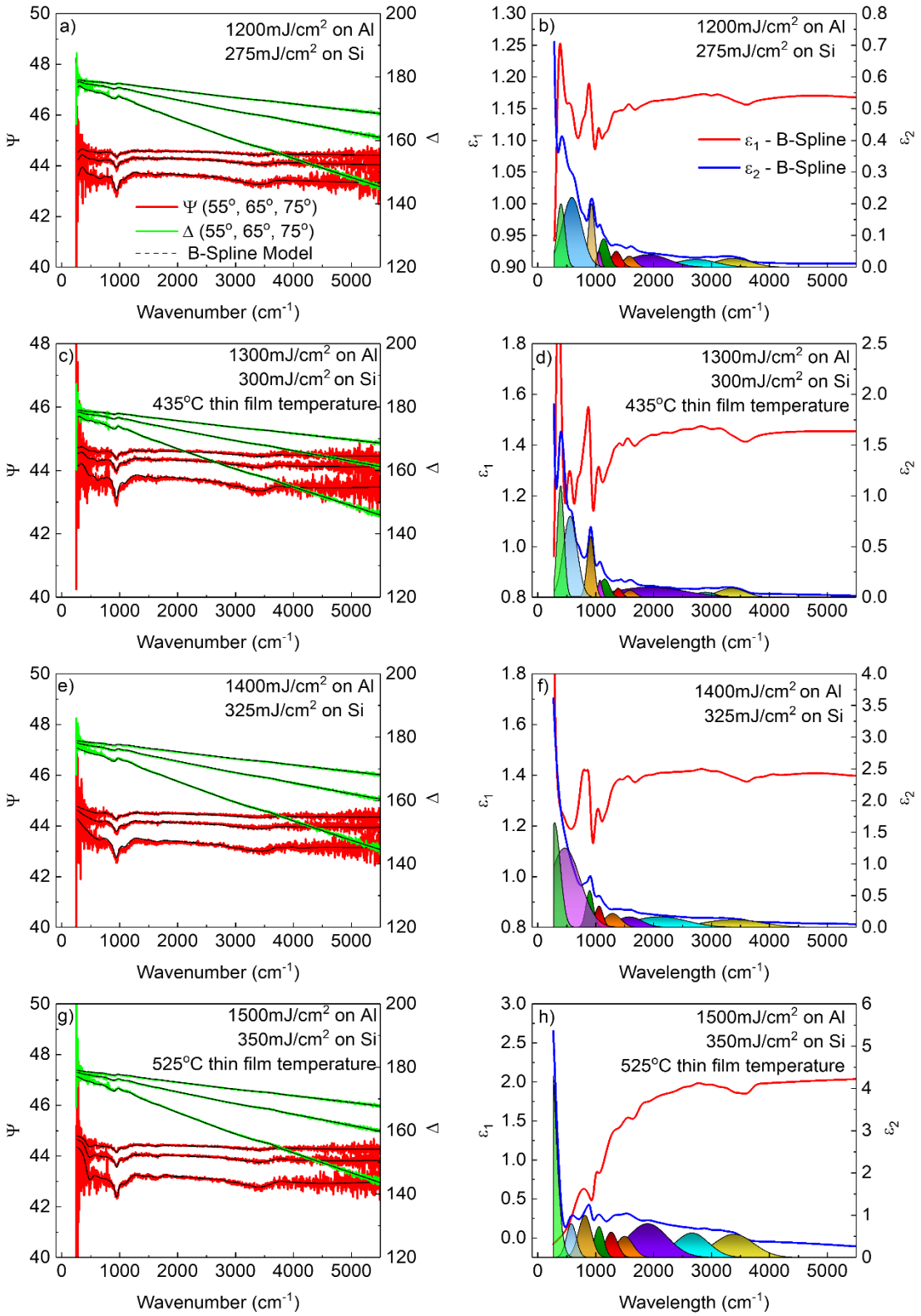

Figure 6.5. Measured $\Psi(E)$ (red lines) and $\Delta(E)$ (green lines) with the B-Spline models (blacked dashed line), and the optical constants extracted from the B-Spline, for various LA $Zr(AcAc)_4$ samples on Al substrate. a) $\Psi(E)$ and $\Delta(E)$ for the $Zr(AcAc)_4$ sample LA with one pulse at $1200\ mJ/cm^2$, with the extracted ε_1 and ε_2 in b). c) $\Psi(E)$ and $\Delta(E)$ for the $Zr(AcAc)_4$ sample LA with one pulse at $1300\ mJ/cm^2$, with the ε_1 and ε_2 in d). e) $\Psi(E)$ and $\Delta(E)$ for the $Zr(AcAc)_4$ sample LA with one pulse at $1400\ mJ/cm^2$, with the extracted ε_1 and ε_2 in f). g) $\Psi(E)$ and $\Delta(E)$ for the $Zr(AcAc)_4$ sample LA with one pulse at $1500\ mJ/cm^2$, with the extracted optical constants in h).

In the case of the $1200\ \mathrm{mJ/cm^2}$ sample, the ρCH_3 mode, $ZrO(CH_3COO)_2$, ν_{c-o} symmetric mode and ν_{c-o} antisymmetric mode peaks reside at wavenumbers of $1056\ \mathrm{cm^{-1}}$, $1137\ \mathrm{cm^{-1}}$ $1355\ \mathrm{cm^{-1}}$ and $1580\ \mathrm{cm^{-1}}$, respectively. $Zr-O$ modes are also presented in similar wavenumbers for the $1200\ \mathrm{mJ/cm^2}$ at $399\ \mathrm{cm^{-1}}$, $587\ \mathrm{cm^{-1}}$ and $927\ \mathrm{cm^{-1}}$. For the $1300\ \mathrm{mJ/cm^2}$ sample, the ρCH_3 mode, $ZrO(CH_3COO)_2$, ν_{c-o} symmetric mode and ν_{c-o} antisymmetric mode peaks reside at wavenumbers of $1072\ \mathrm{cm^{-1}}$, $1153\ \mathrm{cm^{-1}}$ $1387\ \mathrm{cm^{-1}}$ and $1588\ \mathrm{cm^{-1}}$, respectively. $Zr-O$ modes are presented at $393\ \mathrm{cm^{-1}}$, $558\ \mathrm{cm^{-1}}$ and $911\ \mathrm{cm^{-1}}$. In relation to other LA samples and eqs. 6.2-6.4, the results are consistent with each other. An increase in fluence from $1100\ \mathrm{mJ/cm^2}$ to $1200\ \mathrm{mJ/cm^2}$ removes peaks in the $770-820\ \mathrm{cm^{-1}}$ range due to $Zr-O-H$, progressing the conversion process. However, the increase from $1200\ \mathrm{mJ/cm^2}$ to $1300\ \mathrm{mJ/cm^2}$, as it doesn't exceed $450℃$, does not progress the photochemical conversion process any further. Thus, the peak locations stay the same and only the amplitude of ε_2 changes.

For the $1400\ \mathrm{mJ/cm^2}$ sample (Figure 6.5 e-f), there is a marked change in the presented peaks. The broad absorption from $2000-3500\ \mathrm{cm^{-1}}$ can now be fitted with two peaks around $2100\ \mathrm{cm^{-1}}$ and $3400\ \mathrm{cm^{-1}}$, suggesting the removal of some $-OH$ groups. $1057\ \mathrm{cm^{-1}}$ and $1582\ \mathrm{cm^{-1}}$ peaks - for ρCH_3 and ν_{c-o} antisymmetric mode - remain while the $ZrO(CH_3COO)_2$ peak has vanished. There are also now two $Zr-O$ peaks in the far-IR at $287\ \mathrm{cm^{-1}}$ and $463\ \mathrm{cm^{-1}}$, though the $287\ \mathrm{cm^{-1}}$ peak is based on modelling outside of the IRSE measurement range. The $Zr-O$ peak at $895\ \mathrm{cm^{-1}}$ is also present. Finally, the peak at $1290\ \mathrm{cm^{-1}}$ represents the ν_{C-C} mode in the acetate ligand. The modification of $Zr-O$ peaks in the far-IR, removal of some OH groups and the removal of the $ZrO(CH_3COO)_2$ peak demonstrates further progression via partial decomposition of the acetate, though not as far as the temperature of the thin film from opto-thermal simulations would suggest.

For the $1500\ \mathrm{mJ/cm^2}$ sample (Figure 6.5 e-f), the conversion of the sample begins to regress. The broad peak from $2000-3500\ \mathrm{cm^{-1}}$ is now fitted with 3 peaks again, suggesting the hydrophilic nature of the film has allowed adsorption during the LA process. The additional OH bonds further contribute to this at $799\ \mathrm{cm^{-1}}$, where OH stretching occurs when bonded as $Zr-OH$ [392]. Since Zr may be taken up by hydroxyl bonding and $Zr-O$, the acetate ligands may now be freely dispersed, thus peaks at $1057\ \mathrm{cm^{-1}}$ ρCH_3 and $1282\ \mathrm{cm^{-1}}$ for ν_{C-C} that show the acetate is still present. Due to high instrumental noise, the $Zr-O$ peak is difficult to fit. A peak at $211\ \mathrm{cm^{-1}}$ is in close proximity to some far-IR modes reported in the literature [399], but the noise and its existence outside the range of IRSE means it cannot be assured with certainty. Other $Zr-O$ peaks at $602\ \mathrm{cm^{-1}}$ and $887\ \mathrm{cm^{-1}}$ have been previously reported in other $Zr(AcAc)_4$ samples in this work.

Table 6.5. ε_2 peaks for $Zr(AcAc)_4$ samples on Al substrate, with the $Zr(AcAc)_4$ precursor LA with several different fluences. Their corresponding physical interpretations are also given.

No of peak	$Zr(AcAc)_4 - 1200\ mJ/cm^2$	$Zr(AcAc)_4 - 1300\ mJ/cm^2$	$Zr(AcAc)_4 - 1400\ mJ/cm^2$	$Zr(AcAc)_4 - 1500\ mJ/cm^2$	Interpretation
1	-	-	287	211	$Zr-O$
2	399	393	-	-	$Zr-O$
3	-	-	463	-	$Zr-O$
4	587	558	-	602	$Zr-O$
5	-	-	-	799	$Zr-OH$
6	927	911	895	887	$Zr-O$
7	1056	1072	1057	1057	ρCH_3
8	1137	1153	-	-	$ZrO(CH_3COO)_2$
9	-	-	1290	1282	$\nu(C-C)$
10	1355	1387	-	-	ν_{c-o}
11	-	-	-	1476	$\nu(C-C)$
12	1580	1588	1582	-	$\nu(C-O)$ (acetate)
13	2111	2127	2106	1782	$H-O-H$
14	2734	2787	-	2726	$\nu(O-H)$
15	3371	3347	3375	3460	$\nu(O-H)$

Combined with the $Al(NO_3)_3$ sample, there is consistent evidence that fluence providing a peak temperature rise equivalent to the conventional thermal approaches is not sufficient. In the case of the $Al(NO_3)_3$, even fluences producing temperatures close to $450°C$ allow nitrate ions to remain. For $Zr(AcAc)_4$, temperatures of over $500°C$ do not remove acetate

ligands and don't reach the zirconium carbonate product due to decomposition that would be expected. Thus, the number of pulses is of great interest to display these decomposition pathways *via* IRSE.

6.5 Concluding Remarks and Summary

The work demonstrated in this chapter shows IRSE can be used as a novel technique for compositional characterisation of sol-gel precursors ($\mathrm{Al(NO_3)_3}$ and ($\mathrm{Zr(AcAc)_4}$) on Al substrate to gain knowledge on their LA precursor conversion mechanism to functional dielectric thin films, which can then be linked to the performance of TFTs. Opto-thermal simulations were used to determine the LA fluence window to be applied for each precursor (of different chemical pathways) on Al substrate. Fittings involving both oscillator models and B-Splines were used to determine the most accurate (and rapid) extraction of optical constants relating to the composition of the thin films. Based on comparisons of B-Spline and the oscillator models when applied to $\mathrm{Al(NO_3)_3}$, either can be used to determine the organic residues leftover in the mid-IR.

For $\mathrm{Al(NO_3)_3}$, the stabilised and TA samples were consistent with the literature, with the $450℃$ leading to a full aluminium oxide hydroxide compound and removal of undesired organic groups. In contrast, none of the LA $\mathrm{Al(NO_3)_3}$ samples led to full conversion with any of the fluences on single pulses as nitrate peaks remained throughout each sample, despite achieving high temperatures of above $400℃$ that previous literature has shown can lead to conversion into a thin film. Via IRSE, this has demonstrated the photochemical conversion process from a nitrate precursor to a thin film via LA, and how it differs to the typical TA process.

For $\mathrm{Zr(AcAc)_4}$, stabilised and TA sample composition agreed with the findings of the literature when characterised with IRSE. The incremental change in composition of the LA $\mathrm{Zr(AcAc)_4}$ thin films could be measured and explained via IRSE, attributing several peaks to a complex multi-stage decomposition process. It was confirmed none of these samples achieved photochemical conversion to a thin film, since acetate ligands from the decomposition process remained. For $1100\ \mathrm{mJ/cm^2}$ on Al – a LA fluence comparable to the LA fluence for dielectrics in TFTs presented earlier in this thesis – the larger ratio of acetate ligands and adsorbed water in the $\mathrm{Zr(AcAc)_4}$ thin film that were determined via IRSE were linked to the low μ_{FE} in the TFTs due to increased charge traps in the film and at the dielectric-semiconductor interface. As well as characterising an acetylacetonate precursor composition via IRSE, this is the first time this type of analysis has been utilised to link composition to TFT performance.

7. Schottky diodes fabricated via adhesion lithography and laser patterning

This chapter was completed in collaboration with King Abdullah University of Science and Technology, Saudi Arabia. NTU (Matthew Spink, the author of this thesis, with supervision from Dr Nikolaos Kalfagiannis and Dr Demosthenes Koutsogeorgis) consulted the laser patterning stage of this work, processing samples for KAUST to continue their experimental work. KAUST subsequently produced Schottky diodes and their electrical characterisation. All of the above are featured in this chapter.

While previous work focussed on laser annealing and TFTs, photonic processing has other pathways to be implemented into modern electronics. Schottky diodes are key in the implementation of RFIDs, which are vital to the IoT paradigm and have faced development challenges with large-area RFIDs at ultra-high operating frequencies. This chapter demonstrates the use of laser ablation as a substitute to photolithography to pattern substrates and thin films using the adhesion lithography (a-lith) fabrication methodology to pave the way to ultra-high frequency RFIDs. Several laser sources were trialled for laser patterning on borosilicate glass substrates with $100\ \mathrm{nm}$ Al electrode acting as metal 1 (M1), with a $532\ \mathrm{nm}$ laser source firing through the backside of the substrate being preferential. Several laser conditions were tested, with visual inspection under a microscope to investigate the effect on the glass substrate. The Al/Glass samples then underwent laser patterning with optimised conditions and were characterised with transmission spectroscopy, AFM and optical profilometry to elucidate the effects of the metal ablation on the substrate. Schottky diodes were subsequently fabricated via the a-lith manufacturing process using Au and ZnO as metal 2 (M2) and the semiconductor respectively, with an octadecylphosphonic acid (ODPA) SAM. Devices underwent electrical characterisation for rectification ratios and cut-off frequency measurements. Devices showed a range of rectification ratios while extrinsic and intrinsic frequency exhibited two different behaviours that resulted in GHz frequency operation.

7.1 Selecting Laser Source

Several laser sources were considered for ablating aluminum (Al) from borosilicate glass substrates. An excimer laser, utilized in previous experiments (discussed in Chapter 5), offers a highly uniform spot size via its integrated optical delivery system, and its wavelength ensures sufficient absorption within the Al for effective ablation. However, the borosilicate glass also absorbs this wavelength, inducing undesirable thermal effects and excessive nanostructure formation at the substrate/Al interface. This compromises the a-lith methodology due to impaired SAM and M2 adhesion.

7. Schottky diodes fabricated via adhesion lithography and laser patterning

To mitigate substrate-induced nanostructure, longer wavelengths were investigated using Trumpf DPSS lasers (532 nm and 1064 nm). These wavelengths enhance Al absorption while minimizing borosilicate glass absorption. Furthermore, the transparency of borosilicate glass to 532 nm light enables backside irradiation, potentially reducing surface damage and nanogap disruption during a-lith processing. However, the Trumpf lasers lack the advanced optics of the excimer laser, resulting in an unfiltered Gaussian beam and uneven heat distribution.

Detailed laser parameters for both the excimer and Trumpf DPSS lasers are provided in the experimental methodology (Chapter 3, Sections 3.2.1 and 3.2.2). To systematically screen processing parameters, the Trumpf TruTops Mark CAD software with its integrated navigator grid was employed. This navigator grid software concurrently and systematically varies laser parameters across a series of square spots (Figure 7.1 shows an example for 532 nm). Laser power was generally held constant to reduce experimental variables, while scan speed and repetition rate were maintained at a constant hatch spacing at the pre-defined focal point (verified via focus tests).

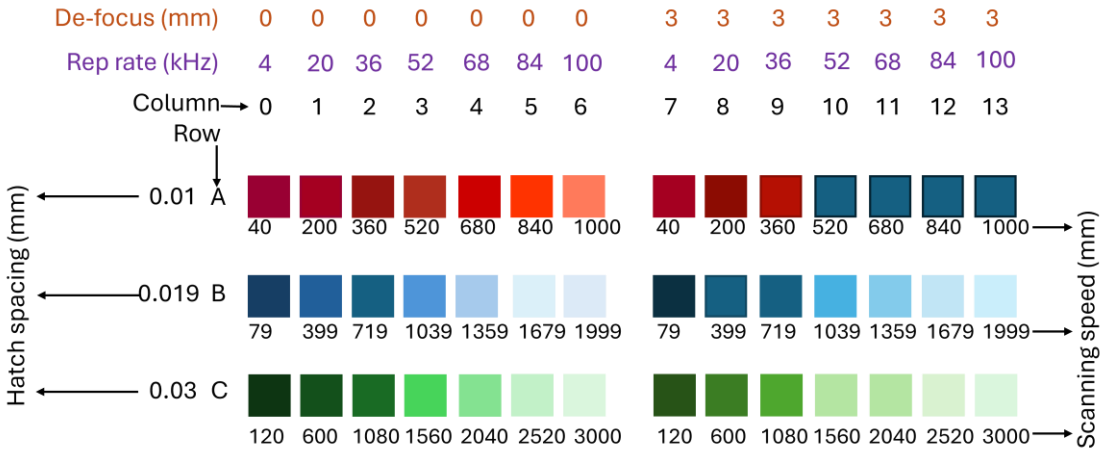

Figure 7.1. A recreation of the navigator grid used with the 532 nm laser, created by the CAD software to systematically and rapidly screen laser parameters. The first row of number (from the top of the figure) indicates the defocus (in mm) added during processing, the second row the repetition rate in kHz and third row the column number. The numbers beneath each square indicate the scan speed (n mm/s). Each row represents a different hatch spacing (in mm), attached to a row letter on the far left of the grid.

To investigate the influence of size and geometry on diode characteristics, a custom CAD design (Figure 7.2a) was employed. This design, shown from the backside perspective (as most samples were backside-irradiated), facilitated testing of diodes with varying dimensions and configurations. Figure 7.2b presents a representative laser-patterned sample fabricated using this CAD design. The CAD design incorporated six repeated rows, each featuring a series of 2 mm, 1 mm and 0.5 mm diameter circles, squares with 2 mm, 1 mm and 0.5 mm width,

diamonds of $1\,\mathrm{mm}$ and $0.5\,\mathrm{mm}$ width and rectangles of $1\,\mathrm{mm} \times 0.5\,\mathrm{mm}$ in different orientations. A $0.5\,\mathrm{mm}$ gap separated each ablated feature. The remaining space at the sample's base was used for laser-scribing sample identification.

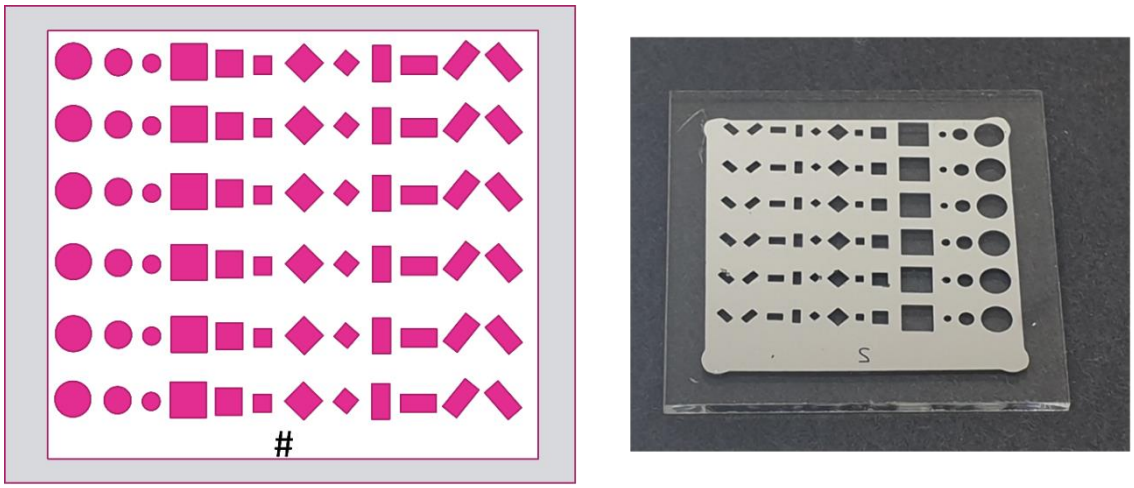

Figure 7.2. a) Schematic of the CAD design used with the Trumpf lasers. The design utilises several different geometries in different sizes due to their effects on diode performance, with each ablated area separated by a $0.5\,\mathrm{mm}$ gap. The number is scribed on the bottom. Depending on if the sample is irradiated on the frontside or the backside, the design on the ablated film may be reversed. b) An example of a sample with the CAD design, after ablation via laser irradiation through the backside (since the design is inverted).

7.1.1 248 nm Excimer Laser

The $248\,\mathrm{nm}$ excimer laser was first tested via irradiation from the frontside of the sample (Al side). The fluence and number of pulses range were dictated by a series of preliminary experiments before proceeding. This also included tests for ablation via the frontside and backside, with the frontside ablation being evidently superior. Through the backside, fluences and number of pulses as high as $5000\,\mathrm{mJ/cm^2}$ and 50 pulses (at $10\,\mathrm{Hz}$ repetition rate) were required to only partially ablate the film with detrimental effects to the substrate. Table 7.1 shows the LA parameters tested for ablation from the Al side using the $248\,\mathrm{nm}$ excimer laser. Only a $1\,\mathrm{Hz}$ repetition rate was used. Fluences were varied from $800 - 1600\,\mathrm{mJ/cm^2}$ in steps of $100\,\mathrm{mJ/cm^2}$, with anywhere from $1 - 20$ pulses. Each sample contains a 5×5 grid of square laser spots that are $2.4\,\mathrm{mm} \times 2.4\,\mathrm{mm}$. Despite parameter optimisation, the numerous laser processing conditions necessitated an initial pragmatic approach to characterisation, employing visual inspection using a Brunel SP600 microscope.

Table 7.1 List of conditions used to test the fluence and number of pulses for the $248\ \mathrm{nm}$ excimer laser for the ablation of Al on borosilicate glass.

Fluence ($\mathrm{mJ/cm^2}$)	Number of Pulses	Rep Rate (Hz)
800	1, 2, 3, 5, 10, 20	1
900	1, 2, 3, 5, 10, 20	1
1000	1, 2, 3, 5, 10, 20	1
1100	1, 2, 3, 5, 10, 20	1
1200	1, 2, 3, 5, 10, 20	1
1300	1, 2, 3, 5, 10	1
1400	1, 2, 3, 5, 10	1
1500	1, 2, 3, 5, 10	1
1600	1, 2, 3, 5, 10	1

Figures 7.3a and 7.3c show representative samples processed using various fluences and pulse numbers. The corresponding schematic diagrams are shown in Figures 7.3b and 7.3d. Complete ablation required fluences of $1500\ \mathrm{mJ/cm^2}$ or higher for single pulses, and above $1100\ \mathrm{mJ/cm^2}$ for three pulses; higher pulse numbers allowed ablation at almost any fluence. However, several unusual ablation phenomena were observed, independent of apparent Al structural variations. Incomplete ablation (e.g., $900\ \mathrm{mJ/cm^2}$ with two or three pulses) exhibited a bottom-to-top ablation pattern, indicating uneven material removal across the laser spot. This effect was consistent across the entire Al film. Furthermore, post-ablation marks, resembling the ablation pattern, were consistently observed on the glass substrate (Figures 7.3e and 7.3f). The origin of these marks is unknown and has not been previously reported in the literature or observed in similar experiments at NTU.

It was postulated that these marks could potentially be removed via ensuring the mask, iris and mirror tilt are completely aligned and cleaned. The uneven ablation and marks are of massive concern to the fabrication of the Schottky diodes via a-lith, since the ablated area will have uneven Au deposition and potentially poor peel-off. The visible light microscope was used to elucidate the difference between these marks and the glass, as well as investigate the quality of the laser spot edge. The formation of a smooth and even edge is also of importance, since this is where the nanogap will form during the fabrication of the Schottky diode. Figure 7.4a shows a close-up of the laser spot for $1300\ \mathrm{mJ/cm^2}$ with 10 pulses, with a circled area showing the area under scrutiny, towards the middle and bottom the laser spot to capture each distinct region of the laser spot. Figure 7.4b shows the microscope image of this area. At the edge (blue circle), several gradients can be seen moving towards the edge. The green circled area shows the grey area, which is smoother with some levels of patchiness. This is speculated to be the glass surface itself. The red circled area shows the darker area of the spot, which has large clusters of features emerging. These features are also seen in parts of the edge from high heat.

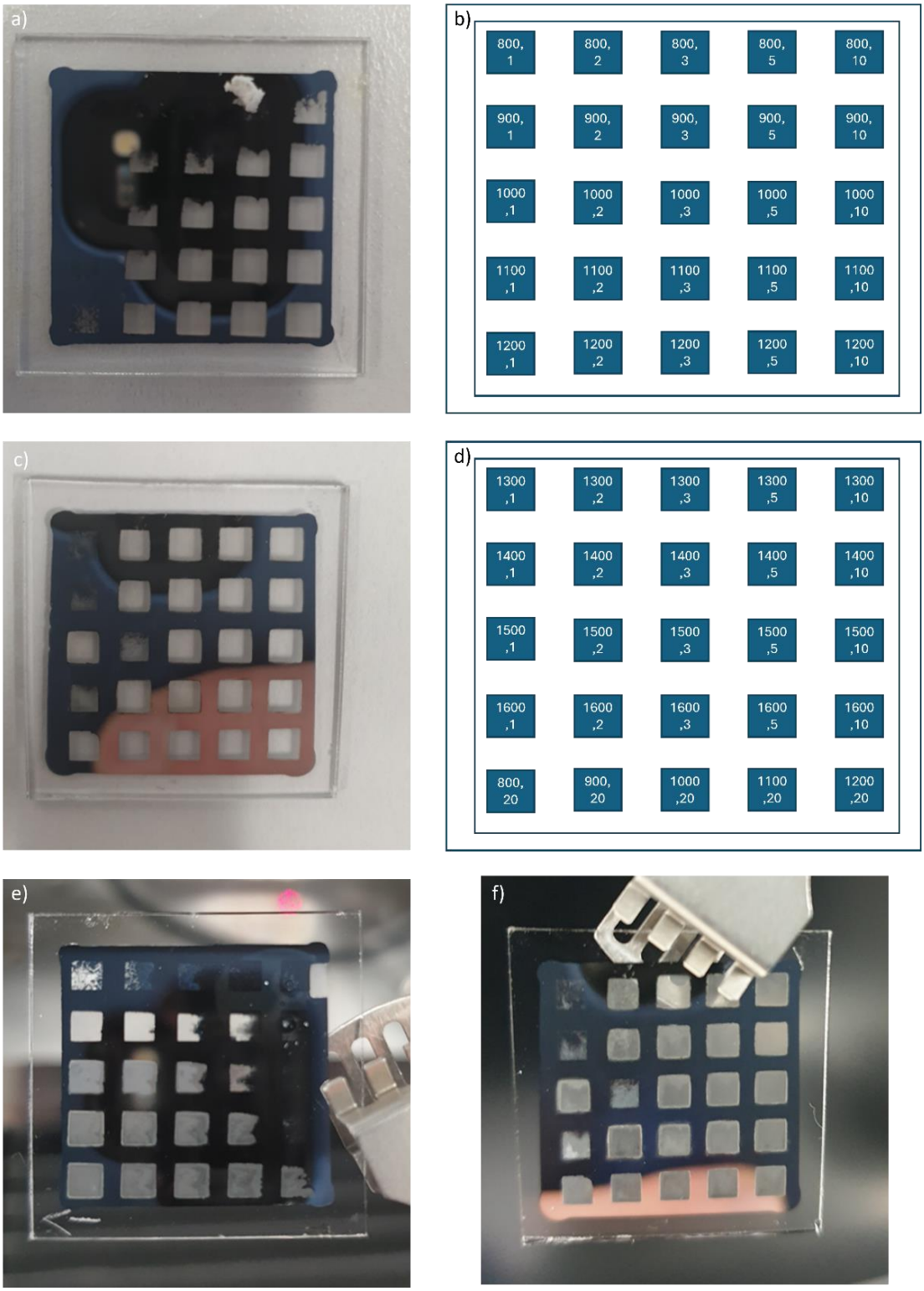

Figure 7.3 a) Picture of the one of the samples used to investigate the effects of one set of fluence and number of pulses on the laser patterning of Al on glass. b) Schematic for the processing conditions for the sample in a). The first larger number indicates the fluence, while the second number is the number of pulses. c) picture of the second sample for testing fluence and number of pulses on the laser patterning of Al on glass. d) Schematic for the processing conditions for the sample in c). Pictures of both samples rotated $90°$ and on a different background to demonstrate and elucidate the strange marks on the glass substrate are shown in e) and f).

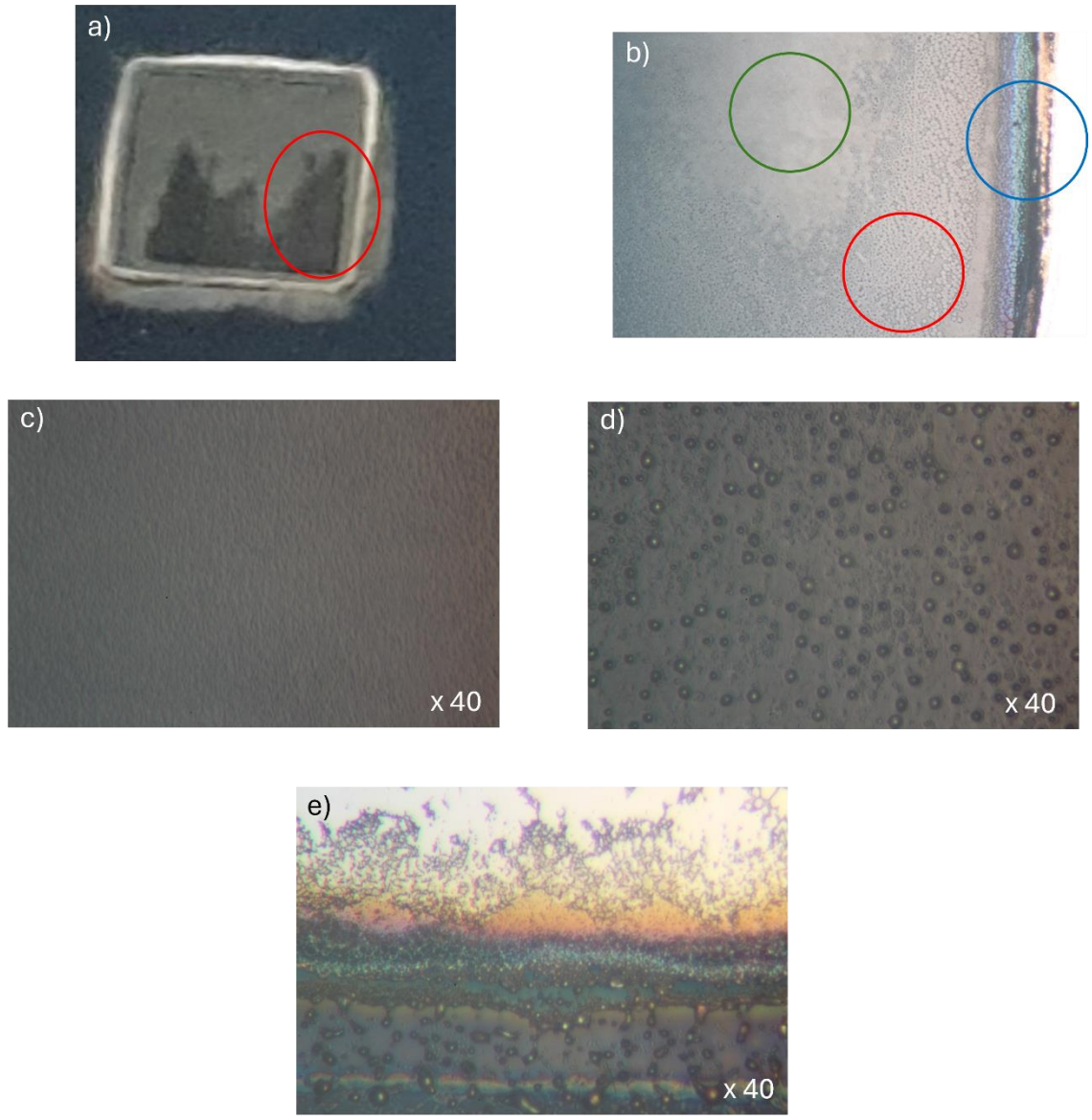

Figure 7.4 Investigating the impact of $248\ \mathrm{nm}$ excimer laser on the borosilicate glass surface. a) Picture of the laser spot from $1300\ \mathrm{mJ/cm^2}$ with 10 pulses, with the area of interest for the microscope highlighted by the red circle. b) The area of interest under a microscope at $\times\ 5$ magnification. The image reveals the glass surface showing three distinct types of surface. c) The smoother area (green circle in b) at $\times\ 40$ magnification. d) The structured area (red circle in b) at $\times\ 40$ magnification. e) The edge of the ablated area (blue circle) at $\times\ 40$ magnification.

The bottom (darker area) of the spot ablated before the top (lighter area) of the spot during LA. Thus, it is expected that these dots represent roughness and nanostructure introduced to the substrate, due to overexposure to laser irradiation. Further microscope images at higher magnifications were taken. Figure 7.4c shows the seemingly smoother area at $\times\ 40$ magnification objective. The lack of features suggests this area of the glass has far lower nanostructure, though it cannot be concluded if there is no roughness on the glass surface. The features in Figure 7.4d at $\times\ 40$ magnification objective show different levels of brightness, potentially suggesting nanostructure that is scattering light to differing extents. These features

are not in present in Figure 7.4c, confirming the large inhomogeneity across the sample. Non-uniform substrate topography, resulting from the laser ablation process, could negatively impact M2 deposition and peel-off during a-lith fabrication. Surface roughness can enhance thin-film adhesion in certain circumstances [400] which makes subsequent films difficult to remove during peel-off, as well as even uneven application of whichever peel-off process is used. Previous a-lith processes (KAUST method) employed photolithography and wet etching, yielding highly uniform patterns with acceptable roughness [264]. However, Figure 7.4e (at $\times 40$ magnification) highlights a region of concern at the ablation spot edge, showing a high density of the nanostructures depicted in Figure 7.4d, accompanied by significant gradients and multiple interfaces between the processed and unprocessed Al. Such non-uniformity, particularly if the resulting gap exceeds previously observed dimensions, would likely disrupt the patterning process and severely compromise Schottky diode performance. This drastic temperature gradient at the ablation edge is likely a consequence of the laser's thermal effects; this is evident in Figure 7.4a, where significant light scattering from the edge is visible under microscopic illumination.

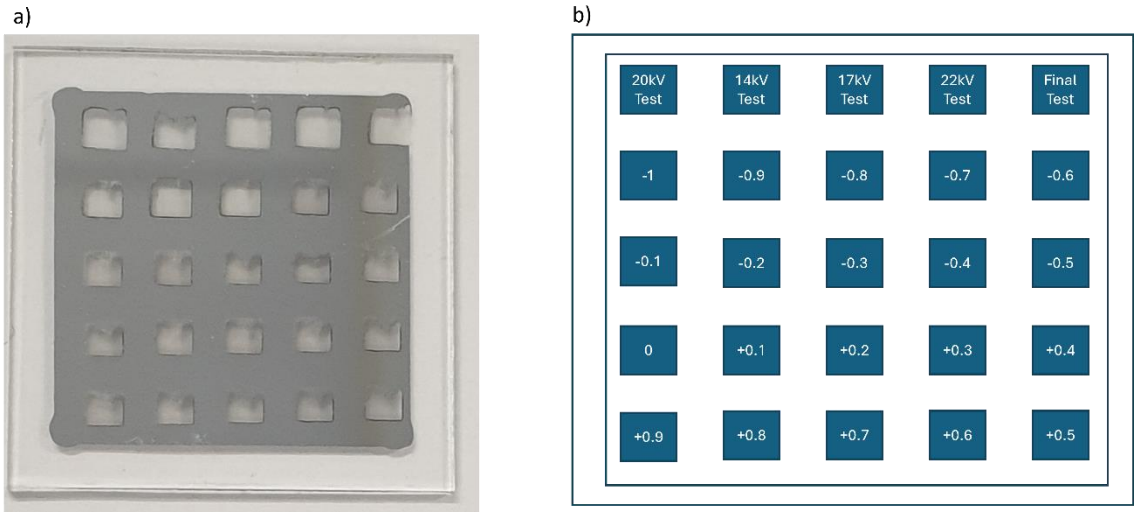

Figure 7.5 a) Picture of the sample used to investigate the effect of focus and the laser optics, attempting to remove the strange marks on the glass surface after ablation. b) Schematic of the laser conditions used. The top row is a series of test spots before proceeding. The other rows show the level of change (in mm) of the z-alignment of the excimer laser stage relative to the pre-determined point of focus.

To assess the feasibility of achieving uniform ablation, a series of experiments were conducted to optimize laser parameters and spot uniformity. A specific laser condition ($900\ \mathrm{mJ/cm^2}$, 10 pulses) was selected to partially ablate the Al film, minimizing excessive thermal effects that might obscure the impact of focal changes on image quality. Figure 7.5a shows the sample and its schematic. While improved spot uniformity was achieved by adjusting the z-axis alignment, the nanostructure and surface marks observed previously (Figure 7.4)

persisted. Given the consistent observation of uneven ablation and substantial nanostructure on the glass substrate, regardless of excimer laser parameter optimization, the $248\ \mathrm{nm}$ excimer laser was deemed unsuitable for Schottky diode laser patterning.

7.1.2 532 nm Laser

The navigator grid (defined in section 3.2.2) from Figure 7.1 was imposed onto the Al/glass sample via irradiation through the backside of the substrate after defining focus at a sub-mm level. Figure 7.6a and 7.6b shows the samples with the navigator grid as viewed from the frontside of the sample, creating a mirror image of the navigator grid. Since full ablation without nanostructure is what is sought, conditions with opaqueness or translucency due to incomplete ablation (A2-A6, B2-B6, C3-C6) or nanostructure to the point of etching (A7, A8, B7, B8) could be eliminated from the optimisation process.

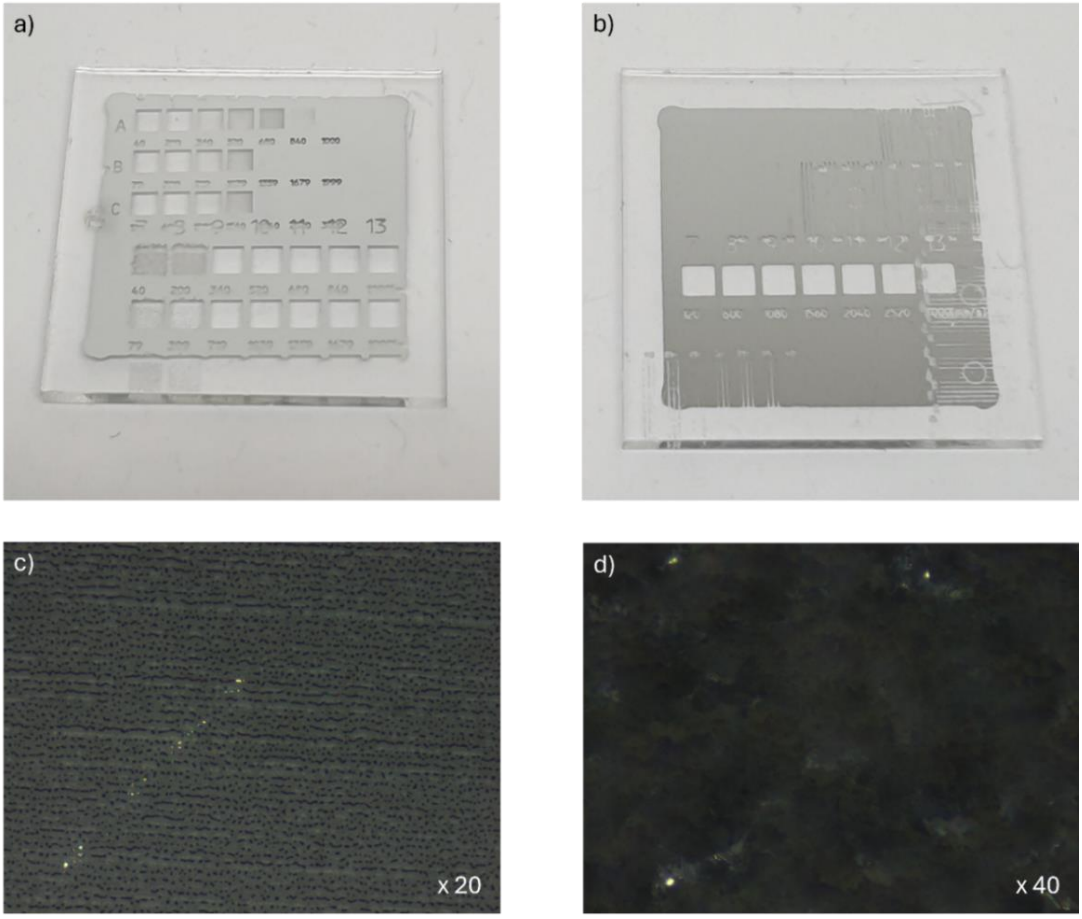

Figure 7.6 Pictures of samples used to test the $532\ \mathrm{nm}$ navigator grid. a) Sample with laser conditions A0 – A6, B0 – B6 and C0 – C6 on the top half of the sample, with laser conditions A7 – A13 and B7 – B13 on the bottom. b) Sample with laser conditions C7 – C13. Various laser conditions clearly show light scattering from roughness or even more severe damage to the glass. c) A microscope image at $\times\ 20$ magnification of laser condition A2, shoeing an example of incomplete ablation of the Al thin film. d) A microscope image at $\times\ 40$ magnification of laser condition B7, exemplifying excessive processing and nanostructure in the glass substrate.

In the case of exaggerated examples of incomplete ablation, the large reflectivity of Al returns a bright and featureless picture. The appearance of these laser conditions in microscope images and their extreme points of failure for application to the a-lith process can then be used to eliminate further conditions, since certain trends emerged that made this simple first approach of visual inspection adequate. Figure 7.6c shows an example of a more minor example of incomplete ablation from laser condition A2 which becomes more obvious when compared to laser parameters that more blatantly fully ablate the Al thin film. The hatch pattern is more obvious, as well as highly reflective parts of the image on the left-hand side suggesting Al remains. Thus, these features can be linked to a visual appearance of a laser condition like that of A2 in Figure 7.6a, which is slightly more translucent. Figure 7.6d shows a $\times\, 20$ magnification objective of the laser condition B7, which shows a far darker colour palette and irregular pattern to the extent the hatch is obscured. This can then be linked to undesired nanostructure or damage in the glass. The edge quality for where the nanogap is formed is also of critical importance.

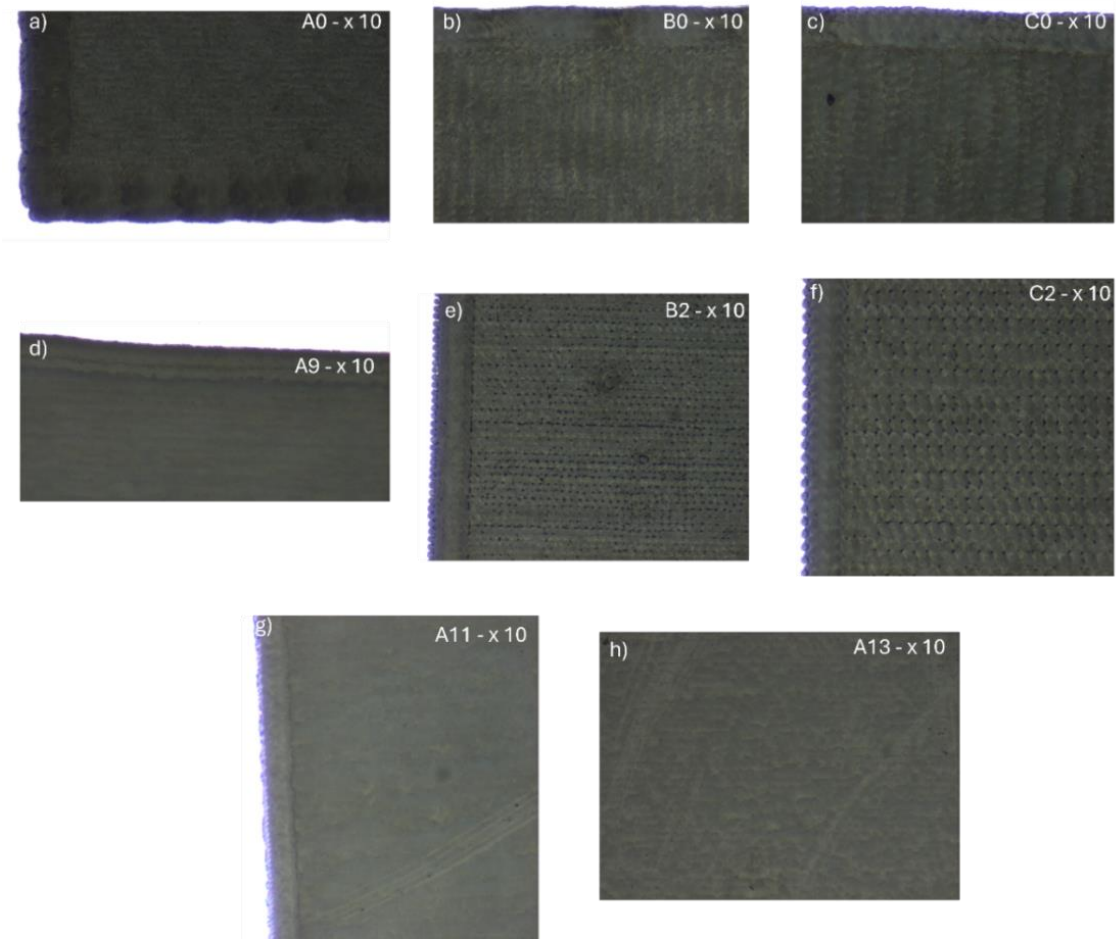

Figure 7.7. Microscope images of samples used to evaluate the $532\ \mathrm{nm}$ laser for metal ablation on glass. Samples are labelled according to their designation in the navigator grid, with the laser parameters described in Table 7.1. Each condition was taken with a $\times\, 10$ objective magnification. a) Laser condition A0. b) Laser condition B0. c) Laser condition C0. d) Laser condition A9. e) Laser condition B2. f) Laser condition C2. g) Laser condition A11. h) Laser condition A13.

The remaining conditions were evaluated *via* optical microscopy, focusing on ablation quality and edge definition. This process aimed to further reduce the number of conditions proceeding to advanced characterisation and device fabrication. Some laser parameters immediately demonstrated non-ideal impact on the glass substrate. Figure 7.7a shows a section of the glass after experiencing the laser condition A0 ($4\ \mathrm{kHz}$ repetition rate, $0.01\ \mathrm{mm}$ hatch spacing, $40\ \mathrm{mm/s}$ scan speed with 100% power), showing a large variation and faltering in the edge of the ablated area while also appearing darker which is linked to increased damage of the glass surface. As previously discussed, this can be linked to excessive irradiation that is damaging the glass as well as gaps far larger than the nanogap desired. The above observations and conclusions can be similarly applied to laser conditions B0 (Figure 7.7b), C0 (Figure 7.7c), and A9 (Figure 7.7d), whose parameters are described in Figure 7.1. Other conditions such as B2 (Figure 7.7e) and C2 (Figure 7.7f) swayed the other way, where the laser conditions were not effective in leaving well-defined edges due to low laser flux. The conditions A11 and A13 (Figure 7.7g and Figure 7.7h) produced a combination of the two, where ablation of the edge was incomplete but the ablated area showed inconsistent structure across the surface. Overall, this eliminates 26 different sets of laser parameters at this stage.

7.1.3 1064 nm Laser

The same approach as the $532\ \mathrm{nm}$ laser was taken for the $1064\ \mathrm{nm}$ laser, using a different navigator grid than that of Figure 7.1 but still processing through the backside. Figure 7.8 shows a schematic of the navigator grid.

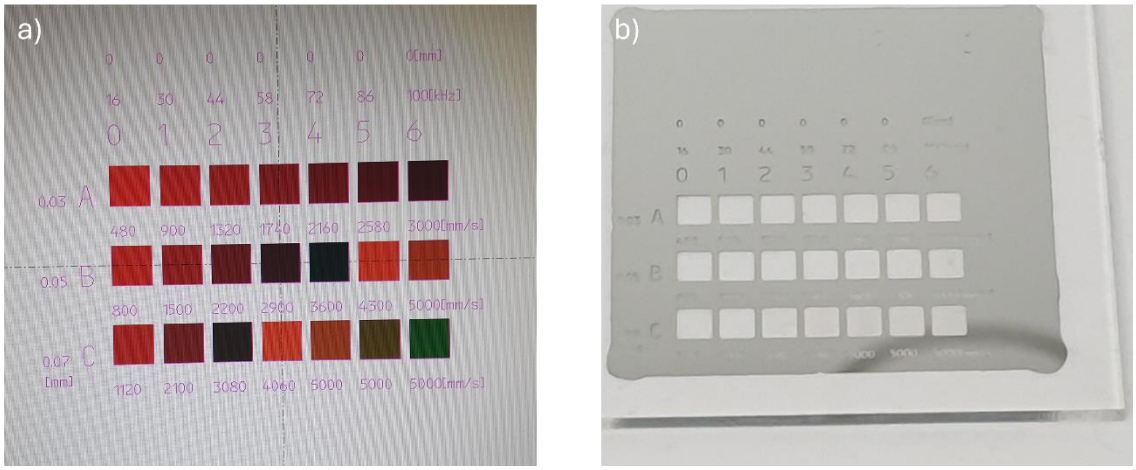

Figure 7.8 Production of the $1064\ \mathrm{nm}$ laser ablation test sample. a) Navigator grid used on the Al/Glass sample. b) Picture of the resulting sample after processing using the navigator grid.

The $1064\ \mathrm{nm}$ laser doesn't use a defocus as standard, which limits the number of conditions used. Visually, none of the sets of laser parameters caused ablation of the glass substrate or milkiness, thus microscope images were necessary for all of the spots to determine the effect of laser parameters on ablation quality. It's also noteworthy that the processing with

the 1064 nm produced a lot of debris after processing, which needed to be cleaned off using DI water and IPA. As removal of debris was necessary to view the ablated areas, it is unknown how the use of solvent affects the ablated area after processing. From the images of rows B and C, a clear limit on hatch spacing while varying other parameters emerges, as there is clearly Al left over between the laser spots.

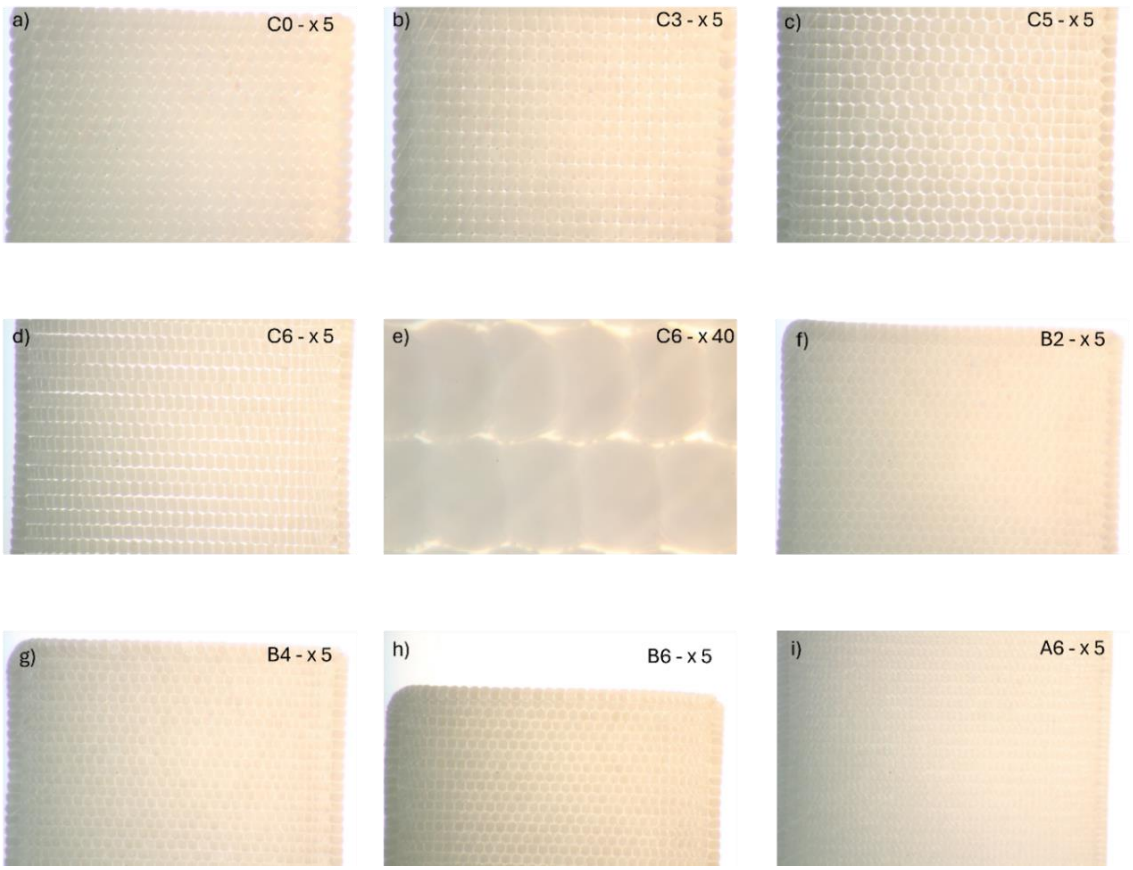

Figure 7.9. Microscope images of sample used to determine the effectiveness of the 1064 nm laser for laser patterning via metal ablation. The laser parameter designation from the navigator grid, along with the microscope objective magnification, are indicated in the top-right of this image. Row C is contained within a-e, row B in f-h and i) an example of a condition for row A.

Figure 7.9 a-e shows various conditions of row C from the 1064 nm sample at × 5 objective magnification. As the frequency and scan speed increase throughout row C (Figure 7.9a-d), white gaps indicating reflection from the Al appear, as well as poorly defined edges that would increase nanogap size variability. A high magnification image of this (Figure 7.9e) shows that the hatch spacing horizontally is too large, thus overlap of each row vertically is not sufficient to cover all the surrounding area. This occurs in row B, but only for medium to high frequencies and scan speeds. Row A does not show this issue, with the highest frequency and scan speed still allowing a sharp edge and complete ablation of the irradiated area. For the 1064 nm laser, the increased hatch spacing is necessary due to a larger spot size. The 532 nm laser uses 25 μm spot compared to a 45 μm spot for the 1064 nm, thus bigger spacings are

used for theoretically the same coverage. However, the bigger spot sizes become increasingly difficult to tesselate and overlap, resulting in the leftover Al. Because of this intrinsic requirement, making the $1064\ \mathrm{nm}$ optimised for the a-lith process is extremely restrictive.

7.2 Optimisation of 532 nm laser

Based on the results of section 7.1, the $532\ \mathrm{nm}$ laser was selected as the source, with the Al irradiated through the backside of the substrate to reduce damage and any resulting microstructure and disruption to the nanogap. To determine the correlation between the laser parameters, substrate morphology and Schottky diode $\mathrm{I-V}$ characteristics and frequency, select conditions from the navigator grid were used to fabricate Schottky diodes to begin to understand the relationship between these variables. The selection of conditions was based on microscope inspection of some of the samples for ablation quality, as well as ensuring a spread of high frequency, high scan speed and low frequency, low scan speed laser conditions. As before, power was kept constant. The location of the eight conditions (whose parameters are described in Table 7.2) across the samples were systematically varied so they occupied different spaces across the samples – at the top, middle and bottom of the Al thin film. Since evaporated Al films may have shadows or taper towards the edges, as well as have different grain sizes that affect the distribution of thermal load, it is essential to accommodate for these differences that may skew the results. Section A1 of the appendix shows the schematics and tables for how these conditions were distributed across the four samples.

Table 7.2. A list of conditions that were trialled with a $532\ \mathrm{nm}$ Nd:YAG laser via a navigator grid. The grid systematically varies the scan speed, repetition rate and hatch spacing in and out of focus as an initial way to screen conditions for a process. The last column shows the ratio between scan speed and repetition rate, which is preserved to closely match the hatch spacing along the line of scanning.

Nav Grid Indicator	Hatch Spacing (mm)	Scan Speed (mm/s)	Rep Rate (kHz)	Power (%)	De-focus (mm)	Scan Speed/Rep Rate (mm)
A10	0.010	520	52	100	3	0.01000
B1	0.019	399	20	100	0	0.01995
B9	0.019	719	36	100	3	0.01997
B11	0.019	1359	68	100	3	0.01999
B12	0.019	1679	84	100	3	0.01999
C1	0.030	600	20	100	0	0.03000
C7	0.030	600	20	100	3	0.03000
C11	0.030	2040	68	100	3	0.03000

7. Schottky diodes fabricated via adhesion lithography and laser patterning

Figures 7.10a shows the samples after the peel-off stage for the $\mathrm{SAM/Au}$. There are large regions of unremoved material in the majority of the samples, including near the sites of nanogap formation. During processing, some of the laser parameters etched the ablated areas, immediately creating microstructure. Figure 7.10b shows microscope images of the samples after the peel-off stage, demonstrating the disruption caused by laser parameters. B9 and C7 that are described in Table 7.2 were the most aggressive. The issue of peel-off has been tested on early laser ablated samples with a variety of tapes and adhesives including first contact glue, label sticker, Sellotape and electrical tape. Electrical tape was found to be preferred, as it was not overly aggressive towards removing the Al in addition to the $\mathrm{SAM/Au}$ (though this is dependent on operator usage).

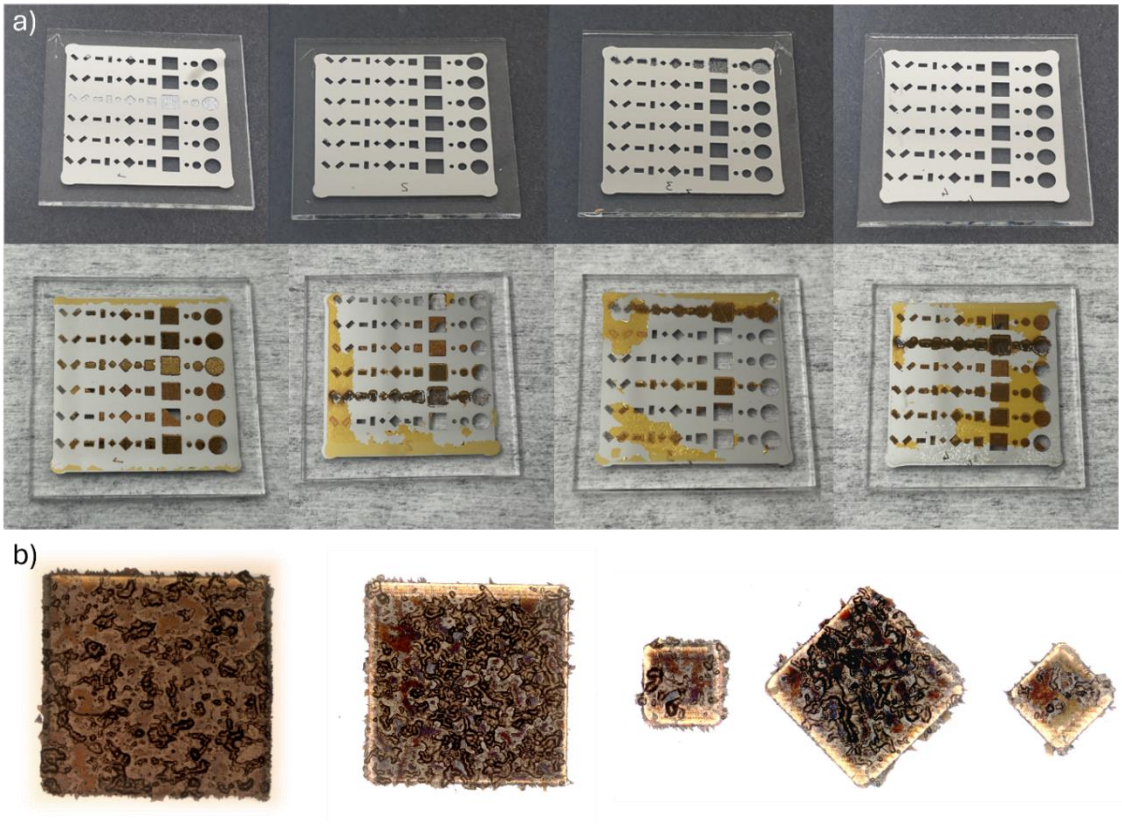

Figure 7.10. a) Photos of the samples after the $\mathrm{SAM/Au}$ deposition and the subsequent peel-off stage using electrical tape. While sample 1 shows a reasonable peel-off, samples 2-4 show swathes of leftover Au remaining that negatively affect nanogap formation and diode performance. b) Microscope images of the areas after $\mathrm{SAM/Au}$ deposition and the peel-off process. The images show how the Au deposition and remaining material are heavily disrupted due to the laser processing.

After the peel-off stage, ZnO was spin-coated onto the $\mathrm{Al-Au}$ co-planar electrodes to complete fabrication of the Schottky diodes. These diodes were then electrically characterised. Discussion of these $\mathrm{I-V}$ characteristics at each condition on each sample takes place on a case-by-case basis, before assessing any trends among the laser parameters and device quality.

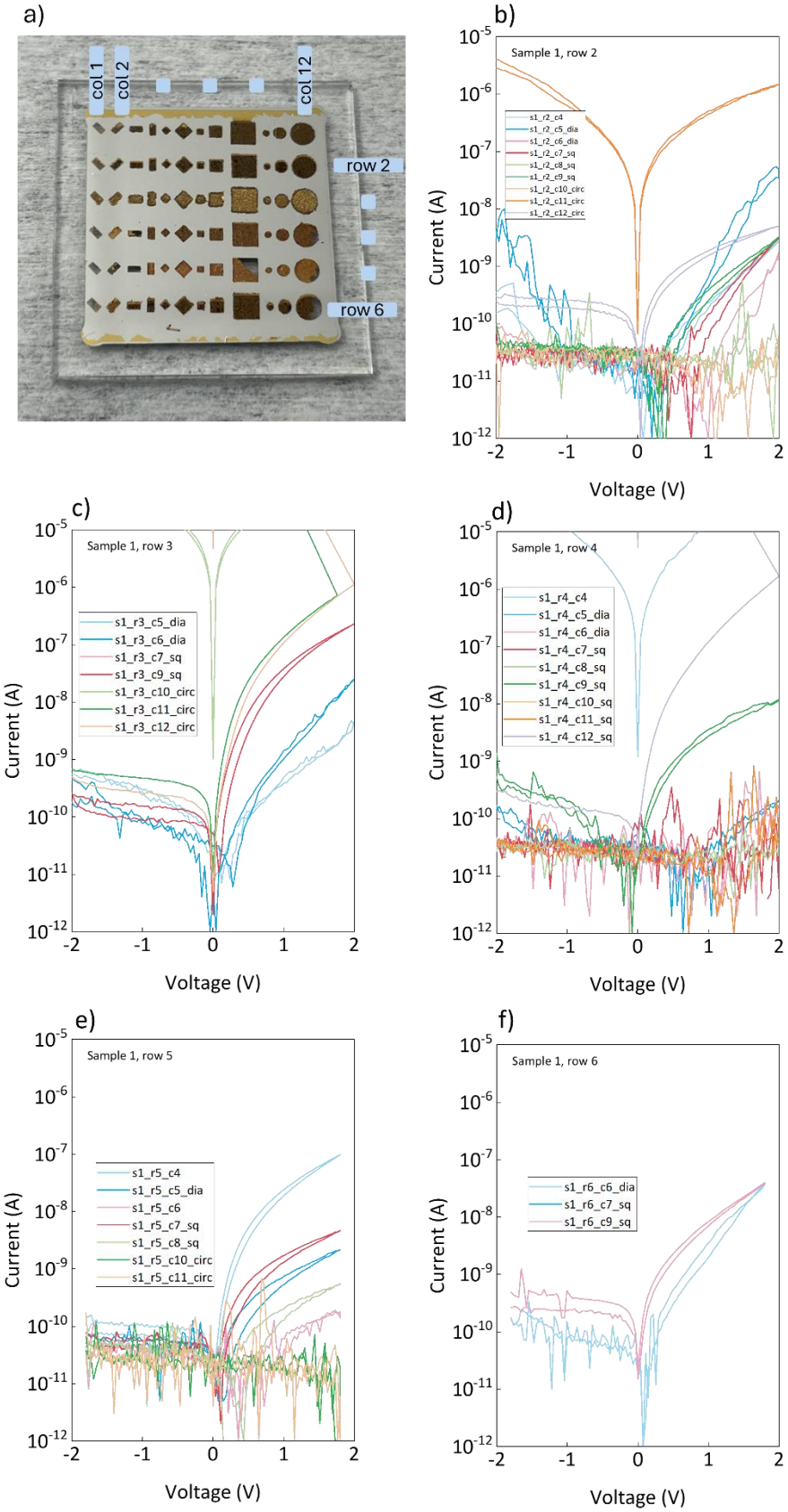

Figure 7.11. Sample 1 of the Schottky diodes fabricated via laser patterning using the $532\ \mathrm{nm}$ laser. a) Picture of the sample after SAM/Au deposition and peel-off, before semiconductor deposition. The rows and columns, corresponding to those measured and shown in subsequent $\mathrm{I}-\mathrm{V}$ characteristics, are indicated. The $\mathrm{I}-\mathrm{V}$ characteristics of the diode after semiconductor deposition are of b) row 2, c) row 3, d) row 4, e) row 5 and f) row 6.

7. Schottky diodes fabricated via adhesion lithography and laser patterning

Figure 7.11 shows the $\mathrm{I}-\mathrm{V}$ characteristics of each row of sample 1 alongside its picture. The column number indicates each shape, while the row applies to the condition, which is restated here. Row 1 had no working devices to be tested. Row 2 (B1, Figure 7.11b) shows a mixture of not working devices (not linked to geometry or size) with low rectification ratios of 10^2-10^3 and some low reverse currents. Some devices struggle to switch on at the lower voltages that Schottky diodes are expected to switch at. It is generally difficult to show a trend in diode behaviour in relation to the size or geometry. Row 3 (B9, Figure 7.11c) shows the ablated area of the diodes are all visibly etched. Despite this, over half of the devices show rectifying behaviour. One speculation is that enough damage is caused near the edge (towards the Au) to produce vertical diodes instead of planar diodes across the nanogap. The reverse currents of these devices are higher than any other laser parameters on the sample, which is perhaps linked to the etching from laser ablation. The diodes show switching behaviour close to $0\ \mathrm{V}$ and reasonable forward currents. However, the rectification ratios are lower than desired due to the high reverse current. The best device of row 4 (B11, Figure 7.11d) shows a reasonable forward current and switches very close to $0\ \mathrm{V}$, but also exhibits a high reverse current and abnormal hysteresis behaviour, like row 3. For this set of laser parameters, there is an overall poor yield of working devices. Row 5 (B12, Figure 7.11e) displays a better yield of devices and more favourable characteristics than other devices such as on voltages close to $0\ \mathrm{V}$ and low reverse currents. However, forward currents aren't very high, leading to lower rectification ratios than desired. Finally, sample 1, row 6 (C1, Figure 7.11f) shows only two working devices, showing similar performance issues to previous devices on this sample e.g. low rectification ratios of 10^2.

For sample 2, there were multiple rows with no working devices. From the picture of the sample, this is clearly linked to the peel-off stage, as substantial quantities of the Au deposition on the ablated areas and edges was also removed. Since the sample was so heavily compromised, only laser parameters inducing the lowest possible damage to the glass substrate would be expected to produce rectifying diodes. Row 3 (B12, Figure 7.12b) produces very few diodes, all of which possess switching voltages further from $0\ \mathrm{V}$ than desired. However, rectification ratios were higher than many devices on sample 1. Row 4 (C1, Figure 7.12c) produced a far greater yield than row 3, with several diodes achieving reasonable rectification ratios. There is a wide spread of reverse currents. Since the Au deposition and peel-off was so poor on sample 3, only one row of devices was able to be measured. This row (row 4, C1, Figure 7.13b) produced devices with high forward current and rectification ratio, switching at around the ideal expected value of $0.45\ \mathrm{V}$. For sample 4, there were yet again several rows without working devices, but the conditions that did function produced desirable results. Row 3 (B12,

Figure 7.14b) has several devices with low reverse current and rectification ratios above 10^4, with some devices showing ideal Schottky diode behaviour. Row 5 (B1, Figure 7.14c) show characteristics with lots of noise but low reverse currents of below 10^{-10}, rectification ratios of 10^3 and on voltages as expected for Schottky diodes. However, lower yield is achieved with this condition. The combination of noise and lower yield after the peel-off implies sufficient nanostructure in the glass to disrupt charge accumulation at the metal-semiconductor interface and the peel-off process.

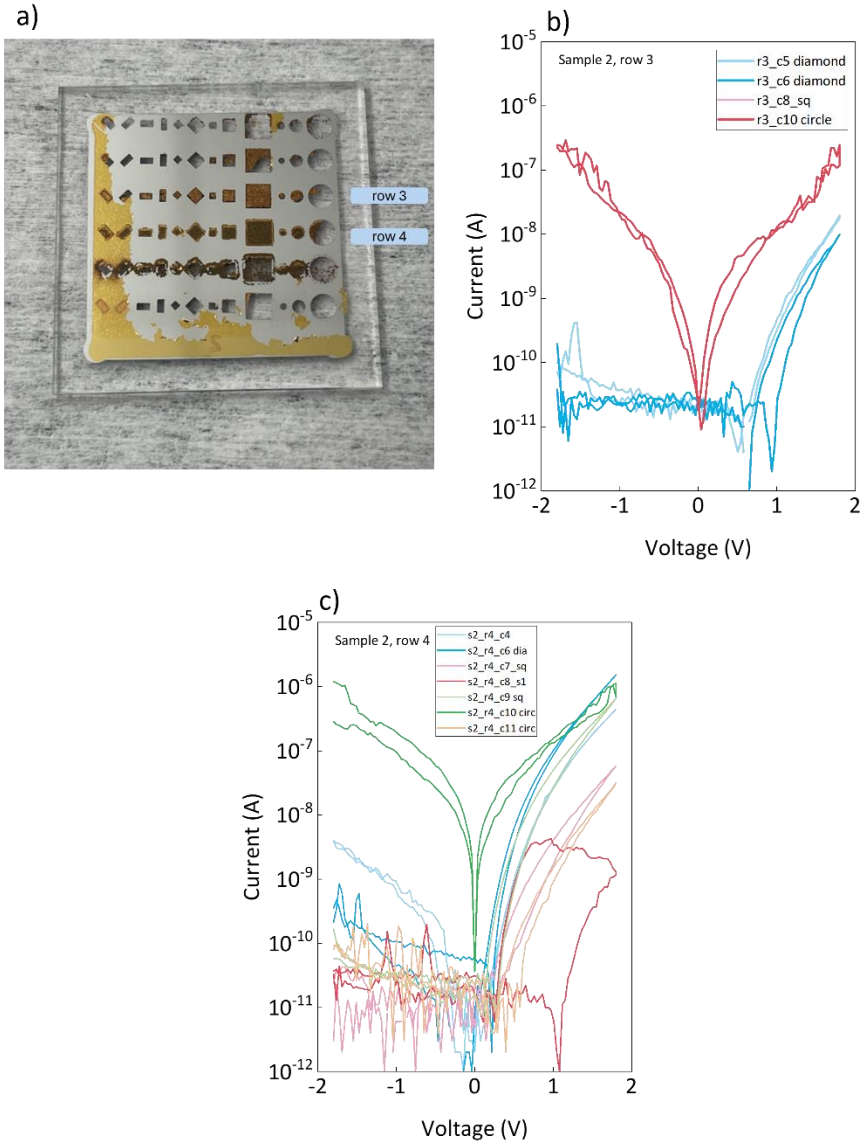

Figure 7.12. Sample 2 of the Schottky diodes fabricated via laser patterning using the $532\ \mathrm{nm}$ laser. a) Picture of the sample after SAM/Au deposition and peel-off, before semiconductor deposition. The rows and columns, corresponding to those measured and shown in subsequent $\mathrm{I}-\mathrm{V}$ characteristics, are indicated. The poorer peel-off is more evident in this sample. The $\mathrm{I}-\mathrm{V}$ characteristics of the diode after semiconductor deposition are of b) row 3, and c) row 4.

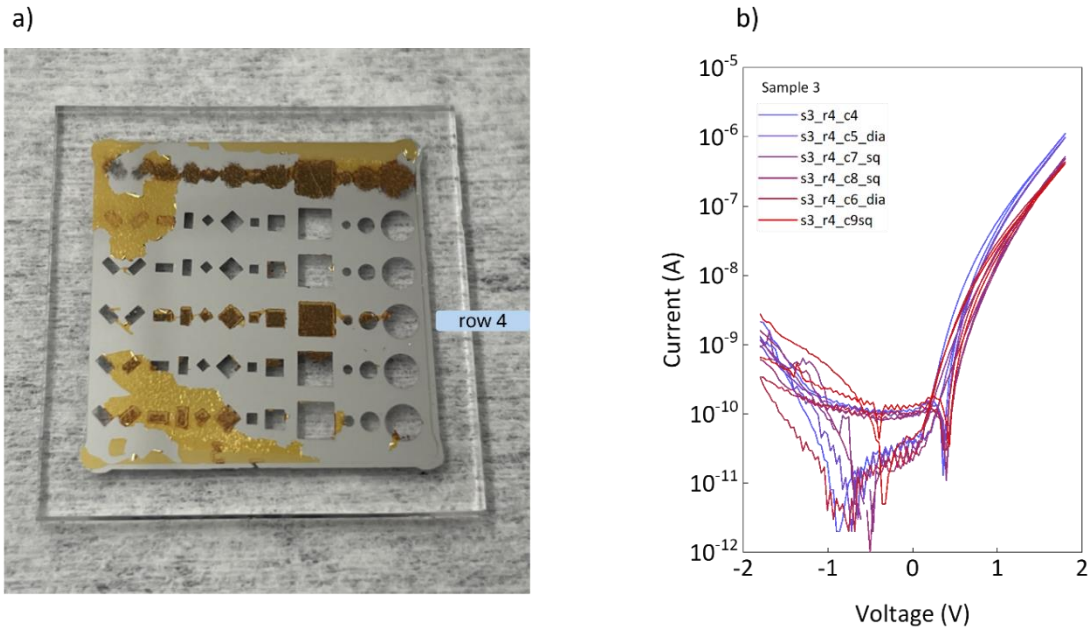

Figure 7.13 Sample 3 of the Schottky diodes fabricated via laser patterning using the $532\ \mathrm{nm}$ laser. a) Picture of the sample after SAM/Au deposition and peel-off, before semiconductor deposition. The rows and columns, corresponding to those measured and shown in subsequent I-V characteristics, are indicated. The poorer peel-off is more evident in this sample. b) The I-V characteristics diodes on row 4 of the sample after semiconductor deposition.

No condition truly showed a sufficient yield due to the poor peel-off. Reverse currents were noisy but often desirably low in working diodes (with some exceptions). Though it is difficult to show a trend between diode size or geometry and the $\mathrm{I}-\mathrm{V}$ characteristics at this stage, the rotated rectangles (columns 1—3) showed very little evidence of producing rectifying diodes. For many diodes that did work, a switching voltage close to $0\ \mathrm{V}$ was achieved, likely due to the intrinsic nature of the Schottky diode's carrier transport rather than exceptional device manufacture. Despite several issues with the peel-off and yield that can, in part, linked to screening a wider range of laser parameters, several diodes were produced with desirable characteristics and typical diode behaviour. This first round of devices immediately demonstrated the potential for this laser patterning with the proven a-lith methodology.

To pragmatically proceed to improve on the above devices, the number of laser conditions needed to be narrowed. Due to their demonstration of working diodes across all samples, conditions B12 and C1 were highlighted as candidates to further investigate laser ablation for diodes. B12 and C1 also produced some of the best performing diodes out of the working devices. The capability for both devices to achieve working devices is interesting, since the two conditions are completely contrasting. B12 utilises a large defocus, with a high repetition rate and high scan speed with a medium hatch spacing. Meanwhile, C1 uses a lower repetition

rate and scan speed (relative to some other conditions in the navigator grid) with a large hatch spacing. The repetition rate of C1 also maximises the peak pulse power. Such large differences in laser parameters both producing rectifying diodes also opens the opportunity for investigating the effect of a plethora of laser parameterisation with minimal sample throughput.

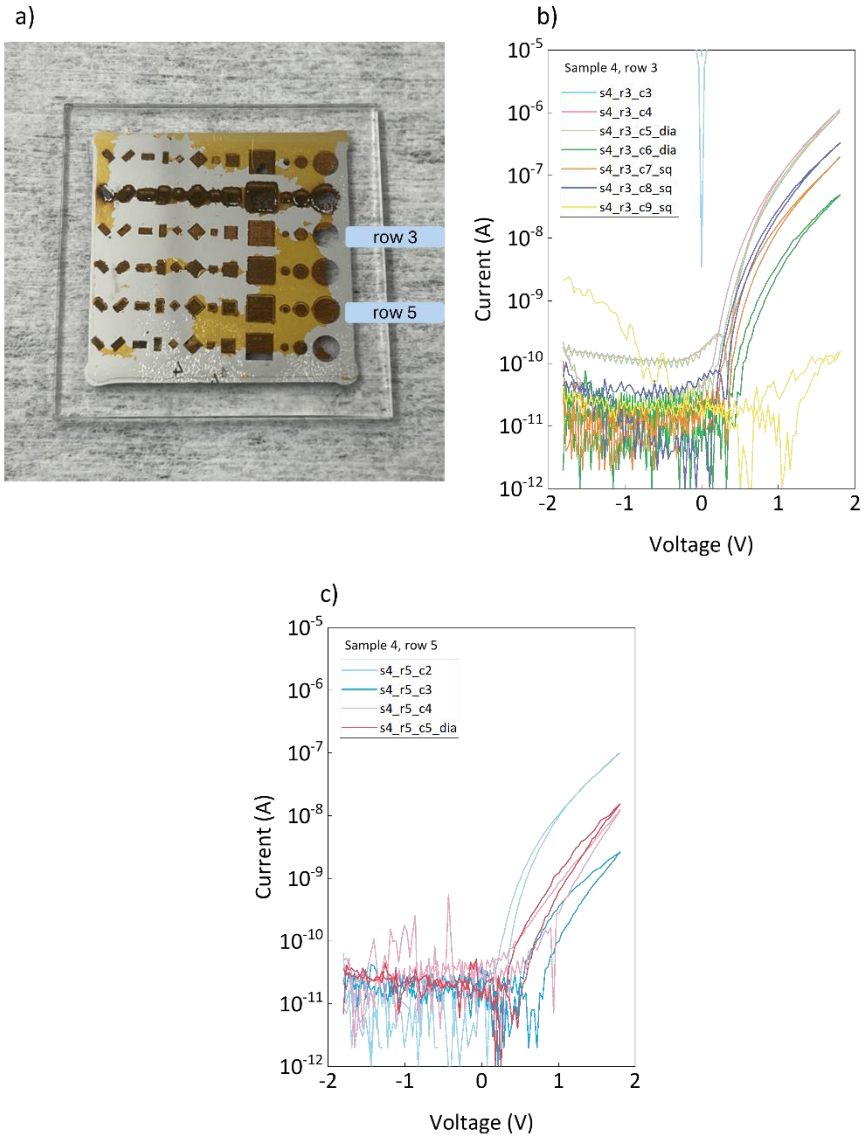

Figure 7.14 Sample 4 of the Schottky diodes fabricated via laser patterning using the 532 nm laser. a) Picture of the sample after SAM/Au deposition and peel-off, before semiconductor deposition. The rows and columns, corresponding to those measured and shown in subsequent I-V characteristics, are indicated. The poorer peel-off is more evident in this sample. The I-V characteristics of the diode after semiconductor deposition are of b) row 3, and c) row 5.

7.3 Effect of laser parameters on nanostructure

Having identified the two conditions of B12 and C1 being linked to better device performance, further investigations were necessary to investigate reproducibility, establish better methodologies for quality control and establish the link between laser parameters and the nanostructure induced into the substrate surface. Diodes produced in section 7.2, while demonstrating good performance comparable to the state-of-the-art, had shown difficulty in fabrication via the adhesion lithography methodology during the deposition and peel-off of M2. Due to the rapid pace at which laser patterned samples can be produced and the volume of samples used to test reproducibility, at least one of the characterisation techniques needed to permit high throughput. Once satisfied by the quality control imposed by transmission spectroscopy, a few (carefully selected) samples were investigated for their topography with each set of laser parameters (B12 and C1), via AFM and optical profilometry.

7.3.1 Transmission Spectroscopy

The optical constants of borosilicate glass (n, k as well as reflection-transmission-absorption) are well known in the literature. The methodology of transmission spectroscopy can be found in chapter 3, section 3.4.5. A key detail of the experimental setup that should be emphasized is the use of the fibre optic lens, which reduces the light source spot size to smaller than the dimensions of the ablated square, avoiding reflections from Al down through the glass and into the spectrometer. Thus, all changes in transmission correspond to changes in the glass substrate. Figure 7.15 demonstrates indicative transmission data obtained in six samples. Each measurement was taken from the square spots.

In Figure 7.15, we observe distinct patterns in the transmission properties of samples subjected to different laser processing conditions. Rows 1-3, which correspond to condition B12, are depicted by red lines and are situated on the top half of the sample. Conversely, rows 4-6 relate to condition C1, represented by blue lines on the bottom half. For comparative purposes, a black solid line denotes an unprocessed glass reference. The measurements reveal that rows 1-3 (condition B12) consistently exhibit a transmission efficiency of 95% above the $350\ \mathrm{nm}$ wavelength, surpassing the 92% transmission of unprocessed glass. This variance in transmission is indicative of alterations or damage within the ablated region of the glass. In contrast, rows 4-6 (condition C1) display reduced transmission below $550\ \mathrm{nm}$, extending into the ultraviolet spectrum. This suggests that laser ablation under condition C1 induces structural changes or damage that results in light scattering, thereby diminishing transmission efficiency. Additionally, a notable visual change is observed with condition C1, where the ablated areas acquire a milky appearance upon exposure to white light. This effect corroborates the transmission data and highlights the alteration not previously detected, as direct light exposure

to the ablated area under condition C1 had not been conducted prior.

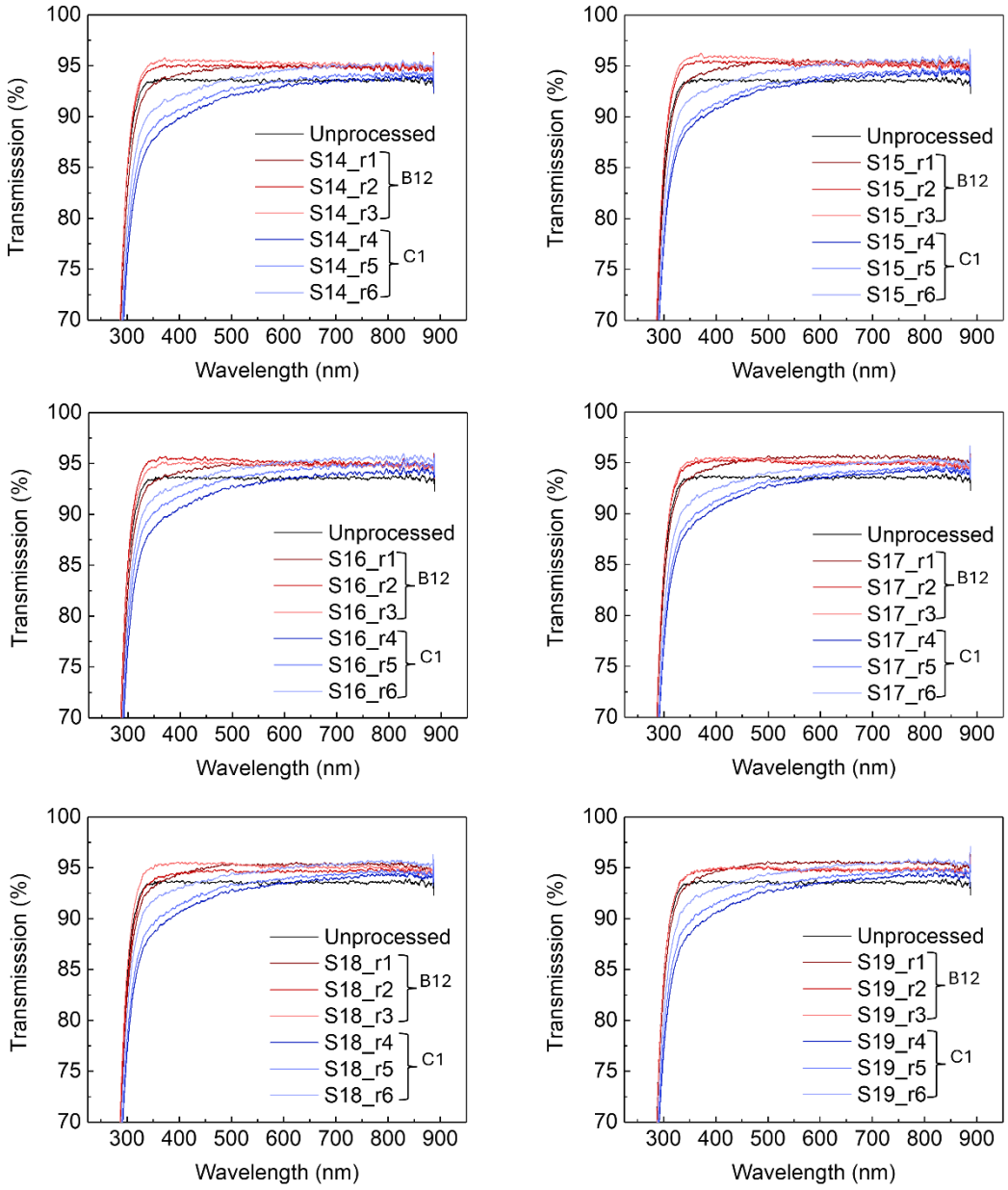

Figure 7.15. Typical Transmission Spectroscopy data obtained from six different Al/Glass sample laser ablated with conditions B12 and C1. Rows 1-3 contain condition B12 (red lines) while rows 4-6 contain condition C1 (blue lines). A reference measurement of the unprocessed glass is shown by the solid black line.

It is important to note that condition B12 does not evoke a similar visual or transmission effect. The distinct grouping of rows for each condition across multiple samples attests to the high consistency and repeatability of the laser processing technique. Each condition remains distinct from the unprocessed glass benchmark. A particularly interesting finding is the progressive decline in transmission from top to bottom of the sample, with maximum values at row 3 declining steadily to a minimum at row 6, suggesting a gradation in the extent of laser-

induced effects. This pattern indicates a systematic influence of laser processing on the material's transmission properties and structural integrity.

The increase in transmission from 92% to 95% in condition B12 can be explained by a large periodic roughness that leads to interference effects. Figure 7.16 shows the transmission of a smooth borosilicate glass substrate (BK7, Schott, n-k values retrieved from the CompleteEASE software database) before processing (black line) compared to the transmission of the same glass with varying levels of roughness, generated within the CompleteEASE ellipsometry software. As with other optical models in CompleteEASE, a layer of roughness is an Effective Medium Approximation of 50 % air and 50 % the optical constants of the main layer (in this case the glass is the only layer). The elevated roughness causes interference that increases the transmission above the normal value, with the case of condition B12 causing a roughness that only causes a single small oscillation above the bandgap. Visually, thicknesses from $80 - 150$ nm on this glass would cause a similar effect. In the case of C1, roughness causing interference, as well as a thin layer of material with different refractive index on the bulk glass, could be linked to the change in transmission.

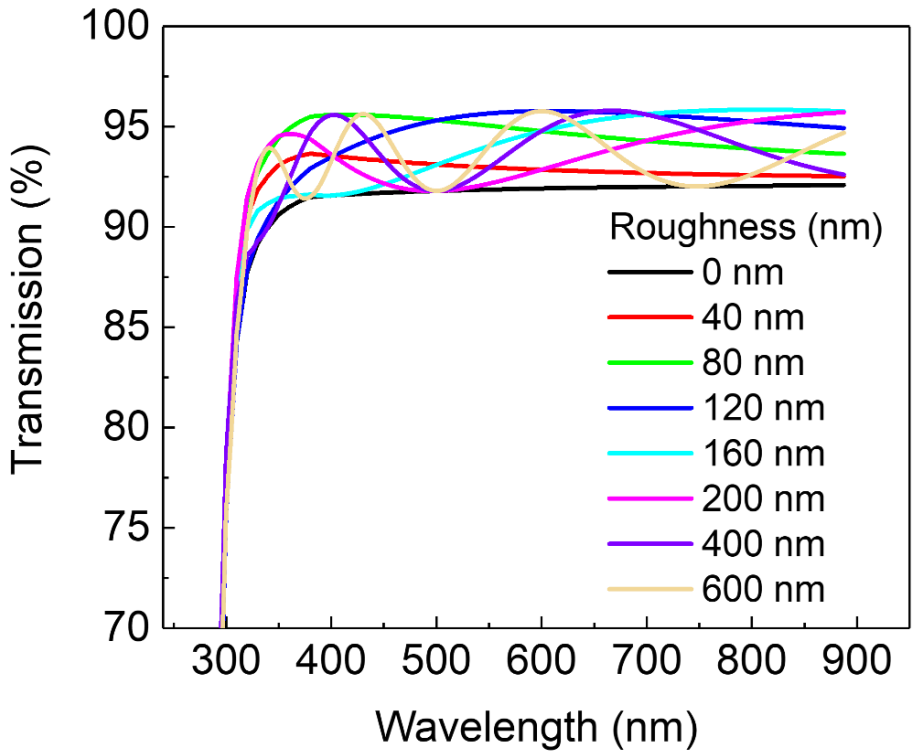

Figure 7.16. Depiction of how surface roughness alters the transmission through a borosilicate glass substrate. Regular periodic roughness via an EMA leads to interference that increases the transmission compared to a smooth surface.

7.3.2 Topography Analysis

To further explore the nanostructure from laser ablation, further characterisation with Atomic Force Microscopy (AFM) and Optical Profilometry was performed. First, a reference AFM image of the unprocessed glass was taken to establish the surface character before laser ablation. Figure 7.17 shows the $50\ \mu m \times 50\ \mu m$ image of the unprocessed borosilicate glass substrate. While there is a peak roughness value of $4.7\ nm$, most of the glass is extremely smooth with a R_q of $0.466\ nm$ and R_a of $0.353\ nm$. This AFM image establishes the glass is flat and without nanostructure in the topography, thus any nanostructure in subsequent AFM images is resultant from laser patterning.

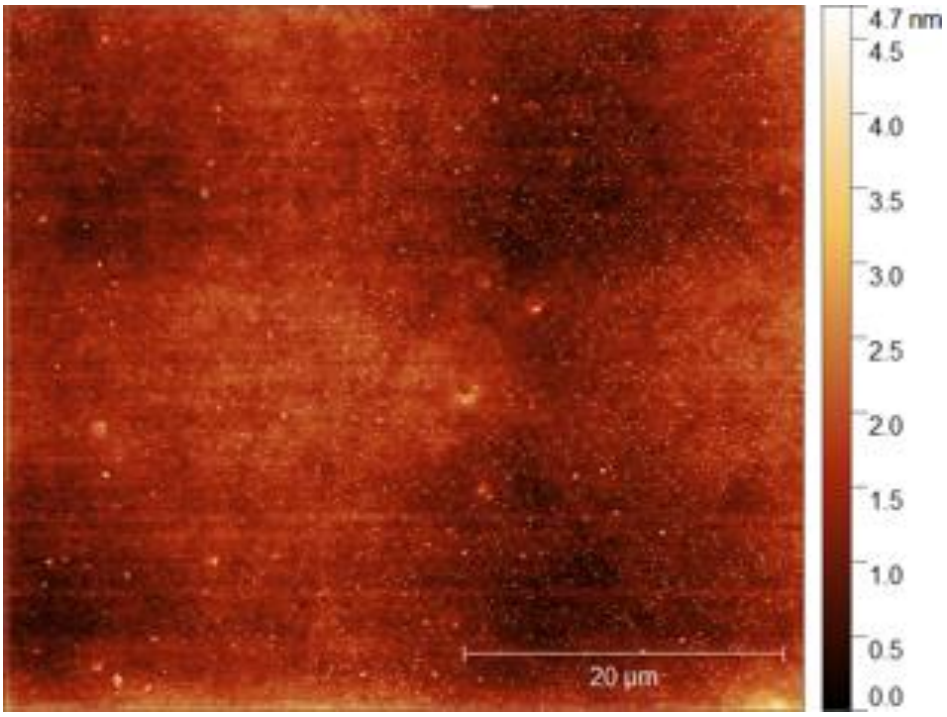

Figure 7.17. $50\ \mu m \times 50\ \mu m$ AFM image taken in Tapping Mode of the unprocessed glass. A low peak-to-peak and RMSR values confirm the glass is extremely flat, and is overall featureless.

Figure 7.18a shows an AFM image of B12 taken in Tapping Mode, while Figure 7.18b shows the horizontal line profile (indicated by the solid blue lines on Figure 7.18a) measuring the height variation across the sample. The image reveals the laser spot spatial profile is embedded in the surface – this is highlighted by the dotted circle on the image. The line profile measured the periodicity of these spots as $0.21\ mm$, which matches closely to the hatch spacing of B12. The peak-to-valley height is approximately $160\ nm$. The vertical line profile (not shown in this report) agrees with this value, showing the uniformity across the ablated area. The WYKO Optical Profilometer was used to corroborate the findings of AFM. Figure 7.18c and 7.18d shows the 3D image and horizontal line profile of B12. B12 shows a more regular structure with holes and spikes that form trenches in certain regions. This can be attributed to where the hatch

overlaps more, causing further indentation in the glass. The line profile of this image reveals a spacing between these holes of 19 μm, matching closely with the B12 condition and AFM data.

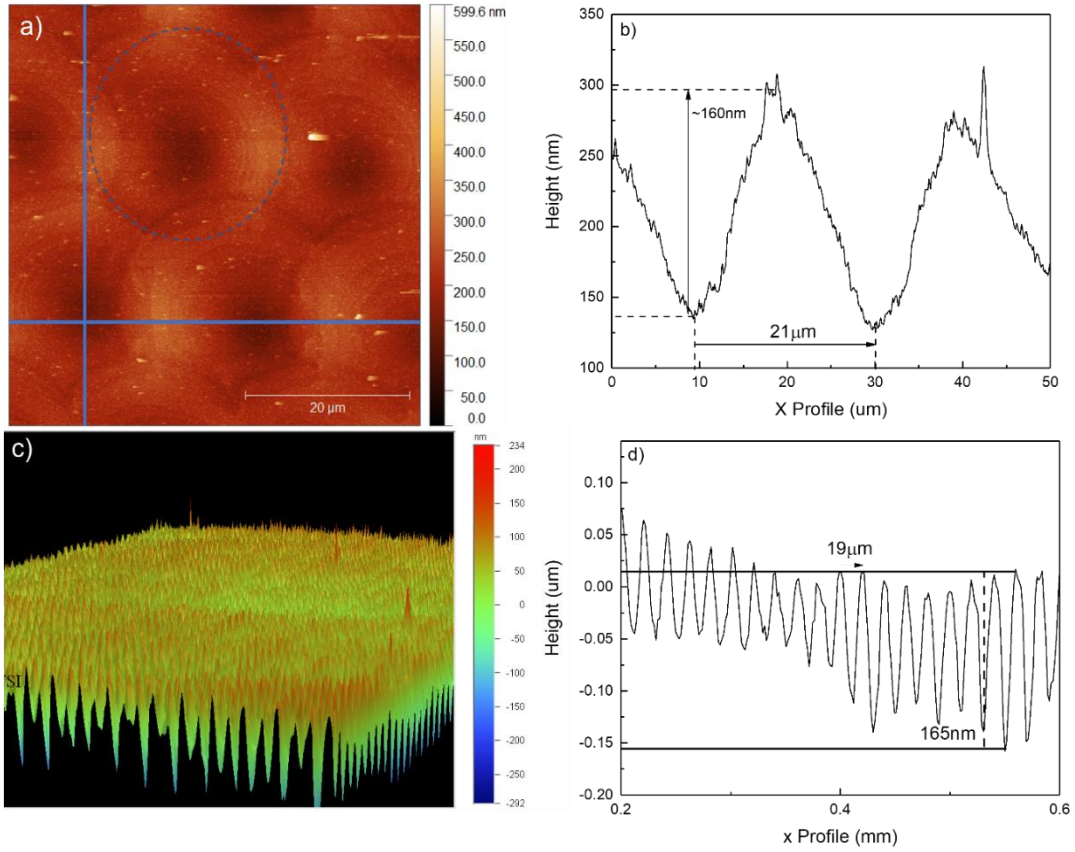

Figure 7.18: a) 50 μm × 50 μm AFM image taken in Tapping Mode of condition B12. The thin dotted line forming a circle highlights the laser spot formed on the surface during laser ablation of the Al, while the thick solid blue lines indicate where line profiles were taken to determine the variation in surface topography. b) Horizontal line profile of the AFM of B12, taken so it is incident with the centres of several laser spots. Spacings between oscillations and the visual character of the image match the hatch spacing used for this condition closely, while the peak-to-valley for the height is consistent across the sample. c) A 0.9 mm × 1.2 mm WYKO Optical Profilometer image of the processing condition B12. The regular periodic nature of the holes and spikes matches closely to the AFM image. d) A section of a horizontal line profile for the WYKO optical profiler image. The spacing between the peaks of 19 μm matches exactly to the B12 condition while the peak-to-valley is similar to the AFM.

Figure 7.19a shows the AFM image of C1 taken in Tapping Mode, while Figure 7.19b shows the horizontal line profile (indicated by the solid blue lines on Figure 7.19a) measuring the height variation across the sample. The AFM image shows no consistent structure or topography relating to the laser spot or C1 processing condition used. C1 displays a lower peak roughness of 70 nm compared to B12, suggesting the type of structure on the glass surface has reduced the transmission in the VIS-UV. WYKO Optical Profilometer images were also taken here for further investigation. Figure 7.19c and 7.19d shows the 3D image and horizontal (x) line

profile of C1 respectively. C1 shows a more irregular structure, though it still retains some periodicity. The retainment of this structure can be seen in Figure 7.19d, where even spacings between craggy peaks is displayed. This periodicity occurs approximately every $30\ \mu m$, which agrees with the C1 condition. The peak roughness of $60\ nm$ is also similar to the AFM, corroborating most observations.

Overall, the conditions currently used for laser patterning cause a large amount of damage to the glass substrate that impedes the standard approach in a-lith methodology. In performing this characterisation, a standardised methodology for quality control of laser patterned samples has been developed using standard practices.

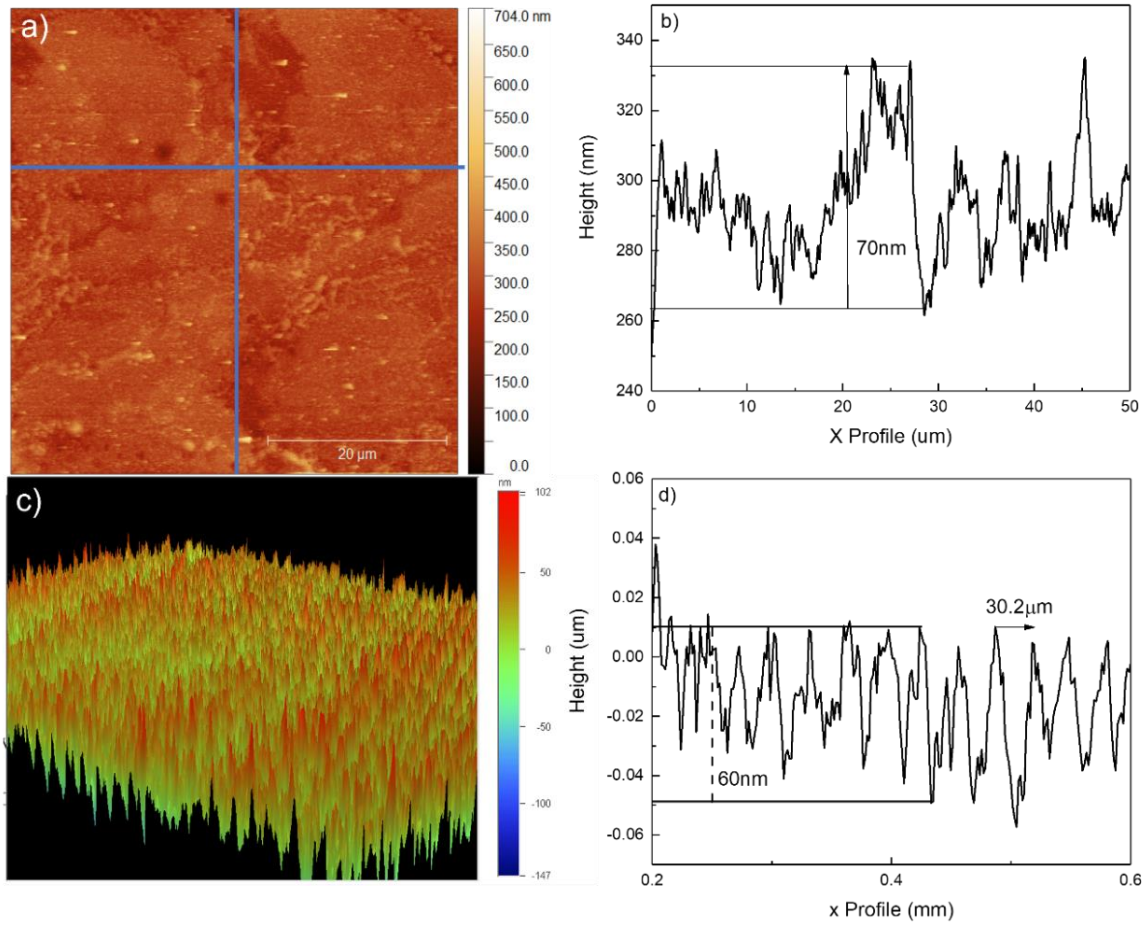

Figure 7.19: a) $50\ \mu m \times 50\ \mu m$ AFM image taken in Tapping Mode of condition C1, with the thick solid lines indicating the line profiles taken for height measurements. b) Horizontal line profile of the AFM image of C1. Over this short range, there is no periodicity as in condition B12. The peak roughness is approximately $70\ nm$. c) A $0.9\ mm \times 1.2\ mm$ WYKO Optical Profiler image of condition C1. The image displays a topography that shows holes and spikes like B12, but with less periodicity and lower peak roughness. d) Horizontal line profile of the WYKO image of C1. The peak roughness of $60\ nm$ corroborates the AFM image while the spacing of the peaks is that of the $30\ \mu m$ hatch spacing used for C1, suggesting the features of the AFM image are real.

7.4 Reproducibility and Cut-off Frequency

The surface morphology of the samples with B12 and C1 laser parameters revealed large periodic features that may not be compatible with the typical a-lith peel-off methods. Thus, with many of the new samples used to test reproducibility, a new chemical wash peel-off method was used. After the SAM and Au deposition, the samples are ultra sonicated in acetone for $4\ \mathrm{mins}$, followed by $1\ \mathrm{min}$ of ultra sonication in IPA. The results of this markedly improved peel-off can be seen in Figure 7.20a.

To assess insulation properties, the empty electrodes were evaluated for their current-voltage (I-V) characteristics, as detailed in Figure 7.20b. The blue lines depict a complete row of devices processed under condition B12, while the orange lines represent those for condition C1. It was observed that, although the empty electrodes do not achieve perfect insulation, they maintain sufficiently low leakage currents (approximately $10^{-8}\ \mathrm{A}$) suitable for diode fabrication. Notably, condition C1 $\mathrm{I}-\mathrm{V}$ characteristics cluster tightly between $10^{-8}\ \mathrm{A}$ and $10^{-9}\ \mathrm{A}$, whereas condition B12 experiences a broader range from $10^{-8}\ \mathrm{A}$ to $10^{-10}\ \mathrm{A}$. Figure 7.20c presents the optimal I-V characteristics for each laser condition, with B12 in blue and C1 in orange. The larger reverse currents under condition C1 result in lower rectification ratios, not exceeding 10^4, despite achieving forward currents around $10^{-5}\ \mathrm{A}$.

In contrast, condition B12, benefiting from its reduced reverse currents, manages to reach rectification ratios of 10^4 in some scenarios. The threshold voltage for an increase in forward current is noted at $0.4\ \mathrm{V}$ for C1 and $0.55\ \mathrm{V}$ for B12, representing reasonable initiation values. The 10^4 rectification ratios are reasonable values but are not exceptional. For example, the a-lith methodology using photolithography and less developed peel-off processes – also glass substrate, $\mathrm{Al}-\mathrm{Au}$ co-planar electrodes and ZnO - was able to achieve 10^5 rectification ratios and above [265]. However, Figure 7.20d illustrates the replication inconsistency of these characteristics, showing rectification ratios across 144 tested devices (from two samples). The mean values, indicated by the coloured horizontal lines, and the data point distribution reveal that devices with performance similar to those in Figure 7.20c are sparse, amounting to only a couple of dozen per 144 tested devices. The maximum average rectification ratio for any column barely surpasses 10^3, with condition B12 consistently outperforming C1. In summary, while the potential to achieve reasonable rectification ratios is evident, the yield of devices replicating these performance levels remains unsatisfactory. This highlights a need for further refinement in fabrication processes to enhance the reproducibility and yield of high-performance diode devices.

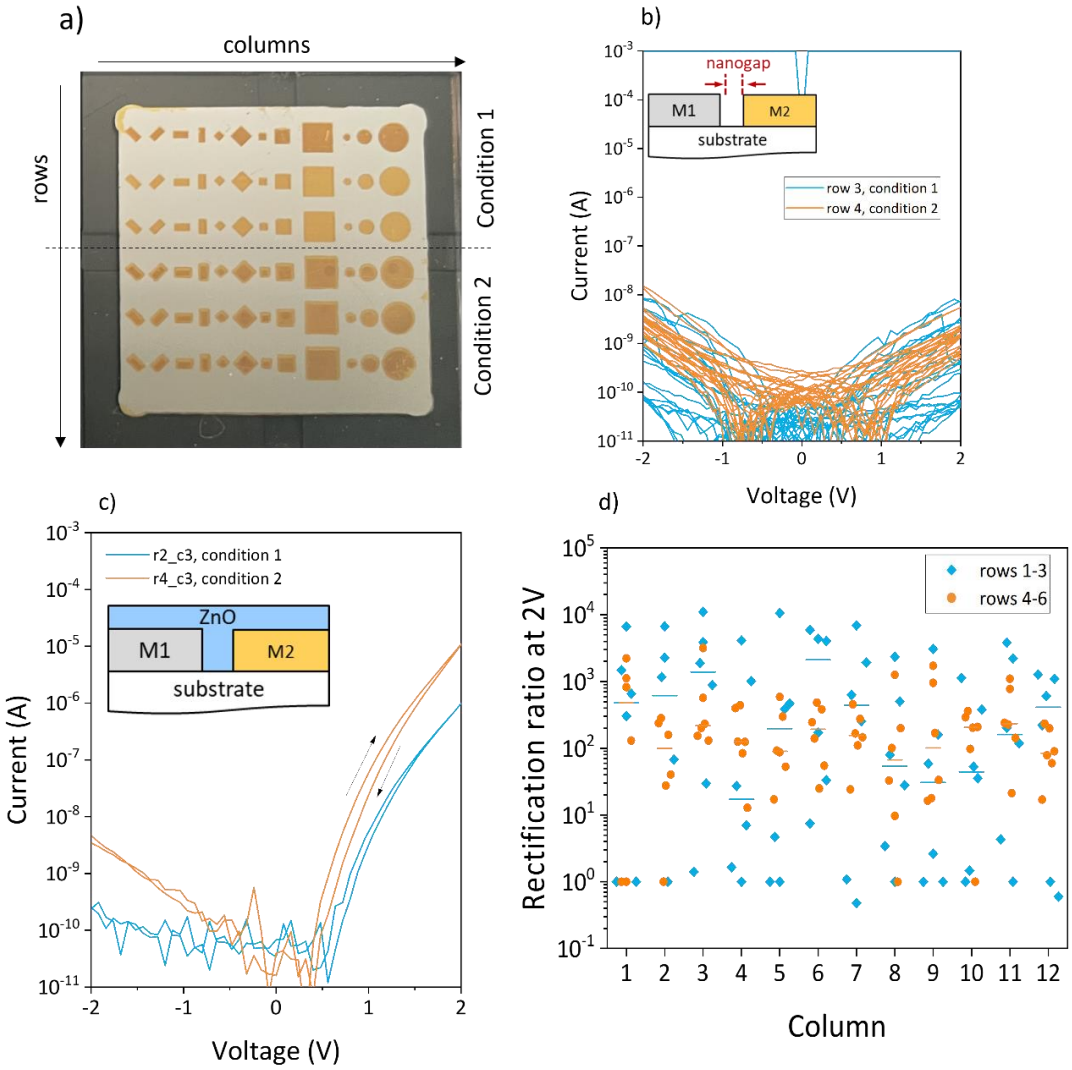

Figure 7.20 a) Example of the $\mathrm{Al}-\mathrm{Au}$ co-planar electrodes after the peel-off step, using a chemical removal step instead of tape. The peel-off was improved compared to the first batch of devices. The split between condition 1 (B12) and condition 2 (C1) is shown via the dotted line across the picture. b) I-V characteristics of the empty electrodes (as per the inset schematic), prior to semiconductor deposition, to test for electrical insulation. The blue lines indicate the B12 parameters, while the orange line indicate the C1 parameters. The majority of devices show currents below 10^{-8}. c) Examples of the best I-V characteristics of the diode for each condition after semiconductor deposition. Condition 1 (B12) shows good insulation and reasonable forward current, while condition 2 (C1) shows good forward current. d) Summary of rectification ratios for 144 devices (two substrates). There is a wide span of device performance shown, though it is unknown if electrode size or shape coincides with these variations.

Finally, cut-off frequency was measured on a group of the diodes. Several devices, despite providing positive results on their rectification ratios, did not show a response in the $\mathrm{V_{out}}$ measurement, indicating voltage values within or lower than the $\mu\mathrm{V}$ range (instead of expected mV outputs). For those devices that did produce mV outputs, there were two outcomes that will be discussed. Figure 7.21a and 7.21b shows the intrinsic and extrinsic frequency – respectively for one device, while Figure 7.21c and 7.21d show a device exhibiting

a different device's intrinsic and extrinsic frequency. devices were produced from the laser condition B12, with a large defocus and smaller hatch spacing. In Figure 7.21a and 7.21c, intrinsic frequencies of $8.9\ \mathrm{GHz}$ and $9.6\ \mathrm{GHz}$ are achieved, demonstrating Schottky diodes that can theoretically achieve fast RF operation. In the case of the diodes tested here, $9.6\ \mathrm{GHz}$ was also the highest value achieved. However, the measurement of extrinsic frequency produced two distinct cases. For the device producing $\mathrm{V_{out}}$ in Figure 7.21b, a higher ($\approx 20\ \mathrm{mV}$) initial $\mathrm{V_{out}}$ is achieved that drops quickly. Although the output remains high for a reasonable frequency range, the proportion of the drop in relation to the magnitude of $\mathrm{V_{out}}$ results in an extrinsic frequency of $0.32\ \mathrm{GHz}$.

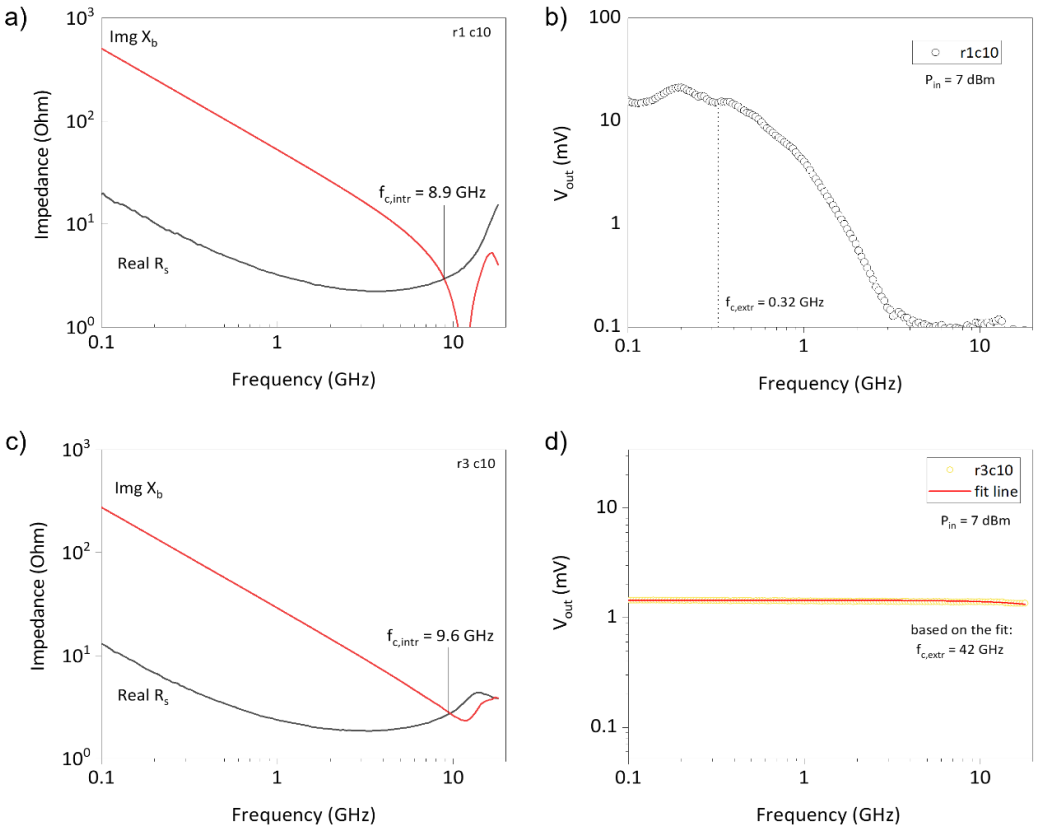

Figure 7.21. Examples of cut-off frequency measurements of some of the Schottky diodes. Two distinct expressions of the cutoff frequency are shown. a) Intrinsic frequency of one device, paired with b) the extrinsic frequency measurement of the same device in a), showing a mV output that rapidly drops. c) Intrinsic frequency measurement of a different device, paired with d) the extrinsic frequency measurement of the device in c), displaying an erroneously high cut-off frequency measurement based on a fit extrapolating to the value.

In the device presented in Figure 7.21d, a typical mV value of $1 - 3\ \mathrm{mV}$ is stable across the measurement range and produces an extrinsic frequency of around $40\ \mathrm{GHz}$ based on the fit of the line (sufficient drop in $\mathrm{V_{out}}$ was not achieved within the measurement range due to the limit of the bias tee in the measurement setup). While this is an excellent value, it should be treated with large scepticism since it vastly exceeds the intrinsic frequency value that acts as a

theoretical minimum. As with the rectification ratios, a large range of values is achieved. Between the laser conditions B12 and C1, no apparent difference was found between their cut-off frequencies, and both were partial to both of the above cases. Reviewing all of the electrical characteristics of the diodes in this chapter, it can be argued that the condition B12, with a defocus and larger scan speeds and frequencies, is preferable to the condition C1. B12 was capable of higher rectification ratios with GHz cut-off frequencies. Further tests with conditions similar to B12 may continue to reduce surface roughness and improve the consistency of device performance and yield.

7.5 Concluding Remarks and Summary

The work presented in this chapter indicates a significant advancement in integrating laser patterning into a-lith processes, facilitating the production of high-frequency diodes. We have explored the fabrication of Schottky diodes using an innovative approach that substitutes traditional photolithography with laser patterning to create the metal contact layer (M1). Specifically, a $100\ \mathrm{nm}$ Al layer was deposited on borosilicate glass, followed by the deposition of an octadecylphosphonic acid (ODPA) self-assembled monolayer (SAM) and a subsequent gold layer (M2). The peel-off process, essential for revealing the laser-patterned substrate, was experimentally optimized using various tape types and chemical ultrasonication, with the latter emerging as the most effective method for the laser-patterned samples.

The selection of laser sources for Al ablation was critical to ensure minimal damage to the underlying glass substrate. Following extensive evaluation, the $532\ \mathrm{nm}$ laser was identified as the most advantageous option due to the transparency of borosilicate glass at this wavelength, which mitigates thermal damage. This wavelength also proved beneficial for processing flexible polymer substrates with similar transparency characteristics. Initial experimental efforts focused on refining the laser parameters for optimal diode fabrication through visual inspection across a broad spectrum of conditions. This led to the identification of relationships between surface roughness induced by Al ablation, laser hatch spacing, and focusing conditions. Notably, two laser parameters – B12 ($0.019\ \mathrm{mm}$ hatch spacing, $1679\ \mathrm{mm/s}$ scan speed, $84\ \mathrm{kHz}$ repetition rate, $3\ \mathrm{mm}$ defocus, 100% power) and C1 ($0.03\ \mathrm{mm}$ hatch spacing, $600\ \mathrm{mm/s}$ scan speed, $20\ \mathrm{kHz}$ repetition rate, $0\ \mathrm{mm}$ defocus, 100% power) emerged as particularly promising for enhancing diode quality, warranting further exploration of their impacts on the glass substrate post-ablation.

Characterisation techniques, including transmission spectroscopy, atomic force microscopy (AFM), and optical profilometry, provided valuable insights into the substrate surface modifications resulting from laser patterning. Transmission spectroscopy revealed a high

degree of reproducibility in laser processing, with twenty samples demonstrating consistent transmission values. Both AFM and profilometry confirmed that significant roughness was introduced into the glass, with periodicity directly correlating with hatch spacing. The Schottky diodes produced from these laser-patterned substrates achieved notable rectification ratios of up to 10^4 and cut-off frequencies reaching $9.6\ \mathrm{GHz}$.

.

8. Conclusions and Future Work

8.1 Conclusions

The work in this PhD thesis aimed to generate new knowledge in light-matter interactions to efficiently convert and process MO precursors to sequentially stacked thin films for fabricating high performance, state-of-the-art TFTs amenable to flexible, large-area substrates. This was *via* a combination of theoretical (opto-thermal simulations) and experimental (device fabrication/characterisation) routes, to unravel the photochemical conversion process and utilise the knowledge for the development of high performing vital electrical devices. To achieve this aim, three **ROs** were pursued. **RO1** focused on the development of LA processing protocols for the growth and processing of MO precursors to produce semiconductor and dielectric thin films. **RO2** was to gain knowledge on the light-matter interactions critical for efficient photochemical conversion of precursor material to its targeted stoichiometry. **RO3** intended to utilise the results on LA parameterisation for the best performing material systems (outputs of **RO1** and **RO2**) to develop prototype LA MO electronic devices including fully sol-gel, LA TFTs. **RO1** was further extended by using laser processing as a patterning tool (as well as or instead of a processing tool) within the established a-lith methodology, substituting conventional photolithography.

In this thesis, the efficacy of the opto-thermal simulations was first developed via comparison of the theoretical temperature rise with electrical characteristics of $\mathrm{In(NO_3)_3}/\mathrm{SiO_2}/\mathrm{Si}$ TFTs fabricated at NTU and how the performance may be linked with the selected temperature rise. This is the first time the temperature rise of sol-gel layers due to LA has been simulated, as well as coupling the temperature rise to the electrical performance or composition of sol-gel, LA devices and layers. Targeting these samples in particular allowed opto-thermal simulations with materials of well-known optical and thermal properties, thus the novel simulations and initial development of a ubiquitous tool can be completed with a high degree of confidence and accuracy. Along with these opto-thermal properties (and thermal non-linearities), the laser temporal and spectral profiles, material thicknesses and phase changes due to precursor decomposition and exceeding of melting points, were combined to track temperature rise. The opto-thermal simulation results had varying levels of agreement with the experimental results that comprised the different current-voltage curves. In all $\mathrm{SiO_2}$ thicknesses, the temperature rise increase with fluence was linear in nature. At a lower and medium thicknesses of $100\ \mathrm{nm}$ and $200\ \mathrm{nm}\ \mathrm{SiO_2}$ dielectric, the temperature rises predicted predominantly agree with the observations of the $\mathrm{I-V}$ characteristics. In the case of $100\ \mathrm{nm}\ \mathrm{SiO_2}$, the high absorption into $\mathrm{In(NO_3)_3}$ due to the chosen $\mathrm{SiO_2}$ thickness results in high temperature rises above the precursor conversion temperature at low fluences, leading to

a somewhat uncontrolled modification of the precursor thin film and excessive conductivity. This leads to the high μ_{FE}, negative V_{th} and low $I_{On/Off}$ observed. For $200\ nm\ SiO_2$ dielectric, the increases in temperature with fluence are more moderate, thus desirable levels of control over the precursor conversion process could be achieved. The moderate to high temperature rises can be confidently coupled to the controlled changes and optimisation in TFT conductivity, μ_{FE} and $I_{On/Off}$ observed. However, confidence in the opto-thermal simulations is slightly reduced by cases where different fluences in $100\ nm\ SiO_2$ and $200\ nm\ SiO_2$ result in temperature rise equivalence, but with drastically different $I-V$ characteristics. This implies that different compositions are present, since TFT performance is heavily correlated to the composition of the sol-gel layers. Further discrepancies are underscored by several cases with $400\ nm\ SiO_2$. At this thickness, nearly all fluences are predicted to be incapable of achieving sufficient temperature rise for conversion and clearly defined TFT channel. This is in contradiction to experimental results, where most fluences clearly demonstrate switching behaviour and high-performance characteristics. These opto-thermal simulations are a novel demonstration of predicting temperature rise from pulsed LA incorporating several complex properties and has contributed knowledge to light-matter interactions for photochemical conversion, linking this developed understanding to performance of materials and devices. Thus, contributions to **RO2** were made through a theoretical approach. However, it is clear that further work can be done to improve their accuracy, particularly with higher thicknesses.

Afterwards, work progressed to implementing novel sol-gel, LA ZrO_x MO dielectric within MOS capacitors and TFTs devices, with the TFT devices comprised of both a sol-gel MO dielectric and sol-gel InO_x semiconductor. AlO_x from sol-gel and ALD deposition were also fabricated, as a reference to a well-established MO dielectric. Electrical ($C-V, C-f, I-V$), optical (ORS, SE) and topographical (AFM) techniques were utilised to investigate the effect of LA fluence and number of pulses on the dielectric thin films at several thicknesses and optimise their fabrication. Since the dielectric thickness is vital as part of this optimisation step, the characterisation took place on 1, 2 and 3 deposited sol-gel layers at concentrations of $0.1\ M$, $0.15\ M$ and $0.2\ M$. Unanimously, 1-layer samples were unsuitable as high frequency dispersion made them unstable across high frequencies, despite their high areal capacitance C_i and high breakdown field E_{br}. 3-layer samples did not show this extreme dispersion but showed the lowest areal capacitance and dielectric constants compared to other samples. Additionally, AFM of 3-layer samples showed alleged crystallisation and visible modification to the surface after LA (from light scattering off the surface), creating a rougher surface and rougher dielectric-semiconductor interface that would impede μ_{FE} in the case of BGTC TFT. On the other hand, 2-layer samples showed an excellent balance between minimising high frequency dispersion,

maximising dielectric constant ε_r and E_{br}, and maintaining a surface with minimal roughness after LA. VIS-UV SE confirmed a band-gap below $5\ eV$ ($248\ nm$ excimer LA wavelength), highlighting the semi-absorbing nature of the ZrO_x film compared to AlO_x and that it cannot necessarily be considered an optical spacer. The ZrO_x and reference AlO_x films were integrated into TFTs with InO_x in a BGTC configuration, with both TA and LA samples fabricated. Electrical characterisation of InO_x/ZrO_x TFT devices demonstrated switching behaviour as desired in TA and LA samples, though both LA and TA samples demonstrated poorer performance than expected, while LA devices exhibited poorer performance than the TA samples. Despite the lacking performance, the samples provided a proof-of-concept for opto-electronic devices involving both sol-gel, LA dielectrics and semiconductors. Devices based on all forms of InO_x/AlO_x (i.e. ALD AlO_x or sol-gel AlO_x) did not show desirable TFT performance and, in some cases, no switching behaviour at all. Thus, further investigations on the optimisation of combining the different sol-gel layers is necessary to fully realise the potential of the LA approach. By developing protocols for the development of sol-gel, LA thin films, implementing a process flow to integrate them and showing advantages and limitations of the thin films and process thus far, a large contribution to **RO1** was made. The fabrication of the MOS capacitors and TFTs using the knowledge and methodology developed means **RO3** was achieved.

To further elucidate the effects of LA on the dielectric thin films, IRSE was used to investigate the thin film properties, especially chemical composition and precursor conversion into a metal oxide thin film due to the origin of organometallic bond absorption wavelengths in the IR. Thin films of ZrO_x and AlO_x using acetylacetonate and nitrate precursors, respectively, were deposited on $100\ nm\ Al$ substrate that enhances IRSE sensitivity. Single pulse LA at a range of fluences were investigated alongside TA sol-gel reference samples (at several temperatures). The selection of fluences was based on temperature rises from opto-thermal simulations to determine identical temperature rises from differing fluences while compensating for different optical and thermal properties. Several fitting strategies with Cauchy dispersion models, B-Spline models and oscillator models were explored to most accurately but efficiently extract thin film thickness and chemical composition. In both precursors and thin films, absorption peaks relating to organometallic bonds could be fitted and identified as specific bond types, demonstrating the novel compositional characterisation of LA samples using IRSE and its potential for probing the LA photochemical conversion process from a precursor into a MO thin film. For AlO_x, tested using a new recipe with a thicker film, thermal treatment at $300℃$ did not convert the film via removal of nitrate anions, demonstrating the necessity to increase process temperature for dielectrics when ultra-thin films may be counterintuitive for functional opto-electronic devices. Higher thermal treatment of $450℃$ did illicit the expected conversion

process. LA of AlO_x with single pulses did not demonstrate full conversion with any fluence, despite the vast differences in temperature rise expected. For ZrO_x, TA treatments of $300°C$ expectedly left several remaining organic species and did not fully convert the film. TA at $450°C$ did not cause conversion to a thin film as expected, which was explained by the presence of adsorbed water and hydrophilic nature of the thin film. For ZrO_x LA thin films, single-pulse LA did not result in precursor conversion in any condition. Comparing the TFTs in chapter 5 (with both AlO_x and ZrO_x) to IRSE characterisation reveals that the desired thin film composition was not achieved, leading to charge traps in the dielectric and hence non-satisfactory performance in the devices. This compositional characterisation also revealed how ZrO_x LA and TA sol-gel thin films resulted in different TFT performances. In doing so, clarification on the photochemical conversion mechanism (and the role of LA fluence in it) and the potential link to the performance of electrical devices in chapter 5 were achieved and contributed to **RO1** and **RO2.** The work is the first demonstration that IRSE can be used as an alternative to traditional techniques (e.g. XPS, FTIR) to investigate chemical composition for thin films, unravel the LA photochemical conversion mechanism and subsequently link these results to the electrical characteristics of a device.

Aside from the work on MOS capacitors and TFTs, laser processing was also explored as a method to pattern electrodes as an alternative to photolithography. Electrodes of $100\ nm$ Al on $1\ mm$ thick borosilicate glass were initially laser patterned with several different laser sources at systematically varied laser parameters, with the effect of laser processing on the glass substrate surface assessed via an optical microscope. In several cases, ablation was also trialled through the backside of the glass with the hypothesis that any induced roughness of the glass would be minimised. In the case of $248\ nm$ and $1064\ nm$, the Al was ablated but with moderate to significant increase in roughness or damage to the glass – observed via optical microscopy - that would impede the deposition of the SAM and M2 during the a-lith methodology. In contrast, $532\ nm$ through the backside produced markedly lower roughness, thus was selected as the primary source for laser patterning. Several laser parameters were rapidly screened, establishing a link between laser focus, hatch spacing and the substrate surface quality. Two sets of laser parameters were selected to fabricate Schottky diodes, testing for reproducibility and yield in the process. Characterisation with several techniques (transmission spectroscopy, optical profilometry, AFM) revealed varying levels of roughness and periodic nanostructure linked directly to the laser spot and hatch spacing. Despite this nanostructure and with only a rough screening of laser parameters, the Schottky diodes produced with laser patterning as part of the a-lith methodology demonstrated a relatively high yield, a reasonable rectification ratio of 10^4 and cut-off frequencies in the GHz regime. This

work demonstrates the potential of the laser patterning approach to replace the photolithography step in a-lith and other methodologies amenable to LAE. While not utilising LA for the processing of materials, laser parameterisation

8.2 Future Work

The trajectory of the work in this PhD has left several unexplored pathways of research work and revealed a plethora of new routes of research. A limited list of those that could deliver high impact results are listed below, also acting as progressions to the chapters in this thesis.

1) **IRSE investigation of the composition of $\mathbf{InO_x}$ thin films in TFTs**: the opto-thermal simulations in chapter 4 showed in some cases temperature rise and electrical performance are closely related, while other cases showed deviation between the experimental and theoretical work. While experimental data already comprises electrical and AFM, compositional data across all thicknesses of SiO_2 is lacking and is vital to completely link the theoretical and experimental data. The use of IRSE on $InO_x/SiO_2/Al/Si$ samples would be the first demonstration of compositional characterisation via IRSE of a full TFT. Such a study would also deliver full sol-gel, LA devices on an Al electrode that is mandatory for devices on flexible substrates. Completion of this investigation also would demonstrate the applicability of IRSE as a possible in-line quality control tool for electrical layers. This study could occur alongside thermal annealing of $In(NO_3)_3$ on each thickness of SiO_2 at a variety of temperatures analogous to those seen in the simulations, with I-V characterisation seeking similarities to previous data, or extend to include the number of pulses of LA as a parameter.

2) **Electronic transport simulations of sol-gel semiconductors and conductors**: charge transport inside sol-gel semiconductors and conductors (and across their interfaces), evaluated by electrical simulations considering drift-diffusion equations, remains unexplored. The optoelectronic nature of the electronic devices in this thesis results in electrical behaviour being coupled with optical properties of the materials involved, which in turn becomes linked to temperature rises in the materials due to optical absorption, Joule heating effects and heat diffusion. The drift-diffusion equations would allow the study of transport along surfaces and interfaces, Fermi level, charge injection across interfaces and current-voltage curves for elementary devices. The electronic transport simulations, combined with an extended material property database and the opto-thermal simulation component, would begin to describe the full effects of LA on sol-gel materials used in opto-electronics.

3) **Further optimisation of $\mathbf{ZrO_x}$, $\mathbf{AlO_x}$ and $\mathbf{InO_x}$ for TFTs**: ZrO_x and AlO_x dielectrics have demonstrated good performance in MOS capacitors and proof of concept for sol-gel, LA TFTs was demonstrated, but the low carrier mobility and high leakage currents were less than desirable. The IRSE characterisation of chapter 6 revealed full photochemical conversion from precursor to thin film for the dielectrics had not been achieved. By re-tuning the LA fluence and number of pulses based on further IRSE compositional characterisation and preventing surface traps on the dielectrics during and after thin film deposition, performance can be improved so on-off current ratio of 10^5, μ_{FE} of > 20 and near-zero V_{th} values can be achieved. The use of the opto-thermal simulations will help to guide this process, predicting temperature rises and the impact of varying thicknesses (different optical behaviour) after laser pulses on the heat propagation through the thin film.

4) **Fabrication of Schottky diodes on flexible substrates via a-lith**: the work of chapter 7 exhibits proof of concept for laser patterning as a key step in the development of large-area Schottky diodes via a-lith. Similar to the TFTs and MOS capacitors in this thesis, these were on a rigid, thermally stable substrate and could be further optimised to achieve higher performance than what was demonstrated. The two sets of laser parameters can be fine-tuned to further reduce nanostructure on the glass, demonstrating the full potential of laser patterning for a-lith. Re-optimisation of laser parameters and the peel-off step with flexible substrates - with assistance from opto-thermal simulations - would begin the process of this transfer to flexible substrates.

9. References

[1] D. Zhang, T. Huang, and L. Duan, 'Emerging Self-Emissive Technologies for Flexible Displays', *Advanced Materials*, vol. 32, no. 15, Apr. 2020, doi: 10.1002/adma.201902391.

[2] A. R. Patil, T. D. Dongale, R. K. Kamat, and K. Y. Rajpure, 'Binary metal oxide-based resistive switching memory devices: A status review', *Mater Today Commun*, vol. 34, p. 105356, Mar. 2023, doi: 10.1016/j.mtcomm.2023.105356.

[3] A. Dey, 'Semiconductor metal oxide gas sensors: A review', *Materials Science and Engineering: B*, vol. 229, pp. 206–217, Mar. 2018, doi: 10.1016/j.mseb.2017.12.036.

[4] J. K. Jeong, 'The status and perspectives of metal oxide thin-film transistors for active matrix flexible displays', *Semicond Sci Technol*, vol. 26, no. 3, p. 034008, Mar. 2011, doi: 10.1088/0268-1242/26/3/034008.

[5] J. G. Labram, N. D. Treat, Y. H. Lin, C. H. Burgess, M. A. McLachlan, and T. D. Anthopoulos, 'Energy Quantization in Solution-Processed Layers of Indium Oxide and Their Application in Resonant Tunneling Diodes', *Adv Funct Mater*, vol. 26, no. 10, pp. 1656–1663, Mar. 2016, doi: 10.1002/adfm.201503732.

[6] F. Eisner *et al.*, 'Solution-Processed In2O3/ZnO Heterojunction Electron Transport Layers for Efficient Organic Bulk Heterojunction and Inorganic Colloidal Quantum-Dot Solar Cells', *Solar RRL*, vol. 2, no. 7, Jul. 2018, doi: 10.1002/solr.201800076.

[7] S. Calnan and A. N. Tiwari, 'High mobility transparent conducting oxides for thin film solar cells', *Thin Solid Films*, vol. 518, no. 7, pp. 1839–1849, Jan. 2010, doi: 10.1016/j.tsf.2009.09.044.

[8] L. Atzori, A. Iera, and G. Morabito, 'The Internet of Things: A survey', *Computer Networks*, vol. 54, no. 15, pp. 2787–2805, Oct. 2010, doi: 10.1016/j.comnet.2010.05.010.

[9] A. N. Hanna, A. T. Kutbee, R. C. Subedi, B. Ooi, and M. M. Hussain, 'Wavy Architecture Thin-Film Transistor for Ultrahigh Resolution Flexible Displays', *Small*, vol. 14, no. 1, Jan. 2018, doi: 10.1002/smll.201703200.

[10] G. Wyatt-Moon, D. G. Georgiadou, A. Zoladek-Lemanczyk, F. A. Castro, and T. D. Anthopoulos, 'Flexible nanogap polymer light-emitting diodes fabricated via adhesion lithography (a-Lith)', *JPhys Materials*, vol. 1, no. 1, Dec. 2018, doi: 10.1088/2515-7639/aadd57.

[11] A. Samouco, A. C. Marques, A. Pimentel, R. Martins, and E. Fortunato, 'Laser-induced electrodes towards low-cost flexible UV ZnO sensors', *Flexible and Printed Electronics*, vol. 3, no. 4, Dec. 2018, doi: 10.1088/2058-8585/aaed77.

[12] A. C. Arias, J. D. MacKenzie, I. McCulloch, J. Rivnay, and A. Salleo, 'Materials and Applications for Large Area Electronics: Solution-Based Approaches', *Chem Rev*, vol. 110, no. 1, pp. 3–24, Jan. 2010, doi: 10.1021/cr900150b.

[13] C. Miller, *Chip War: The Fight for the World's Most Critical Technology*, 1st ed. Scribner, 2022.

[14] 'From Microchips to Medical Devices: Semiconductors as an Essential Industry during the COVID-19 Pandemic ', 2020.

[15] J. M. Barrero, N. Bloom, and S. J. Davis, 'Why Working from Home will Stick', 28731, Apr. 2021.

[16] L. Kelion, 'Factory blaze adds to computer chip supply crisis', BBC.

[17] 'Impact of the February 13 Earthquake in the Coast of Fukushima Prefecture on Renesas Electronics Operation', Renesas. Accessed: Oct. 31, 2024. [Online]. Available: https://www.renesas.com/en/node/1491366?srsltid=AfmBOoq3mrMSWuVnaKYsjQmHfZQWoNdj2EraIKtu7dFjFO5ruvdbZ5Ci

[18] NXP Semiconductors, 'NXP Provides Update Regarding Impact of Severe Winter Weather on Austin, Texas Facilities'. Accessed: Oct. 30, 2024. [Online]. Available: https://www.nxp.com/company/about-nxp/newsroom/NW-NXP-PROVIDES-FACILITIES-TEXAS

[19] 'Samsung, Infineon, and NXP Halt Production in Texas due to Winter Storm', Sourcengine. Accessed: Oct. 31, 2024. [Online]. Available: https://www.sourcengine.com/blog/samsung-infineon-nxp-halt-production-texas-winter-storm-2021-02-18?srsltid=AfmBOoqy313B9dYh6dKnC5Cad04wSk0mdxmrASGORk8xGXyErDZ8wFxW

[20] A. Ananthalakshmi, 'Malaysia's COVID-19 lockdown to be extended - PM', Reuters.

[21] H. Davidson and C. Lin, 'How Taiwan secured semiconductor supremacy – and why it won't give it up', The Guardian. Accessed: Oct. 30, 2024. [Online]. Available: https://www.theguardian.com/world/article/2024/jul/19/taiwan-semiconductor-industry-booming

[22] E. Barbiroglio, 'No Water No Microchips: What Is Happening In Taiwan?', Forbes. Accessed: Oct. 30, 2024. [Online]. Available: https://www.forbes.com/sites/emanuelabarbiroglio/2021/05/31/no-water-no-microchips-what-is-happening-in-taiwan/

[23] ASML, 'Fire incident at ASML Berlin'. Accessed: Oct. 30, 2024. [Online]. Available: https://www.asml.com/en/news/press-releases/2022/fire-incident-at-asml-berlin

[24] Bureau of Industry and Security, 'Commerce Implements New Export Controls on Advanced Computing and Semiconductor Manufacturing Items to the People's Republic of China (PRC) ', Oct. 2022.

[25] C. Cytera, 'Gallium, Germanium, and China — The Minerals Inflaming the Global Chip War', CEPA. Accessed: Oct. 30, 2024. [Online]. Available: https://cepa.org/article/china-gallium-and-germanium-the-minerals-inflaming-the-global-chip-war/

[26] M. Blackwood and C. DeFilippo, 'Germanium and Gallium: U.S. Trade and Chinese Export Controls ', Mar. 2024.

[27] 'Rare Gases (Krypton, Neon, Xenon): Impact assessment for supply security', 2022.

[28] G. Arcuri and S. Lu, 'Taiwan's Semiconductor Dominance: Implications for Cross-Strait Relations and the Prospect of Forceful Unification', Center for Strategic and International Studies. Accessed: Oct. 31, 2024. [Online]. Available: https://www.csis.org/blogs/perspectives-innovation/taiwans-semiconductor-dominance-implications-cross-strait-relations

[29] European Commission Directorate, 'European Chips Act'. Accessed: Oct. 30, 2024. [Online]. Available: https://commission.europa.eu/strategy-and-policy/priorities-2019-2024/europe-fit-digital-age/european-chips-act_en

[30] 117th Congress, 'H.R.4346 - CHIPS and Science Act'. Accessed: Oct. 30, 2024. [Online]. Available: https://www.congress.gov/bill/117th-congress/house-bill/4346

[31] G. E. Moore, 'Cramming more components onto integrated circuits', *Electronics (Basel)*, vol. 38, no. 8, pp. 114–117, Apr. 1965.

[32] R. H. Dennard, F. H. Gaensslen, H.-N. Yu, V. L. Rideout, E. Bassous, and A. R. LeBlanc, 'Design of ion-implanted MOSFET's with very small physical dimensions', *IEEE J Solid-State Circuits*, vol. 9, no. 5, pp. 256–268, Oct. 1974, doi: 10.1109/JSSC.1974.1050511.

[33] Imec, 'Smaller, better, faster: imec presents chip scaling roadmap'. Accessed: Oct. 30, 2024. [Online]. Available: https://www.imec-int.com/en/articles/smaller-better-faster-imec-presents-chip-scaling-roadmap

[34] H. J. Levinson, 'High-NA EUV lithography: current status and outlook for the future', *Jpn J Appl Phys*, vol. 61, no. SD, p. SD0803, Jun. 2022, doi: 10.35848/1347-4065/ac49fa.

[35] N. Fu, Y. Liu, X. Ma, and Z. Chen, 'EUV Lithography: State-of-the-Art Review', *Journal of Microelectronic Manufacturing*, vol. 2, no. 2, pp. 1–6, 2019, doi: 10.33079/jomm.19020202.

[36] V. Bakshi, *EUV Lithography*, vol. 178. SPIE Press, 2009.

[37] I. Cutress, '"Better Yield on 5nm than 7nm": TSMC Update on Defect Rates for N5', ANandTech. Accessed: Jun. 26, 2024. [Online]. Available: https://www.anandtech.com/show/16028/better-yield-on-5nm-than-7nm-tsmc-update-on-defect-rates-for-n5

[38] ASML, 'Lithography Principles - Light and lasers'. Accessed: Oct. 31, 2024. [Online]. Available: https://www.asml.com/en/technology/lithography-principles/light-and-lasers

[39] W. Witkowski, '"Moore's Law's dead," Nvidia CEO Jensen Huang says in justifying gaming-card price hike', MarketWatch. Accessed: Oct. 30, 2024. [Online]. Available: https://www.marketwatch.com/story/moores-laws-dead-nvidia-ceo-jensen-says-in-justifying-gaming-card-price-hike-11663798618

[40] R. F. P. Martins *et al.*, 'Recyclable, Flexible, Low-Power Oxide Electronics', *Adv Funct Mater*, vol. 23, no. 17, pp. 2153–2161, May 2013, doi: 10.1002/adfm.201202907.

[41] OECD, 'Green technology and innovation'. Accessed: Oct. 30, 2024. [Online]. Available: https://www.oecd.org/en/topics/policy-issues/green-technology-and-innovation.html#related-publications

[42] A. Dechezlepretre and T. Kruse, 'The effect of climate policy on innovation and economic performance along the supply chain', Feb. 2022. doi: 10.1787/3569283a-en.

[43] M. Hegde *et al.*, '3D Printing All-Aromatic Polyimides using Mask-Projection Stereolithography: Processing the Nonprocessable', *Advanced Materials*, vol. 29, no. 31, Aug. 2017, doi: 10.1002/adma.201701240.

[44] C. Freitag, M. Berners-Lee, K. Widdicks, B. Knowles, G. Blair, and A. Friday, 'The climate impact of ICT: A review of estimates, trends and regulations', Feb. 2021.

[45] University of Cambridge, 'Cambridge spin-out starts producing graphene at commercial scale'. Accessed: Mar. 07, 2025. [Online]. Available: https://www.cam.ac.uk/research/news/cambridge-spin-out-starts-producing-graphene-at-commercial-scale

[46] K. Nomura, H. Ohta, A. Takagi, T. Kamiya, M. Hirano, and H. Hosono, 'Room-temperature fabrication of transparent flexible thin-film transistors using amorphous oxide semiconductors', *Nature*, vol. 432, no. 7016, pp. 488–492, Nov. 2004, doi: 10.1038/nature03090.

[47] Antonio. Facchetti and T. J. Marks, *Transparent electronics : from synthesis to applications*. Wiley, 2010.

[48] S. R. Forrest, 'The path to ubiquitous and low-cost organic electronic appliances on plastic', *Nature*, vol. 428, no. 6986, pp. 911–918, Apr. 2004, doi: 10.1038/nature02498.

[49] J. E. Anthony, 'Addressing challenges', *Nat Mater*, vol. 13, no. 8, pp. 773–775, Aug. 2014, doi: 10.1038/nmat4034.

[50] Q. Cao *et al.*, 'Medium-scale carbon nanotube thin-film integrated circuits on flexible plastic substrates', *Nature*, vol. 454, no. 7203, pp. 495–500, Jul. 2008, doi: 10.1038/nature07110.

[51] Z. Li, Z. Liu, H. Sun, and C. Gao, 'Superstructured Assembly of Nanocarbons: Fullerenes, Nanotubes, and Graphene', *Chem Rev*, vol. 115, no. 15, pp. 7046–7117, Aug. 2015, doi: 10.1021/acs.chemrev.5b00102.

[52] H. Schmidt, F. Giustiniano, and G. Eda, 'Electronic transport properties of transition metal dichalcogenide field-effect devices: surface and interface effects', *Chem Soc Rev*, vol. 44, no. 21, pp. 7715–7736, 2015, doi: 10.1039/C5CS00275C.

[53] X. Yu, T. J. Marks, and A. Facchetti, 'Metal oxides for optoelectronic applications', *Nat Mater*, vol. 15, no. 4, pp. 383–396, Mar. 2016, doi: 10.1038/nmat4599.

[54] K. Nomura, H. Ohta, K. Ueda, T. Kamiya, M. Hirano, and H. Hosono, 'Thin-film transistor fabricated in single-crystalline transparent oxide semiconductor', *Science (1979)*, vol. 300, no. 5623, pp. 1269–1272, May 2003, doi: 10.1126/science.1083212.

[55] J. G. Labram *et al.*, 'Signatures of Quantized Energy States in Solution-Processed Ultrathin Layers of Metal-Oxide Semiconductors and Their Devices', *Adv Funct Mater*, vol. 25, no. 11, pp. 1727–1736, Jan. 2015, doi: 10.1002/adfm.201403862.

[56] A. Liu *et al.*, 'Eco-friendly water-induced aluminum oxide dielectrics and their application in a hybrid metal oxide/polymer TFT', *RSC Adv*, vol. 5, no. 105, pp. 86606–86613, 2015, doi: 10.1039/c5ra15370k.

[57] Y. H. Kim *et al.*, 'Flexible metal-oxide devices made by room-temperature photochemical activation of solĝ€"gel films', *Nature*, vol. 489, no. 7414, pp. 128–132, Sep. 2012, doi: 10.1038/nature11434.

[58] Y. M. Park, J. Daniel, M. Heeney, and A. Salleo, 'Room-temperature fabrication of ultrathin oxide gate dielectrics for low-voltage operation of organic field-effect transistors', *Advanced Materials*, vol. 23, no. 8, pp. 971–974, Feb. 2011, doi: 10.1002/adma.201003641.

[59] T. Jun *et al.*, 'High-performance low-temperature solution-processable ZnO thin film transistors by microwave-assisted annealing', *J Mater Chem*, vol. 21, no. 4, pp. 1102–1108, Jan. 2011, doi: 10.1039/c0jm02178d.

[60] S. Logothetidis, D. Georgiou, A. Laskarakis, C. Koidis, and N. Kalfagiannis, 'In-line spectroscopic ellipsometry for the monitoring of the optical properties and quality of roll-to-roll printed nanolayers for organic photovoltaics', *Solar Energy Materials and Solar Cells*, vol. 112, pp. 144–156, May 2013, doi: 10.1016/j.solmat.2013.01.007.

[61] E. Yarali *et al.*, 'Recent Progress in Photonic Processing of Metal-Oxide Transistors', May 01, 2020, *Wiley-VCH Verlag*. doi: 10.1002/adfm.201906022.

[62] E. Carlos *et al.*, 'Laser induced ultrafast combustion synthesis of solution-based AlO: Xfor thin film transistors', *J Mater Chem C Mater*, vol. 8, no. 18, pp. 6176–6184, May 2020, doi: 10.1039/d0tc01204a.

[63] S. Dellis, I. Isakov, N. Kalfagiannis, K. Tetzner, T. D. Anthopoulos, and D. C. Koutsogeorgis, 'Rapid laser-induced photochemical conversion of sol-gel precursors to In2O3 layers and their application in thin-film transistors', *J Mater Chem C Mater*, vol. 5, no. 15, pp. 3673–3677, 2017, doi: 10.1039/c7tc00169j.

[64] C. Koutsiaki, 'Photonic conversion of sol-gel organometallic precursors into inorganic thin films', 2023.

[65] J. Semple, S. Rossbauer, and T. D. Anthopoulos, 'Analysis of Schottky contact formation in coplanar Au/ZnO/Al nanogap radio frequency diodes processed from solution at low temperature', *ACS Appl Mater Interfaces*, vol. 8, no. 35, pp. 23167–23174, Sep. 2016, doi: 10.1021/acsami.6b07099.

[66] C. Koutsiaki, D. C. Koutsogeorgis, and N. Kalfagiannis, 'Physicochemical Analysis of Nanoscale Metal Oxide Thin Film Precursors via Infrared Spectroscopic Ellipsometry', *Journal of Physical Chemistry C*, vol. 127, pp. 15876–15886, 2023.

[67] A. A. Toropov and T. V. Shubina, *Plasmonic Effects in Metal-Semiconductor Nanostructures*. Oxford University Press, 2015.

[68] M. Fox and G. F. Bertsch, *Optical Properties of Solids* , 2nd ed., no. 12. Oxford University Press, 2010. doi: 10.1119/1.1691372.

[69] D. J. Griffiths, *Introduction to Electrodynamics*. Cambridge University Press, 2017. doi: 10.1017/9781108333511.

[70] N. Bleistein and V. Barcilon, *Mathematical Methods for Wave Phenomena*. Elsevier, 1984. doi: 10.1016/C2009-0-21864-2.

[71] M. N. Berberan-Santos, 'Beer's law revisited', *J Chem Educ*, vol. 67, no. 9, pp. 757–759, Sep. 1990, doi: 10.1021/ed067p757.

[72] T. M. Atanackovic and A. Guran, *Theory of Elasticity for Scientists and Engineers*, 1st ed. Boston, MA: Birkhäuser Boston, 2000. doi: 10.1007/978-1-4612-1330-7.

[73] C. C. Murdock, 'Coulomb's Law and the Dielectric Constant', *Am J Phys*, vol. 12, no. 4, pp. 201–203, Aug. 1944, doi: 10.1119/1.1990594.

[74] L. E. Sutton, 'Electric dipole moments and resonance in molecules', *Transactions of the Faraday Society*, vol. 30, pp. 789–801, 1934, doi: 10.1039/tf9343000789.

[75] A. F. J. Levi, *Essential Classical Mechanics for Device Physics*, 1st ed. Morgan & Claypool Publishers, 2016. doi: 10.1088/978-1-6817-4413-1.

[76] H. G. Tompkins and J. N. Hilfiker, *Spectroscopic Ellipsometry: Practical Application to Thin Film Characterization*. New York: Momentum Press, 2016.

[77] M. Aburas, V. Soebarto, T. Williamson, R. Liang, H. Ebendorff-Heidepriem, and Y. Wu, 'Thermochromic smart window technologies for building application: A review', *Appl Energy*, vol. 255, p. 113522, Dec. 2019, doi: 10.1016/j.apenergy.2019.113522.

[78] C. G. Granqvist, 'Electrochromics for smart windows: Oxide-based thin films and devices', *Thin Solid Films*, vol. 564, pp. 1–38, Aug. 2014, doi: 10.1016/j.tsf.2014.02.002.

[79] A. Piccolo and F. Simone, 'Performance requirements for electrochromic smart window', *Journal of Building Engineering*, vol. 3, pp. 94–103, Sep. 2015, doi: 10.1016/j.jobe.2015.07.002.

[80] H. Xu *et al.*, 'A flexible AMOLED display on the PEN substrate driven by oxide thin-film transistors using anodized aluminium oxide as dielectric', *J. Mater. Chem. C*, vol. 2, no. 7, pp. 1255–1259, 2014, doi: 10.1039/C3TC31710B.

[81] J. Jo, S. Kang, J. S. Heo, Y. Kim, and S. K. Park, 'Flexible Metal Oxide Semiconductor Devices Made by Solution Methods', *Chemistry – A European Journal*, vol. 26, no. 42, pp. 9126–9156, Jul. 2020, doi: 10.1002/chem.202000090.

[82] Y. Nakajima *et al.*, 'Development of 8-in. oxide-TFT-driven flexible AMOLED display using high-performance red phosphorescent OLED', *J Soc Inf Disp*, vol. 22, no. 3, pp. 137–143, Mar. 2014, doi: 10.1002/jsid.227.

[83] P. Yianoulis and M. Giannouli, 'Thin Solid Films and Nanomaterials for Solar Energy Conversion and Energy Saving Applications', *Journal of Nano Research*, vol. 2, pp. 49–60, Aug. 2008, doi: 10.4028/www.scientific.net/JNanoR.2.49.

[84] T. D. Lee and A. U. Ebong, 'A review of thin film solar cell technologies and challenges', *Renewable and Sustainable Energy Reviews*, vol. 70, pp. 1286–1297, Apr. 2017, doi: 10.1016/j.rser.2016.12.028.

[85] S. Babu Krishna Moorthy, Ed., *Thin Film Structures in Energy Applications*. Cham: Springer International Publishing, 2015. doi: 10.1007/978-3-319-14774-1.

[86] C. Wang, L. Yin, L. Zhang, D. Xiang, and R. Gao, 'Metal Oxide Gas Sensors: Sensitivity and Influencing Factors', *Sensors*, vol. 10, no. 3, pp. 2088–2106, Mar. 2010, doi: 10.3390/s100302088.

[87] P. Lin and F. Yan, 'Organic Thin-Film Transistors for Chemical and Biological Sensing', *Advanced Materials*, vol. 24, no. 1, pp. 34–51, Jan. 2012, doi: 10.1002/adma.201103334.

[88] L. Babun, K. Denney, Z. B. Celik, P. McDaniel, and A. S. Uluagac, 'A survey on IoT platforms: Communication, security, and privacy perspectives', *Computer Networks*, vol. 192, p. 108040, Jun. 2021, doi: 10.1016/j.comnet.2021.108040.

[89] P. Heremans *et al.*, 'Mechanical and Electronic Properties of Thin-Film Transistors on Plastic, and Their Integration in Flexible Electronic Applications', *Advanced Materials*, vol. 28, no. 22, pp. 4266–4282, Jun. 2016, doi: 10.1002/adma.201504360.

[90] K. Myny, 'The development of flexible integrated circuits based on thin-film transistors'.

[91] J. W. Borchert *et al.*, 'Flexible low-voltage high-frequency organic thin-film transistors', *Sci Adv*, vol. 6, no. 21, May 2020, doi: 10.1126/sciadv.aaz5156.

[92] Y. Li, G. Xu, C. Cui, and Y. Li, 'Flexible and Semitransparent Organic Solar Cells', *Adv Energy Mater*, vol. 8, no. 7, Mar. 2018, doi: 10.1002/aenm.201701791.

[93] K. Seshan and D. Schepis, Eds., *Handbook of Thin Film Deposition*, 4th ed. Elsevier, 2018. doi: 10.1016/C2016-0-03243-6.

[94] L. Venema, 'Silicon electronics and beyond', *Nature*, vol. 479, no. 7373, pp. 309–309, Nov. 2011, doi: 10.1038/479309a.

[95] IEEE, 'International Roadmap for Devices and Systems: More Moore', 2021.

[96] S. C. Song *et al.*, '2nm Node: Benchmarking FinFET vs Nano-Slab Transistor Architectures for Artificial Intelligence and Next Gen Smart Mobile Devices', in *2019 Symposium on VLSI Technology*, IEEE, Jun. 2019, pp. T206–T207. doi: 10.23919/VLSIT.2019.8776478.

[97] R. W. Keyes, 'Fundamental limits of silicon technology', *Proceedings of the IEEE*, vol. 89, no. 3, pp. 227–239, Mar. 2001, doi: 10.1109/5.915372.

[98] R. W. Keyes, 'Fundamental limits of silicon technology', *Proceedings of the IEEE*, vol. 89, no. 3, pp. 227–239, Mar. 2001.

[99] J. D. Meindl, Q. Chen, and J. A. Davis, 'Limits on Silicon Nanoelectronics for Terascale Integration', *Science (1979)*, vol. 293, no. 5537, pp. 2044–2049, Sep. 2001, doi: 10.1126/science.293.5537.2044.

[100] Q. Wu, Y. Li, and Y. Zhao, 'The Evolution of Photolithography Technology, Process Standards, and Future Outlook', in *2020 IEEE 15th International Conference on Solid-State & Integrated Circuit Technology (ICSICT)*, IEEE, Nov. 2020, pp. 1–5. doi: 10.1109/ICSICT49897.2020.9278164.

[101] H. A. Klasens and H. Koelmans, 'A tin oxide field-effect transistor', *Solid State Electron*, vol. 7, no. 9, pp. 701–702, Sep. 1964, doi: 10.1016/0038-1101(64)90057-7.

[102] H. Schroeder, 'Properties and Applications of Oxide Layers Deposited on Glass from Organic Solutions', *Optica Acta: International Journal of Optics*, vol. 9, no. 3, pp. 249–254, Jul. 1962, doi: 10.1080/713826428.

[103] K. Nomura, H. Ohta, A. Takagi, T. Kamiya, M. Hirano, and H. Hosono, 'Room-temperature fabrication of transparent flexible thin-film transistors using amorphous oxide semiconductors', *Nature*, vol. 432, no. November, p. 488, 2004, [Online]. Available: https://www.nature.com/articles/nature03090.pdf

[104] M. Lorenz *et al.*, 'The 2016 oxide electronic materials and oxide interfaces roadmap', *J Phys D Appl Phys*, vol. 49, no. 43, p. 433001, Nov. 2016, doi: 10.1088/0022-3727/49/43/433001.

[105] T. D. Anthopoulos, J.-S. Chen, and A. Facchetti, 'Metal oxide thin film electronics', *Appl Phys Lett*, vol. 124, no. 19, May 2024, doi: 10.1063/5.0215543.

[106] H. Takagi and H. Y. Hwang, 'An Emergent Change of Phase for Electronics', *Science (1979)*, vol. 327, no. 5973, pp. 1601–1602, Mar. 2010, doi: 10.1126/science.1182541.

[107] D. -H. Lee, Y. -J. Chang, G. S. Herman, and C. -H. Chang, 'A General Route to Printable High-Mobility Transparent Amorphous Oxide Semiconductors', *Advanced Materials*, vol. 19, no. 6, pp. 843–847, Mar. 2007, doi: 10.1002/adma.200600961.

[108] Yu. N. Zhuravlev and O. S. Obolonskaya, 'Structure, mechanical stability, and chemical bond in alkali metal oxides', *Journal of Structural Chemistry*, vol. 51, no. 6, pp. 1005–1013, Dec. 2010, doi: 10.1007/s10947-010-0157-1.

[109] D. Khim *et al.*, 'Modulation-Doped In2O3/ZnO Heterojunction Transistors Processed from Solution', *Advanced Materials*, vol. 29, no. 19, May 2017, doi: 10.1002/adma.201605837.

[110] Z. Sun *et al.*, 'Generalized self-assembly of scalable two-dimensional transition metal oxide nanosheets', *Nat Commun*, vol. 5, no. 1, p. 3813, May 2014, doi: 10.1038/ncomms4813.

[111] F. Trier, D. V Christensen, and N. Pryds, 'Electron mobility in oxide heterostructures', *J Phys D Appl Phys*, vol. 51, no. 29, p. 293002, Jul. 2018, doi: 10.1088/1361-6463/aac9aa.

[112] H. Faber *et al.*, 'Heterojunction oxide thin-film transistors with unprecedented electron mobility grown from solution', *Sci Adv*, vol. 3, no. 3, pp. 1–10, 2017, doi: 10.1126/sciadv.1602640.

[113] Y. S. Rim *et al.*, 'Boost Up Mobility of Solution-Processed Metal Oxide Thin-Film Transistors via Confining Structure on Electron Pathways', *Advanced Materials*, vol. 26, no. 25, pp. 4273–4278, Jul. 2014, doi: 10.1002/adma.201400529.

[114] L. Petti *et al.*, 'Metal oxide semiconductor thin-film transistors for flexible electronics', Jun. 01, 2016, *American Institute of Physics Inc.* doi: 10.1063/1.4953034.

[115] S. R. Thomas, P. Pattanasattayavong, and T. D. Anthopoulos, 'Solution-processable metal oxide semiconductors for thin-film transistor applications', *Chem Soc Rev*, vol. 42, no. 16, pp. 6910–6923, Jul. 2013, doi: 10.1039/c3cs35402d.

[116] D. G. . Rethwisch and W. D. Callister Jr, *Materials Science and Engineering: An Introduction*, 10th ed. Wiley, 2018.

[117] J. Robertson, 'High dielectric constant oxides', *EPJ Applied Physics*, vol. 28, no. 3, pp. 265–291, Dec. 2004, doi: 10.1051/epjap:2004206.

[118] K. Yim *et al.*, 'Novel high-κ dielectrics for next-generation electronic devices screened by automated ab initio calculations', *NPG Asia Mater*, vol. 7, no. 6, pp. e190–e190, Jun. 2015, doi: 10.1038/am.2015.57.

[119] S. Steudel *et al.*, 'Influence of the dielectric roughness on the performance of pentacene transistors', *Appl Phys Lett*, vol. 85, no. 19, pp. 4400–4402, 2004.

[120] A. D. Mottram *et al.*, 'Electron mobility enhancement in solution-processed low-voltage In2O3 transistors via channel interface planarization', *AIP Adv*, vol. 8, no. 6, Jun. 2018, doi: 10.1063/1.5036809.

[121] J. Robertson, 'Interfaces and defects of high-K oxides on silicon', *Solid State Electron*, vol. 49, no. 3, pp. 283–293, Mar. 2005, doi: 10.1016/j.sse.2004.11.011.

[122] S. Park, C.-H. Kim, W.-J. Lee, S. Sung, and M.-H. Yoon, 'Sol-gel metal oxide dielectrics for all-solution-processed electronics', *Materials Science and Engineering: R: Reports*, vol. 114, pp. 1–22, Apr. 2017, doi: 10.1016/j.mser.2017.01.003.

[123] E. N. Bunting, G. R. Shelton, and A. S. Creamer, 'Properties of Barium-Strontium Titanate Dielectrics'.

[124] R. Liu *et al.*, 'Materials and physical properties of novel high-k and medium-k gate dielectrics', *Materials Research Society Symposium - Proceedings*, vol. 670, pp. K111–K1112, 2001, doi: 10.1557/proc-670-k1.1.

[125] M. G. Elmahgary, A. M. Mahran, M. Ganoub, and S. O. Abdellatif, 'Optical investigation and computational modelling of BaTiO3 for optoelectronic devices applications', *Sci Rep*, vol. 13, no. 1, Dec. 2023, doi: 10.1038/s41598-023-31652-2.

[126] A. Piccirillo and A. L. Gobbi, 'Physical-Electrical Properties of Silicon Nitride Deposited by PECVD on I II-V Semiconductors'.

[127] R. D. Clark, 'Emerging applications for high K materials in VLSI technology', 2014, *MDPI AG*. doi: 10.3390/ma7042913.

[128] W. T. Lin *et al.*, 'Optical Properties of Silicon Nitride You may also like Kinetics of Thermal Growth of HCl 0 2 Oxides on Silicon K. Hirabayashi and J. Iwamura-Ion Implantation and Annealing Effects on the Superconductivity and Microstructure of BiSrCaCuO Superconducting Films Electrical Properties of a Native Oxide on Gallium Phosphide'.

[129] 'PEA_24_2_305-311'.

[130] C. L. Ücker *et al.*, 'Investigation of the properties of niobium pentoxide for use in dye-sensitized solar cells', *Journal of the American Ceramic Society*, vol. 102, no. 4, pp. 1884–1892, Apr. 2019, doi: 10.1111/jace.16080.

[131] A. Callegari, E. Cartier, M. Gribelyuk, H. F. Okorn-Schmidt, and T. Zabel, 'Physical and electrical characterization of Hafnium oxide and Hafnium silicate sputtered films', *J Appl Phys*, vol. 90, no. 12, pp. 6466–6475, Dec. 2001, doi: 10.1063/1.1417991.

[132] K. Yim *et al.*, 'Novel high-K dielectrics for next-generation electronic devices screened by automated ab initio calculations', *NPG Asia Mater*, vol. 7, no. 6, Jun. 2015, doi: 10.1038/am.2015.57.

[133] O. A. Lukianova and V. V. Sirota, 'Dielectric properties of silicon nitride ceramics produced by free sintering', *Ceram Int*, vol. 43, no. 11, pp. 8284–8288, Aug. 2017, doi: 10.1016/j.ceramint.2017.03.161.

[134] K. Van Benthem, C. Elsässer, and R. H. French, 'Bulk electronic structure of SrTiO3: Experiment and theory', *J Appl Phys*, vol. 90, no. 12, pp. 6156–6164, Dec. 2001, doi: 10.1063/1.1415766.

[135] G. Nanda *et al.*, 'Temperature dependent conductivity and broadband dielectric response of precursor-derived Nb2O5', *Ceram Int*, vol. 46, no. 7, pp. 9512–9518, May 2020, doi: 10.1016/j.ceramint.2019.12.213.

[136] X. Wang *et al.*, 'Structural Properties Characterized by the Film Thickness and Annealing Temperature for La2O3 Films Grown by Atomic Layer Deposition', *Nanoscale Res Lett*, vol. 12, no. 1, Dec. 2017, doi: 10.1186/s11671-017-2018-8.

[137] R. C. Neville, B. Hoeneisen, and C. A. Mead, 'Permittivity of strontium titanate', *J Appl Phys*, vol. 43, no. 5, pp. 2124–2131, 1972, doi: 10.1063/1.1661463.

[138] G. D. Wilk, R. M. Wallace, and J. M. Anthony, 'High-κ gate dielectrics: Current status and materials properties considerations', *J Appl Phys*, vol. 89, no. 10, pp. 5243–5275, May 2001, doi: 10.1063/1.1361065.

[139] C. Bartic, H. Jansen, A. Campitelli, and S. Borghs, 'Ta2O5 as gate dielectric material for low-voltage organic thin-film transistors', *Org Electron*, vol. 3, no. 2, pp. 65–72, Jun. 2002, doi: 10.1016/S1566-1199(02)00034-4.

[140] M. Matsui, H. Nagayoshi, G. Muto, S. Tanimoto, K. Kuroiwa, and Y. Tarui, 'Amorphous Silicon Thin-Film Transistors Employing Photoprocessed Tantalum Oxide Films as Gate Insulators', *Jpn J Appl Phys*, vol. 29, no. 1R, p. 62, Jan. 1990, doi: 10.1143/JJAP.29.62.

[141] F. Xu, A. Liu, G. Liu, B. Shin, and F. Shan, 'Solution-processed yttrium oxide dielectric for high-performance IZO thin-film transistors', *Ceram Int*, vol. 41, pp. S337–S343, Jul. 2015, doi: 10.1016/j.ceramint.2015.03.120.

[142] K. Song, W. Yang, Y. Jung, S. Jeong, and J. Moon, 'A solution-processed yttrium oxide gate insulator for high-performance all-solution-processed fully transparent thin film transistors', *J Mater Chem*, vol. 22, no. 39, p. 21265, 2012, doi: 10.1039/c2jm34162j.

[143] R. Z. Wang, S. L. Wu, X. Y. Li, and J. T. Zhang, 'The electrical performance and gate bias stability of an amorphous InGaZnO thin-film transistor with HfO 2 high-k dielectrics', *Solid State Electron*, vol. 133, pp. 6–9, Jul. 2017, doi: 10.1016/j.sse.2017.04.004.

[144] F. Zhang, G. Liu, A. Liu, B. Shin, and F. Shan, 'Solution-processed hafnium oxide dielectric thin films for thin-film transistors applications', *Ceram Int*, vol. 41, no. 10, pp. 13218–13223, Dec. 2015, doi: 10.1016/j.ceramint.2015.07.099.

[145] K. J. Hubbard and D. G. Schlom, 'Thermodynamic stability of binary oxides in contact with silicon', *J Mater Res*, vol. 11, no. 11, pp. 2757–2776, Nov. 1996, doi: 10.1557/JMR.1996.0350.

[146] K. Yim *et al.*, 'Novel high-κ dielectrics for next-generation electronic devices screened by automated ab initio calculations', *NPG Asia Mater*, vol. 7, no. 6, pp. e190–e190, Jun. 2015, doi: 10.1038/am.2015.57.

[147] D. S. Ginley, Ed., *Handbook of Transparent Conductors*. Boston, MA: Springer US, 2011. doi: 10.1007/978-1-4419-1638-9.

[148] H. Hosono, 'Recent progress in transparent oxide semiconductors: Materials and device application', *Thin Solid Films*, vol. 515, no. 15, pp. 6000–6014, May 2007, doi: 10.1016/j.tsf.2006.12.125.

[149] N. Münzenrieder, C. Zysset, L. Petti, T. Kinkeldei, G. A. Salvatore, and G. Tröster, 'Flexible double gate a-IGZO TFT fabricated on free standing polyimide foil', *Solid State Electron*, vol. 84, pp. 198–204, 2013, doi: 10.1016/j.sse.2013.02.025.

[150] G. J. Lee, J. Kim, J. H. Kim, S. M. Jeong, J. E. Jang, and J. Jeong, 'High performance, transparent a-IGZO TFTs on a flexible thin glass substrate', *Semicond Sci Technol*, vol. 29, no. 3, Mar. 2014, doi: 10.1088/0268-1242/29/3/035003.

[151] F. Xu, A. Liu, G. Liu, B. Shin, and F. Shan, 'Solution-processed yttrium oxide dielectric for high-performance IZO thin-film transistors', *Ceram Int*, vol. 41, pp. S337–S343, Jul. 2015, doi: 10.1016/j.ceramint.2015.03.120.

[152] A. Mancinelli, D. Briand, S. Bolat, J. Kim, and Y. E. Romanyuk, 'Deep-UV-enhanced approach for low-temperature solution processing of IZO transistors with high-K AlOx/YALOX dielectric', *ACS Appl Electron Mater*, vol. 2, no. 10, pp. 3141–3151, Oct. 2020, doi: 10.1021/acsaelm.0c00444.

[153] T. Minami, H. Sato, K. Ohashi, T. Tomofuji, and S. Takata, 'Conduction mechanism of highly conductive and transparent zinc oxide thin films prepared by magnetron sputtering', *J Cryst Growth*, vol. 117, no. 1–4, pp. 370–374, Feb. 1992, doi: 10.1016/0022-0248(92)90778-H.

[154] R. Branquinho *et al.*, 'Towards environmental friendly solution-based ZTO/AlO $_x$ TFTs', *Semicond Sci Technol*, vol. 30, no. 2, p. 024007, Feb. 2015, doi: 10.1088/0268-1242/30/2/024007.

[155] J. W. Park, B. H. Kang, and H. J. Kim, 'A Review of Low-Temperature Solution-Processed Metal Oxide Thin-Film Transistors for Flexible Electronics', May 01, 2020, *Wiley-VCH Verlag*. doi: 10.1002/adfm.201904632.

[156] K. Song *et al.*, 'Solution-processable tin-doped indium oxide with a versatile patternability for transparent oxide thin film transistors', *J Mater Chem*, vol. 21, no. 38, p. 14646, 2011, doi: 10.1039/c1jm11418b.

[157] W. Seiler, M. Nistor, C. Hebert, and J. Perrière, 'Epitaxial undoped indium oxide thin films: Structural and physical properties', *Solar Energy Materials and Solar Cells*, vol. 116, pp. 34–42, Sep. 2013, doi: 10.1016/j.solmat.2013.04.002.

[158] H. Sato, T. Minami, S. Takata, and T. Yamada, 'Transparent conducting p-type NiO thin films prepared by magnetron sputtering', *Thin Solid Films*, vol. 236, no. 1–2, pp. 27–31, Dec. 1993, doi: 10.1016/0040-6090(93)90636-4.

[159] A. O. Musa, T. Akomolafe, and M. J. Carter, 'Production of cuprous oxide, a solar cell material, by thermal oxidation and a study of its physical and electrical properties', *Solar Energy Materials and Solar Cells*, vol. 51, no. 3–4, pp. 305–316, Feb. 1998, doi: 10.1016/S0927-0248(97)00233-X.

[160] A. Kudo, H. Yanagi, H. Hosono, and H. Kawazoe, 'SrCu 2 O 2 : A *p* -type conductive oxide with wide band gap', *Appl Phys Lett*, vol. 73, no. 2, pp. 220–222, Jul. 1998, doi: 10.1063/1.121761.

[161] H. Kawazoe, M. Yasukawa, H. Hyodo, M. Kurita, H. Yanagi, and H. Hosono, 'P-type electrical conduction in transparent thin films of CuAlO2', *Nature*, vol. 389, no. 6654, pp. 939–942, Oct. 1997, doi: 10.1038/40087.

[162] H. Hosono, 'Ionic amorphous oxide semiconductors: Material design, carrier transport, and device application', *J Non Cryst Solids*, vol. 352, no. 9–20, pp. 851–858, Jun. 2006, doi: 10.1016/j.jnoncrysol.2006.01.073.

[163] J. E. Medvedeva, I. A. Zhuravlev, C. Burris, D. B. Buchholz, M. Grayson, and R. P. H. Chang, 'Origin of high carrier concentration in amorphous wide-bandgap oxides: Role of disorder in defect formation and electron localization in In2O3- x', *J Appl Phys*, vol. 127, no. 17, May 2020, doi: 10.1063/1.5144219.

[164] A. D. Mottram, Y. H. Lin, P. Pattanasattayavong, K. Zhao, A. Amassian, and T. D. Anthopoulos, 'Quasi Two-Dimensional Dye-Sensitized In2O3 Phototransistors for Ultrahigh Responsivity and Photosensitivity Photodetector Applications', *ACS Appl Mater Interfaces*, vol. 8, no. 7, pp. 4894–4902, Feb. 2016, doi: 10.1021/acsami.5b11210.

[165] P. K. Nayak, M. N. Hedhili, D. Cha, and H. N. Alshareef, 'High performance In2O3 thin film transistors using chemically derived aluminum oxide dielectric', *Appl Phys Lett*, vol. 103, no. 3, p. 033518, Jul. 2013, doi: 10.1063/1.4816060.

[166] K. Tetzner, I. Isakov, A. Regoutz, D. J. Payne, and T. D. Anthopoulos, 'The impact of post-deposition annealing on the performance of solution-processed single layer In2O3 and

isotype In2O3/ZnO heterojunction transistors', *J Mater Chem C Mater*, vol. 5, no. 1, pp. 59–64, 2017, doi: 10.1039/c6tc04907a.

[167] J. E. Medvedeva and A. J. Freeman, 'Combining high conductivity with complete optical transparency: A band structure approach', *Europhys Lett*, vol. 69, no. 4, pp. 583–587, Feb. 2005, doi: 10.1209/epl/i2004-10386-y.

[168] J. E. Medvedeva and C. L. Hettiarachchi, 'Tuning the properties of complex transparent conducting oxides: Role of crystal symmetry, chemical composition, and carrier generation', *Phys Rev B Condens Matter Mater Phys*, vol. 81, no. 12, Mar. 2010, doi: 10.1103/PhysRevB.81.125116.

[169] H. O. Hidefumi Odaka, Y. S. Yuzo Shigesato, T. M. Takashi Murakami, and S. I. Shuichi Iwata, 'Electronic Structure Analyses of Sn-doped In $_2$ O $_3$', *Jpn J Appl Phys*, vol. 40, no. 5R, p. 3231, May 2001, doi: 10.1143/JJAP.40.3231.

[170] Y. M. Yiming Mi, H. O. Hidefumi Odaka, and S. I. Shuichi Iwata, 'Electronic Structures and Optical Properties of ZnO, SnO $_2$ and In $_2$ O $_3$', *Jpn J Appl Phys*, vol. 38, no. 6R, p. 3453, Jun. 1999, doi: 10.1143/JJAP.38.3453.

[171] O. Mryasov and A. Freeman, 'Electronic band structure of indium tin oxide and criteria for transparent conducting behavior', *Phys Rev B*, vol. 64, no. 23, p. 233111, Dec. 2001, doi: 10.1103/PhysRevB.64.233111.

[172] M. Feneberg *et al.*, 'Many-electron effects on the dielectric function of cubic <math> <mrow> <msub> <mi>In</mi> <mn>2</mn> </msub> <msub> <mi mathvariant="normal">O</mi> <mn>3</mn> </msub> </mrow> </math> : Effective electron mass, band nonparabolicity, band gap renormalization, and Burstein-Moss shift', *Phys Rev B*, vol. 93, no. 4, p. 045203, Jan. 2016, doi: 10.1103/PhysRevB.93.045203.

[173] A. Walsh *et al.*, 'Nature of the Band Gap of <math display="inline"> <msub> <mi>In</mi> <mn>2</mn> </msub> <msub> <mi mathvariant="normal">O</mi> <mn>3</mn> </msub> </math> Revealed by First-Principles Calculations and X-Ray Spectroscopy', *Phys Rev Lett*, vol. 100, no. 16, p. 167402, Apr. 2008, doi: 10.1103/PhysRevLett.100.167402.

[174] D. R. Lide, Ed., *Handbook of Chemistry and Physics*, 85th ed. Boca Raton: CRC Press, 2005.

[175] H. K. Hideo Hosono, Masahiro Yasakawa, 'Novel oxide amorphous semiconductors : transparent conducting amorphous oxides Possible Candidate for HMCs', *J Non Cryst Solids*, vol. 203, pp. 334–344, 1996.

[176] R. L. Weiher, 'Electrical Properties of Single Crystals of Indium Oxide', *J Appl Phys*, vol. 33, no. 9, pp. 2834–2839, Sep. 1962, doi: 10.1063/1.1702560.

[177] T. Kamiya and H. Hosono, 'Material characteristics and applications of transparent amorphous oxide semiconductors', *NPG Asia Mater*, vol. 2, no. 1, pp. 15–22, Jan. 2010, doi: 10.1038/asiamat.2010.5.

[178] T. Kamiya, K. Nomura, and H. Hosono, 'Origins of High Mobility and Low Operation Voltage of Amorphous Oxide TFTs: Electronic Structure, Electron Transport, Defects and Doping', *Journal of Display Technology*, vol. 5, no. 7, pp. 273–288, Jul. 2009, doi: 10.1109/JDT.2009.2021582.

[179] J. Y. W. Seto, 'The electrical properties of polycrystalline silicon films', *J Appl Phys*, vol. 46, no. 12, pp. 5247–5254, Dec. 1975, doi: 10.1063/1.321593.

[180] G. Baccarani, B. Riccò, and G. Spadini, 'Transport properties of polycrystalline silicon films', *J Appl Phys*, vol. 49, no. 11, pp. 5565–5570, Nov. 1978, doi: 10.1063/1.324477.

[181] R. Clanget, 'Ionized impurity scattering in degenerate In2O3', *Applied Physics*, vol. 2, no. 5, pp. 247–256, Nov. 1973, doi: 10.1007/BF00889507.

[182] M. Jothibas, C. Manoharan, S. Ramalingam, S. Dhanapandian, S. Johnson Jeyakumar, and M. Bououdina, 'Preparation, characterization, spectroscopic (FT-IR, FT-Raman, UV and visible) studies, optical properties and Kubo gap analysis of In2O3 thin films', *J Mol Struct*, vol. 1049, pp. 239–249, Oct. 2013, doi: 10.1016/j.molstruc.2013.06.047.

[183] A. Rogozin, M. Vinnichenko, N. Shevchenko, U. Kreissig, A. Kolitsch, and W. Möller, 'Real-time evolution of electrical properties and structure of indium oxide and indium tin oxide during crystallization', *Scr Mater*, vol. 60, no. 4, pp. 199–202, Feb. 2009, doi: 10.1016/j.scriptamat.2008.09.020.

[184] M. Parashar, V. K. Shukla, and R. Singh, 'Metal oxides nanoparticles via sol–gel method: a review on synthesis, characterization and applications', *Journal of Materials Science: Materials in Electronics*, vol. 31, no. 5, pp. 3729–3749, Mar. 2020, doi: 10.1007/s10854-020-02994-8.

[185] V. Stavila, A. A. Talin, and M. D. Allendorf, 'MOF-based electronic and opto-electronic devices', *Chem. Soc. Rev.*, vol. 43, no. 16, pp. 5994–6010, 2014, doi: 10.1039/C4CS00096J.

[186] Y. Dimitriev, Y. Ivanova, and R. Iordanova, 'History of sol-gel science and technology', *Journal of University of Chemical Technology and Metallurgy*, vol. 43, no. 2, pp. 181–192, 2008.

[187] W. M. Cranton *et al.*, 'Excimer laser processing of inkjet-printed and sputter-deposited transparent conducting SnO2:Sb for flexible electronics', *Thin Solid Films*, vol. 515, no. 24 SPEC. ISS., pp. 8534–8538, Oct. 2007, doi: 10.1016/j.tsf.2007.03.118.

[188] H. Faber *et al.*, 'Indium oxide thin-film transistors processed at low temperature via ultrasonic spray pyrolysis', *ACS Appl Mater Interfaces*, vol. 7, no. 1, pp. 782–790, Jan. 2015, doi: 10.1021/am5072139.

[189] G. Adamopoulos, S. Thomas, P. H. Wöbkenberg, D. D. C. Bradley, M. A. McLachlan, and T. D. Anthopoulos, 'High-mobility low-voltage ZnO and Li-doped ZnO transistors based on ZrO2 high-k dielectric grown by spray pyrolysis in ambient air', *Advanced Materials*, vol. 23, no. 16, pp. 1894–1898, 2011, doi: 10.1002/adma.201003935.

[190] T. Puangpetch, T. Sreethawong, S. Yoshikawa, and S. Chavadej, 'Synthesis and photocatalytic activity in methyl orange degradation of mesoporous-assembled SrTiO3 nanocrystals prepared by sol-gel method with the aid of structure-directing surfactant', *J Mol Catal A Chem*, vol. 287, no. 1–2, pp. 70–79, May 2008, doi: 10.1016/j.molcata.2008.02.027.

[191] E. Carlos, R. Branquinho, A. Kiazadeh, P. Barquinha, R. Martins, and E. Fortunato, 'UV-Mediated Photochemical Treatment for Low-Temperature Oxide-Based Thin-Film Transistors', *ACS Appl Mater Interfaces*, vol. 8, no. 45, pp. 31100–31108, Nov. 2016, doi: 10.1021/acsami.6b06321.

[192] A. Bashir, M. Farooq, A. Malik, S. Naseem, and A. S. Bhatti, 'UV-a treatment of ZrO2 thin films fabricated by environmental friendlier water-based solution processing: Structural and optical studies', *Coatings*, vol. 11, no. 7, Jul. 2021, doi: 10.3390/coatings11070821.

[193] M. Yabuki, R. Takahashi, S. Sato, T. Sodesawa, and K. Ogura, 'Silica–alumina catalysts prepared in sol–gel process of TEOS with organic additives', *Phys. Chem. Chem. Phys.*, vol. 4, no. 19, pp. 4830–4837, 2002, doi: 10.1039/B205645C.

[194] B. E. Yoldas, 'Monolithic glass formation by chemical polymerization', *J Mater Sci*, vol. 14, no. 8, pp. 1843–1849, Aug. 1979, doi: 10.1007/BF00551023.

[195] I. Bretos, R. Jiménez, J. Ricote, and M. L. Calzada, 'Low-temperature crystallization of solution-derived metal oxide thin films assisted by chemical processes', *Chem Soc Rev*, vol. 47, no. 2, pp. 291–308, 2018, doi: 10.1039/C6CS00917D.

[196] A. E. Danks, S. R. Hall, and Z. Schnepp, 'The evolution of "sol-gel" chemistry as a technique for materials synthesis', *Mater Horiz*, vol. 3, no. 2, pp. 91–112, Mar. 2016, doi: 10.1039/c5mh00260e.

[197] C. de Coelho Escobar and J. H. Z. dos Santos, 'Effect of the sol–gel route on the textural characteristics of silica imprinted with Rhodamine <scp>B</scp>', *J Sep Sci*, vol. 37, no. 7, pp. 868–875, Apr. 2014, doi: 10.1002/jssc.201301143.

[198] L. Velardi, L. Scrimieri, A. Serra, D. Manno, and L. Calcagnile, 'The synergistic role of pH and calcination temperature in sol–gel titanium dioxide powders', *Applied Physics A*, vol. 125, no. 10, p. 735, Oct. 2019, doi: 10.1007/s00339-019-3038-2.

[199] G. W. Scherer, 'Aging and drying of gels', *J Non Cryst Solids*, vol. 100, no. 1–3, pp. 77–92, Mar. 1988, doi: 10.1016/0022-3093(88)90008-7.

[200] E. A. Cochran, K. N. Woods, D. W. Johnson, C. J. Page, and S. W. Boettcher, 'Unique chemistries of metal-nitrate precursors to form metal-oxide thin films from solution: materials for electronic and energy applications', *J Mater Chem A Mater*, vol. 7, pp. 24124–24149, 2019.

[201] J. D. Wright and N. A. J. M. Sommerdijk, *Sol-Gel Materials Chemistry and Applications*. CRC Press, 2001.

[202] I. Isakov *et al.*, 'Exploring the Leidenfrost Effect for the Deposition of High-Quality In2O3 Layers via Spray Pyrolysis at Low Temperatures and Their Application in High Electron Mobility Transistors', *Adv Funct Mater*, vol. 27, no. 22, Jun. 2017, doi: 10.1002/adfm.201606407.

[203] M. M. Collinson, H. Wang, R. Makote, and A. Khramov, 'The effects of drying time and relative humidity on the stability of sol–gel derived silicate films in solution', *Journal of Electroanalytical Chemistry*, vol. 519, no. 1–2, pp. 65–71, Feb. 2002, doi: 10.1016/S0022-0728(01)00723-9.

[204] S. Park *et al.*, 'In-depth studies on rapid photochemical activation of various sol-gel metal oxide films for flexible transparent electronics', *Adv Funct Mater*, vol. 25, no. 19, pp. 2807–2815, May 2015, doi: 10.1002/adfm.201500545.

[205] K.-H. Lim *et al.*, 'A systematic study on effects of precursors and solvents for optimization of solution-processed oxide semiconductor thin-film transistors', *J Mater Chem C Mater*, vol. 5, no. 31, pp. 7768–7776, 2017, doi: 10.1039/C7TC01779K.

[206] S. Jeong, J.-Y. Lee, S. S. Lee, Y. Choi, and B.-H. Ryu, 'Impact of Metal Salt Precursor on Low-Temperature Annealed Solution-Derived Ga-doped In_2O_3 Semiconductor for Thin-Film Transistors', *The Journal of Physical Chemistry C*, vol. 115, no. 23, pp. 11773–11780, Jun. 2011, doi: 10.1021/jp202522s.

[207] N. Ben Moussa *et al.*, 'Synthesis of ZnO sol–gel thin-films CMOS-Compatible', *RSC Adv*, vol. 11, pp. 22723–22733, 2021.

[208] W. J. Scheideler, R. Kumar, A. R. Zeumault, and V. Subramanian, 'Low-Temperature-Processed Printed Metal Oxide Transistors Based on Pure Aqueous Inks', *Adv Funct Mater*, vol. 27, no. 14, Apr. 2017, doi: 10.1002/adfm.201606062.

[209] A. Nadarajah, M. E. Carnes, M. G. Kast, D. W. Johnson, and S. W. Boettcher, 'Aqueous Solution Processing of F-Doped SnO_2 Transparent Conducting Oxide Films Using a Reactive Tin(II) Hydroxide Nitrate Nanoscale Cluster', *Chemistry of Materials*, vol. 25, no. 20, pp. 4080–4087, Oct. 2013, doi: 10.1021/cm402424c.

[210] R. M. Pasquarelli, D. S. Ginley, and R. O'Hayre, 'Solution processing of transparent conductors: from flask to film', *Chem Soc Rev*, vol. 40, no. 11, p. 5406, 2011, doi: 10.1039/c1cs15065k.

[211] S. Y. Park *et al.*, 'Low-temperature, solution-processed and alkali metal doped zno for high-performance thin-film transistors', *Advanced Materials*, vol. 24, no. 6, pp. 834–838, Feb. 2012, doi: 10.1002/adma.201103173.

[212] S. W. Han, J. H. Park, Y. B. Yoo, K. H. Lee, K. H. Kim, and H. K. Baik, 'Solution-processed laminated ZrO2/Al2O3 dielectric for low-voltage indium zinc oxide thin-film transistors', *J Solgel Sci Technol*, vol. 81, no. 2, pp. 570–575, Feb. 2017, doi: 10.1007/s10971-016-4205-y.

[213] W. Xia, G. Xia, G. Tu, X. Dong, S. Wang, and R. Liu, 'Sol-gel processed high-k aluminum oxide dielectric films for fully solution-processed low-voltage thin-film transistors', *Ceram Int*, vol. 44, no. 8, pp. 9125–9131, Jun. 2018, doi: 10.1016/j.ceramint.2018.02.120.

[214] C. Avis and J. Jang, 'High-performance solution processed oxide TFT with aluminum oxide gate dielectric fabricated by a sol-gel method', *J Mater Chem*, vol. 21, no. 29, pp. 10649–10652, Aug. 2011, doi: 10.1039/c1jm12227d.

[215] M. Olam, 'Mechanical and Thermal Properties of HDPE/PET Microplastics, Applications, and Impact on Environment and Life', 2023. doi: 10.5772/intechopen.110390.

[216] S. Jeong, Y. Ha, J. Moon, A. Facchetti, and T. J. Marks, 'Role of Gallium Doping in Dramatically Lowering Amorphous-Oxide Processing Temperatures for Solution-Derived Indium Zinc Oxide Thin-Film Transistors', *Advanced Materials*, vol. 22, no. 12, pp. 1346–1350, Mar. 2010, doi: 10.1002/adma.200902450.

[217] W. Xu, H. Li, J.-B. Xu, and L. Wang, 'Recent Advances of Solution-Processed Metal Oxide Thin-Film Transistors', *ACS Appl Mater Interfaces*, vol. 10, no. 31, pp. 25878–25901, Aug. 2018, doi: 10.1021/acsami.7b16010.

[218] Y. Tao and P. P. Pescarmona, 'Nanostructured Oxides Synthesised via scCO2-Assisted Sol-Gel Methods and Their Application in Catalysis', *Catalysts*, vol. 8, no. 5, p. 212, May 2018, doi: 10.3390/catal8050212.

[219] V. G. Kessler, G. I. Spijksma, G. A. Seisenbaeva, S. Håkansson, D. H. A. Blank, and H. J. M. Bouwmeester, 'New insight in the role of modifying ligands in the sol-gel processing of metal alkoxide precursors: A possibility to approach new classes of materials', *J Solgel Sci Technol*, vol. 40, no. 2–3, pp. 163–179, Dec. 2006, doi: 10.1007/s10971-006-9209-6.

[220] M.-G. Kim, M. G. Kanatzidis, A. Facchetti, and T. J. Marks, 'Low-temperature fabrication of high-performance metal oxide thin-film electronics via combustion processing', *Nat Mater*, vol. 10, no. 5, pp. 382–388, May 2011, doi: 10.1038/nmat3011.

[221] B. Wang *et al.*, 'Carbohydrate-Assisted Combustion Synthesis To Realize High-Performance Oxide Transistors', *J Am Chem Soc*, vol. 138, no. 22, pp. 7067–7074, Jun. 2016, doi: 10.1021/jacs.6b02309.

[222] X. Yu *et al.*, 'Spray-combustion synthesis: Efficient solution route to high-performance oxide transistors', *Proceedings of the National Academy of Sciences*, vol. 112, no. 11, pp. 3217–3222, Mar. 2015, doi: 10.1073/pnas.1501548112.

[223] F. Shan *et al.*, 'High-mobility p-type NiOx thin-film transistors processed at low temperatures with Al2O3 high-k dielectric', *J Mater Chem C Mater*, vol. 4, no. 40, pp. 9438–9444, 2016, doi: 10.1039/c6tc02137a.

[224] S. Ullah *et al.*, 'Boosting highly transparent and conducting indium zinc oxide thin films through solution combustion synthesis: Influence of rapid thermal annealing', *Semicond Sci Technol*, vol. 33, no. 10, Sep. 2018, doi: 10.1088/1361-6641/aad5cc.

[225] E. Carlos *et al.*, 'Boosting Electrical Performance of High-κ Nanomultilayer Dielectrics and Electronic Devices by Combining Solution Combustion Synthesis and UV Irradiation', *ACS*

Appl Mater Interfaces, vol. 9, no. 46, pp. 40428–40437, Nov. 2017, doi: 10.1021/acsami.7b11752.

[226] R. Branquinho *et al.*, 'Solution Combustion Synthesis: Applications in Oxide Electronics', in *Developments in Combustion Technology*, InTech, 2016. doi: 10.5772/64761.

[227] M. S. Kang and W. J. Cho, 'High-performance amorphous indium gallium zinc oxide thin-film transistors with sol-gel processed gate dielectric and channel layer fabricated using microwave irradiation', *Current Applied Physics*, vol. 18, no. 9, pp. 1080–1086, Sep. 2018, doi: 10.1016/j.cap.2018.06.003.

[228] A. Pimentel *et al.*, 'Effect of solvents on ZnO nanostructures synthesized by solvothermal method assisted by microwave radiation: a photocatalytic study', *J Mater Sci*, vol. 50, no. 17, pp. 5777–5787, Sep. 2015, doi: 10.1007/s10853-015-9125-7.

[229] K. Tetzner, Y. H. Lin, A. Regoutz, A. Seitkhan, D. J. Payne, and T. D. Anthopoulos, 'Sub-second photonic processing of solution-deposited single layer and heterojunction metal oxide thin-film transistors using a high-power xenon flash lamp', *J Mater Chem C Mater*, vol. 5, no. 45, pp. 11724–11732, 2017, doi: 10.1039/c7tc03721j.

[230] E. Yarali *et al.*, 'Low-Voltage Heterojunction Metal Oxide Transistors via Rapid Photonic Processing', *Adv Electron Mater*, vol. 6, no. 6, Jun. 2020, doi: 10.1002/aelm.202000028.

[231] C. J. Moon and H. S. Kim, 'Intense Pulsed Light Annealing Process of Indium-Gallium-Zinc-Oxide Semiconductors via Flash White Light Combined with Deep-UV and Near-Infrared Drying for High-Performance Thin-Film Transistors', *ACS Appl Mater Interfaces*, vol. 11, no. 14, pp. 13380–13388, Apr. 2019, doi: 10.1021/acsami.8b22458.

[232] W. Chung, M. O. Thompson, P. Wickboldt, D. Toet, and P. G. Carey, 'Room temperature indium tin oxide by XeCl excimer laser annealing for flexible display', *Thin Solid Films*, vol. 460, no. 1–2, pp. 291–294, Jul. 2004, doi: 10.1016/j.tsf.2004.01.050.

[233] Y. H. Yang, S. S. Yang, and K. Sen Chou, 'Characteristic enhancement of solution-processed In-Ga-Zn oxide thin-film transistors by laser annealing', *IEEE Electron Device Letters*, vol. 31, no. 9, pp. 969–971, Sep. 2010, doi: 10.1109/LED.2010.2055821.

[234] H. Pan *et al.*, 'Melt-mediated coalescence of solution-deposited ZnO nanoparticles by excimer laser annealing for thin-film transistor fabrication', *Appl Phys A Mater Sci Process*, vol. 94, no. 1, pp. 111–115, Jan. 2009, doi: 10.1007/s00339-008-4925-0.

[235] Q. Nian *et al.*, 'Large scale laser crystallization of solution-based alumina-doped zinc oxide (AZO) Nanoinks for highly transparent conductive electrode', *Sci Rep*, vol. 5, Oct. 2015, doi: 10.1038/srep15517.

[236] M. Noh *et al.*, 'Spectroscopic ellipsometry investigation on the excimer laser annealed indium thin oxide sol-gel films', *Current Applied Physics*, vol. 16, no. 2, pp. 145–149, Feb. 2016, doi: 10.1016/j.cap.2015.11.007.

[237] B. jia Li *et al.*, 'Performance optimization of fluorine-doped tin oxide thin films by introducing ultrasonic vibration during laser annealing', *Ceram Int*, vol. 43, no. 9, pp. 7329–7337, Jun. 2017, doi: 10.1016/j.ceramint.2017.03.036.

[238] C. Y. Tsay and T. T. Huang, 'Improvement of physical properties of IGZO thin films prepared by excimer laser annealing of sol-gel derived precursor films', *Mater Chem Phys*, vol. 140, no. 1, pp. 365–372, Jun. 2013, doi: 10.1016/j.matchemphys.2013.03.051.

[239] J. P. S. Bermundo, C. Kulchaisit, Y. Ishikawa, M. N. Fujii, H. Ikenoue, and Y. Uraoka, 'Rapid photo-assisted activation and enhancement of solution-processed InZnO thin-film transistors', *J Phys D Appl Phys*, vol. 53, no. 4, 2020, doi: 10.1088/1361-6463/ab5085.

[240] X. Huang, G. Yu, and C. Wu, 'IGZO TFT-based circuit with tunable threshold voltage by laser annealing', *Superlattices Microstruct*, vol. 111, pp. 1172–1176, Nov. 2017, doi: 10.1016/j.spmi.2017.08.027.

[241] V. S. Teodorescu *et al.*, 'Structure and dielectric properties of low fluence excimer laser annealing of sol-gel HfO<inf>2</inf> thin films deposited on Si wafer', in *CAS 2013 (International Semiconductor Conference)*, IEEE, Oct. 2013, pp. 77–80. doi: 10.1109/SMICND.2013.6688094.

[242] C.-H. Wu, K.-M. Chang, Y.-M. Chen, B.-W. Huang, Y.-X. Zhang, and S.-J. Wang, ' Using KrF ELA to Improve Gate-Stacked LaAlO 3 /ZrO 2 Indium Gallium Zinc Oxide Thin-Film Transistors with Novel Atmospheric Pressure Plasma-Enhanced Chemical Vapor Deposition Technique ', *J Nanosci Nanotechnol*, vol. 18, no. 3, pp. 1917–1921, Oct. 2017, doi: 10.1166/jnn.2018.14976.

[243] H. W. Zan, W. T. Chen, C. W. Chou, C. C. Tsai, C. N. Huang, and H. W. Hsueh, 'Low temperature annealing with solid-state laser or UV lamp irradiation on amorphous IGZO thin-film transistors', *Electrochemical and Solid-State Letters*, vol. 13, no. 5, 2010, doi: 10.1149/1.3313201.

[244] M. Nakata *et al.*, 'Fabrication method for self-aligned bottom-gate oxide thin-film transistors by utilizing backside excimer-laser irradiation through substrate', *Appl Phys Lett*, vol. 103, no. 14, Sep. 2013, doi: 10.1063/1.4824301.

[245] D. V. Bellas *et al.*, 'Simulating the opto-thermal processes involved in laser induced self-assembly of surface and sub-surface plasmonic nano-structuring', *Thin Solid Films*, vol. 630, pp. 7–24, May 2017, doi: 10.1016/j.tsf.2016.12.046.

[246] A. Siozios *et al.*, 'Sub-surface laser nanostructuring in stratified metal/dielectric media: A versatile platform towards flexible, durable and large-scale plasmonic writing', *Nanotechnology*, vol. 26, no. 15, 2015, doi: 10.1088/0957-4484/26/15/155301.

[247] N. Kalfagiannis *et al.*, 'Selective modification of nanoparticle arrays by laser-induced self assembly (MONA-LISA): Putting control into bottom-up plasmonic nanostructuring', *Nanoscale*, vol. 8, no. 15, pp. 8236–8244, Apr. 2016, doi: 10.1039/c5nr09192f.

[248] S. O. Kasap, *Principles of Electronic Materials and Devices*, 4th ed. McGraw Hill, 2017.

[249] S. Lee, Y. Chen, J. Jeon, C. Park, and J. Jang, 'Reduction of Parasitic Capacitance in Indium-Gallium-Zinc Oxide (a-IGZO) Thin-Film Transistors (TFTs) without Scarifying Drain Currents by Using Stripe-Patterned Source/Drain Electrodes', *Adv Electron Mater*, vol. 4, no. 4, Apr. 2018, doi: 10.1002/aelm.201700550.

[250] J. Bardeen and W. H. Brattain, 'The Transistor, A Semi-Conductor Triode', *Physical Review*, vol. 74, no. 2, pp. 230–231, Jul. 1948, doi: 10.1103/PhysRev.74.230.

[251] F. Braun, 'Ueber die Stromleitung durch Schwefelmetalle', *Ann Phys*, vol. 229, no. 12, pp. 556–563, Jan. 1875, doi: 10.1002/andp.18752291207.

[252] J. Semple, D. G. Georgiadou, G. Wyatt-Moon, G. Gelinck, and T. D. Anthopoulos, 'Flexible diodes for radio frequency (RF) electronics: A materials perspective', Oct. 30, 2017, *Institute of Physics Publishing*. doi: 10.1088/1361-6641/aa89ce.

[253] B. K. Kanaujia, N. Singh, and S. Kumar, *Rectenna: Wireless Energy Harvesting System*. Singapore: Springer Singapore, 2021. doi: 10.1007/978-981-16-2536-7.

[254] N. F. Mott, 'Note on the contact between a metal and an insulator or semi-conductor', *Mathematical Proceedings of the Cambridge Philosophical Society*, vol. 34, no. 4, pp. 568–572, Oct. 1938, doi: 10.1017/S0305004100020570.

[255] W. Schottky, 'Zur Halbleitertheorie der Sperrschicht- und Spitzengleichrichter', *Zeitschrift f*[illegible]*r Physik*, vol. 113, no. 5–6, pp. 367–414, May 1939, doi: 10.1007/BF01340116.

[256] S. M. Sze and K. K. Ng, *Physics of Semiconductor Devices*, 3rd ed. John Wiley and Sons, 2006.

[257] D. K. Schroder, *Semiconductor Material and Device Characterization*. Wiley, 2005. doi: 10.1002/0471749095.

[258] S. K. Cheung and N. W. Cheung, 'Extraction of Schottky diode parameters from forward current-voltage characteristics', *Appl Phys Lett*, vol. 49, no. 2, pp. 85–87, Jul. 1986, doi: 10.1063/1.97359.

[259] A. S. Bhuiyan, A. Martinez, and D. Esteve, 'A new Richardson plot for non-ideal schottky diodes', *Thin Solid Films*, vol. 161, pp. 93–100, Jul. 1988, doi: 10.1016/0040-6090(88)90239-8.

[260] D. K. de Vries, P. Stelmaszyk, and A. D. Wieck, 'Intrinsic and extrinsic capacitances of in-plane-gated transistors', *J Appl Phys*, vol. 79, no. 10, pp. 8087–8090, May 1996, doi: 10.1063/1.362364.

[261] P. Periasamy *et al.*, 'Metal–Insulator–Metal Diodes: Role of the Insulator Layer on the Rectification Performance', *Advanced Materials*, vol. 25, no. 9, pp. 1301–1308, Mar. 2013, doi: 10.1002/adma.201203075.

[262] S. J. Yang *et al.*, 'Ultrafast 27 GHz cutoff frequency in vertical WSe2 Schottky diodes with extremely low contact resistance', *Nat Commun*, vol. 11, no. 1, p. 1574, Mar. 2020, doi: 10.1038/s41467-020-15419-1.

[263] J. Zhang, Y. Li, B. Zhang, H. Wang, Q. Xin, and A. Song, 'Flexible indium–gallium–zinc–oxide Schottky diode operating beyond 2.45 GHz', *Nat Commun*, vol. 6, no. 1, p. 7561, Jul. 2015, doi: 10.1038/ncomms8561.

[264] K. Loganathan *et al.*, 'Rapid and up-scalable manufacturing of gigahertz nanogap diodes', *Nat Commun*, vol. 13, no. 1, Dec. 2022, doi: 10.1038/s41467-022-30876-6.

[265] D. G. Georgiadou *et al.*, '100 GHz zinc oxide Schottky diodes processed from solution on a wafer scale', *Nat Electron*, vol. 3, no. 11, pp. 718–725, Nov. 2020, doi: 10.1038/s41928-020-00484-7.

[266] A. U. N. S.N. *et al.*, 'Near Field Communication – Applications and Performance Studies', 2012, pp. 1–10. doi: 10.1007/978-3-642-31686-9_1.

[267] M. Patel and J. Wang, 'Applications, challenges, and prospective in emerging body area networking technologies', *IEEE Wirel Commun*, vol. 17, no. 1, pp. 80–88, Feb. 2010, doi: 10.1109/MWC.2010.5416354.

[268] A. J. D. Rathnayaka, V. M. Potdar, and S. J. Kuruppu, 'Evaluation of wireless home automation technologies', in *5th IEEE International Conference on Digital Ecosystems and Technologies (IEEE DEST 2011)*, IEEE, May 2011, pp. 76–81. doi: 10.1109/DEST.2011.5936601.

[269] K. V. S. Rao, P. V. Nikitin, and S. F. Lam, 'Antenna design for UHF RFID tags: a review and a practical application', *IEEE Trans Antennas Propag*, vol. 53, no. 12, pp. 3870–3876, Dec. 2005, doi: 10.1109/TAP.2005.859919.

[270] R. Garcia, A. W. Knoll, and E. Riedo, 'Advanced scanning probe lithography', *Nat Nanotechnol*, vol. 9, no. 8, pp. 577–587, Aug. 2014, doi: 10.1038/nnano.2014.157.

[271] D. Qin, Y. Xia, and G. M. Whitesides, 'Soft lithography for micro- and nanoscale patterning', *Nat Protoc*, vol. 5, no. 3, pp. 491–502, Mar. 2010, doi: 10.1038/nprot.2009.234.

[272] J. Moreland and J. W. Ekin, 'Electron tunneling experiments using Nb-Sn "'break'" junctions', *J Appl Phys*, vol. 58, no. 10, pp. 3888–3895, Nov. 1985, doi: 10.1063/1.335608.

[273] C. J. Muller, J. M. van Ruitenbeek, and L. J. de Jongh, 'Conductance and supercurrent discontinuities in atomic-scale metallic constrictions of variable width', *Phys Rev Lett*, vol. 69, no. 1, pp. 140–143, Jul. 1992, doi: 10.1103/PhysRevLett.69.140.

[274] J. Reichert, H. B. Weber, M. Mayor, and H. v. Löhneysen, 'Low-temperature conductance measurements on single molecules', *Appl Phys Lett*, vol. 82, no. 23, pp. 4137–4139, Jun. 2003, doi: 10.1063/1.1574844.

[275] A. F. Morpurgo, C. M. Marcus, and D. B. Robinson, 'Controlled fabrication of metallic electrodes with atomic separation', *Appl Phys Lett*, vol. 74, no. 14, pp. 2084–2086, Apr. 1999, doi: 10.1063/1.123765.

[276] Y. V. Kervennic, D. Vanmaekelbergh, L. P. Kouwenhoven, and H. S. J. Van der Zant, 'Planar nanocontacts with atomically controlled separation', *Appl Phys Lett*, vol. 83, no. 18, pp. 3782–3784, Nov. 2003, doi: 10.1063/1.1623317.

[277] C. Vieu *et al.*, 'Electron beam lithography: resolution limits and applications', *Appl Surf Sci*, vol. 164, no. 1–4, pp. 111–117, Sep. 2000, doi: 10.1016/S0169-4332(00)00352-4.

[278] T. Thio, H. F. Ghaemi, H. J. Lezec, P. A. Wolff, and T. W. Ebbesen, 'Surface-plasmon-enhanced transmission through hole arrays in Cr films', *Journal of the Optical Society of America B*, vol. 16, no. 10, p. 1743, Oct. 1999, doi: 10.1364/JOSAB.16.001743.

[279] A. Hatzor and P. S. Weiss, 'Molecular Rulers for Scaling Down Nanostructures', *Science (1979)*, vol. 291, no. 5506, pp. 1019–1020, Feb. 2001, doi: 10.1126/science.1057553.

[280] D. J. Beesley *et al.*, 'Sub-15-nm patterning of asymmetric metal electrodes and devices by adhesion lithography', *Nat Commun*, vol. 5, May 2014, doi: 10.1038/ncomms4933.

[281] J. Semple *et al.*, 'Large-area plastic nanogap electronics enabled by adhesion lithography', *npj Flexible Electronics*, vol. 2, no. 1, Dec. 2018, doi: 10.1038/s41528-018-0031-3.

[282] J. Semple *et al.*, 'Radio Frequency Coplanar ZnO Schottky Nanodiodes Processed from Solution on Plastic Substrates', *Small*, vol. 12, no. 15, pp. 1993–2000, Apr. 2016, doi: 10.1002/smll.201503110.

[283] J. Semple *et al.*, 'Large-area plastic nanogap electronics enabled by adhesion lithography', *npj Flexible Electronics*, vol. 2, no. 1, p. 18, Jun. 2018, doi: 10.1038/s41528-018-0031-3.

[284] J. Semple, G. Wyatt-Moon, D. G. Georgiadou, M. A. McLachlan, and T. D. Anthopoulos, 'Semiconductor-Free Nonvolatile Resistive Switching Memory Devices Based on Metal Nanogaps Fabricated on Flexible Substrates via Adhesion Lithography', *IEEE Trans Electron Devices*, vol. 64, no. 5, pp. 1973–1980, May 2017, doi: 10.1109/TED.2016.2638499.

[285] G. Wyatt-Moon, D. G. Georgiadou, J. Semple, and T. D. Anthopoulos, 'Deep Ultraviolet Copper(I) Thiocyanate (CuSCN) Photodetectors Based on Coplanar Nanogap Electrodes Fabricated via Adhesion Lithography', *ACS Appl Mater Interfaces*, vol. 9, no. 48, pp. 41965–41972, Dec. 2017, doi: 10.1021/acsami.7b12942.

[286] L. E. Scriven, 'Physics and Applications of DIP Coating and Spin Coating', *MRS Proceedings*, vol. 121, p. 717, Feb. 1988, doi: 10.1557/PROC-121-717.

[287] A. G. Emslie, F. T. Bonner, and L. G. Peck, 'Flow of a Viscous Liquid on a Rotating Disk', *J Appl Phys*, vol. 29, no. 5, pp. 858–862, May 1958, doi: 10.1063/1.1723300.

[288] D. Meyerhofer, 'Characteristics of resist films produced by spinning', *J Appl Phys*, vol. 49, no. 7, pp. 3993–3997, Jul. 1978, doi: 10.1063/1.325357.

[289] D. M. Mattox, *The Foundations of Vacuum Coating Technology*. Berlin, Heidelberg: Springer Berlin Heidelberg, 2003. doi: 10.1007/978-3-662-10329-6.

[290] N. Kalfagiannis, D. C. Koutsogeorgis, E. Lidorikis, and P. Patsalas, 'Laser Annealing as a Platform for Plasmonic Nanostructuring', in *Nanoplasmonics - Fundamentals and Applications*, InTech, 2017. doi: 10.5772/67670.

[291] J. A. Hillier *et al.*, 'Reactive laser annealing of indium tin oxide: implications to crystal structure, defect composition, and plasma energy', *Opt Mater Express*, vol. 12, no. 11, p. 4310, Nov. 2022, doi: 10.1364/OME.464918.

[292] P. A. Franken, A. E. Hill, C. W. Peters, and G. Weinreich, 'Generation of Optical Harmonics', *Phys Rev Lett*, vol. 7, no. 4, pp. 118–119, Aug. 1961, doi: 10.1103/PhysRevLett.7.118.

[293] ThorLabs, 'F-Theta Scan Lenses'. Accessed: Oct. 31, 2024. [Online]. Available: https://www.thorlabs.com/newgrouppage9.cfm?objectgroup_id=6430

[294] H. Salar Amoli and B. Fathi, 'Effect of pulse Nd-YAG laser beam interaction on annealing of nanopowder ITO using spin-on-glass', *J Solgel Sci Technol*, vol. 59, no. 1, pp. 32–35, Jul. 2011, doi: 10.1007/s10971-011-2457-0.

[295] R. A. Ganeev, *Laser - Surface Interactions*. Dordrecht: Springer Netherlands, 2014. doi: 10.1007/978-94-007-7341-7.

[296] M. von Allmen and A. Blatter, *Laser-Beam Interactions with Materials*, vol. 2. Berlin, Heidelberg: Springer Berlin Heidelberg, 1995. doi: 10.1007/978-3-642-57813-7.

[297] D. Bäuerle, 'Laser processing and chemistry: recent developments', *Appl Surf Sci*, vol. 186, no. 1–4, pp. 1–6, Jan. 2002, doi: 10.1016/S0169-4332(01)00655-9.

[298] G. Jo, J.-H. Ji, K. Masao, J.-G. Ha, S.-K. Lee, and J.-H. Koh, 'CO2 laser annealing effects for Al-doped ZnO multilayered films', *Ceram Int*, vol. 44, pp. S211–S215, Nov. 2018, doi: 10.1016/j.ceramint.2018.08.112.

[299] M. Lluscà *et al.*, 'Activation of visible up-conversion luminescence in transparent and conducting ZnO:Er:Yb films by laser annealing', *J Lumin*, vol. 167, pp. 101–105, Nov. 2015, doi: 10.1016/j.jlumin.2015.06.017.

[300] P. Yeh, *Optical Waves in Layered Media*, 1st ed. Wiley, 2005.

[301] E. Lampadariou, K. Kaklamanis, D. Goustouridis, I. Raptis, and E. Lidorikis, 'Nonlocal Effective Medium (NLEM) for Quantitative Modelling of Nanoroughness in Spectroscopic Reflectance', *Photonics*, vol. 9, no. 7, p. 499, Jul. 2022, doi: 10.3390/photonics9070499.

[302] A. L. Crosbie and R. Viskanta, 'Transient heating or cooling of a plate by combined convection and radiation', *Int J Heat Mass Transf*, vol. 11, no. 2, pp. 305–317, Feb. 1968, doi: 10.1016/0017-9310(68)90159-2.

[303] D. R. Lide, *CRC Handbook of Chemistry and Physics*, 85th ed. Boca Raton, FL: CRC Press, 2005.

[304] B. Pacewska and M. Keshr, 'Thermal transformations of aluminium nitrate hydrate', *Thermochim Acta*, vol. 385, no. 1, pp. 73–80, Mar. 2002, doi: 10.1016/S0040-6031(01)00703-1.

[305] S. Grimm, S. J. Baik, P. Hemberger, T. Kasper, A. M. Kempf, and B. Atakan, 'Insights into the decomposition of zirconium acetylacetonate using synchrotron radiation: Routes to the formation of volatile Zr-intermediates', *J Mater Res*, vol. 37, no. 9, pp. 1558–1575, May 2022, doi: 10.1557/s43578-022-00566-6.

[306] C. Kittel, *Introduction to Solid State Physics*, 8th ed. Berkeley: John Wiley and Sons, 2005.

[307] H. Hojjati and S. Rohani, 'Measurement and Prediction of Solubility of Paracetamol in Water-Isopropanol Solution. Part 2. Prediction', *Org Process Res Dev*, vol. 10, pp. 1110–1118, 2006.

[308] J. G. Cordaro, A. M. Kruizenga, R. Altmaier, M. Sampson, and A. Nissen, 'Thermodynamic Properties of Molten Nitrate Salts', 2011.

[309] Y. Xiong, Z. Wang, P. Xu, C. Hongbing, and Y. Wu, 'Experimental investigation into the thermos-physical properties by dispersing nanoparticles to the nitrates', *Energy Procedia*, vol. 158, 2019.

[310] C. Marchbanks and Z. Wu, 'Reduction of heat capacity and phonon group velocity in silicon nanowires', *J Appl Phys*, vol. 117, p. 084305, 2015.

[311] A. Ziabari, Z. Bian, and A. Shakouri, 'Adaptive Power Blurring Techniques to Calculate IC Temperature Profile under Large Temperature Variations'.

[312] M. P. Bellmann, E. A. Meese, M. Syvertsen, A. Solheim, H. Sørheim, and L. Arnberg, 'Silica versus silicon nitride crucible: Influence of thermophysical properties on the solidification of multi-crystalline silicon by Bridgman technique', *J Cryst Growth*, vol. 318, no. 1, pp. 265–268, Mar. 2011, doi: 10.1016/j.jcrysgro.2010.10.073.

[313] D. Dragulin and M. Ruther, 'Specific heat capacity of aluminium and aluminium alloys', *Heat Treatment*, 2018.

[314] A. I. Oliva and J. M. Lugo, 'The physical properties of nanomaterials: A challenge in materials science', in *2015 12th International Conference on Electrical Engineering, Computing Science and Automatic Control (CCE)*, IEEE, Oct. 2015, pp. 1–6. doi: 10.1109/ICEEE.2015.7357902.

[315] J. M. Lugo, A. I. Oliva, H. G. Riveros, and O. Ceh, 'Heat capacity determination of metallic thin films using temperature profiles at room conditions: Theory', in *2010 7th International Conference on Electrical Engineering Computing Science and Automatic Control*, IEEE, Sep. 2010, pp. 504–509. doi: 10.1109/ICEEE.2010.5608603.

[316] V. I. Mazhukin, O. N. Koroleva, A. V. Shapranov, M. M. Demin, and A. A. Aleksashkina, 'Determination of Thermal Properties of Gold in the Region of Melting–Crystallization Phase Transition: Molecular Dynamics Approach', *Mathematical Models and Computer Simulations*, vol. 14, no. 4, pp. 662–676, Aug. 2022, doi: 10.1134/S2070048222040068.

[317] M. Bauccio, *ASM Engineering Materials Reference Book*, 2nd ed. CRC Press, 1994.

[318] A. Cappella *et al.*, 'High Temperature Thermal Conductivity of Amorphous Al $_2$ <scp>O</scp> $_3$ Thin Films Grown by Low Temperature ALD', *Adv Eng Mater*, vol. 15, no. 11, pp. 1046–1050, Nov. 2013, doi: 10.1002/adem.201300132.

[319] I. Stark, M. Stordeur, and F. Syrowatka, 'Thermal conductivity of thin amorphous alumina films', *Thin Solid Films*, vol. 226, pp. 185–190, 1993.

[320] J. T. Gaskins *et al.*, 'Review—Investigation and Review of the Thermal, Mechanical, Electrical, Optical, and Structural Properties of Atomic Layer Deposited High- *k* Dielectrics: Beryllium Oxide, Aluminum Oxide, Hafnium Oxide, and Aluminum Nitride', *ECS Journal of Solid State Science and Technology*, vol. 6, no. 10, pp. N189–N208, 2017, doi: 10.1149/2.0091710jss.

[321] M. W. Chase, *NIST-JANAF Thermochemical Tables, monograph 9*, 4th ed., vol. 9. Washington DC: American Chemical Society, 1998.

[322] S. R. Gul, M. Khan, Y. Zeng, and B. Wu, 'Understanding the thermodynamic properties of 20% CeO $_2$ stabilized ZrO $_2$ coatings with atomistic modeling and simulations', *Mater Res Express*, vol. 6, no. 7, p. 076532, Apr. 2019, doi: 10.1088/2053-1591/ab1424.

[323] D. R. Clarke, 'Materials selection guidelines for low thermal conductivity thermal barrier coatings', *Surf Coat Technol*, vol. 163–164, pp. 67–74, Jan. 2003, doi: 10.1016/S0257-8972(02)00593-5.

[324] S. R. Gul, M. Khan, Y. Zeng, and B. Wu, 'Understanding the improved stability and reduced thermal conductivity of yttria stabilized zirconia: A combined experimental and atomistic modeling study', *Comput Mater Sci*, vol. 153, pp. 208–216, Oct. 2018, doi: 10.1016/j.commatsci.2018.06.045.

[325] M. R. Winter and D. R. Clarke, 'Oxide Materials with Low Thermal Conductivity', *Journal of the American Ceramic Society*, vol. 90, no. 2, pp. 533–540, Feb. 2007, doi: 10.1111/j.1551-2916.2006.01410.x.

[326] Q. Mistarihi, M. A. Umer, J. H. Kim, S. H. Hong, and H. J. Ryu, 'Fabrication of ZrO2-based nanocomposites for transuranic element-burning inert matrix fuel', *Nuclear Engineering and Technology*, vol. 47, no. 5, pp. 617–623, Aug. 2015, doi: 10.1016/j.net.2015.05.003.

[327] K. Koski, J. Hölsä, and P. Juliet, 'Properties of zirconium oxide thin films deposited by pulsed reactive magnetron sputtering', *Surf Coat Technol*, vol. 120–121, pp. 303–312, Nov. 1999, doi: 10.1016/S0257-8972(99)00501-0.

[328] A. Mehner, W. Datchary, N. Bleil, H.-W. Zoch, M. J. Klopfstein, and D. A. Lucca, 'The Influence of Processing on Crack Formation, Microstructure, Density and Hardness of Sol-Gel Derived Zirconia Films', *J Solgel Sci Technol*, vol. 36, no. 1, pp. 25–32, Oct. 2005, doi: 10.1007/s10971-005-4792-5.

[329] J. J. Low, N. H. Paulson, M. D'Mello, and M. Stan, 'Thermodynamics of monoclinic and tetragonal hafnium dioxide (HfO2) at ambient pressure', *Calphad*, vol. 72, p. 102210, Mar. 2021, doi: 10.1016/j.calphad.2020.102210.

[330] R. L. Orr, 'High Temperature Heat Contents of Hafnium Dioxide and Hafnium Tetrachloride', *J Am Chem Soc*, vol. 75, no. 5, pp. 1231–1232, Mar. 1953, doi: 10.1021/ja01101a065.

[331] H. Zhang, H. Wei, and H. Bao, 'Thermal Transport Mechanism of Amorphous HfO2: A Molecular Dynamics Based Study', *Journal of Thermal Science*, vol. 31, no. 4, pp. 1052–1060, Jul. 2022, doi: 10.1007/s11630-022-1626-5.

[332] E. A. Scott, J. T. Gaskins, S. W. King, and P. E. Hopkins, 'Thermal conductivity and thermal boundary resistance of atomic layer deposited high- *k* dielectric aluminum oxide, hafnium oxide, and titanium oxide thin films on silicon', *APL Mater*, vol. 6, no. 5, May 2018, doi: 10.1063/1.5021044.

[333] M. A. Panzer *et al.*, 'Thermal Properties of Ultrathin Hafnium Oxide Gate Dielectric Films', *IEEE Electron Device Letters*, vol. 30, no. 12, pp. 1269–1271, Dec. 2009, doi: 10.1109/LED.2009.2032937.

[334] D. S. Tsagareishvili and G. G. Gvelesiani, 'Enthalpy and heat capacity of indium sesquioxide at high temperatures', *High Temp*, vol. 13, p. 7349473, 1975.

[335] K. J. Bachmann, F. S. L. Hsu, and J. P. Remeika, 'The low temperature heat capacities of SnO2 and In2O3', *physica status solidi (a)*, vol. 67, no. 1, pp. K39–K42, 1981, doi: 10.1002/pssa.2210670144.

[336] J. Le Lan, Y. Liu, Y. H. Lin, C. W. Nan, Q. Cai, and X. Yang, 'Enhanced thermoelectric performance of In2O3-based ceramics via nanostructuring and point defect engineering', *Sci Rep*, vol. 5, 2015, doi: 10.1038/srep07783.

[337] V. I. Brinzari, A. I. Cocemasov, D. L. Nika, and G. S. Korotcenkov, 'Ultra-low thermal conductivity of nanogranular indium tin oxide films deposited by spray pyrolysis', *Appl Phys Lett*, vol. 110, no. 7, Feb. 2017, doi: 10.1063/1.4976629.

[338] J. Lan, Y. Lin, Y. Liu, S. Xu, and C. Nan, 'High Thermoelectric Performance of Nanostructured <scp> <scp>In</scp> </scp> $_2$ <scp> <scp>O</scp> </scp> $_3$ -Based Ceramics', *Journal of the American Ceramic Society*, vol. 95, no. 8, pp. 2465–2469, Aug. 2012, doi: 10.1111/j.1551-2916.2012.05284.x.

[339] H. Y. Kim *et al.*, 'Low-Temperature Growth of Indium Oxide Thin Film by Plasma-Enhanced Atomic Layer Deposition Using Liquid Dimethyl(*N* -ethoxy-2,2-dimethylpropanamido)indium for High-Mobility Thin Film Transistor Application', *ACS Appl Mater Interfaces*, vol. 8, no. 40, pp. 26924–26931, Oct. 2016, doi: 10.1021/acsami.6b07332.

[340] P. Mpofu, P. Rouf, N. J. O'Brien, U. Forsberg, and H. Pedersen, 'Thermal atomic layer deposition of In_2O_3 thin films using a homoleptic indium triazenide precursor and water', *Dalton Transactions*, vol. 51, no. 12, pp. 4712–4719, 2022, doi: 10.1039/D1DT03748J.

[341] 'Evaluating Oxide Reliability Using V-Ramp and J-Ramp Techniques'.

[342] JEDEC, 'PROCEDURE FOR WAFER-LEVEL-TESTING OF THIN DIELECTRICS: JESD35A - https://www.jedec.org/standards-documents/docs/jesd-35'.

[343] J. N. Hilfiker and J. A. Woollam, 'Spectroscopic Ellipsometry: Practical Application to Thin Film Characterization', 2016. [Online]. Available: https://www.researchgate.net/publication/298344032

[344] C. M. Herzinger, B. Johs, W. A. McGahan, J. A. Woollam, and W. Paulson, 'Ellipsometric determination of optical constants for silicon and thermally grown silicon dioxide via a multi-sample, multi-wavelength, multi-angle investigation', *J Appl Phys*, vol. 83, no. 6, pp. 3323–3336, Mar. 1998, doi: 10.1063/1.367101.

[345] B. Johs and J. S. Hale, 'Dielectric function representation by B-splines', *Physica Status Solidi (A) Applications and Materials Science*, vol. 205, no. 4, pp. 715–719, Apr. 2008, doi: 10.1002/pssa.200777754.

[346] T. E. Tiwald, D. W. Thompson, J. A. Woollam, W. Paulson, and R. Hance, 'Application of IR variable angle spectroscopic ellipsometry to the determination of free carrier concentration depth profiles', *Thin Solid Films*, vol. 313–314, pp. 661–666, Feb. 1998, doi: 10.1016/S0040-6090(97)00973-5.

[347] H. P. Gavin, 'The Levenberg-Marquardt algorithm for nonlinear least squares curve-fitting problems', 2024.

[348] H. Fujiwara, *Spectroscopic Ellipsometry*. Wiley, 2007. doi: 10.1002/9780470060193.

[349] B. D. Johs, W. A. McGahan, and J. A. Woollam, 'Optical analysis of complex multilayer structures using multiple data types', *Thin Solid Films*, vol. 253, no. 1–2, pp. 25–27, Dec. 1994, doi: 10.1016/0040-6090(94)90288-7.

[350] R. A. Synowicki, 'Suppression of backside reflections from transparent substrates', in *Physica Status Solidi (C) Current Topics in Solid State Physics*, 2008, pp. 1085–1088. doi: 10.1002/pssc.200777873.

[351] M. Born, E. Wolf, and E. Hecht, '*Principles of Optics: Electromagnetic Theory of Propagation, Interference and Diffraction of Light*', *Phys Today*, vol. 53, no. 10, pp. 77–78, Oct. 2000, doi: 10.1063/1.1325200.

[352] H. Wöhler, G. Haas, M. Fritsch, and D. A. Mlynski, 'Faster 4 × 4 matrix method for uniaxial inhomogeneous media', *Journal of the Optical Society of America A*, vol. 5, no. 9, p. 1554, Sep. 1988, doi: 10.1364/JOSAA.5.001554.

[353] O. S. Heavens, 'Optical properties of thin films', *Reports on Progress in Physics*, vol. 23, no. 1, p. 301, Jan. 1960, doi: 10.1088/0034-4885/23/1/301.

[354] J. A. Hillier, 'Photo-engineered Optoelectronic Properties of Transparent Conductive Oxides via Reactive Laser Annealing (ReLA): The Consequence of Defects', Nottingham Trent University, 2021.

[355] R. Jagtap and A. Ambre, 'Atomic force microscopy (AFM): Basics and its important applications for polymer characterization: An overview', *Indian Journal of Engineering and Material Sciences*, vol. 13, pp. 368–384, 2006.

[356] G. Friedbacher and H. Bubert, *Surface and Thin Film Analysis: A Compendium of Principles, Instrumentation, and Applications*, 2nd ed. Wiley, 2011. doi: 10.1002/9783527636921.

[357] B. Voigtländer, *Atomic Force Microscopy*, 2nd ed. Springer, 2019.

[358] A. San Paulo and R. García, 'High-Resolution Imaging of Antibodies by Tapping-Mode Atomic Force Microscopy: Attractive and Repulsive Tip-Sample Interaction Regimes', *Biophys J*, vol. 78, no. 3, pp. 1599–1605, Mar. 2000, doi: 10.1016/S0006-3495(00)76712-9.

[359] B. Bhushan, J. C. Wyant, and J. Meiling, 'A new three-dimensional non-contact digital optical profiler', *Wear*, vol. 122, no. 3, pp. 301–312, Mar. 1988, doi: 10.1016/0043-1648(88)90016-6.

[360] J. A. Woollam Co., 'Elllipsometry database (WVASE Software)', 2018, *J. A. Wooll*.

[361] J. W. Barkby *et al.*, 'Fabrication of nitrogen-hyperdoped silicon by high-pressure gas immersion excimer laser doping', *Sci Rep*, vol. 14, no. 1, p. 19640, Aug. 2024, doi: 10.1038/s41598-024-69552-8.

[362] S. M. Hu, D. R. Kerr, and L. V. Gregor, 'Evidence of hole injection and trapping in silicon nitride films prepared by reactive sputtering', *Appl Phys Lett*, vol. 10, pp. 97–99, 1967.

[363] L. Liu *et al.*, 'Theoretical study of oxygen-vacancy distribution in indium oxide', *Journal of Physical Chemistry C*, vol. 125, pp. 7077–7085, 2021.

[364] K. Jensen, *Introduction to the Physics of Electron Emission*. Wiley, 2017. doi: 10.1002/9781119051794.

[365] O. Obregon, S. Alcantara, S. Soto, and M. A. Dominguez, 'Effects of Electrical Stress in Solution-Processed Spin-On Glass Dielectric Films: Frequency Dependence', in *The 1st International Conference on Micromachines and Applications*, Basel Switzerland: MDPI, May 2021, p. 2. doi: 10.3390/Micromachines2021-09543.

[366] S. Kaya, R. Lok, A. Aktag, J. Seidel, and E. Yilmaz, 'Frequency dependent electrical characteristics of BiFeO3 MOS capacitors', *J Alloys Compd*, vol. 583, pp. 476–480, Jan. 2014, doi: 10.1016/j.jallcom.2013.08.204.

[367] J. H. Park *et al.*, 'Low-Temperature, High-Performance Solution-Processed Thin-Film Transistors with Peroxo-Zirconium Oxide Dielectric', *ACS Appl Mater Interfaces*, vol. 5, no. 2, pp. 410–417, Jan. 2013, doi: 10.1021/am3022625.

[368] M. A. Dominguez, O. Obregon, and J. A. Luna-Lopez, 'Study of stability of solution-processed dielectric film under electrical stress', *J Alloys Compd*, vol. 688, pp. 893–896, Dec. 2016, doi: 10.1016/j.jallcom.2016.07.126.

[369] T. Böscke, 'Crystalline Hafnia and Zirconia Based Dielectrics for Memory Applications', Hamburg University of Technology, 2010.

[370] W. Kleber, 'Einführung in die Kristallographie', *Geologiska Föreningen i Stockholm Förhandlingar*, vol. 80, no. 4, pp. 504–505, Nov. 1958, doi: 10.1080/11035895809447264.

[371] M. ANWAR and C. A. HOGARTH, 'Structural investigations and colour centres in MoO_3 films deposited by vacuum evaporation', *International Journal of Electronics*, vol. 67, no. 4, pp. 567–576, Oct. 1989, doi: 10.1080/00207218908921110.

[372] I. Georgieva, N. Danchova, S. Gutzov, and N. Trendafilova, 'DFT modeling, UV-Vis and IR spectroscopic study of acetylacetone-modified zirconia sol-gel materials', *J Mol Model*, vol. 18, no. 6, pp. 2409–2422, Jun. 2012, doi: 10.1007/s00894-011-1257-3.

[373] J. S. Toll, 'Causality and the Dispersion Relation: Logical Foundations', *Physical Review*, vol. 104, no. 6, pp. 1760–1770, Dec. 1956, doi: 10.1103/PhysRev.104.1760.

[374] V. Lucarini, J. J. Saarinen, K. Peiponen, and E. M. Vartiainen, *Kramers-Kronig Relations in Optical Materials Research*, vol. 110. Springer, 2005.

[375] Y. Xu, P. Liu, and Y. Zhang, 'Mid-infrared spectroscopy of hemispherical water droplets', *Spectrochim Acta A Mol Biomol Spectrosc*, vol. 264, p. 120256, Jan. 2022, doi: 10.1016/j.saa.2021.120256.

[376] C. Kemball, 'Physical and Chemical Aspects of Adsorbents and Catalysts', *Physics Bulletin*, vol. 21, no. 12, pp. 559–559, Dec. 1970, doi: 10.1088/0031-9112/21/12/035.

[377] S. Ramanathan, S. K. Roy, R. Bhat, D. D. Upadhyaya, and A. R. Biswas, 'Alumina powders from aluminium nitrate-urea and aluminium sulphate-urea reactions — The role of the precursor anion and process conditions on characteristics', *Ceram Int*, vol. 23, pp. 45–53, 1997.

[378] W. W. Rudolph, D. Fischer, M. R. Tomney, and C. C. Pye, 'Indium(<scp>iii</scp>) hydration in aqueous solutions of perchlorate, nitrate and sulfate. Raman and infrared

spectroscopic studies and ab-initio molecular orbital calculations of indium(<scp>iii</scp>)–water clusters', *Phys. Chem. Chem. Phys.*, vol. 6, no. 22, pp. 5145–5155, 2004, doi: 10.1039/B407419J.

[379] J. T. Kloprogge and R. L. Frost, 'Raman and infrared spectroscopic investigation of the neutralisation of aluminium in the presence of monomeric orthosilicic acid', *Spectrochim Acta A Mol Biomol Spectrosc*, vol. 55, no. 7, pp. 1359–1369, 1999.

[380] J. Kischkat *et al.*, 'Mid-infrared optical properties of thin films of aluminum oxide, titanium dioxide, silicon dioxide, aluminum nitride, and silicon nitride', *Appl Opt*, vol. 51, no. 28, p. 6789, Oct. 2012, doi: 10.1364/AO.51.006789.

[381] C. Barone *et al.*, 'Kondo-like transport and magnetic field effect of charge carrier fluctuations in granular aluminum oxide thin films', *Sci Rep*, vol. 8, no. 1, p. 13892, Sep. 2018, doi: 10.1038/s41598-018-32298-1.

[382] H. D. Ruan, R. L. Frost, J. T. Kloprogge, and L. Duong, 'Far-infrared spectroscopy of alumina phases', *Spectrochim Acta A Mol Biomol Spectrosc*, vol. 58, no. 2, pp. 265–272, Jan. 2002, doi: 10.1016/S1386-1425(01)00532-7.

[383] Z. Piasek and T. Urbanski, 'The infra-red absorption spectrum and structure of urea', *B Pol. Acad. Sci.-Tech.*, vol. 10, pp. 113–120, 1962.

[384] V. Timón, B. Maté, V. J. Herrero, and I. Tanarro, 'Infrared spectra of amorphous and crystalline urea ices', *Physical Chemistry Chemical Physics*, vol. 23, no. 39, pp. 22344–22351, 2021, doi: 10.1039/D1CP03503G.

[385] N. Zhu, F. Qian, X. Xu, M. Wang, and Q. Teng, 'Thermogravimetric Experiment of Urea at Constant Temperatures', *Materials*, vol. 14, no. 20, p. 6190, Oct. 2021, doi: 10.3390/ma14206190.

[386] N. Matsumoto, T. Hosokura, T. Nagashima, and M. Hangyo, 'Measurement of the dielectric constant of thin films by terahertz time-domain spectroscopic ellipsometry', *Opt Lett*, vol. 36, no. 2, p. 265, Jan. 2011, doi: 10.1364/OL.36.000265.

[387] J. M. Reyes, B. M. Perez Ramos, C. Z. Islas, W. C. Arriaga, P. R. Quintero, and A. T. Jacome, 'Chemical and Morphological Characteristics of ALD Al_2O_3 Thin-Film Surfaces after Immersion in pH Buffer Solutions', *J Electrochem Soc*, vol. 160, no. 10, pp. B201–B206, 2013, doi: 10.1149/2.060310jes.

[388] C. Liu, K. Shih, Y. Gao, F. Li, and L. Wei, 'Dechlorinating transformation of propachlor through nucleophilic substitution by dithionite on the surface of alumina', *J Soils Sediments*, vol. 12, no. 5, pp. 724–733, May 2012, doi: 10.1007/s11368-012-0506-0.

[389] C. Morterra and G. Magnacca, 'A case study: surface chemistry and surface structure of catalytic aluminas, as studied by vibrational spectroscopy of adsorbed species', *Catal Today*, vol. 27, no. 3–4, pp. 497–532, Feb. 1996, doi: 10.1016/0920-5861(95)00163-8.

[390] J. T. Kloprogge, H. D. Ruan, and R. L. Frost, 'Thermal decomposition of bauxite minerals: infrared emission spectroscopy of gibbsite, boehmite and diaspore', *J Mater Sci*, vol. 37, no. 6, pp. 1121–1129, 2002, doi: 10.1023/A:1014303119055.

[391] B. Pacewska, 'Some physicochemical properties of aluminium oxides obtained from basic aluminium sulphates', *Thermochim Acta*, vol. 200, pp. 387–400, Jul. 1992, doi: 10.1016/0040-6031(92)85132-F.

[392] I. Georgieva, N. Danchova, S. Gutzov, and N. Trendafilova, 'DFT modeling, UV-Vis and IR spectroscopic study of acetylacetone-modified zirconia sol-gel materials', *J Mol Model*, vol. 18, no. 6, pp. 2409–2422, Jun. 2012, doi: 10.1007/s00894-011-1257-3.

[393] H. M. Ismail, 'Characterization of the decomposition products of zirconium acetylacetonate: nitrogen adsorption and spectrothermal investigation', *Powder Technol*, vol. 85, no. 3, pp. 253–259, Dec. 1995, doi: 10.1016/0032-5910(95)03025-7.

[394] R. M. Mahfouz, G. A.-W. Ahmed, A. I. Al-Wassil, M. R. H. Siddiqui, and A. M. Al-Otaibi, 'Radiation-induced synthesis of ZrO_2 nanoparticles by thermal decomposition of zirconium acetylacetonate', *Radiation Effects and Defects in Solids*, vol. 168, no. 11–12, pp. 950–958, Dec. 2013, doi: 10.1080/10420150.2013.784909.

[395] J. Sun *et al.*, 'Moisture-indicating cellulose aerogels for multiple atmospheric water harvesting cycles driven by solar energy', *J Mater Chem A Mater*, vol. 9, no. 43, pp. 24650–24660, 2021, doi: 10.1039/D1TA07498A.

[396] G. O. Noonan and J. S. Ledford, 'Structure and Chemical Sensing Applications of Zirconium Acetate Sol-Gel Films', *Chemistry of Materials*, vol. 7, no. 6, pp. 1117–1123, Jun. 1995, doi: 10.1021/cm00054a011.

[397] A. Q. Wang and T. D. Golden, 'Electrodeposition of Oriented Cerium Oxide Films', *International Journal of Electrochemistry*, vol. 2013, pp. 1–10, 2013, doi: 10.1155/2013/482187.

[398] G. Guo, Y. Chen, and S. Xu, 'The Physico-Chemical Characterization of Mesoporous Sulfated Zirconia Nanoparticles Prepared under Structure-Directing-Free for <i>n</i>-Hexane Isomerization', *Journal of Minerals and Materials Characterization and Engineering*, vol. 08, no. 03, pp. 59–83, 2020, doi: 10.4236/jmmce.2020.83005.

[399] E. Bonera, G. Scarel, and M. Fanciulli, 'Structure evolution of atomic layer deposition grown ZrO2 films by deep-ultra-violet Raman and far-infrared spectroscopies', *J Non Cryst Solids*, vol. 322, no. 1–3, pp. 105–110, Jul. 2003, doi: 10.1016/S0022-3093(03)00188-1.

[400] L. Ouyang, Y. Gao, and H. Zheng, 'Research on the improvement of the adhesion strength of the Cu films deposited on the Al2O3 films', *Journal of Vacuum Science & Technology B*, vol. 42, no. 4, Jul. 2024, doi: 10.1116/6.0003649.

10. Appendices

A1: Optimisation of 532 nm Laser

In chapter 7, section 7.2, multiple sets of laser parameters were used on four Al/glass samples. The location of these parameters across the samples were systematically varied so they occupied different spaces across the samples – at the top, middle and bottom of the Al thin film – to account for variations in properties of the Al film. Figures A1.1-A1.4 show the colour mapped CAD design used for patterning the Al/glass samples, with corresponding Tables A1-A4 describing each laser parameter in relation to the colour mapping.

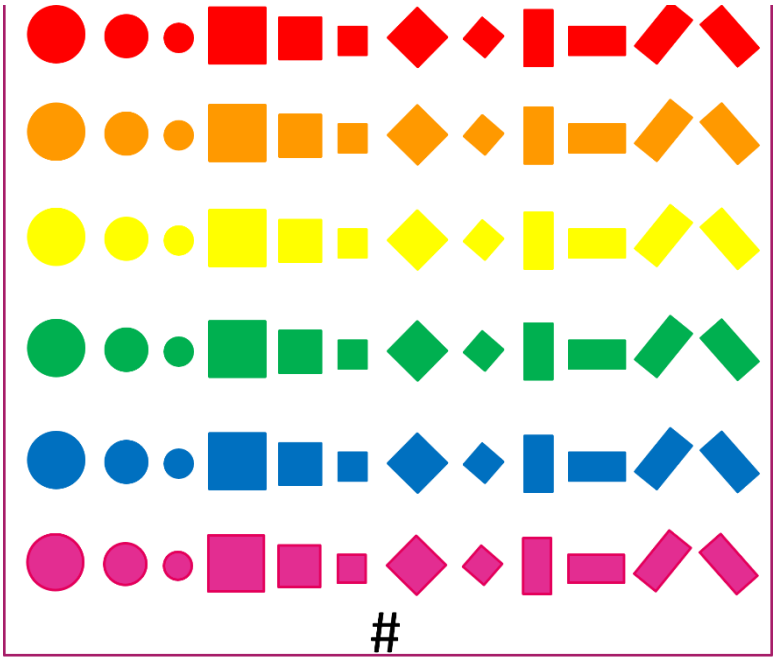

Figure A1.1. Schematic of the CAD design, using colours for each row that indicate the use of a different set of laser parameters each row.

Table A1.1. List of laser parameters for sample 1, with each processing condition linked to a colour in Figure A1.1.

Colour	Hatch spacing (mm)	Scan Speed (mm/s)	Rep Rate (kHz)	De-focus (mm)	Power (%)	Navigator Grid #
Red	0.010	520	52	3	100	A10
Orange	0.019	399	20	0	100	B1
Yellow	0.019	719	36	3	100	B9
Green	0.019	1359	68	3	100	B11
Blue	0.019	1679	84	3	100	B12
Pink	0.030	600	20	0	100	C1

Table A1.2. List of laser parameters for sample 2, with each processing condition linked to a colour in Figure A1.1.

Colour	Hatch spacing (mm)	Scan Speed (mm/s)	Rep Rate (kHz)	De-focus (mm)	Power (%)	Navigator Grid #
Red	0.010	719	36	0	100	B9
Orange	0.019	1359	68	0	100	B11
Yellow	0.019	1679	84	0	100	B12
Green	0.010	600	20	3	100	C1
Blue	0.010	120	4	3	100	C7
Pink	0.010	2040	68	3	100	C11

Table A1.3. List of laser parameters for sample 3, with each processing condition linked to a colour in Figure A1.1.

Colour	Hatch spacing (mm)	Scan Speed (mm/s)	Rep Rate (kHz)	De-focus (mm)	Power (%)	Navigator Grid #
Red	0.019	120	4	3	100	C7
Orange	0.019	2040	68	3	100	C11
Yellow	0.030	1359	68	3	100	B11
Green	0.030	600	20	3	100	C1
Blue	0.019	520	52	0	100	A10
Pink	0.010	399	20	3	100	B1

Table A1.4. List of laser parameters for sample 4, with each processing condition linked to a colour in Figure A1.1.

Colour	Hatch spacing (mm)	Scan Speed (mm/s)	Rep Rate (kHz)	De-focus (mm)	Power (%)	Navigator Grid #
Red	0.019	2040	68	3	100	C11
Orange	0.019	120	4	3	100	C7
Yellow	0.019	1679	84	3	100	B12
Green	0.030	719	36	3	100	B9
Blue	0.030	399	20	3	100	B1
Pink	0.030	520	52	3	100	A10